THE UNIVERSITY OF CHICAGO

BIOMACROMOLECULAR CONSTRUCTS FOR IMMUNOMODULATION

A DISSERTATION SUBMITTED TO

THE FACULTY OF THE DIVISION OF THE PHYSICAL SCIENCES

IN CANDIDACY FOR THE DEGREE OF

DOCTOR OF PHILOSOPHY

DEPARTMENT OF CHEMISTRY

BY

ADAM MICHAEL WEISS

CHICAGO, ILLINOIS

JUNE 2023

DEDICATION

To my family and friends for supporting me.

To the city of Youngstown for shaping me.

Table of Contents.

List of Figures.

List of Tables.

List of Schemes.

Acknowledgements.

When I entered graduate school, I expected that the next five years were just a stepping-stone to my future career. I expected to work hard, go about my business, and maybe make a friend or two along the way (emphasis on the *maybe*). I could have never imagined all the love, support, and community I gave and received from countless individuals over the past five years. I hope that the science might make an impact one day, but even if it doesn't, I feel so thankful for the people who made this experience one of the best times in my life.

I am immensely grateful to my friends. Brad, Ben, Nate, Sarah, and Adam A. – thank you for all the memories and great times at 5491. You made graduate school more fun than I ever imagined it could be. I also want to thank Norman, Kate, Nick M., Matt R., Adarsh, Greg, Joseph, Coach Laura, Coach Tim G., Tim L., Spencer, Maia, Lauren, Alex C., Ethan, Liv, Josh W., Miah, Patrick, and everyone else who was a part of this wild ride for being fun, crazy, weird, and supportive. Finally, I want to thank the members of the Pamphlet fantasy football league: Will, Nick, Rollin, Sam, Ed, Dan, Bill, Alec, and TK for being incredible lifelong friends and supporting me even as time and geography have separated us.

Next, I want to thank my labmates in the Esser-Kahn and Rowan labs for teaching me everything, dealing with my nonsense, and creating a supportive environment. In particular, I thank Nihesh, Britteny, Jorge, Jainu, Flora, Ethan, Brittany, James, Celine, and Ben R. for being patient and supportive mentors. I also thank Matt, Brad, Sophia, Uri, Jeremiah, Adarsh, Nick M., Hongyi, and Elise for growing and learning as scientists with me. I want to thank Jingjing, Qing, and Yoseline for doing so much work behind the scenes to make our experiments in the Esser-Kahn lab successful. I want to thank Jainu, Tyler, and Saikat, as well as the teams in the Maurer lab and at Vaxcyte Inc., for being excellent collaborators. Finally, I want to thank Marcos, Delaney, Udoka, and Maria for being smart, capable, and enthusiastic mentees – you are the future, and I am so excited to see what you will accomplish over the next few years. I hope I was able to teach you a thing or two along the way.

While my labmates made the day-to-day in lab bearable, I also owe a great deal of thanks to Aaron and Stuart, as well as the other faculty and staff at University of Chicago who have supported my research. Aaron: your patience and kindness as a mentor is one-of-a-kind. Stuart: your excitement about research is truly infectious. Thank you both for taking me under your wings, even when I am not sure I deserved your unwavering support in the early days of my PhD. I also thank my committee members, Peter Savage and Bozhi Tian. Pete: thank you for tolerating my interest in immunology as a misguided chemist—it has meant a great deal to me. Bozhi: thank you for being one of my biggest cheerleaders throughout the PhD. To Joe Piccirilli, Jeff Hubbell, Yamuna Krishnan, and Scott Snyder: thank you for serving as mentors at various stages of my PhD. I am also greatly indebted to the Committee of Immunology, who allowed me to face one of my greatest challenges in my PhD by enrolling in the Advanced Immunology course. I hope I represented the chemistry department well. Finally, I owe innumerable thanks to staff who run our campus. I cannot possibly name everyone, but I want to give special thanks to Laura L. and Vera for running various aspects of the Chemistry Department, Max and Thaddeus for keeping Kovler functional, and Tracy and Keturah for always making time for me in my advisors' busy schedules.

Lastly, I want to thank my family for supporting me since day one. Graduate school is not without its challenges, but it is easy compared to running a dry-cleaning business in Youngstown, Ohio. Mom and Dad: thank you for teaching me by example what it means to work hard and persevere in the face of adversity. Morgan and Ben: thank you for travelling life in all its ups and downs with me. To Bobby, Debbie, Zach, Jacob, Mollie, Dan, Emmy, Miles, Carol, Bruce, and Nola: thank you for always providing a warm meal and great company when I needed some family love. Finally, I want to thank my grandparents, Grammy, Grandma Ava, and Grandpa Alan, for being my biggest cheerleaders. Grammy: I cannot tell you how much our Sunday phone calls mean to me, and I am so thankful that you have taught me the value of family and community. Grandma Ava: Thank you for being such a great role model in pursuing your PhD and teaching me what it means to be a lifelong learner. Finally, Grandpa Alan: Thank you for being an incredible

sounding board and reminding me to enjoy the finer things in life. Your battle with COVID-19 was a terrible irony for me, and I only hope that future research will help prevent people like you from getting sick in the future. I love you all, and my thesis is dedicated to you.

Abstract.

(Bio)macromolecules ranging from proteins and carbohydrates to synthetic polymers and nanoparticles are critical components of many therapeutics, including vaccines. These materials can deliver molecular cargo, interact with receptors, and alter cellular processes on account of their physicochemical properties to modulate the immune response. Despite the promise of these materials, there are few studies probing how different physicochemical parameters (*e.g.*, size, shape, charge, or valency) can generate divergent immune responses. As such, there are a limited number of chemical approaches which use these materials toward the design of new, more effective vaccines. This thesis explores several approaches toward the design, characterization, and implementation of (bio)macromolecules that engage the immune system in controlled manners to facilitate desired immunological responses in the context of vaccination. Libraries of cationic polymers and cellulose nanocrystals with different physicochemical properties are generated to understand how these materials engage the immune system. By mapping the physicochemical parameters that result in toxic, immunogenic, and biocompatible responses, better materials for drug and gene delivery, vaccine adjuvants, and antimicrobial coatings can be rationally designed. Additionally, small molecule vaccine adjuvants are formulated both as liposomes and as bioconjugate materials to control their biodistribution and enhance the innate and adaptive immune response. A class of small molecules, the Cyclin Dependent Kinase inhibitors, which target the NLRP3 inflammasome are identified and formulated to induce robust Th1-biased immune responses. Moreover, antigen-adjuvant bioconjugates comprised of Toll-like receptor 9 agonists are synthesized and shown to allow for dose sparing in the adaptive immune response toward a model antigen. Altogether, these works serve to grow the repertoire of macromolecular tools available toward vaccine design.

CHAPTER 1 Introduction.

Portions of this chapter are adapted from a published Perspective in Macromolecules.[1]

1.1 The Innate and Adaptive Immune System.

The immune system's chief function is to protect the body from disease. It does so by identifying "non-self" or "damaged-self" from "self" (*i.e.*, distinguishing viral or cancerous proteins from endogenous proteins). Immune recognition is achieved by innate and adaptive components of the immune system. The innate immune system confers non-specific immunity in response to signals secreted by foreign and/or damaged cells and provides a first line of defense against threats to one's health. Activation of innate immunity results in recruitment of monocyte-lineage cells, removal of damaged or foreign cells by those cells, and induction of adaptive immunity, Once activated, the adaptive immune system confers specialized protection against threats that cannot be cleared by innate immunity alone via rapid proliferation of lymphocytes. These lymphocytes then produce antibodies and/or cytotoxins that can block further infection of the host and/or kill the foreign or damaged cells altogether. While greater detail about the immune system cannot be fully covered in this thesis, we provide a brief overview of some major components of innate and adaptive immunity relevant for the design of vaccine and immunotherapies in the next paragraphs (**Figure 1.1**). More information about specific aspects of immunity necessary in the design of next-generation therapeutics can be found in excellent texts and reviews.[2-6]

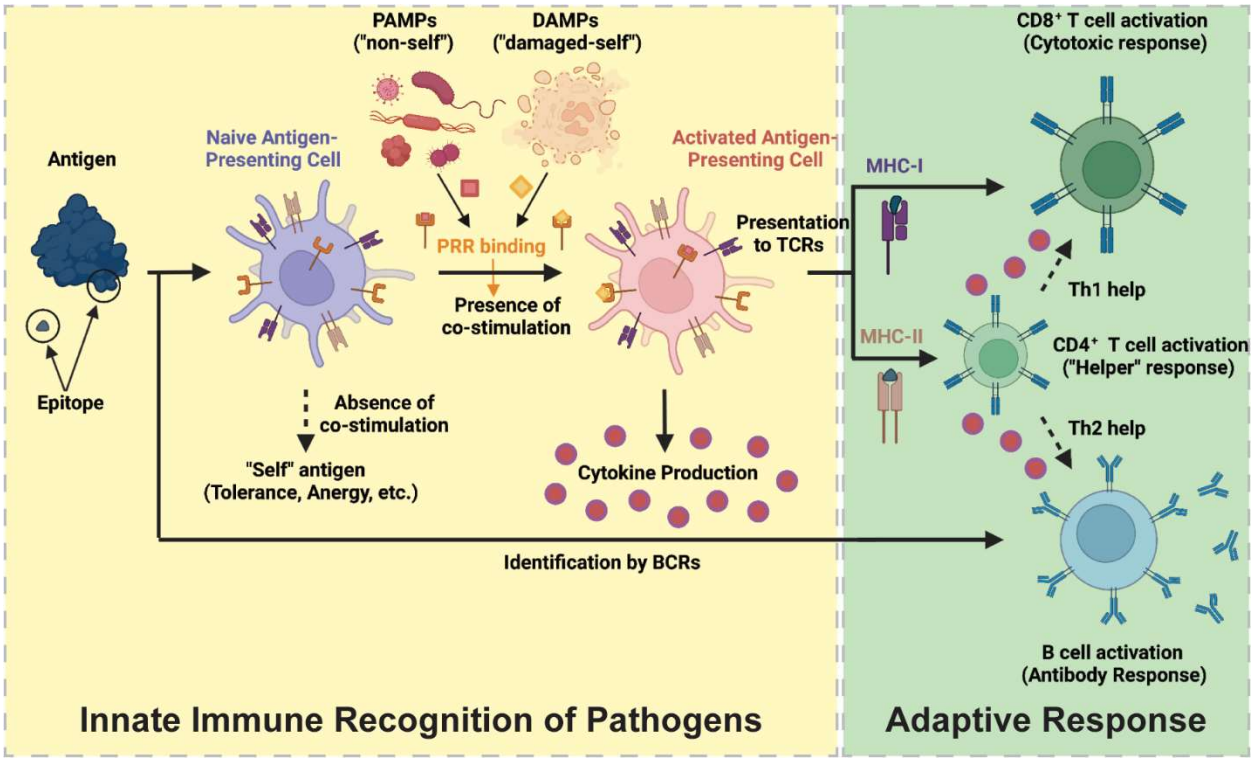

Figure 1.1: Schematic overview of relevant components of the innate and adaptive immune systems for vaccination and cancer immunotherapy. Under a disruption of homeostasis, antigen presenting cells (APCs) of the innate immune system identifies “non-self” and “damaged-self” molecular motifs (PAMPs and DAMPs) through their major histocompatibility complexes (MHC-I and MHC-II) and pattern recognition receptors (PRRs). APCs then become activated, secrete immunostimulatory cytokines, and present antigens on MHC-I or MHC-II to stimulate a response by the adaptive immune system. The adaptive response is coordinated by B cells, which bind antigens with their B cell receptor (BCR), as well as $CD4^+$ and $CD8^+$ T cells, which bind peptide:MHC complexes with their T cell receptor (TCR). Together, T and B cells facilitate the destruction of the pathogen. Reprinted from (1); copyright 2022 ACS.

In the context of host-pathogen response or vaccination, foreign antigens (any proteins or carbohydrates to which an immune response is mounted) must be identified by the immune system with the appropriate co-stimulatory molecules to generate an immune response. Antigen presenting cells (APCs), such as dendritic cells and macrophages, sample circulating proteins as they pass through secondary lymphoid organs. These notably include the lymph nodes, where APCs sample contents of the lymph draining from peripheral tissues, and in the spleen, where APCs sample contents of the blood. Under homeostatic conditions, APCs endocytose protein antigens and enzymatically process them into short peptides (epitopes), which can be loaded

onto major histocompatibility complex I or II (MHC-I and MHC-II). APCs then present these epitopes on MHC-I or MHC-II to naïve T cells in the spleen and lymph nodes. In the absence of co-stimulatory molecules (*i.e.*, in the case of an endogenous or "self" antigen), such antigen presentation fails to induce a productive immune response and results in anergy, exhaustion, or immune regulation (*i.e.*, T cell differentiation toward a regulatory phenotype). During a disruption to homeostasis, such as the presence of an infection or cancer (*e.g.*, presence of "non-self" or "damaged self"), APCs are further stimulated by pathogen associated molecular patterns (PAMPs) and/or damage associated molecular patterns (DAMPs) binding to PRRs. Activation of these PRRs can induce production of co-stimulatory factors, such as cytokines (which are immune signaling proteins) and cell surface markers (which facilitate antigen presentation), which are needed to license naïve T cells to become activated, proliferate, and facilitate a memory-inducing adaptive response. APCs also reside in lesser numbers in peripheral tissues, such as the skin, and sample the local environment for antigens. Under stimulation by PAMPs or DAMPs, they migrate to the secondary lymphoid organs where they similarly initiate an adaptive response.

The adaptive component of the immune response is mediated by T cell receptors (TCRs) and B cell-bound immunoglobulins (the B cell receptor, or BCR). TCRs, in coordination with CD4 and CD8, bind antigenic epitopes presented by APCs on MHC-II or MHC-I, respectively, to bridge innate and adaptive immunity. T cell responses can be separated into a $CD8^+$ cytotoxic T lymphocyte (CTL) response, critical for killing and clearing pathogen-infected or tumor cells, or a $CD4^+$ "helper" T cell (Th) response, important for secreting soluble immune mediators, such as cytokines, which enhance $CD8^+$ T cell and B cell responses.[7] Helper T cells can be further separated into Th1 and Th2 subtypes, where Th1 responses support CTL-mediated killing and Th2 responses support B cell maturation and differentiation. BCRs, meanwhile, bind antigenic macromolecules such as proteins and carbohydrates (or, in some cases, synthetic materials) on account of their secondary structure. Naïve B cells that bind an antigen and subsequently receive stimulation by Th2-biasing cytokines differentiate into plasma cells that can both secrete

antibodies and allow for phagocytosis to mediate destruction of pathogens. Alternatively, arrayed binding of a repeating chemical motif, as found in carbohydrates, can induce B cell maturation and antibody production independent of T cell signaling.[8] Stimulation of B cells with appropriate cytokines can induce isotype class switching from conventional IgM and IgD antibodies to those with increased affinity and specialized functions, such as IgG2 (which specialize in responding to bacterial capsular polysaccharides) and IgA (which specialize in responding to mucosal infections).[9] Concurrent B and T cell responses are often necessary to neutralize pathogens.

1.2 Pattern Recognition Receptor Agonists as Adjuvants.

Given the importance of innate immune co-stimulation in mounting a productive adaptive immune response, providing PAMPs and/or DAMPs that can bind pattern recognition receptors (PRRs) concurrently with delivery of antigen is critical for vaccines and immunotherapies.[5, 10] Such molecular agonists and other helper molecules, which modulate adaptive responses, are called adjuvants. Adjuvant comes from the Latin *adjuvare* meaning “to help.” While the word adjuvant is used loosely by immunologists to describe a host of formulants in current vaccines, adjuvants will be classified in this thesis as (1) immunologically active PRR agonists or (2) particulate and depot adjuvants. This section focuses on the former class, while the latter are discussed in **Section 1.3**.

While prophylactic vaccines were historically generated from attenuated or inactivated pathogens, which intrinsically contain PAMPs, newer systems such as subunit and RNA/DNA-based vaccines or neoantigen cancer vaccines may lack natural immunostimulatory components. As such, these systems can require supplementation with immunologically active agents, namely PRR agonists, to induce productive immune responses. There are >20 known PRRs that bind a diverse range of molecular patterns, and the design of synthetic PRR agonists that induce specific cytokine profiles and transcriptional programs for use in therapeutics is an active area of research (**Table 1.1**). Among the most well-studied PRR agonists include the Toll-like receptors (TLRs), which bind a breadth of molecular patterns specific to microbes, and the C-type lectin receptors,

which bind carbohydrates present in microbes or damaged cells.[11, 12] PRR agonists can be expressed on the cell surface (e.g., TLR1/2, TLR2/6, TLR4, and Dectin-1), in the endosome (e.g., TLR3, TLR7/8, TLR9, DNGR-1), or in the cytosol (e.g., STING, NLRP3, RIG-1, NOD1/2) – a factor which must be considered in the co-delivery of antigens and adjuvants for vaccination. Adjuvants can aid in the delivery and biodistribution of antigens, the intracellular localization of antigens, and the production of cytokines to facilitate an adaptive immune response (**Figure 1.2**).

PRR	Ligand Class	Phase III (with trial number) or Approval Status?
TLR1/2	Lipopeptides	No
TLR2/6	Lipopeptides	No
TLR3	dsRNA	No
TLR4	Lipopolysaccharide	FDA Approved for vaccination (AS01: Shingrix, Mosquirix; AS04: Cervarix; mRNA LNP: Comirnaty, Spikevax)[13-17], In Phase III for vaccination (AS01: NCT04319380, NCT05059301)
TLR5	Bacterial flagellin	No
TLR7/8	ssRNA	In Phase III for vaccination (Imiquimod: NCT04083157, NCT04143451)[18]
TLR9	CpG ssDNA	FDA Approved for vaccination (CpG-1018: Heplisav B)[19], In Phase III (CpG-1018: NCT04864561 NCT04672395)
NOD (1&2)	Peptidoglycan	No
NLRP3	Ion flux, membrane disruption, reactive oxygen species	FDA Approved for vaccination (AS01: Shingrix, Mosquirix; AS04: Cervarix; mRNA LNP: Comirnaty, Spikevax)[13-16], In Phase III for vaccination (AS01: NCT04319380, NCT05059301; Matrix-M: NCT04704830, NCT04611802, NCT04120194)
STING	Cytosolic cyclic DNA	No
RIG-I	Short viral dsRNA	No
DNGR-1	F-actin-myosin	No
Dectin-1	β-Glucan	In Phase III as a cancer immunotherapy supplement (β-Glucan dietary supplement: NCT04710290)
Dectin-2	α-Mannan	No
C-type lectins	Mannose, Fucose, GlcNAc	No
DC-SIGN	High Mannose glycans	No

Table 1.1: Selected PRR agonists and regulatory approval status. Note that TLR1/2 and TLR2/6 form heterodimers and were therefore included as one construct. Clinical trial status was identified by searching each PRR and known agonists for active or recruiting Phase III clinical trial status on https://clinicaltrials.gov as of 8/2022. Abbreviations: TLR = Toll-like receptor, NOD = Nucleotide-binding oligomerization domain-containing protein, NLRP3 = NACHT, LRR and PYD domains-containing protein 3, STING = Stimulator of interferon genes, RIG = retinoic acid-inducible gene, DNGR = dendritic cell natural killer lectin group receptor, DC-SIGN = dendritic cell-specific ICAM-grabbing non-integrin, LNP = lipid nanoparticle.

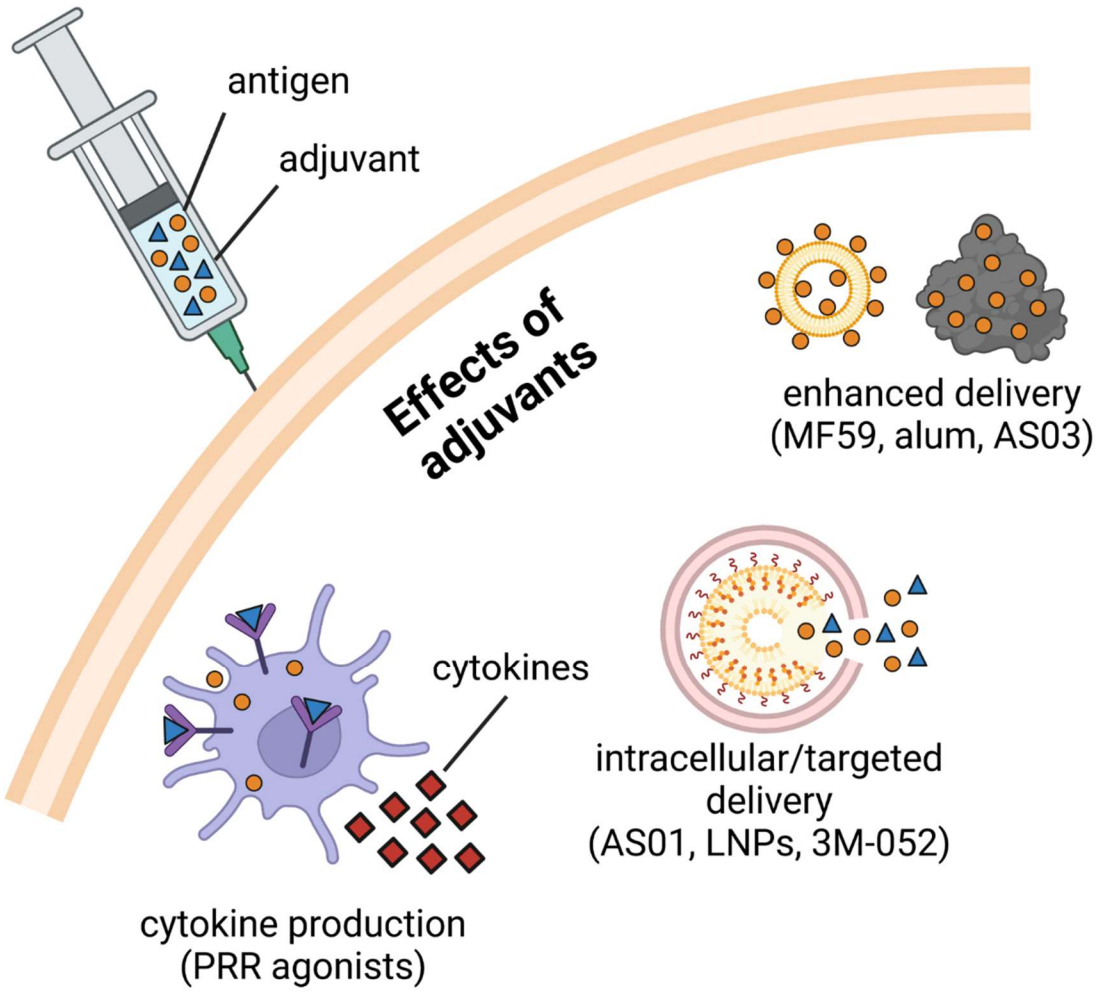

Figure 1.2: Schematic describing some effect of adjuvants on the innate immune response to vaccination. Adjuvanted vaccines can enhance delivery of antigens, target the delivery of antigens to (intra)cellular loci, and facilitate cytokine production to coordinate an adaptive response. Figure prepared with Biorender.com.

PRR agonists bind their receptors, which are expressed on specific cell populations to drive signaling of key innate immune signaling pathways. These include nuclear factor κ-light-chain enhancer of activated B cells (NF-κB), myeloid differentiation primary response 88 (MyD88), interferon regulatory transcription factor (IRF), Janus kinase – signal transducer and activator of transcription proteins (JAK-STAT), and others. Collectively, these signaling pathways regulate more than 2,000 genes associated with the immune response.[20] While the complexities of immunological signaling are beyond the scope of this thesis, one must appreciate how distinct

cell types, combinations of agonists, and spatiotemporal dynamics of immune signaling can play a profound and interconnected role in modulating efficacy of different vaccine formulations.[20-22]

Two key outcomes of PRR signaling are the secretion of cytokines and the upregulation of cell surface activation markers. Cytokines play a role in molding the adaptive immune response by binding to their cognate receptors expressed on specific cellular subsets (**Table 1.2**). For instance, secretion of IFN-γ and IL-12 can drive Th1 polarized responses, while secretion of IL-4 and IL-6 can drive Th2 polarized responses.[11, 23] Moreover, cytokine secretion can regulate differentiation of mature B cells, suppression of regulatory T cells, and induction of long-term immune memory.[11, 24] Upregulation of co-stimulatory receptors on APCs and lymphocytes also plays a role in successful immune responses.[11, 25] For successful binding of MHC:peptide complexes to the TCR, APCs must express B7.1 or B7.2 (also known as CD80 and CD86), while T cells must express CD28. This CD28:B7.1/2 binding interaction can be aided by additional co-stimulatory APC and T cell receptor:ligand interactions, including those of CD40:CD40L, ICOS:ICOSL, CD70:CD27, 4-1BB:4-1BBL, and OX40:OX40L.[25] Alternatively, co-inhibitory receptor:ligand interactions, including those of CTLA4:B7.1/2 and PD-1:PD-L1/2 can inhibit binding of MHC:peptide complexes to the TCR, resulting in T cell anergy.[25-27] B cells also express CD40, and CD40:CD40L binding between B cells and helper $CD4^+$ T cells is critical for B cell maturation.[28] Measuring up-regulation of co-stimulatory ligands and secreted cytokines serve as tools to quantify the efficacy and Th-biasing of immune responses garnered by PRR agonists.

Cytokine	Receptor	Effects
TNF-α	TNF receptor superfamily (TNFRSF)	Inflammation, inflammatory cell death[29]
IFN-α/β	IFNAR	Induction of JAK-STAT, MAPK, and PI3K, adaptive immunity[20]
IFN-γ	IFNGR	Induction of JAK-STAT, Th1 bias, adaptive immunity[20, 30]
IL-1α	IL-1R1/IL-1R2	MyD88 signaling, COX-2 activation, fever, NO production[31]
IL-1β	IL-1R1/IL-1R2	MyD88 signaling, COX-2 activation, fever, NO production[31]
IL-1ra	IL-1R1/IL-1R2	Inhibitor of IL-1 signaling[31]
IL-2	IL-2R	T cell proliferation[32]
IL-4	IL-4Rα	Th2 bias, IgE antibodies, IL-4 production[30]
IL-6	IL-6R	Inflammation, B cell help, fever, blocks TNF-α and IL-1 production[33]
IL-10	IL-10R	Treg differentiation, blocks Th1 bias, immunosuppression[34]
IL-12	IL-12Rβ1/2	Th1 bias, IFN-γ and TNF-α production[30]
IL-17A	IL-17R	Th17 bias, inflammation, macrophage recruitment[35]
IL-18	IL-1R1/IL-1R2/IL-18R	MyD88 signaling, COX-2 activation, fever, NO production[31]

Table 1.2: Selected cytokines involved in bridging the innate and adaptive immune responses. Abbreviations: IL = interleukin, TNF = tumor necrosis factor, IFN = interferon, IL-1ra = IL-1 receptor antagonist, COX = cyclooxygenase, NO = nitric oxide, IgE = immunoglobulin E.

Despite promising work in the design of synthetic adjuvants, many candidate molecules have been limited by systemic toxicity and inconsistent or poorly understood immune responses.[10] Local secretion of cytokines is critical for successful induction of adaptive immunity; however, systemic PRR activation can also result in immunotoxic cytokine production and lead to fever, injection site pain, or other side effects. In severe cases, excessive PRR stimulation can result in a life-threatening pathology known as “cytokine storm” (sometimes called Cytokine Release Syndrome, or CRS).[36, 37] As a notable example, small molecule TLR7/8 agonists, such as Imiquimod and Resiquimod, have found success pre-clinically but failed at the clinical level due to toxic systemic side effects.[18] Reducing systemic side effects is critical for enhancing patient compliance in receiving common vaccines, especially those such as influenza that require booster immunizations on a regular interval. Reducing cytokines while maintaining efficacy can be

challenging, as cytokines induced during the innate immune response can be critical for stimulating adaptive immunity. On the other hand, pathogens with poorly immunogenic antigens require robust stimulation of innate immunity to generate long term immune memory.[37] There are currently no FDA-approved vaccines for human immunodeficiency virus,[38] Q fever (caused by *C. burnetii*),[39] or tick-borne diseases (caused by *B. burgdorferi* and others),[40, 41] as well as many neglected tropical diseases.[42] Moreover, approved vaccines against malaria[17, 43] and tuberculosis[44] suffer from poor protective efficacy (<75%), and those against rabies[45] and anthrax[46] only offer short-term and/or incomplete protection. To overcome these challenges, adjuvants that stimulate more robust innate immune responses and result in long-term immune memory without overwhelming toxicity are needed. Overall, the design of improved adjuvants is desirable to advance human health and an active area of research in the Esser-Kahn group.

1.3 Particulate Adjuvants and Vaccine Delivery Systems.

In addition to PRR agonist-based adjuvants, emulsions and nanoparticles which form "antigen depots" or otherwise aid in the delivery of antigenic cargo have found considerable success as adjuvants. The first adjuvant, alum (one or more aluminum salt(s) including aluminum hydroxyphosphate sulfate, aluminum hydroxide, aluminum phosphate, potassium aluminum sulfate), has been used for almost 100 years and is currently employed in >10 FDA approved vaccines.[47, 48] Squalene emulsion-based systems such as MF59 and AS03 have also been FDA approved for commercial influenza vaccines.[49-51] Most recently, lipid nanoparticles (LNPs) comprised of mRNA or DNA complexed with ionizable lipid polymers and stabilizing agents were found to generate remarkable adjuvanticity, resulting in their FDA approval for COVID-19 vaccination.[15, 16] While the mechanism of depot-based vaccines is poorly understood, they appear to invoke B cell mediated immunity by stabilizing antigen at the injection site, altering cell adhesion, and inducing inflammation to recruit and activate peripheral tissue-resident APCs.[48, 50-56] Depot-based adjuvant systems have been suggested to activate the NLRP3 inflammasome

and other danger sensors, but these data are debated among immunologists.[15, 53, 57-60] While depot-based adjuvants are attractive for their low cost, safety, and high efficacy, they lack chemical tunability, have a poorly defined mode of action, and are ineffective in some diseases. As such, the design of precisely defined adjuvant systems is of significant research interest.

Polymers and nanoparticles have recently gained attention as tools to facilitate controlled delivery of antigen while facilitating adjuvanticity through the formation of antigen depots or PRR binding.[1, 61-63] These materials can mimic the size, shape, and biodistribution of pathogens, target and deliver cargo selectively via the incorporation of molecular patterns, and slow the systemic release of immunostimulatory components into the bloodstream.[22] Particle size can control routing of molecular cargo to the immune system. Larger particles (>500 nm) form antigen depots at the injection site for processing by tissue-resident APCs, while smaller particles (<100 nm) quickly and directly drain to the lymph node and afford efficient presentation by lymph node-resident APCs.[64, 65] Unformulated soluble cargoes (<10 nm), meanwhile, rapidly enter the bloodstream where they can induce off-target systemic side effects before being removed by the liver and/or kidneys.[66] Particle size can also modulate activation of damage sensors, as Muñoz-Wolf, *et al.* recently found that 50 nm polymeric nanoparticles, but not 100 nm – 100 μm particles, induce generation of intracellular reactive oxygen species and activate the Caspase-11 inflammasome.[67] While the favorable pharmacokinetics of particulate systems are beneficial relative to those of soluble systems for the controlled delivery of adjuvants, both injection site- and lymph node-targeting strategies have found use in FDA-approved vaccines. Despite the advantages of particulate systems, controlling the size and physicochemical properties of such systems remains challenging and is limited by poor encapsulation efficiency of chemically incompatible cargo.

Even amongst similarly sized nanoparticles, shape, charge, and texture can modulate immune responses. The Mitragotri group and others have shown that particle shape plays a distinct role in phagocytosis and processing of antigen, with smaller, spherical particles (mimicking that of natural pathogens) exhibiting maximum phagocytosis by APCs. In contrast,

high aspect ratio materials induce poor cellular uptake and damage consistent with inflammasome activation and/or necrotic cell death.[68-71] Charge can similarly modulate immunological activity of polymer-containing systems. Cationic polymers such as poly(ethyleneimine) (PEI), poly(2-aminoethyl methacrylate) (AEMA), poly(N,N'-dimethylaminoethyl methacrylate) (DMAEMA), and polyarginine have been employed to complex negatively charged PRR agonists such as CpG (a TLR9 agonist) or poly(I:C) (a TLR3 agonist) and enhance uptake and cytosolic delivery.[72-75] Such cationic polymers can effectively facilitate cytosolic delivery to enhance cross-presentation of antigen on MHC-I or to deliver mRNA and DNA.[76-78] Lastly, the Kurt-Jones group has shown that particle texture can alter immune responses, with rough polystyrene nanoparticles inducing greater immunostimulatory activity and neutrophil infiltration than smooth particles.[79]

In addition to controlling the physicochemical properties of immunogenic formulations, polymers and nanoparticles can also be used to release cargo to specific cell subsets with a reduction in systemic immunotoxic side effects.[62, 80] To achieve this requirement, polymer-drug systems can be imparted with stimulus responsive characteristics using reversible chemistries or reactive linkers. These chemistries allow release of molecular cargo under specific cellular or subcellular conditions, such as the reductive tumor microenvironment or acidic endolysosome. Alternatively, targeting ligands (often peptides that bind receptors found on specific cells or organelles) can allow delivery to specific locations in the body. Some chemistries which have been employed in pre-clinical vaccines include pH-responsive materials for endo/lysosomal disruption,[81-83] reactive oxygen species (ROS)-responsive materials for tumoral delivery,[73, 84] biodegradable polymers and peptides for slow release of cargo,[22, 85-87] and thermally responsive materials for delivery to metabolically active tissues.[88-90] Furthermore, targeting peptides can be incorporated into the formulation for the delivery of molecular cargo to specific cell subsets and/or organelles.[91-93] Stimuli responsive polymers used for drug delivery are reviewed in greater depth elsewhere.[1, 94] As design principles are better understood and greater synthetic control can be achieved, polymers and nanoparticles will emerge as key components of future therapeutics.

1.4 Vaccines and Immunotherapies.

Vaccines are perhaps the greatest advance to public health in the modern era. They have reduced morbidity and mortality of once-devastating diseases like polio and smallpox, and they have allowed a remarkably fast recovery from the COVID-19 pandemic. At the fundamental level, vaccines are a weakened or altered form of an infectious pathogen that, when administered to a patient, generates protective immunity against that pathogen without causing infection.[5, 10, 22, 37] Vaccines can be prophylactic, meaning that they generate protective immunity prior to pathogen exposure, or therapeutic, meaning that they facilitate an immune response after infection is underway. The first vaccines were comprised of attenuated (*i.e.,* weakened by serial passaging of the virus through an intermediary species) or inactivated (*i.e.*, killed by heat or chemical treatment) pathogens, which intrinsically contained the necessary antigens and adjuvants to induce a productive immune response. An example of one such early vaccine is Edward Jenner's smallpox vaccine. This vaccine contained a cowpox virus that was non-infectious to humans but generated protective immunity against the biologically similar and deadly smallpox virus. Despite their effectiveness, attenuated and inactivated vaccines can contain harmful pathogenic material, can undergo spontaneous mutations to revert to their infectious form, and risk infecting the patient if incompletely inactivated.[95-97] These vaccines are often not recommended for use in elderly and immunocompromised individuals and cannot be rapidly changed to treat emergent diseases. As a result, there is interest in designing safer and alternatives to whole-pathogen derived vaccines.

In the past twenty years, a variety of alternatives to attenuated and inactivated pathogens have emerged and found success in the clinic, including subunit vaccines,[10, 95, 98] nucleotide vaccines,[99, 100] and viral vector vaccines (**Table 1.3**).[97, 101] Subunit vaccines are comprised of a protein or peptide "subunit" of the pathogen of interest. These vaccines are advantageous because they do not risk reverting to an infectious form, and they have a high degree of synthetic tunability. Synthetic tunability affords the ability to edit antigens more quickly in response to

pathogenic drift and remove autoreactive epitopes that are suggested by some to be responsible for autoimmune conditions like Guillain–Barré syndrome.[102] With that said, these protein and peptide subunits suffer from low immunogenicity and therefore must be co-administered with immunostimulatory adjuvants as described in previous sections to facilitate protective immunity.[97] Protein-based subunit vaccines adjuvanted with TLR9,[19] TLR4,[13-17] and NLRP3[13-17] agonists or alum[48] and MF-59[103] depot-based systems have been FDA-approved (**Table 1.1**), but many other adjuvanted subunit vaccines (such as those containing TLR7/8 agonists[18]) have failed clinical trials.[37, 95] While no peptide-based subunit vaccines have been FDA-approved, at least one prophylactic vaccine (BiondVax's M-001 infleunza vaccine, which is adjuvanted with NLRP3 and TLR4 agonists[104]) recently underwent Phase III clinical trials (NCT03450915), and therapeutic peptide vaccines are expected to play a growing role in personalized cancer medicine.[105] More recently, nucleotide-based vaccines found clinical use in response to the COVID-19 pandemic.[99, 106, 107] Nucleotide-based vaccines encode for antigenic proteins that are translated by the patient's own cellular machinery. While these systems require challenging formulation and cold-chain storage (-70 °C) to stabilize and prevent degradation of nucleotides, when designed to overcome these issues, they can induce a highly localized and robust immune response against protein antigens.[15, 16, 99, 108, 109] By using the body's own transcription and translation machinery along with modified non-inflammatory nucleotides, these vaccines can be advantageous over subunit protein vaccines for proteins that are difficult to express recombinantly or that can induce systemic immunotoxicity.[99] Finally, viral vector vaccines use attenuated or weak pathogens as a vector to deliver nucleic acids coding for an antigen of interest. While both replicating and non-replicating viruses can be used, most research to date has focused on non-replicating adenoviruses because of their safety, high levels of antigen expression, and Th1-biased cellular immune responses.[101] The viral vector is transfected with genetic material encoding for the antigen of interest, and the resulting vaccine has an innate immunostimulatory capacity due to the presence of viral materials from the carrier. These vaccines have shown promise for emergent viral infections such as

Ebola[110] and COVID-19,[111, 112] as they can be manufactured rapidly and with a high degree of tunability. With that said, there remain concerns about the safety of genetically modified viruses, and these vaccines have proven less effective for bacterial infections. Overall, the selection of a vaccine format plays a considerable role in informing the immune response and must be carefully considered in the design of next-generation vaccines.

Vaccine Type	FDA-approved examples (not comprehensive)
Live Attenuated Vaccine	MMR, Chickenpox, Smallpox, Tuberculosis
Inactivated Vaccine	Polio, Influenza, Rabies, Typhoid
Subunit Protein Vaccine	HPV, Hepatitis B, Shingles, Malaria
Subunit Peptide Vaccine	None
mRNA Vaccine	COVID-19
DNA Vaccine	None
Replicating Viral Vector Vaccine	None
Non-replicating Viral Vector Vaccine	Ebola
Carbohydrate Conjugate Vaccine	Tetanus, Pneumococcus, Meningococcus

Table 1.3: List of vaccine subtypes and FDA approved examples of each. Data were obtained as of 10/2022 from https://www.fda.gov/vaccines-blood-biologics/vaccines/vaccines-licensed-use-united-states.

In addition to vaccines that provide protection against pathogens, neoantigen vaccines have emerged as a critical tool in the fight against cancer.[105, 113-115] Neoantigens are “non-self” antigens that emerge from the high mutation rate of many tumors. Among the more pernicious features of cancer is its ability to generate an immunosuppressive, or “cold,” microenvironment where antigen presentation is limited, and cytotoxic $CD8^+$ T cells are excluded. Developing therapeutic vaccines against antigens in the tumor microenvironment can jump-start the immune system, turning “cold” tumors “hot” by generating a supportive milieu (white blood cell infiltration, antigen presentation, and cytokine production) for anti-tumor $CD8^+$ T cell responses.[113, 115] RNA sequencing and proteomics technology can now be used to identify neoantigen peptides for personalized medicine.[115-117] Neoantigens specific to a given tumor can be identified using these

screening strategies, synthesized *ex vivo*, formulated with one or more adjuvants, and finally re-administered to the patient to invoke a response. In contrast to prophylactic vaccines, where the mitigation of immunostimulatory side effects is critical for translation, more robust immune responses are needed for cancer vaccines – as such, highly immunogenic PRR agonists such as imiquimod (a TLR7/8 agonist) are tolerated for these applications and have found clinical success in a cancer setting.[115, 118] Cancer vaccines can also be combined with autologous cell therapies to induce highly targeted responses.[115] Indeed, the first FDA approved cancer vaccine, Sipuleucel-T, uses autologous dendritic cells that are activated ex-vivo with a common prostate cancer neoantigen and then reintroduced to the patient.[119] As personalized cancer medicine becomes more scalable, cancer vaccines are expected to emerge as key therapeutics.

To overcome the immunosuppressive tumor microenvironment, one or more checkpoint blockade is often administered as part of the therapeutic regime in cancer medicine.[114] Immune checkpoints are a series of negative feedback systems, such as the up-regulation of the co-inhibitory surface markers, CTLA4 and PD-1, that prevent the body from expending too many resources during a chronic infection. This feature is critical during homeostasis to prevent an aberrant response against self-antigens, but in cancer, it prevents effective long-term anti-tumor responses. Checkpoint therapies block these negative feedback loops to allow long lived immune cell activation. For example, anti-CTLA4[27] and anti-PD-1[26] antibodies block T cells exhaustion, a phenotype characterized by down-regulation of TCR expression, decreased effector function, and cell death in the face of chronic stimulation. A host of CTLA4 and PD-1 blockade therapeutics, including ipilimumab, pembrolizumab, and others, are now FDA-approved for the treatment of cancer and are widely considered to be the most important advances in cancer medicine in the past twenty years.[114] There are also a host of investigational checkpoint blockades under investigation, including anti-CD47 and anti-TGF-β. CD47 is a “don’t eat me” signal expressed on most cells that binds CD172a (also called SIRPα) on macrophages to prevent phagocytosis.[120] Tumors have been shown to upregulate CD47 to prevent immune responses by macrophages.

As such, treatment with anti-CD47 has been shown to be a powerful tool restore effective APC function in the tumor microenvironment.[121] Similarly, tumors produce high levels of inhibitory cytokines, such as TGF-β, to generate an immunosuppressive environment, so blockade of these antibodies can restore innate immune function.[122] Combining checkpoint blockade with cancer neoantigen vaccines and other modern therapeutics is a powerful tool to activate the immune system and invoke potent cytotoxic tumor specific immune responses.

1.5 Inflammasomes and the IL-1 Family of Cytokines in Disease and Therapeutics.

While many cytokines play a role in orchestrating the immune response in disease, few are more potent than the IL-1 family of cytokines. The IL-1 family, including IL-1α, IL-1β, IL-18, and IL-33, as well as the IL-1 receptor antagonist (IL-1ra), have been implicated in the pathology of various diseases as well as the efficacy of modern vaccines.[15, 31, 123-125] Gout,[126] Alzheimer's disease,[127] Type 2 Diabetes,[128] Rheumatoid Arthritis,[129] COVID-19 CRS,[130] and various autoimmune diseases[31] have been associated with high levels of IL-1β. Meanwhile, IL-1β is known to be critical in generating protection in the Shingrix,[131-133] Mosquirix,[131-133] Comirnaty,[15] and Spikevax[15] vaccines. This differential response highlights a key facet of IL-1β and other cytokines: the immunological response toward IL-1 cytokines is context-dependent. The IL-1 family of cytokines bind the IL-1 family of receptors (IL-1Rs), of which IL-1R1, IL-1R2, and IL-18R are the most common. IL-1R1 and IL-18R induce CD8- and Th1-biased immune response via the MyD88 signaling pathway.[31, 67] They also induce activation of cyclooxygenase 2 (COX2), secretion of nitric oxide (NO), and transcription of phospholipidases, all of which contribute to fever and vasodilation to neutralize pathogenic threats.[31] Meanwhile, IL-1R2 is a decoy receptor which serves as a sink for high levels of secreted IL-1 cytokines.[31] Secretion of IL-18 in concert with IL-12 and IL-15 has been shown to induce potent cytotoxic responses for cancer immunotherapy,[133-135] while administration of recombinant IL-1ra (Anakinra), anti-IL-1β (Canakinumab), or IL-1R antagonist (Rilonacept) are all used clinically to reduce inflammation.[135]

One key challenge in the study of IL-1-producing compounds is that mice express higher levels of IL-1ra than humans, challenging pre-clinical interpretation of immunogenicity and toxicity.[15] This thesis will focus on IL-1β and IL-18 in the context of vaccination and immunotherapy, but the study of IL-1 cytokines in a variety of disease contexts is an active and exciting area of research.

Secretion of IL-1β and IL-18 is induced primarily by PRRs called inflammasomes.[136] These intracellular damage sensors include the NACHT, LRR and PYD domains-containing proteins 1 and 3 (NLRP1 and NLRP3) inflammasomes, NOD-like receptor C4 (NLRC4) inflammasome, absent in melanoma 2 (AIM2) inflammasome, Caspase-11 inflammasome, and others.[136] IL-1β and IL-18 exist as a "pro-form" which, upon activation of these inflammasome receptors, are cleaved by enzymes called Caspases to their active form.[136] Of these inflammasomes, NLRP3 is the most well-studied since its discovery in 2003.[137] NLRP3 undergoes conformational change in response to a broad class of stimuli that behave as danger signals (DAMPs) after disruptions of homeostasis.[137] While diverse stimuli have been implicated in NLRP3 activation, including reactive oxygen species,[138-140] extracellular ATP,[141] and lysosomal disruption,[126, 142, 143] these stimuli seem to converge on cellular potassium efflux as a causative agent of the NLRP3 conformational change (**Figure 1.3**).[137, 144] Once activated, NLRP3 can interact with ASC, NEK7, and pro-Caspase 1 to form an inflammasome, which is a megadalton protein complex with a host of effector functions.[137, 145, 146] Specifically, NLRP3 inflammasome formation catalyzes cleavage of pro-Caspase 1 to Caspase 1. Active Caspase 1 then facilitates secretion of IL-1β and IL-18 and induces pyroptosis, a form of inflammatory cell death characterized by GSDMD N-terminal cleavage, membrane pore formation, and eventual cell lysis (**Figure 1.3**).[147-149]

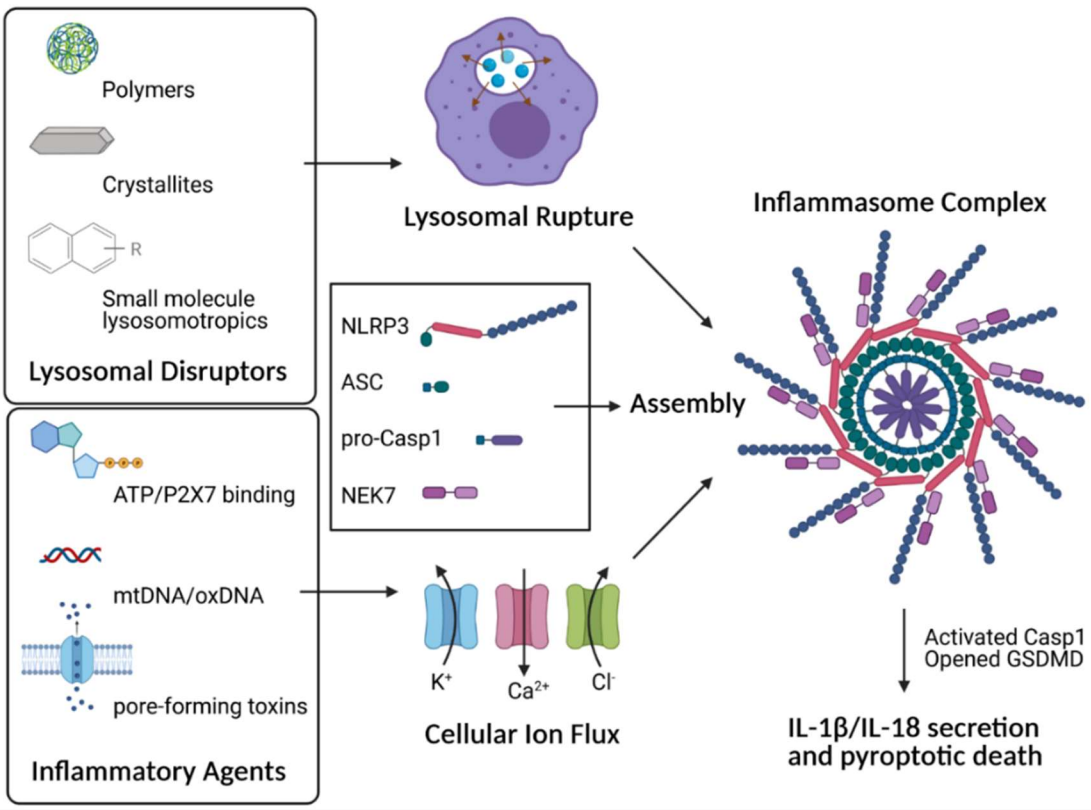

Figure 1.3: Overview of NLRP3 inflammasome activation pathways. Figure prepared with BioRender.com.

A variety of particulate agents have been shown to activate the NLRP3 inflammasome. Early studies demonstrated that uric acid crystals, present in Gout, activate the inflammasome via lysosomal disruption.[126] Since then, a variety of other particulates and crystallites, including silica,[142] asbestos,[142] amyloid plaques,[127] Charcot-Leyden crystals,[150] and others[151] have been similarly shown to activate the inflammasome – all playing a role in pathological inflammatory disease. Indeed, recombinant IL-1ra or antibodies raised against IL-1R are used as therapeutics for a variety of autoimmune contexts including rheumatoid arthritis, gout, and COVID-19 related CRS.[135] Alternatively, activators of the NLRP3 inflammasome can stimulate protective Th1-biased immune responses in vaccines and immunotherapies.[125, 152] As mentioned previously, alum- or emulsion-based particulate adjuvant systems may activate the inflammasome via lysosomal disruption, but this has not been conclusively demonstrated.[53-58, 60] While saponins (extracts from

the *Quillaia saponaria* tree) and immunostimulatory complexes (ISCOMs) of saponins, lipids, and cholesterol have been used as adjuvants for more than 50 years, it was recently found in 2016 that these materials' adjuvanticity results in part from NLRP3 inflammasome activation.[131, 132, 153-156] Works by Marty-Roix, *et al.*,[131] and Welsby, *et al.*,[132] independently reported that QS-21, the 21st chromatographic isolate of *Q. saponaria*, activates the NLRP3 inflammasome via lysosomal rupture. While effective, saponin-based systems are costly, derived from limited natural resources, synthetically complex, and prone to toxicity.[157] Indeed, mature (30+ year-old) *Q. saponaria* must be killed in the production of saponin adjuvants used in Mosquirix and Shingrix vaccines, and the limited availability of this resource threatens the broad and equitable distribution of these vaccines.[157] Finally, various lipid-based particles used both in the COVID-19 vaccines and clinical immunotherapies were recently found to induce robust IL-1β secretion. Tähtinen, *et al.*[15] observed that the polymer and lipid components of these systems derive their adjuvant effects, in part, from IL-1β secretion. These recent findings highlight the potential of IL-1-producing adjuvants, yet both saponins and lipid nanoparticles are complex formulations with high cost, poor tunability, and toxic side effects.[109, 157] Synthetic alternatives are desirable for use as adjuvants which overcome these limitations and allow broad applicability of this technology.

Recently, it was shown that cationic polymers similarly activate the NLRP3 inflammasome via lysosomal disruption.[81, 143, 158-162] The properties of polymers can modulate the extent of lysosomal rupture and thereby provide an avenue by which controlled NLRP3 inflammasome activation can be achieved.[159-162] Moreover, such lysosome-disrupting polymeric adjuvants can be formulated to deliver immunostimulatory cargo to the cytosol and activate cytosolic PRRs (such as STING) to afford multi-adjuvant synergies. In a recent publication, Manna *et al.* showed that the composition of dendrimeric scaffolds composed of cationic amino acid and tetra(ethylene glycol) (TEG) domains in varied ratios were found to modulate the extent of osmotic swelling in the lysosome following cellular uptake, thereby controlling the extent of rupture and the degree of downstream Caspase 1 and IL-1β activity (**Figure 1.4A**).[159] Likewise, Baljon *et al.* report that the

ratio of butyl methacrylate to 2-(dimethylamino)ethyl methacrylate in a pH-responsive co-polymer could control the extent of lysosomal disruption and IL-1β secretion in human monocytes,[161] and Nandi *et al.* report that the (hydrophobic) alkyl content in poly[(ethylene glycol)-*b*-[(coumarin methacrylate)-*r*-(octyl methacrylate)] similarly influenced the extent of lysosomal disruption and inflammasome activation in murine macrophages (**Figure 1.4B**).[160] These results highlight that changes in physicochemical properties can have drastic impacts on endo/lysosomal rupture and provide methods for the screening of NLRP3 inflammasome activation via IL-1β activity. Future work must be conducted to better elucidate how polymer properties and related inflammasome activation correlate with *in-vivo* responses.[125, 152, 163] Such structure-bioactivity relationships will better allow for the rational design of polymers for vaccines and therapies.

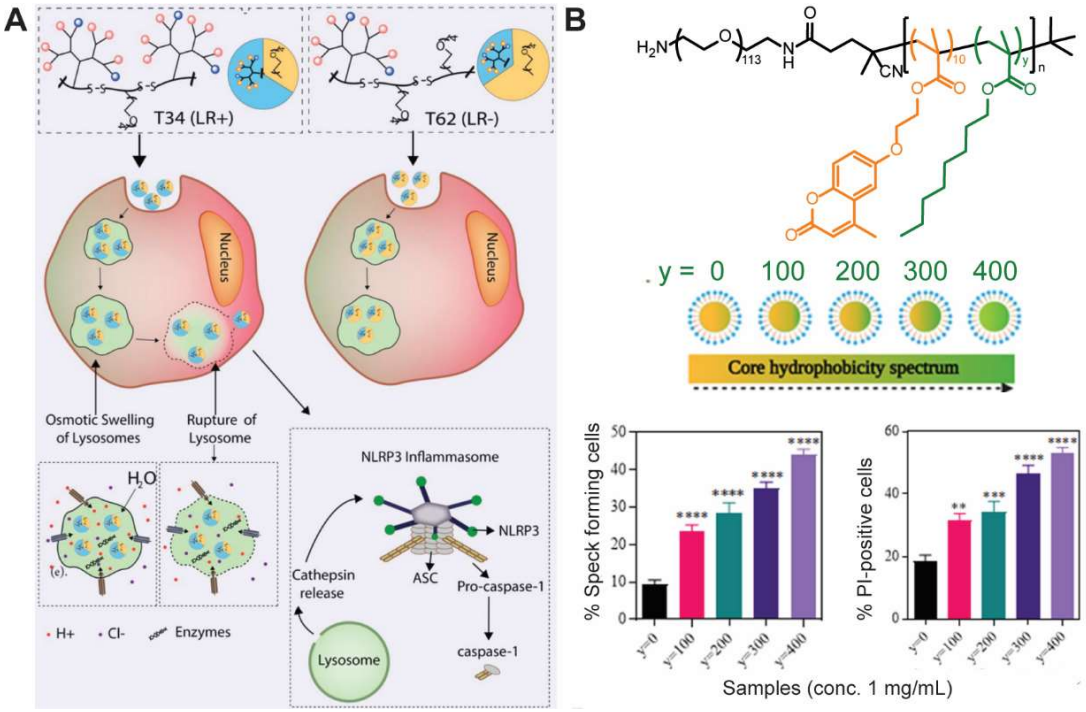

Figure 1.4: Examples of inflammasome activating polymeric adjuvant systems. (A) Dendrimeric histidine- and tryptophan-containing scaffolds with 34% or 62% ethylene glycol (T34 and T62) were synthesized and shown to mediate NLRP3 inflammasome activation via a lysosomal rupture- and cathepsin-dependent mechanism. (B) Self-assembling polymer nanoparticles induce ASC speck formation and immunotoxic responses in a composition dependent fashion, with increasing core octyl methacrylate content mediating maximal immunogenicity. Reprinted from (1); copyright 2022 ACS.

1.6 Cell Division and Death and their Role in Innate Immune Signaling.

Inflammatory cell death is a possible result of PRR overstimulation, inflammatory cytokine production, and inflammasome activation, and it is increasingly recognized as an important signaling mechanism of innate immunity.[149, 152, 164, 165] Under homeostasis, a series of feedback loops provide the signaling mechanisms needed for proper cell growth and division. The cellular growth and division cycle is split into four phases: G1 or growth phase 1, S or (DNA) synthesis phase, G2 or growth phase 2, and M or mitosis phase. When stressed, these pathways become dysregulated, and cells can die via controlled or uncontrolled pathways. These include intrinsic apoptosis, extrinsic apoptosis, necrosis, necroptosis, or pyroptosis. Cell death via apoptosis results in the recruitment of phagocytes to prevent the release of cellular contents and allow for non-inflammatory cell death. On the other hand, cell death via necrosis, necroptosis, and pyroptosis results in the release of damage associated molecular patterns (DAMPs) into the extracellular milieu, providing further inflammatory signals to neighboring cells.[149, 165] Controlled cell death is executed largely by Caspases, which are a class of 12 cysteine-dependent aspartate-directed proteases (10 in mice) with a host of effector functions. Many adjuvants induce low levels of cell death *in vivo*. Understanding how cell death informs innate immune responses is important to understand why some adjuvants succeed while others fail.

In the steady state, cell cycle is regulated by a family of proteins called cyclins and the associated cyclin-dependent kinases (CDKs) (**Figure 1.5**).[166, 167] During normal cellular growth (G1 phase), Cyclin D is produced and builds up in the cytosol. Upon reaching a critical concentration, Cyclin D binds CDK4/6, which in turn, phosphorylates retinoblastoma protein (Rb) to inactivate it. Upon Rb inactivation, the E2F protein becomes active and induces transcription of Cyclin E. Cyclin E binds CDK2 and initiates the onset of S phase and DNA replication. Transcription of Cyclin A increases as DNA replication comes to a completion, binding CDK1/2 to initiate the start of G2 phase. Finally, upon sufficient Cyclin A—CDK1 binding, the nuclear envelope breaks down, and Cyclin A is enzymatically degraded. At this point, Cyclin B can bind

CDK1 and initiate the onset of mitosis. Other CDKs are involved in cell cycle process, but their functions are currently poorly understood.[166] Failure to progress in the cell cycle, particularly in the G1 to S phase transition, results in apoptosis via the intrinsic pathway. This process is sometimes referred to as senescence.[168] On the other hand, mutations in the Cyclin—CDK signaling pathway are involved in many cancers, and CDK inhibitors have been FDA approved as highly effective cancer therapeutics.[169] As many PRR agonists alter cellular metabolism and division, it is believed that there is interplay between innate immune signaling and cell cycle. This interplay is still poorly understood and of significant interest for further study.[128, 170]

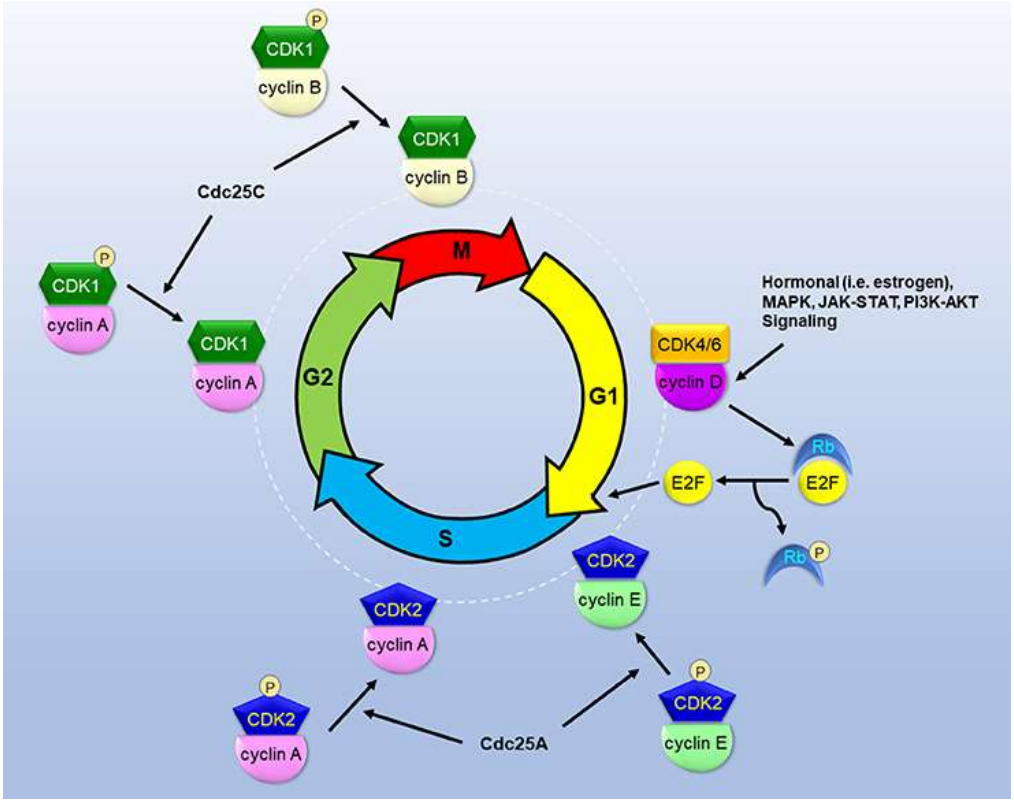

Figure 1.5: Overview of cell cycle signaling pathways involving cyclins and their cognate receptors, the cyclin-dependent kinases (CDKs). Figure reprinted from (167).

Apoptosis was the first mechanistic form of cell death to be discovered, when J.F.R. Kerr found that cells can die from a controlled mode of death independent from traumatic rupture.[171]

Since then, scientists have uncovered that apoptosis can be initiated either by receptor-mediated signaling (the extrinsic pathway) or intrinsic mitochondrial signaling (the intrinsic pathway).[172] The extrinsic pathway is regulated by a subset of the TNF receptor superfamily (TNFRSF, see **Table 1.2**) that contain a cytoplasmic death domain, including Fas and TNFR-I. Upon binding of these receptors by Fas ligand or TNF-α, respectively, the death domain recruits initiator pro-Caspases, 8 and 10, and induces their cleavage to an active form. Active Caspases 8 and 10 then activate the effector Caspases 3, 6, and 7, which in turn cleave and degrade a series of proteins that allow for apoptosis. Similarly, the intrinsic pathway is regulated by cytochrome C (Cyt c). In the presence of mitochondrial stressors or the absence of survival signals (orchestrated by the Bcl-2 family of proteins[173]), Cyt c is released into the cytosol. Cyt c binds an intermediary enzyme, Apaf-1, which in turn, recruits and facilitates the cleavage of the alternative initiator pro-Caspase, 9, to its active form. Caspase 9 then functions similarly to Caspases 8 and 10, activating the effector Caspases, 3, 6, and 7, to initiate apoptosis.[172] Key features of apoptotic cells include cell shrinkage, chromatin condensation, and DNA fragmentation. Dying cell fragments are then packaged in apoptotic bodies marked by high levels of phosphatidylserine for disposal by macrophages.[172, 174] Alternative mechanisms of apoptosis exist and are discussed elsewhere.[172]

In contrast to apoptosis, other modes of cell death result in the release of cellular contents *via* controlled or uncontrolled mechanisms. Necrosis is a form of inflammatory cell death where the cell becomes compromised and rapidly bursts due to a chemical or physical insult, releasing its cellular contents in an uncontrolled manner. Necrosis can be regulated, as with complement-mediated necrosis, or unregulated, as in the case of a traumatic wound.[175] In contrast, pyroptosis and necroptosis are precisely controlled modes of inflammatory cell death. As described in **Section 1.5**, pyroptosis is initiated by the activation of inflammasomes, where active Caspase 1 (or 11, in the case of non-canonical inflammasomes[176]) cleaves the GSDMD N-terminus to allow membrane pore formation and secretion of cellular contents.[148, 177-180] Specifically, cleaved GSDMD has been shown to self-assemble into ~21 nm diameter 33-mers that preferentially

release positively charged proteins, such as the IL-1 family of cytokines, into the extracellular space.[180] Necroptosis functions via an evolutionarily similar mechanism to pyroptosis and exists as an alternative mode of cell death to apoptosis. In the presence of high levels of TNFR-I signaling, an alternative signaling pathway emerges where the death domain recruits receptor-interacting serine/threonine-protein kinase 1 and 3 (RIPK1 and RIPK3). RIPK1 and RIPK3 phosphorylate one another and form fibrous complexes called necrosomes. Necrosomes, in turn, phosphorylate Mixed Lineage Kinase Domain Like Pseudokinase (MLKL), which causes it to insert in the lipid bilayer and form pores in the cell membrane.[181, 182] Phospho-MLKL pores are much smaller than GSDMD pores and only allow for ion fluxes, though their precise structure has not been resolved at an atomic level.[182] Ion fluxes into the cell upon MLKL pore formation result in osmolytic swelling that eventually causes the cell to burst.[181] The balance between apoptosis and necroptosis is currently thought to be regulated, in part, both by the extent of TNFRSF signaling and intracellular levels of pro-Caspase 8.[183-185] Other modes of inflammatory cell death exist, such as ferroptosis (death initiated by excessive iron levels) and NETosis (neutrophil extracellular trap mediated necrosis), but these remain incompletely understood and are outside the scope of this thesis.[186] A visual overview of the cell death pathways described herein in is provided in **Figure 1.6**.

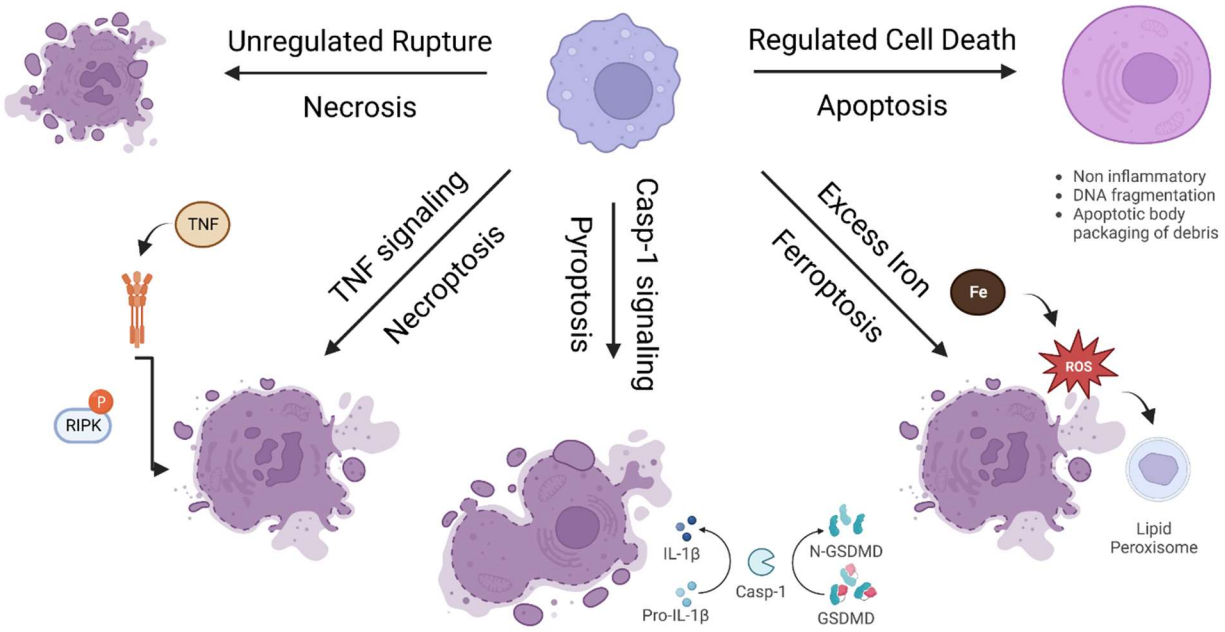

Figure 1.6: Overview of some common cell death signaling pathways. Healthy cells can undergo non-inflammatory, regulated cell death known as apoptosis or undergo necrosis in response to damaging chemical or mechanical insults. Alternatively, a variety of chemical signals, such as TNF-α, Casp-1, or Iron, can initiate controlled modes of inflammatory cell death such as necroptosis, pyroptosis, and ferroptosis, respectively. Figure prepared with Biorender.com.

The release of cellular contents has been shown to play a key role in the generation of an immune response.[187] In **Section 1.5**, it is already described how release of mature IL-1 cytokines during pyroptosis can stimulate a Th1-biased immune response. Additionally, release of DAMPs such as nucleic acids (which activate TLR3, TLR7/8, TLR9, STING, and RIG-I), heat shock proteins (which activate TLR2 and TLR4), cytoskeletal proteins (which activate DNGR-1 and C-type lectin receptors), and mitochondrial contents (which activate NLRP3 and others) during can activate PRRs on neighboring cells to further invoke an immune response (see **Table 1.1**).[187] Notably, it was recently demonstrated that extracellular F-actin binds DNGR-1 (a C-type lectin) to induce lysosomal rupture and cross-presentation of antigens.[188] It is believed that this is a dedicated signaling pathway for the immune system to respond to dead cell-associated antigens, which may be productive in cancer or degenerative disease. Indeed, one mechanism of cancer evasion is the down-regulation of proteins associated with apoptosis, such as Apaf-1,[189] and using

inflammatory cell death as a tool to stimulate innate immunity and facilitate an anti-tumor T cell response is an active area of research.[187] I hypothesize that controlled, *in vivo* cell death could be a valuable tool in next generation adjuvants. To achieve this goal, better methods to screen inflammatory cell death *in vitro* and control the location and extent of cell death *in vivo* are needed.

1.7 Living Polymerization and Controlled High Throughput Polymer Synthesis in Biology.

Developing polymers with better binding affinity and avidity or that can disrupt organelle homeostasis and/or activate innate immunity is an attractive strategy for the design of novel therapeutics. As described herein, small differences to material properties, such as size or charge, can have large impacts on immunostimulatory activity of materials targeting the innate immune system. As such, better methods for synthesis, characterization, and screening of the immunostimulatory activity of polymers targeting immune receptors will allow structure-bioactivity relationships to be developed over a larger domain space. Living polymerization strategies, in concert with advances in high throughput polymer synthesis make such screens possible.

Polymers are macromolecules comprised of repeating units, called monomers. The number of monomers incorporated in a polymer of interest is the degree of polymerization (DP), calculated by dividing the average molecular weight, M_n, by the molecular weight of the monomer, M_i (**1**). Because bulk polymerization techniques yield a statistical distribution of chain lengths, the statistical variation in the DP of a matrix is known as the dispersity, Đ. The dispersity is calculated by dividing the weight average molecular weight (M_w, **2**) by the number average molecular weight (M_n, **3**) as shown in **4**. Most polymer synthesis schemes can be described as step growth or chain growth polymerizations. In step growth, monomers with reactive chain ends combine to form oligomers of increasing chain length. This approach is advantageous because requires no chemical initiator and is less susceptible to reaction termination; however, as growing oligomers become more viscous and kinetically trapped, it is difficult to achieve high M_n polymers with this approach. In contrast, during chain growth, monomers are attached sequentially to the growing

polymer from an initiation site. This approach can more quickly yield polymers with higher M_n, but it is challenging to control the growing polymer chain and remove unreacted monomer after the polymerization has completed. By introducing an initiator or monomer with multiple reactive sites, polymers with sophisticated architectures such as stars, brushes, or networks can be achieved.[190] Furthermore, co-polymers comprised of two or more monomers (either incorporated randomely or in blocks to the growing chain) can be synthesized to afford materials with optimized properties or self-assembly behavior.[191] Excellent texts on the basic chemistry of polymerizations exist.[192]

(1) Degree of polymerization $\boldsymbol{DP = \frac{M_n}{M_i}}$

(2) Number average molecular weight $\boldsymbol{M_n = \frac{\sum_i N_i M_i}{\sum_i N_i}}$

(3) Weight average molecular weight $\boldsymbol{M_w = \frac{\sum_i N_i {M_i}^2}{\sum_i N_i M_i}}$

(4) Degree of polymerization $Đ = \boldsymbol{\frac{M_w}{M_n}}$

Since polymers were first described nearly 100 years ago,[193] polymer chemists have developed many tools to synthesize polymers from a breadth of monomers with controlled molecular weights and low dispersities. Control over these properties is critical for biological applications, as they define the reproducibility of the synthesis and the material properties of the resultant materials. Perhaps the most important technique has been the ascent of reversible deactivation radical polymerization (RDRP), a chain growth technique that can be used to prepare polymers with $Đ \leq 1.3$.[194] In RDRP, the radical chain end of a growing polymer is reversibly capped by a chain transfer agent (CTA) that controls the rate of reaction (**Scheme 1.1A**). Several RDRP strategies have emerged, including nitroxide mediated polymerization (NMP) in 1986,[195, 196] atom transfer radical polymerization (ATRP) in 1995,[197-199] and reversible addition-fragmentation transfer polymerization (RAFT) in 1998 (**Scheme 1.1B**).[200-202] NMP employs a nitroxide radical as the CTA, ATRP employs a transition metal such as copper as the CTA, and RAFT employs a thiocarbonylthio moiety (or related functional group) as the CTA. A key to all RDRP approaches

is that the rate of radical chain transfer to the CTA must be much faster than that of radical addition to the growing polymer chain. As such, the growing polymer will spend most of its time in a non-reactive state, allowing all polymers to grow at a similar rate.[194] CTA groups can be designed with different stereoelectronic properties to control the on/off rate for monomers with different rates of chain growth. Key challenges in the design of RDRPs are defining solvent and monomer compatibility for a given system, developing "green" versions of these chemistries, and creating low-cost and scalable strategies to use these technologies in the supply chain.[194]

Despite challenges in the scalable synthesis of well-controlled polymers for biological applications, advances in process chemistry have now enabled high throughput RDRP synthesis of polymers in drug delivery contexts.[203] In one example, Mann *et al.* synthesized and screened 90 acrylamide-based insulin excipients using RAFT chemistry with a Chemspeed Swing XL process chemistry instrument. With this approach, they developed an optimized, ultrafast acting insulin formulation with greater stability and efficacy.[204] Here, polymer composition was shown to alter the biodistribution, pharmacokinetics, and activity, highlighting the impact that polymer design and high throughput screening can have on downstream applications. In an alternative example, Ulkoski *et al.* synthesized a library of polymers containing one of two tertiary amine monomers statistically co-polymerized with alkyl monomers of varying length using an Agilent Bravo liquid handling robot.[77] These materials were then screened for their ability to disrupt endosomal membranes and deliver mRNA for use in gene delivery, and design principles were elucidated for clinical applications. Unfortunately, the high cost and limited accessibility of this instrumentation has prevented further applications of automated RDRP in biomedicine.

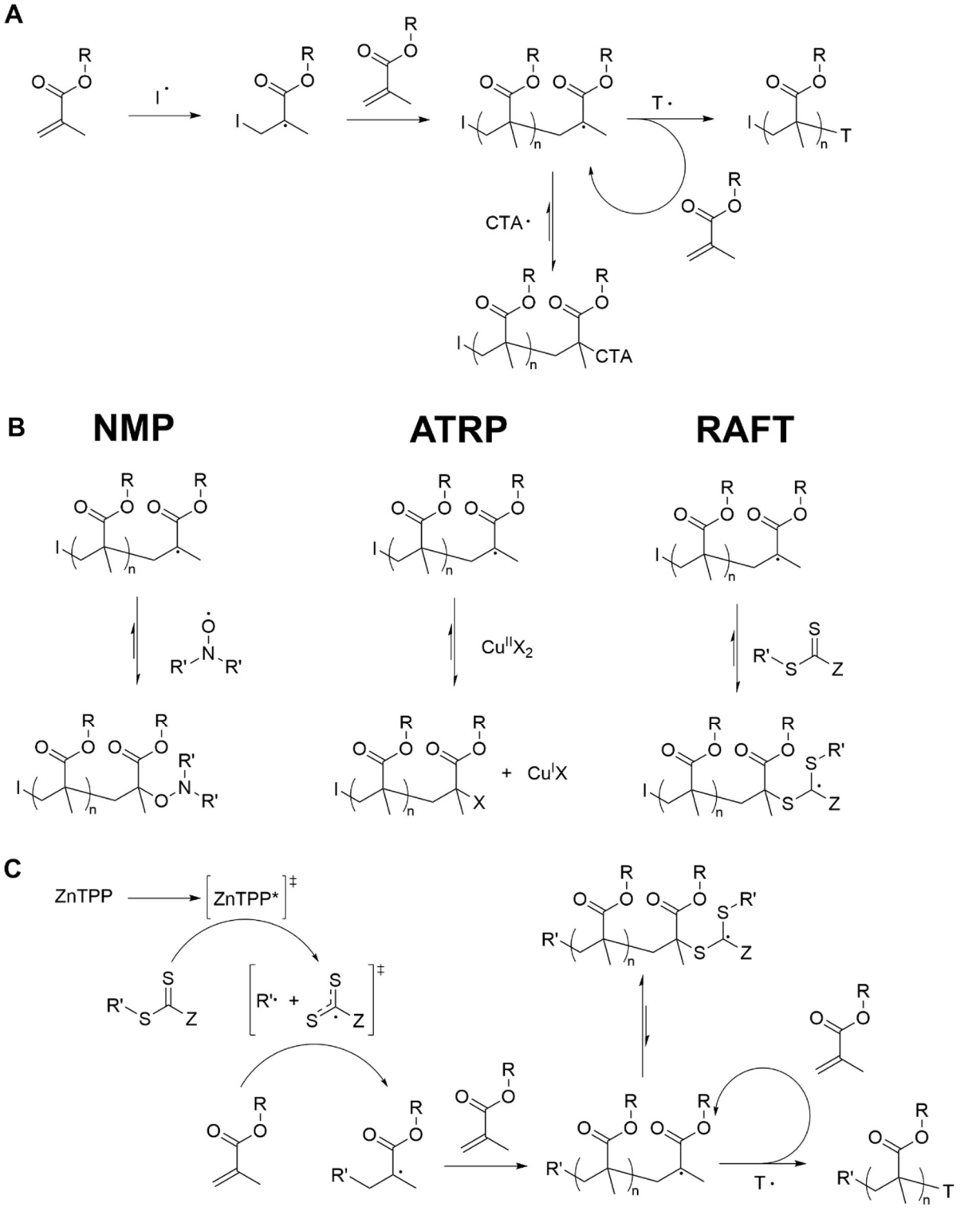

Scheme 1.1: Overview of some reversible deactivation radical polymerization (RDRP) approaches. (A) General reaction scheme for RDRP of a methacrylate using an initiator, I, terminator, T, and chain transfer agent, CTA. (B) Chain transfer agents used in three types of RDRP. (C) Scheme for the photoinitiation of PET-RAFT systems based on the model reported by Corrigan, *et al*.[205]

Perhaps the most exciting new technology in high throughput RDRP chemistry is the photo-electron transfer (PET)-RAFT reaction.[206] In this reaction, a photoredox agent such as Eosin Y[207] or tetraphenylporphyrin zinc (ZnTPP)[208] initiates the polymerization when exposed to an excitatory wavelength of light. In contrast to a thermal initiator, the reaction is initiated by triplet energy transfer from the redox agent directly to the chain transfer agent (**Scheme 1.1C**).[205] This approach (1) does not require heat, (2) can be conducted in well plates, (3) affords spatial and temporal control, and (4) is compatible with a breadth of monomers and solvent systems. Recent work by the Boyer group has demonstrated that, when DMSO is used as a solvent, ZnTPP-catalyzed PET-RAFT reactions are tolerant of oxygen, allowing high throughput reactions to move from stringently air-free conditions (such as a glovebox) to the benchtop and improve accessibility of these techniques.[209] The Gormley group has pioneered this use of PET-RAFT technique to design new and improved materials for biological applications. They demonstrated that a cyclopropenone-protected dibenzocyclooctyne (cp-DIBAC) could tolerate polymer synthesis under PET-RAFT conditions in a 96-well plate format.[210] This functionality could be cleaved with ultraviolet light to unveil a reactive cyclooctyne to allow reactions with azide modified biomacromolecules. With this approach, many polymer conjugates can be prepared in one-pot to rapidly generate libraries for downstream analysis. In 2022, they showed that PET-RAFT could be employed in parallel with machine learning to predict the stabilizing effects of polymers on proteins.[211] Using the mechanistic insight gained from their high throughput screening and computational datasets, they identified polymers that could stabilize a series of enzymes under otherwise-denaturing conditions. These works provide a glimpse into the promise of high throughput screening. As this chemistry is developed and computational tools are applied in new contexts,[203] high throughput screens of systems prepared via PET-RAFT or other mild polymerization conditions will allow advances in the production of new materials for biomedicine.

1.8 Polymers in Innate Immunity and Vaccination.

The premise that polymers can modulate innate and adaptive immune responses has a remarkably long precedent. In the 1930s, Goebel and Avery reported several landmark studies demonstrating that conjugation of carbohydrate polymers to proteins could modulate the immune response in a pneumococcus vaccine.[212, 213] Later, work in the 1960s showed that hydrophilic polymers such as polyethylene glycol, alginates, and methylcelluloses were safe for use as drug excipients or surgical tools, while other hydrocarbons such as polystyrene and poly(vinyl chloride) were less favorable for biological applications.[214, 215] Similar property-activity relationships were developed through the 1980s and provide foundational understanding of polymer biocompatibility today. Work in the 1990s demonstrated that polymers could be synthesized with precise chemistries to deliver small molecules, proteins, or oligonucleotides with controlled release kinetics, biodistribution, and immune responses.[216-219] Today, the ascent of controlled polymerization techniques combined with sophisticated monomer design[194, 220] has allowed a breadth of polymers to be used in biomedical applications such as tissue scaffolds, drug delivery systems, drug excipients, antimicrobial coatings, and gene therapies, to name a few. Specific to clinical immunology, polymers are critical components of liposomal and nanoparticulate vaccine formulations,[61, 221, 222] transfection reagents for CAR T cell production and oncological gene therapies,[218, 223] and compatibilizing agents for stents and devices.[63] Growth in the use of polymers in these applications requires an increased molecular understanding of interactions between polymers and the immune system to allow for the development of safe and improved therapeutics. Recently, advances in the design of (1) covalent polymer-drug systems, (2) non-covalent polymer-drug systems, and (3) innately immunostimulatory polymers have shown great pre-clinical potential and are expected to emerge as clinically relevant therapeutics in the next decade.

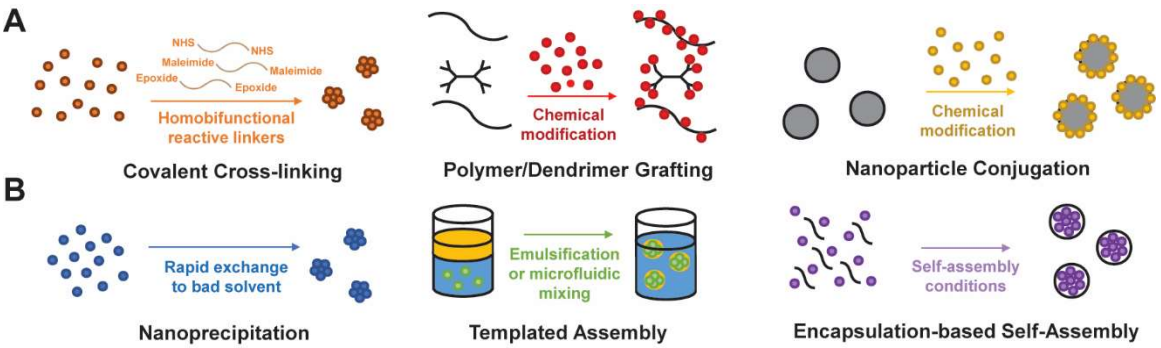

Figure 1.7: Overview of selected (A) covalent and (B) non-covalent strategies used to synthesize polymer-based vaccines or immunotherapies. Overview of selected (A) covalent and (B) non-covalent strategies used to synthesize polymer-based vaccines or immunotherapies. Reprinted from (1); copyright 2022 ACS.

Covalent Polymer-Drug Systems. Covalent polymer-drug systems have gained attention as a method by which enhanced immunostimulatory activity can be achieved. Polymers covalently conjugated to immunogenic groups such as PRR agonists can allow for polyvalent receptor-ligand interactions, localized delivery of cargo, or delivery of multiple cargoes to a single locus. Moreover, covalently linked combinations of synthetic polymers and additional immunostimulatory components are attractive for the design of adjuvants with precise molecular composition and behavior in solution. Several of the most attractive strategies for the design of covalent systems include linear polymers with PRR agonist grafts, dendrimers, functionalized solid nanoparticles (such as gold, silica, or poly(lactic-co-glycolic acid)), cross-linked hydrogels, and mechanically interlocked polymers (**Figure 1.7A**).[62] The Hubbell group has demonstrated one application of polymer-drug conjugates to enhance the efficacy of vaccines.[224] In this work, a TLR7 agonist-containing methacrylamide monomer based on the imidazoquinolinone class (pTLR7) and a mannose-containing methacrylamide monomer (pMan) were polymerized using reversible addition-fragmentation transfer (RAFT) to obtain p(Man-*s*-TLR7). This polymer was conjugated to a model antigen, ovalbumin (OVA), using a self-immolative disulfide-based linker to form an antigen-docked synthetic scaffold for immune activation (**Figure 1.8**).[224] *In vitro,* this platform show improved uptake and presentation of antigen using BMDC and T cell co-culture

experiments, and competition experiments using anti-CD206 and anti-CD209 antibodies (which block mannose and DC-SIGN receptors) reveal that synthetic mannosylation was responsible for this response. After demonstrating the efficacy of this model using OVA, p(Man-*s*-TLR7) was conjugated to the malaria circumsporozoite protein (CSP) and used in a murine vaccination study. Here, p(Man-*s*-TLR7) conjugated to CSP was shown to induce improved antigen specific T and B cell responses relative to unlinked controls. The Hubbell group has demonstrated in other works that this synthetic glycosylation strategy can be similarly employed using GalNac and GlcNac as glycans to route antigens to the liver and induce tolerance in a model of diabetes,[225] as well as the applicability of this system to other disease contexts such as COVID-19.[226]

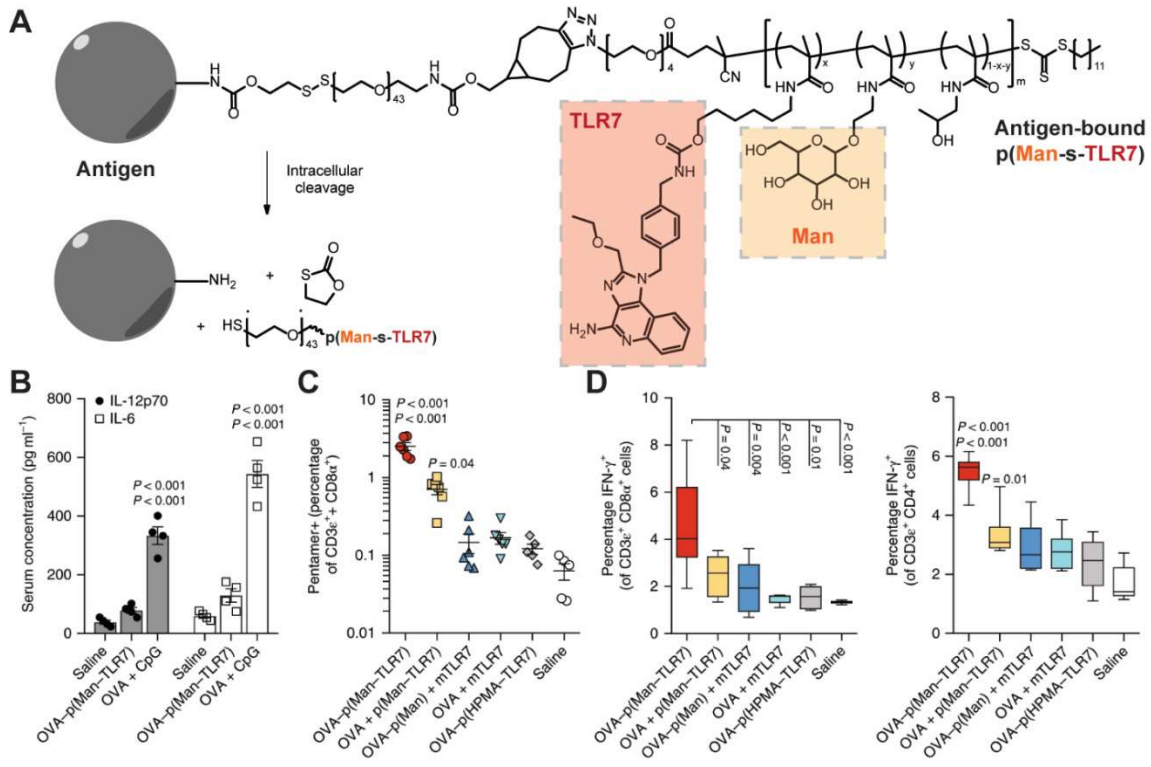

Figure 1.8: Example of one successful polymer-drug system used for vaccination. (A) Synthesis of p(Man-*s*-TLR7) glycoadjuvant containing a self-immolative disulfide linker to afford intracellular co-delivery of antigen, mannose, and TLR7 agonist. (B) Vaccination with p(Man-s-TLR7) reduces systemic IL-6 and IL-12p70 production relative to soluble TLR9 agonist. (C) Antigen specific CD8 T cell production as well as (D) antigen-specific $CD8^+$ and $CD4^+$ T cell activation after re-stimulation with the model antigen, OVA, were enhanced in the splenocytes of mice treated with p(Man-s-TLR7). Reprinted from (1); copyright 2022 ACS.

Beyond linear polymer scaffolds, dendrimers, functionalized nanoparticles, and cross-linked hydrogels can allow for higher density display of antigen or ligand as well-defined (and potentially stimulus-responsive) nanocarriers. Specifically, dendrimers can improve solubility and biocompatibility while displaying adjuvants at their surface on account of their globular structure.[227] Wang and colleagues recently reported a light-responsive adjuvant therapy based on a TLR7-activating 2-aminoimidazole derivative and a poly(lysine) dendron.[228] When complexed with an anti-cancer agent and antigen, dendrimeric light- and hypoxia-responsive nanoassemblies are formed which were found to display robust anti-cancer therapy against multiple tumor models.[228] Cationic poly(amidoamine) (PAMAM)-based systems have also been extensively employed for gene therapies and cancer therapeutics, but their toxic side-effects have limited use in other applications such as vaccination or drug delivery.[229, 230] Similarly, polymeric or inorganic nanoparticles can be functionalized with PRR agonists to afford polyvalent display and reduce systemic side effects relative to soluble ligands. Such materials been extensively reviewed elsewhere, with the chief limitation of this approach being that many solid materials are poorly biocompatible and biodegradable.[231, 232] Chemically cross-linked hydrogels, meanwhile, show great potential for generating immunogenic adjuvant systems with tailored physicochemical properties, biocompatibility, and release of synthetic or biologically-derived cargoes.[233-235] Demonstrating the potential of this synthetic approach, the Irvine lab has developed protein nanogel “backpacks,” which can be tethered to CAR T cells (engineered T cells with a scFv acting as a TCR) to support proliferation after adoptive cell transfer therapy.[234] The backpacks contain recombinant IL-15, which supports T cells proliferation, and CD45, which serves as an anchor to the T cell surface, and are cross-linked at lysine residues using a disulfide-containing NHS-ester linker.[234] The backpacks were found to enhance T cell proliferation 16-fold relative to CAR T cells delivered with soluble IL-15, and this technology is now in clinical trials for the treatment of solid tumors (NCT03815682). While reversible bonds have found use in both chemistry and biology

during the past decade, better strategies for the stimulus-responsive release of cross-linked biologicals under specific conditions will allow targeting of various immune cell subsets.

Non-covalent Polymer-Drug Systems. Spontaneous self-assembly or other non-covalent formulation is an alternative strategy to achieve immunogenic systems derived from multiple macromolecular components (**Figure 1.5B**). Advantages of such non-covalent strategies is that they are easily prepared from low-cost starting materials, break down on biologically relevant timescales into biocompatible biproducts, and can be imparted with stimuli responsive or other desirable properties.[234, 236] Formulations including imiquimod (a small molecule TLR7/8 agonist) serve as an example of the promise of formulated nanomaterials; while systemic toxicity after injection has prevented clinical translation of imiquimod as vaccine adjuvant,[18] a lipid-modified derivative, 3M-052, adsorbed onto alum has shown remarkable safety and efficacy in pre-clinical studies and is now undergoing early-stage clinical trials for influenza vaccination when co-delivered with antigen (NCT04177355).[237] Self-assembled delivery systems such as liposomes, lipid nanoparticles, micelles, and polymersomes are perhaps the most common non-covalent systems. On account of their amphiphilic properties, they can encapsulate both hydrophilic and hydrophobic cargoes, making them highly versatile for the delivery of chemically diverse materials. While liposomes and lipid micelles have been extensively reviewed for drug delivery,[232, 238] perhaps the most notable recent application of self-assembled lipid-based nanocarriers for immunological applications has been in the delivery of mRNA. Here, lipid nanoparticles have been FDA-approved for vaccination against SARS-Cov-2 in 2021.[109] In these systems, the ionizable lipid nanocarrier stabilizes mRNA from degradation and, upon endocytosis, assists in endosomal escape to deliver mRNA to the cytosol.[109, 239] mRNA plays a dual role in encoding for the production of antigen while also behaving as an adjuvant, though many current systems use modified nucleosides with decreased immunostimulatory capacity.[108, 109] The lipid composition plays an important but poorly understood role in the resultant immune response and remains an active area of research.[15, 109] Alternative to lipid-based systems, polymersomes and

polymeric micelles can be prepared that allow greater synthetic control over the molecular architecture and can confer stimuli-responsive behavior to the delivery system.[240] Dowling and Scott *et al*.[241] synthesized a series of poly(ethylene glycol-*b*-propylene sulfide) polymersome-based vaccines loaded with a small-molecule TLR8 adjuvant and antigen. They compare the effects of different polymersome size and antigen loads on immunogenicity of the polymersome-based vaccines relative to live attenuated *Bacillus Calmette-Guérin* (BCG) vaccine.[241] Maximum innate and adaptive immune responses are achieved with the polymersomes when physicochemical properties and antigen load are matched to the properties of the live attenuated virus, providing further design principles for next-generation therapies.

In contrast to self-assembled systems, chemically irregular non-covalent formulations can be achieved by nanoprecipitation or *in-situ* hydrogel formation. Nanoprecipitation involves rapid transfer of cargo from a good solvent (often methanol or dimethyl sulfoxide) to a bad solvent (such as aqueous phosphate buffer) via dialysis or microfluidic mixing. As an example of this strategy, the Esser-Kahn lab has synthetized a poly(orthoester) scaffold which assembles by nanoprecipitation with a heterodimeric TLR2/6 and TLR7 agonist and antigen.[242] When the resultant ~50 nm constructs are administered as a cancer immunotherapy to mice bearing an aggressive B16.F10 melanoma, complete remission of the tumor is achieved.[242] This formulation furthermore reduced systemic side effects relative to soluble TLR2/6 and TLR7 agonists, likely by prolonging bioavailability relative to the soluble formulation.[62, 242] Nanoprecipitation is a powerful approach to encapsulate large quantities of immunogenic materials and deliver them to specific cell subsets; however, it is limited by solvent compatibility of the cargo needed for successful nanoaggregate formation.[62] Alternatively, the solvent compatibility requirement can be eliminated entirely by encapsulating cargo in hydrogels.[243] In a recent example applied to vaccine delivery, the Appel lab has synthesized a polymer-nanoparticle hydrogel formulation comprised of dodecyl-modified hydroxypropyl methylcellulose (C12-HPMC) loaded with poly(ethylene glycol-*b*-lactic acid) (PEG-PLA) nanoparticles.[85] This system is desirable because it can be formulated with both

hydrophilic and hydrophobic cargo and injected through a syringe on account of its shear thinning behavior. The hydrogels, when formulated with a hydrophilic protein antigen and a hydrophobic TLR3 agonist, displayed a depot effect at the injection site for more than one week and enhanced antibody responses 90 d after injection relative to a soluble formulation.[85] Such delayed release formulations could enhance vaccine compliance and accessibility, but tuning formulations to control release over relevant timescales remains challenging and an active area of research.[244]

Synthetic Polymers with Immunostimulatory Capacity. More recently, it has become appreciated that innately immunostimulatory polymers can be used to alter the immune response. The prevailing theory of pattern recognition supposes that the immune system responds to PAMPs and DAMPs. Many biologically derived polymers, such as carbohydrates and nucleotides, activate these receptors and can be formulated with antigenic cargo to facilitate an immune response. Some examples of immunostimulatory polymers derived from biology include CpG oligodeoxynucleotide, mannose, β-glucan, and chitosan – more details about the modes of action and therapeutic examples of these polymers are discussed in Weiss, *et al*.[1] While synthetic polymers (such as (meth)acrylamides and (meth)acrylates) were not designed with the expressed goal of activating such systems, recent studies found that polymer coils retain physicochemical properties and/or structural motifs that can allow them to activate PRRs to induce an immune response. As PRR ligation is better understood at the molecular level and polymers of increasing complexity can be facilely prepared, rational design could be employed to prepare polymers that interact with biological receptors to induce immunostimulatory activity in a controlled manner.[245] If achieved, synthetic (i.e., non-biologically derived or inspired) polymers that bind PRRs (or otherwise stimulate innate immunity) would be advantageous over conventional PRR agonists on account of their relative low cost, high tunability, and facile compatibility with existing vaccine or immunotherapy formulations. Indeed, **Section 1.5** already described how polymers and nanoparticles can activate the NLRP3 inflammasome via modulating cellular ion fluxes and/or lysosomal integrity. In a different example, recent work by Jinming Gao's laboratory has shown

that a synthetic block co-polymer, poly[(ethylene glycol)-*b*-(2-(hexamethyleneimino)ethyl methacrylate)] (PC7A), can bind the Stimulator of Interferon Genes (STING) to induce robust interferon production.[245-247] In this work, it was shown that PC7A can access the cytosol and bind a non-competitive site on both the mouse and human STING proteins. PC7A can therefore be used in combination with 2'-3' cGAMP or other small molecule STING agonists for dual STING-targeted therapy. The polymer was further demonstrated to have robust efficacy for the treatment of multiple tumor models (**Figure 1.9**). Additional screening of other cyclic amine methacrylates by the Gao group has shown that innate immune activation induced by PC7A is unique to the 7-membered ring structure,[246] highlighting the specificity which will be required for future non-biological polymeric agonists. Overall, polymers hold great potential for the modulation of immune responses, and advances in high throughput strategies (as discussed in **Section 1.7**) will only serve to further increase the rate of progress in this field.

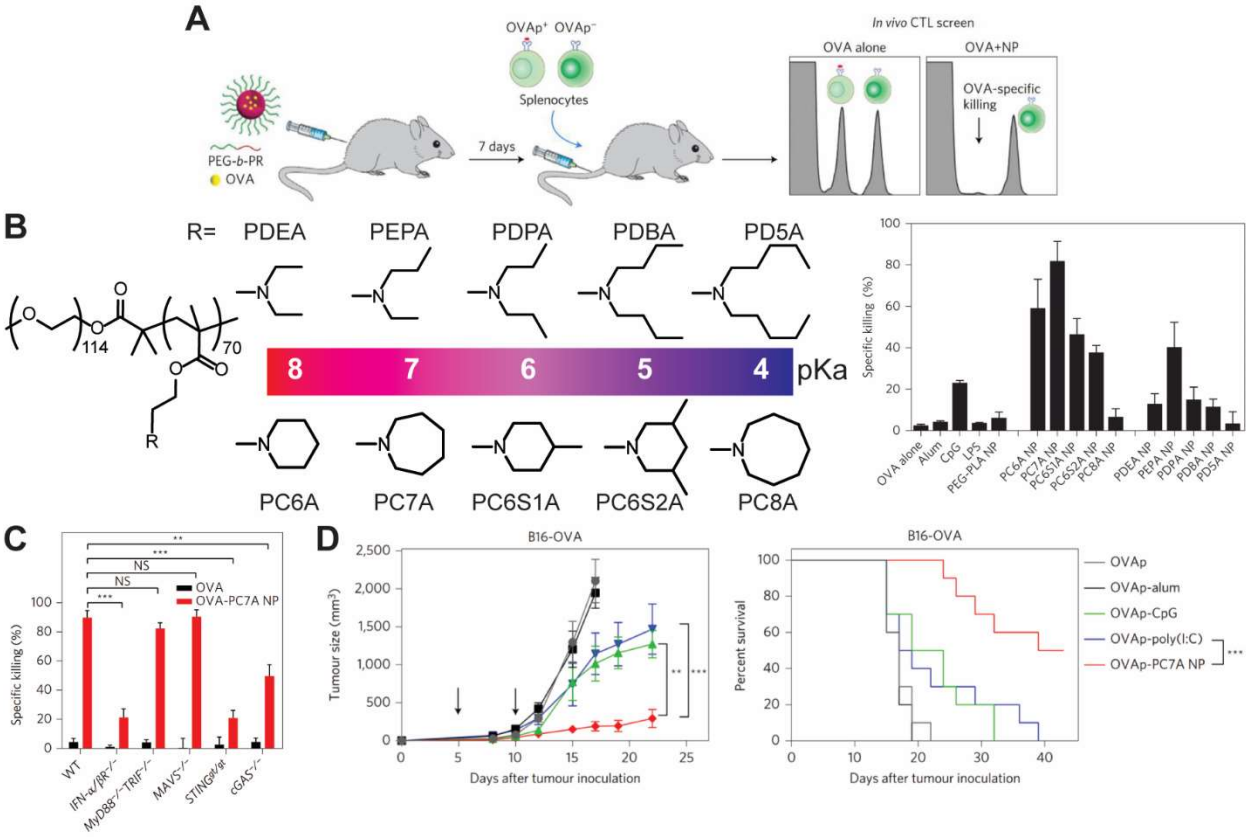

Figure 1.9: Synthesis and characterization of a STING-activating nanovaccine. (A) Schematic representation and screening method used to determine OVA-specific T cell-mediated killing of various cyclic amine nanoparticles loaded with OVA. (B) Efficacy of various cyclic amine nanoparticles or controls screened identified PC7A as an optimal adjuvant candidate. (C) Repeat of screening experiments in STING-, cGAS-, or IFN-α/β receptor-deficient mice identify a role of STING in PC7A nanovaccine efficacy. (D) Therapeutic vaccination with PC7A nanovaccine is shown to slow growth of an aggressive B16-OVA melanoma. Reprinted from (1); copyright 2022 ACS.

1.9 Cellulose Nanocrystals as Tools for Drug Delivery.

In the design of a polymer-drug systems, materials that are (1) lower cost, (2) biologically compatible, and (3) chemically tunable are of significant interest to stabilize cargo and facilitate their delivery. Synthetic polymers including poly(ethylene glycol) (PEG) and poly(vinylpyrrolidone) (PVP) have been used as excipients for more than fifty years, but there is now national security and public health interest in designing bio-derived alternatives to these petroleum-based products. In addition to their lower cost and environmentally friendly synthesis, biologically derived

materials have been shown to interact more compatibly with the immune system than their synthetic counterparts, inducing a wound healing niche rather than a pro-inflammatory niche.[248]

One attractive biomaterial for use in excipients and other biomedical applications is cellulose. Cellulose is a β(1→4)-linked D-glucose polymer found in many plants and some animals. It is comprised of highly crystalline domains, referred to as cellulose nanocrystals (CNCs) (sometimes also referred to as nanocellulose or cellulose nanowhiskers) hierarchically organized within amorphous cellulose to afford structural rigidity (**Figure 1.10A**).[249-251] CNCs can be isolated from bulk cellulose via hydrolysis of the amorphous regions to achieve mechanically rigid, rodlike materials with a length of 50-5,000 nm. The length and aspect ratio (*e.g.*, length-to-width ratio) are dependent on the biosource (**Figure 1.10B**).[250-252] Various acids have been employed for hydrolysis to yield materials with C6 hydroxyl (CNC-OH), sulfate half-ester (CNC-OSO_3^-), or phosphate half-ester (CNC-OPO_3H^-) functional groups. While CNC-OH containing a C6 hydroxyl is colloidally unstable, it can be oxidized with 2,2,6,6-tetramethylpiperidine-1-oxyl (TEMPO) to yield water-dispersible crystals with carboxylate groups at the C6 site (CNC-COO^-).[253] In contrast to many inorganic nanorods, CNC-OSO_3^-, CNC-OPO_3H^-, and CNC-COO^- are dispersible in water and can be chemically functionalized using chemistries at the C2, C3, or C6 positions.[253-255] As a result of their chemical tunability and material properties, CNCs have found use in a breadth of systems including polymer composites, hydrogels, and stabilizers. While the many applications of CNCs are outside the scope of this thesis, excellent reviews are available.[249-251]

A

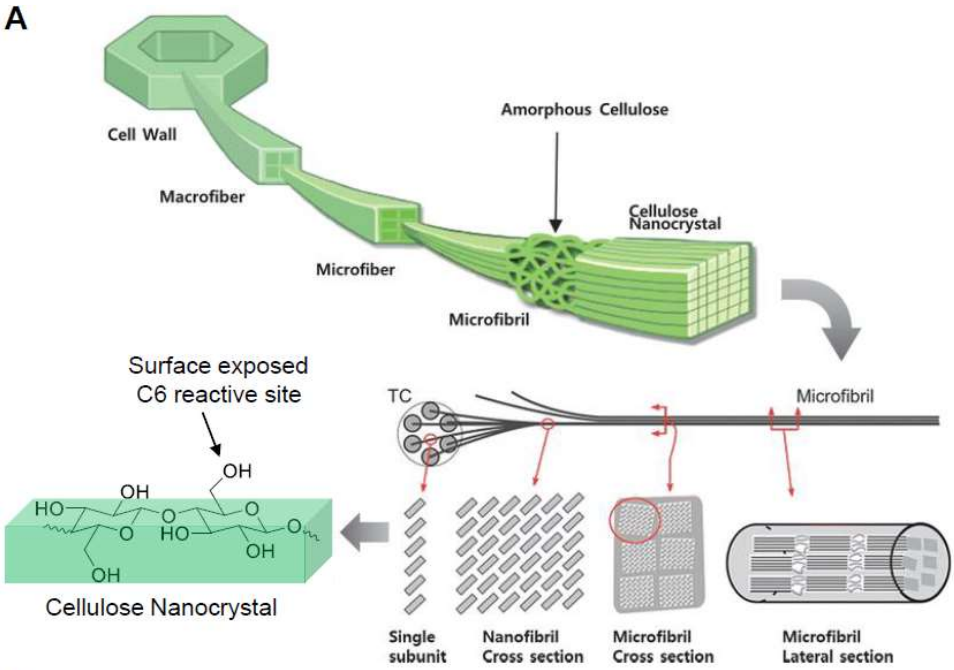

B

Source	Length	Aspect Ratio
Lyocell	25-100 nm	1-2
Cotton	75-150 nm	10-15
Wood	100-200 nm	10-25
Miscanthus giganteus	150-300 nm	50-75
Agave sisalana	100-500 nm	50-100
Tunicate	500-3000 nm	>75

Figure 1.10: Overview of cellulose nanocrystalline structure. A) Cellulose forms a hierarchical structure in the cell walls of plants to provide structural rigidity. CNCs are the rigid units that comprise these macromolecular constructs. Reactions can take place at exposed C6 hydroxyl groups without disrupting the integrity of the crystallinity. Figure adapted from (256). B) Length and aspect ratio of CNCs from various biosources.[250-252]

Recently, the material properties of CNCs have facilitated a growing interest in their use as biomaterials for applications in drug delivery, tissue regeneration, and antimicrobial coatings. In many ways, this field was foreshadowed by Lin and Dufresne, who in 2014, wrote a pioneering article discussing the potential of CNCs for various biological applications.[249] Since this article was first published, this potential has been realized in many notable publications. De France *et al*. reported the development of a shear thinning, injectable CNC—poly(oligoethylene glycol ethyl ether methacrylate) (POEGMA) hydrogel that can retain cargo at the injection site following subcutaneous injection for slow release.[257] The mechanical and charge properties of this hydrogel

can be tuned by altering the POEGMA component, allowing the delivery of diverse small molecule and biomacromolecular cargoes.[257] In an alternative example, Nguyen *et al.* report the design of a CNC—poly(vinyl acetate) (PVAc) composite material for use as an intracortical recording probe.[258] Traditionally, materials used for this application are rigid and have a large degree of mechanical mismatch with brain tissue, resulting in inflammation. The CNC—PVAc composite afforded more similar mechanical properties to the brain and reduced neuroinflammatory side effects following injection.[258] In this system, the CNCs provided sufficient mechanical rigidity to facilitate site-specific injection, while the PVAc provided a softer matrix to facilitate healing. Finally, recent work in the Rowan group has explored the use of CNC-based latexes for application as sweat-wicking liners in prosthetic limbs (unpublished). Despite the promise of these examples, many other reports of CNCs in biomedicine lack advantages relative to other, better-established materials. The advancement of CNC-based tools for biomedicine will require careful consideration of the advantages and disadvantages of CNCs and their chemistry to provide clinical benefit.

Despite the interest in CNCs for biomedical applications, few studies have interrogated the biocompatibility of these materials. While cellulose, as a biologically derived carbohydrate, is assumed to interact favorably with biological systems, its high aspect ratio and charge properties may pose problems for biological interrogation. *In-vitro*, early cytotoxicity studies by the Roman,[259] Chinga-Carrasco,[260] and Um,[261] research groups found that CNCs were generally well-tolerated at clinically relevant doses in a variety of cell lines. With that said, derivatization of CNCs can alter these results. One study by Sunasee *et al*. found that CNCs functionalized with cationic groups induced reactive oxygen production to activate the NLRP3 inflammasome,[262] while a second by Lin *et al*. found that cationic CNCs coated with alginate were both biocompatible and effective in delivering small molecule cargo.[263] The results of *in-vivo* biocompatibility experiments have been even less conclusive. A study by Yanamala *et al.* found that inhaled CNCs induced an acute inflammatory response characteristic of other rod-like materials (like silica or asbestos),[264] and a follow-up study found that this pulmonary response had negative effects on the reproductive

system of male mice.[265] Though concerning, these effects can be mitigated by using CNCs in a slurry or suspension. Wang *et al.* found that CNCs injected intraperitoneally with an antigen exhibited a length-dependent adjuvant effect, which they hypothesize to result from NLRP3 inflammasome activation.[266] However, the dose of CNC (2 mg) and antigen (400 μg) used in this study are physiologically irrelevant, weakening the conclusions that can be made from this study. In contrast, Colombo *et al.* found that CNCs induced no adverse immunological effects when administered via oral or topical routes.[267] In this study, the biodistribution of CNCs after oral administration was assessed, and it was found that CNCs localized over one week to the liver and spleen. It is currently unknown what the longer term (>1 month) consequences of CNC administration are *in-vivo*. Overall, a more comprehensive characterization of the immune responses of CNCs must be conducted if these materials are to be translated to the clinic.

1.10 Bioconjugate Chemistry in Innate Immunity and Vaccination.

Bioconjugates, such as antibody-drug conjugates, protein-polymer constructs, and proteolysis targeting chimeras (PROTACs), are emerging as critical tools in biomedicine. Bioconjugates are broadly defined as materials in which two or more biomolecule(s) (protein, nucleotide, or carbohydrate) and/or small molecule drug(s) are covalently linked together. These systems afford enhanced co-localization of cargo, targeting to specific cell and organelle subsets, solubility control (via changing the chemical linker), and temporal release profiles (via introducing biodegradable functionality within the linker). Advances in fast, selective, and bioorthogonal chemistries – termed “click” chemistries by Sharpless in 1998[268] – in the past twenty years have made the synthesis of these materials accessible to a wide variety of scientists for a breadth of approaches. The first click reactions widely employed for bioconjugation in the literature were the copper-promoted or strain-promoted azide-alkyne [3+2] cycloaddition reactions,[268, 269] but they have since expanded to describe a wide a variety of bio-orthogonal reactions. Selected click chemistries are presented in **Table 1.4** and reviewed in greater depth in texts and reviews.[270-272]

Name/Abbreviation	Reactive Group 1	Reactive Group 2	Catalyst
CuAAC	Azide	Alkyne	Cu(I)
SPAAC	Azide	Cyclooctyne	None
SPANC	Azide	Nitrone	None
Thiol-Maleimide	Thiol	Maleimide	pH > 7
Thiol-Alkene	Thiol	Alkene	*hv*
IEDDA	Tetrazine	trans-Cyclooctene	None
Peptide coupling	Amine	Activated ester	None
Hydrazone/Oxime click	Hydrazone/Oxime	Ketone/Aldehyde	pH > 7

Table 1.4: List of "click" and click-like reactions commonly used in the synthesis of bioconjugates. CuAAC = Copper-catalyzed azide-alkyne cycloaddition, SPAAC = Strain-promoted azide-alkyne cycloaddition, SPANC = Strain-promoted azide-nitrone cycloaddition, IEDDA = Inverse electron demand Diels Alder.

Conjugates vaccines comprised of two or more antigens linked together have been FDA-approved and show enormous clinical potential.[273] There are two key advantages of such systems. First, conjugate vaccines comprised of a weakly immunogenic antigen conjugated to a more strongly immunogenic antigen can increase immunogenicity, especially in the case of carbohydrate-based vaccines. Indeed, several FDA-approved *Haemophilus influenzae type B* (Hib) vaccines contain the Hib polysaccharide outer capsule conjugated to tetanus toxoid antigen to enhance immunogenicity. Second, conjugate vaccines can allow conjugation of many different antigens to a single carrier to increase the breadth of protection against pathogens with high mutation rates or diverse antigenic profiles.[273] Polyvalent pneumococcus and meningococcus vaccines comprised of multiple antigens conjugated to a single carrier are FDA-approved and have shown remarkable breadth of potential. Currently limitations in the design of conjugate vaccines are poor control over chemical conjugation to antigens and challenging purification.

As an alternative to multiple antigen systems, conjugate vaccines having immunogenic haptens or PRR agonists conjugated to an antigen can also be used for vaccination. Haptens are small molecules that reacts with a specific antibody when bound to a protein carrier. Hapten-protein conjugate vaccines can combat challenges in public heath such as opioid dependency.[274]

At least one Phase I/II clinical trial is in progress wherein an opioid agonist is conjugated to a protein carrier and used in adjuvanted vaccines (NCT04458545), and a bevy of exciting pre-clinical studies using similar strategies have been published in the past five years.[275-277] The premise of this technology is that surface conjugation to a protein carrier allows the body to develop antibodies against the hapten of interest, preventing the hapten from exerting its effects on the body (in the case of opiates, blocking the "high" that results in long-term dependence).[274] Antigen-adjuvant conjugates hold promise for different reasons. Here, conjugating an intracellular PRR agonist to an antigen helps ensure that the same cells that receive antigen become activated by PRR binding – better recapitulating the natural response to a pathogen and reducing off-target effects.[278] With this technology, the immune response can be localized to APCs, and the dose of adjuvant needed can be reduced. Several pre-clinical examples of antigen-adjuvant conjugates comprised of PRR agonists have been reported in the literature, but a key challenge for clinical translation is controlling the site of conjugation.[279-281] High levels of adjuvant conjugation were reported to result in the formation of poorly immunogenic aggregates.[280] Uncontrolled conjugation can block immunodominant epitopes or create inhomogeneities in structure that result in spurious side effects or difficulties in regulatory approval. The advent of more controlled conjugation strategies, such as cell-free expression of proteins containing non-native amino acids[282] or development of more specific N- or C-terminal protein conjugation techniques,[283] will be critical in allowing these technologies to translate from the bench to the clinic.

1.11 Dissertation Scope.

The remaining chapters will discuss a variety of approaches toward using macromolecular chemistry to enhance immune responses in vaccines and immunotherapies. Macromolecules provide chemical tools to control the spatiotemporal delivery of biomolecules within the cell and body writ large. The overarching goal of this thesis is to rationally design biomacromolecules that can manipulate these cellular and biological interactions to inform immunological responses. This

is achieved in multiple forms, including (1) the design of polymers that induce cell membrane or lysosomal rupture to manipulate cell death, (2) the formulation of small molecule inflammasome activating drugs into liposomal formulation to target the draining lymph node, and (3) the conjugation of antigens and adjuvants in controlled ratios to achieve co-delivery and reduce off-target effects. Specific information discussed in each chapter is outlined below.

Chapter 2 will discuss high throughput synthesis and screening approaches toward the design of cationic polymers that activate the NLRP3 inflammasome. By synthesizing a library of polymers varied parametrically in composition and probing their immunostimulatory activity in-vitro and in-vivo, mechanistic insights toward the design of toxic and immunogenic materials were elucidated. This work will have broad implications for the design of biomaterials for drug and gene delivery, medical device, and antimicrobial applications.

Chapter 3 will discuss the use of polymers that activate the NLRP3 inflammasome as adjuvants. It was envisioned that the screening data generated in Chapter 2 could be applied toward the design of tunable polymeric adjuvants for vaccination and immunotherapy. Ultimately, these approaches were unsuccessful, but various design strategies and technical considerations are presented that could benefit future research in this area.

Chapter 4 will discuss the identification, formulation, and application of small molecule inflammasome adjuvants. Having been unsuccessful in the design of tunable polymeric adjuvants for vaccination in Chapter 3, small molecules that induce high levels of IL-1β were targeted. Using high throughput screening data generated by others in the Esser-Kahn laboratory, a novel class of IL-1β producing compounds were identified. These compounds' mechanisms of action were explored, and they were formulated as alternatives to saponin adjuvants for use in vaccination.

Chapter 5 discusses a long-standing collaboration between the Esser-Kahn laboratory and Vaxcyte, Inc., a biotechnology corporation with a proprietary cell-free protein synthesis (CFPS) technology that allows for incorporation of azides at specific sites within expressed proteins. In this collaboration, antigen-adjuvant conjugates targeting Toll-like receptors 7 and 9

(TLR7 and TLR9) are synthesized and used in vaccination. This work demonstrates application of the CFPS platform toward antigen-adjuvant conjugation.

Chapter 6 will discuss the immunocompatibility of various cellulose nanocrystals (CNCs) and efforts toward their use in peptide-based vaccines. CNCs were isolated from various biosources, functionalized to confer different charge characteristics, and purified to remove bacterial endotoxins on their surface. The resulting materials' biocompatibilities were assayed in-vitro and in-vivo, providing design principles for future applications of these materials.

1.12 References.

1. Weiss, A. M.; Hossainy, S.; Rowan, S. J.; Hubbell, J. A.; Esser-Kahn, A. P., Immunostimulatory Polymers as Adjuvants, Immunotherapies, and Delivery Systems. *Macromolecules* **2022,** *55* (16), 6913-6937.

2. Murphy, K., *Janeway's Immunobiology*. 8 ed.; Garland Science: New York, NY, 2012.

3. Pulendran, B.; Ahmed, R., Immunological mechanisms of vaccination. *Nat Immunol* **2011,** *12* (6), 509-517.

4. Coffman, R. L.; Sher, A.; Seder, R. A., Vaccine adjuvants: putting innate immunity to work. *Immunity* **2010,** *33* (4), 492-503.

5. Iwasaki, A.; Medzhitov, R., Control of adaptive immunity by the innate immune system. *Nat Immunol* **2015,** *16* (4), 343-353.

6. Demaria, O.; Cornen, S.; Daeron, M.; Morel, Y.; Medzhitov, R.; Vivier, E., Harnessing innate immunity in cancer therapy. *Nature* **2019,** *574* (7776), 45-56.

7. Swain, S. L.; McKinstry, K. K.; Strutt, T. M., Expanding roles for CD4(+) T cells in immunity to viruses. *Nat Rev Immunol* **2012,** *12* (2), 136-148.

8. Defrance, T.; Taillardet, M.; Genestier, L., T cell-independent B cell memory. *Curr Opin Immunol* **2011,** *23* (3), 330-336.

9. Stavnezer, J.; Guikema, J. E.; Schrader, C. E., Mechanism and regulation of class switch recombination. *Annu Rev Immunol* **2008,** *26*, 261-292.

10. Reed, S. G.; Orr, M. T.; Fox, C. B., Key roles of adjuvants in modern vaccines. *Nat Med* **2013,** *19* (12), 1597-608.

11. Tom, J. K.; Albin, T. J.; Manna, S.; Moser, B. A.; Steinhardt, R. C.; Esser-Kahn, A. P., Applications of Immunomodulatory Immune Synergies to Adjuvant Discovery and Vaccine Development. *Trends Biotechnol* **2018**, *37* (4), 373-388.

12. Brown, G. D.; Willment, J. A.; Whitehead, L., C-type lectins in immunity and homeostasis. *Nat Rev Immunol* **2018,** *18* (6), 374-389.

13. Cunningham, A. L.; Lal, H.; Kovac, M.; Chlibek, R.; Hwang, S. J.; Diez-Domingo, J.; Godeaux, O.; Levin, M. J.; McElhaney, J. E.; Puig-Barbera, J.; Vanden Abeele, C.; Vesikari, T.; Watanabe, D.; Zahaf, T.; Ahonen, A.; Athan, E.; Barba-Gomez, J. F.; Campora, L.; de Looze, F.; Downey, H. J.; Ghesquiere, W.; Gorfinkel, I.; Korhonen, T.; Leung, E.; McNeil, S. A.; Oostvogels, L.; Rombo, L.; Smetana, J.; Weckx, L.; Yeo, W.; Heineman, T. C.; Group, Z. O. E. S., Efficacy of the Herpes Zoster Subunit Vaccine in Adults 70 Years of Age or Older. *N Engl J Med* **2016,** *375* (11), 1019-1032.

14. Didierlaurent, A. M.; Laupeze, B.; Di Pasquale, A.; Hergli, N.; Collignon, C.; Garcon, N., Adjuvant system AS01: helping to overcome the challenges of modern vaccines. *Expert Rev Vaccines* **2017,** *16* (1), 55-63.

15. Tahtinen, S.; Tong, A. J.; Himmels, P.; Oh, J.; Paler-Martinez, A.; Kim, L.; Wichner, S.; Oei, Y.; McCarron, M. J.; Freund, E. C.; Amir, Z. A.; de la Cruz, C. C.; Haley, B.; Blanchette, C.; Schartner, J. M.; Ye, W.; Yadav, M.; Sahin, U.; Delamarre, L.; Mellman, I., IL-1 and IL-1ra are key regulators of the inflammatory response to RNA vaccines. *Nat Immunol* **2022,** *23* (4), 532-542.

16. Li, C.; Lee, A.; Grigoryan, L.; Arunachalam, P. S.; Scott, M. K. D.; Trisal, M.; Wimmers, F.; Sanyal, M.; Weidenbacher, P. A.; Feng, Y.; Adamska, J. Z.; Valore, E.; Wang, Y.; Verma, R.; Reis, N.; Dunham, D.; O'Hara, R.; Park, H.; Luo, W.; Gitlin, A. D.; Kim, P.; Khatri, P.; Nadeau, K. C.; Pulendran, B., Mechanisms of innate and adaptive immunity to the Pfizer-BioNTech BNT162b2 vaccine. *Nat Immunol* **2022,** *23* (4), 543-555.

17. RTS,S Clinical Trial Partnership, Efficacy and safety of RTS,S/AS01 malaria vaccine with or without a booster dose in infants and children in Africa: final results of a phase 3, individually randomised, controlled trial. *The Lancet* **2015,** *386* (9988), 31-45.

18. Dowling, D. J., Recent Advances in the Discovery and Delivery of TLR7/8 Agonists as Vaccine Adjuvants. *Immunohorizons* **2018,** *2* (6), 185-197.

19. Jackson, S.; Lentino, J.; Kopp, J.; Murray, L.; Ellison, W.; Rhee, M.; Shockey, G.; Akella, L.; Erby, K.; Heyward, W. L.; Janssen, R. S.; Group, H. B. V. S., Immunogenicity of a two-dose investigational hepatitis B vaccine, HBsAg-1018, using a toll-like receptor 9 agonist adjuvant compared with a licensed hepatitis B vaccine in adults. *Vaccine* **2018,** *36* (5), 668-674.

20. Platanitis, E.; Decker, T., Regulatory Networks Involving STATs, IRFs, and NFkappaB in Inflammation. *Front Immunol* **2018,** *9*, 2542.

21. Hagan, T.; Gerritsen, B.; Tomalin, L. E.; Fourati, S.; Mule, M. P.; Chawla, D. G.; Rychkov, D.; Henrich, E.; Miller, H. E. R.; Diray-Arce, J.; Dunn, P.; Lee, A.; Human Immunology Project; Levy, O.; Gottardo, R.; Sarwal, M. M.; Tsang, J. S.; Suarez-Farinas, M.; Sekaly, R. P.; Kleinstein, S. H.; Pulendran, B., Transcriptional atlas of the human immune response to 13 vaccines reveals a common predictor of vaccine-induced antibody responses. *Nat Immunol* **2022**, *23* (12), 1788-1798.

22. Bachmann, M. F.; Jennings, G. T., Vaccine delivery: a matter of size, geometry, kinetics and molecular patterns. *Nat Rev Immunol* **2010,** *10* (11), 787-796.

23. Zhu, J.; Yamane, H.; Paul, W. E., Differentiation of effector CD4 T cell populations. *Annu Rev Immunol* **2010,** *28*, 445-489.

24. Hoebe, K.; Janssen, E.; Beutler, B., The interface between innate and adaptive immunity. *Nat Immunol* **2004,** *5* (10), 971-974.

25. Chen, L.; Flies, D. B., Molecular mechanisms of T cell co-stimulation and co-inhibition. *Nat Rev Immunol* **2013,** *13* (4), 227-242.

26. Barber, D. L.; Wherry, E. J.; Masopust, D.; Zhu, B.; Allison, J. P.; Sharpe, A. H.; Freeman, G. J.; Ahmed, R., Restoring function in exhausted CD8 T cells during chronic viral infection. *Nature* **2006,** *439* (7077), 682-687.

27. Leach, D. R.; Krummel, M. F.; Allison, J. P., Enhancement of antitumor immunity by CTLA-4 blockade. *Science* **1996,** *271* (5256), 1734-1736.

28. Spriggs, M. K.; Armitage, R. J.; Strockbine, L.; Clifford, K. N.; Macduff, B. M.; Sato, T. A.; Maliszewski, C. R.; Fanslow, W. C., Recombinant human CD40 ligand stimulates B cell proliferation and immunoglobulin E secretion. *J Exp Med* **1992,** *176* (6), 1543-1550.

29. Idriss, H. T.; Naismith, J. H., TNFa and the TNF receptor superfamily: Structure-function relationship(s). *Microsc Res Tech* **2000,** *50* (3), 184-195.

30. Spellberg, B.; Edwards, J. E., Jr., Type 1/Type 2 immunity in infectious diseases. *Clin Infect Dis* **2001,** *32* (1), 76-102.

31. Dinarello, C. A., Immunological and inflammatory functions of the interleukin-1 family. *Annu Rev Immunol* **2009,** *27*, 519-550.

32. Williams, M. A.; Tyznik, A. J.; Bevan, M. J., Interleukin-2 signals during priming are required for secondary expansion of CD8+ memory T cells. *Nature* **2006,** *441* (7095), 890-893.

33. Kaur, S.; Bansal, Y.; Kumar, R.; Bansal, G., A panoramic review of IL-6: Structure, pathophysiological roles and inhibitors. *Bioorg Med Chem* **2020,** *28* (5), 115327.

34. Ouyang, W.; Rutz, S.; Crellin, N. K.; Valdez, P. A.; Hymowitz, S. G., Regulation and functions of the IL-10 family of cytokines in inflammation and disease. *Annu Rev Immunol* **2011,** *29*, 71-109.

35. Korn, T.; Bettelli, E.; Oukka, M.; Kuchroo, V. K., IL-17 and Th17 Cells. *Annu Rev Immunol* **2009,** *27*, 485-517.

36. Petrovsky, N., Comparative Safety of Vaccine Adjuvants: A Summary of Current Evidence and Future Needs. *Drug Saf* **2015,** *38* (11), 1059-74.

37. Pulendran, B.; P, S. A.; O'Hagan, D. T., Emerging concepts in the science of vaccine adjuvants. *Nat Rev Drug Discov* **2021,** *20* (6), 454-475.

38. Burton, D. R.; Ahmed, R.; Barouch, D. H.; Butera, S. T.; Crotty, S.; Godzik, A.; Kaufmann, D. E.; McElrath, M. J.; Nussenzweig, M. C.; Pulendran, B.; Scanlan, C. N.; Schief, W. R.; Silvestri, G.; Streeck, H.; Walker, B. D.; Walker, L. M.; Ward, A. B.; Wilson, I. A.; Wyatt, R., A Blueprint for HIV Vaccine Discovery. *Cell Host Microbe* **2012,** *12* (4), 396-407.

39. Ruiz, S.; Wolfe, D. N., Vaccination against Q fever for biodefense and public health indications. *Front Microbiol* **2014,** *5*, 726.

40. Muhanguzi, D.; Ndekezi, C.; Nkamwesiga, J.; Kalayou, S.; Ochwo, S.; Vuyani, M.; Kimuda, M. P., Anti-Tick Vaccines: Current Advances and Future Prospects. In *Vaccine Design: Methods and Protocols, Volume 2. Vaccines for Veterinary Diseases*, Thomas, S., Ed. Springer US: New York, NY, 2022; pp 253-267. DOI: 10.1007/978-1-0716-1888-2_15

41. Steere, A. C.; Strle, F.; Wormser, G. P.; Hu, L. T.; Branda, J. A.; Hovius, J. W. R.; Li, X.; Mead, P. S., Lyme borreliosis. *Nat Rev Dis Primers* **2016,** *2* (1), 16090.

42. Hotez, P. J.; Molyneux, D. H.; Fenwick, A.; Kumaresan, J.; Sachs, S. E.; Sachs, J. D.; Savioli, L., Control of neglected tropical diseases. *N Engl J Med* **2007,** *357* (10), 1018-27.

43. Olotu, A.; Fegan, G.; Wambua, J.; Nyangweso, G.; Leach, A.; Lievens, M.; Kaslow, D. C.; Njuguna, P.; Marsh, K.; Bejon, P., Seven-Year Efficacy of RTS,S/AS01 Malaria Vaccine among Young African Children. *N Engl J Med* **2016,** *374* (26), 2519-2529.

44. Schrager, L. K.; Vekemens, J.; Drager, N.; Lewinsohn, D. M.; Olesen, O. F., The status of tuberculosis vaccine development. *Lancet Infect Dis* **2020,** *20* (3), 28-37.

45. Rupprecht, C. E.; Nagarajan, T.; Ertl, H., Current Status and Development of Vaccines and Other Biologics for Human Rabies Prevention. *Expert Rev Vaccines* **2016,** *15* (6), 731-749.

46. Clark, A.; Wolfe, D. N., Current State of Anthrax Vaccines and Key R&D Gaps Moving Forward. *Microorganisms* **2020,** *8* (5), 651.

47. Glenny, A. T. P., C. G.; Waddington, H.; Wallace, U., The antigenic value of toxoid precipitated by potassium alum. *J Pathol Bacteriol* **1926,** *29*, 38-45.

48. Oleszycka, E.; Lavelle, E. C., Immunomodulatory properties of the vaccine adjuvant alum. *Curr Opin Immunol* **2014,** *28*, 1-5.

49. O'Hagan, D. T.; van der Most, R.; Lodaya, R. N.; Coccia, M.; Lofano, G., "World in motion" - emulsion adjuvants rising to meet the pandemic challenges. *NPJ Vaccines* **2021,** *6* (1), 158.

50. O'Hagan, D. T.; Ott, G. S.; De Gregorio, E.; Seubert, A., The mechanism of action of MF59 - an innately attractive adjuvant formulation. *Vaccine* **2012,** *30* (29), 4341-8.

51. Garcon, N.; Chomez, P.; Van Mechelen, M., GlaxoSmithKline Adjuvant Systems in vaccines: concepts, achievements and perspectives. *Expert Rev Vaccines* **2007,** *6* (5), 723-39.

52. Gavin, A. L.; Hoebe, K.; Duong, B.; Ota, T.; Martin, C.; Beutler, B.; Nemazee, D., Adjuvant-enhanced antibody responses in the absence of toll-like receptor signaling. *Science* **2006,** *314* (5807), 1936-1938.

53. Franchi, L.; Nunez, G., The Nlrp3 inflammasome is critical for aluminium hydroxide-mediated IL-1beta secretion but dispensable for adjuvant activity. *Eur J Immunol* **2008,** *38* (8), 2085-2089.

54. McKee, A. S.; Munks, M. W.; MacLeod, M. K.; Fleenor, C. J.; Van Rooijen, N.; Kappler, J. W.; Marrack, P., Alum induces innate immune responses through macrophage and mast cell sensors, but these sensors are not required for alum to act as an adjuvant for specific immunity. *J Immunol* **2009,** *183* (7), 4403-4414.

55. Flach, T. L.; Ng, G.; Hari, A.; Desrosiers, M. D.; Zhang, P.; Ward, S. M.; Seamone, M. E.; Vilaysane, A.; Mucsi, A. D.; Fong, Y.; Prenner, E.; Ling, C. C.; Tschopp, J.; Muruve, D. A.; Amrein, M. W.; Shi, Y., Alum interaction with dendritic cell membrane lipids is essential for its adjuvanticity. *Nat Med* **2011,** *17* (4), 479-487.

56. Hutchison, S.; Benson, R. A.; Gibson, V. B.; Pollock, A. H.; Garside, P.; Brewer, J. M., Antigen depot is not required for alum adjuvanticity. *FASEB J* **2012,** *26* (3), 1272-1279.

57. Hornung, V.; Bauernfeind, F.; Halle, A.; Samstad, E. O.; Kono, H.; Rock, K. L.; Fitzgerald, K. A.; Latz, E., Silica crystals and aluminum salts activate the NALP3 inflammasome through phagosomal destabilization. *Nat Immunol* **2008,** *9* (8), 847-856.

58. Spreafico, R.; Ricciardi-Castagnoli, P.; Mortellaro, A., The controversial relationship between NLRP3, alum, danger signals and the next-generation adjuvants. *Eur J Immunol* **2010,** *40* (3), 638-642.

59. Seubert, A.; Calabro, S.; Santini, L.; Galli, B.; Genovese, A.; Valentini, S.; Aprea, S.; Colaprico, A.; D'Oro, U.; Giuliani, M. M.; Pallaoro, M.; Pizza, M.; O'Hagan, D. T.; Wack, A.; Rappuoli, R.; De Gregorio, E., Adjuvanticity of the oil-in-water emulsion MF59 is independent of Nlrp3 inflammasome but requires the adaptor protein MyD88. *Proc Natl Acad Sci U S A* **2011,** *108* (27), 11169-11174.

60. Neumann, S.; Burkert, K.; Kemp, R.; Rades, T.; Rod Dunbar, P.; Hook, S., Activation of the NLRP3 inflammasome is not a feature of all particulate vaccine adjuvants. *Immunol Cell Biol* **2014,** *92* (6), 535-542.

61. Irvine, D. J.; Hanson, M. C.; Rakhra, K.; Tokatlian, T., Synthetic Nanoparticles for Vaccines and Immunotherapy. *Chem Rev* **2015,** *115* (19), 11109-11146.

62. Ulbrich, K.; Hola, K.; Subr, V.; Bakandritsos, A.; Tucek, J.; Zboril, R., Targeted Drug Delivery with Polymers and Magnetic Nanoparticles: Covalent and Noncovalent Approaches, Release Control, and Clinical Studies. *Chem Rev* **2016,** *116* (9), 5338-5431.

63. Sadtler, K.; Collins, J.; Byrne, J. D.; Langer, R., Parallel evolution of polymer chemistry and immunology: Integrating mechanistic biology with materials design. *Adv Drug Deliv Rev* **2020,** *156*, 65-79.

64. Reddy, S. T.; van der Vlies, A. J.; Simeoni, E.; Angeli, V.; Randolph, G. J.; O'Neil, C. P.; Lee, L. K.; Swartz, M. A.; Hubbell, J. A., Exploiting lymphatic transport and complement activation in nanoparticle vaccines. *Nat Biotechnol* **2007,** *25* (10), 1159-1164.

65. Wang, N.; Chen, M.; Wang, T., Liposomes used as a vaccine adjuvant-delivery system: From basics to clinical immunization. *J Control Release* **2019,** *303*, 130-150.

66. Mosquera, J.; Garcia, I.; Liz-Marzan, L. M., Cellular Uptake of Nanoparticles versus Small Molecules: A Matter of Size. *Acc Chem Res* **2018,** *51* (9), 2305-2313.

67. Munoz-Wolf, N.; Ward, R. W.; Hearnden, C. H.; Sharp, F. A.; Geoghegan, J.; O'Grady, K.; McEntee, C. P.; Shanahan, K. A.; Guy, C.; Bowie, A. G.; Campbell, M.; Roces, C. B.; Anderluzzi, G.; Webb, C.; Perrie, Y.; Creagh, E.; Lavelle, E. C., Non-canonical inflammasome activation mediates the adjuvanticity of nanoparticles. *Cell Rep Med* **2023**, *4* (1), 100899.

68. Champion, J. A.; Mitragotri, S., Role of target geometry in phagocytosis. *Proc Natl Acad Sci U S A* **2006,** *103* (13), 4930-4934.

69. Champion, J. A.; Mitragotri, S., Shape induced inhibition of phagocytosis of polymer particles. *Pharm Res* **2009,** *26* (1), 244-249.

70. Kumar, S.; Anselmo, A. C.; Banerjee, A.; Zakrewsky, M.; Mitragotri, S., Shape and size-dependent immune response to antigen-carrying nanoparticles. *J Control Release* **2015,** *220* (Pt A), 141-148.

71. Niikura, K.; Matsunaga, T.; Suzuki, T.; Kobayashi, S.; Yamaguchi, H.; Orba, Y.; Kawaguchi, A.; Hasegawa, H.; Kajino, K.; Ninomiya, T.; Ijiro, K.; Sawa, H., Gold nanoparticles as a vaccine platform: influence of size and shape on immunological responses in vitro and in vivo. *ACS Nano* **2013,** *7* (5), 3926-3938.

72. Kelly, S. H.; Cossette, B. J.; Varadhan, A. K.; Wu, Y.; Collier, J. H., Titrating Polyarginine into Nanofibers Enhances Cyclic-Dinucleotide Adjuvanticity in Vitro and after Sublingual Immunization. *ACS Biomat Sci Eng* **2021**, *7* (5), 1876-1888.

73. Liang, J.; Wang, H.; Ding, W.; Huang, J.; Zhou, X.; Wang, H.; Dong, X.; Li, G.; Chen, E.; Zhou, F.; Fan, H.; Xia, J.; Shen, B.; Cai, D.; Lan, P.; Jiang, H.; Ling, J.; Cheng, Z.; Liu, X.; Sun, J., Nanoparticle-enhanced chemo-immunotherapy to trigger robust antitumor immunity. *Sci Adv* **2020,** *6* (35), eabc3646.

74. Li, A. W.; Sobral, M. C.; Badrinath, S.; Choi, Y.; Graveline, A.; Stafford, A. G.; Weaver, J. C.; Dellacherie, M. O.; Shih, T. Y.; Ali, O. A.; Kim, J.; Wucherpfennig, K. W.; Mooney, D. J., A facile approach to enhance antigen response for personalized cancer vaccination. *Nat Mater* **2018,** *17* (6), 528-534.

75. Shen, C.; Li, J.; Zhang, Y.; Li, Y.; Shen, G.; Zhu, J.; Tao, J., Polyethylenimine-based micro/nanoparticles as vaccine adjuvants. *Int J Nanomedicine* **2017,** *12*, 5443-5460.

76. Anderson, D. G.; Akinc, A.; Hossain, N.; Langer, R., Structure/property studies of polymeric gene delivery using a library of poly(beta-amino esters). *Mol Ther* **2005,** *11* (3), 426-434.

77. Ulkoski, D.; Munson, M. J.; Jacobson, M. E.; Palmer, C. R.; Carson, C. S.; Sabirsh, A.; Wilson, J. T.; Krishnamurthy, V. R., High-Throughput Automation of Endosomolytic Polymers for mRNA Delivery. *ACS Appl Bio Mater* **2021,** *4* (2), 1640-1654.

78. Kauffman, K. J.; Webber, M. J.; Anderson, D. G., Materials for non-viral intracellular delivery of messenger RNA therapeutics. *J Control Release* **2016,** *240*, 227-234.

79. Vaine, C. A.; Patel, M. K.; Zhu, J.; Lee, E.; Finberg, R. W.; Hayward, R. C.; Kurt-Jones, E. A., Tuning innate immune activation by surface texturing of polymer microparticles: the role of shape in inflammasome activation. *J Immunol* **2013,** *190* (7), 3525-3532.

80. Oldenhuis, N. J.; Eldredge, A. C.; Burts, A. O.; Ryu, K. A.; Chung, J.; Johnson, M. E.; Guan, Z., Biodegradable Dendronized Polymers for Efficient mRNA Delivery. *ChemistrySelect* **2016,** *1* (15), 4413-4417.

81. Gong, N.; Zhang, Y.; Teng, X.; Wang, Y.; Huo, S.; Qing, G.; Ni, Q.; Li, X.; Wang, J.; Ye, X.; Zhang, T.; Chen, S.; Wang, Y.; Yu, J.; Wang, P. C.; Gan, Y.; Zhang, J.; Mitchell, M. J.; Li, J.; Liang, X. J., Proton-driven transformable nanovaccine for cancer immunotherapy. *Nat Nanotechnol* **2020,** *15* (12), 1053-1064.

82. Chen, B.; Yan, Y.; Yang, Y.; Cao, G.; Wang, X.; Wang, Y.; Wan, F.; Yin, Q.; Wang, Z.; Li, Y.; Wang, L.; Xu, B.; You, F.; Zhang, Q.; Wang, Y., A pyroptosis nanotuner for cancer therapy. *Nat Nanotechnol* **2022**, *17* (7), 788-798.

83. Kocak, G.; Tuncer, C.; Bütün, V., pH-Responsive polymers. *Polym Chem* **2017,** *8* (1), 144-176.

84. Song, C. C.; Du, F. S.; Li, Z. C., Oxidation-responsive polymers for biomedical applications. *J Mater Chem B* **2014,** *2* (22), 3413-3426.

85. Roth, G. A.; Gale, E. C.; Alcantara-Hernandez, M.; Luo, W.; Axpe, E.; Verma, R.; Yin, Q.; Yu, A. C.; Lopez Hernandez, H.; Maikawa, C. L.; Smith, A. A. A.; Davis, M. M.; Pulendran, B.; Idoyaga, J.; Appel, E. A., Injectable Hydrogels for Sustained Codelivery of Subunit Vaccines Enhance Humoral Immunity. *ACS Cent Sci* **2020,** *6* (10), 1800-1812.

86. Ajit, J.; Cassaidy, B.; Tang, S.; Solanki, A.; Chen, Q.; Shen, J.; Esser Kahn, A. P., Temporal Control of Trained Immunity via Encapsulated Release of β-Glucan Improves Therapeutic Applications. *Adv Healthc Mater* 2022, *11* (18), e2200819

87. Boopathy, A. V.; Mandal, A.; Kulp, D. W.; Menis, S.; Bennett, N. R.; Watkins, H. C.; Wang, W.; Martin, J. T.; Thai, N. T.; He, Y.; Schief, W. R.; Hammond, P. T.; Irvine, D. J., Enhancing humoral immunity via sustained-release implantable microneedle patch vaccination. *Proc Natl Acad Sci U S A* **2019,** *116* (33), 16473-16478.

88. Kotsuchibashi, Y., Recent advances in multi-temperature-responsive polymeric materials. *Polym J* **2020,** *52* (7), 681-689.

89. Qin, S.; Geng, Y.; Discher, D. E.; Yang, S., Temperature-Controlled Assembly and Release from Polymer Vesicles of Poly(ethylene oxide)-block- poly(N-isopropylacrylamide). *Adv Mater* **2006,** *18* (21), 2905-2909.

90. Nishimura, T.; Sasaki, Y.; Akiyoshi, K., Thermoresponsive glycopolymer vesicles: in situ observation of morphological changes and triggered cargo release. *Polym J* **2021,** *53* (11), 1251-1258.

91. Field, L. D.; Delehanty, J. B.; Chen, Y.; Medintz, I. L., Peptides for specifically targeting nanoparticles to cellular organelles: quo vadis? *Acc Chem Res* **2015,** *48* (5), 1380-90.

92. Wang, Y.; Cheetham, A. G.; Angacian, G.; Su, H.; Xie, L.; Cui, H., Peptide-drug conjugates as effective prodrug strategies for targeted delivery. *Adv Drug Deliv Rev* **2017,** *110-111*, 112-126.

93. Cerrato, C. P.; Kunnapuu, K.; Langel, U., Cell-penetrating peptides with intracellular organelle targeting. *Expert Opin Drug Deliv* **2017,** *14* (2), 245-255.

94. Cheng, R.; Meng, F.; Deng, C.; Klok, H. A.; Zhong, Z., Dual and multi-stimuli responsive polymeric nanoparticles for programmed site-specific drug delivery. *Biomaterials* **2013,** *34* (14), 3647-57.

95. Moyle, P. M.; Toth, I., Modern subunit vaccines: development, components, and research opportunities. *ChemMedChem* **2013,** *8* (3), 360-376.

96. Lauring, A. S.; Jones, J. O.; Andino, R., Rationalizing the development of live attenuated virus vaccines. *Nat Biotechnol* **2010,** *28* (6), 573-579.

97. Brisse, M.; Vrba, S. M.; Kirk, N.; Liang, Y.; Ly, H., Emerging Concepts and Technologies in Vaccine Development. *Front Immunol* **2020,** *11*, 583077.

98. Oscherwitz, J., The promise and challenge of epitope-focused vaccines. *Hum Vaccin Immunother* **2016,** *12* (8), 2113-2116.

99. Barbier, A. J.; Jiang, A. Y.; Zhang, P.; Wooster, R.; Anderson, D. G., The clinical progress of mRNA vaccines and immunotherapies. *Nat Biotechnol* **2022,** *40*, 840-854.

100. Hobernik, D.; Bros, M., DNA Vaccines-How Far From Clinical Use? *Int J Mol Sci* **2018,** *19* (11), 3605.

101. Ura, T.; Okuda, K.; Shimada, M., Developments in Viral Vector-Based Vaccines. *Vaccines (Basel)* **2014,** *2* (3), 624-641.

102. Principi, N.; Esposito, S., Vaccine-preventable diseases, vaccines and Guillain-Barre' syndrome. *Vaccine* **2019,** *37* (37), 5544-5550.

103. Vesikari, T.; Knuf, M.; Wutzler, P.; Karvonen, A.; Kieninger-Baum, D.; Schmitt, H. J.; Baehner, F.; Borkowski, A.; Tsai, T. F.; Clemens, R., Oil-in-water emulsion adjuvant with influenza vaccine in young children. *N Engl J Med* **2011,** *365* (15), 1406-16.

104. Atsmon, J.; Caraco, Y.; Ziv-Sefer, S.; Shaikevich, D.; Abramov, E.; Volokhov, I.; Bruzil, S.; Haima, K. Y.; Gottlieb, T.; Ben-Yedidia, T., Priming by a novel universal influenza vaccine (Multimeric-001)-a gateway for improving immune response in the elderly population. *Vaccine* **2014,** *32* (44), 5816-5823.

105. Gubin, M. M.; Artyomov, M. N.; Mardis, E. R.; Schreiber, R. D., Tumor neoantigens: building a framework for personalized cancer immunotherapy. *J Clin Invest* **2015,** *125* (9), 3413-3421.

106. Polack, F. P.; Thomas, S. J.; Kitchin, N.; Absalon, J.; Gurtman, A.; Lockhart, S.; Perez, J. L.; Perez Marc, G.; Moreira, E. D.; Zerbini, C.; Bailey, R.; Swanson, K. A.; Roychoudhury, S.; Koury, K.; Li, P.; Kalina, W. V.; Cooper, D.; Frenck, R. W., Jr.; Hammitt, L. L.; Tureci, O.; Nell, H.; Schaefer, A.; Unal, S.; Tresnan, D. B.; Mather, S.; Dormitzer, P. R.; Sahin, U.; Jansen, K. U.; Gruber, W. C.; C4591001 Clinical Trial Group, Safety and Efficacy of the BNT162b2 mRNA Covid-19 Vaccine. *N Engl J Med* **2020**, *383* (27), 2603-2615.

107. Baden, L. R.; El Sahly, H. M.; Essink, B.; Kotloff, K.; Frey, S.; Novak, R.; Diemert, D.; Spector, S. A.; Rouphael, N.; Creech, C. B.; McGettigan, J.; Kehtan, S.; Segall, N.; Solis, J.; Brosz, A.; Fierro, C.; Schwartz, H.; Neuzil, K.; Corey, L.; Gilbert, P.; Janes, H.; Follmann, D.; Marovich, M.; Mascola, J.; Polakowski, L.; Ledgerwood, J.; Graham, B. S.; Bennett, H.; Pajon, R.; Knightly, C.; Leav, B.; Deng, W.; Zhou, H.; Han, S.; Ivarsson, M.; Miller, J.; Zaks, T.; COVE Study Group, Efficacy and Safety of the mRNA-1273 SARS-CoV-2 Vaccine. *N Engl J Med* **2020**, *384* (5), 403-416

108. Kariko, K.; Buckstein, M.; Ni, H.; Weissman, D., Suppression of RNA recognition by Toll-like receptors: the impact of nucleoside modification and the evolutionary origin of RNA. *Immunity* **2005,** *23* (2), 165-175.

109. Hou, X.; Zaks, T.; Langer, R.; Dong, Y., Lipid nanoparticles for mRNA delivery. *Nat Rev Mater* **2021,** *6* (12), 1078-1094.

110. Regules, J. A.; Beigel, J. H.; Paolino, K. M.; Voell, J.; Castellano, A. R.; Hu, Z.; Munoz, P.; Moon, J. E.; Ruck, R. C.; Bennett, J. W.; Twomey, P. S.; Gutierrez, R. L.; Remich, S. A.; Hack, H. R.; Wisniewski, M. L.; Josleyn, M. D.; Kwilas, S. A.; Van Deusen, N.; Mbaya, O. T.; Zhou, Y.; Stanley, D. A.; Jing, W.; Smith, K. S.; Shi, M.; Ledgerwood, J. E.; Graham, B. S.; Sullivan, N. J.; Jagodzinski, L. L.; Peel, S. A.; Alimonti, J. B.; Hooper, J. W.; Silvera, P. M.; Martin, B. K.; Monath, T. P.; Ramsey, W. J.; Link, C. J.; Lane, H. C.; Michael, N. L.; Davey, R. T., Jr.; Thomas, S. J.; r, V.-Z.-G. P. S. G., A Recombinant Vesicular Stomatitis Virus Ebola Vaccine. *N Engl J Med* **2017,** *376* (4), 330-341.

111. Madhi, S. A.; Baillie, V.; Cutland, C. L.; Voysey, M.; Koen, A. L.; Fairlie, L.; Padayachee, S. D.; Dheda, K.; Barnabas, S. L.; Bhorat, Q. E.; Briner, C.; Kwatra, G.; Ahmed, K.; Aley, P.; Bhikha, S.; Bhiman, J. N.; Bhorat, A. E.; du Plessis, J.; Esmail, A.; Groenewald, M.; Horne, E.; Hwa, S. H.; Jose, A.; Lambe, T.; Laubscher, M.; Malahleha, M.; Masenya, M.; Masilela, M.; McKenzie, S.; Molapo, K.; Moultrie, A.; Oelofse, S.; Patel, F.; Pillay, S.; Rhead, S.; Rodel, H.; Rossouw, L.; Taoushanis, C.; Tegally, H.; Thombrayil, A.; van Eck, S.; Wibmer, C. K.; Durham, N. M.; Kelly, E. J.; Villafana, T. L.; Gilbert, S.; Pollard, A. J.; de Oliveira, T.; Moore, P. L.; Sigal, A.; Izu, A.; NGS-SA Group; Wits-VIDA COVID Group, Efficacy of the ChAdOx1 nCoV-19 Covid-19 Vaccine against the B.1.351 Variant. *N Engl J Med* **2021**, *384* (20), 1885-1898.

112. Sadoff, J.; Gray, G.; Vandebosch, A.; Cardenas, V.; Shukarev, G.; Grinsztejn, B.; Goepfert, P. A.; Truyers, C.; Fennema, H.; Spiessens, B.; Offergeld, K.; Scheper, G.; Taylor, K. L.; Robb, M. L.; Treanor, J.; Barouch, D. H.; Stoddard, J.; Ryser, M. F.; Marovich, M. A.; Neuzil, K. M.; Corey, L.; Cauwenberghs, N.; Tanner, T.; Hardt, K.; Ruiz-Guinazu, J.; Le Gars, M.; Schuitemaker, H.; Van Hoof, J.; Struyf, F.; Douoguih, M.; Group, E. S., Safety and Efficacy of Single-Dose Ad26.COV2.S Vaccine against Covid-19. *N Engl J Med* **2021,** *384* (23), 2187-2201.

113. Sellars, M. C.; Wu, C. J.; Fritsch, E. F., Cancer vaccines: Building a bridge over troubled waters. *Cell* **2022,** *185* (15), 2770-2788.

114. Waldman, A. D.; Fritz, J. M.; Lenardo, M. J., A guide to cancer immunotherapy: from T cell basic science to clinical practice. *Nat Rev Immunol* **2020**, *20* (11), 651-668.

115. Saxena, M.; van der Burg, S. H.; Melief, C. J. M.; Bhardwaj, N., Therapeutic cancer vaccines. *Nat Rev Cancer* **2021,** *21* (6), 360-378.

116. Robbins, P. F.; Lu, Y. C.; El-Gamil, M.; Li, Y. F.; Gross, C.; Gartner, J.; Lin, J. C.; Teer, J. K.; Cliften, P.; Tycksen, E.; Samuels, Y.; Rosenberg, S. A., Mining exomic sequencing data

to identify mutated antigens recognized by adoptively transferred tumor-reactive T cells. *Nat Med* **2013,** *19* (6), 747-52.

117. Schumacher, T. N.; Scheper, W.; Kvistborg, P., Cancer Neoantigens. *Annu Rev Immunol* **2019,** *37*, 173-200.

118. Bowen, W. S.; Svrivastava, A. K.; Batra, L.; Barsoumian, H.; Shirwan, H., Current challenges for cancer vaccine adjuvant development. *Expert Rev Vaccines* **2018,** *17* (3), 207-215.

119. Higano, C. S.; Schellhammer, P. F.; Small, E. J.; Burch, P. A.; Nemunaitis, J.; Yuh, L.; Provost, N.; Frohlich, M. W., Integrated data from 2 randomized, double-blind, placebo-controlled, phase 3 trials of active cellular immunotherapy with sipuleucel-T in advanced prostate cancer. *Cancer* **2009,** *115* (16), 3670-3679.

120. Liu, X.; Pu, Y.; Cron, K.; Deng, L.; Kline, J.; Frazier, W. A.; Xu, H.; Peng, H.; Fu, Y. X.; Xu, M. M., CD47 blockade triggers T cell-mediated destruction of immunogenic tumors. *Nat Med* **2015,** *21* (10), 1209-1215.

121. Chao, M. P.; Alizadeh, A. A.; Tang, C.; Myklebust, J. H.; Varghese, B.; Gill, S.; Jan, M.; Cha, A. C.; Chan, C. K.; Tan, B. T.; Park, C. Y.; Zhao, F.; Kohrt, H. E.; Malumbres, R.; Briones, J.; Gascoyne, R. D.; Lossos, I. S.; Levy, R.; Weissman, I. L.; Majeti, R., Anti-CD47 antibody synergizes with rituximab to promote phagocytosis and eradicate non-Hodgkin lymphoma. *Cell* **2010,** *142* (5), 699-713.

122. Li, S.; Liu, M.; Do, M. H.; Chou, C.; Stamatiades, E. G.; Nixon, B. G.; Shi, W.; Zhang, X.; Li, P.; Gao, S.; Capistrano, K. J.; Xu, H.; Cheung, N. V.; Li, M. O., Cancer immunotherapy via targeted TGF-beta signalling blockade in TH cells. *Nature* **2020,** *587* (7832), 121-125.

123. Sims, J. E.; Smith, D. E., The IL-1 family: regulators of immunity. *Nat Rev Immunol* **2010,** *10* (2), 89-102.

124. Jain, A.; Song, R.; Wakeland, E. K.; Pasare, C., T cell-intrinsic IL-1R signaling licenses effector cytokine production by memory CD4 T cells. *Nat Commun* **2018,** *9* (1), 3185.

125. Hatscher, L.; Lehmann, C. H. K.; Purbojo, A.; Onderka, C.; Liang, C.; Hartmann, A.; Cesnjevar, R.; Bruns, H.; Gross, O.; Nimmerjahn, F.; Ivanovic-Burmazovic, I.; Kunz, M.; Heger, L.; Dudziak, D., Select hyperactivating NLRP3 ligands enhance the TH1- and TH17-inducing potential of human type 2 conventional dendritic cells. *Sci Signal* **2021,** *14* (680), eabe1757.

126. Martinon, F.; Petrilli, V.; Mayor, A.; Tardivel, A.; Tschopp, J., Gout-associated uric acid crystals activate the NALP3 inflammasome. *Nature* **2006,** *440* (7081), 237-241.

127. Ising, C.; Venegas, C.; Zhang, S.; Scheiblich, H.; Schmidt, S. V.; Vieira-Saecker, A.; Schwartz, S.; Albasset, S.; McManus, R. M.; Tejera, D.; Griep, A.; Santarelli, F.; Brosseron, F.; Opitz, S.; Stunden, J.; Merten, M.; Kayed, R.; Golenbock, D. T.; Blum, D.; Latz, E.; Buee, L.; Heneka, M. T., NLRP3 inflammasome activation drives tau pathology. *Nature* **2019,** *575* (7784), 669-673.

128. Sharma, B. R.; Kanneganti, T. D., NLRP3 inflammasome in cancer and metabolic diseases. *Nat Immunol* **2021**, *22* (5), 550-559.

129. Guo, C.; Fu, R.; Wang, S.; Huang, Y.; Li, X.; Zhou, M.; Zhao, J.; Yang, N., NLRP3 inflammasome activation contributes to the pathogenesis of rheumatoid arthritis. *Clin Exp Immunol* **2018,** *194* (2), 231-243.

130. Rodrigues, T. S.; de Sa, K. S. G.; Ishimoto, A. Y.; Becerra, A.; Oliveira, S.; Almeida, L.; Goncalves, A. V.; Perucello, D. B.; Andrade, W. A.; Castro, R.; Veras, F. P.; Toller-Kawahisa, J. E.; Nascimento, D. C.; de Lima, M. H. F.; Silva, C. M. S.; Caetite, D. B.; Martins, R. B.; Castro, I. A.; Pontelli, M. C.; de Barros, F. C.; do Amaral, N. B.; Giannini, M. C.; Bonjorno, L. P.; Lopes, M. I. F.; Santana, R. C.; Vilar, F. C.; Auxiliadora-Martins, M.; Luppino-Assad, R.; de Almeida, S. C. L.; de Oliveira, F. R.; Batah, S. S.; Siyuan, L.; Benatti, M. N.; Cunha, T. M.; Alves-Filho, J. C.; Cunha, F. Q.; Cunha, L. D.; Frantz, F. G.; Kohlsdorf, T.; Fabro, A. T.; Arruda, E.; de Oliveira, R. D. R.; Louzada-Junior, P.; Zamboni, D. S., Inflammasomes are activated in response to SARS-CoV-2 infection and are associated with COVID-19 severity in patients. *J Exp Med* **2021,** *218* (3), e20201707.

131. Marty-Roix, R.; Vladimer, G. I.; Pouliot, K.; Weng, D.; Buglione-Corbett, R.; West, K.; MacMicking, J. D.; Chee, J. D.; Wang, S.; Lu, S.; Lien, E., Identification of QS-21 as an Inflammasome-activating Molecular Component of Saponin Adjuvants. *J Biol Chem* **2016,** *291* (3), 1123-1136.

132. Welsby, I.; Detienne, S.; N'Kuli, F.; Thomas, S.; Wouters, S.; Bechtold, V.; De Wit, D.; Gineste, R.; Reinheckel, T.; Elouahabi, A.; Courtoy, P. J.; Didierlaurent, A. M.; Goriely, S., Lysosome-Dependent Activation of Human Dendritic Cells by the Vaccine Adjuvant QS-21. *Front Immunol* **2016,** *7*, 663.

133. Coccia, M.; Collignon, C.; Herve, C.; Chalon, A.; Welsby, I.; Detienne, S.; van Helden, M. J.; Dutta, S.; Genito, C. J.; Waters, N. C.; Deun, K. V.; Smilde, A. K.; Berg, R.; Franco, D.; Bourguignon, P.; Morel, S.; Garcon, N.; Lambrecht, B. N.; Goriely, S.; Most, R. V.; Didierlaurent, A. M., Cellular and molecular synergy in AS01-adjuvanted vaccines results in an early IFNgamma response promoting vaccine immunogenicity. *NPJ Vaccines* **2017,** *2*, 25.

134. Lusty, E.; Poznanski, S. M.; Kwofie, K.; Mandur, T. S.; Lee, D. A.; Richards, C. D.; Ashkar, A. A., IL-18/IL-15/IL-12 synergy induces elevated and prolonged IFN-gamma production by ex vivo expanded NK cells which is not due to enhanced STAT4 activation. *Mol Immunol* **2017,** *88*, 138-147.

135. Chauhan, D.; Vande Walle, L.; Lamkanfi, M., Therapeutic modulation of inflammasome pathways. *Immunol Rev* **2020,** *297* (1), 123-138.

136. Latz, E.; Xiao, T. S.; Stutz, A., Activation and regulation of the inflammasomes. *Nat Rev Immunol* **2013,** *13* (6), 397-411.

137. Swanson, K. V.; Deng, M.; Ting, J. P., The NLRP3 inflammasome: molecular activation and regulation to therapeutics. *Nat Rev Immunol* **2019,** *19* (8), 477-489.

138. Zhou, R.; Tardivel, A.; Thorens, B.; Choi, I.; Tschopp, J., Thioredoxin-interacting protein links oxidative stress to inflammasome activation. *Nat Immunol* **2010,** *11* (2), 136-140.

139. Shimada, K.; Crother, T. R.; Karlin, J.; Dagvadorj, J.; Chiba, N.; Chen, S.; Ramanujan, V. K.; Wolf, A. J.; Vergnes, L.; Ojcius, D. M.; Rentsendorj, A.; Vargas, M.; Guerrero, C.; Wang, Y.; Fitzgerald, K. A.; Underhill, D. M.; Town, T.; Arditi, M., Oxidized mitochondrial DNA activates the NLRP3 inflammasome during apoptosis. *Immunity* **2012,** *36* (3), 401-414.

140. Zhou, R.; Yazdi, A. S.; Menu, P.; Tschopp, J., A role for mitochondria in NLRP3 inflammasome activation. *Nature* **2011,** *469* (7329), 221-225.

141. Mariathasan, S.; Weiss, D. S.; Newton, K.; McBride, J.; O'Rourke, K.; Roose-Girma, M.; Lee, W. P.; Weinrauch, Y.; Monack, D. M.; Dixit, V. M., Cryopyrin activates the inflammasome in response to toxins and ATP. *Nature* **2006,** *440* (7081), 228-232.

142. Dostert, C.; Petrilli, V.; Van Bruggen, R.; Steele, C.; Mossman, B. T.; Tschopp, J., Innate immune activation through Nalp3 inflammasome sensing of asbestos and silica. *Science* **2008,** *320* (5876), 674-677.

143. Sharp, F. A.; Ruane, D.; Claass, B.; Creagh, E.; Harris, J.; Malyala, P.; Singh, M.; O'Hagan, D. T.; Petrilli, V.; Tschopp, J.; O'Neill, L. A.; Lavelle, E. C., Uptake of particulate vaccine adjuvants by dendritic cells activates the NALP3 inflammasome. *Proc Natl Acad Sci U S A* **2009,** *106* (3), 870-875.

144. Munoz-Planillo, R.; Kuffa, P.; Martinez-Colon, G.; Smith, B. L.; Rajendiran, T. M.; Nunez, G., K(+) efflux is the common trigger of NLRP3 inflammasome activation by bacterial toxins and particulate matter. *Immunity* **2013,** *38* (6), 1142-1153.

145. He, Y.; Zeng, M. Y.; Yang, D.; Motro, B.; Nunez, G., NEK7 is an essential mediator of NLRP3 activation downstream of potassium efflux. *Nature* **2016,** *530* (7590), 354-357.

146. Agostini, L.; Martinon, F.; Burns, K.; McDermott, M. F.; Hawkins, P. N.; Tschopp, J., NALP3 Forms an IL-1β-Processing Inflammasome with Increased Activity in Muckle-Wells Autoinflammatory Disorder. *Immunity* **2004,** *20* (3), 319-325.

147. Fink, S. L.; Cookson, B. T., Caspase-1-dependent pore formation during pyroptosis leads to osmotic lysis of infected host macrophages. *Cell Microbiol* **2006,** *8* (11), 1812-1825.

148. Liu, X.; Zhang, Z.; Ruan, J.; Pan, Y.; Magupalli, V. G.; Wu, H.; Lieberman, J., Inflammasome-activated gasdermin D causes pyroptosis by forming membrane pores. *Nature* **2016,** *535* (7610), 153-158.

149. Hachim, M. Y.; Khalil, B. A.; Elemam, N. M.; Maghazachi, A. A., Pyroptosis: The missing puzzle among innate and adaptive immunity crosstalk. *J Leukoc Biol* **2020,** *108* (1), 323-338.

150. Persson, E. K.; Verstraete, K.; Heyndrickx, I.; Gevaert, E.; Aegerter, H.; Percier, J. M.; Deswarte, K.; Verschueren, K. H. G.; Dansercoer, A.; Gras, D.; Chanez, P.; Bachert, C.; Goncalves, A.; Van Gorp, H.; De Haard, H.; Blanchetot, C.; Saunders, M.; Hammad, H.; Savvides, S. N.; Lambrecht, B. N., Protein crystallization promotes type 2 immunity and is reversible by antibody treatment. *Science* **2019,** *364* (6442), eaaw4295.

151. Franklin, B. S.; Mangan, M. S.; Latz, E., Crystal Formation in Inflammation. *Annu Rev Immunol* **2016,** *34*, 173-202.

152. Evavold, C. L.; Kagan, J. C., How Inflammasomes Inform Adaptive Immunity. *J Mol Biol* **2018,** *430* (2), 217-237.

153. Dalsgaard, K., Saponin adjuvants. III. Isolation of a substance from Quillaja saponaria Molina with adjuvant activity in food-and-mouth disease vaccines. *Arch Gesamte Virusforsch* **1974,** *44* (3), 243-254.

154. Wu, J. Y.; Gardner, B. H.; Murphy, C. I.; Seals, J. R.; Kensil, C. R.; Recchia, J.; Beltz, G. A.; Newman, G. W.; Newman, M. J., Saponin adjuvant enhancement of antigen-specific immune responses to an experimental HIV-1 vaccine. *J Immunol* **1992,** *148* (5), 1519-1525.

155. Garcon, N.; Friede, M. Vaccines Containing a Saponin and Sterol. 1996.

156. den Brok, M. H.; Bull, C.; Wassink, M.; de Graaf, A. M.; Wagenaars, J. A.; Minderman, M.; Thakur, M.; Amigorena, S.; Rijke, E. O.; Schrier, C. C.; Adema, G. J., Saponin-based adjuvants induce cross-presentation in dendritic cells by intracellular lipid body formation. *Nat Commun* **2016,** *7*, 13324.

157. Fernandez-Tejada, A.; Tan, D. S.; Gin, D. Y., Development of Improved Vaccine Adjuvants Based on the Saponin Natural Product QS-21 through Chemical Synthesis. *Acc Chem Res* **2016,** *49* (9), 1741-1756.

158. Lima, H., Jr.; Jacobson, L. S.; Goldberg, M. F.; Chandran, K.; Diaz-Griffero, F.; Lisanti, M. P.; Brojatsch, J., Role of lysosome rupture in controlling Nlrp3 signaling and necrotic cell death. *Cell Cycle* **2013,** *12* (12), 1868-1878.

159. Manna, S.; Howitz, W. J.; Oldenhuis, N. J.; Eldredge, A. C.; Shen, J.; Nihesh, F. N.; Lodoen, M. B.; Guan, Z.; Esser-Kahn, A. P., Immunomodulation of the NLRP3 Inflammasome through Structure-Based Activator Design and Functional Regulation via Lysosomal Rupture. *ACS Cent Sci* **2018,** *4* (8), 982-995.

160. Nandi, D.; Shivrayan, M.; Gao, J.; Krishna, J.; Das, R.; Liu, B.; Thayumanavan, S.; Kulkarni, A., Core Hydrophobicity of Supramolecular Nanoparticles Induces NLRP3 Inflammasome Activation. *ACS Appl Mater Interfaces* **2021,** *13* (38), 45300-45314.

161. Baljon, J. J.; Dandy, A.; Wang-Bishop, L.; Wehbe, M.; Jacobson, M. E.; Wilson, J. T., The efficiency of cytosolic drug delivery using pH-responsive endosomolytic polymers does not correlate with activation of the NLRP3 inflammasome. *Biomater Sci* **2019,** *7* (5), 1888-1897.

162. Li, T.; Zehner, M.; He, J.; Prochnicki, T.; Horvath, G.; Latz, E.; Burgdorf, S.; Takeoka, S., NLRP3 inflammasome-activating arginine-based liposomes promote antigen presentations in dendritic cells. *Int J Nanomedicine* **2019,** *14*, 3503-3516.

163. Deets, K. A.; Vance, R. E., Inflammasomes and adaptive immune responses. *Nat Immunol* **2021,** *22*, 412–422.

164. Yatim, N.; Cullen, S.; Albert, M. L., Dying cells actively regulate adaptive immune responses. *Nat Rev Immunol* **2017,** *17* (4), 262-275.

165. Orzalli, M. H.; Kagan, J. C., Apoptosis and Necroptosis as Host Defense Strategies to Prevent Viral Infection. *Trends Cell Biol* **2017,** *27* (11), 800-809.

166. Malumbres, M.; Barbacid, M., Cell cycle, CDKs and cancer: a changing paradigm. *Nat Rev Cancer* **2009,** *9* (3), 153-166.

167. Lin, Z. P.; Zhu, Y. L.; Ratner, E. S., Targeting Cyclin-Dependent Kinases for Treatment of Gynecologic Cancers. *Front Oncol* **2018,** *8*, 303.

168. Zhou, C.; Chen, X.; Zeng, W.; Peng, C.; Huang, G.; Li, X.; Ouyang, Z.; Luo, Y.; Xu, X.; Xu, B.; Wang, W.; He, R.; Zhang, X.; Zhang, L.; Liu, J.; Knepper, T. C.; He, Y.; McLeod, H. L., Propranolol induced G0/G1/S phase arrest and apoptosis in melanoma cells via AKT/MAPK pathway. *Oncotarget* **2016,** *7* (42), 68314-68327.

169. Klein, M. E.; Kovatcheva, M.; Davis, L. E.; Tap, W. D.; Koff, A., CDK4/6 Inhibitors: The Mechanism of Action May Not Be as Simple as Once Thought. *Cancer Cell* **2018,** *34* (1), 9-20.

170. Capece, D.; Verzella, D.; Flati, I.; Arboretto, P.; Cornice, J.; Franzoso, G., NF-kappaB: blending metabolism, immunity, and inflammation. *Trends Immunol* **2022,** *43* (9), 757-775.

171. Kerr, J. F. R., A histochemical study of hypertrophy and ischaemic injury of rat liver with special reference to changes in lysosomes. *J Pathol Bacteriol* **1965,** *90* (2), 419-35.

172. Elmore, S., Apoptosis: a review of programmed cell death. *Toxicol Pathol* **2007,** *35* (4), 495-516.

173. Czabotar, P. E.; Lessene, G.; Strasser, A.; Adams, J. M., Control of apoptosis by the BCL-2 protein family: implications for physiology and therapy. *Nat Rev Mol Cell Biol* **2014,** *15* (1), 49-63.

174. Li, M. O.; Sarkisian, M. R.; Mehal, W. Z.; Rakic, P.; Flavell, R. A., Phosphatidylserine receptor is required for clearance of apoptotic cells. *Science* **2003,** *302* (5650), 1560-1563.

175. Proskuryakov, S. Y. a.; Konoplyannikov, A. G.; Gabai, V. L., Necrosis: a specific form of programmed cell death? *Exp Cell Res* **2003,** *283* (1), 1-16.

176. Kayagaki, N.; Warming, S.; Lamkanfi, M.; Vande Walle, L.; Louie, S.; Dong, J.; Newton, K.; Qu, Y.; Liu, J.; Heldens, S.; Zhang, J.; Lee, W. P.; Roose-Girma, M.; Dixit, V. M., Non-canonical inflammasome activation targets caspase-11. *Nature* **2011,** *479* (7371), 117-121.

177. Kayagaki, N.; Stowe, I. B.; Lee, B. L.; O'Rourke, K.; Anderson, K.; Warming, S.; Cuellar, T.; Haley, B.; Roose-Girma, M.; Phung, Q. T.; Liu, P. S.; Lill, J. R.; Li, H.; Wu, J.; Kummerfeld, S.; Zhang, J.; Lee, W. P.; Snipas, S. J.; Salvesen, G. S.; Morris, L. X.; Fitzgerald, L.; Zhang, Y.; Bertram, E. M.; Goodnow, C. C.; Dixit, V. M., Caspase-11 cleaves gasdermin D for non-canonical inflammasome signalling. *Nature* **2015,** *526* (7575), 666-671.

178. Shi, J.; Zhao, Y.; Wang, K.; Shi, X.; Wang, Y.; Huang, H.; Zhuang, Y.; Cai, T.; Wang, F.; Shao, F., Cleavage of GSDMD by inflammatory caspases determines pyroptotic cell death. *Nature* **2015,** *526* (7575), 660-665.

179. He, W. T.; Wan, H.; Hu, L.; Chen, P.; Wang, X.; Huang, Z.; Yang, Z. H.; Zhong, C. Q.; Han, J., Gasdermin D is an executor of pyroptosis and required for interleukin-1beta secretion. *Cell Res* **2015,** *25* (12), 1285-98.

180. Xia, S.; Zhang, Z.; Magupalli, V. G.; Pablo, J. L.; Dong, Y.; Vora, S. M.; Wang, L.; Fu, T. M.; Jacobson, M. P.; Greka, A.; Lieberman, J.; Ruan, J.; Wu, H., Gasdermin D pore structure reveals preferential release of mature interleukin-1. *Nature* **2021,** *593* (7860), 607-611.

181. Wang, H.; Sun, L.; Su, L.; Rizo, J.; Liu, L.; Wang, L. F.; Wang, F. S.; Wang, X., Mixed lineage kinase domain-like protein MLKL causes necrotic membrane disruption upon phosphorylation by RIP3. *Mol Cell* **2014,** *54* (1), 133-146.

182. Chen, X.; He, W. T.; Hu, L.; Li, J.; Fang, Y.; Wang, X.; Xu, X.; Wang, Z.; Huang, K.; Han, J., Pyroptosis is driven by non-selective gasdermin-D pore and its morphology is different from MLKL channel-mediated necroptosis. *Cell Res* **2016,** *26* (9), 1007-20.

183. Fritsch, M.; Gunther, S. D.; Schwarzer, R.; Albert, M. C.; Schorn, F.; Werthenbach, J. P.; Schiffmann, L. M.; Stair, N.; Stocks, H.; Seeger, J. M.; Lamkanfi, M.; Kronke, M.; Pasparakis, M.; Kashkar, H., Caspase-8 is the molecular switch for apoptosis, necroptosis and pyroptosis. *Nature* **2019,** *575* (7784), 683-687.

184. Gunther, C.; Martini, E.; Wittkopf, N.; Amann, K.; Weigmann, B.; Neumann, H.; Waldner, M. J.; Hedrick, S. M.; Tenzer, S.; Neurath, M. F.; Becker, C., Caspase-8 regulates TNF-alpha-induced epithelial necroptosis and terminal ileitis. *Nature* **2011,** *477* (7364), 335-339.

185. Vanden Berghe, T.; Vanlangenakker, N.; Parthoens, E.; Deckers, W.; Devos, M.; Festjens, N.; Guerin, C. J.; Brunk, U. T.; Declercq, W.; Vandenabeele, P., Necroptosis, necrosis and secondary necrosis converge on similar cellular disintegration features. *Cell Death Differ* **2010,** *17* (6), 922-930.

186. Nomenclature Committee on Cell Death, Molecular mechanisms of cell death: recommendations of the Nomenclature Committee on Cell Death 2018. *Cell Death Differ* **2018,** *25* (3), 486-541.

187. Krysko, D. V.; Garg, A. D.; Kaczmarek, A.; Krysko, O.; Agostinis, P.; Vandenabeele, P., Immunogenic cell death and DAMPs in cancer therapy. *Nat Rev Cancer* **2012,** *12* (12), 860-875.

188. Canton, J.; Blees, H.; Henry, C. M.; Buck, M. D.; Schulz, O.; Rogers, N. C.; Childs, E.; Zelenay, S.; Rhys, H.; Domart, M. C.; Collinson, L.; Alloatti, A.; Ellison, C. J.; Amigorena, S.; Papayannopoulos, V.; Thomas, D. C.; Randow, F.; Reis, E. S. C., The receptor DNGR-1 signals for phagosomal rupture to promote cross-presentation of dead-cell-associated antigens. *Nat Immunol* **2020**. *22* (2), 140-153.

189. Razaghi, A.; Heimann, K.; Schaeffer, P. M.; Gibson, S. B., Negative regulators of cell death pathways in cancer: perspective on biomarkers and targeted therapies. *Apoptosis* **2018,** *23* (2), 93-112.

190. Hawker, C. J.; Wooley, K. L., The convergence of synthetic organic and polymer chemistries. *Science* **2005,** *309* (5738), 1200-1205.

191. Penfold, N. J. W.; Yeow, J.; Boyer, C.; Armes, S. P., Emerging Trends in Polymerization-Induced Self-Assembly. *ACS Macro Letters* **2019,** *8* (8), 1029-1054.

192. Lodge, T. P.; Hiemenz, P. C., *Polymer Chemistry*. 2 ed.; CRC Press: Boca Raton, FL, 2013.

193. Staudinger, H., Über polymerisation. *Berichte der deutschen chemischen Gesellschaft* **1920,** *53*, 1073-1085.

194. Corrigan, N.; Jung, K.; Moad, G.; Hawker, C. J.; Matyjaszewski, K.; Boyer, C., Reversible-deactivation radical polymerization (Controlled/living radical polymerization): From discovery to materials design and applications. *Prog Polym Sci* **2020,** *111*, 103111.

195. Solomon, D. H.; Rizzardo, E.; Cacioli, P. Polymerization process and polymers produced thereby. US Patent US4581429A, April 08 1986.

196. Nicolas, J.; Guillaneuf, Y.; Lefay, C.; Bertin, D.; Gigmes, D.; Charleux, B., Nitroxide-mediated polymerization. *Prog Polym Sci* **2013,** *38* (1), 63-235.

197. Wang, J.-S.; Matyjaszewski, K., Controlled/"living" radical polymerization. atom transfer radical polymerization in the presence of transition-metal complexes. *J Am Chem Soc* **1995,** *117* (20), 5614-5615.

198. Kato, M.; Kamigaito, M.; Sawamoto, M.; Higashimura, T., Polymerization of Methyl Methacrylate with the Carbon Tetrachloride/Dichlorotris-(triphenylphosphine)ruthenium(II)/Methylaluminum Bis(2,6-di-tert-butylphenoxide) Initiating System: Possibility of Living Radical Polymerization. *Macromolecules* **1995,** *28* (5), 1721-1723.

199. Matyjaszewski, K., Advanced Materials by Atom Transfer Radical Polymerization. *Adv Mater* **2018,** *30* (23), e1706441.

200. Chiefari, J.; Chong, Y. K.; Ercole, F.; Krstina, J.; Jeffery, J.; Le, T. P. T.; Mayadunne, R. T. A.; Meijs, G. F.; Moad, C. L.; Moad, G.; Rizzardo, E.; Thang, S. H., Living Free-Radical Polymerization by Reversible Addition−Fragmentation Chain Transfer: The RAFT Process. *Macromolecules* **1998,** *31* (16), 5559-5562.

201. Boyer, C.; Bulmus, V.; Davis, T. P.; Ladmiral, V.; Liu, J.; Perrier, S., Bioapplications of RAFT polymerization. *Chem Rev* **2009,** *109* (11), 5402-5436.

202. Gregory, A.; Stenzel, M. H., Complex polymer architectures via RAFT polymerization: From fundamental process to extending the scope using click chemistry and nature's building blocks. *Prog Polym Sci* **2012,** *37* (1), 38-105.

203. Upadhya, R.; Kosuri, S.; Tamasi, M.; Meyer, T. A.; Atta, S.; Webb, M. A.; Gormley, A. J., Automation and data-driven design of polymer therapeutics. *Adv Drug Deliv Rev* **2021,** *171*, 1-28.

204. Mann, J. L.; Maikawa, C. L.; Smith, A. A. A.; Grosskopf, A. K.; Baker, S. W.; Roth, G. A.; Meis, C. M.; Gale, E. C.; Liong, C. S.; Correa, S.; Chan, D.; Stapleton, L. M.; Yu, A. C.; Muir, B.; Howard, S.; Postma, A.; Appel, E. A., An ultrafast insulin formulation enabled by high-throughput screening of engineered polymeric excipients. *Sci Transl Med* **2020,** *12* (550), eaba6676.

205. Corrigan, N.; Xu, J.; Boyer, C.; Allonas, X., Exploration of the PET-RAFT Initiation Mechanism for Two Commonly Used Photocatalysts. *ChemPhotoChem* **2019,** *3* (11), 1193-1199.

206. Ng, G.; Yeow, J.; Chapman, R.; Isahak, N.; Wolvetang, E.; Cooper-White, J. J.; Boyer, C., Pushing the Limits of High Throughput PET-RAFT Polymerization. *Macromolecules* **2018,** *51* (19), 7600-7607.

207. Xu, J.; Shanmugam, S.; Duong, H. T.; Boyer, C., Organo-photocatalysts for photoinduced electron transfer-reversible addition–fragmentation chain transfer (PET-RAFT) polymerization. *Polym Chem* **2015,** *6* (31), 5615-5624.

208. Shanmugam, S.; Xu, J.; Boyer, C., Exploiting Metalloporphyrins for Selective Living Radical Polymerization Tunable over Visible Wavelengths. *J Am Chem Soc* **2015,** *137* (28), 9174-9185.

209. Gormley, A. J.; Yeow, J.; Ng, G.; Conway, O.; Boyer, C.; Chapman, R., An Oxygen-Tolerant PET-RAFT Polymerization for Screening Structure-Activity Relationships. *Angew Chem Int Ed Engl* **2018,** *57* (6), 1557-1562.

210. Li, Z.; Kosuri, S.; Foster, H.; Cohen, J.; Jumeaux, C.; Stevens, M. M.; Chapman, R.; Gormley, A. J., A Dual Wavelength Polymerization and Bioconjugation Strategy for High Throughput Synthesis of Multivalent Ligands. *J Am Chem Soc* **2019,** *141* (50), 19823-19830.

211. Tamasi, M. J.; Patel, R. A.; Borca, C. H.; Kosuri, S.; Mugnier, H.; Upadhya, R.; Murthy, N. S.; Webb, M. A.; Gormley, A. J., Machine Learning on a Robotic Platform for the Design of Polymer-Protein Hybrids. *Adv Mater* **2022,** *34* (30), e2201809.

212. Avery, O. T.; Goebel, W. F., Chemo-Immunological Studies on Conjugated Carbohydrate-Proteins: II. Immunological Specificity of Synthetic Sugar-Protein Antigens. *J Exp Med* **1929,** *50* (4), 533-550.

213. Avery, O. T.; Goebel, W. F., Chemo-Immunological Studies on Conjugated Carbohydrate-Proteins: V. The Immunological Specifity of an Antigen Prepared by Combining the Capsular Polysaccharide of Type Iii Pneumococcus with Foreign Protein. *J Exp Med* **1931,** *54* (3), 437-447.

214. Homsy, C. A.; Ansevin, K. D.; O'Bannon, W.; Thompson, S. A.; Hodge, R.; Estrella, M. E., Rapid In Vitro Screening of Polymers for Biocompatibility. *J Macromol Sci Part A* **1970,** *4* (3), 615-634.

215. Singh, P.; Guillory, J. K.; Sokoloski, T. D.; Benet, L. Z.; Bhatia, V. N., Effect of inert tablet ingredients on drug absorption. I. Effect of polyethylene glycol 4000 on the intestinal absorption of four barbiturates. *J Pharm Sci* **1966,** *55* (1), 63-68.

216. Behr, J. P.; Demeneix, B.; Loeffler, J. P.; Perez-Mutul, J., Efficient gene transfer into mammalian primary endocrine cells with lipopolyamine-coated DNA. *Proc Natl Acad Sci U S A* **1989,** *86* (18), 6982-6986.

217. Langer, R., Polymer-Controlled Drug-Delivery Systems. *Accounts of Chemical Research* **1993,** *26* (10), 537-542.

218. Panyam, J.; Labhasetwar, V., Biodegradable nanoparticles for drug and gene delivery to cells and tissue. *Adv Drug Deliv Rev* **2003,** *55* (3), 329-347.

219. Stuart, M. A.; Huck, W. T.; Genzer, J.; Muller, M.; Ober, C.; Stamm, M.; Sukhorukov, G. B.; Szleifer, I.; Tsukruk, V. V.; Urban, M.; Winnik, F.; Zauscher, S.; Luzinov, I.; Minko, S., Emerging applications of stimuli-responsive polymer materials. *Nat Mater* **2010,** *9* (2), 101-113.

220. Hakobyan, K.; Xu, J.; Müllner, M., The challenges of controlling polymer synthesis at the molecular and macromolecular level. *Polym Chem* **2022**, *13*, 5431-5446.

221. Wibowo, D.; Jorritsma, S. H. T.; Gonzaga, Z. J.; Evert, B.; Chen, S.; Rehm, B. H. A., Polymeric nanoparticle vaccines to combat emerging and pandemic threats. *Biomaterials* **2020**, *268*, 120597.

222. Vincent, M. P.; Navidzadeh, J. O.; Bobbala, S.; Scott, E. A., Leveraging self-assembled nanobiomaterials for improved cancer immunotherapy. *Cancer Cell* **2022**, *40* (3), 255-276.

223. Samal, S. K.; Dash, M.; Van Vlierberghe, S.; Kaplan, D. L.; Chiellini, E.; van Blitterswijk, C.; Moroni, L.; Dubruel, P., Cationic polymers and their therapeutic potential. *Chem Soc Rev* **2012,** *41* (21), 7147-7194.

224. Wilson, D. S.; Hirosue, S.; Raczy, M. M.; Bonilla-Ramirez, L.; Jeanbart, L.; Wang, R.; Kwissa, M.; Franetich, J. F.; Broggi, M. A. S.; Diaceri, G.; Quaglia-Thermes, X.; Mazier, D.; Swartz, M. A.; Hubbell, J. A., Antigens reversibly conjugated to a polymeric glyco-adjuvant induce protective humoral and cellular immunity. *Nat Mater* **2019,** *18* (2), 175-185.

225. Wilson, D. S.; Damo, M.; Hirosue, S.; Raczy, M. M.; Brunggel, K.; Diaceri, G.; Quaglia-Thermes, X.; Hubbell, J. A., Synthetically glycosylated antigens induce antigen-specific tolerance and prevent the onset of diabetes. *Nat Biomed Eng* **2019,** *3* (10), 817-829.

226. Gray, L. T.; Raczy, M. M.; Briquez, P. S.; Marchell, T. M.; Alpar, A. T.; Wallace, R. P.; Volpatti, L. R.; Sasso, M. S.; Cao, S.; Nguyen, M.; Mansurov, A.; Budina, E.; Watkins, E. A.; Solanki, A.; Mitrousis, N.; Reda, J. W.; Yu, S. S.; Tremain, A. C.; Wang, R.; Nicolaescu, V.; Furlong, K.; Dvorkin, S.; Manicassamy, B.; Randall, G.; Wilson, D. S.; Kwissa, M.; Swartz, M. A.; Hubbell, J. A., Generation of potent cellular and humoral immunity against SARS-CoV-2 antigens via conjugation to a polymeric glyco-adjuvant. *Biomaterials* **2021,** *278*, 121159.

227. Dias, A. P.; da Silva Santos, S.; da Silva, J. V.; Parise-Filho, R.; Igne Ferreira, E.; Seoud, O. E.; Giarolla, J., Dendrimers in the context of nanomedicine. *Int J Pharm* **2020,** *573*, 118814.

228. Wang, Y.; Gong, N.; Ma, C.; Zhang, Y.; Tan, H.; Qing, G.; Zhang, J.; Wang, Y.; Wang, J.; Chen, S.; Li, X.; Ni, Q.; Yuan, Y.; Gan, Y.; Chen, J.; Li, F.; Zhang, J.; Ou, C.; Zhao, Y.; Liu, X.; Liang, X. J., An amphiphilic dendrimer as a light-activable immunological adjuvant for in situ cancer vaccination. *Nat Commun* **2021,** *12* (1), 4964.

229. Bodewein, L.; Schmelter, F.; Di Fiore, S.; Hollert, H.; Fischer, R.; Fenske, M., Differences in toxicity of anionic and cationic PAMAM and PPI dendrimers in zebrafish embryos and cancer cell lines. *Toxicol Appl Pharmacol* **2016,** *305*, 83-92.

230. Markowicz-Piasecka, M.; Luczak, E.; Chalubinski, M.; Broncel, M.; Mikiciuk-Olasik, E.; Sikora, J., Studies towards biocompatibility of PAMAM dendrimers--overall hemostasis potential and integrity of the human aortic endothelial barrier. *Int J Pharm* **2014,** *473* (1-2), 158-169.

231. Pola, R.; Braunová, A.; Laga, R.; Pechar, M.; Ulbrich, K., Click chemistry as a powerful and chemoselective tool for the attachment of targeting ligands to polymer drug carriers. *Polym. Chem.* **2014,** *5* (4), 1340-1350.

232. Blanco, E.; Shen, H.; Ferrari, M., Principles of nanoparticle design for overcoming biological barriers to drug delivery. *Nat Biotechnol* **2015,** *33* (9), 941-951.

233. Deng, L.; Mohan, T.; Chang, T. Z.; Gonzalez, G. X.; Wang, Y.; Kwon, Y. M.; Kang, S. M.; Compans, R. W.; Champion, J. A.; Wang, B. Z., Double-layered protein nanoparticles induce broad protection against divergent influenza A viruses. *Nat Commun* **2018,** *9* (1), 359.

234. Tang, L.; Zheng, Y.; Melo, M. B.; Mabardi, L.; Castano, A. P.; Xie, Y. Q.; Li, N.; Kudchodkar, S. B.; Wong, H. C.; Jeng, E. K.; Maus, M. V.; Irvine, D. J., Enhancing T cell therapy through TCR-signaling-responsive nanoparticle drug delivery. *Nat Biotechnol* **2018,** *36* (8), 707-716.

235. Fang, L.; Zhao, Z.; Wang, J.; Zhang, P.; Ding, Y.; Jiang, Y.; Wang, D.; Li, Y., Engineering autologous tumor cell vaccine to locally mobilize antitumor immunity in tumor surgical bed. *Sci Adv* **2020,** *6* (25), eaba4024.

236. Toy, R.; Roy, K., Engineering nanoparticles to overcome barriers to immunotherapy. *Bioeng Transl Med* **2016,** *1* (1), 47-62.

237. Smirnov, D.; Schmidt, J. J.; Capecchi, J. T.; Wightman, P. D., Vaccine adjuvant activity of 3M-052: an imidazoquinoline designed for local activity without systemic cytokine induction. *Vaccine* **2011,** *29* (33), 5434-5442.

238. Kraft, J. C.; Freeling, J. P.; Wang, Z.; Ho, R. J., Emerging research and clinical development trends of liposome and lipid nanoparticle drug delivery systems. *J Pharm Sci* **2014,** *103* (1), 29-52.

239. Wittrup, A.; Ai, A.; Liu, X.; Hamar, P.; Trifonova, R.; Charisse, K.; Manoharan, M.; Kirchhausen, T.; Lieberman, J., Visualizing lipid-formulated siRNA release from endosomes and target gene knockdown. *Nat Biotechnol* **2015,** *33* (8), 870-876.

240. Lee, J. S.; Feijen, J., Polymersomes for drug delivery: design, formation and characterization. *J Control Release* **2012,** *161* (2), 473-483.

241. Dowling, D. J.; Scott, E. A.; Scheid, A.; Bergelson, I.; Joshi, S.; Pietrasanta, C.; Brightman, S.; Sanchez-Schmitz, G.; Van Haren, S. D.; Ninkovic, J.; Kats, D.; Guiducci, C.; de Titta, A.; Bonner, D. K.; Hirosue, S.; Swartz, M. A.; Hubbell, J. A.; Levy, O., Toll-like receptor 8 agonist nanoparticles mimic immunomodulating effects of the live BCG vaccine and enhance neonatal innate and adaptive immune responses. *J Allergy Clin Immunol* **2017,** *140* (5), 1339-1350.

242. Nihesh, N.; Manna, S.; Studnitzer, B.; Shen, J.; Esser-Kahn, A. P., A synthetic pathogen mimetic molecule induces a highly amplified synergistic immune response via activation of multiple signaling pathways. *Chem Sci* **2021,** *12* (19), 6646-6651.

243. Wechsler, M. E.; Stephenson, R. E.; Murphy, A. C.; Oldenkamp, H. F.; Singh, A.; Peppas, N. A., Engineered microscale hydrogels for drug delivery, cell therapy, and sequencing. *Biomed Microdevices* **2019,** *21* (2), 31.

244. Roth, G. A.; Picece, V. C. T. M.; Ou, B. S.; Luo, W.; Pulendran, B.; Appel, E. A., Designing spatial and temporal control of vaccine responses. *Nat Rev Mater* **2021**, *7* (3), 174-195.

245. Li, S.; Luo, M.; Wang, Z.; Feng, Q.; Wilhelm, J.; Wang, X.; Li, W.; Wang, J.; Cholka, A.; Fu, Y. X.; Sumer, B. D.; Yu, H.; Gao, J., Prolonged activation of innate immune pathways by a polyvalent STING agonist. *Nat Biomed Eng* **2021**, *5* (5), 455-466.

246. Luo, M.; Wang, H.; Wang, Z.; Cai, H.; Lu, Z.; Li, Y.; Du, M.; Huang, G.; Wang, C.; Chen, X.; Porembka, M. R.; Lea, J.; Frankel, A. E.; Fu, Y. X.; Chen, Z. J.; Gao, J., A STING-activating nanovaccine for cancer immunotherapy. *Nat Nanotechnol* **2017,** *12* (7), 648-654.

247. Wilhelm, J.; Quinones-Perez, M.; Wang, J.; Wang, X.; Basava, V. S.; Gao, J., Antigen folding improves loading efficiency and antitumor efficacy of PC7A nanoparticle vaccine. *J Control Release* **2021,** *329*, 353-360.

248. Sadtler, K.; Wolf, M. T.; Ganguly, S.; Moad, C. A.; Chung, L.; Majumdar, S.; Housseau, F.; Pardoll, D. M.; Elisseeff, J. H., Divergent immune responses to synthetic and biological scaffolds. *Biomaterials* **2019,** *192*, 405-415.

249. Lin, N.; Dufresne, A., Nanocellulose in biomedicine: Current status and future prospect. *Eur Polym J* **2014,** *59*, 302-325.

250. Calvino, C.; Macke, N.; Kato, R.; Rowan, S. J., Development, processing and applications of bio-sourced cellulose nanocrystal composites. *Prog Polym Sci* **2020**, *103*, 101221.

251. Habibi, Y.; Lucia, L. A.; Rojas, O. J., Cellulose nanocrystals: chemistry, self-assembly, and applications. *Chem Rev* **2010,** *110* (6), 3479-3500.

252. Cheng, M.; Qin, Z.; Liu, Y.; Qin, Y.; Li, T.; Chen, L.; Zhu, M., Efficient extraction of carboxylated spherical cellulose nanocrystals with narrow distribution through hydrolysis of lyocell fibers by using ammonium persulfate as an oxidant. *J. Mater. Chem. A* **2014,** *2* (1), 251-258.

253. Habibi, Y.; Chanzy, H.; Vignon, M. R., TEMPO-mediated surface oxidation of cellulose whiskers. *Cellulose* **2006,** *13* (6), 679-687.

254. Sun, B.; Hou, Q.; Liu, Z.; Ni, Y., Sodium periodate oxidation of cellulose nanocrystal and its application as a paper wet strength additive. *Cellulose* **2015,** *22* (2), 1135-1146.

255. Rana, A. K.; Frollini, E.; Thakur, V. K., Cellulose nanocrystals: Pretreatments, preparation strategies, and surface functionalization. *Int J Biol Macromol* **2021,** *182*, 1554-1581.

256. Kim, J.; Mun, S.; Ko, H.-U.; Zhai, L.; Min, S.-K.; Kim, H. C., A Comprehensive Review of Electroactive Paper Actuators. In *Ionic Polymer Metal Composites (IPMCs): Smart Multi-Functional Materials and Artificial Muscles*, Shahinpoor, M., Ed. Royal Society of Chemistry: 2015; pp. 398-422. DOI: 10.1039/9781782627234-00398.

257. De France, K. J.; Badv, M.; Dorogin, J.; Siebers, E.; Panchal, V.; Babi, M.; Moran-Mirabal, J.; Lawlor, M.; Cranston, E. D.; Hoare, T., Tissue Response and Biodistribution of Injectable Cellulose Nanocrystal Composite Hydrogels. *ACS Biomat Sci Eng* **2019,** *5* (5), 2235-2246.

258. Nguyen, J. K.; Park, D. J.; Skousen, J. L.; Hess-Dunning, A. E.; Tyler, D. J.; Rowan, S. J.; Weder, C.; Capadona, J. R., Mechanically-compliant intracortical implants reduce the neuroinflammatory response. *J Neural Eng* **2014,** *11* (5), 056014.

259. Dong, S.; Hirani, A. A.; Colacino, K. R.; Lee, Y. W.; Roman, M., Cytotoxicity and Cellular Uptake of Cellulose Nanocrystals. *Nano LIFE* **2012,** *02* (03).

260. Alexandrescu, L.; Syverud, K.; Gatti, A.; Chinga-Carrasco, G., Cytotoxicity tests of cellulose nanofibril-based structures. *Cellulose* **2013,** *20* (4), 1765-1775.

261. Hanif, Z.; Ahmed, F. R.; Shin, S. W.; Kim, Y. K.; Um, S. H., Size- and dose-dependent toxicity of cellulose nanocrystals (CNC) on human fibroblasts and colon adenocarcinoma. *Colloids Surf B Biointerfaces* **2014,** *119*, 162-165.

262. Sunasee, R.; Araoye, E.; Pyram, D.; Hemraz, U. D.; Boluk, Y.; Ckless, K., Cellulose nanocrystal cationic derivative induces NLRP3 inflammasome-dependent IL-1beta secretion associated with mitochondrial ROS production. *Biochem Biophys Rep* **2015,** *4*, 1-9.

263. Lin, N.; Geze, A.; Wouessidjewe, D.; Huang, J.; Dufresne, A., Biocompatible Double-Membrane Hydrogels from Cationic Cellulose Nanocrystals and Anionic Alginate as Complexing Drugs Codelivery. *ACS Appl Mater Interfaces* **2016,** *8* (11), 6880-6889.

264. Yanamala, N.; Farcas, M. T.; Hatfield, M. K.; Kisin, E. R.; Kagan, V. E.; Geraci, C. L.; Shvedova, A. A., In Vivo Evaluation of the Pulmonary Toxicity of Cellulose Nanocrystals: A Renewable and Sustainable Nanomaterial of the Future. *ACS Sustain Chem Eng* **2014,** *2* (7), 1691-1698.

265. Farcas, M. T.; Kisin, E. R.; Menas, A. L.; Gutkin, D. W.; Star, A.; Reiner, R. S.; Yanamala, N.; Savolainen, K.; Shvedova, A. A., Pulmonary exposure to cellulose nanocrystals caused deleterious effects to reproductive system in male mice. *J Toxicol Environ Health A* **2016,** *79* (21), 984-997.

266. Wang, X.; Chang, C. H.; Jiang, J.; Liu, Q.; Liao, Y. P.; Lu, J.; Li, L.; Liu, X.; Kim, J.; Ahmed, A.; Nel, A. E.; Xia, T., The Crystallinity and Aspect Ratio of Cellulose Nanomaterials Determine Their Pro-Inflammatory and Immune Adjuvant Effects In Vitro and In Vivo. *Small* **2019,** *15* (42), e1901642.

267. Colombo, L.; Zoia, L.; Violatto, M. B.; Previdi, S.; Talamini, L.; Sitia, L.; Nicotra, F.; Orlandi, M.; Salmona, M.; Recordati, C.; Bigini, P.; La Ferla, B., Organ Distribution and Bone Tropism of Cellulose Nanocrystals in Living Mice. *Biomacromolecules* **2015,** *16* (9), 2862-2871.

268. Kolb, H. C.; Finn, M. G.; Sharpless, K. B., Click Chemistry: Diverse Chemical Function from a Few Good Reactions. *Angew Chem Int Ed Engl* **2001,** *40* (11), 2004-2021.

269. Agard, N. J.; Prescher, J. A.; Bertozzi, C. R., A strain-promoted [3 + 2] azide-alkyne cycloaddition for covalent modification of biomolecules in living systems. *J Am Chem Soc* **2004,** *126* (46), 15046-15047.

270. Hermanson, G. T., *Bioconjugate Techniques*. 3 ed.; Academic Press: Waltham, MA, 2013.

271. Tang, W.; Becker, M. L., "Click" reactions: a versatile toolbox for the synthesis of peptide-conjugates. *Chem Soc Rev* **2014,** *43* (20), 7013-7039.

272. Moses, J. E.; Moorhouse, A. D., The growing applications of click chemistry. *Chem Soc Rev* **2007,** *36* (8), 1249-1262.

273. Pichichero, M. E., Protein carriers of conjugate vaccines: characteristics, development, and clinical trials. *Hum Vaccin Immunother* **2013,** *9* (12), 2505-2523.

274. Pravetoni, M.; Comer, S. D., Development of vaccines to treat opioid use disorders and reduce incidence of overdose. *Neuropharmacology* **2019,** *158*, 107662.

275. Townsend, E. A.; Blake, S.; Faunce, K. E.; Hwang, C. S.; Natori, Y.; Zhou, B.; Bremer, P. T.; Janda, K. D.; Banks, M. L., Conjugate vaccine produces long-lasting attenuation of fentanyl vs. food choice and blocks expression of opioid withdrawal-induced increases in fentanyl choice in rats. *Neuropsychopharmacology* **2019,** *44* (10), 1681-1689.

276. Blake, S.; Bremer, P. T.; Zhou, B.; Petrovsky, N.; Smith, L. C.; Hwang, C. S.; Janda, K. D., Developing Translational Vaccines against Heroin and Fentanyl through Investigation of Adjuvants and Stability. *Mol Pharm* **2021,** *18* (1), 228-235.

277. Barrientos, R. C.; Bow, E. W.; Whalen, C.; Torres, O. B.; Sulima, A.; Beck, Z.; Jacobson, A. E.; Rice, K. C.; Matyas, G. R., Novel Vaccine That Blunts Fentanyl Effects and Sequesters Ultrapotent Fentanyl Analogues. *Mol Pharm* **2020,** *17* (9), 3447-3460.

278. Datta, S. K.; Cho, H. J.; Takabayashi, K.; Horner, A. A.; Raz, E., Antigen-immunostimulatory oligonucleotide conjugates: mechanisms and applications. *Immunol Rev* **2004,** *199*, 217-226.

279. Tighe, H.; Takabayashi, K.; Schwartz, D.; Marsden, R.; Beck, L.; Corbeil, J.; Richman, D. D.; Eiden, J. J., Jr.; Spiegelberg, H. L.; Raz, E., Conjugation of protein to immunostimulatory DNA results in a rapid, long-lasting and potent induction of cell-mediated and humoral immunity. *Eur J Immunol* **2000,** *30* (7), 1939-1947.

280. Clauson, R. M.; Berg, B.; Chertok, B., The Content of CpG-DNA in Antigen-CpG Conjugate Vaccines Determines Their Cross-Presentation Activity. *Bioconjug Chem* **2019,** *30* (3), 561-567.

281. Wille-Reece, U.; Flynn, B. J.; Lore, K.; Koup, R. A.; Kedl, R. M.; Mattapallil, J. J.; Weiss, W. R.; Roederer, M.; Seder, R. A., HIV Gag protein conjugated to a Toll-like receptor 7/8 agonist improves the magnitude and quality of Th1 and CD8+ T cell responses in nonhuman primates. *Proc Natl Acad Sci U S A* **2005,** *102* (42), 15190-4.

282. Carlson, E. D.; Gan, R.; Hodgman, C. E.; Jewett, M. C., Cell-free protein synthesis: applications come of age. *Biotechnol Adv* **2012,** *30* (5), 1185-1194.

283. Chen, D.; Disotuar, M. M.; Xiong, X.; Wang, Y.; Chou, D. H., Selective N-terminal functionalization of native peptides and proteins. *Chem Sci* **2017,** *8* (4), 2717-2722.

CHAPTER 2 Understanding How Cationic Polymers' Properties Inform Toxic or Immunogenic Responses *Via* Parametric Analysis.

This chapter is currently under review for publication.

2.1 Introduction.

Cationic materials have found extensive use in immunology and biomedicine on account of their physicochemical properties. They both traverse and disrupt cell and organelle membranes and are therefore used as transfection reagents and antimicrobial coatings[1-3] They are also widely used in drug and gene delivery as they interact with negatively charged biomacromolecules.[3-5] Clinically, cationic materials ranging from poly(ethyleneimine) to Lipofectamine-2000 to chitosan remain key components of gene editing technologies,[6, 7] drug delivery systems,[8, 9] and most recently as ionizable lipid-polymer hybrids that comprise lipid nanoparticles (LNPs).[10, 11]

Despite excellent work optimizing these materials for each application, there is an inherent compromise between functionality, immunogenicity, and toxicity. Immunogenicity and toxicity can be unintended consequences of a desired cellular interaction, such as endosomal disruption. These unintended consequences can limit the clinical translation of a polymer-based system. In this work, we explore what features of cationic polymers lead to an immunogenic or toxic response. Polymers that disrupt cellular membranes for endosomolysis or transfection can cause cell membrane rupture, neutrophil recruitment, and necrosis in the tissue niche.[12-14] Likewise, polymers that complex with negatively charged biomacromolecules for drug delivery can activate pattern recognition receptors or the complement system when unbound from their cargo and released systemically.[15] Specifically, cationic polymers activate the NOD-, LRR- and pyrin domain- containing protein 3 (NLRP3) inflammasome via lysosomal rupture, resulting in IL-1β secretion and pyroptosis.[16-22] IL-1β can initiate productive or damaging immune responses, depending on delivery context.[23-28] Notably, cationic polymers and lipids in mRNA vaccines induce high levels of IL-1β secretion.[23] Currently, costly *in vivo* models of (pre)-clinical biocompatibility

are required before new materials can be translated in the clinic – slowing research progress and leading to costly failures. We hypothesized that mapping the immunogenic and toxic chemical space of cationic polymers would allow researchers to be better informed while designing materials so they can avoid or generate a particular response.

To date, research on the interactions between cationic polymers and the innate immune system has been sporadic and application-driven, led to conflicting conclusions about the ideal material properties for an application [9] In gene delivery, positive charge, hydrophobicity, molecular weight, and formation of self-assembled nanostructures can modulate toxicity.[29-33] In innate immunology, the ratio of charged to hydrophobic groups in a co-polymer can modulate lysosomal rupture, inflammasome activation, and IL-1β secretion.[18] Charge, hydrophobicity, and pK_a can further inform lysosomal rupture and inflammasome activation.[17-20] Finally, physicochemical properties can modulate hemolytic and anti-fouling capacities of antimicrobial polymer coatings.[1, 13, 34-39] Paslay *et al.* assayed the antimicrobial properties of water-soluble poly(methacrylamides) and found that primary amines were superior to tertiary amines in neutralizing *E. coli* growth.[34] While each result provides structure-function information related to one specific application, they do not connect the polymers' properties to their interactions with cells at a mechanistic level.

To explore large parameter spaces in polymer chemistry, new high-throughput synthesis methods enable precise and systematic variation of material properties. Recent advances allow the rapid, high-throughput synthesis of materials with controlled chemical compositions and molecular weights using living polymerization strategies such as reversible addition-fragmentation transfer (RAFT) or atom transfer radical polymerization (ATRP).[40, 41] In particular, the Gormley and Boyer groups have developed high-throughput, air-tolerant, photo-induced electron transfer (PET)-RAFT polymerizations in dimethyl sulfoxide. With this strategy, biocompatible acrylamides containing functional handles for additional modification with biomolecules can be prepared.[41-43] Alternatively, the increasing availability of process chemistry instruments allows rapid and facile synthesis and screening of large polymeric libraries.[36, 40, 44] Using one such instrument, Mann *et*

al. reported the synthesis of 90 PEGylated insulin derivatives to develop an optimized formulation for management of diabetes.[44] With access to these technologies, the toolbox to prepare libraries of polymers for screening is now accessible.

In this work, our goal was to map cationic polymer structure and cellular responses using high-throughput screening. Specifically, we sought to probe how polymers with different charged groups, hydrophobic/hydrophilic groups, and molecular weights induce immunogenicity via the NLRP3 inflammasome or toxicity via necrotic cell death. The polymers targeted for this study were varied parametrically in structure and were designed not to self-assemble, as Lynn *et al.* and others have already confirmed that polymers' size and shape can influence immune activation.[9, 45, 46] To eliminate confounding factors of toxicity, metal- and azide-free reactions were employed. Using RAFT polymerization, we prepared 107 methacrylate-based statistical co-polymers that varied charge, amine identity, hydrophilicity, and hydrophobicity in different proportions and ratios within the co-polymers. We used two amine-containing monomers, *N*,*N*-(dimethylamino)ethyl methacrylate (DMAEMA) and 2-aminoethyl methacrylate (AEMA). These monomers allowed us to test if it was charge or amine identity that contributed to an observed response. To probe hydrophilicity and hydrophobicity, we included two additional monomers, triethylene glycol methyl ether methacrylate (TEGMA) and butyl methacrylate (BMA). A series of co-polymers were synthesized that contain either of the amine monomers with 0, 10, 20, 30, 40, or 50 mol.% of TEGMA or BMA statistically incorporated into the backbone to create a systematic sweep of this domain space. For each combination, polymers were prepared at five molecular weights (7.5, 15, 30, 45, and 60 kg/mol). The resulting polymer library is comprised of water-soluble polymers that vary in charge (10-50 mol.%), hydrophilicity/hydrophobicity (10-50 mol.%), and molecular weight (7.5-60 kg/mol) (**Figure 1**). This parametric and minimalist design allowed us to probe how polymers' structures impact resultant immunogenic or immunotoxic responses of immune cells.

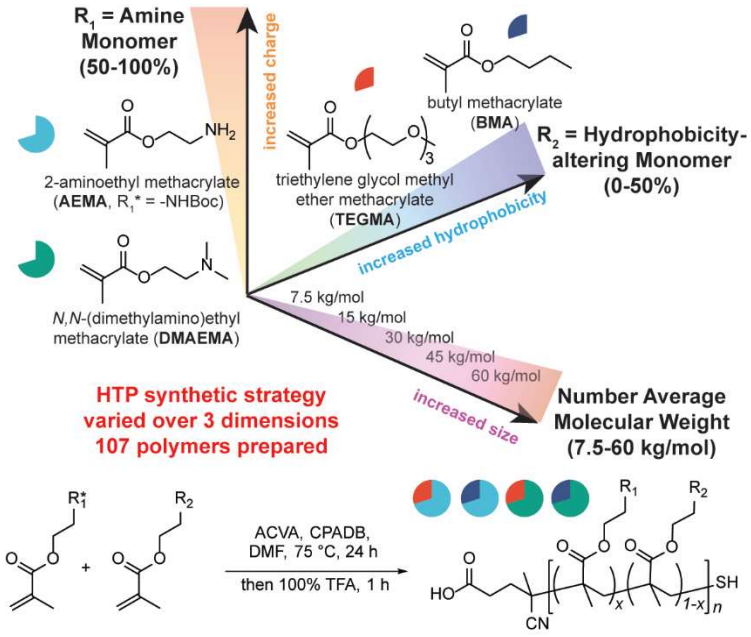

Figure 2.1: High throughput synthesis strategy for polymeric library**.** 107 statistical co-polymers were prepared via RAFT polymerization using 50-100% of the amine-containing monomers (R_1 = BocAEMA or DMAEMA) and 0-50% of the hydrophobicity-modifying monomers (R_2 = TEGMA or BMA) at five different molecular weights (M_n = 7.5-60 kg/mol) to map a broad domain space of physicochemical properties.

2.2 Results and Discussion.

2.2.1 Cationic polymer library synthesis via RAFT polymerization.

To evaluate the ability of cationic polymers with a breadth of physicochemical properties to invoke immunogenic or toxic responses, a library of 107 water-soluble polymers containing two amine monomers (R_1 = 50-100 mol.% DMAEMA or AEMA) and two hydrophilicity/hydrophobicity modifying monomers (R_2 = 0-50 mol.% BMA or TEGMA) at different monomer ratios and number average molecular weights (M_n = 7,500 – 60,000 g/mol) were synthesized. RAFT polymerization was employed with 4,4′-azobis(4-cyanovaleric acid) (ACVA) as initiator and 4-cyanopentanoic acid dithiobenzoate (CPADB) as chain transfer agent (**Figure 2.1**). A Boc-protected form of AEMA (BocAEMA) was used as the monomer for AEMA-containing polymers to prevent side reactions with the primary amine (**Figure S2.1**).[47] All polymers were synthesized on a 100 mg scale in high-throughput manner under an oxygen-free atmosphere using an automated process chemistry robot. The reactions were conducted on a 100 mg scale in 1 mL of DMF, as this dissolved all

monomers and allowed for synthesis of polymers with low dispersities. In contrast to previous analyses of self-assembled polymers,[19] statistical co-polymers lacking a secondary structure were targeted to rule out any effects of the size, shape, or orientation of assemblies on the immune response. Analysis of the polymerizations of DMAEMA or BocAEMA with TEGMA or BMA in DMF confirmed similar rates of incorporation of amine monomers with hydrophilicity- and hydrophobicity-modifying monomers into the polymer scaffold, and the target molecular weights were achieved after 18 h (**Figure S2.2**). In a typical synthesis, 50-70 mg of polymer was obtained after purification (50-70% yield) for chemical characterization and immunological screening.

To characterize the polymer library, size exclusion chromatography (SEC) and proton nuclear magnetic resonance (^{1}H-NMR) spectroscopy were used to evaluate molecular weight and monomer composition, respectively (data are tabulated in **Table S2.1**, while full SEC and ^{1}H-NMR spectra are provided in **Appendix A**). The crude, Boc-protected form of AEMA-containing polymers was used for SEC analysis as they were soluble in DMF. After synthesis, polymers were precipitated, deprotected by treatment with trifluoroacetic acid (TFA) for 1 h, precipitated again, and dialyzed sequentially against 0.5 M aqueous NaCl and deionized water for purification. DMAEMA-containing polymers were similarly treated with TFA, though they did not require Boc deprotection, as a control. Polymers were then freeze dried and analyzed via ^{1}H-NMR in D_2O. The final molar ratio of monomers in the polymers (*i.e.,* mol.% of AEMA or DMAEMA and BMA or TEGMA after purification) was determined by ^{1}H-NMR as described in **Figure S2.3-S2.4**. To confirm that TFA treatment did not result in decomposition or cross-linking of the polymers during deprotection, DOSY-NMR was conducted on a subset of the polymer library after deprotection and purification to determine diffusion constants (D) (**Figure S2.5**). Indeed, log(D) obtained via DOSY correlated linearly with M_n, suggesting that polymers did not decompose during TFA treatment.[48] Most experimentally determined M_n values and NMR compositional ratios were consistent with expectations, having a composition of monomers within 7% of the target, narrow dispersities (usually $Đ < 1.4$), and molecular weight within 30% of the target M_n (**Table S2.1**). It

was observed that high M_n, DMAEMA-containing co-polymers had higher dispersities of $Đ$ = 1.3-1.7, consistent with previous reported trends and considered sufficient for preliminary screening.[49]

After successfully synthesizing the polymers, additional characterization was conducted on a subset of polymers to confirm their desired behavior in solution. Eight polymers were selected that spanned each of the four monomer combinations in a 70:30 molar ratio ($AEMA_{70}$-BMA_{30}, $AEMA_{70}$-$TEGMA_{30}$, $DMAEMA_{70}$-BMA_{30}, $DMAEMA_{30}$-$TEGMA_{70}$) and two different molecular weights (15 and 60 kg/mol) for analysis. First, to confirm that the statistical co-polymers did not self-assemble under biological conditions, dynamic light scattering (DLS) was conducted in cell culture medium (**Table S2.2**). The selected polymers were found to have hydrodynamic radii of 4-11 nm, consistent with other reports of hydrophobic, single polymer chains in water.[50] To confirm the different ionization of AEMA- and DMAEMA-containing co-polymers in biological solutions, polymers were titrated with aqueous NaOH (**Figure S2.6**). It was found that AEMA-containing co-polymers had pK_as *ca.* 7.1-7.2 while DMAEMA-containing co-polymers had pK_as *ca.* 6.4-6.7. Finally, to confirm that polymers would not alter pH beyond a tolerable level when dissolved in cell culture medium, 100 µg/mL of the polymers (or strong acid and base controls) were added to phenol-red containing culture medium, and the pH was monitored by absorbance spectroscopy (**Figure S2.7**). Again, no significant changes to pH were observed when polymers were added to the culture medium, supporting the use of these polymers in biological settings. Having successfully synthesized and characterized 107 polymers in the domain space of interest, we then moved on to screen immune activity and cell death in a high-throughput *in vitro* fashion.

2.2.2 Polymers' compositions inform immunogenicity and toxicity.

Synthetic polymers have the potential to interact with a large range of biomolecules and organelles to induce an immune response.[9, 51] This response might be characterized by protein adsorption, immune cell activation, and/or tissue necrosis dependent on the physicochemical properties of the polymer and the route of administration. Optimizing such responses for specific

applications is of critical importance for the safe implementation of biomaterials. Gene editing, mRNA vaccines, and antibacterial coatings all employ cationic polymers.[3] Many more polymer-based technologies which complex nucleic acids or other biomolecules are in development. Preventing unwanted toxicity and immunogenicity induced by the polymers while maximizing intended biological responses could improve patient outcomes and lower the cost of development. Most *in vitro* screens focus only on maximizing biological responses, leading to the possibility for expensive, late-stage biocompatibility failures. As such, our initial studies sought to broadly map the ability of the synthesized polymers to induce an immunogenic or toxic response. With our library of 107 polymers that vary parametrically over several dimensions, we can correlate toxicity and immunogenicity with polymer structure – namely charge, hydrophobicity/hydrophilicity, and molecular weight. Such a structure-property map can allow early and rapid identification of monomer compositions that generate desired biocompatibility features while still maintaining their functionality for a breadth of biological applications.

Our goal was to determine which characteristics of the polymer correlated with which types of responses. Activation of the NLRP3 inflammasome and subsequent IL-1β secretion are regulators of pro-inflammatory pathways, and many polymers have been shown to activate this immune sensor via disruption of homeostasis.[16-21, 26] Alternatively, many polymers induce toxic responses independently of inflammatory pathways (*e.g.*, via direct membrane disruption).[13, 34, 52] Cells were treated with each of the 107 polymers, and secretion of IL-1β and an intracellular enzyme, lactate dehydrogenase (LDH), were assayed in the supernatant. In this way, polymers' charge, hydrophobicity/hydrophilicity, and molecular weight could be mapped against their cellular responses, and emergent features could be observed. The THP-1 human monocyte cell line was employed, as these secondary cells express key components of the immune system, retain high phagocytic capacity, and have been transduced with a variety of reporter constructs for mechanistic analysis.[53] THP-1 cells were treated with lipopolysaccharide (LPS) for 3 h to prime inflammasome formation and then with each of the 107 polymers at 6.25, 12.5, 25, 50, or 100

μg/mL for 5 h. Toxicity was evaluated by LDH secretion using a commercially available assay, and IL-1β secretion was evaluated by enzyme-linked immunosorbent assay (ELISA). It is key to note that, while IL-1β secretion was selected as the main readout in this study, this workflow is amenable to analysis of other pro-inflammatory cytokine (such as TNF-α) or multiplexed readouts.

The results of high-throughput *in vitro* immunogenicity and toxicity screening at three concentrations are presented in **Figure 2.2A-B**, while full results of this initial screen are provided in **Figure S2.8-S2.9**. We quantified observed trends by assuming that the results at each of the five concentrations tested were independent (5 concentrations x 2 assays = 10 conditions). A principal component analysis was then conducted and used to map each polymer structure against the observed biological response (**Figure 2.2C**). Principal component axes 1 and 2 (PCA-1 and PCA-2) comprised 80% of the variance in the data and revealed three regions of interest. First, the presence of the hydrophobic monomer, BMA, or the charged monomer, AEMA, resulted in toxic polymers regardless of molecular weight or other co-monomer identity. These results imply that the presence of ≥50 mol.% charged, primary amine-containing monomers or ≥10 mol.% hydrophobic monomers in a polymer will likely result in at least partial toxicity. The greatest toxicity was observed when either amine monomer, AEMA or DMAEMA, was co-polymerized with 10-20 mol.% BMA, demonstrating that positive charge and hydrophobicity interplay to inform toxic responses. These results are consistent with previous reports that highly charged, hydrophobic materials are effective as anti-microbial coatings and anti-cancer chemotherapies on account of their high toxicity.[34, 35, 54] In most cases, toxicity is reduced as molecular weight decreases, particularly in hydrophobic compounds (≥30 mol.% BMA). Second, high molecular weight (M_n = 45 or 60 kg/mol), hydrophobic co-polymers comprised of DMAEMA and BMA induced IL-1β secretion, particularly when >20 mol.% of BMA was incorporated into the polymer scaffold. This result suggests that increasing the ratio of hydrophobic monomer (BMA) to tertiary amine monomer (DMAEMA) in high molecular weight systems can shift the biological response from a toxic phenotype to an immunogenic phenotype. Interestingly, this observation is consistent with

work recently reported by Baljon, *et al.* in a small library of self-assembled block co-polymers containing DMAEMA and BMA in different molar ratios.[18] Finally, co-polymers derived from DMAEMA and TEGMA only resulted in a toxic response at high molecular weight ($M_n \geq 45$ kg/mol) and with <20 mol.% TEGMA. This result demonstrates that, in the design of polymers for non-toxic applications like gene delivery, a composition of DMAEMA and TEGMA with ≥20 mol.% of TEGMA and/or molecular weights below 45 kg/mol would be expected to be biocompatible.

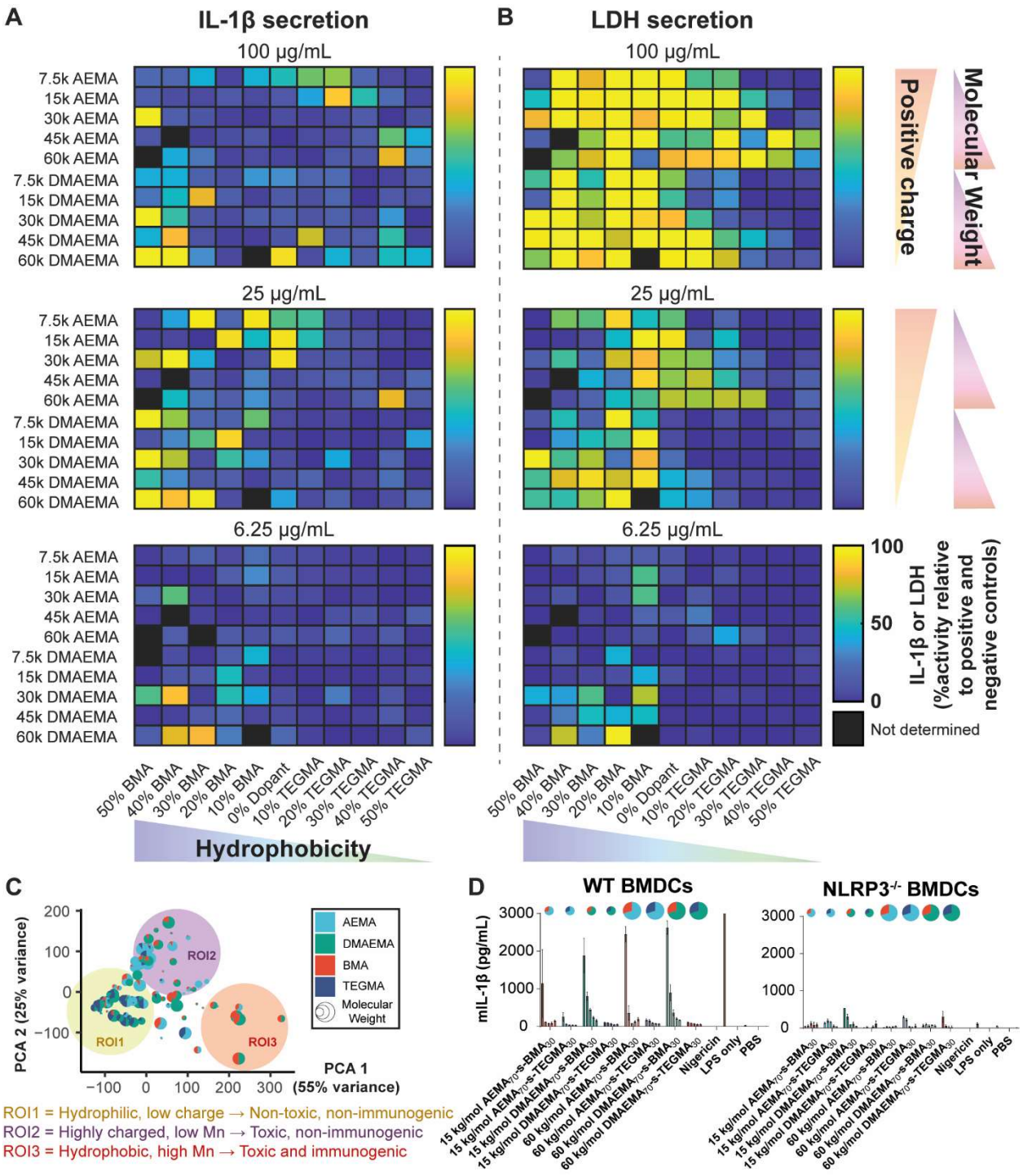

Figure 2.2: Results and analysis of high-throughput immunological and toxicity screening. (A) IL-1β and (B) LDH screens at high (100 µg/mL), medium (25 µg/mL), and low (6.25 µg/mL) concentrations for each of the 107 polymer library entries. (C) Principal component analysis was used to elucidate trends in the screen. The first two principal component axes (PCA-1 and PCA-2) are plotted, and polymer composition and size are represented using size and color of dots. Three regions of interest are identified as shown. (D) Validation of IL-1β secretion results in bone marrow derived dendritic cells (BMDCs) from wild-type and NLRP3$^{-/-}$ mice demonstrate NLRP3-dependence of cytokine production. From left to right, the bars shown indicate 100, 50, 25, 12.5, and 6.25 µg/mL of polymer incubated with LPS-primed BMDCs for 5 h.

These combinations of features, placed in context, present the compelling observation that it is not any single feature that drives toxicity or immunogenicity. Rather, it is the ratio between hydrophobicity, charge, and ethylene glycol in a polymeric scaffold. The overall molecular weight act as an amplifier, increasing the effects of a physicochemical parameter such as hydrophobicity. While reducing positive charge density and introducing ethylene glycol moieties (such as TEGMA) have long been known to enhance biocompatibility, our screening methods provide a map of cationic polymer structures that can afford different responses. With these principles and "map" of design parameters in place, a particular polymer might be adjusted to accommodate functional performance. For example, DNA binding can be enhanced by using a low quantity of a charged monomer, while toxicity and immunogenicity can be mitigated by adjusting the ratio of corresponding hydrophobic and ethylene glycol-containing monomers. In essence, we envision that polymers which avoid the "hot spots" of immunogenicity and toxicity within this map can be designed while still maintaining their desired functionality for one of many possible applications. In addition, this screening workflow employs a rapid and low-cost strategy to synthesize and characterize a polymeric library and select a candidate for use. Similar to approaches taken in medicinal chemistry, ELISAs and other colorimetric readouts (such as the LDH toxicity assay) can allow multiplexed characterization of polymers *in vitro*, narrowing the scope of a screen prior to *in vivo* testing. We envision broad applicability of this screening strategy to accelerate research in polymer-based drug delivery systems, antimicrobial materials, and tissue scaffolds.

After conducting this broad screen, we sought to determine if these observed trends held in primary cells. Eight representative polymers representing each of the major categories of charge, hydrophobicity/hydrophilicity, and molecular weights (based on the preliminary screening data) were employed in primary cell studies. The eight polymers consist of each of the four co-monomer combinations at a 70:30 ratio ($AEMA_{70}$-BMA_{30}, $AEMA_{70}$-$TEGMA_{30}$, $DMAEMA_{70}$-BMA_{30}, and $DMAEMA_{70}$-$TEGMA_{30}$) prepared at 15 and 60 kg/mol. Within this set, 15 kg/mol $AEMA_{70}$-BMA_{30} is representative of polymers with the highest toxicity, 60 kg/mol $DMAEMA_{70}$-BMA_{30} is

representative of inflammasome-activating polymers, and 15 kg/mol $DMAEMA_{70}$-$TEGMA_{30}$ is representative of non-toxic polymers. LDH production and IL-1β secretion were assayed in monocyte-derived dendritic cells (MoDCs), isolated from peripheral human blood, and bone marrow derived dendritic cells (BMDCs), isolated from wild-type or NLRP3-deficient C57Bl/6J mice (**Figure 2.2D** and **S2.10-S2.11**). In MoDCs and wild-type BMDCs, comparable IL-1β and LDH secretion trends were observed relative to THP-1 cells, supporting the clinical relevance and cross-species translatability of the primary screen results. Moreover, repeating the assay in BMDCs from NLRP3-deficient mice reduced IL-1β secretion while having a minimal effect on toxicity (**Figure 2.2D** and **S2.11**). It is worthy of note that, after treatment of NLRP3-deficient BMDCs with any of the polymers or nigericin, low levels of IL-1β are observed suggesting either incomplete knock out of NLRP3 gene or IL-1β secretion through alternative pathways.[26]

We then sought to test whether the map of physicochemical properties and immunotoxic responses generated in this screen would match other positively charged, hydrophobic polymers. Some of the most common polymers in this class are branched poly(ethyleneimine) (PEI)-based systems used to deliver nucleic acids.[15] These polymers are water-soluble and contain a dendrimer-like scaffold of secondary and tertiary amines. Based on our screening data, PEI should fall within the ratio of positive charge to hydrophobicity that induces IL-1β production and cellular toxicity. LDH and IL-1β production were assayed when BMDCs were treated with branched PEI with three molecular weights: 60, 10, and 1.8 kg/mol. It was found that branched PEI behaved similarly to co-polymers comprised of DMAEMA and >20 mol.% BMA. 60 kg/mol branched PEI induced IL-1β secretion at all concentrations tested, while 10 kg/mol and 1.8 kg/mol PEI induced toxicity in the absence of inflammasome activation except at the highest concentration tested (**Figure S2.12**). It is important to note that typical gene delivery protocols employ 10-20 μg/mL of PEI, so the lower concentrations tested hold important insight to the immune responses generated by clinically relevant gene delivery systems. Altogether, these results suggest that polymer-cell interactions induce cell death independent of NLRP3

inflammasome activation but that NLRP3 is required for IL-1β secretion. Moreover, this screen can broadly inform the design of water-soluble, cationic polymers used in gene delivery applications. Given these results, mechanistic studies were undertaken to address why the different physicochemical properties of each polymer induced different responses. While it is likely that multiple mechanisms are involved, a greater understanding of these responses would inspire design principles for new materials in a breadth of applications.

2.2.3 Cells treated with polymers undergo morphological changes.

After validating the activity of the polymers in primary cells, time-lapse microscopy was employed to observe the polymer-cell interactions that mediated the immunogenic and toxic responses. Polymer-induced changes to organelle pH, lysosomal rupture, or cell membrane integrity could all play a role in the subsequent toxic or immunogenic responses. Lysosomal rupture is already a well-documented component of NLRP3 inflammasome activation and various cell death pathways, yet not all toxic polymers in the data set were found to induce inflammasome activation.[17-20] To probe the mechanisms behind observed immunogenicity and toxicity, THP-1 cells were treated with phorbol 12-myristate-13-acetate (PMA) to induce an adherent, macrophage-like phenotype and provide stability for time-lapse imaging.[53] DND-189 was then used to probe lysosomal pH, as it localizes in acidic compartments of the cell and decreases in fluorescence as pH increases.[55] PMA-differentiated THP-1 cells were primed with LPS, stained with DND-189, treated with the indicated polymers, and imaged for 1 h in 2 min intervals (**Figures 2.3** and **S2.13**). No changes in lysosomal pH were found in live cells prior to death; however, large changes to cellular morphology upon death were observed in cells treated with polymers that induced non-specific lysis relative to those which underwent osmotic swelling upon death. 60 kg/mol $DMAEMA_{70}$-BMA_{30} polymers underwent swelling upon death consistent with NLRP3-mediated pyroptosis and osmolytic lysis (as has been shown previously[20]), whereas 15 kg/mol $AEMA_{70}$-BMA_{30} polymers did not display swelling upon death. The polymers that underwent

osmolytic lysis were the same polymers that induced IL-1β production in the preliminary screen, suggesting that this lysis could be related to inflammasome activation. To test whether this result occurred due to polymer-cell interactions or NLRP3-driven pore formation, the experiment was repeated in NLRP3-deficient THP-1 cells (**Figures 2.3** and **S2.14**). Similar swelling behavior was observed for the wild-type THP-1 cells, supporting the hypothesis that differences in polymer-cell interactions underlie the cell death observed in our high-throughput screen. Finally, the assays were repeated in A549 (human epithelial cells), HeLa (human cervical cancer cells), and murine BMDCs to evaluate the relevance of these results in different cell lines and species, which might have different lysosomal characteristics. Similar swelling phenomena were observed in all cells tested (**Figures 2.3** and **S2.15**), demonstrating that swelling is a basic and consistent feature of cells treated with 60 kg/mol $DMAEMA_{70}$-BMA_{30} and other similar hydrophobic, high M_n polymers.

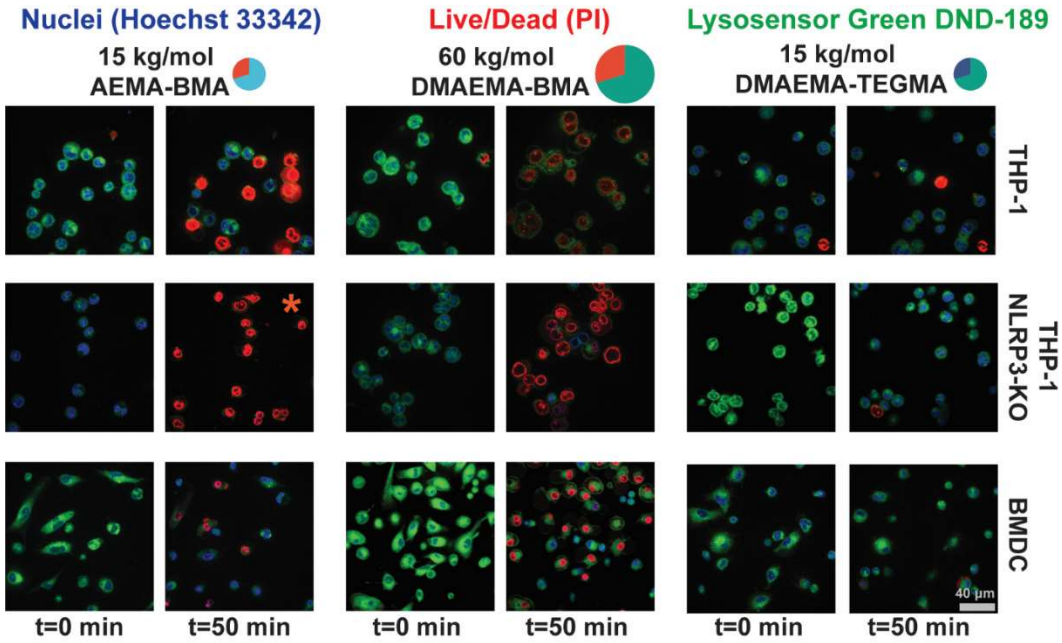

Figure 2.3: Imaging the rupture of cells treated with representative polymers reveals distinct modes of rupture and death. Time-lapse imaging reveals cellular swelling induced by inflammasome-activating 60 kg/mol DMAEMA-BMA co-polymer but not toxic 15 kg/mol AEMA-BMA co-polymer when treated with three different cell lines. This phenomenon was found to persist independently of NLRP3 using NLRP3-KO cells. Time lapse images can be found in and **Figures S2.13-S2.15**. For the (*) denoted image, t = 40 min as all cells died and imaging was stopped. Scale bar is representative of all images.

As DND-189 can non-specifically localize in acidic organelles, these experiments were further validated using HEK-293T cells containing a genetically encoded biosensor for lysosomal pH called FIRE-pHLy.[56] The HEK FIRE-pHLy cells contain a lysosome associated membrane protein 1 (LAMP-1) fusion protein bound to mCherry, which is pH invariant, and mTFP1, which exhibits pH-sensitive fluorescence (pK_a = 4.3), to allow ratiometric pH determination. When HEK FIRE-pHLy cells were treated with the eight polymers of interest and pH was analyzed via flow cytometry 1 h later, no significant changes in lysosomal pH were observed in live cells prior to cell death (**Figure S2.16**). These results show that these polymers do not directly modulate lysosomal pH and therefore this is not their mechanism for inflammasome activation. It is possible that they undergo physicochemical changes in response to endosomal maturation as has been reported previously.[20, 31] With this caveat in mind, it was important to explore the differential mechanisms which might explain the polymer-induced lysis by different classes of polymers.

2.2.4 Cationic polymers disrupt cell membranes to induce cell death and enter the cytosol for immunogenic responses.

Having observed that DND-189-stained THP-1 cells treated with polymers induced cell swelling responses in a polymer composition-dependent fashion, it was important to identify where polymers with different compositions localize in the cell. To do so, fluorescently tagged versions of the eight polymers of interest (**Figure S2.17**) were generated. AEMA-containing polymers ($AEMA_{70}$-BMA/$TEGMA_{30}$) were directly labelled with 5 mol.% Alexa Fluor 488 (AF488) dye (relative to total moles of monomers) using an NHS-ester activated form of the dye. As DMAEMA-containing polymers lack a functional site for AF488 modification, DMAEMA-containing polymers with 5 mol.% AEMA ($DMAEMA_{65}$-BMA/$TEGMA_{30}$-$AEMA_5$) were synthesized and subsequently labelled with AF488 dye using analogous NHS ester chemistry (**Figure S2.17**). With fluorescently labelled polymers in hand, PMA-differentiated, LPS-primed THP-1 cells were treated with the fluorescently tagged polymers for 15, 30, and 60 min, washed to reduce background

AF488 signal, and imaged by confocal microscopy (**Figure 2.4**). It was observed that toxic polymers (*e.g.*, 15 kg/mol $AEMA_{70}$-BMA_{30}) did not enter the cell and instead stuck to the outer cell membrane. On the other hand, the high molecular weight, hydrophobic co-polymers such as 60 kg/mol $DMAEMA_{70}$-BMA_{30} entered the cell prior to rupture. These results suggest that differences in immunogenic or toxic behavior could be explained by polymer-cell interactions. Highly charged polymers disrupt the outer cell membrane to facilitate toxic responses, while less charged, hydrophobic polymers enter the cell to induce lysosomal rupture and immunogenic responses.

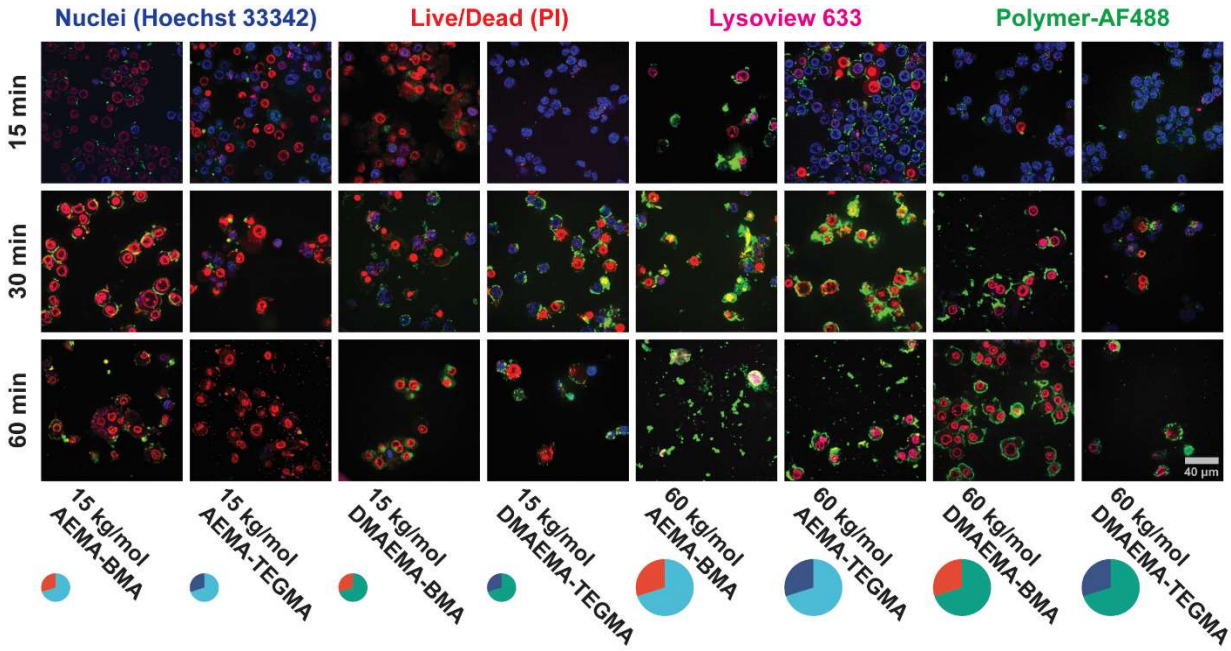

Figure 2.4: Analysis of cationic polymer localization in the cell for 8 representative polymers. Treatment of THP-1 cells with AF488-labelled polymers was employed to determine cellular localization of polymers at 15, 30, and 60 min after treatment with cells. Cells were LPS primed, stained with the indicated dyes, treated with polymers for the indicated times, then washed and immediately imaged using a confocal microscope (40x oil lens). Scale bar is representative of all images.

With some possibilities eliminated and a clear set of biological phenomena identified, the next step was to evaluate whether the observed cell-polymer interactions corresponded with IL-1β and LDH secretion identified in the primary screen. To do so, THP-1 cells that contain a green fluorescent protein-labelled ASC inflammasome adaptor protein (THP-1 ASC-GFP) were used.

Upon inflammasome activation, cytosolic ASC-GFP condenses into one or more “specks” which can be identified visually by confocal microscopy.[57] THP-1 ASC-GFP cells were primed, stained, and then treated with polymers immediately prior to the onset of imaging. Speck-containing cells were counted in each image, plotted as the percentage of total cells in plane, and compared to cells treated with nigericin as control (**Figures 2.5A** and **Figure S2.18-S2.19**). Treatment of the cells with 60 kg/mol $DMAEMA_{70}$-BMA_{30} and 60 kg/mol $AEMA_{70}$-BMA_{30} resulted in speck formation in about 20% of cells (compared to 24% of cells treated with 5 μM nigericin as a positive control), while cells treated with 15 kg/mol $AEMA_{70}$-BMA_{30} and $AEMA_{70}$-$TEGMA_{30}$ polymers induced toxicity without the formation of specks. While a few specks (<10%) were observed in the non-toxic, non-immunogenic polymers, these results are likely a result of stressors from the imaging environment (though this was mitigated as best as possible by using an environmental control chamber with exogenous CO_2 and heating during imaging) and can result from other cell death pathways, some of which also use the ASC adaptor protein.[58]

The above results raise the question of whether the inflammasome activation was the result of conventional phagocytic pathways or transcytosis across the cell membrane, as was previously reported for acetylated PEI dendrimers.[59] To test this hypothesis, the assay was repeated in the presence of Cytochalasin D (CytoD), an inhibitor of actin polymerization which, in turn, prevents active transport into the cell. This assay probed whether active transport into the cell was necessary for the observed inflammatory and toxic responses. In the presence of CytoD, ASC speck formation was almost completely inhibited, providing strong evidence that active transport of polymers into the cell is required for NLRP3 inflammasome activation (**Figures 2.5B** and **S2.20-S2.21**). Moreover, cell death in the presence of CytoD was unaffected. In accordance with polymer-AF488 tracking studies, this result suggests that polymers induce a toxic phenotype by membrane disruption in an active transport-independent fashion. Taken together with our IL-1β, LDH, and cell swelling analyses, we conclude that large, hydrophobic polymers induce NLRP3 inflammasome activation and cell death via swelling and rupture of membrane organelles, such

as lysosomes. Meanwhile, small, highly charged polymers induce necrotic death by alternative means, such as direct membrane disruption (**Figure 2.5C**). An open question that remains is the mechanism of active transport into the cell, as PEI-based systems undergo different mechanisms of endocytosis or transcytosis based on their physicochemical properties.[59] These results provide mechanistic insight to the behavior of cells that are treated with cationic polymers and could inspire rational design of new polymers for a breadth of applications.

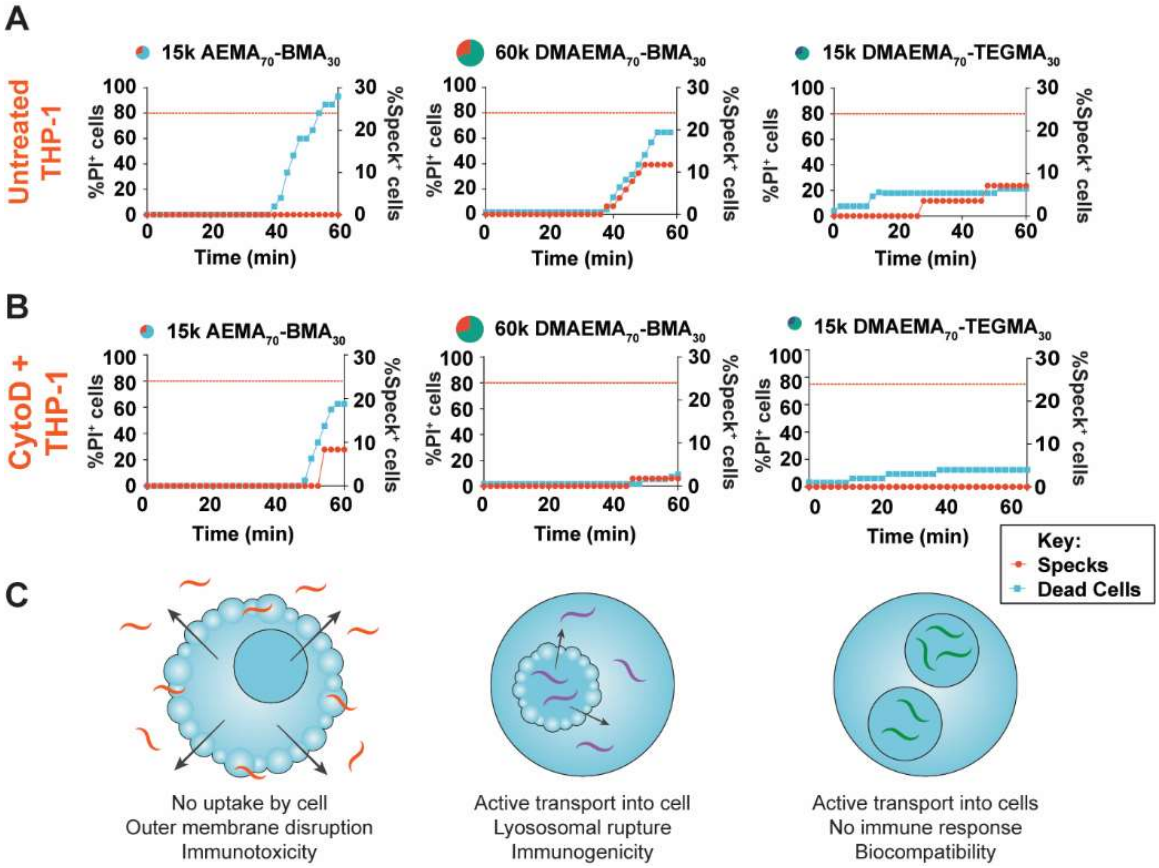

Figure 2.5: Probing the role of active transport on inflammasome activation induced by representative polymers. THP-1 ASC-GFP cells were treated with (A) the indicated polymers or (B) the indicated polymers + Cytochalasin D, and cell death and ASC speck formation were evaluated as a function of time and plotted as shown. Time lapse images and data for additional polymers can be found in **Figures S2.18-S2.21**. (C) Based on the results of A-B in conjunction with other data from this work, models of cell-polymer interactions for each of the three polymers shown are depicted.

2.2.5 Immunogenic and immunotoxic phenotypes can be observed in vivo.

Having conducted this extensive screen and mechanistic analysis, the next goal was to demonstrate the functional relevance of these data for biological applications. To probe the immunotoxic behavior of inflammasome-activating polymers *in vivo*, three polymers representing the classes of materials described in **Figure 2.5C** were administered intravenously to the tail vein. 15 kg/mol $AEMA_{70}$-BMA_{30} represents a toxic membrane rupturing polymer, 60 kg/mol $DMAEMA_{70}$-BMA_{30} represents an immunogenic, lysosome-rupturing polymer, and 15 kg/mol $DMAEMA_{70}$-$TEGMA_{30}$ represents a non-toxic polymer. Using the model of Tahtinen *et al.*, the parameters of immune response and IL-1β mediated toxicity were measured including cytokine production, body temperature, and splenic immune responses. (**Figure 2.6A**).[23] Recent reports on mRNA liposome and lipid nanoparticle vaccine formulations, bearing charged amines, indicated that IL-1 was a key mediator of immunogenicity and reactogenicity toward such formulations in a composition dependent manner. It was hypothesized that the physicochemical properties of these polymers could similarly bias the immune response and inspire design principles for future therapeutics.

After injection of 50 μg polymer, mice (n=4/group) treated with 15 kg/mol $AEMA_{70}$-BMA_{30} or 15 kg/mol $DMAEMA_{70}$-$TEGMA_{30}$ did not exhibit changes to body temperature or other adverse health outcomes. On the other hand, two mice treated with 60 kg/mol $DMAEMA_{70}$-BMA_{30} died within 1 h after injection, possibly a result of cytokine storm or clotting of the polymers, and the remaining mice showed a large decrease in body temperature indicative of a sickness response (**Figure 2.6B**). After 6 h, mice were sacrificed. Cytokines in the sera were evaluated, and it was observed that mice treated with 60 kg/mol $DMAEMA_{70}$-BMA_{30} had significant increases in IL-1α and IL-1β (**Figure 2.6C-D**). Surprisingly, this increase in IL-1 cytokines was not accompanied by increases in other pro-inflammatory cytokines such as TNF-α and MCP-1 (**Figures 2.6E-F**), which were found to be increased in mice treated with the non-immunogenic, 15 kg/mol $DMAEMA_{70}$-$TEGMA_{30}$ polymers. This TNF-α and MCP-1 cytokine profile was unexpected and could result from improved systemic trafficking of hydrophilic, TEGMA-containing polymers relative to the

more positively charged polymers (which are more likely to adsorb serum proteins and be rapidly cleared). A non-significant increase in spleen size was observed in mice treated with 60 kg/mol $DMAEMA_{70}$-BMA_{30}, although there were no changes in leukocyte composition (**Figures 2.6G** and **S2.21-S2.22**). When intracellular cytokine staining was conducted on leukocytes for IL-1α, pro-IL-1β, and TNF-α, few differences between groups were observed (**Figure S2.23**). Notably, mice treated with 15 kg/mol $DMAEMA_{70}$-$TEGMA_{30}$ had an increase in IL-1α$^+$ macrophages, which again suggests that these polymers could be more effectively transported to the spleen for endocytosis, but more work must be conducted to formulate these materials for optimized delivery.

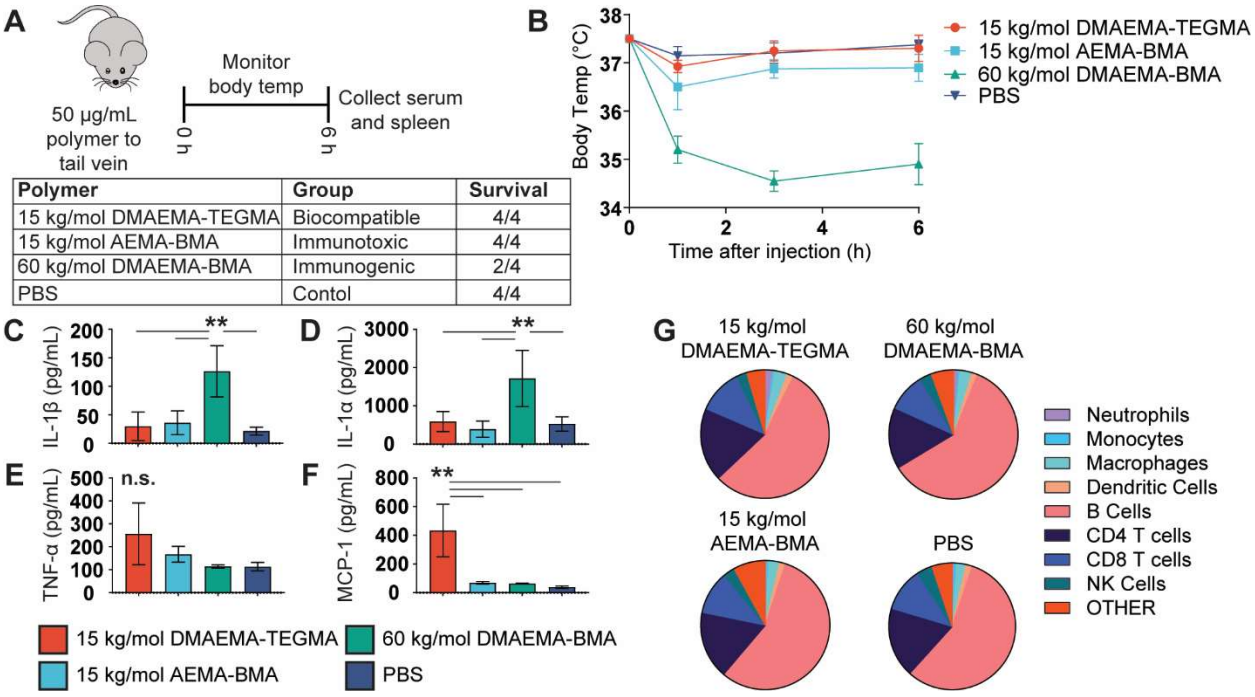

Polymer	Group	Survival
15 kg/mol DMAEMA-TEGMA	Biocompatible	4/4
15 kg/mol AEMA-BMA	Immunotoxic	4/4
60 kg/mol DMAEMA-BMA	Immunogenic	2/4
PBS	Contol	4/4

Figure 2.6: In-vivo model of immunotoxicity induced by representative polymers. (A) Experimental paradigm for immunotoxicity study and survival after injection. (B) Body weight was monitored 1, 3, and 6 h after injection for mice treated with each polymer. (C-F) Serum cytokines assayed 6 h after injection of polymers was determined via multiplex cytokine panel. (G) Spleen leukocyte composition (% of live CD45$^+$ cells) averaged for mice treated with each polymer. **, $p < 0.01$ using Tukey's multiple comparisons test.

Understanding the physicochemical properties that induce an inflammatory response is a central requirement for the synthesis of next-generation biomaterials. While these immunogenic

polymers were found to induce IL-1β and systemic toxicity when administered intravenously in mice, IL-1β producing materials can also be used as immunological adjuvants for vaccination and immunotherapy.[21, 23, 60] This highlights an insight similarly reported by Tähtinen, *et al.*, and others regarding IL-1β-inducing lipid nanoparticles: the immunogenicity of IL-1β is context-dependent.[23, 26] IL-1 receptor activation modulates innate immunity indirectly via prostaglandins, nitric oxide synthases, cyclooxygenases, and MyD88 signaling, which in turn result in vasodilation, hypotension, and production of cytokines such as IL-6.[26, 61] As such, systemic release of IL-1β can cause fever and inflammation, and it is commonly observed during cytokine release syndrome and autoinflammatory disease.[27, 28, 62, 63] On the other hand, lymphatic secretion of IL-1β concomitant with NLRP3 inflammasome activation has been shown to play a key role in adjuvanticity of mRNA lipid nanoparticles and saponins used in the FDA-approved AS01 adjuvant systems.[23, 64] Developing methods to formulate cationic polymers for lymphatic delivery will therefore be of importance for the design of next-generation adjuvants, as cationic polymers provide a low-cost, tunable framework for immune modulation. While the cationic methacrylate platform holds promise for such applications, studies with PEI (**Figure S2.12**) demonstrate that the screening data described herein could be applied to a breadth of drug and gene delivery systems. Altogether, these results show that cationic, water-soluble polymers with $M_n \geq 45$ kg/mol and >20 mol.% BMA can induce IL-1 cytokine production via NLRP3 inflammasome activation both *in vitro* and *in vivo*, inspiring design principles for the next generation of biomaterials.

2.3 Conclusion and Future Directions.

Polymers have emerged as key components of many biotechnologies. For the safe and effective implementation of polymers for these technologies, better methods are needed to rapidly probe their characteristics, such as charge or hydrophobicity, and determine how they affect immunological and/or toxic responses.[9] Here, we show that physicochemical characterization of a polymeric library in tandem with *in vitro* high-throughput screening can elucidate immunogenic

and toxic responses emergent from polymers' compositions. Polymers present challenges in high-throughput synthesis and screening resulting from batch-to-batch variability in their synthesis and complex behavior in solution. Recent technological advances, including commercially available process chemistry instruments and scalable living polymerization strategies, now make such screens feasible. Our model system was prepared using a process chemistry robot and RAFT polymerization. Two positively charged amine-containing monomers, AEMA and DMAEMA, and two hydrophobicity/hydrophilicity altering monomers, BMA and TEGMA, were co-polymerized at various molar ratios and molecular weights. Using a screening approach based on two assays, the IL-1β ELISA and LDH toxicity assay, we generated a structure-property map of 107 water-soluble, cationic polymers representative of materials used in drug or gene delivery systems, antimicrobial coatings, and other biomaterials. We then conducted time lapse microscopy studies to identify a mechanistic basis for the observed responses. With these microscopy experiments, we observe that classes of polymers with different IL-1β and/or LDH secretion profiles correspond with underlying differences in polymer-cell interactions (**Figure 2.5C**). Finally, an *in vivo* biocompatibility study was undertaken, where we showed that it is possible to extrapolate the *in vitro* results from the high-throughput screening dataset to *in vivo* responses with reasonable fidelity. These results can inform the development of future cationic biomaterials.

Overall, this study provides three key insights: (1) the correlation of immunogenicity and toxicity with polymer-cell interactions, (2) a "map" of the composition of polymers which result in these interactions, and (3) a simple and low-cost workflow to identify immunotoxic behavior of a polymer prior to *in vivo* testing. First, we correlated immunogenicity and toxicity induced by polymers with underlying polymer-cell interactions. Baljon, *et al.*[18] recently reported that the ratio of DMAEMA to BMA in a polymer can modulate NLRP3 inflammasome activation. Adding to this finding, we report that the mechanistic feature behind this phenomenon is the polymer's ability to enter the cell. Hydrophobic, high M_n polymers (*i.e.*, those ≥ 45 kg/mol and containing DMAEMA and >20 mol.% BMA) displayed robust inflammasome activation in an active transport-dependent

fashion. These results strongly suggest that polymer entry into the cell is the determining factor for homeostatic changes that result in NLRP3 inflammasome activation. Highly charged, low M_n polymers (*i.e.,* those ≤ 30 kg/mol and comprised of ≥50 mol.% AEMA) induced toxicity via outer cell membrane disruption. Finally, less charged, hydrophilic polymers (*i.e.,* those containing DMAEMA and ≥20 mol.% TEGMA) were taken up to a lower extent but did not disrupt membranes and were therefore biocompatible at all concentrations tested. Of course, one open question that remains is the mechanism of polymer-induced membrane and organelle disruption. This question is one of great interest and beyond the scope of this study, as several pore-forming mechanisms have already been proposed and studied for antimicrobial peptides and polymers.[52, 59]

Second, we provide a "map" of cationic polymers' immunogenic and toxic behavior. By systematically mapping the response generated by cells treated with 107 polymers varied over several dimensions, we find that subtle variations in a polymer's structure can have large effects on the resultant immunogenicity and toxicity. These effects can largely be attributed to changes in the proportional ratio between hydrophobicity, charge, and ethylene glycol in a polymeric scaffold. Polymers containing 10-20 mol.% of a hydrophobic monomer (BMA) within an amine monomer backbone (AEMA or DMAEMA) were among the most toxic tested, displaying toxicity at all concentrations tested. Those with any proportion of AEMA or BMA tested were toxic at higher concentrations. High M_n, DMAEMA-containing polymers with ≥20 mol.% of BMA activated the NLRP3 inflammasome upon active transport into the cell. Co-polymers of DMAEMA and BMA are highly effective gene delivery platforms,[31, 32] so reducing M_n or BMA content to avoid immunogenic side effects might serve as a valuable tool for safe translation of these systems. Finally, co-polymers of DMAEMA and TEGMA were found to be non-toxic and non-immunogenic, particularly when low molecular weights (≤30 kg/mol) and/or >20 mol.% TEGMA were employed. These results provide "points of no return" of polymer composition that, when avoided by a reasonable margin, can ensure that a positively charged and hydrophobic polymer will have a low probability of being immunologically active or toxic. Understanding what compositions must be

avoided can narrow the scope of future functional screens to accelerate polymer-based therapeutic development.

Third, and perhaps of greatest importance, we present a simple method to screen the immunogenicity and toxicity of polymers prior to costly *in vivo* experiments. While highly specialized, application driven readouts are appealing to maximize effectiveness of a material for a given application, they are poorly translated between different fields and often fail due to unanticipated biocompatibility challenges. While this study focused on IL-1β and LDH release induced by cationic polymers, the workflow used herein can be applied toward other markers of immunotoxicity, such as TNF-α, IL-1α, or reactive oxygen species. It can also be applied toward different polymer structures, such as anionic water-soluble polymers or self-assembled polymers. Applying these insights in new and existing therapeutics should streamline (pre)-clinical testing to design tailored materials for applications in biomedicine. By using common monomers with general features, such as primary or tertiary amines, we sought to make this initial "map" general to many common applications of cationic polymers. In verification studies, branched PEI fell within the toxicity and immunogenicity parameters outlined by DMAEMA and BMA (**Figure S2.12**). While the information generated from our screen may not be general to every cationic polymer, we suggest it will provide a robust starting point for any application driven study (*e.g.*, designing polymers for mRNA delivery). As structure-property information is obtained on additional polymeric libraries, high-throughput screening can be combined with machine learning to unveil emergent properties and develop new, optimized materials for specific applications.[40]

Many studies have used structure-function information to identify polymers for biological applications without recognizing the inherent compromise between functionality, immunogenicity, and toxicity. A combination of physicochemical properties, such as charge, hydrophobicity, or molecular weight, that lead to a desired response can behave as a double-edged sword, causing lysosomal rupture and inflammasome activation or cell necrosis. Understanding the polymer-cell interactions which govern these responses can accelerate polymer development and reduce late-

stage biocompatibility screening failures. By varying parameters in a systematic fashion, we present a single parameterized map rather than disparate outputs generated in application-driven studies. Using the screening data presented in this work, researchers can make informed choices and design polymer compositions which might be suitable for a variety of applications. For example, in drug delivery, small quantities of positive charge in a polymer can improve performance (*e.g.* using a primary amine co-monomer to facilitate protein adsorption), but too much positive charge might result in toxicity. This study suggests a small quantity (<10 mol.%) of positive charge could be accommodated by applying the heuristics outlined herein to build polymers which balance the charge with hydrophilic, ethylene glycol containing components. Overall, the screening strategies and mechanistic results in this study provide a framework from which future materials can be built, accelerating the development of new biomaterials.

2.4 Methods and Materials.

Mice and Chemical Sourcing. All chemicals and cell culture reagents were obtained from Sigma Aldrich or Thermo Fisher and used without further purification unless otherwise noted. Alexa Fluor 488 (AF488)-NHS Ester was obtained from Click Chemistry Tools. Nigericin and phorbol 12-myristate 13-acetate (PMA) were obtained from Cayman Chemical Company. LysoView 633 was obtained from Biotium. Cytochalasin D was obtained from R&D Systems. THP-1, THP-1 NLRP3-KO, and THP-1 ASC-GFP cells were obtained from InvivoGen and cultured at 37 °C and 5% CO_2 in RPMI-1640 medium with 10% (v/v) heat inactivated fetal bovine serum (HI-FBS), 100 U/mL penicillin, 100 µg/mL streptomycin, and selection antibiotics ("THP-1 medium"). A549 and HeLa cells were purchased from ATCC, and HEK FIRE-pHLy cells[56] were obtained as a gift from Aimee Kao (Stanford University). A549, HeLa, and HEK FIRE-pHLy cells were cultured at 37 °C and 5% CO_2 in Dulbecco's Modified Eagle Medium (DMEM) with 10% (v/v) FBS, 1 µg/mL puromycin, 100 U/mL penicillin, and 100 µg/mL streptomycin ("HEK medium"). PBMCs were purchased from Precision Medicine Group. Antibodies used for flow cytometry are listed in **Table**

S2.3. 6-week-old C57Bl/6J or B6.129S6-Nlrp3^{tm1Bhk}/J mice were purchased from Jackson Laboratory, housed under controlled light, temperature, and humidity, and allowed to acclimatize for at least one week prior to use. All experiments were conducted with the approval of the University of Chicago Institutional Animal Care and Use Committee, and animals were maintained in accordance with guidelines and regulations of the National Institutes of Health. All data unless otherwise noted are analyzed and plotted in GraphPad Prism 9 and/or Igor Pro 7.

Synthesis of 2-(N-(tert-butoxycarbonyl)amino)ethyl methacrylate (BocAEMA). BocAEMA was prepared as reported previously with minor changes.[47] Briefly, 60.0 g di-tert-butyl dicarbonate was dissolved in 100 mL DCM in a 250 mL flask containing a stir bar. The reaction was placed under an addition funnel, pleaced in an ice bath, and sealed under Argon. 25.0 mL 2-aminoethan-1-ol was added to the addition funnel and added dropwise under rapid stirring. After addition was complete, the reaction was warmed to room temperature and stirred for 16 h. The reaction was then extracted sequentially with 100 mL 0.1 M NaOH, 100 mL H_2O, and 100 mL brine, and the organic phase was collected and dried over $MgSO_4$. The solvent was removed under reduced pressure to crude obtain N-(tert-Butoxycarbonyl)ethanolamine, which was used without further purification. 10.0 g of N-(tert-Butoxycarbonyl)ethanolamine was then added to a flame dried flask with 8.0 mL triethylamine and a stir bar, dissolved in 100 mL dry DCM, and sealed under argon. The flask was placed in an ice bath, and 9.0 mL methacryloyl chloride in 50 mL dry DCM was added over 30 min with rapid stirring. Upon complete addition, the reaction was warmed to room temperature and stirred for 16 h. The reaction was then quenched by addition of 100 mL 0.1 M NaOH, and the organic phase was washed with 2 x 100 mL H_2O and 100 mL brine prior to drying over $MgSO_4$. The product was filtered, concentrated under reduced pressure, and recrystallized from 1:1 Hexanes:DCM to obtain 2-(N-(tert-butoxycarbonyl)amino)ethyl methacrylate as a white crystalline solid. ^{1}H-NMR: 6.13 (s, 1H), 5.59 (s, 1H), 4.79 (br s, 1H), 4.21 (t, 2H), 3.45 (q, 2H), 1.95 (s, 3H), 1.45 (s, 9H).

Synthesis of Polymer Library. The polymer library was synthesized on a 100 mg scale in a glovebox using an Unchained Junior process chemistry instrument. Triethylene glycol methyl ether methacrylate (TEGMA) and butyl methacrylate (BMA) were passed through a column of basic alumina prior to use. N,N'-(dimethylamino)ethyl methacrylate (DMAEMA) was distilled under reduced pressure prior to use. 4-cyanopentanoic acid dithiobenzoate (CPADB) and 4,4′-Azobis(4-cyanovaleric acid) (ACVA) were recrystallized from methanol prior to use. Boc-(2-aminoethyl) methacrylate (BocAEMA) was recrystallized from 1:1 hexanes:DCM prior to use. Under a nitrogen atmosphere, purified BocAEMA, DMAEMA, BMA, and TEGMA were dissolved at 250 mg/mL in dry DMF, and CPADB and ACVA were dissolved at 10 mg/mL in DMF. All reagents were added in appropriate ratios to 2 mL vessels and diluted to a final volume of 1 mL in DMF. The vessels were then heated to 72 °C and shaken at 1500 rpm. After 24 h, the vessels were cooled and exposed to air to quench the reaction. 25 µL aliquots were collected for size exclusion chromatography. The polymers were protonated by addition of 500 µL TFA, precipitated into 50 mL of 1:1 diethyl ether:hexanes, and collected by centrifugation. All polymers were then treated with 1 mL TFA for 1 h to remove Boc protecting groups or as a control. After 1 h, the polymers were re-precipitated into 50 mL of 1:1 diethyl ether:hexanes, collected by centrifugation, and taken up in 5 mL dH_2O. The polymers were dialyzed sequentially for 24 h each against 0.5 M NaCl and dH_2O and then freeze dried to obtain the polymers as white or pink aerogels. Additional co-polymers for analysis of monomer consumption or AF488 labelling were synthesized by hand using an analogous method; here, air-free conditions were achieved by bubbling argon through the reaction for 30 mins prior to heating, and the reaction was stirred with a stir bar.

Characterization of Polymer Library. Size exclusion chromatography (SEC) was conducted in DMF with 0.01 M LiBr additive at 50 ºC using a Tosoh EcoSEC system equipped in series with Tosoh SuperAW3000 and Tosoh SuperAW4000 columns. 25 µL aliquots of crude reaction mixture were diluted in 1 mL of DMF + 0.01 M LiBr, and 15 µL was injected for each

chromatograph. Polymer molecular weight was calculated relative to PMMA standards using the Tosoh EcoSEC analysis software. ^{1}H-NMR was conducted at 400 MHz on a Bruker DRX instrument equipped with a BBO probe using Topspin 1.3 and analyzed using MestreNova software (64 scans/polymer). All NMR spectra were referenced to the residual D_2O solvent peak (4.79 ppm), and the area under the curve of diagnostic peaks were used to calculate the mol.% of co-monomers incorporated into the polymer scaffold. DOSY-NMR molecular weight validation and kinetic analyses were conducted at 500 MHz Bruker Avance-II+ spectrometer equipped with a QNP probe using Topspin 2.1.

Analysis of Monomer Consumption. To confirm the random incorporation of monomer into the polymer backbone, polymerizations were subjected to ^{1}H-NMR spectroscopy using a 60-to-40 mol.% ratio of AEMA or DMAEMA to BMA or TEGMA and M_n = 30 kg/mol target. Purified monomers, CTA, ACVA, and a stir bar were added to a flame-dried flask for a 1.0 g scale reaction. The flask was sealed, 2.5 mL dry DMF was transferred by syringe, and the reaction sparged with argon for 30 min. The flask was then added to a pre-heated oil bath at 72 °C and stirred. At 1, 2, 4, 6, and 18 h, 50 µL aliquots of crude reaction mixture were collected, quenched by rapid addition to an ice bath, and diluted in 600 µL DMSO-*d6*. The mixtures were analyzed by ^{1}H-NMR spectroscopy to evaluate relative consumption of monomers as well as the reaction conversion. The ^{1}H-NMR spectra in DMSO-*d6* were referenced to a TMS standard and analyzed in MestReNova. After 18 h, the reaction mixtures were quenched by exposure to air, deprotected, and purified. The aerogels were then re-analyzed by ^{1}H-NMR spectroscopy in D_2O to confirm that molar ratios of polymers were consistent with expected molar ratios of AEMA or DMAEMA to BMA or TEGMA. Monomer consumption over time for each co-monomer system were conducted at least twice to confirm the results shown. The results shown are representative of replicate trials.

Diffusion Ordered Spectroscopy-Nuclear Magnetic Resonance (DOSY-NMR). Selected samples were analyzed using a 500 MHz Bruker Avance-II+ spectrometer equipped with a QNP probe using Topspin 2.1. Samples were analyzed using the ledbpgps2 pulse program

with P30 = 1900 μs, Δ20 = 1 s, and D1 = 5 s, and 32 ramp increments (16 scans/spectrum, linear gradient) ranging from a gradient amplitude (GPZ6) of 5-95% were obtained for each sample. Diffusion analysis was subsequently conducted using MestreNova, and the diffusion constant was calculated by determining the largest non-solvent peak from each sample, plotting the integral intensity as a function of field strength, and fitting the resultant curve to a mono-exponential fit function y = B*Exp(-x*F), where F is the diffusion constant.

In vitro IL-1β and LDH Screening. Prior to analysis, polymers were dissolved at 1,000 μg/mL in sterile PBS and serially diluted to achieve 10x stock solutions at the indicated concentrations. THP-1 cells were plated at 180,000 cells/well in a 96 well plate and primed with 100 EU/mL ultrapure LPS-EB (InvivoGen). After 3 h, cells were pelleted, washed once with PBS, resuspended in THP-1 media, and treated in triplicate with a final concentration of 100, 50, 25, 12.5, or 6.25 μg/mL of the polymers (or 10 μM nigericin and PBS as positive and negative controls, respectively). After 5 h, the supernatant was collected and subjected to human IL-1β ELISA Kit (Thermo Scientific) and CyQUANT LDH Cytotoxicity Assay (Thermo Fisher) according to the manufacturer's procedures. Similar protocols were conducted with BMDCs and MoDCs. Principal component analysis was conducted using MATLAB 2020B, and data were plotted using RStudio with the scatterpie package (https://github.com/GuangchuangYu/scatterpie).

Monocyte-derived Dendritic Cell Validation Assay. Peripheral blood samples were thawed and isolated by magnetic separation using EasySep Human Monocyte Isolation Kit (StemCell Technologies) according to the manufacturer's protocol. Isolated monocytes were then cultured in RPMI + 10% FBS with IL-4 and GM-CSF supplementation to induce a dendritic cell-like phenotype. After 6 d, the monocyte-derived dendritic cells (MoDCs) were released with EDTA, pelleted by centrifugation, and plated at 90,000 cells/well in RPMI + 10% HI-FBS. Cells were primed with 100 EU/mL ultrapure LPS-EB for 3 h. Media was then removed and replaced with fresh media containing polymer solutions at the indicated concentration. Cells were incubated with polymers for 5 h and then medium was collected and analyzed with human IL-1β ELISA Kit

(Thermo Scientific) and CyQUANT LDH Cytotoxicity Assay (Thermo Fisher) according to the manufacturer's procedures.

Bone Marrow Derived Dendritic Cell Validation Assay. Bone-marrow-derived dendritic cells (BMDCs) were harvested from C57Bl/6J or B6.129S6-Nlrp3^{tm1Bhk}/J mice (Jackson Laboratory) and differentiated with GM-CSF to a dendritic cell-like phenotype as previously reported.[S17] After 6 d, cells were released with EDTA, pelleted by centrifugation, and plated at 180,000 cells/well in a 96-well plate in DMEM with 10% HI-FBS, 10 mM HEPES buffer, 55 μM β-mercaptoethanol, 100 U/mL penicillin, and 100 μg/mL streptomycin ("BMDM medium"). After allowing adhesion for 1 h, cells were primed with 100 EU/mL ultrapure LPS-EB for 3 h. Media was then removed and replaced with fresh BMDM medium containing polymer solutions at the indicated concentration. Cells were incubated with polymers for 5 h and then medium was collected and analyzed with mouse IL-1β ELISAMAX Kit (BioLegend) and CyQUANT LDH Cytotoxicity Assay (Thermo Fisher) according to the manufacturer's procedures.

Time Lapse Confocal Microscopy. For confocal imaging, 50,000 cells were plated in each well of a four chambered, 35 mm glass bottom microscope dish (Grenier Bio-One) and allowed to adhere for 24-48 h. THP-1, THP-1 ASC-GFP and THP-1 NLRP3-KO cells were differentiated for 24-48 h with 25 nM PMA to induce an adherent macrophage-like phenotype. Cells were then washed and primed with 100 EU/mL ultrapure LPS-EB (InvivoGen) in THP-1 or HEK medium as appropriate for 3 h. In the last 30 min of priming, lysosomal dyes (2 μM LysoSensor Green DND-189 or 1:1000 dilution of LysoView 633) and 2.5 μg/mL Cytochalasin D were added as appropriate. Cells were then washed, treated with phenol red-free THP-1 or HEK medium containing 10 μg/mL Hoechst 33342 and/or 10 μg/mL Propidium Iodide, and placed into focus using a 3i Marianas confocal microscope (40x oil lens) with an OKO full environmental control chamber. The imaging chamber was held at 37 °C and supplemented with CO_2 for the duration of imaging. After focusing cells within the imaging plane, 100 μg/mL polymer stocks were added in a 1:10 dilution, and time-lapse images were collected in 2 min intervals for 60 min. Data

were processed using the 3i SlideBook 6 software. For studies with THP-1 ASC-GFP cells, specks were counted by a single blind volunteer.

Polymer Labelling and Imaging. Polymers containing a 70:30 amine:TEGMA/BMA monomer ratio with molecular weights of 15 and 60 kg/mol were used for labelling studies. AEMA-containing polymers were directly labelled, while DMAEMA-containing polymers containing 5 mol% AEMA were synthesized as described above for functionalization with AF488 NHS Ester. For labelling, 20 mg of polymer was dissolved in 5 mL of ultrapure water, the vial was wrapped in foil, and 20 µL of 5 mg/mL AF488 NHS Ester (in DMSO) was added with stirring. The reaction was allowed to proceed overnight, unreacted AF488 was removed by dialysis against 4 L of water for 3 d in the dark (changing dialysate twice daily), and polymers were lyophilized to obtain yellow aerogels. THP-1 cells were then plated in a 4-chambered dish, differentiated with PMA, primed with ultrapure LPS-EB, and stained with LysoView 633 as described above. Cells were then washed and incubated with 100 ug/mL final concentration of the AF488-tagged polymers, 10 µg/mL Hoechst 33342, and 10 µg/mL Propidium Iodide in phenol red-free THP-1 medium for 30 mins. Cells were washed again, plated in 500 µL phenol red-free medium, and imaged using a Marianas 3i confocal microscope (40x oil lens).

Lysosomal pH Analysis Using FIRE-pHLy Construct. HEK FIRE-pHLy cells were plated at 50,000 cells/well in a 96 well plate in 200 µL HEK media, rested for 2 h, and then treated with 25 µg/mL of the indicated polymers for 1 h. Cells were then detached with EDTA, washed, resuspended in PBS + 2% FBS + 5 mM EDTA, and analyzed analyzed with a LSR Fortessa (BD Biosciences) flow cytometer. The median fluorescence intensity ratio of mTFP1 (measured on the BV510 detector) to mCherry (measured on the PE-CF594 detector) was used to determine the lysosomal pH.

Biocompatibility Study with Polymers. 8-week-old female C57Bl/6J mice were injected with 50 µL of 1 mg/mL of the indicated polymers in PBS and monitored for adverse effects for 30 min. Body weight was monitored at 1, 3, and 6 h after injection using a digital, no-touch infrared

thermometer (Home Depot). At 6 h, mice were bled via the submandibular vein and then sacrificed for spleen harvest. Systemic cytokines in the serum were assayed via LEGENDplex™ Mouse Inflammation 13-plex (BioLegend). Splenocytes were prepared, counted via hemocytometer, and then plated at 2.5 x 10^6 cells/well in a 96-well plate. Cells were stained for viability and cell surface markers, fixed using Cytofix/Cytoperm (BD Biosciences), stained for intracellular cytokines, and analyzed with a Novocyte Penteon (Agilent) flow cytometer. Antibodies used for staining are provided in **Table S2.3**. Flow cytometry data was analyzed using FlowJo v10.8.1.

2.5 Supplementary Information.

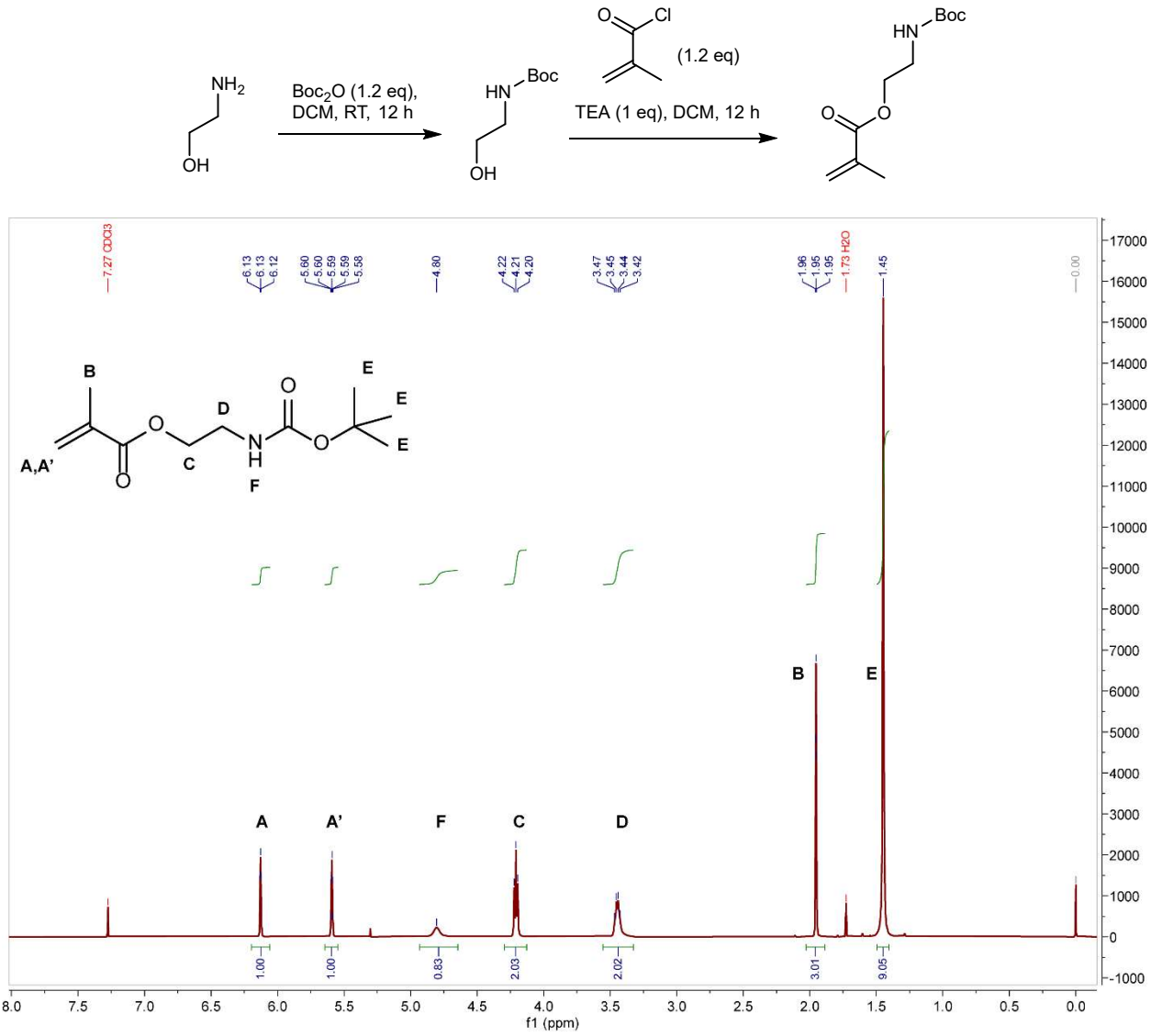

Figure S2.1: Synthesis of 2-(N-(tert-butoxycarbonyl)amino)ethyl methacrylate. Synthetic scheme and ^{1}H-NMR of 2-(N-(tert-butoxycarbonyl)amino)ethyl methacrylate (BocAEMA) in $CDCl_3$ at 400 MHz.

A)

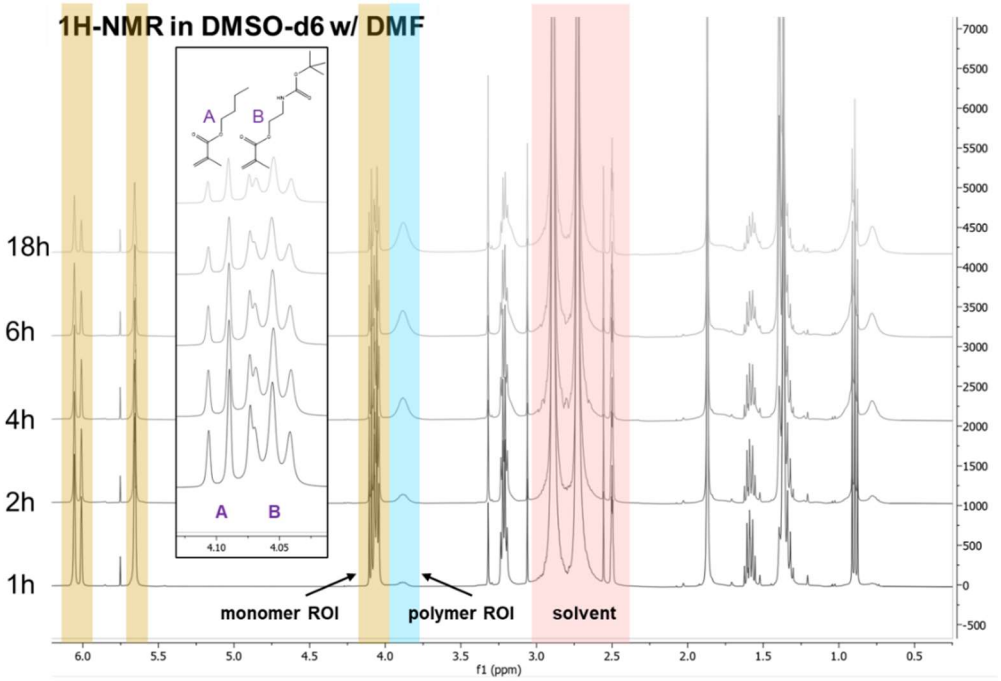

Time (h)	Conversion	%BocAEMA in solution	%BocAEMA in polymer
1	2%	60.0%	N/A
2	10%	61.3%	N/A
4	31%	60.5%	N/A
6	41%	60.6%	N/A
18	56%	63.4%	N/A
Final	N/A	N/A	57.9%

Figure S2.2: Analysis of Monomer Incorporation Over Time for Polymerizations.

B)

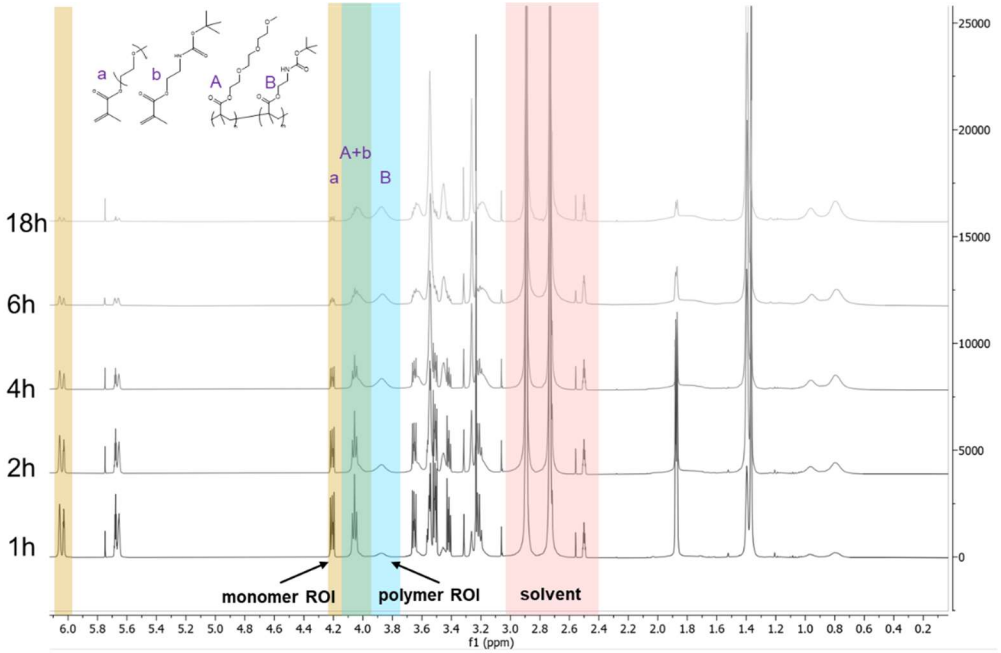

Time (h)	Conversion	%BocAEMA in solution	%BocAEMA in polymer
1	20%	59.5%	N/A
2	45%	59.0%	N/A
4	71%	58.5%	N/A
6	82%	62.5%	N/A
18	96%	58.0%	N/A
Final	N/A	N/A	57.5%

Figure S2.2 (cont.): Analysis of Monomer Incorporation Over Time for Polymerizations.

C)

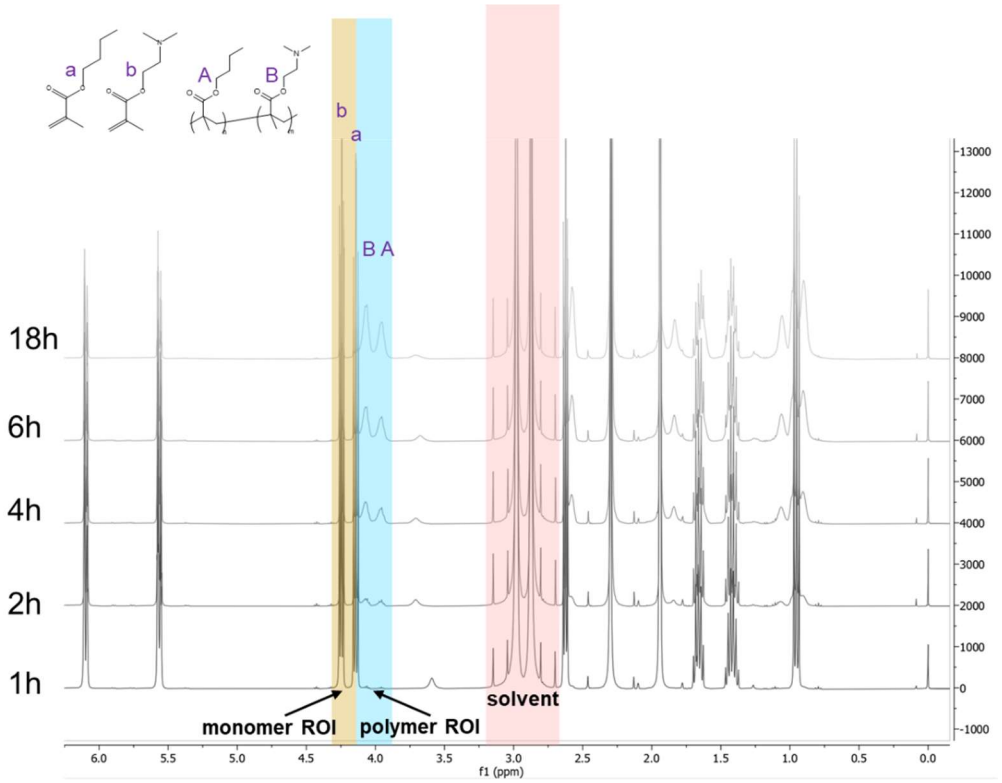

Time (h)	Conversion	%DMAEMA in solution	%DMAEMA in polymer
1	1%	58.1%	N/A
2	7%	57.8%	N/A
4	24%	57.5%	N/A
6	36%	57.5%	N/A
18	58%	57.5%	N/A
Final	N/A	N/A	57.3%

Figure S2.2 (cont.): Analysis of Monomer Incorporation Over Time for Polymerizations.

D)

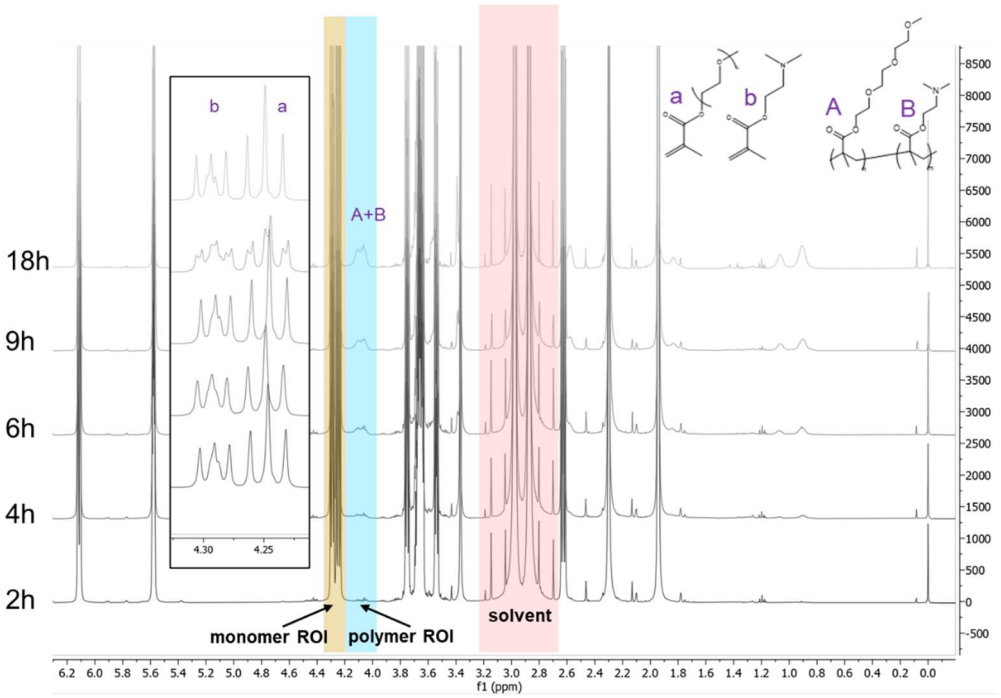

Time (h)	Conversion	%DMAEMA in solution	%DMAEMA in polymer
2	1%	56.7%	N/A
4	3%	56.3%	N/A
6	5%	56.9%	N/A
9	10%	56.5%	N/A
18	17%	56.1%	N/A
Final	N/A	N/A	58.1%

Figure S2.2 (cont.): Analysis of Monomer Incorporation Over Time for Polymerizations. Monomer consumption in each co-polymer system, (A) BocAEMA-BMA, (B) BocAEMA-TEGMA, (C) DMAEMA-BMA, and (D) DMAEMA-TEGMA, employed in this work was assessed by 400 MHz ^{1}H-NMR spectroscopy. Analysis of monomer consumption versus time for a polymer containing 60 mol.% of the amine-containing monomer and 40 mol.% of the hydrophobicity-altering monomer was conducted by ^{1}H-NMR using DMF as reaction solvent and DMSO-d6 as a locking solvent. The indicated regions of interest (ROI) were integrated to determine the conversion of monomer at each time point. For each combination, monomers were incorporated into the polymer backbone at a similar rate, which was important to prevent self-assembly behavior in solution.

Polymer Name	Mon1	Mon2	M_n (theory)	%Mon1 (theory)	% Mon1 (^{1}H-NMR)	M_n_Boc (SEC)	M_n (SEC)	$Đ$ (SEC)
7.5k $AEMA_{50}$-s-BMA_{50}	AEMA	BMA	7,500	50%	52%	6,600	5,000	1.22
7.5k $AEMA_{60}$-s-BMA_{40}	AEMA	BMA	7,500	60%	62%	8,900	6,800	1.19
7.5k $AEMA_{70}$-s-BMA_{30}	AEMA	BMA	7,500	70%	76%	10,700	7,500	1.22
7.5k $AEMA_{80}$-s-BMA_{20}	AEMA	BMA	7,500	80%	82%	8,800	5,900	1.23
7.5k $AEMA_{90}$-s-BMA_{10}	AEMA	BMA	7,500	90%	91%	14,200	8,800	1.14
7.5k AEMA	AEMA		7,500	100%	100%	10,900	6,300	1.22
7.5k $AEMA_{90}$-s-$TEGMA_{10}$	AEMA	TEGMA	7,500	90%	91%	12,000	7,400	1.18
7.5k $AEMA_{80}$-s-$TEGMA_{20}$	AEMA	TEGMA	7,500	80%	79%	14,400	9,600	1.16
7.5k $AEMA_{70}$-s-$TEGMA_{30}$	AEMA	TEGMA	7,500	70%	76%	9,500	6,700	1.26
7.5k $AEMA_{60}$-s-$TEGMA_{40}$	AEMA	TEGMA	7,500	60%	64%	12,000	8,800	1.19
7.5k $AEMA_{50}$-s-$TEGMA_{50}$	AEMA	TEGMA	7,500	50%	43%	12,700	10,100	1.30
15k $AEMA_{50}$-s-BMA_{50}	AEMA	BMA	15,000	50%	54%	16,200	12,700	1.17
15k $AEMA_{60}$-s-BMA_{40}	AEMA	BMA	15,000	60%	63%	18,200	12,700	1.17
15k $AEMA_{70}$-s-BMA_{30}	AEMA	BMA	15,000	70%	68%	26,800	18,800	1.17
15k $AEMA_{80}$-s-BMA_{20}	AEMA	BMA	15,000	80%	81%	22,400	14,700	1.17
15k $AEMA_{90}$-s-BMA_{10}	AEMA	BMA	15,000	90%	91%	25,700	15,700	1.14
15k AEMA	AEMA		15,000	100%	100%	25,700	14,600	1.25
15k $AEMA_{90}$-s-$TEGMA_{10}$	AEMA	TEGMA	15,000	90%	89%	24,600	15,000	1.18
15k $AEMA_{80}$-s-$TEGMA_{20}$	AEMA	TEGMA	15,000	80%	79%	26,700	17,600	1.18
15k $AEMA_{70}$-s-$TEGMA_{30}$	AEMA	TEGMA	15,000	70%	75%	19,000	13,300	1.21
15k $AEMA_{60}$-s-$TEGMA_{40}$	AEMA	TEGMA	15,000	60%	63%	22,700	16,600	1.17
15k $AEMA_{50}$-s-$TEGMA_{50}$	AEMA	TEGMA	15,000	50%	45%	24,900	19,700	1.25
30k $AEMA_{50}$-s-BMA_{50}	AEMA	BMA	30,000	50%	44%	40,400	31,800	1.20
30k $AEMA_{60}$-s-BMA_{40}	AEMA	BMA	30,000	60%	62%	31,300	23,200	1.19
30k $AEMA_{70}$-s-BMA_{30}	AEMA	BMA	30,000	70%	65%	40,000	27,900	1.36
30k $AEMA_{80}$-s-BMA_{20}	AEMA	BMA	30,000	80%	83%	38,400	25,100	1.20
30k $AEMA_{90}$-s-BMA_{10}	AEMA	BMA	30,000	90%	92%	56,900	34,700	1.22
30k AEMA	AEMA		30,000	100%	100%	44,100	25,000	1.16
30k $AEMA_{90}$-s-$TEGMA_{10}$	AEMA	TEGMA	30,000	90%	91%	56,400	34,400	1.26
30k $AEMA_{80}$-s-$TEGMA_{20}$	AEMA	TEGMA	30,000	80%	82%	36,300	23,700	1.25
30k $AEMA_{70}$-s-$TEGMA_{30}$	AEMA	TEGMA	30,000	70%	74%	48,300	33,700	1.22
30k $AEMA_{60}$-s-$TEGMA_{40}$	AEMA	TEGMA	30,000	60%	66%	30,900	22,300	1.24
30k $AEMA_{50}$-s-$TEGMA_{50}$	AEMA	TEGMA	30,000	50%	57%	41,200	32,400	1.22
45k $AEMA_{50}$-s-BMA_{50}	AEMA	BMA	45,000	50%	42%	53,700	42,200	1.28
45k $AEMA_{70}$-s-BMA_{30}	AEMA	BMA	45,000	70%	70%	41,800	29,200	1.20
45k $AEMA_{80}$-s-BMA_{20}	AEMA	BMA	45,000	80%	80%	63,400	41,400	1.40
45k $AEMA_{90}$-s-BMA_{10}	AEMA	BMA	45,000	90%	92%	68,800	41,900	1.39
45k AEMA	AEMA		45,000	100%	100%	58,900	33,300	1.18
45k $AEMA_{90}$-s-$TEGMA_{10}$	AEMA	TEGMA	45,000	90%	91%	76,800	46,800	1.32
45k $AEMA_{80}$-s-$TEGMA_{20}$	AEMA	TEGMA	45,000	80%	81%	71,200	46,500	1.29
45k $AEMA_{70}$-s-$TEGMA_{30}$	AEMA	TEGMA	45,000	70%	72%	55,800	38,900	1.47
45k $AEMA_{60}$-s-$TEGMA_{40}$	AEMA	TEGMA	45,000	60%	57%	52,800	41,500	1.34
45k $AEMA_{50}$-s-$TEGMA_{50}$	AEMA	TEGMA	45,000	50%	53%	72,600	53,800	1.40

Table S2.1: Polymer Characterization Data Table.

Polymer Name	Mon1	Mon2	M_n (theory)	%Mon1 (theory)	% Mon1 (^{1}H-NMR)	M_n_Boc (SEC)	M_n (SEC)	$Đ$ (SEC)
60k $AEMA_{60}$-s-BMA_{40}	AEMA	BMA	60,000	60%	60%	66,900	49,500	1.25
60k $AEMA_{70}$-s-BMA_{30}	AEMA	BMA	60,000	70%	67%	76,800	53,500	1.35
60k $AEMA_{80}$-s-BMA_{20}	AEMA	BMA	60,000	80%	82%	81,100	52,900	1.26
60k $AEMA_{90}$-s-BMA_{10}	AEMA	BMA	60,000	90%	88%	76,100	46,300	1.58
60k AEMA	AEMA		60,000	100%	100%	90,100	50,900	1.23
60k $AEMA_{90}$-s-$TEGMA_{10}$	AEMA	TEGMA	60,000	90%	90%	106,200	64,600	1.27
60k $AEMA_{80}$-s-$TEGMA_{20}$	AEMA	TEGMA	60,000	80%	82%	73,000	47,600	1.37
60k $AEMA_{70}$-s-$TEGMA_{30}$	AEMA	TEGMA	60,000	70%	72%	85,000	59,100	1.31
60k $AEMA_{60}$-s-$TEGMA_{40}$	AEMA	TEGMA	60,000	60%	66%	66,700	49,300	1.26
60k $AEMA_{50}$-s-$TEGMA_{50}$	AEMA	TEGMA	60,000	50%	57%	68,800	54,000	1.31
7.5k $DMAEMA_{50}$-s-BMA_{50}	DMAEMA	BMA	7,500	50%	45%		6,000	1.37
7.5k $DMAEMA_{60}$-s-BMA_{40}	DMAEMA	BMA	7,500	60%	59%		7,000	1.35
7.5k $DMAEMA_{70}$-s-BMA_{30}	DMAEMA	BMA	7,500	70%	69%		5,900	1.37
7.5k $DMAEMA_{80}$-s-BMA_{20}	DMAEMA	BMA	7,500	80%	76%		5,600	1.32
7.5k $DMAEMA_{90}$-s-BMA_{10}	DMAEMA	BMA	7,500	90%	91%		5,400	1.37
7.5k DMAEMA	DMAEMA		7,500	100%	100%		8,700	1.33
7.5k $DMAEMA_{90}$-s-$TEGMA_{10}$	DMAEMA	TEGMA	7,500	90%	86%		5,900	1.39
7.5k $DMAEMA_{80}$-s-$TEGMA_{20}$	DMAEMA	TEGMA	7,500	80%	81%		6,100	1.45
7.5k $DMAEMA_{70}$-s-$TEGMA_{30}$	DMAEMA	TEGMA	7,500	70%	66%		5,700	1.39
7.5k $DMAEMA_{60}$-s-$TEGMA_{40}$	DMAEMA	TEGMA	7,500	60%	60%		7,800	1.39
7.5k $DMAEMA_{50}$-s-$TEGMA_{50}$	DMAEMA	TEGMA	7,500	50%	51%		5,600	1.37
15k $DMAEMA_{50}$-s-BMA_{50}	DMAEMA	BMA	15,000	50%	52%		12,300	1.28
15k $DMAEMA_{60}$-s-BMA_{40}	DMAEMA	BMA	15,000	60%	65%		11,500	1.35
15k $DMAEMA_{70}$-s-BMA_{30}	DMAEMA	BMA	15,000	70%	70%		11,500	1.39
15k $DMAEMA_{80}$-s-BMA_{20}	DMAEMA	BMA	15,000	80%	79%		13,200	1.27
15k $DMAEMA_{90}$-s-BMA_{10}	DMAEMA	BMA	15,000	90%	93%		13,000	1.32
15k DMAEMA	DMAEMA		15,000	100%	100%		10,800	1.32
15k $DMAEMA_{90}$-s-$TEGMA_{10}$	DMAEMA	TEGMA	15,000	90%	90%		9,700	1.26
15k $DMAEMA_{80}$-s-$TEGMA_{20}$	DMAEMA	TEGMA	15,000	80%	79%		9,300	1.20
15k $DMAEMA_{70}$-s-$TEGMA_{30}$	DMAEMA	TEGMA	15,000	70%	64%		11,500	1.37
15k $DMAEMA_{60}$-s-$TEGMA_{40}$	DMAEMA	TEGMA	15,000	60%	55%		18,700	1.56
15k $DMAEMA_{50}$-s-$TEGMA_{50}$	DMAEMA	TEGMA	15,000	50%	50%		11,400	1.36
30k $DMAEMA_{50}$-s-BMA_{50}	DMAEMA	BMA	30,000	50%	43%		30,900	1.35
30k $DMAEMA_{60}$-s-BMA_{40}	DMAEMA	BMA	30,000	60%	62%		23,600	1.31
30k $DMAEMA_{70}$-s-BMA_{30}	DMAEMA	BMA	30,000	70%	73%		22,200	1.53
30k $DMAEMA_{80}$-s-BMA_{20}	DMAEMA	BMA	30,000	80%	83%		24,000	1.37
30k $DMAEMA_{90}$-s-BMA_{10}	DMAEMA	BMA	30,000	90%	86%		30,700	1.49
30k DMAEMA	DMAEMA		30,000	100%	100%		36,900	1.35
30k $DMAEMA_{90}$-s-$TEGMA_{10}$	DMAEMA	TEGMA	30,000	90%	85%		30,800	1.53
30k $DMAEMA_{80}$-s-$TEGMA_{20}$	DMAEMA	TEGMA	30,000	80%	74%		21,100	1.53
30k $DMAEMA_{70}$-s-$TEGMA_{30}$	DMAEMA	TEGMA	30,000	70%	68%		34,400	1.43
30k $DMAEMA_{60}$-s-$TEGMA_{40}$	DMAEMA	TEGMA	30,000	60%	56%		33,900	1.51
30k $DMAEMA_{50}$-s-$TEGMA_{50}$	DMAEMA	TEGMA	30,000	50%	50%		32,000	1.47

Table S2.1 (cont.): Polymer Characterization Data Table.

Polymer Name	Mon1	Mon2	M_n (theory)	%Mon1 (theory)	% Mon1 (^{1}H-NMR)	M_n_Boc (SEC)	M_n (SEC)	$Đ$ (SEC)
45k DMAEMA$_{50}$-s-BMA$_{50}$	DMAEMA	BMA	45,000	50%	48%		39,600	1.46
45k DMAEMA$_{60}$-s-BMA$_{40}$	DMAEMA	BMA	45,000	60%	61%		34,400	1.32
45k DMAEMA$_{70}$-s-BMA$_{30}$	DMAEMA	BMA	45,000	70%	67%		38,500	1.58
45k DMAEMA$_{80}$-s-BMA$_{20}$	DMAEMA	BMA	45,000	80%	82%		32,000	1.47
45k DMAEMA$_{90}$-s-BMA$_{10}$	DMAEMA	BMA	45,000	90%	91%		38,200	1.66
45k DMAEMA	DMAEMA		45,000	100%	100%		40,000	1.51
45k DMAEMA$_{90}$-s-TEGMA$_{10}$	DMAEMA	TEGMA	45,000	90%	83%		42,500	1.57
45k DMAEMA$_{80}$-s-TEGMA$_{20}$	DMAEMA	TEGMA	45,000	80%	76%		35,100	1.43
45k DMAEMA$_{70}$-s-TEGMA$_{30}$	DMAEMA	TEGMA	45,000	70%	68%		42,800	1.66
45k DMAEMA$_{60}$-s-TEGMA$_{40}$	DMAEMA	TEGMA	45,000	60%	54%		46,100	1.70
45k DMAEMA$_{50}$-s-TEGMA$_{50}$	DMAEMA	TEGMA	45,000	50%	51%		42,900	1.65
60k DMAEMA$_{50}$-s-BMA$_{50}$	DMAEMA	BMA	60,000	50%	54%		46,400	1.61
60k DMAEMA$_{60}$-s-BMA$_{40}$	DMAEMA	BMA	60,000	60%	67%		48,700	1.44
60k DMAEMA$_{70}$-s-BMA$_{30}$	DMAEMA	BMA	60,000	70%	67%		47,900	1.65
60k DMAEMA$_{80}$-s-BMA$_{20}$	DMAEMA	BMA	60,000	80%	82%		46,900	1.73
60k DMAEMA	DMAEMA		60,000	100%	100%		45,400	1.36
60k DMAEMA$_{90}$-s-TEGMA$_{10}$	DMAEMA	TEGMA	60,000	90%	88%		48,200	1.85
60k DMAEMA$_{80}$-s-TEGMA$_{20}$	DMAEMA	TEGMA	60,000	80%	79%		50,800	1.24
60k DMAEMA$_{70}$-s-TEGMA$_{30}$	DMAEMA	TEGMA	60,000	70%	67%		48,300	1.88
60k DMAEMA$_{60}$-s-TEGMA$_{40}$	DMAEMA	TEGMA	60,000	60%	59%		47,200	1.57
60k DMAEMA$_{50}$-s-TEGMA$_{50}$	DMAEMA	TEGMA	60,000	50%	48%		78,800	1.58

Table S2.1 (cont.): Polymer Characterization Data Table. ^{1}H-NMR and SEC characterization data of polymer library. Full 400 MHz ^{1}H-NMR spectra and SEC analyses in DMF are provided in **Appendix A**.

A) 30 kg/mol poly(AEMA$_{60}$-*s*-BMA$_{40}$)

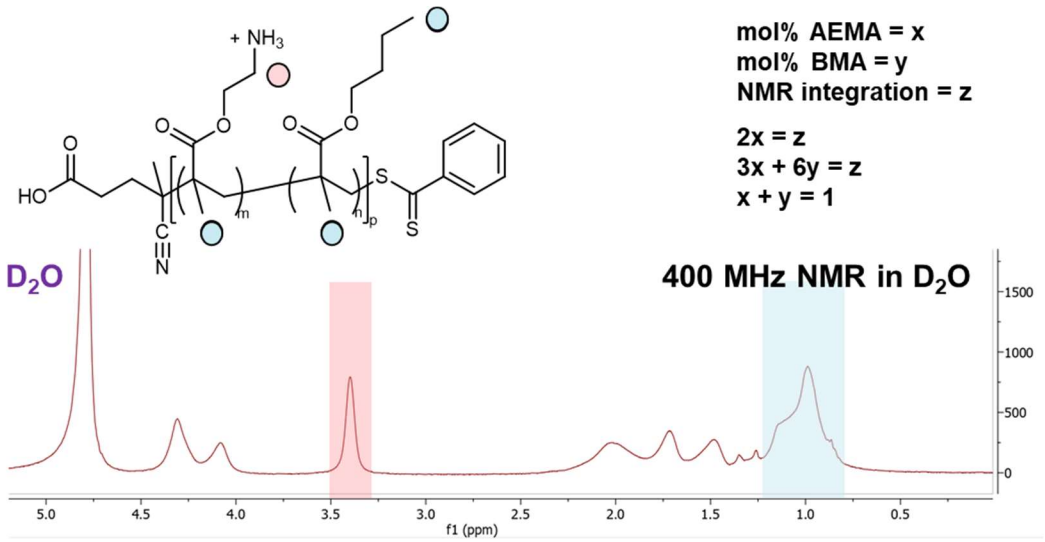

B) 30 kg/mol poly(AEMA$_{60}$-*s*-TEGMA$_{40}$)

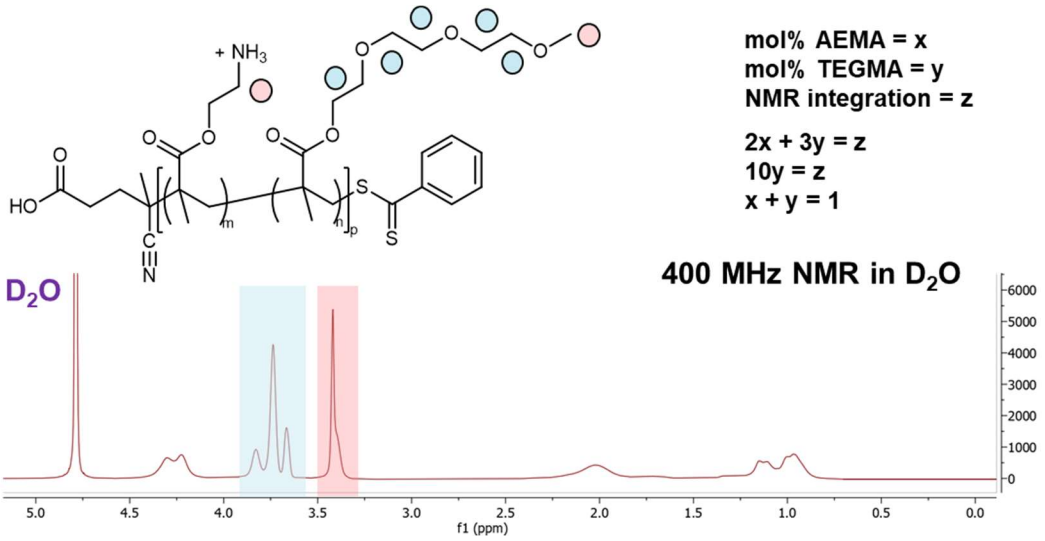

Figure S2.3: NMR Diagnostic Peaks for AEMA-containing polymers. Schematic analysis of 400 MHz ^{1}H-NMR spectra used to determine polymer composition for combinations of AEMA and BMA or TEGMA after deprotection and dialysis. NMR spectra correspond to the 60:40 core:dopant polymers prepared for monomer consumption analysis in **Figure S2.2**. Integration of the red ROI is defined as “x”, and integration of the blue ROI is defined as “y”. Based on the relative integrations, a system of equations was defined to determine the relative ratio of core and dopant monomer incorporated into the polymer backbone.

A) 30 kg/mol poly(DMAEMA$_{60}$-*s*-BMA$_{40}$)

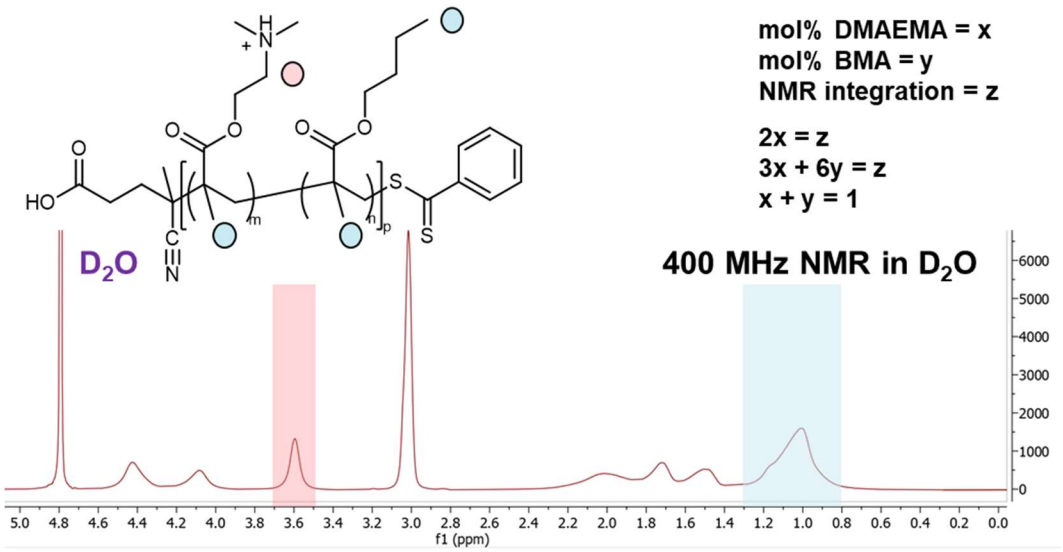

B) 30 kg/mol poly(DMAEMA$_{60}$-*s*-TEGMA$_{40}$)

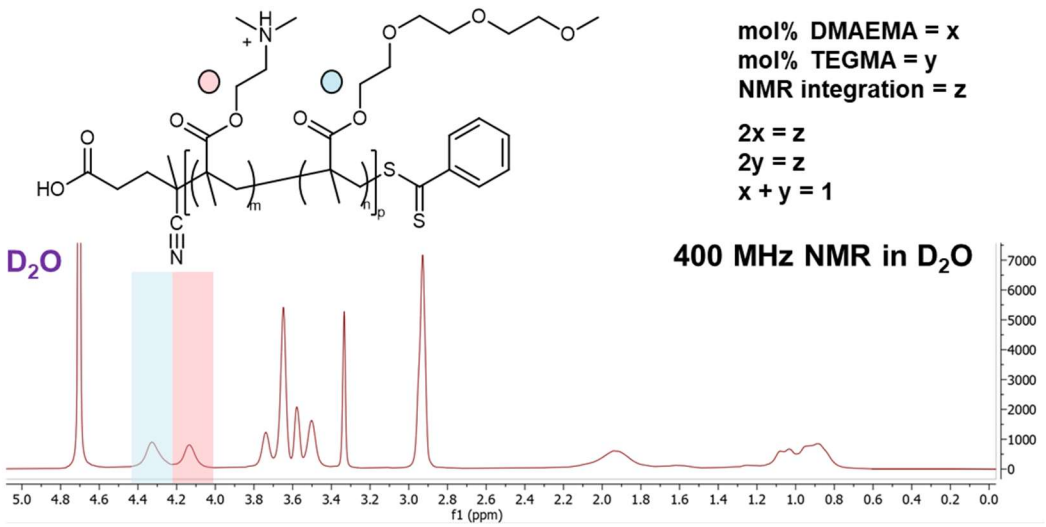

Figure S2.4: NMR Diagnostic Peaks for DMAEMA-containing polymers. NMR Diagnostic Peaks for DMAEMA-containing polymers. Schematic analysis of 400 MHz ^{1}H-NMR spectra used to determine polymer composition for combinations of DMAEMA and BMA or TEGMA after deprotection and dialysis. NMR spectra correspond to the 60:40 core:dopant polymers prepared for monomer consumption analysis in **Figure S2.2**. Integration of the red ROI is defined as “x”, and integration of the blue ROI is defined as “y”. Based on the relative integrations, a system of equations was defined to determine the relative ratio of core and dopant monomer incorporated into the polymer backbone.

Polymer ID	M_n (SEC)	D (DOSY-NMR)
15k $AEMA_{70}$-BMA_{30}	18,800 g/mol	2.2 x 10^{-11} m^2/s
15k $AEMA_{70}$-$TEGMA_{30}$	13,300 g/mol	1.8 x 10^{-12} m^2/s
15k $DMAEMA_{70}$-BMA_{30}	11,500 g/mol	3.4 x 10^{-12} m^2/s
15k $DMAEMA_{70}$-$TEGMA_{30}$	11,500 g/mol	2.9 x 10^{-12} m^2/s
60k $AEMA_{70}$-BMA_{30}	53,500 g/mol	7.0 x 10^{-12} m^2/s
60k $AEMA_{70}$-$TEGMA_{30}$	59,100 g/mol	7.1 x 10^{-12} m^2/s
60k $DMAEMA_{70}$-BMA_{30}	47,900 g/mol	1.0 x 10^{-12} m^2/s
60k $DMAEMA_{70}$-$TEGMA_{30}$	48,300 g/mol	1.2 x 10^{-12} m^2/s

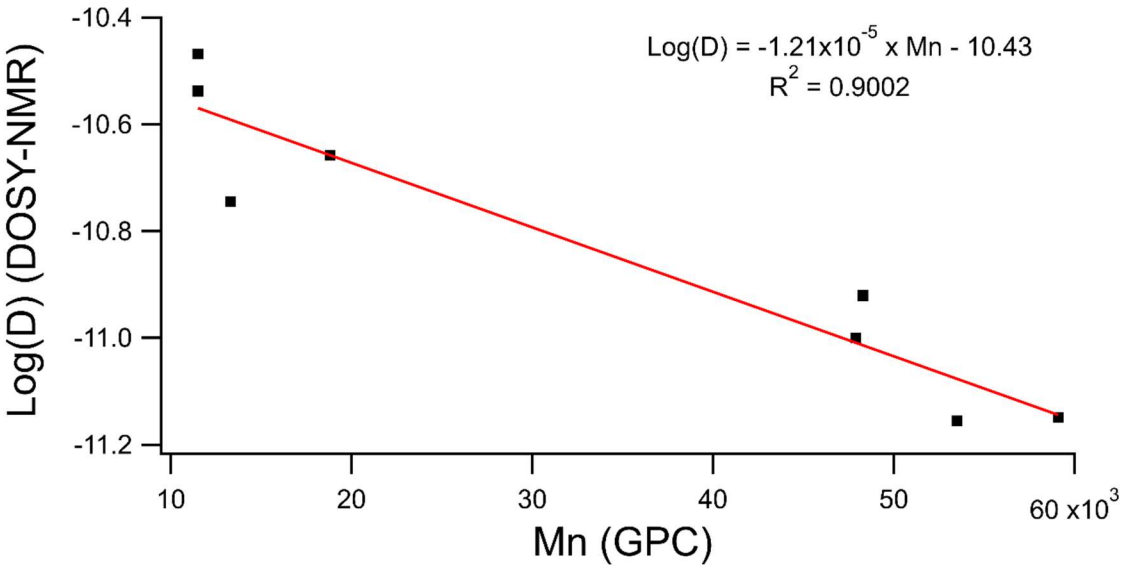

Figure S2.5: DOSY-NMR of Selected Polymers and Comparison to GPC. Diffusion constants determined by DOSY-NMR of polymers in D_2O after deprotection with TFA were used to develop a correlation between diffusion constants (D) determined by DOSY-NMR and M_n determined by SEC prior to deprotection. For a monodisperse polymer in dilute solution, M_n and Log(D) have a linear relationship, thereby providing evidence that polymer molecular weight was maintained during the deprotection process.

Polymer ID	Number Avg. Hydrodynamic Radius (R_h, DLS)
15k $AEMA_{70}$-BMA_{30}	11.32 ± 1.84 nm
15k $AEMA_{70}$-$TEGMA_{30}$	3.90 ± 0.06 nm
15k $DMAEMA_{70}$-BMA_{30}	9.92 ± 3.46 nm
15k $DMAEMA_{70}$-$TEGMA_{30}$	4.28 ± 0.06 nm
60k $AEMA_{70}$-BMA_{30}	10.37 ± 0.16 nm
60k $AEMA_{70}$-$TEGMA_{30}$	11.17 ± 0.97 nm
60k $DMAEMA_{70}$-BMA_{30}	6.89 ± 0.51 nm
60k $DMAEMA_{70}$-$TEGMA_{30}$	14.03 ± 0.49 nm

Table S2.2: DLS of Selected Polymers for Aggregation Analysis. Aggregation of polymers in cell culture medium (100 µg/mL polymer in phenol red-free RPMI + 10% FBS) was assessed using dynamic light scattering. The hydrodynamic radii (R_h) observed suggest that the polymers used in this study do not self-assemble under cell culture conditions.

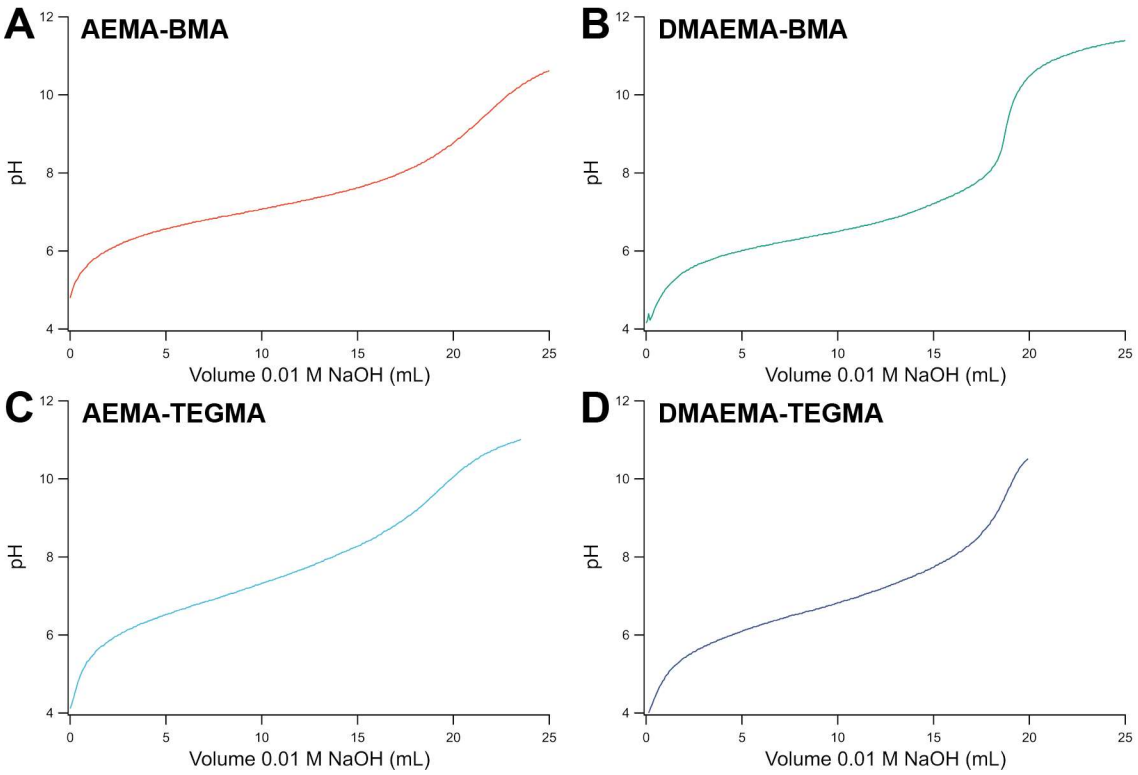

E) Calculated pK_a values for each co-polymer

Co-polymer	pK_a
15k AEMA-BMA	7.18
15k DMAEMA-BMA	6.44
15k AEMA-TEGMA	7.25
15k DMAEMA-TEGMA	6.71

Figure S2.6: Titration and pKa Values of Selected Polymers. (A-D) Polymers from each of the four monomer combinations (70:30 ratio, 15 kg/mol) were dissolved at 1 mg/mL in deionized water and adjusted to pH = 4.0. They were then titrated with 0.01 M NaOH to determine the approximate pK_a of each co-polymer. (E) The pK_a values determined via titration are shown in the accompanying table.

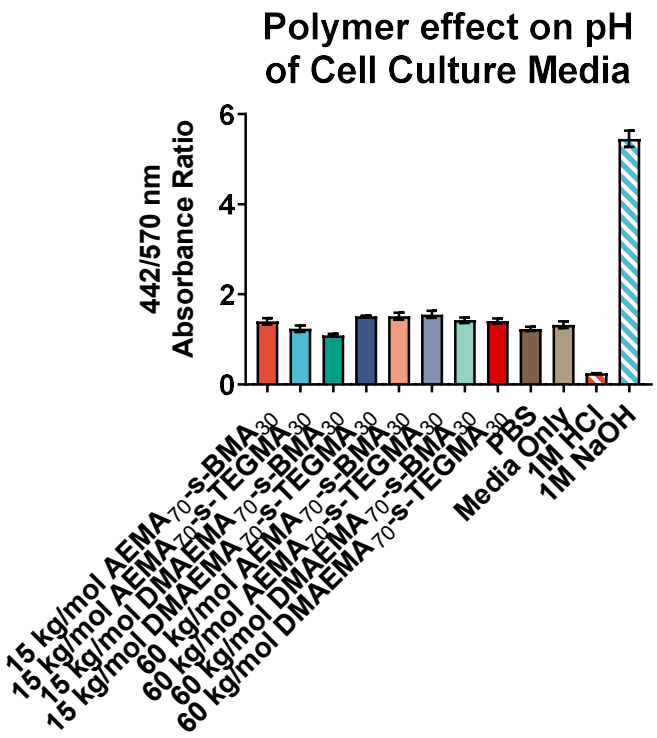

Figure S2.7: Effect of Polymers on pH of Cell Culture Media. To determine the effect of polymers on the pH of cell culture medium, polymers or controls were added to cell culture medium (100 μg/mL polymer in phenol red-containing RPMI + 10% FBS), and the emission spectrum of phenol red (a colorimetric pH indicator between 6.8 and 8.2) was analyzed by plate reader using a broad-spectrum scan (350-750 nm, 2 nm step size). The ratio of absorbance at 442 and 570 nm was used to determine the acidity of solution.

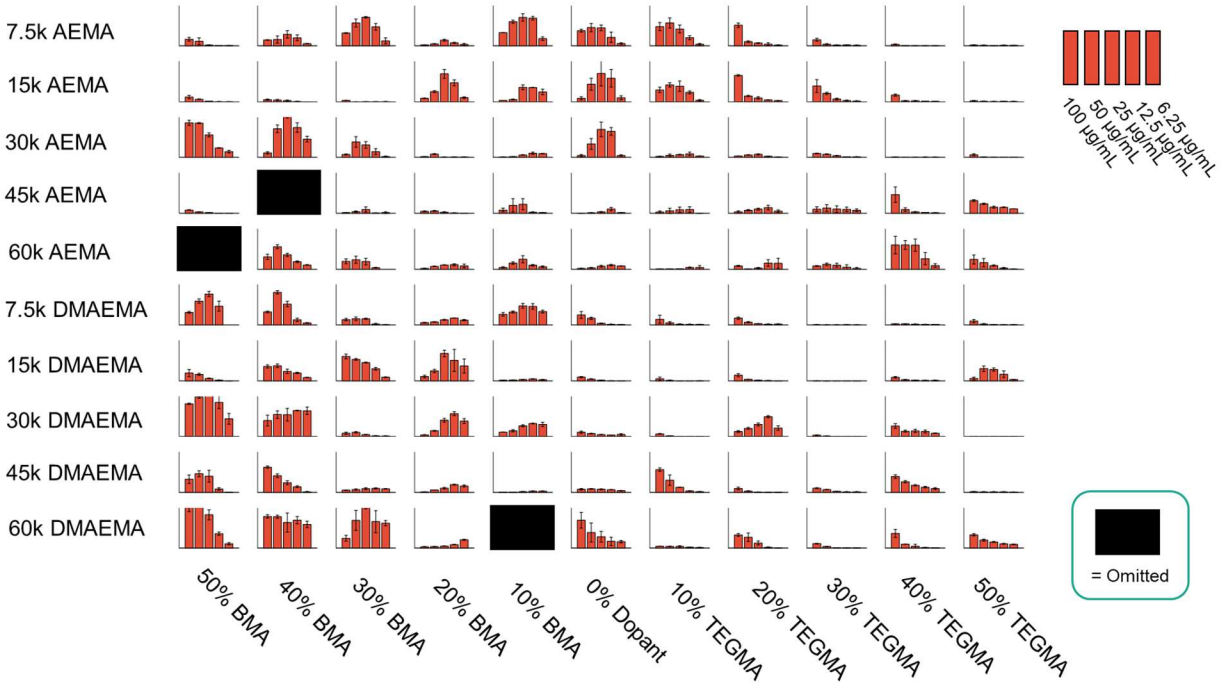

Figure S2.8: Full Results of In-Vitro IL-1β Screening. High throughput screening was conducted for each of the 107 polymers five concentrations tested, and IL-1β was assayed via human IL-1β ELISA.

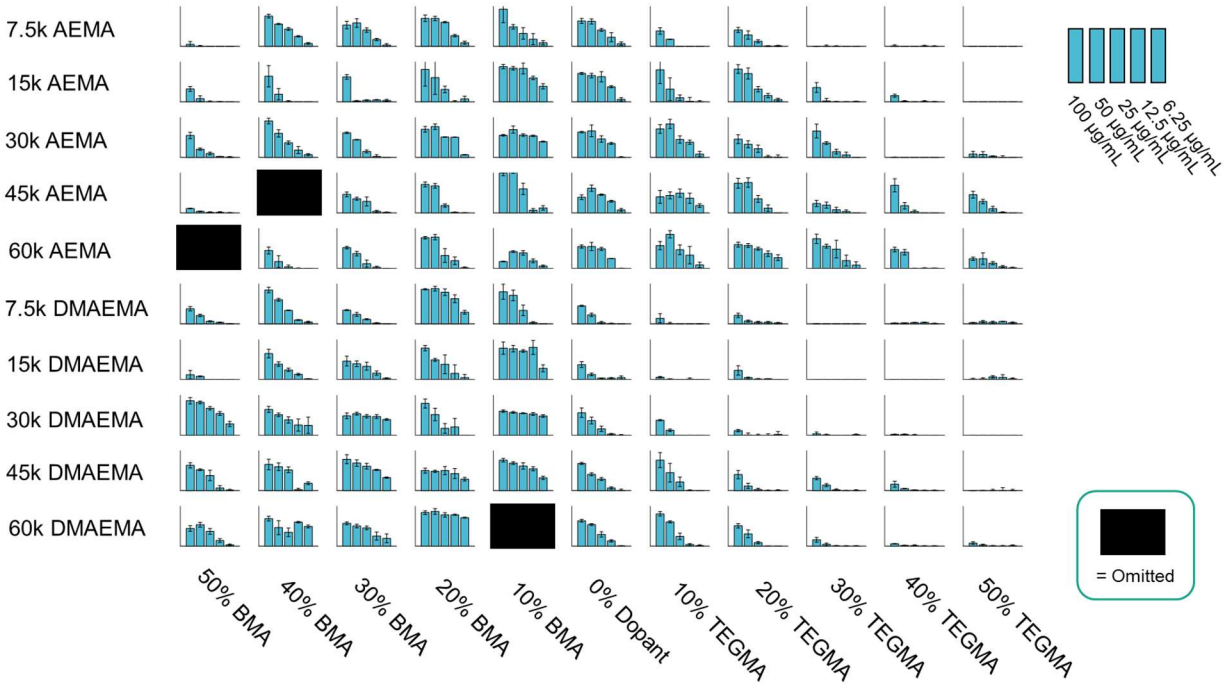

Figure S2.9: Full Results of In-Vitro LDH Screening. High throughput screening was conducted for each of the 107 polymers five concentrations tested, and LDH was assayed via CyQUANDT LDH assay.

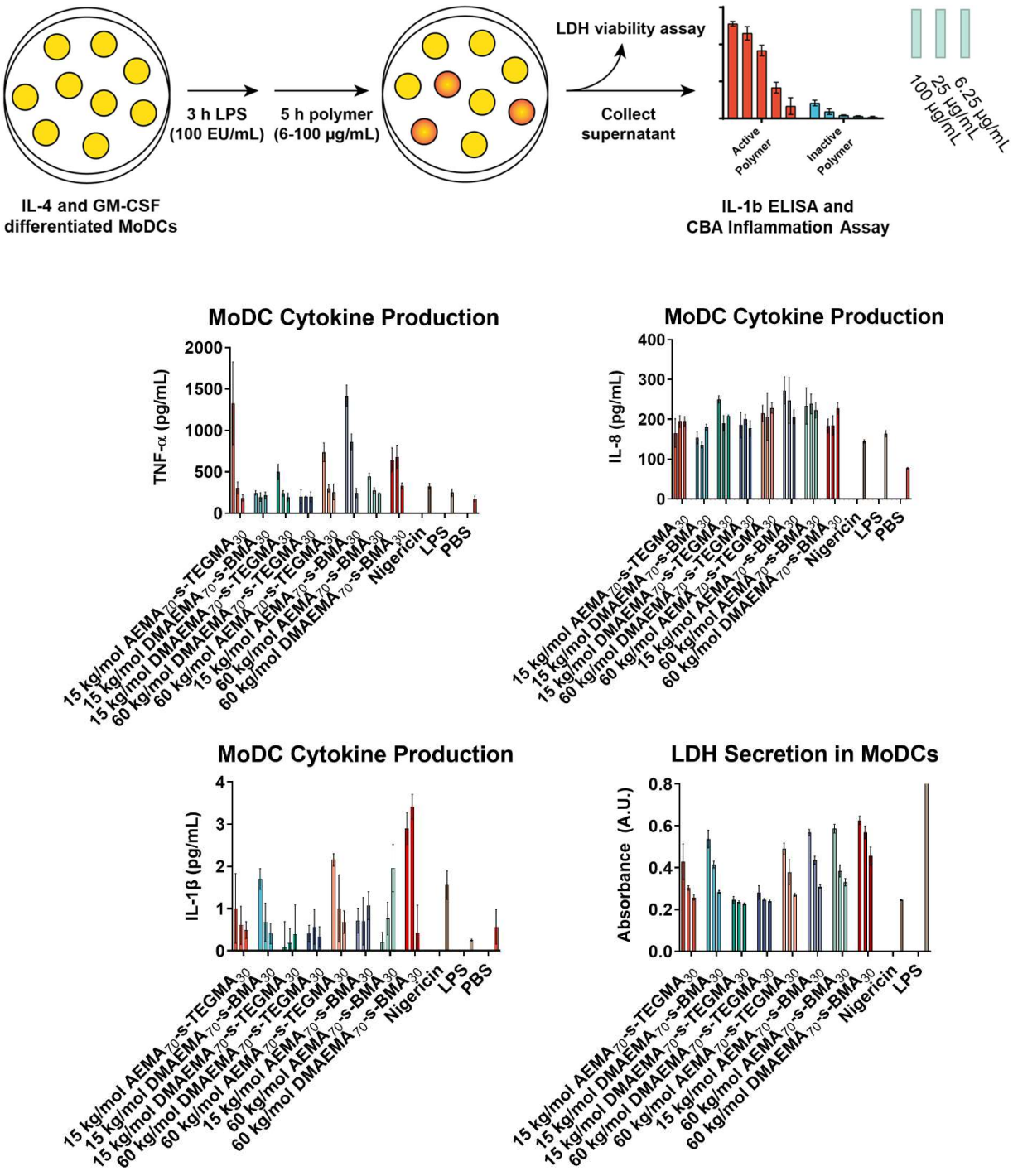

Figure S2.10: Polymer-Induced LDH and Cytokine Production in MoDCs. IL-4 and GM-CSF differentiated primary human monocytes (MoDCs) were primed with 100 EU/mL LPS and then treated with polymers. Cytokine production was then assayed using human CBA inflammation kit (TNF-α and IL-8) or ELISA (IL-1β), and LDH was assayed by CyQUANT LDH Cytotoxicity assay.

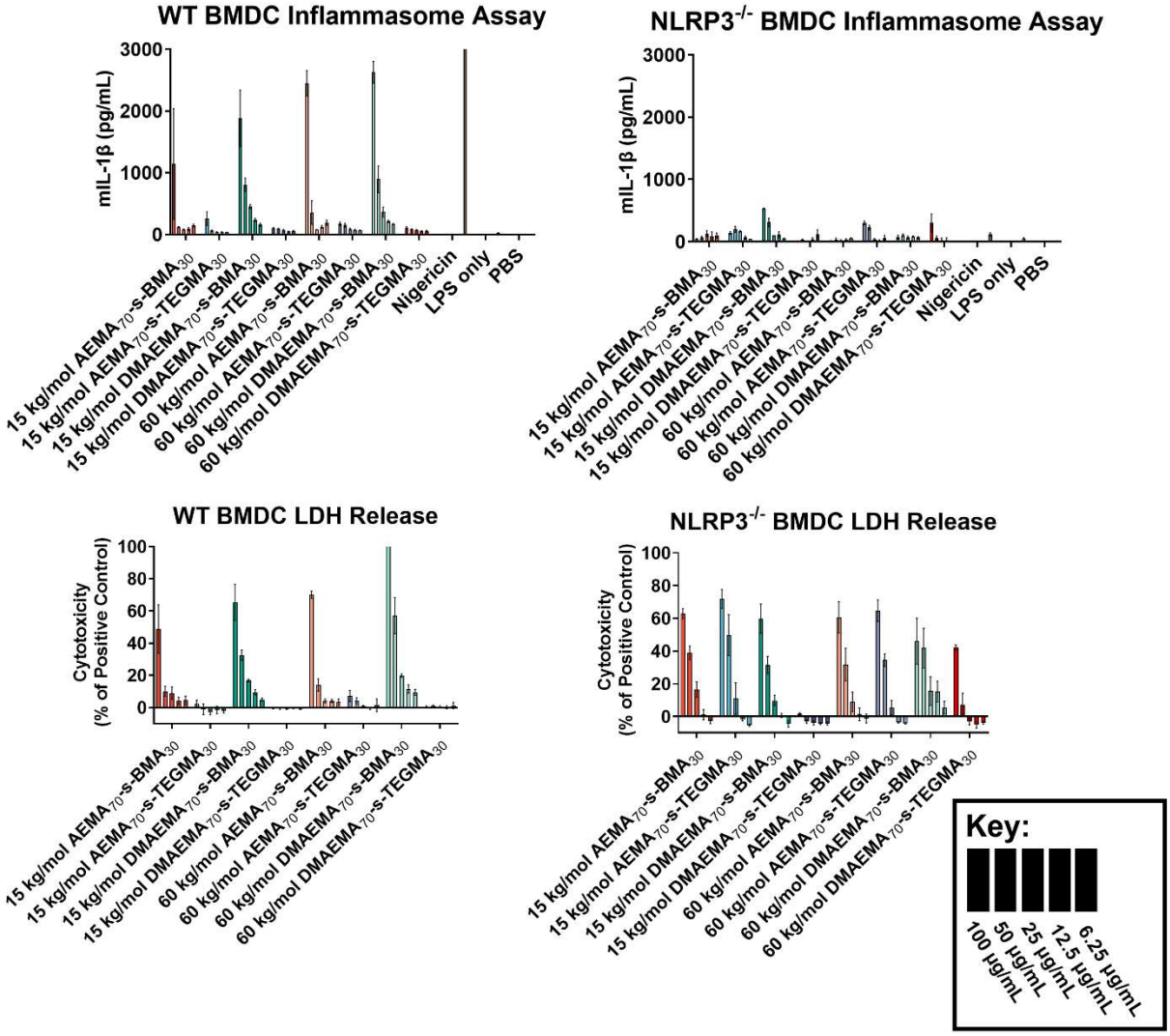

Figure S2.11: Polymer-Induced LDH and Cytokine Production in BMDCs. GM-CSF differentiated murine dendritic cells (BMDCs) from wild-type or NLRP3-KO C57Bl6/J mice were primed with 100 EU/mL LPS and then treated with polymers. IL-1β production was analyzed by ELISA, and LDH was assayed by CyQUANT LDH Cytotoxicity assay. The IL-1β production results shown are also plotted in **Figure 2.2D** in the manuscript.

A

Polymer (with Mn)	Vendor	Product Number	Reported Đ
60 kg/mol branched PEI	Sigma	181978	12.5
10 kg/mol branched PEI	Sigma	408727	2.5
1.8 kg/mol branched PEI	Sigma	408700	1.11

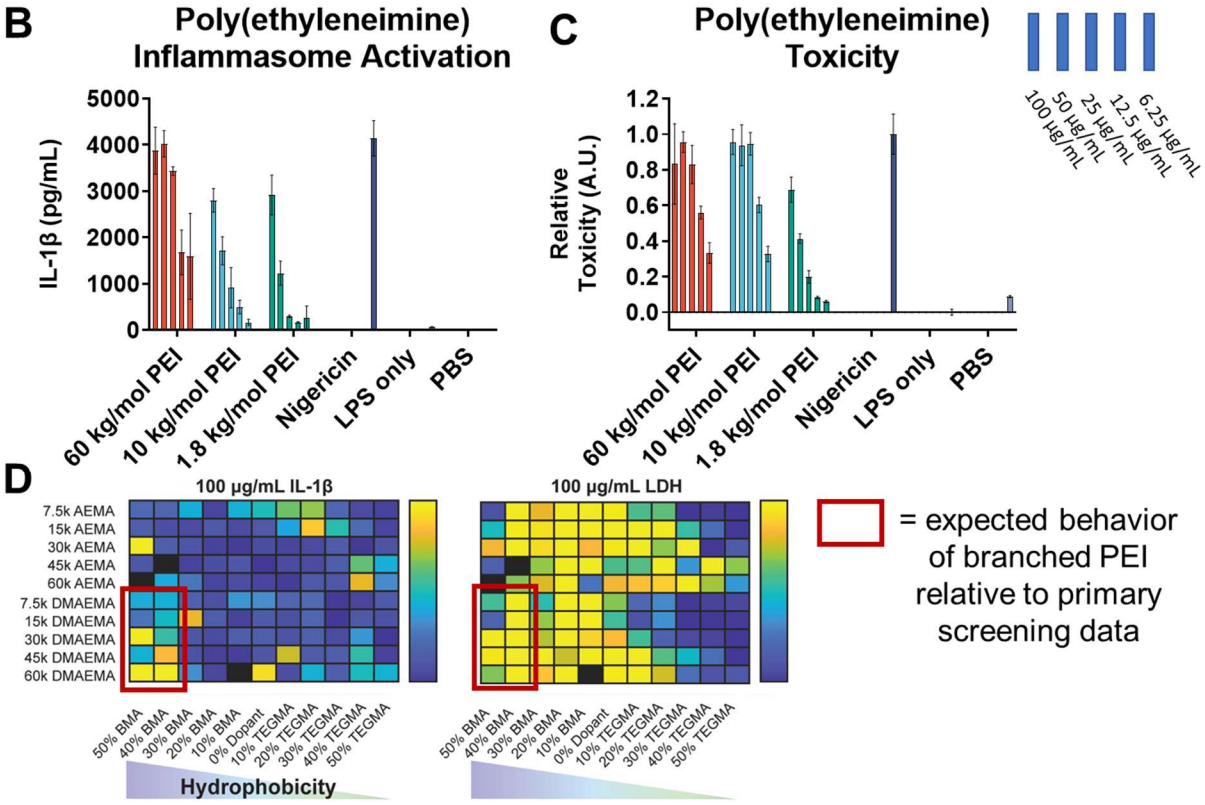

Figure S2.12: In-vitro Screening of Branched Poly(ethyleneimine). (A) Three branched poly(ethyleneimine) (PEI) compounds with different molecular weights were purchased with the reported characteristics. LPS-primed BMDCs were treated with the indicated polymers for 5 h, and (B) IL-1β and (C) LDH were assayed in the supernatant. (D) Based on the results of (B) and (C), branched PEI is expected to behave similarly to the polymers noted in red from the high throughput screen.

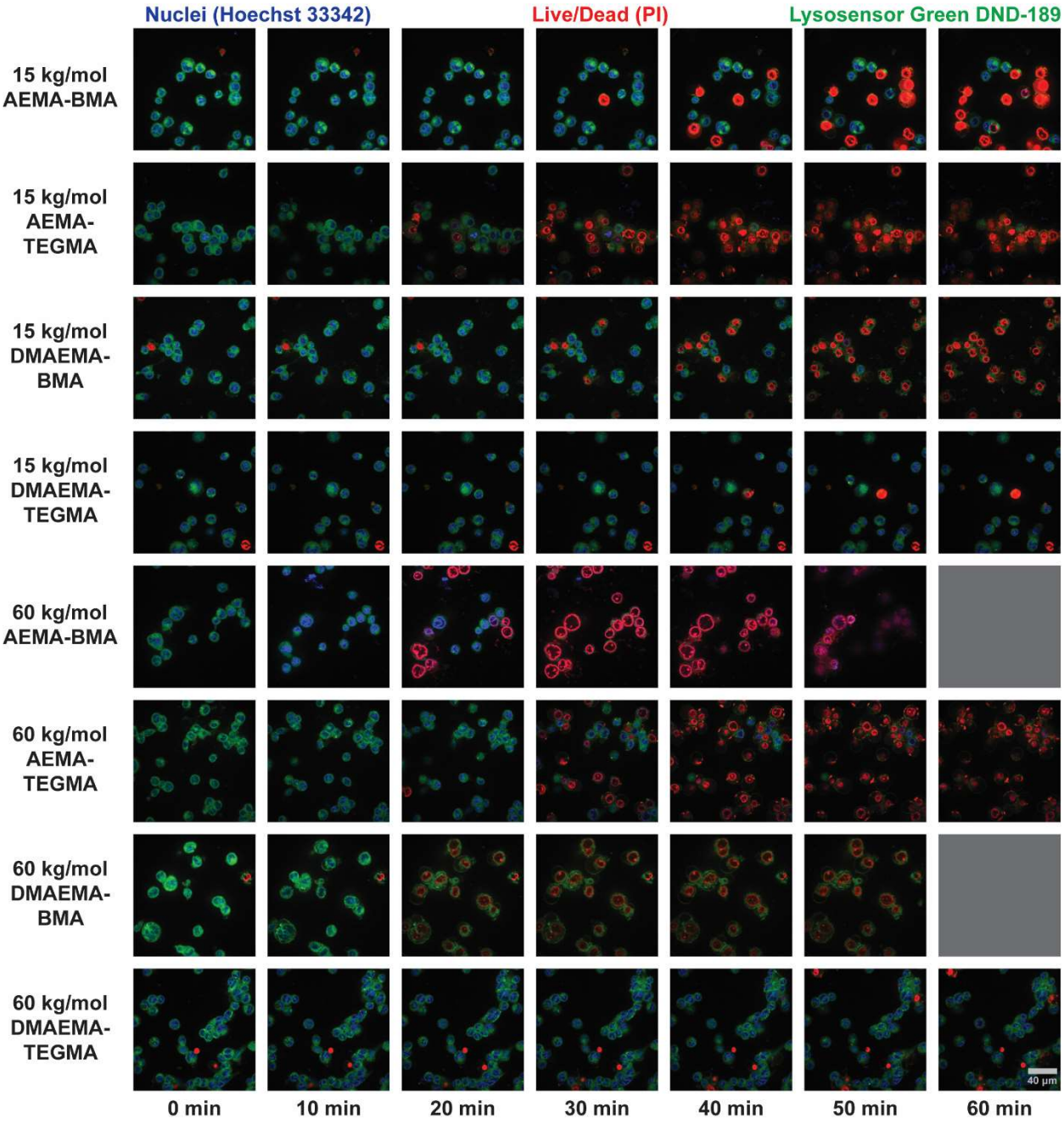

Figure S2.13: Raw Images of Lysosensor Green Assay in WT THP-1 Cells. THP-1 cells were stained with LysoSensor Green DND-189, Propidium Iodide, and Hoechst 33342 and then treated with 100 µg/mL of the indicated polymers. Cells were then imaged every 2 min for 1 h using confocal microscopy (40x oil lens) to evaluate lysosomal pH and cellular morphology. 10 min intervals of selected polymers are shown. Scale bar is representative of all images.

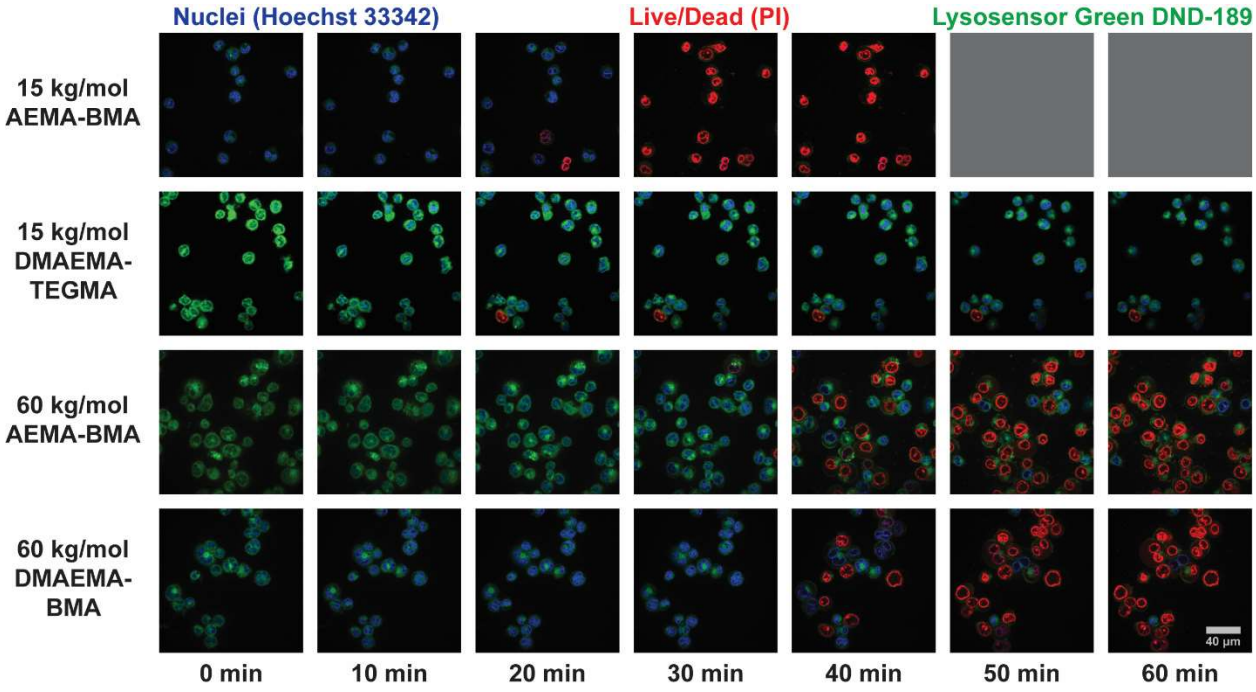

Figure S2.14: Raw Images of Lysosensor Green Assay in NLRP3-KO THP-1 Cells. NLRP3-KO THP-1 cells were stained with LysoSensor Green DND-189, Propidium Iodide, and Hoechst 33342 and then treated with 100 µg/mL of the indicated polymers. Cells were then imaged every 2 min for 1 h using confocal microscopy to evaluate lysosomal pH and cellular morphology. 10 min intervals of selected polymers are shown. Scale bar is representative of all images.

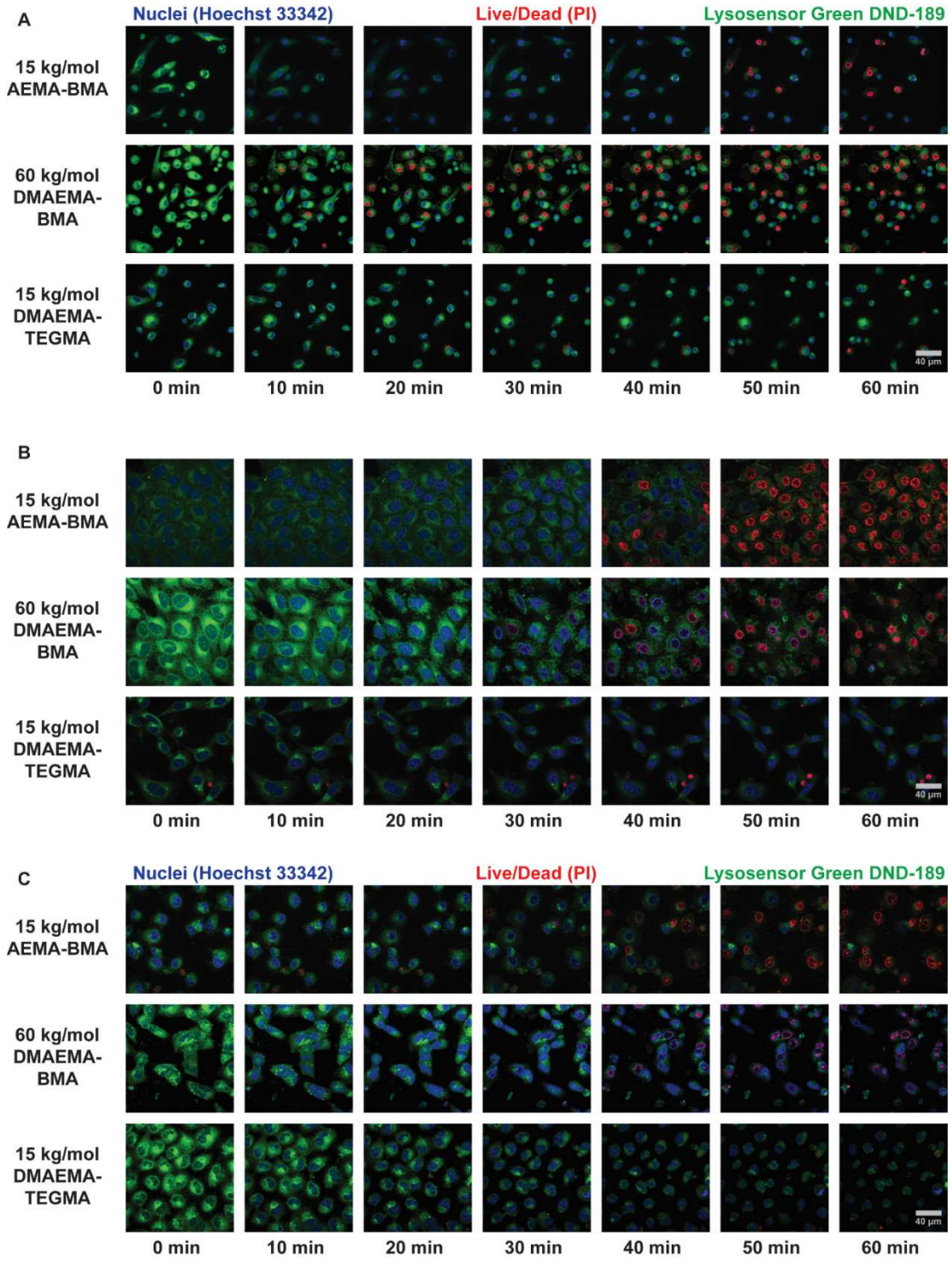

Figure S2.15: Raw Images of Lysosensor Green Assay in Other Cell Lines. (A) Bone marrow-derived dendritic cells (BMDCs), (B) HeLa cells, or (C) A549 cells were stained with LysoSensor Green DND-189, Propidium Iodide, and Hoechst 33342 and then treated with 100 µg/mL of the indicated polymers. Cells were then imaged every 2 min for 1 h using confocal microscopy to evaluate lysosomal pH and cellular morphology. 10 min intervals of selected polymers are shown. Scale bar is representative of all images.

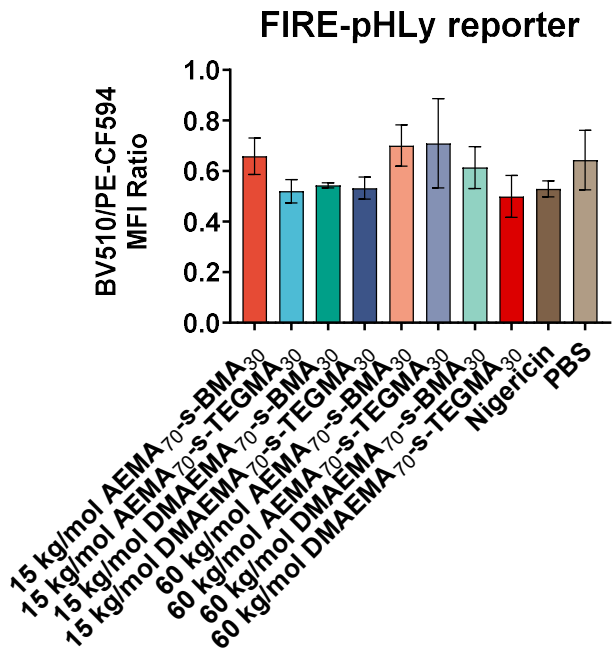

Figure S2.16: HEK FIRE-pHLy Lysosomal pH Assay. HEK FIRE-pHLy cells were treated with polymers at 25 µg/mL for 1 h, and the ratio of mTFP1 to mCherry fluorescence was analyzed by flow cytometry. mTFP1 is a pH sensitive lysosomal reporter where greater fluorescence (relative to the pH insensitive mCherry reporter) indicates lysosomal acidification.

A) Synthetic Scheme

Synthesis of DMAEMA-containing polymers with 5 mol.% AEMA for fluorescent tagging

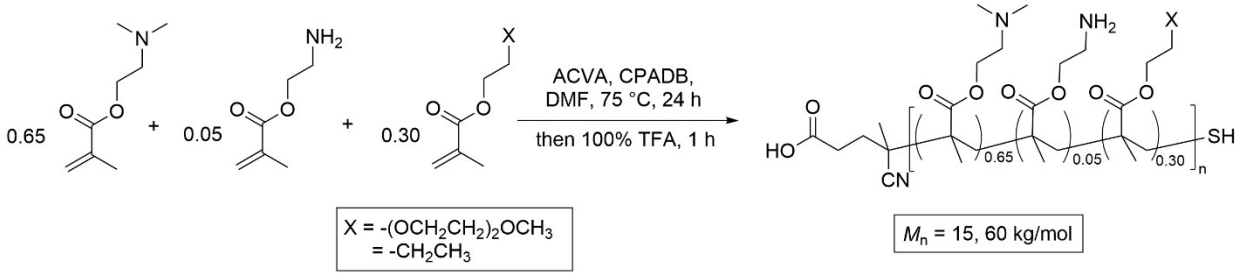

Fluorescent tagging of polymers with AF488-NHS Ester

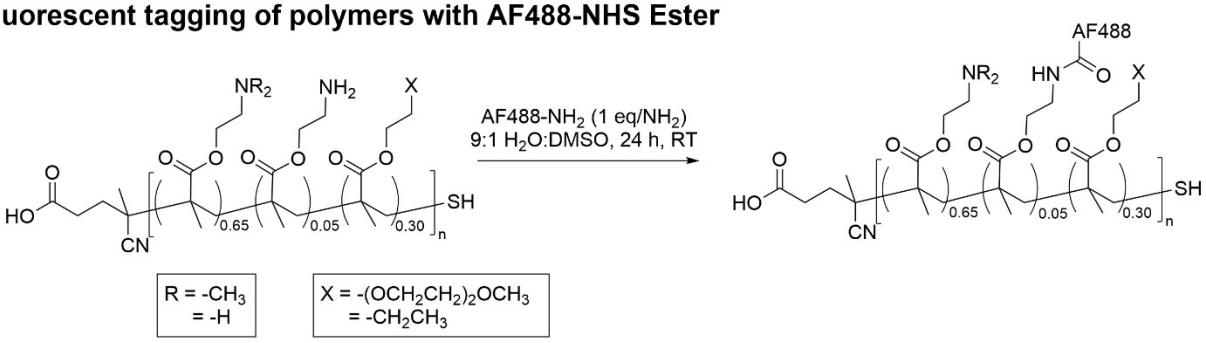

B) Characterization Table

Polymer Name	Mon1	Mon2	M_n (theory)	%Mon1 (theory)	% Mon1 (^{1}H-NMR)	M_n (SEC)	$Đ$ (SEC)
15k $AEMA_{70}$-s-BMA_{30}	AEMA	BMA	15,000	70%	68%	18,800	1.17
15k $AEMA_{70}$-s-$TEGMA_{30}$	AEMA	TEGMA	15,000	70%	75%	13,300	1.21
60k $AEMA_{70}$-s-BMA_{30}	AEMA	BMA	60,000	70%	67%	53,500	1.35
60k $AEMA_{70}$-s-$TEGMA_{30}$	AEMA	TEGMA	60,000	70%	72%	59,100	1.31
15k $DMAEMA_{65}$-s-BMA_{30}-s-$AEMA_5$	DMAEMA	BMA	15,000	65%	68%	14,100*	1.33
15k $DMAEMA_{65}$-s-$TEGMA_{30}$-s-$AEMA_5$	DMAEMA	TEGMA	15,000	65%	63%	10,600*	1.60
60k $DMAEMA_{65}$-s-BMA_{30}-s-$AEMA_5$	DMAEMA	BMA	60,000	65%	61%	37,500*	1.39
60k $DMAEMA_{65}$-s-$TEGMA_{30}$-s-$AEMA_5$	DMAEMA	TEGMA	60,000	65%	61%	31,800*	1.35

Figure S2.17: Synthesis and characterization of AF488-Labelled Polymers. (A) Synthetic strategy to prepare polymers for AF488 conjugation and subsequent imaging studies. (B) Characterization of polymers prepared for conjugation to AF488-NHS Ester. Raw NMR and SEC spectra are provided in **Appendix A**. Where starred (*), we note that DMF-SEC was conducted on deprotected polymers containing primary amines, so the SEC values reported for are expected to be under-estimations due to primary amine-column interactions.

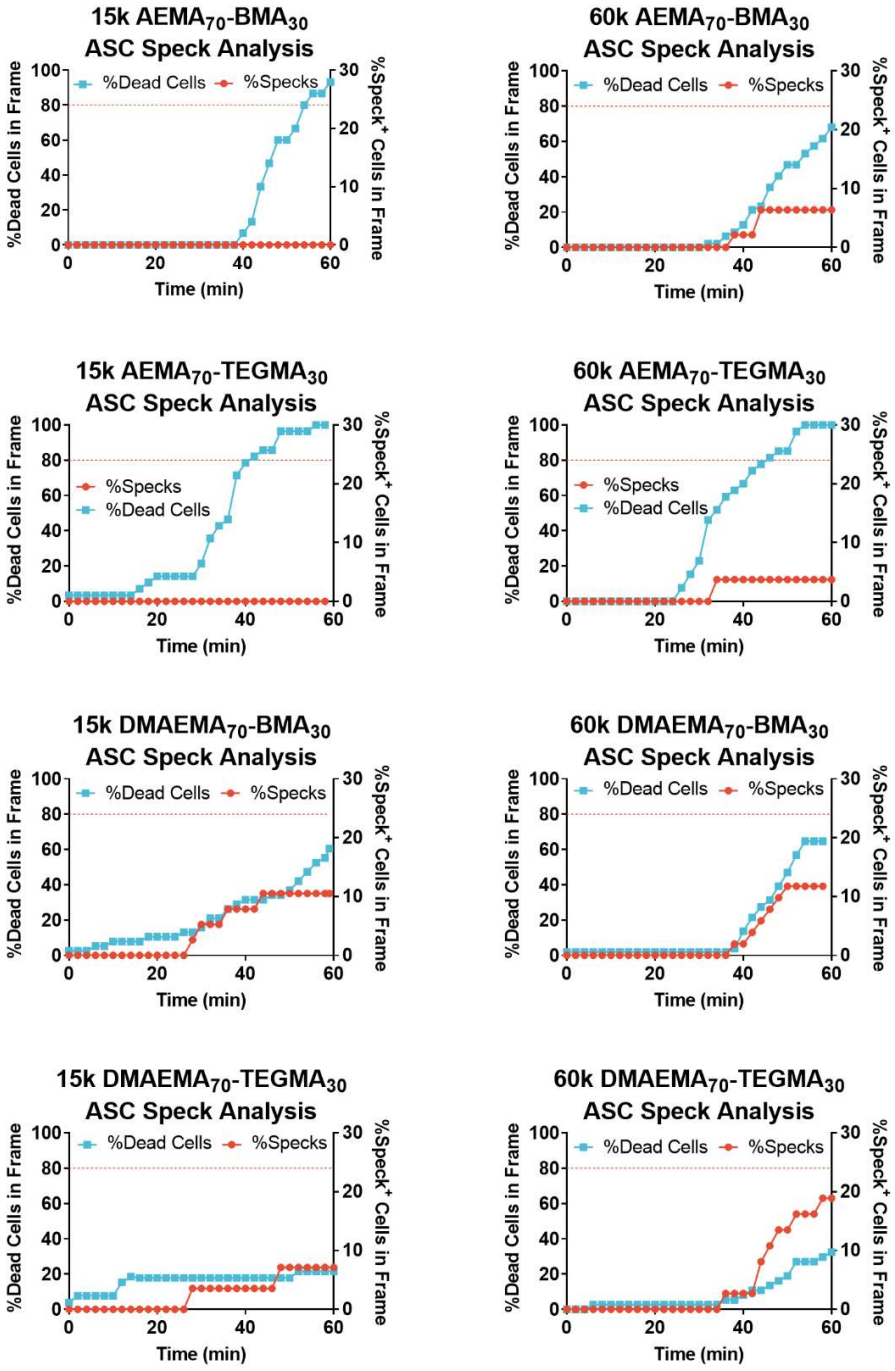

Figure S2.18: THP-1 ASC-GFP Speck Formation. ASC speck formation and propidium iodide staining of THP-ASC-GFP cells were analyzed in 2 min intervals for 60 min after treatment with the eight polymers of interest at 100 µg/mL. Selected results are also presented in **Figure 2.5A**.

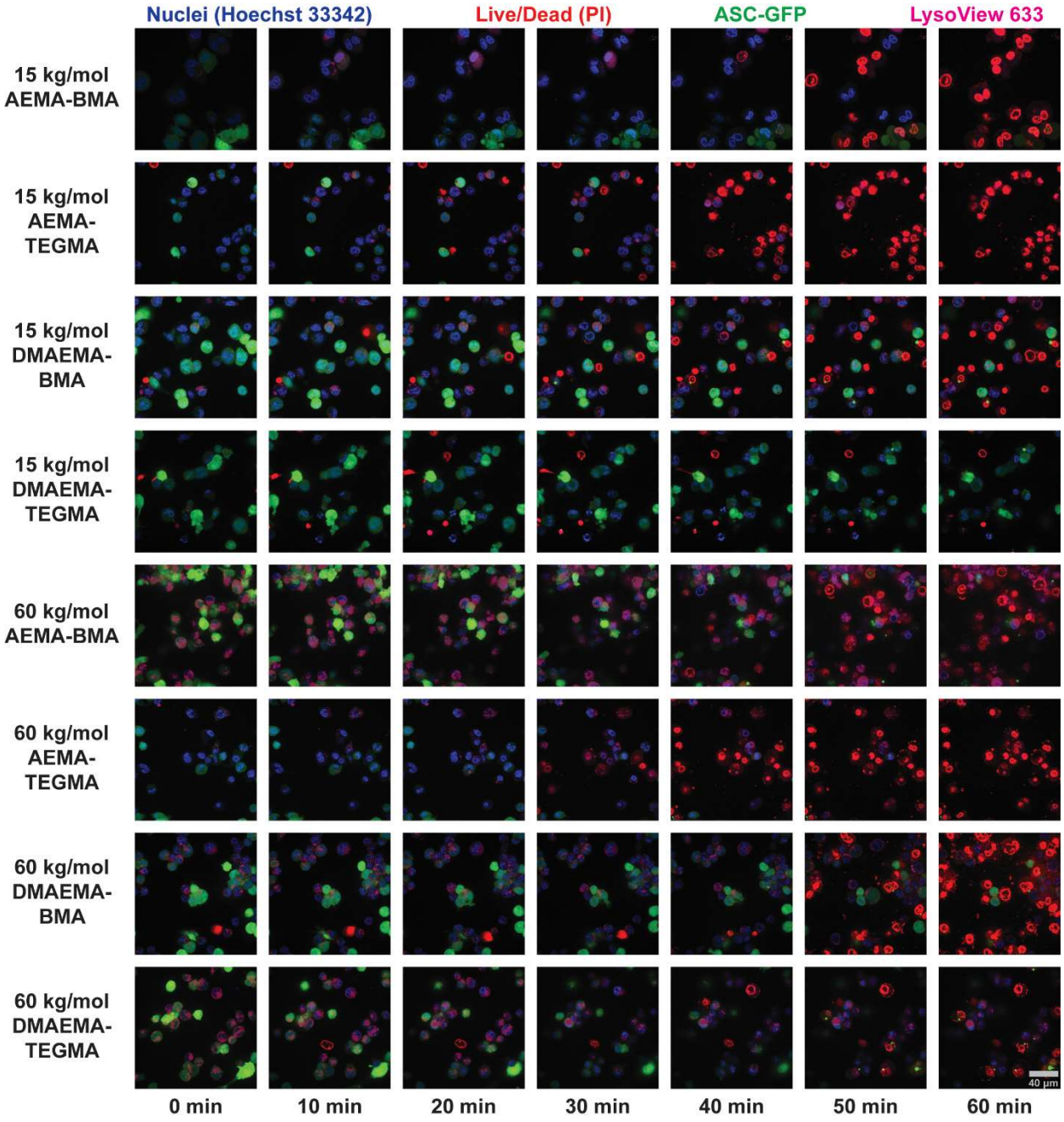

Figure S2.19: THP-1 ASC-GFP Speck Raw Images. THP-1 ASC-GFP cells were stained with LysoView 633, Propidium Iodide, and Hoechst 33342 and then treated with 100 µg/mL of the indicated polymers. Cells were then imaged every 2 min for 1 h using confocal microscopy (40x oil lens) to evaluate speck formation and cell death. 10 min intervals of selected polymers are shown. Images were used to determine results shown in **Figures 2.6A** and **S2.18**. Scale bar is representative of all images.

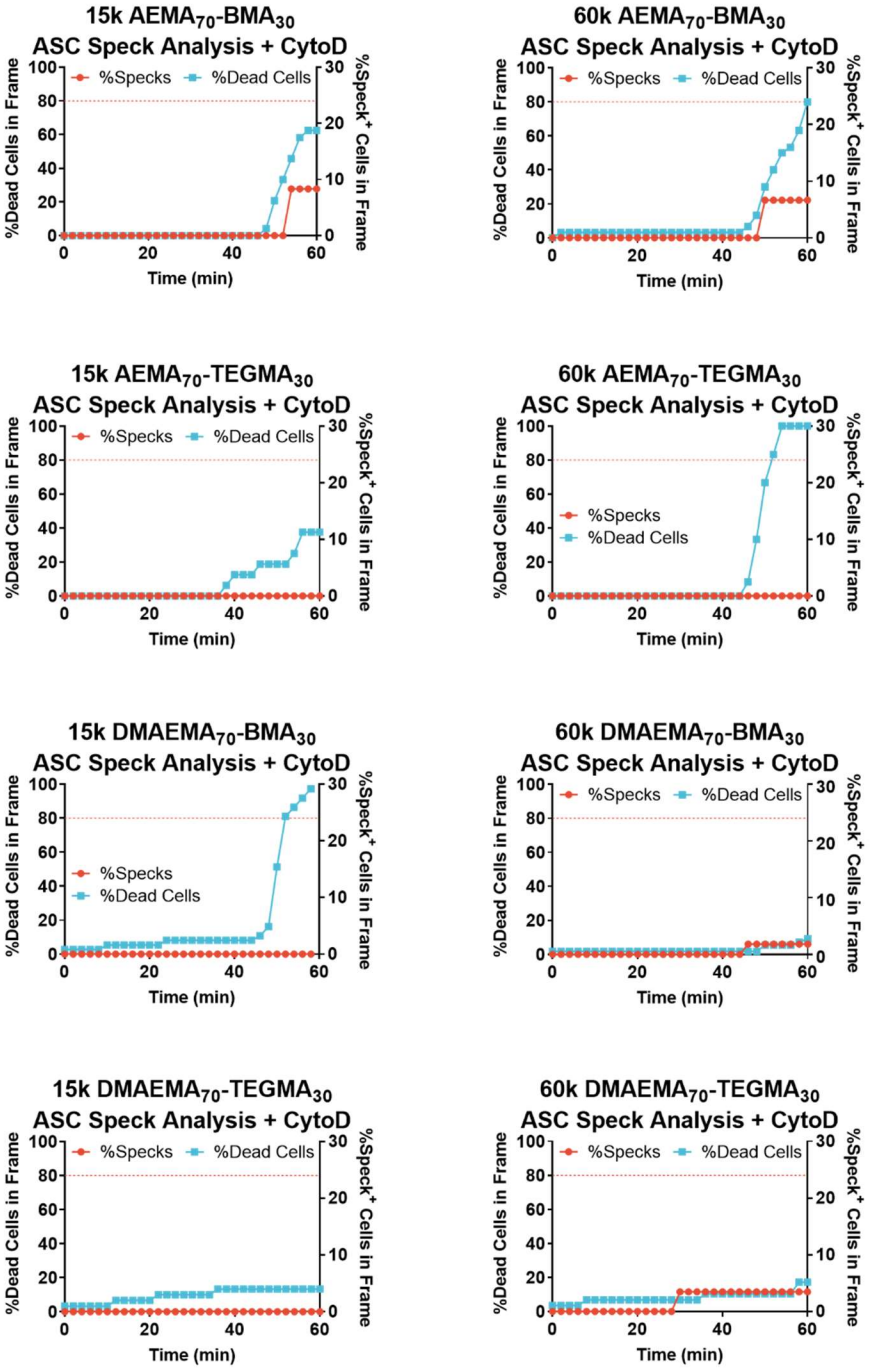

Figure S2.20: THP-1 ASC-GFP Speck Formation + Cytochalasin D. Cells were pre-treated with cytochalasin D (CytoD), and ASC speck formation and propidium iodide staining were analyzed in 2 min intervals for 60 min after treatment with the eight polymers of interest at 100 µg/mL (analogously as in **Figure S2.18**). Selected results are also presented in **Figure 2.5B**.

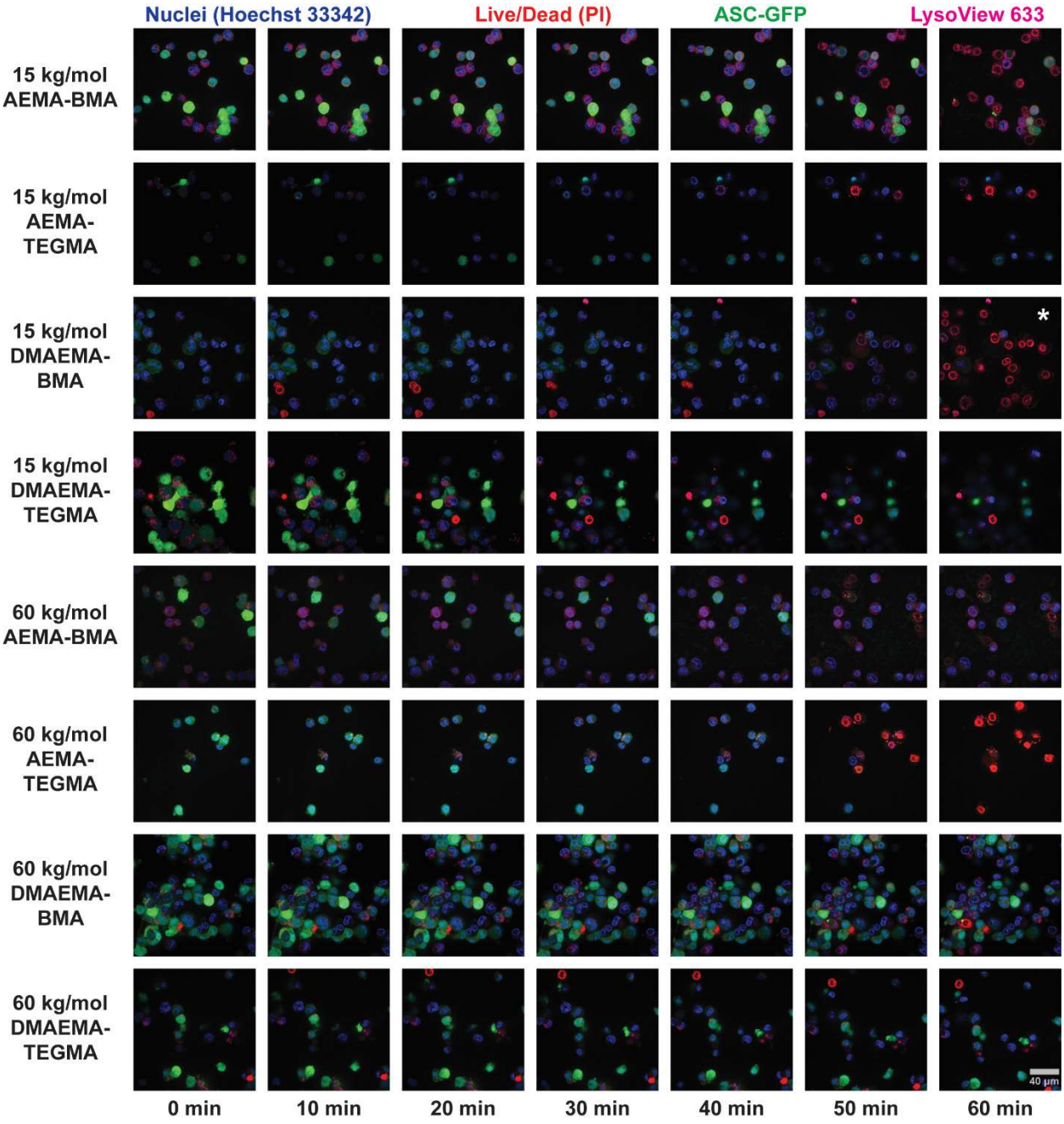

Figure S2.21: ASC-GFP Speck Raw Images + Cytochalasin D. THP-1 ASC-GFP cells were pre-treated with Cytochalasin D, stained as in **Figure S2.19**, and treated with 100 µg/mL of the indicated polymers. Cells were then imaged every 2 min for 1 h using confocal microscopy (40x oil lens) to evaluate speck formation and cell death. 10 min intervals of selected polymers are shown (* = imaged at 58 min). Images were used to determine results shown in **Figures 2.5B** and **S2.20**. Scale bar is representative of all images.

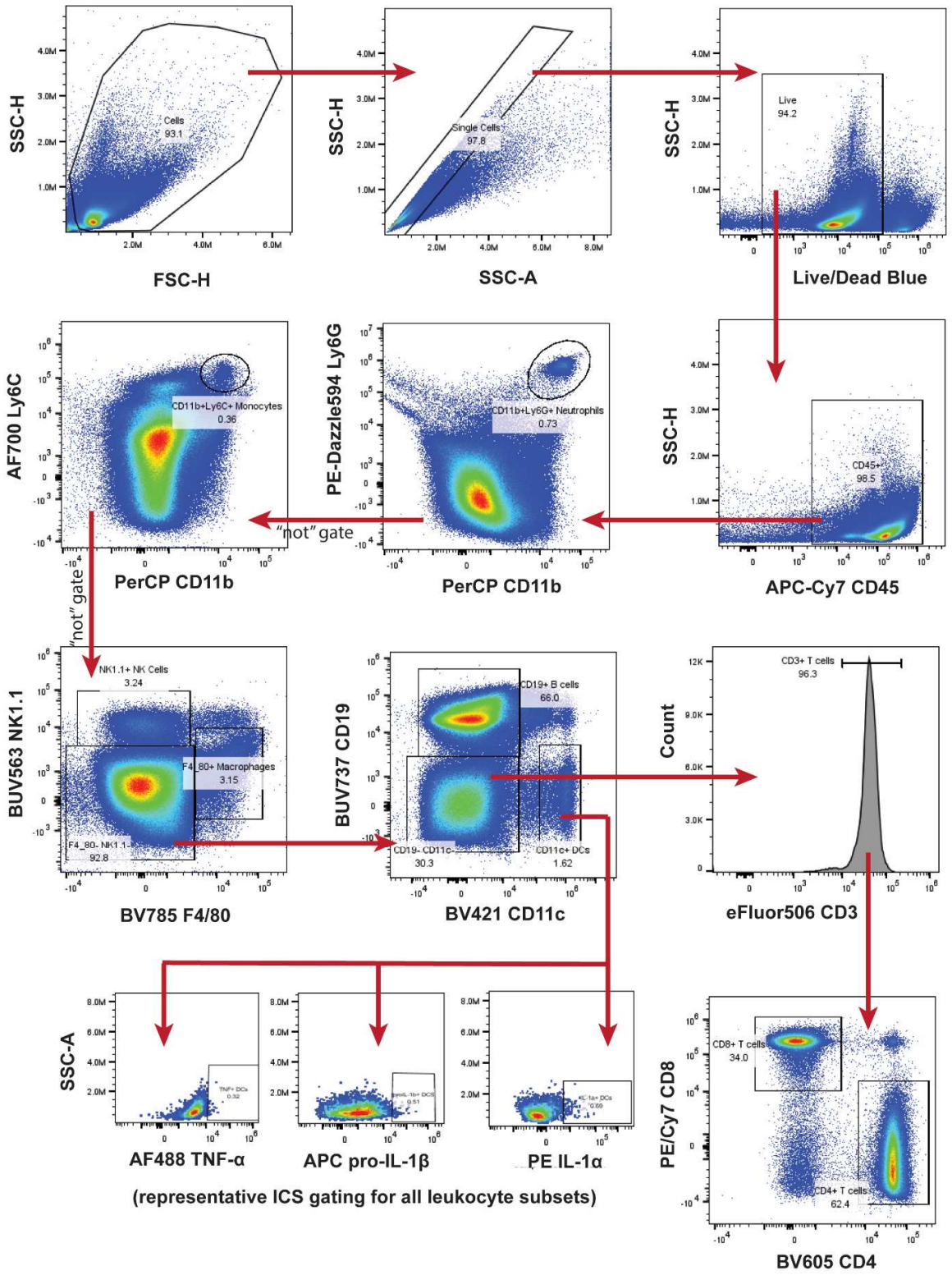

Figure S2.22: Flow Cytometry Gating Strategy for Intravenous Polymer Administration Study. Flow cytometry gating for the immunophenotyping experiment described in **Figures 2.6** and **S2.23-24**.

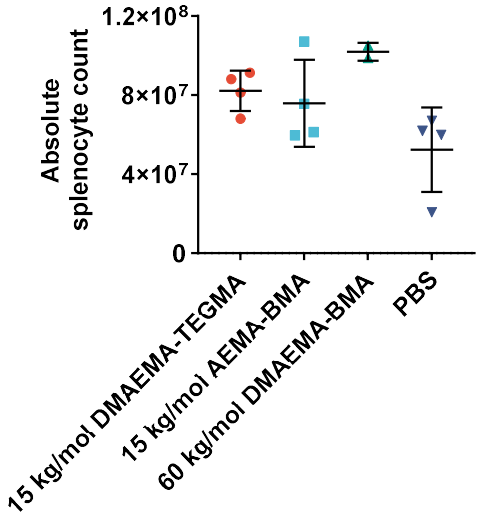

Figure S2.23: Absolute Cell Counts in Spleen after I.V. Polymer Administration. Absolute splenocyte count 6 h after intravenous injection of 50 µg of the indicated polymers as described in **Figure 2.6A**. Cells were counted manually using a hemocytometer.

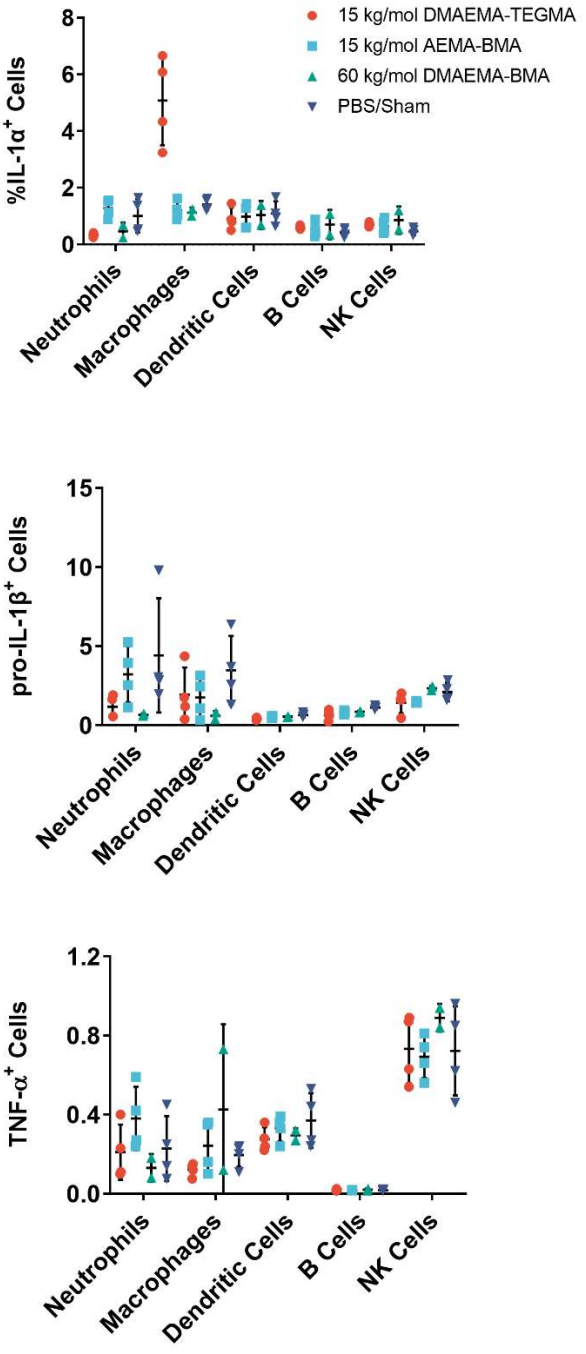

Figure S2.24: Intracellular IL-1 and TNF-α in Spleen after I.V. Polymer Administration. Splenocytes collected 6 h after I.V. injection of the indicated polymers were immunophenotyped as described in **Figure S2.22**, and the percentage of IL-1α$^+$, pro-IL-1β$^+$, and TNF-α$^+$ cells in each leukocyte subset were quantified via intracellular cytokine staining and flow cytometry.

Antibody	Fluorophore	Clone	Vendor
Live/Dead Blue	N/A	N/A	Thermo
Anti-mouse CD45	APC/Cy7	I3/2.3	BioLegend
Anti-mouse CD11b	PerCP	M1/70	BioLegend
Anti-mouse CD11c	BV421	N418	BioLegend
Anti-mouse F4/80	BV785	BM8	BioLegend
Anti-mouse Ly6G	PE-CF594	1A8	BioLegend
Anti-mouse CD19	BUV737	1D3	BD
Anti-mouse Ly6C	AF700	HK1.4	BioLegend
Anti-mouse NK1.1	BUV563	PK136	BD
Anti-mouse CD3	eFluor506	17A2	Thermo
Anti-mouse CD4	BV605	RM4-5	BioLegend
Anti-mouse CD8	PE/Cy7	53.6-7	BioLegend
Anti-mouse TNF-α	AF488	MP6-XT22	BioLegend
Anti-mouse pro-IL-1β	APC	NJTEN3	Thermo
Anti-mouse IL-1α	PE	ALF-161	BioLegend
CD16/32 (TruStain FcX™)	N/A	93	BioLegend

Table S2.3: List of antibodies used for flow cytometry analysis in **Chapter 2**.

2.6 References.

1. Zhao, S.; Huang, W.; Wang, C.; Wang, Y.; Zhang, Y.; Ye, Z.; Zhang, J.; Deng, L.; Dong, A., Screening and Matching Amphiphilic Cationic Polymers for Efficient Antibiosis. *Biomacromolecules* **2020,** *21* (12), 5269-5281.

2. Monnery, B. D., Polycation-Mediated Transfection: Mechanisms of Internalization and Intracellular Trafficking. *Biomacromolecules* **2021,** *22* (10), 4060-4083.

3. Samal, S. K.; Dash, M.; Van Vlierberghe, S.; Kaplan, D. L.; Chiellini, E.; van Blitterswijk, C.; Moroni, L.; Dubruel, P., Cationic polymers and their therapeutic potential. *Chem Soc Rev* **2012,** *41* (21), 7147-7194.

4. Lv, J.; Fan, Q.; Wang, H.; Cheng, Y., Polymers for cytosolic protein delivery. *Biomaterials* **2019,** *218*, 119358.

5. Lostalé-Seijo, I.; Montenegro, J., Synthetic materials at the forefront of gene delivery. *Nat Rev Chem* **2018,** *2* (10), 258-277.

6. Schuster, S. J.; Bishop, M. R.; Tam, C. S.; Waller, E. K.; Borchmann, P.; McGuirk, J. P.; Jager, U.; Jaglowski, S.; Andreadis, C.; Westin, J. R.; Fleury, I.; Bachanova, V.; Foley, S. R.; Ho, P. J.; Mielke, S.; Magenau, J. M.; Holte, H.; Pantano, S.; Pacaud, L. B.; Awasthi, R.; Chu, J.; Anak, O.; Salles, G.; Maziarz, R. T.; Investigators, J., Tisagenlecleucel in Adult Relapsed or Refractory Diffuse Large B-Cell Lymphoma. *N Engl J Med* **2019,** *380* (1), 45-56.

7. Russell, S.; Bennett, J.; Wellman, J. A.; Chung, D. C.; Yu, Z.-F.; Tillman, A.; Wittes, J.; Pappas, J.; Elci, O.; McCague, S.; Cross, D.; Marshall, K. A.; Walshire, J.; Kehoe, T. L.; Reichert, H.; Davis, M.; Raffini, L.; George, L. A.; Hudson, F. P.; Dingfield, L.; Zhu, X.; Haller, J. A.; Sohn, E. H.; Mahajan, V. B.; Pfeifer, W.; Weckmann, M.; Johnson, C.; Gewaily, D.; Drack, A.; Stone, E.; Wachtel, K.; Simonelli, F.; Leroy, B. P.; Wright, J. F.; High, K. A.; Maguire, A. M., Efficacy and safety of voretigene neparvovec (AAV2-hRPE65v2) in patients with RPE65 -mediated inherited retinal dystrophy: a randomised, controlled, open-label, phase 3 trial. *The Lancet* **2017,** *390* (10097), 849-860.

8. Atmar, R. L.; Bernstein, D. I.; Harro, C. D.; Al-Ibrahim, M. S.; Chen, W. H.; Ferreira, J.; Estes, M. K.; Graham, D. Y.; Opekun, A. R.; Richardson, C.; Mendelman, P. M., Norovirus vaccine against experimental human Norwalk Virus illness. *N Engl J Med* **2011,** *365* (23), 2178-2187.

9. Weiss, A. M.; Hossainy, S.; Rowan, S. J.; Hubbell, J. A.; Esser-Kahn, A. P., Immunostimulatory Polymers as Adjuvants, Immunotherapies, and Delivery Systems. *Macromolecules* **2022,** *55* (16), 6913-6937.

10. Chahal, J. S.; Khan, O. F.; Cooper, C. L.; McPartlan, J. S.; Tsosie, J. K.; Tilley, L. D.; Sidik, S. M.; Lourido, S.; Langer, R.; Bavari, S.; Ploegh, H. L.; Anderson, D. G., Dendrimer-RNA nanoparticles generate protective immunity against lethal Ebola, H1N1 influenza, and Toxoplasma gondii challenges with a single dose. *Proc Natl Acad Sci U S A* **2016,** *113* (29), 4133-4142.

11. Barbier, A. J.; Jiang, A. Y.; Zhang, P.; Wooster, R.; Anderson, D. G., The clinical progress of mRNA vaccines and immunotherapies. *Nat Biotechnol* **2022,** *40*, 840-854.

12. Breunig, M.; Lungwitz, U.; Liebl, R.; Goepferich, A., Breaking up the correlation between efficacy and toxicity for nonviral gene delivery. *Proc Natl Acad Sci U S A* **2007,** *104* (36), 14454-14459.

13. Mortazavian, H.; Foster, L. L.; Bhat, R.; Patel, S.; Kuroda, K., Decoupling the Functional Roles of Cationic and Hydrophobic Groups in the Antimicrobial and Hemolytic Activities of Methacrylate Random Copolymers. *Biomacromolecules* **2018,** *19* (11), 4370-4378.

14. Wei, X.; Shao, B.; He, Z.; Ye, T.; Luo, M.; Sang, Y.; Liang, X.; Wang, W.; Luo, S.; Yang, S.; Zhang, S.; Gong, C.; Gou, M.; Deng, H.; Zhao, Y.; Yang, H.; Deng, S.; Zhao, C.; Yang, L.; Qian, Z.; Li, J.; Sun, X.; Han, J.; Jiang, C.; Wu, M.; Zhang, Z., Cationic nanocarriers induce cell necrosis through impairment of Na(+)/K(+)-ATPase and cause subsequent inflammatory response. *Cell Res* **2015,** *25* (2), 237-253.

15. Toy, R.; Pradhan, P.; Ramesh, V.; Di Paolo, N. C.; Lash, B.; Liu, J.; Blanchard, E. L.; Pinelli, C. J.; Santangelo, P. J.; Shayakhmetov, D. M.; Roy, K., Modification of primary amines to higher order amines reduces in vivo hematological and immunotoxicity of cationic nanocarriers through TLR4 and complement pathways. *Biomaterials* **2019,** *225*, 119512.

16. Swanson, K. V.; Deng, M.; Ting, J. P., The NLRP3 inflammasome: molecular activation and regulation to therapeutics. *Nat Rev Immunol* **2019,** *19* (8), 477-489.

17. Manna, S.; Howitz, W. J.; Oldenhuis, N. J.; Eldredge, A. C.; Shen, J.; Nihesh, F. N.; Lodoen, M. B.; Guan, Z.; Esser-Kahn, A. P., Immunomodulation of the NLRP3 Inflammasome through Structure-Based Activator Design and Functional Regulation via Lysosomal Rupture. *ACS Cent Sci* **2018,** *4* (8), 982-995.

18. Baljon, J. J.; Dandy, A.; Wang-Bishop, L.; Wehbe, M.; Jacobson, M. E.; Wilson, J. T., The efficiency of cytosolic drug delivery using pH-responsive endosomolytic polymers does not correlate with activation of the NLRP3 inflammasome. *Biomater Sci* **2019,** *7* (5), 1888-1897.

19. Nandi, D.; Shivrayan, M.; Gao, J.; Krishna, J.; Das, R.; Liu, B.; Thayumanavan, S.; Kulkarni, A., Core Hydrophobicity of Supramolecular Nanoparticles Induces NLRP3 Inflammasome Activation. *ACS Appl Mater Interfaces* **2021,** *13* (38), 45300-45314.

20. Chen, B.; Yan, Y.; Yang, Y.; Cao, G.; Wang, X.; Wang, Y.; Wan, F.; Yin, Q.; Wang, Z.; Li, Y.; Wang, L.; Xu, B.; You, F.; Zhang, Q.; Wang, Y., A pyroptosis nanotuner for cancer therapy. *Nat Nanotechnol* **2022,** *17* (7), 788-798.

21. Gong, N.; Zhang, Y.; Teng, X.; Wang, Y.; Huo, S.; Qing, G.; Ni, Q.; Li, X.; Wang, J.; Ye, X.; Zhang, T.; Chen, S.; Wang, Y.; Yu, J.; Wang, P. C.; Gan, Y.; Zhang, J.; Mitchell, M. J.; Li, J.; Liang, X. J., Proton-driven transformable nanovaccine for cancer immunotherapy. *Nat Nanotechnol* **2020,** *15* (12), 1053-1064.

22. Li, T.; Zehner, M.; He, J.; Prochnicki, T.; Horvath, G.; Latz, E.; Burgdorf, S.; Takeoka, S., NLRP3 inflammasome-activating arginine-based liposomes promote antigen presentations in dendritic cells. *Int J Nanomedicine* **2019,** *14*, 3503-3516.

23. Tahtinen, S.; Tong, A. J.; Himmels, P.; Oh, J.; Paler-Martinez, A.; Kim, L.; Wichner, S.; Oei, Y.; McCarron, M. J.; Freund, E. C.; Amir, Z. A.; de la Cruz, C. C.; Haley, B.; Blanchette, C.; Schartner, J. M.; Ye, W.; Yadav, M.; Sahin, U.; Delamarre, L.; Mellman, I., IL-1 and IL-1ra are key regulators of the inflammatory response to RNA vaccines. *Nat Immunol* **2022,** *23* (4), 532-542.

24. Ghiringhelli, F.; Apetoh, L.; Tesniere, A.; Aymeric, L.; Ma, Y.; Ortiz, C.; Vermaelen, K.; Panaretakis, T.; Mignot, G.; Ullrich, E.; Perfettini, J. L.; Schlemmer, F.; Tasdemir, E.; Uhl, M.; Genin, P.; Civas, A.; Ryffel, B.; Kanellopoulos, J.; Tschopp, J.; Andre, F.; Lidereau, R.; McLaughlin, N. M.; Haynes, N. M.; Smyth, M. J.; Kroemer, G.; Zitvogel, L., Activation of the

NLRP3 inflammasome in dendritic cells induces IL-1beta-dependent adaptive immunity against tumors. *Nat Med* **2009,** *15* (10), 1170-1178.

25. Sagoo, P.; Garcia, Z.; Breart, B.; Lemaitre, F.; Michonneau, D.; Albert, M. L.; Levy, Y.; Bousso, P., In vivo imaging of inflammasome activation reveals a subcapsular macrophage burst response that mobilizes innate and adaptive immunity. *Nat Med* **2016,** *22* (1), 64-71.

26. Gabay, C.; Lamacchia, C.; Palmer, G., IL-1 pathways in inflammation and human diseases. *Nat Rev Rheumatol* **2010,** *6* (4), 232-241.

27. Agostini, L.; Martinon, F.; Burns, K.; McDermott, M. F.; Hawkins, P. N.; Tschopp, J., NALP3 Forms an IL-1β-Processing Inflammasome with Increased Activity in Muckle-Wells Autoinflammatory Disorder. *Immunity* **2004,** *20* (3), 319-325.

28. Martinon, F.; Petrilli, V.; Mayor, A.; Tardivel, A.; Tschopp, J., Gout-associated uric acid crystals activate the NALP3 inflammasome. *Nature* **2006,** *440* (7081), 237-241.

29. Anderson, D. G.; Lynn, D. M.; Langer, R., Semi-automated synthesis and screening of a large library of degradable cationic polymers for gene delivery. *Angew Chem Int Ed Engl* **2003,** *42* (27), 3153-3158.

30. Anderson, D. G.; Akinc, A.; Hossain, N.; Langer, R., Structure/property studies of polymeric gene delivery using a library of poly(beta-amino esters). *Mol Ther* **2005,** *11* (3), 426-434.

31. Nelson, C. E.; Kintzing, J. R.; Hanna, A.; Shannon, J. M.; Gupta, M. K.; Duvall, C. L., Balancing cationic and hydrophobic content of PEGylated siRNA polyplexes enhances endosome escape, stability, blood circulation time, and bioactivity in vivo. *ACS Nano* **2013,** *7* (10), 8870-8880.

32. Ulkoski, D.; Munson, M. J.; Jacobson, M. E.; Palmer, C. R.; Carson, C. S.; Sabirsh, A.; Wilson, J. T.; Krishnamurthy, V. R., High-Throughput Automation of Endosomolytic Polymers for mRNA Delivery. *ACS Appl Bio Mater* **2021,** *4* (2), 1640-1654.

33. Rinkenauer, A. C.; Vollrath, A.; Schallon, A.; Tauhardt, L.; Kempe, K.; Schubert, S.; Fischer, D.; Schubert, U. S., Parallel high-throughput screening of polymer vectors for nonviral gene delivery: evaluation of structure-property relationships of transfection. *ACS Comb Sci* **2013,** *15* (9), 475-482.

34. Paslay, L. C.; Abel, B. A.; Brown, T. D.; Koul, V.; Choudhary, V.; McCormick, C. L.; Morgan, S. E., Antimicrobial poly(methacrylamide) derivatives prepared via aqueous RAFT polymerization exhibit biocidal efficiency dependent upon cation structure. *Biomacromolecules* **2012,** *13* (8), 2472-2482.

35. Wan, P.; Wang, Y.; Guo, W.; Song, Z.; Zhang, S.; Wu, H.; Yan, W.; Deng, M.; Xiao, C., Low-Molecular-Weight Polylysines with Excellent Antibacterial Properties and Low Hemolysis. *ACS Biomater Sci Eng* **2022,** *8* (2), 903-911.

36. Chan, D.; Chien, J. C.; Axpe, E.; Blankemeier, L.; Baker, S. W.; Swaminathan, S.; Piunova, V. A.; Zubarev, D. Y.; Maikawa, C. L.; Grosskopf, A. K.; Mann, J. L.; Soh, H. T.; Appel, E. A., Combinatorial Polyacrylamide Hydrogels for Preventing Biofouling on Implantable Biosensors. *Adv Mater* **2022,** *34* (24), e2109764.

37. Ko, Y.; Truong, V. K.; Woo, S. Y.; Dickey, M. D.; Hsiao, L.; Genzer, J., Counterpropagating Gradients of Antibacterial and Antifouling Polymer Brushes. *Biomacromolecules* **2021,** *23* (1), 424-430.

38. Pham, P.; Oliver, S.; Wong, E. H. H.; Boyer, C., Effect of hydrophilic groups on the bioactivity of antimicrobial polymers. *Polym Chem* **2021,** *12*, 5689-5703.

39. Pham, P.; Oliver, S.; Nguyen, D. T.; Boyer, C., Effect of Cationic Groups on the Selectivity of Ternary Antimicrobial Polymers. *Macromol Rapid Commun* **2022,** *43*, e2200377.

40. Upadhya, R.; Kosuri, S.; Tamasi, M.; Meyer, T. A.; Atta, S.; Webb, M. A.; Gormley, A. J., Automation and data-driven design of polymer therapeutics. *Adv Drug Deliv Rev* **2021,** *171*, 1-28.

41. Ng, G.; Yeow, J.; Chapman, R.; Isahak, N.; Wolvetang, E.; Cooper-White, J. J.; Boyer, C., Pushing the Limits of High Throughput PET-RAFT Polymerization. *Macromolecules* **2018,** *51* (19), 7600-7607.

42. Li, Z.; Kosuri, S.; Foster, H.; Cohen, J.; Jumeaux, C.; Stevens, M. M.; Chapman, R.; Gormley, A. J., A Dual Wavelength Polymerization and Bioconjugation Strategy for High Throughput Synthesis of Multivalent Ligands. *J Am Chem Soc* **2019,** *141* (50), 19823-19830.

43. Gormley, A. J.; Yeow, J.; Ng, G.; Conway, O.; Boyer, C.; Chapman, R., An Oxygen-Tolerant PET-RAFT Polymerization for Screening Structure-Activity Relationships. *Angew Chem Int Ed Engl* **2018,** *57* (6), 1557-1562.

44. Mann, J. L.; Maikawa, C. L.; Smith, A. A. A.; Grosskopf, A. K.; Baker, S. W.; Roth, G. A.; Meis, C. M.; Gale, E. C.; Liong, C. S.; Correa, S.; Chan, D.; Stapleton, L. M.; Yu, A. C.; Muir, B.; Howard, S.; Postma, A.; Appel, E. A., An ultrafast insulin formulation enabled by high-throughput screening of engineered polymeric excipients. *Sci Transl Med* **2020,** *12* (550), eaba6676.

45. Lynn, G. M.; Laga, R.; Darrah, P. A.; Ishizuka, A. S.; Balaci, A. J.; Dulcey, A. E.; Pechar, M.; Pola, R.; Gerner, M. Y.; Yamamoto, A.; Buechler, C. R.; Quinn, K. M.; Smelkinson, M. G.; Vanek, O.; Cawood, R.; Hills, T.; Vasalatiy, O.; Kastenmuller, K.; Francica, J. R.; Stutts, L.; Tom, J. K.; Ryu, K. A.; Esser-Kahn, A. P.; Etrych, T.; Fisher, K. D.; Seymour, L. W.; Seder, R. A., In vivo characterization of the physicochemical properties of polymer-linked TLR agonists that enhance vaccine immunogenicity. *Nat Biotechnol* **2015,** *33* (11), 1201-1210.

46. Manolova, V.; Flace, A.; Bauer, M.; Schwarz, K.; Saudan, P.; Bachmann, M. F., Nanoparticles target distinct dendritic cell populations according to their size. *Eur J Immunol* **2008,** *38* (5), 1404-1413.

47. Fu, L.; Liu, L.; Ruan, Z.; Zhang, H.; Yan, L., Folic acid targeted pH-responsive amphiphilic polymer nanoparticles conjugated with near infrared fluorescence probe for imaging-guided drug delivery. *RSC Adv* **2016,** *6* (46), 40312-40322.

48. Chen, A.; Wu, D.; Johnson, C. S., Determination of Molecular Weight Distributions for Polymers by Diffusion-Ordered NMR. *J Am Chem Soc* **1995,** *117* (30), 7965-7970.

49. Hinton, T. M.; Guerrero-Sanchez, C.; Graham, J. E.; Le, T.; Muir, B. W.; Shi, S.; Tizard, M. L.; Gunatillake, P. A.; McLean, K. M.; Thang, S. H., The effect of RAFT-derived cationic block copolymer structure on gene silencing efficiency. *Biomaterials* **2012,** *33* (30), 7631-7642.

50. Eisele, M.; Burchard, W., Hydrophobic Water-Soluble Polymers 1. Dilute-Solution Properties of Poly(1-Vinyl-2-Piperidone) and Poly(N-Vinylcaprolactam). *Makromol Chem* **1990,** *191* (1), 169-184.

51. Sadtler, K.; Collins, J.; Byrne, J. D.; Langer, R., Parallel evolution of polymer chemistry and immunology: Integrating mechanistic biology with materials design. *Adv Drug Deliv Rev* **2020,** *156*, 65-79.

52. Roy, S.; Sarkhel, S.; Bisht, D.; Hanumantharao, S. N.; Rao, S.; Jaiswal, A., Antimicrobial Mechanisms of Biomaterials: From Macro to Nano. *Biomater Sci* **2022,** *10* (16), 4392-4423.

53. Chanput, W.; Mes, J. J.; Wichers, H. J., THP-1 cell line: an in vitro cell model for immune modulation approach. *Int Immunopharmacol* **2014,** *23* (1), 37-45.

54. Guo, W.; Liu, W.; Wan, P.; Wang, H.; Xiao, C.; Chen, L.; Chen, X., Cationic Amphiphilic Dendrons with Anticancer Activity. *ACS Biomater Sci Eng* **2022,** *8* (5), 2121-2130.

55. Lin, H. J.; Herman, P.; Kang, J. S.; Lakowicz, J. R., Fluorescence lifetime characterization of novel low-pH probes. *Anal Biochem* **2001,** *294* (2), 118-25.

56. Chin, M. Y.; Patwardhan, A. R.; Ang, K. H.; Wang, A. L.; Alquezar, C.; Welch, M.; Nguyen, P. T.; Grabe, M.; Molofsky, A. V.; Arkin, M. R.; Kao, A. W., Genetically Encoded, pH-Sensitive mTFP1 Biosensor for Probing Lysosomal pH. *ACS Sens* **2021,** *6* (6), 2168-2180.

57. Stutz, A.; Horvath, G. L.; Monks, B. G.; Latz, E., ASC Speck Formation as a Readout for Inflammasome Activation. In *The Inflammasome: Methods and Protocols*, De Nardo, C. M.; Latz, E., Eds. Humana Press: Totowa, NJ, 2013; pp 91-101.

58. Van Opdenbosch, N.; Van Gorp, H.; Verdonckt, M.; Saavedra, P. H. V.; de Vasconcelos, N. M.; Goncalves, A.; Vande Walle, L.; Demon, D.; Matusiak, M.; Van Hauwermeiren, F.; D'Hont, J.; Hochepied, T.; Krautwald, S.; Kanneganti, T. D.; Lamkanfi, M., Caspase-1 Engagement and TLR-Induced c-FLIP Expression Suppress ASC/Caspase-8-Dependent Apoptosis by Inflammasome Sensors NLRP1b and NLRC4. *Cell Rep* **2017,** *21* (12), 3427-3444.

59. Chen, S.; Zhou, Q.; Wang, G.; Zhou, Z.; Tang, J.; Xie, T.; Shen, Y., Effect of Cationic Charge Density on Transcytosis of Polyethylenimine. *Biomacromolecules* **2021,** *22* (12), 5139-5150.

60. Li, A. W.; Sobral, M. C.; Badrinath, S.; Choi, Y.; Graveline, A.; Stafford, A. G.; Weaver, J. C.; Dellacherie, M. O.; Shih, T. Y.; Ali, O. A.; Kim, J.; Wucherpfennig, K. W.; Mooney, D. J., A facile approach to enhance antigen response for personalized cancer vaccination. *Nat Mater* **2018,** *17* (6), 528-534.

61. Dinarello, C. A., Immunological and inflammatory functions of the interleukin-1 family. *Annu Rev Immunol* **2009,** *27*, 519-550.

62. Rodrigues, T. S.; de Sa, K. S. G.; Ishimoto, A. Y.; Becerra, A.; Oliveira, S.; Almeida, L.; Goncalves, A. V.; Perucello, D. B.; Andrade, W. A.; Castro, R.; Veras, F. P.; Toller-Kawahisa, J. E.; Nascimento, D. C.; de Lima, M. H. F.; Silva, C. M. S.; Caetite, D. B.; Martins, R. B.; Castro, I. A.; Pontelli, M. C.; de Barros, F. C.; do Amaral, N. B.; Giannini, M. C.; Bonjorno, L. P.; Lopes, M. I. F.; Santana, R. C.; Vilar, F. C.; Auxiliadora-Martins, M.; Luppino-Assad, R.; de Almeida, S. C. L.; de Oliveira, F. R.; Batah, S. S.; Siyuan, L.; Benatti, M. N.; Cunha, T. M.; Alves-Filho, J. C.; Cunha, F. Q.; Cunha, L. D.; Frantz, F. G.; Kohlsdorf, T.; Fabro, A. T.; Arruda, E.; de Oliveira, R. D. R.; Louzada-Junior, P.; Zamboni, D. S., Inflammasomes are activated in response to SARS-CoV-2 infection and are associated with COVID-19 severity in patients. *J Exp Med* **2021,** *218* (3), e20201707.

63. Giavridis, T.; van der Stegen, S. J. C.; Eyquem, J.; Hamieh, M.; Piersigilli, A.; Sadelain, M., CAR T cell-induced cytokine release syndrome is mediated by macrophages and abated by IL-1 blockade. *Nat Med* **2018,** *24* (6), 731-738.

64. Marty-Roix, R.; Vladimer, G. I.; Pouliot, K.; Weng, D.; Buglione-Corbett, R.; West, K.; MacMicking, J. D.; Chee, J. D.; Wang, S.; Lu, S.; Lien, E., Identification of QS-21 as an Inflammasome-activating Molecular Component of Saponin Adjuvants. *J Biol Chem* **2016,** *291* (3), 1123-1136.

CHAPTER 3 Peptides and Polymers that Activate the NLRP3 Inflammasome for Use in Vaccination.

Portions of this chapter are adapted from published work in Biomaterials.[1]

3.1 Introduction.

Vaccination is the most effective medical intervention to prevent disease. It has completely eradicated some diseases like smallpox while dramatically reducing public health burden towards others like influenza.[2] Despite these successes, vaccine development to date has been largely empirical. Vaccinologists lack a comprehensive understanding of the spatiotemporal pattern through which pathogens stimulate innate immunity to facilitate productive cellular and/or humoral responses.[3] This poor understanding has hindered the production of synthetic alternatives to attenuated or inactivated pathogens. As a result, there are no effective vaccines for Tuberculosis, Human Immunodeficiency Virus, Q Fever, and others, where existing vaccines are impractical or have otherwise failed.[4-7] Poor mechanistic understanding of innate immunity has also impeded responses to emergent pathogenic threats, such as Ebola in 2014 and SARS-CoV-2 in 2020. In these cases, semi-empirical vaccine design and testing has led to costly candidate screening and/or sluggish deployment.[8-12] As a result, there is interest in developing a tunable framework for synthetic vaccines with defined safety profiles and predictable immune responses.

One method to improve predictability of immune responses in vaccines is *via* development of tunable subunit vaccine adjuvants.[4] Subunit vaccines allow facile synthesis of recombinant protein antigens or peptides which can be altered in response to genetic drift or emergence of novel pathogens. Co-administration of particulate adjuvants (*e.g.*, aluminum salts or squalene emulsions) or pattern recognition receptor (PRR) agonists (*e.g.*, CpG oligodeoxynucleotides or saponin extracts) provide the pro-inflammatory stimulus needed for highly immunogenic vaccines. Moreover, the adjuvant used in a subunit vaccine can bias the immune response towards cellular or humoral responses which may be most advantageous for a given pathogenic threat. Recently,

vaccine formulations containing combinations of PRR agonists have shown promise to induce immunostimulatory effects once limited to attenuated or inactivated pathogens.[13] FDA-approved subunit vaccines containing synthetic PRR agonists as adjuvants have been developed for Shingles, Malaria, and Hepatitis B, yet other PRR agonist candidates have failed due to immunotoxic side effects or poor protective immune responses.[14-16] As a result, new adjuvants which can precisely control the immune response are desirable for improved subunit vaccines.

Inflammasomes were first identified in 2002 as novel intracellular PRRs.[17-20] In contrast to other innate immune sensors, which bind to pathogen associated molecular patterns (PAMPs), NLR (NOD-, LRR-, and pyrin domain-containing) proteins undergo conformational changes in response to disruptors in homeostasis. Activation by homeostasis-disrupting danger-associated molecular patterns (DAMPs) results in formation of polyprotein complexes called inflammasomes which facilitate inflammatory cytokine production and cell death.[20] The most well-studied of these sensors, the NLRP3 inflammasome, is activated by a multitude of signals present in damaged cells including potassium efflux, reactive oxygen species, or lysosomal enzymes in the cytosol.[20-24] These changes result in activation of the inflammasome complex to facilitate pro-Caspase 1 cleavage to active Caspase 1. Caspase 1, in turn, cleaves pro-IL-1β, pro-IL-18, and GSDMD to their active form and initiates pyroptosis, a mode of inflammatory death characterized by formation of large pores in the cell membrane. IL-1β and IL-18, secreted via GSDMD-mediated pore formation, can initiate an adaptive immune response.[19, 20, 25, 26] Specifically, IL-1β and IL-18 are potent inducers of cellular immunity,[27-36] making the NLRP3 inflammasome a target for novel tunable adjuvants. One of the most effective immunogenic adjuvants, QS-21, is already known to activate the NLRP3 inflammasome via lysosomal rupture, inducing IL-1β secretion and facilitating protective cellular and humoral immune responses when co-administered with a TLR agonist and protein antigen.[15, 37-40] QS-21 is an active component in the AS01 adjuvant systems used in shingles and malaria vaccines, and it has shown promise in other vaccines against viral and parasitic infections.[15, 39, 41-43] Recently, the lipid nanoparticles (LNPs) employed in mRNA vaccines

were also shown to induce high levels of IL-1β production.[44] Despite the promise of these adjuvant systems, both induce high levels of systemic side effects which can prevent use in vulnerable populations, necessitating the need for new, tunable IL-1β-producing adjuvants.

Previous work in the Esser-Kahn laboratory has identified synthetic polymers which can modulate the extent of NLRP3 inflammasome activation on account of their physicochemical properties. These polymers disrupt endo/lysosomal membranes in a property dependent fashion to control levels of IL-1β secretion, providing a case for their use as tunable alternatives to saponin adjuvants. In one example, dendritic polymers were prepared with a histidine- and tryptophan-containing component and 0, 34%, or 62% of a tetraethylene glycol (TEG) component (T0, T34, and T62, respectively). T34 dendrimers induced higher levels of IL-1β activity compared to T0 or T62 dendrimers in LPS-primed cells.[45] Levels of IL-1β activity were correlated with extent of lysosomal rupture, K^+ efflux, and cathepsin activity in an NLRP3 inflammasome-dependent manner. This result provides evidence that polymers' properties can influence innate immune responses via the NLRP3 inflammasome.[45] Furthermore, these dendritic adjuvants afforded protection when used in vaccines against Q Fever, though in this study, adjuvanticity was not confirmed to result from NLRP3 inflammasome activation.[46] The Wilson and Kulkarni labs have also shown that the balance of hydrophobic to cationic contents in polymers can alter IL-1β activity in an inflammasome-dependent manner.[47, 48] These works provide proof of concept that inflammasome activation can be controlled to generate effective adjuvants, yet they fail to address how polymer architectures can modulate such a results in a parametric fashion.

In this work, we attempted using multiple approaches to develop novel inflammasome-activating polymeric adjuvants with advantages over existing inflammasome-activating adjuvants, such as mRNA LNPs,[44] $AS01_B$/QS-21,[37] ISCOMATRIX,[49] and dmLT.[50] Specifically, the proposed polymer systems offer the benefit of tunability, facile synthesis, and iteration of design critical for preparation of optimized polymer adjuvant systems. Based on our work with dendritic inflammasome-activating adjuvants alongside findings from the Wilson and Kulkarni groups, we

hypothesized that polymer properties could control the extent of membrane disruption, which in turn could modulate inflammasome activation, immunotoxicity, and formulation properties. As such, we sought to design a library of polymers that can control the extent of lysosomal disruption for use as inflammasome-activating adjuvants in vaccines. Several different approaches were considered; the approaches described in this chapter were ultimately unsuccessful (see **Chapter 2** for a more successful effort toward using polymers' physicochemical properties to bias the immune response). With that said, several insights can be gained from the strategies attempted here, and this chapter ends with a discussion of methods which could improve the adjuvanticity of future inflammasome-activating polymers.

3.2 Results and Discussion.

3.2.1 Design of a peptide-grafted heterodimeric polymer for immunotherapy.

Previous work in the Esser-Kahn group identified that a linear cell penetrating peptide derived from the human immunodeficiency virus transactivator of transcription (TAT) peptide could activate the NLRP3 inflammasome.[45] By introducing a hydrophobic component connected with a hexa(ethylene glycol) linker to the C-terminus, this cell penetrating peptide was imparted with lysosome-rupturing abilities.[45, 51] A small library of hydrophobic linker groups was probed, and TAT-PEG_6-GWWWG (YGRKKRRQRRR-PEG_6-GWWWG) was identified as the most active peptide (**Figure 3.1A**).[45] We grafted this peptide to a non-inflammatory poly(orthoester) backbone reported by our group previously[52] (**Figure 3.1B**) to achieve a tunable, inflammasome-activating material. A carbohydrate monomer, **2**, containing a C3-alkyne functionality was synthesized and co-polymerized with the standard glucose-based monomer, **1**. Upon successful synthesis and characterization, an N-terminal azide modified TAT-PEG_6-GWWWG and a small-molecule Toll-like receptor 7/8 (TLR7/8) agonist, 2BXy,[53] were grafted to the polymer using sequential, Cu(I)-catalyzed [3+2] azide-alkyne cycloaddition (**Figure 3.1C** and **Figures S3.1-S3.6**).[54] Such a design afforded a series of amphiphilic polymers with varying ratios of 2BXy and TAT-PEG_6-GWWWG.

Owing to the polymeric nature of these adjuvants, we referred to them as Polymeric Activators of Inflammasomes (PAIs). The ratio of 2BXy and TAT-PEG_6-GWWWG peptide in the synthesized PAIs were quantified employing high performance liquid chromatography (HPLC) following degradation of pH-sensitive orthoester linkages using trifluoroacetic acid (**Figures S3.7-S3.8**).

With these polymers in hand, we generated self-assembled nanoparticles (NPs) through a solvent transfer approach (**Figure 3.1D**). The amphiphilic nature of the polymer-conjugates led to generation of well-defined micelles upon transfer from dimethyl sulfoxide (DMSO) to phosphate buffered saline (PBS). Depending on the ratio of 2BXy to TAT-PEG_6-GWWWG, NPs of varying sizes were obtained as confirmed via DLS and TEM (**Figure 3.1E**). Notably, the particles remained stable in PBS, and no significant structural or functional changes were observed when stored at 4 °C for at least 8 weeks. We next investigated the ability of PAIs to elicit immune responses. Initial *in vitro* studies were performed to measure cytokine secretion. PAIs were incubated with bone marrow-derived dendritic cells (BMDCs), and cytokine secretion was analyzed in the supernatant (**Figure 3.1F**). In this case, in addition to analysis of IL-1β to measure inflammasome activation, we also investigated a series of pro-inflammatory cytokines, namely IL-12 and TNF-α. Our study indicated that a PAI with a ratio of 1.5:1 of 2Bxy and TAT-PEG_6-GWWWG generated the highest amount of IL-1β secretion. Notably, this ratio also elicited the highest secretion of TNF-α and IL-12 – important cytokines in innate immune activation and cancer immunosurveillance.[55] Therefore, this PAI (1.5:1) ratio was selected for further studies.

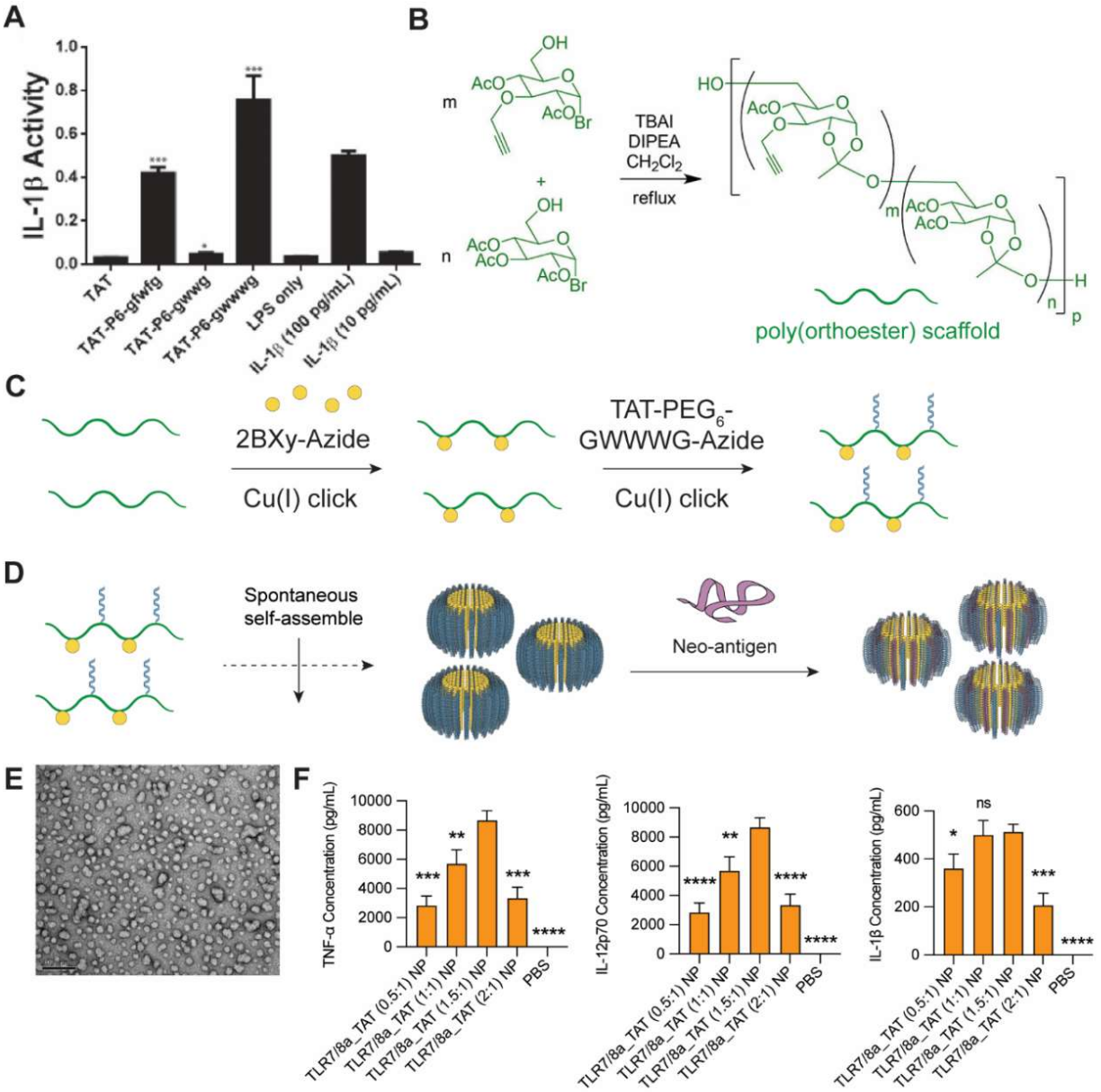

Figure 3.1: Synthesis of functionalized poly(orthoester) polymers containing NLRP3 activating peptides. Synthesis of functionalized poly(orthoester) polymers containing NLRP3 activating peptides. A) Screening of small hydrophobic tails affixed to TAT peptide revealed GWWWG as an optimal motif for inflammasome activation. Adapted from Manna, *et al*.[45] B) Synthetic scheme for preparation of functional poly(othoester) polymer scaffold from carbohydrate monomers. Adapted from Maiti, *et al*.[52] C) Sequential Cu(I) cycloaddition strategy for addition of 2BXy-azide (TLR7/8 agonist) and TAT-PEG_6-GWWWG (NLRP3 agonist) to the poly(orthoester) scaffold. D) PAIs were assembled into nanostructures via solvent transfer from DMSO to PBS and, where appropriate, electrostatically complexed with antigen. E) TEM imaging revealed successful nanoparticulate formation. F) BMDCs were cultured with 25 μg/mL PAIs with various ratios of 2BXy:TAT-P6-GWWWG, and cytokine production was assayed in the supernatant after 18 h. TLR7/8a_TAT (1.5:1) NP was identified as an optimal formulation and used for all subsequent studies.

With the promising *in vitro* studies, we were motivated to evaluate the efficacy of PAI in enhancing immunogenicity of prophylactic and therapeutic cancer vaccines. We initially performed *in vivo* studies to probe the efficacy of prophylactic vaccines containing the OVA-PAI formulation in comparison with unadjuvanted OVA or OVA with molar equivalent quantities of unlinked PAI components. Mice (n=5) were injected subcutaneously with each formulation on days 0 and 14. On day 24, serum was collected for antibody titers, and splenocytes were isolated to assay antigen-specific T-cell responses (**Figure 3.2A**). It was found that PAI significantly enhanced antibody titers compared to the mixture of unlinked components or unadjuvanted formulations (**Figure 3.2B**). Additionally, analysis of antigen-specific splenocytes revealed that PAI formulation enhanced IFN-γ secreting CD4+ T-cell response and IFN-γ secreting CD8+ T-cell response relative to the unlinked formulation (**Figure 3.2C-D**). These results indicated that PAI enhanced antigen-specific immune responses compared with control formulations.

Having confirmed the immunogenicity of PAIs in prophylactic OVA vaccination studies, we next proceeded to investigate the application of PAI in enhancing antigen-specific immune responses in cancer vaccines. First, we performed studies in an E.G7-OVA lymphoma model in which mice (n=6) were implanted with EL4 cells that stably express OVA protein (**Figure 3.2E**). In this study, tumors cells were injected on the right flank of mice on day 0. Vaccines were administered subcutaneously on day 5 and day 12 with OVA loaded PAI or OVA with unlinked agonist formulations. The control group received PBS. Mice were monitored for tumor growth and sacrificed when tumor size reached 20 mm in any linear dimension. To our delight, administration of PAI formulations significantly reduced tumor burden and prolonged survival compared to other formations (**Figure 3.2F-G**). Notably, animals in the PAI formulation-treated group had a median survival of 38 days – significantly higher compared to median survival of 29 days for unlinked agonist formulation and 25 days for PBS treated animals. The enhanced efficacy of PAI formulation is thereby consistent with our previous observation of enhanced antigen-specific immune responses of PAI formulations in OVA vaccination studies.

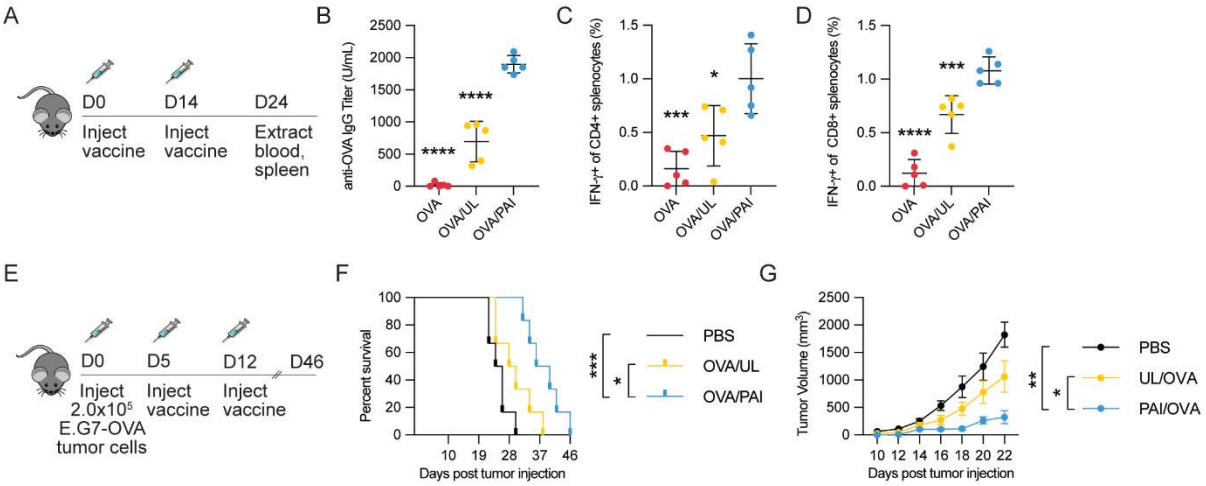

Figure 3.2: Vaccination studies of PAIs or controls formulated with OVA antigen (20 μg). (A) Study design for prophylactic vaccination model (n=5/group). (B) Serum anti-Ova IgG levels were analyzed via ELISA. (C-D) Splenocytes were analyzed for antigen-specific T-cells via intracellular cytokine staining and flow cytometry. (C) Percentage of IFN-γ secreting $CD4^+$ splenocytes after restimulation with OVA323-339. (D) Percentage of IFN-γ secreting $CD8^+$ splenocytes after restimulation with OVA257-264. (E) Study design for therapeutic vaccination model using a E.G7-OVA tumor (n=6/group). Mice were implanted with 2.0 x 10^5 E.G7-OVA cells in the flank and vaccinated with the indicated formulations 5 and 12 d after implantation. (F) Kaplan-Maier survival analysis of mice treated with various formulations. (G) Growth curves of tumors until the first mouse died (day 22). For all assays, *p < 0.05, **p < 0.01, ***p < 0.001, ****p < 0.0001. Statistical analyses were performed using one-way ANOVA with Dunnett's multiple comparisons test in B-D and G and by using log-rank test with Bonferroni-correction in F.

Despite the clear promise of these materials, challenges in the synthesis of derivatives proved limiting for conducting a high throughput screen. The monomers used in this system require 6-7 steps to prepare and are not easily modified. While other members of the Esser-Kahn group continued with further characterization of these materials for use in cancer immunotherapy, I instead moved toward designing more easily tunable systems to probe inflammasome activation.

3.2.2 Using a Copper mediated grafting-to approach to design polymeric adjuvants.

In the design of new polymeric activators of the inflammasome, we again sought to employ TAT-PEG_6-GWWWG by grafting it to a synthetic polymer scaffold. We envisioned that a linear polymeric scaffold derived from simple monomers could be prepared more easily and with tunable physicochemical properties. We could then screen these polymers to elucidate how polymers'

compositions modulate lysosomal rupture and NLRP3 inflammasome activation. Our initial efforts focused on reversible addition-fragmentation transfer (RAFT) polymerization of a hydroxypropyl methacrylamide (HPMA)-based scaffold. Within this scaffold, various dopants can be incorporated to tune polymer properties. HPMA is widely used in biochemistry and materials science as a biocompatible, water-soluble polymer amenable to co-polymerization with a variety of monomers.[56-59] Hydrophobicity and hydrophilicity, respectively, were modified by addition of methyl methacrylate (MMA) or oligoethylene glycol methacrylate (OEGMA). Endosomal escape was facilitated by grafting the TAT-PEG_6-GWWWG motif, which we incorporated into the polymer scaffold using glycidyl methacrylate (GMA). GMA can be reacted with NaN_3 to yield a reactive azide moiety.[60] Using CuAAC chemistry, an N-terminal alkyne-modified TAT-PEG_6-GWWWG peptide could then be grafted to the polymer backbone under ambient temperature (**Scheme 3.1**). Such room-temperature coupling conditions were critical, as previous work with the TAT-PEG_6-GWWWG motif revealed that it decomposed under prolonged treatment above 40 °C. This chemistry could allow facile synthesis of many TAT-functionalized polymers under glove box conditions to probe the role of physicochemical properties in the resultant immune response.

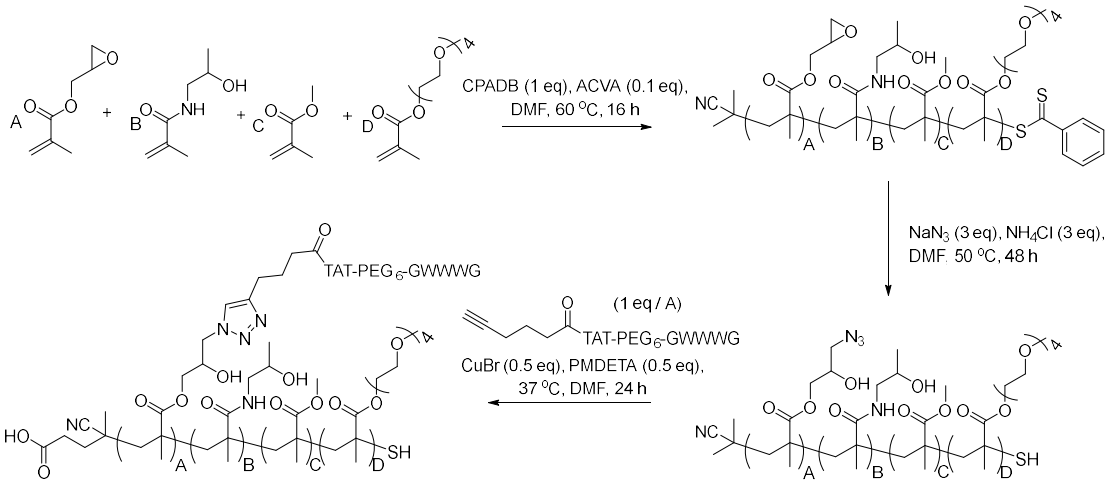

Scheme 3.1: Synthetic scheme for the design of an HPMA-based co-polymer system with functional handles for derivatization with TAT-PEG6-GWWWG.

Initial synthesis of poly[(HPMA)-*stat*-(GMA)] co-polymer scaffold was successfully achieved in a pilot study using five model polymers containing 0, 10, 20, 30, and 40% GMA in a HPMA backbone. Reversible addition-fragmentation transfer (RAFT) polymerization in DMF was conducted overnight, and polymers were precipitated into ether, dried under reduced pressure, and analyzed with FT-IR and aqueous SEC. Other common characterization strategies were not available at the time due to the COVID-19 pandemic. Polymers with a number-average molecular weight of *ca.* 30,000 g/mol and dispersity of *ca.* 1.2 were achieved on a 1 g scale based on aqueous SEC (not shown). Molar ratio of GMA to HPMA was confirmed by FT-IR (**Figure S3.9**). Glycidyl groups were subsequently reacted with sodium azide to open epoxide rings and form β-hydroxy azide-containing structural units. This modification was confirmed using FT-IR (**Figure S3.10**). Having successfully incorporated azides into the polymer scaffold, we attempted to graft TAT-PEG_6-GWWWG using Cu(I)-mediated click chemistry. Under argon, azide-containing polymers were dissolved in anhydrous DMSO. They were stirred with CuBr and a Cu(I) stabilizing agent, PMDETA, and subsequently reacted with TAT-PEG_6-GWWWG containing a 5-hexyn-1-oic acid modification at the N-terminus. Unfortunately, this reaction was unsuccessful, as the polymer and peptide formed insoluble complexes with Cu ligands in solution and could not be removed (**Figure S3.11**). Various copper chelators, such as EDTA and *Cuprisorb*, were used unsuccessfully in attempts to remove the copper.[61] This reaction was also attempted with *in-situ* reduction of Cu(II) using sodium ascorbate in water (not shown), but similar aggregates were obtained. We also attempted to use an alkyne-based propargyl methacrylate monomer in place of azide-modified glycidyl methacrylate (**Figure S3.12**), but again, similar results were obtained. Based on these results, we hypothesize that the methacrylate backbone used in this system chelates copper ions under the conditions used for azide-alkyne bioconjugation.[61] In many systems, this limitation could be overcome by increasing the reaction temperature, but due to thermal instability of TAT-PEG_6-GWWWG peptide above 40 °C, we determined that this reaction

approach was infeasible to produce our grafted co-polymers. Given limitations in characterization and optimization tools at the time due to COVID-19, alternative strategies were considered.

3.2.3 PET-RAFT of peptide-acrylamide co-polymer constructs.

Noting that copper-mediated functionalization proved to be limiting in the design of inflammasome-activating peptide-polymer conjugates, we then attempted an alternative synthetic strategy. In this approach, peptides are modified at their N-terminal with an acrylamide which allows the peptide to be co-polymerized with an N,N'-dimethylacrylamide (DMA)-based polymer scaffold (**Scheme 3.2**). This strategy, pioneered by the Gianneschi group,[62, 63] would alleviate the requirement of incorporating a click-functional handle into the polymer scaffold and allow precise molecular control of the polymeric scaffolds. We first replicated the Gianneschi group's work using a model peptide, KLAKLAKKLAKLAK. The peptide was synthesized using solid-phase peptide synthesis (SPPS) and then reacted with acrylic acid as reported previously[63] to generate a peptide-based acrylamide monomer (**Figure S3.13**). Following synthesis of the peptide acrylamide, aqueous PET-RAFT polymerization was conducted at 450 nm using Eosin Y as a photocatalyst and PMDETA as a sacrificial reductant in a LED-wrapped reaction vessel (**Figure S3.14**). This system was found to be successful in the homo-polymerization of DMA (**Figure S3.14**). A water-soluble chain transfer agent (CTA), 2-(n-butyltrithiocarbonate)-propionic acid (BTPA), was prepared for polymerization of peptide monomers (**Figure S3.15**). When KLA peptide was polymerized using BTPA, polymerization was successful, and polymers with narrow dispersities were achieved (Mn = 30,000 g/mol, Đ < 1.4) (**Figure S3.16**). Furthermore, brief degassing with argon was sufficient to allow the reaction to proceed, supporting the use of this chemistry in a high throughput manner.

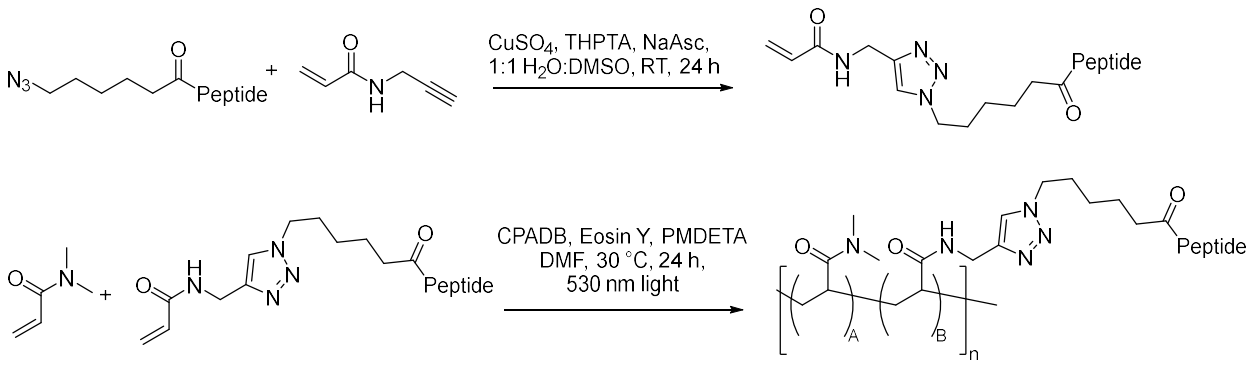

Scheme 3.2: Synthetic scheme for synthesis of peptide brush co-polymers. Peptide acrylamide monomers were prepared using Cu(I) cycloaddition chemistry followed by PET-RAFT co-polymerizations of peptide acrylamides with N,N-dimethylacrylamide. While CPADB is unconventional as a CTA for polymerization of acrylamides, it was found that its high rate of propagation relative to chain transfer facilitated stable RAFT polymerization in the presence of the radical quenching guanidinium and indole moieties of arginine and tryptophan, respectively.

Having successfully replicated their work, I then planned to synthesize polymers with the TAT-PEG_6-GWWWG peptide sequence. TAT-PEG_6-GWWWG was synthesized with an N-terminal azide to allow conjugation to propargyl acrylamide. This acrylamide-modified peptide was successfully synthesized on a 50 mg scale for polymerization (**Figure S3.17**). Unfortunately, while the described method was successful for the peptides reported in their work, we found it unsuccessful when arginine or tryptophan moieties were present. We hypothesize this limitation is due to the radical scavenging abilities of the guanidine and indole functional groups.[64-66] Indeed, the Gianneschi group's reports of this synthesis are limited to a narrow range of peptides lacking these amino acids. Fortunately, following a previous report of polymers containing indole moieties,[64] we found that using a dithiobenzoate CTA (cyanopentanoic acid dithiobenzoate, or CPADB) in DMF in place of the trithiocarbonate in DMSO allowed the reaction to proceed to a limited extent (**Figure S3.18**). Dithiobenzoate CTAs (Z = -Bz) have more electron-withdrawing "Z" groups than trithiocarbonates (Z = -S-R') and therefore have a higher rate of propagation relative to chain transfer for RAFT polymerization.[67] Therefore, while dithiobenzoates often exhibit poor control during acrylamide polymerization on account of their rapid rates of polymerization, we suspect that these reagents are necessary to mitigate radical quenching of tryptophan. While

encouraging, this system was found to require stringent air- and water-free conditions and was poorly scalable or reproducible, limiting its applicability for high throughput screening. With these limitations in mind, we opted to move away from this strategy for subsequent screening work.

3.2.4 Dual wavelength polymerization and functionalization of acrylamide polymers.

After facing poor scalability in the polymerization of acrylamide-modified peptides, we attempted to use an alternative, high throughput approach reported by the Gormley laboratory for post-polymerization functionalization of polymer end groups with azide-containing moieties.[68] In this approach, acrylamide polymers are polymerized using CTAs containing a cyclopropenone-protected dibenzocyclooctyne (cp-DIBAC) as a polymerization-tolerant reactive alkyne group. By employing photo-electron transfer—reversible addition fragmentation transfer (PET-RAFT) polymerization, acrylamide-based co-polymers can be prepared with light-activated, oxygen-tolerant, room temperature conditions. This approach can also be conducted in 96- or 384-well plates, allowing screening of a variety of acrylamide-based monomers. In the previous report by Li *et al.*, PET-RAFT of cp-DIBAC containing acrylamide polymers was achieved using zinc tetraphenylporphyrin (ZnTPP) as a photocatalyst and 565 nm light to initiate polymerization. Azide-modified peptides are then grafted to the polymer end group by releasing the masked hindered alkyne with 365 nm light and subsequently affixing an azide-modified peptide to the DIBAC moiety with strain-promoted azide-alkyne click chemistry (SPAAC).[68] Polymers prepared with this approach can be purified by filtration through a size-exclusion resin,[69] making it highly suitable for synthesis of a polymer library. A cp-DIBAC CTA (**12**) was successfully synthesized in seven steps (**Figure S3.19-S3.24**). With **12** in hand, we conducted proof-of-concept studies to test whether peptides could be grafted to the polymers as described (**Figure 3.3A-C**). A set of four polymers were synthesized and modified with TAT peptide (**13a-d**). 20-40 mol.% of the peptide was engrafted as measured by bicinchoninic acid (BCA) assay. Having successfully prepared a set of four polymers, we then tested their ability to induce IL-1β production in the THP-

1 model cell line. THP-1 cells are an ideal model for studies of inflammasome activation, as they express all components of the NLRP3 inflammasome (including ASC, NLRP3, and IL-1β), retain high phagocytic capacity, and be easily transduced with a wide variety of reporter constructs for subsequent analysis.[70] LPS-primed THP-1 cells were treated with **13a-d** at 100, 10, and 1 μg/mL for 5 h, and IL-1β in the supernatant was quantified by HEK Blue IL-1β assay. All four of the polymers were indeed found to be capable of activating the NLRP3 inflammasome at 100 μg/mL (**Figure 3.3D**). With this promising data in hand, we moved on screen a larger library of polymers.

Unfortunately, these initial successes could not be achieved on a consistent basis. Synthesis of a second set of poly(DMA) polymers engrafted with TAT-PEG_6-GWWWG, **14a-e**, revealed successful reaction by UV-VIS characterization (**Figure S3.25**). However, when the polymers were subjected to SEC analysis, no increase of molecular weight was observed. Characterization proved inconclusive for this system, as NMR revealed a small amount of peptide successfully grafted to the polymers, although far less than the expected molar ratio of peptide to backbone polymer (**Figure S3.25**). Lower grafting of TAT-PEG_6-GWWWG resulted in lower IL-1β production, likely due to decreased peptide-induced lysosomal rupture (**Figure S3.26**). Synthesis of additional polymers, **15a-j**, revealed that the approach could only be achieved using N,N-dimethylacrylamide (DMA) and triethylene glycol methyl ether acrylamide (TEGA) in a controlled manner. Other monomers, including N,N-diethylacrylamide (DEA) or N-isopropylacrylamide (NIPAm), resulted in high dispersities (Đ > 1.4) (**Figure S3.27**). Moreover, upon further evaluation by HPLC, the cp-DIBAC CTAs was found to be prone to degradation even during storage under anhydrous conditions at -80 °C (**Figure S3.28**). This system could prove promising for high throughput synthesis and screening of peptide grafted polymers; however, significant optimization must be conducted to enhance the stability of the CTA and the reaction conditions for a breadth of monomers. Having at this point learned that a lysosomotropic peptide was not necessary for inflammasome activation and developed the chemistry described in Chapter 2, this strategy was

abandoned. Nevertheless, optimizing this system could allow for development of immunogenic water-soluble polymer-peptide conjugates (see **Conclusions and Future Directions**).

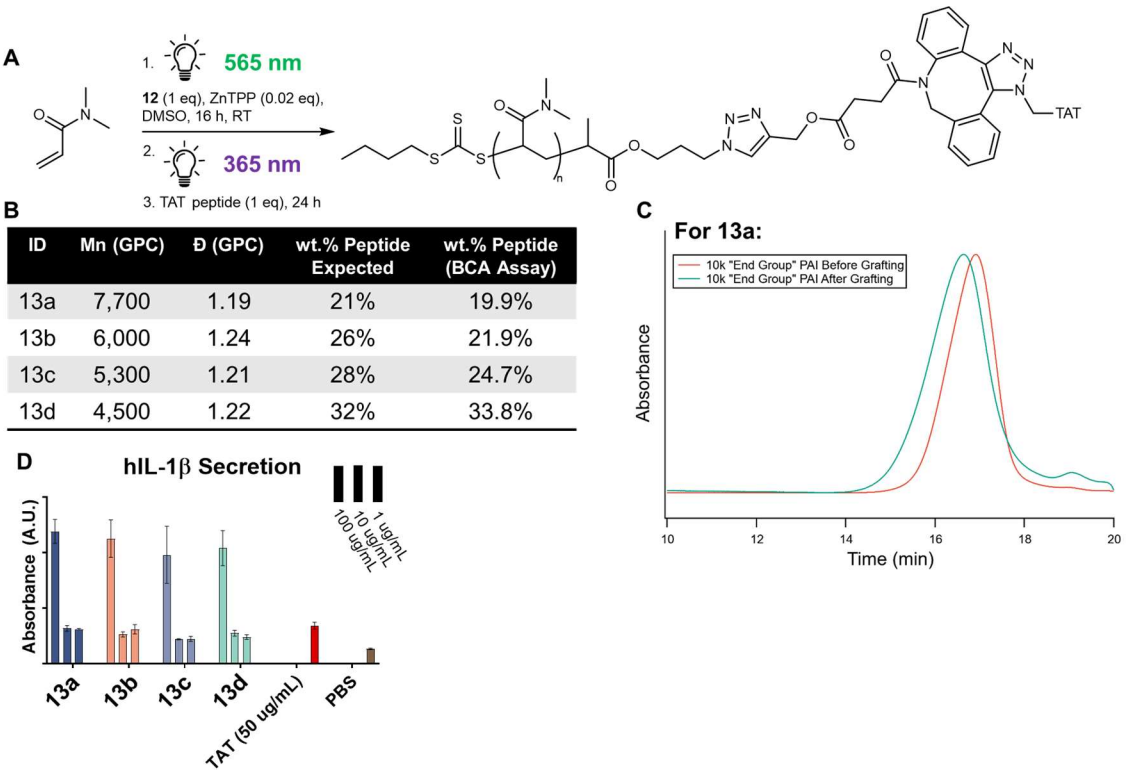

ID	Mn (GPC)	Đ (GPC)	wt.% Peptide Expected	wt.% Peptide (BCA Assay)
13a	7,700	1.19	21%	19.9%
13b	6,000	1.24	26%	21.9%
13c	5,300	1.21	28%	24.7%
13d	4,500	1.22	32%	33.8%

Figure 3.3: Synthesis and characterization of poly(DMA) polymers with cp-DIBAC end groups. A) Synthetic scheme showing dual wavelength PET-RAFT and deprotection of polymers, followed by functionalization with azide-functionalized TAT-PEG_6-GWWWG. B) Characterization of TAT-functionalized poly(DMA) via SEC and BCA assay. C) Representative SEC in DMF of polymer **13a** before and after functionalization with TAT-PEG_6-GWWWG. D) IL-1β secretion was assayed on the synthesized polymers using HEK Blue IL-1β secreted alkaline phosphatase assay after overnight incubation of polymers with LPS-primed THP-1 cells.

3.2.5 Use of cationic polymers as stand-alone adjuvants.

In Chapter 2, it was found that cationic polymers activate inflammasomes in an active transport dependent fashion. In this work, high number average molecular weight (M_n) polymers that contain hydrophobic and charged groups, such as 60 kg/mol poly($DMAEMA_{70}$-*s*-BMA_{30}), activated the NLRP3 inflammasome *via* lysosomal rupture to induce robust IL-1β secretion. Meanwhile, highly charged, low M_n polymers such as 15 kg/mol poly($AEMA_{70}$-*s*-BMA_{30}) disrupted

the cell membrane to induce necrosis without activating inflammasomes. Given these results, we hypothesized that inflammasome-activating hydrophobic and charged polymers would behave as immunological adjuvants when co-administered with an antigen, while toxic polymers would inhibit productive immune responses by inducing necrosis at the injection site. Representative polymers from Chapter 2 were employed for these studies (see Chapter 2 for characterization details), and ovalbumin was used as a model antigen for vaccination. In this way, we could probe whether simple polymers induce IL-1β secretion and display an adjuvant effect *in vivo*.

In a first iteration of this experiment, mice were vaccinated intramuscularly with 50 μg of ovalbumin (OVA), 10 μg of polymer, and either a Toll-like receptor (TLR) 4 or TLR 9 agonist formulation. TLR agonists were included in the formulations as NLRP3 inflammasome activation requires both a priming signal (in the form of TLR stimulation) and an activation signal to induce IL-1β and IL-18 secretion. The TLR 9 agonist, CpG 1018, is FDA approved as a component of the Heplisav B vaccine and was formulated in saline buffer at 25 μg/dose. The TLR 4 agonist, monophosphoryl lipid A (MPLA), is FDA approved in GlaxoSmithKline's AS01 and AS04 adjuvant formulations (used in Shingrix, Mosquirix, and Cervarix vaccines) and formulated in 1:1 saline buffer:squalene emulsion at 10 μg/dose. Mice were vaccinated intramuscularly according to a 14-day prime-boost regimen, and immune responses were characterized 27-28 days after the initial dose (**Figure 3.4A**). Systemic cytokine production was also probed 1 and 24 h after the first dose as a preliminary readout of immunotoxicity. For this initial study, splenic antigen specific $CD8^+$ T cell production and anti-OVA antibody titers were the primary endpoints. Four polymers, representing toxic, immunogenic, and non-inflammatory subsets described in Chapter 2 were used (**Figure 3.4B**). 15 kg/mol poly($AEMA_{70}$-*s*-BMA_{30}) and 60 kg/mol poly($AEMA_{70}$-s-$TEGMA_{30}$) represent toxic polymers, 60 kg/mol poly($DMAEMA_{70}$-*s*-BMA_{30}) represents an immunogenic polymer, and 15 kg/mol poly($DMAEMA_{70}$-*s*-$TEGMA_{30}$) represents a non-inflammatory polymer. MPLA and CpG formulations with no polymer, as well as saline buffer alone, were used as controls. With this study, the efficacy of cationic polymer-based adjuvants could be assayed.

Mice were vaccinated as shown in **Figure 3.4**. At 1 and 24 h after injection, IFN-γ and TNF-α in the serum were assayed (**Figure 3.4C**). While all mice that received CpG had increased levels of IFN-γ at 24 h, IFN-γ levels were highest in the CpG formulation control. Meanwhile, only the CpG formulation control generated increased TNF-α levels at 1 and 24 h after injection. CpG is known to induce more robust cytokine production than MPLA, so this result was expected. On day 27, total anti-OVA antibodies in the serum were assayed using an Ig(G+A+M) enzyme-linked immunosorbent assay (ELISA) (**Figure 3.4D**). It was found that the CpG and MPLA formulation controls had enhanced antibody responses relative to formulations containing the polymers of interest. On day 28, mice were sacrificed, and spleens were isolated to evaluate antigen-specific $CD8^+$ T cell responses *via* tetramer staining (**Figure 3.4E** and **S3.29**). While low levels of tetramer staining (<1%) were observed in all groups, none of the vaccines were found to significantly enhance T cell responses. Based on these results, we hypothesized that polymers could be aiding in diffusion of the vaccine formulations away from the injection site on account of their high charge and/or inducing local tissue necrosis to prevent activation of canonical innate immune sensors.

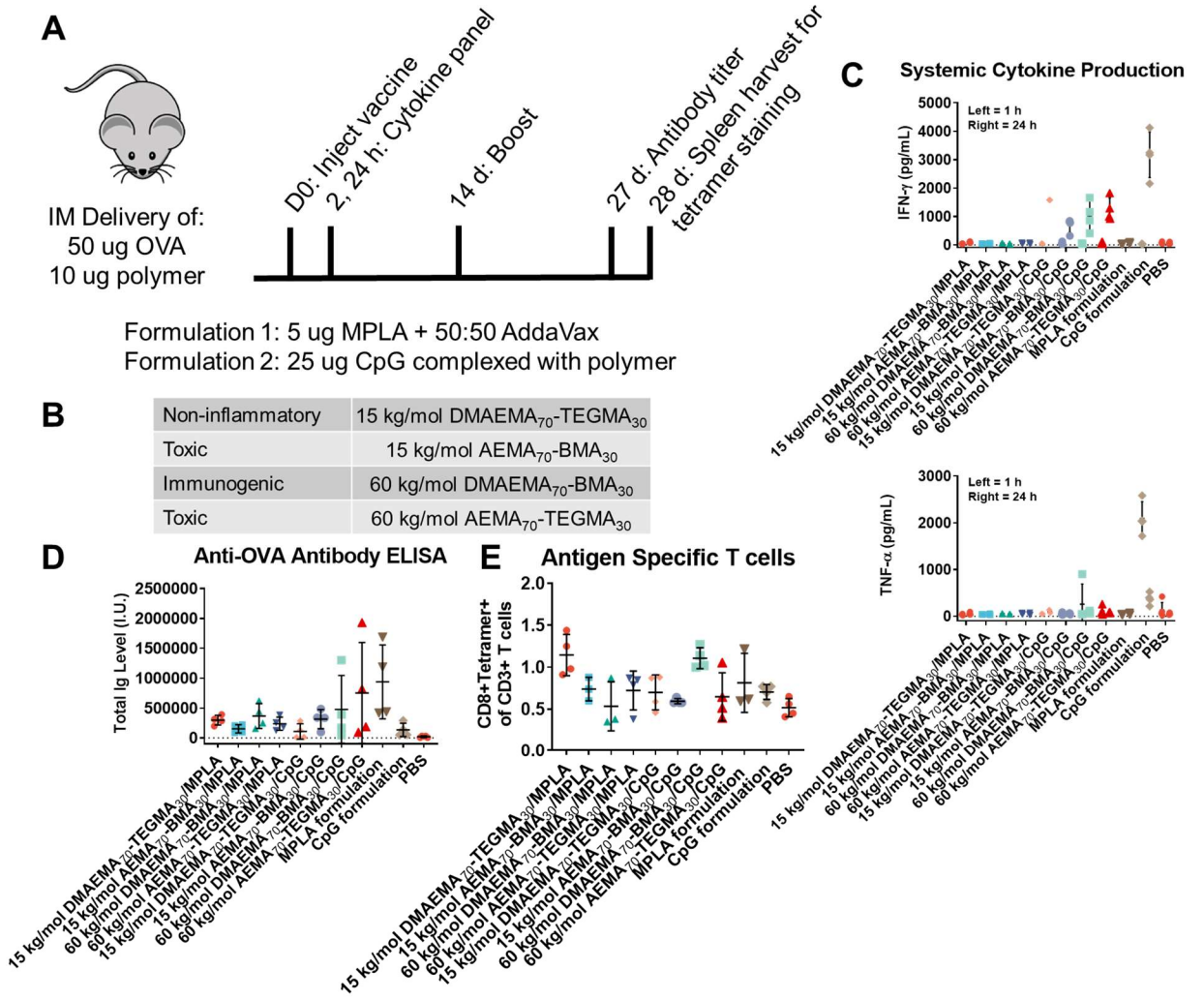

Figure 3.4: Activity of immunogenic, toxic, and non-inflammatory polymers as adjuvants when co-administered with two TLR agonists, MPLA and CpG. A) Polymers were formulated with MPLA or CpG and injected intramuscularly with 50 µg of ovalbumin. B) Four polymers with different biocompatibility features were assayed. C) IFN-γ and TNF-α were assayed in the serum 1 and 24 h after injection with each vaccine. D) Total anti-OVA antibody production was assayed 27 d after vaccination. E) Splenic OVA-specific T cell production was assayed 28 d after vaccination.

With the goal of improving the longevity of cationic polymers at the injection site, we then repeated this vaccine study using a negatively charged particulate adjuvant, alum. Alum is the most successful commercial adjuvant, being FDA approved for use in more than 10 vaccines. While the mechanism of alum's adjuvanticity is poorly understood, it appears to invoke B cell mediated immunity by stabilizing antigen at the injection site, altering cell adhesion, and inducing

inflammation to recruit and activate peripheral tissue-resident APCs.[71-76] Furthermore, it can be chemically modified to alter its physicochemical properties and facilitate adsorption of different charged proteins and macromolecules. In this study, positively charged polymers (10 μg) were adsorbed onto phosphate-modified alum (AdjuPhos, 100 μg) and formulated with OVA (100 μg). It was hypothesized that AdjuPhos, which is negatively charged under biological conditions, would complex with the polymers to form a stable nanocomplex. To characterize the response of polymers with different physicochemical properties, eight polymers comprising two molecular weights (15 and 60 kg/mol) and four compositions ($AEMA_{70}$-*s*-BMA_{30}, $AEMA_{70}$-*s*-$TEGMA_{30}$, $DMAEMA_{70}$-*s*-BMA_{30}, and $DMAEMA_{70}$-*s*-$TEGMA_{30}$) were employed alongside AdjuPhos alone and PBS controls. Mice were vaccinated intramuscularly at days 0 and 14 with these formulations, and antibody responses and $CD8^+$ T cell production were assayed at days 27 and 28 (**Figure 3.5A**). Given that alum induces a Th2 biased, primarily humoral immune response,[76] we hypothesized that a formulation with the immunogenic cationic polymers could stimulate IL-1β secretion to enhance Th1 responses and lead to a balanced cellular and humoral response. Systemic IL-1β was not detected 2 or 24 h after intramuscular injection, and low levels of IL-6 were observed (**Figure 3.5B**). When antibody responses and splenic antigen-specific T cell production were assayed at day 28, the polymer adjuvanted formulations were found to slightly increase $CD4^+$ and $CD8^+$ T cell responses but decrease B cell responses in a property-independent fashion (**Figure 3.5C-D** and **Figure S3.30-S3.31**). We hypothesize that this negative result likely occurred because soluble polymers can diffuse away from the injection site or induce toxicity over long timescales, preventing the alum depot from functioning as intended[73-76] and delivering polymers to antigen presenting cells for transport to the lymph node. Future efforts will be conducted to formulate soluble cationic polymers with antigen for lymphatic delivery and productive immunization (as discussed in the **Conclusions and Future Directions**).

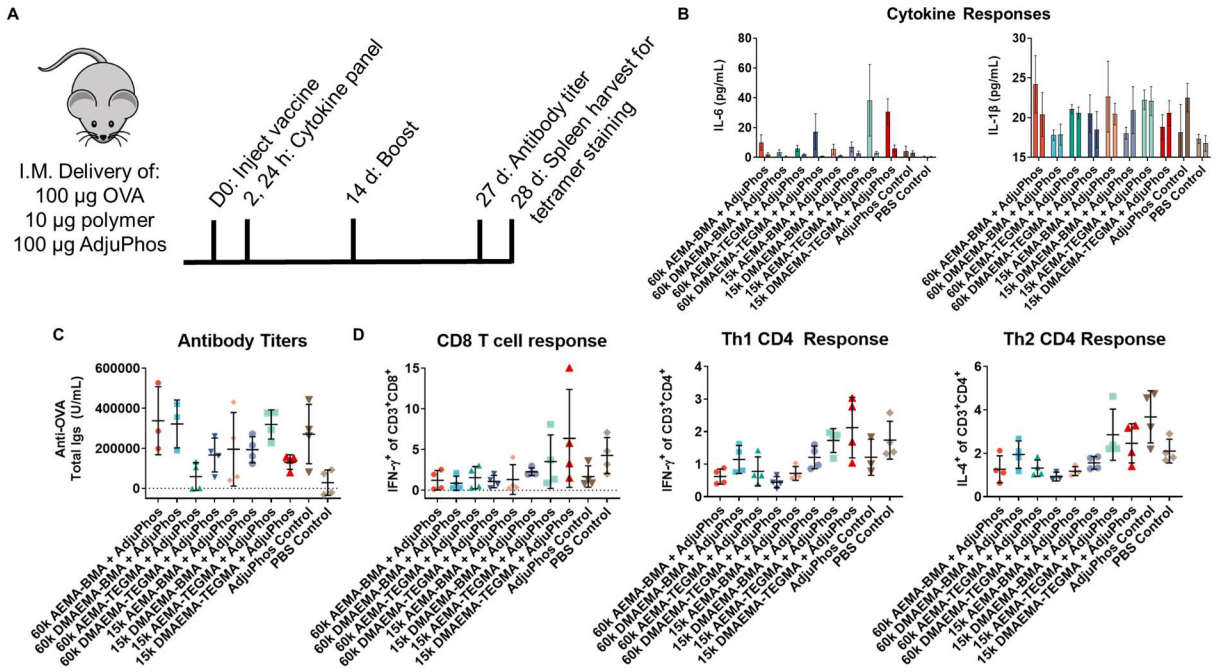

Figure 3.5: Activity of immunogenic, toxic, and non-inflammatory polymers as adjuvants when co-administered with the particulate adjuvant, alum. (A) Schematic timeline of vaccination study conducted using polymers formulated with AdjuPhos as adjuvant with a model antigen, ovalbumin (OVA). (B) IL-6 and IL-1β cytokine production 2 h (left) and 24 h (right) after injection. (C) Anti-OVA antibody production 27 d after vaccination assayed using anti-OVA Total Ig's (G+A+M) kit. (D) T cell responses 28 d after vaccination assayed by restimulating T cells with OVA peptides, conducting intracellular cytokine staining, and quantifying responses by flow cytometry.

3.2.6 Synthesis of lysosome-rupturing Trojan Horse nanogels based on cationic polymers for NLRP3 inflammasome activation and antigen presentation.

Based on our findings using cationic polymers as stand-alone adjuvants, we concluded that formulating cationic polymers to prevent local immunotoxic effects and enhance uptake by APCs was critical for immunogenicity. To prevent immunotoxicity, we envisioned a "Trojan horse" approach where polymers were self-assembled into nanoparticles to enhance uptake by APCs, and positive charge was masked using a stimulus-responsive linker. Upon cellular entry, the linker would be cleaved by intracellular pH and/or reactive oxygen species generation, releasing the positively charged polymer to facilitate inflammasome activation. Moreover, by delivering the antigen concurrently with an endosomolytic polymer, we hypothesized that cross-presentation to

$CD8^+$ T cells would be enhanced. The Irvine group recently reported a homobifunctional, NHS-ester activated carbonate cross-linker for reaction with amines that contains a disulfide bond.[77] The linker, bis[2-(N-succinimidyl-oxycarbonyloxy)ethyl] disulfide (NHS-SS-NHS), was shown to form nanogels with protein cargoes and degrade upon treatment with acid or a reducing agent to reveal the unmodified protein cargo (**Scheme 3.3**). A similar ester-based cross-linker, 3,3'-Dithiobis(sulfosuccinimidylpropionate) (DTSSP) was also purchased (**Scheme 3.3**). DTSSP does not form a traceless linkage, as cross-linked amines will retain a 2-thioethanyl moiety after disulfides are cleaved, but it is advantageous on account of its higher water solubility and stability. A comparative approach for the two linkers was desirable, as polymers and proteins have never been cross-linked in this manner.

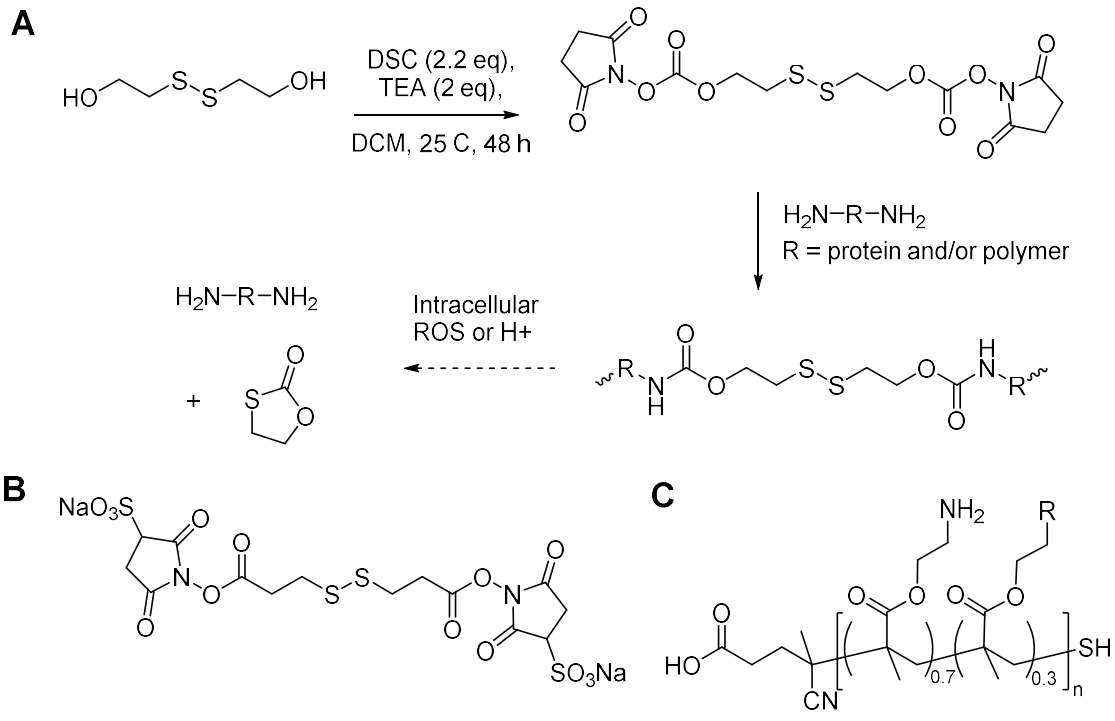

Scheme 3.3: Cross-linkers and polymers employed for the synthesis of "Trojan Horse" nanogels. A) Synthetic scheme and structure of bis[2-(N-succinimidyl-oxycarbonyloxy)ethyl] disulfide and traceless linkage of proteins and polymers via their amine groups. B) Structure of water-soluble, commercially available 3,3'-Dithiobis(sulfosuccinimidylpropionate) (DSTTP) cross linker. C) Structure of 15 kg/mol poly($AEMA_{70}$-*s*-$BMA/TEGMA_{30}$) used in nanogel synthesis studies.

With these linkers in hand, we cross-linked a model antigen, ovalbumin, with AEMA-containing polymers to generate Trojan Horse nanogels for analysis. In Chapter 2, it was identified that highly cationic polymers, such as 15 kg/mol poly($AEMA_{70}$-*s*-BMA_{30}), directly disrupt the cell membrane to induce necrosis, whereas high molecular weight, hydrophobic polymers are uptaken by active transport to induce lysosomal rupture and inflammasome activation. By cross-linking 15 kg/mol poly($AEMA_{70}$-*s*-BMA_{30}) or other low molecular weight, AEMA-containing polymers, we envisioned that the high positive charge density would be masked and phagocytosis would be enhanced, thereby converting this material from a toxic material to an inflammasome activating polymeric adjuvant. In an initial pilot study, 15 kg/mol poly($AEMA_{70}$-*s*-BMA_{30}) and poly($AEMA_{70}$-*s*-$TEGMA_{30}$) were synthesized using reversible addition−fragmentation chain-transfer (RAFT) polymerization using a water soluble dithiobenzoate chain transfer agent and initiator system (**Figure S3.32**). The polymers were then mixed in a 1:3:100 ratio with ovalbumin (OVA) and 2BXy, respectively, for model cross-linking studies. Under rapid stirring, the DSTTP cross-linker was added (**Scheme 3.3B**), and the reaction was stirred for 4 h. Nanogels were then purified from unreacted starting materials *via* centrifugal filtration against a 100 kg/mol filter and lyophilized to dry. For characterization, the nanogels were redispersed in PBS at 1 mg/mL and analyzed by dynamic light scattering (DLS) and transmission electron microscopy (TEM) (**Figure S3.33**). In each case, nanoarchitectures of 100-200 nm in diameter were achieved, supporting use of these materials in subsequent studies.

After successfully synthesizing these materials, we then characterized their ability to facilitate antigen presentation *in vitro*. It was hypothesized that nanogels would afford facile phagocytosis of antigen analogously to other cross-linked antigen systems.[77, 78] Upon entry to the endo/lysosomal compartment, however, the cross-linkage would break, revealing the highly charged polymer, activating inflammasomes, and facilitating cytosolic delivery of antigen for cross-presentation. Cross-presentation is a mechanism whereby antigens enter the cytosol to allow presentation on major histocompatibility complex class I (MHC-I) to $CD8^+$ T cells. This

mechanism of antigen presentation is critical for cell-mediated immune responses. To test this hypothesis, the 15 kg/mol poly(AEMA-*s*-BMA) nanogels or unlinked OVA and polymer controls were incubated with LPS-primed BMDCs overnight, and presentation of an OVA MHC-I restricted epitope, SIINFEKL, was evaluated by flow cytometry (**Figure 3.6A**). To our delight, presentation of SIINFEKL on MHC-I was significantly enhanced in the nanogel-treated BMDCs relative to unlinked controls or PBS. We then tested the functional relevance of this response using a BMDC:T cell co-culture experiment (**Figure 3.6B**). T cells with specificity for the immunodominant $CD8^+$ T cell epitope of ovalbumin (OT-I) were used. After incubating nanogel-treated BMDCs with dye-labelled OT-I T cells for 3 d, antigen-specific T cell responses were measured by dye-dilution and cytokine production (**Figure 3.6C-D**). Again, nanogel-treated BMDCs induced significant OT-I proliferation, as well as production of cytokines such as IFN-γ and IL-2 that are indicative of a productive $CD8^+$ T cell response against OVA. Having validated that the nanogels induced productive immune responses *in vitro*, we moved on to test these systems *in vivo*.

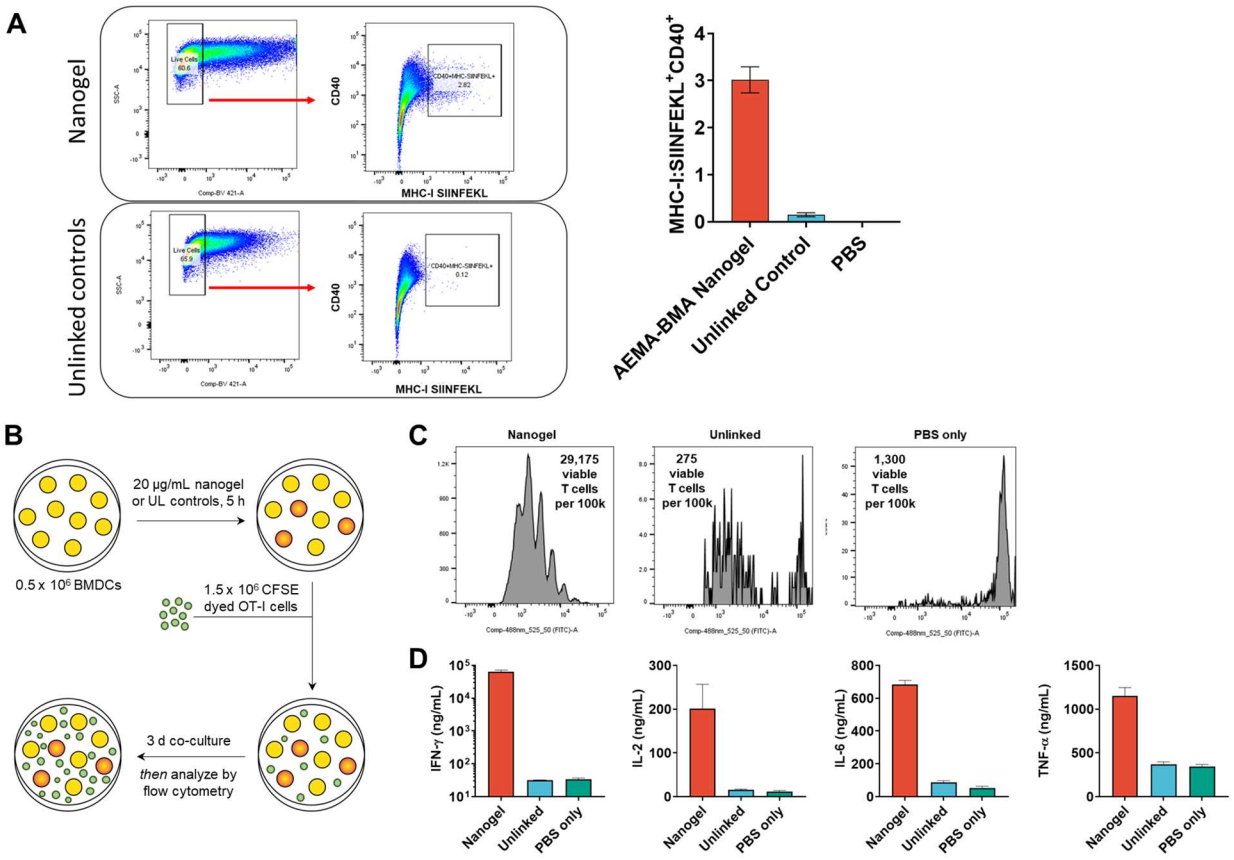

Figure 3.6: In-vitro characterization of nanogels. A) BMDCs were incubated with nanogels for 5 h and then stained with anti-MHC-I:SIINFEKL, anti-CD40, and a viability dye. The percentage of live, $CD40^+$MHC-I:$SIINFEKL^+$ cells were then analyzed *via* flow cytometry. Representative flow gating is presented, and averaged data is representative of four independent trials. B) Workflow for BMDC:OT-I co-culture experiment. C) BMDCs were incubated with nanogels for 5 h and then co-cultured with OT-I T cells for 3 d. Dye dilution was analyzed *via* flow cytometry. Representative flow gating of three independent trials is presented. D) Supernatant was collected after 3 d and analyzed for immunostimulatory cytokine production *via* Legendplex Mouse Inflammation 13-plex.

Given the efficacy of nanogels in producing antigen-specific $CD8^+$ T cell responses, we envisioned that they would be effective formulations for vaccines against viral infections or cancers. As an initial proof of concept, OVA-containing nanogels used in **Figure 3.6** were used in a model vaccination study. Mice were vaccinated with nanogels or equal quantities of unlinked controls on day 0 and boosted on day 14. OVA-specific antibody titers and $CD8^+$ T cell responses were evaluated on day 24 (**Figure S3.34**). While BMA nanogels displayed a trend of increased $CD8^+$ T cell proliferation, this was statistically insignificant relative to the unlinked control. No

changes in antibody responses were observed across groups (**Figure S3.34**). Similar trends were observed in three independent vaccine studies (not shown), shedding doubt on the nanogel platform as a therapeutic. We hypothesized that the DTSSP cross-linker could be hindering the immunogenic capacity of OVA as an antigen by modifying surface amine sites with thiols. Indeed, previous reports of cross-linked nanogels have used traceless linkers rather than DTSSP. With this limitation of the current system in mind, we then explored the traceless linker, NHS-SS-NHS (**Scheme 3.3A**). This linker has the benefit of being labile to both acid and reactive oxygen which are present in the endo/lysosome, increasing the likelihood of intracellular antigen delivery.

Nanogels using the second-generation NHS-SS-NHS linker were prepared to create a nanogel that should release unmodified antigen to the endo/lysosome to allow effective cross-presentation. An identical procedure as with DTSSP was used, and nanogels containing 15 kg/mol poly(AEMA-*s*-BMA) or poly(AEMA-*s*-TEGMA) were synthesized and characterized by TEM and DLS (**Figure S3.35**). Nanogels were prepared with or without 2BXy in this batch of nanogels to assess the role of including a TLR agonist in their activity. Activity was first validated *in vitro* using an antigen presentation study (**Figure S3.36**). After BMDCs were treated with nanogels for 5 h, enhancement in live $CD40^{+}MHC\text{-}I{:}SIINFEKL^{+}$ cells were observed in AEMA-BMA or AEMA-TEGMA nanogels relative to unlinked controls. The incorporation of 2BXy further enhanced the activity of these nanogels (**Figure S3.36**). An *in-vivo* experiment was then conducted. Mice were vaccinated with second-generation nanogels (containing 2BXy) or unlinked controls. The mice were boosted on day 14, and serum antibody production and antigen-specific T cell production were assayed on day 28. Unfortunately, this platform was also unsuccessful, with no increases in antibody production or antigen specific $CD8^{+}$ T cell proliferation being observed relative to unlinked controls (**Figure S3.37**). These results ultimately led us to question whether the nanogel platform was behaving as expected in delivering unmodified antigen to facilitate enhanced T cell responses.

To better understand the failures of the nanogel platform, particularly when using NHS-SS-NHS as a traceless linker, we conducted further physicochemical characterization studies. We hypothesized that nanogels were either ineffective in releasing cargo, incompletely purified of unreacted protein cargo, or unstable in aqueous buffer. To probe these possibilities, a series of SDS-PAGE gel electrophoresis studies were conducted. Nanogels were synthesized as described, purified by various approaches including spin filtration and dialysis, and analyzed *via* gel electrophoresis under denaturing, non-reducing conditions (as reducing conditions would necessarily cleave disulfide cross-linkages) (**Figure S3.38**). It was observed that nanogels cross-linked using NHS-SS-NHS leached free OVA at a low but consistent rate throughout the studies, preventing isolation of nanogel particles. This instability could possibly be avoided in future studies by storing NHS-SS-NHS linked nanogels in acidic conditions to prevent hydrolysis of the carbonate linker. Additionally, an IL-1β ELISA was also conducted on nanogels to confirm their immunological activity. BMDCs were primed with LPS and treated with nanogels for 5 h. Supernatant was collected and analyzed by ELISA (**Figure S3.39**). Fortunately, the nanogels were observed to induce IL-1β secretion, suggesting that they successfully activate inflammasomes. Having gained insight into the mechanism of these failures and moved toward more successful thesis research, this project was ultimately abandoned. With that said, the cross-linked nanogel platform remains promising for inflammasome activation and vaccination, and optimization of the design principles outlined in this section and the **Conclusions and Future Directions** could yield a highly efficacious vaccine platform.

3.3 Conclusion and Future Directions.

In the past ten years, inflammasomes have been recognized as key mediators of adaptive immunity in particle-based adjuvant formulations. In 2018, Li *et al.* prepared poly(ethyleneimine)-coated mesoporous silica rods complexed with CpG (a TLR9 agonist) and the APC maturation- and differentiation-supporting cytokine, GM-CSF.[79] This formulation was found to generate

significant innate immune activation marked by IL-1β secretion and induce anti-tumor immunity against multiple cancer models in only a single dose. This system has since been employed in multiple high impact works.[80, 81] The Takeoka group employed inflammasome-activating, arginine-containing liposomes loaded with a model antigen, ovalbumin (OVA), to probe antigen presentation and T cell activation.[82] Here, it was shown that the ratio of cationic arginine groups to hydrophobic lipid tail influenced the extent of cellular uptake, endo/lysosomal rupture, and NLRP3 inflammasome activation. Most recently, Muñoz-Wolf, *et al.* reported that 50 nm poly(styrene) or poly(lactic-co-glycolic acid) particles maximize cell-mediated immune responses by generating intracellular reactive oxygen species and activating the Caspase-11 inflammasome, while larger particles did not.[83] Other works have highlighted that IL-1β and IL-18 synergize with IL-12 to invoke potent anti-tumor responses,[27, 55] suggesting a key role of inflammasomes in future therapeutics. A meta-analysis of other works where inflammasome activating polymers and nanoparticles were assayed for vaccination is provided in **Table 3.1**. From this analysis, it is evident that particle size of ~50-100 nm and co-administration with other Toll-like receptor agonists appear to be critical parameters for efficacy in vaccines.

Authors	Year	Adjuvant	Inflammasome Mediated Effects
Li... Mooney[79]	2018	PEI-coated mesoporous silica rods (with CpG)	Lysosomal Rupture
Fan… Guan[46]	2022	PEG and peptide dendrimers	Lysosomal Rupture
Gong… Liang[84]	2020	pH responsive peptide nanotransformer	Lysosomal Rupture
Chen… Wang[85]	2022	pH sensitive polymer nanoparticles	Lysosomal Rupture + ROS production
Marty-Roix… Lien[38]	2016	QS-21	Lysosomal Rupture
Munoz-Wolf… Lavelle[86]	2023	PLGA and PS nanoparticles	ROS production
Gan… Qi[87]	2016	Surfactin	ROS production
Wegmann… Sattentau[88]	2012	PEI (with viral glycolipids)	Lysosomal Rupture
Duewell… Schnurr[49]	2011	Saponin-based nanoparticles	Not discussed; lysosomal rupture?
Wang… Xia[89]	2019	Celluosic materials	ROS production
Eisenbarth… Flavell[90]	2008	Alum	Not discussed
Li… Re[91]	2008	Alum	Not discussed
Marichal… Desmet[92]	2011	Alum	dsRNA from damaged cells?
Franchi & Nunez[72]	2008	Alum	Not discussed
Kool… Lambrecht[93]	2008	Alum	Uric acid
Orr… Fox[94]	2019	Alum (nanoparticles)	Not discussed
Forster… Kulkarni[95]	2022	mRNA LNPs	Lysosomal Rupture
Tahtinen… Mellman[44]	2022	mRNA LPX and mRNA LNPs	Not discussed
Wang… Xie[96]	2018	Spiky TiO2 NPs (with MPLA)	"Mechanical Stress" and K+ efflux
Seubert… de Gregorio[97]	2011	Squalene Emulsion	They claim it doesn't activate NLRP3, but MyD88 signaling suggests a role of inflammasomes
Pizzuto… Lonez[98]	2018	Cationic Lipids	Not discussed
Seydoux… Orr[99]	2018	MPLA+Squalene Emulsion Nanoparticles	Extracellular ATP?
Yang… Lavelle[100]	2013	Native CNT/spheres andfunctionalized derivatives	Lysosomal Rupture
Niikura… Sawa[101]	2013	Gold nanoparticles with various size/shapes	Not discussed
Lu… HogenEsch[102]	2015	α-Glucan nanoparticles (~50 nm)	Lysosomal Rupture
Hernandez-Franco… HogenEsch[103]	2021	α-Glucan nanoparticles (~50 nm) + STING	
Swaminathan… Bett[104]	2016	Merck's proprietary LNPs formulated with CpG	Not discussed
Swaminathan… Bett[105]	2016	Merck's proprietary LNPs formulated with CpG	Not discussed
Sharp… Lavelle[106]	2009	PLGA nanoparticles	Lysosomal Rupture
Huang… Kummel[107]	2019	TLR7 agonist functionalized Silica NPs	Lysosomal Accumulation

Table 3.1: Meta-analysis of recent publications where inflammasome activating polymers or nanoparticles were employed for in vivo vaccination experiments. When reported in the publication, the mechanism of inflammasome activation is also reported.

In this chapter, six different approaches toward the design of polymeric adjuvants that target the NLRP3 inflammasome were considered. The goal was to create a system that was easy to synthesize, chemically modular, and compatible with subunit protein vaccines. With this system, we aspired to study how physicochemical parameters, such as charge, hydrophobicity, and molecular weight, could be controlled to optimize the adaptive immune response. Such a low cost and modular system could be of great benefit for future adjuvant design by providing a parametric understanding of how different properties inform the responses tabulated in **Table 3.1**.

The first four approaches each used a polymeric scaffold engrafted with a peptide, TAT-PEG_6-GWWWG, which is known to activate the NLRP3 inflammasome *via* lysosomal rupture (**Figure 3.1A**). In the first approach, this peptide, and a TLR7/8 agonist, 2BXy, were grafted to a non-inflammatory sugar poly(orthoester) scaffold using Cu(I)-mediated azide-alkyne click chemistry. This scaffold self-assembles under solvent transfer from DMSO to PBS to form ~50 nm nano-micelles (**Figure 3.1E**), meeting both the size and co-formulation requirements for effective adjuvanticity *in vivo*. As would therefore be expected, these materials induced potent anti-tumor immunity against an EG.7-OVA when used as adjuvant in a therapeutic cancer vaccine (**Figure 3.2**). Unfortunately, this system was difficult to synthesize, requiring laborious syntheses to prepare the monomers, making physicochemical optimization of derivatives challenging. As such, we moved toward alternative approaches with greater chemical tunability. The second approach used a methacrylate polymer scaffold where inflammasome activation was induced by grafting TAT-PEG_6-GWWWG. In this system, physicochemical properties could be modulated easily by incorporating different co-monomers. Unfortunately, grafting TAT-PEG_6-GWWWG to the polymer scaffold proved unsuccessful, as copper(I) complexed with the methacrylate backbone to form insoluble complexes. To mitigate the need for copper, a TAT-PEG_6-GWWWG acrylamide monomer was synthesized in the third approach, which could be synthesized using PET-RAFT polymerization. While conditions to facilitate this reaction were identified, the stringent air- and water-free conditions needed for this reaction made it impractical to scale. Finally, in the fourth

approach, cyclopropenone-protected cyclooctynes were used to prepare click-reactive reactive monomers and end groups *via* PET-RAFT. The cyclopropenone groups could then be removed by treatment with 365 nm light to form azide-reactive handles for incorporation of TAT-PEG_6-GWWWG. Preliminary data suggested that these polymers induced IL-1β only at high concentrations *in vitro* (**Figure 3.3**). They also lacked a secondary nanostructure, failing to meet the structural requirements postulated to maximize immune responses in-vivo. As such, we were unable to design a tunable system using TAT-PEG_6-GWWWG for inflammasome activation.

Future studies may seek alternative strategies to formulate TAT-PEG_6-GWWWG or other inflammasome activating peptides and small molecules as low-cost adjuvants for vaccines and immunotherapies. Our data with the EG.7-OVA model (**Figure 3.2**) demonstrate that adjuvants comprising this peptide hold great clinical potential if they can be successfully co-formulated into a nanoparticle with other TLR agonists. With that said, this peptide suffers from low chemical stability upon heating and high positive charge density which can cause aggregation. These limitations made the peptide difficult to incorporate into polymeric systems with diverse physicochemical properties, as observed in the second, third, and fourth approaches. As a result, other inflammasome activating agents may be better suited for this higher throughput analysis. In future iterations of this study, one might consider alternative cell penetrating peptides with more desirable physicochemical properties[108] or small molecules that directly activate the inflammasome, such as nigericin, Leu-Leu-OMe, Val-boroPro, or adenosine triphosphate, for engraftment. Alternatively, one could envision an approach where TAT-PEG_6-GWWWG or an alternative peptide is used as a cross-linking agent to formulate water-soluble polymers into nanoparticles.[78] Either approach, if successful, could meet the key requirements for inflammasome activation *in vivo* (nanoaggregate formation and co-delivery with TLR agonists) while simultaneously allowing for the ability to tune physicochemical properties.

Having identified in Chapter 2 that cationic polymers could activate inflammasomes in the absence of the lysosome-rupturing peptide, TAT-PEG_6-GWWWG, the fifth and sixth approaches

sought to formulate these materials directly as adjuvants for vaccination. In the fifth approach, cationic polymers were formulated with CpG, an MPLA/squalene emulsion, or alum. Each of these formulations were expected to form nanoaggregates that would facilitate activity *in-vivo.* Alum and squalene emulsions are known particulate adjuvants, while cationic polymers are known to self-assemble with negatively charged oligonucleotides such as CpG. In these studies, mice were vaccinated with a model antigen, OVA, and each of these formulations, and cellular and humoral immune responses were observed. Unfortunately, incorporation of polymers within these formulations did not enhance the adaptive immune response, and in many cases, reduced the response relative to CpG, MPLA/squalene, or alum alone (**Figures 3.4-3.5**). These results suggest that polymers are not efficiently stimulating NLRP3 inflammasome activation in dendritic cells. It is possible that polymers are diffusing away from the injection site on account of their positive charge and lack of nanostructure. While nanostructured particles can be retained at the injection site due to their low solubility in biological conditions, freely soluble macromolecules (especially those with high charge density) are rapidly transported into the bloodstream and filtered by the liver. Alternatively, it is possible that inflammasome activation must be localized to the lymph node for a productive adaptive immune response. This hypothesis is supported by recent work from Tähtinen, *et al.*, who highlight that inflammasome activating lipid nanoparticles produce an adjuvant effect in the lymphatic tissue but an immunotoxic effect in the bloodstream.[44]

Seeking to overcome these limitations and meet the design criteria for cationic polymer adjuvants described above, we then sought to formulate cationic polymers into biodegradable nanogels. Nanogels were synthesized by cross-linking antigens, polymers, and TLR agonists with one of two homobifunctional linkers, DTSSP and NHS-SS-NHS (**Scheme 3.3**). While the resulting conjugates could enhance antigen presentation and $CD8^+$ T cell activation *in vitro*, they were unsuccessful in enhancing adaptive immune responses *in vivo.* While this result was unexpected, preliminary investigation suggests two possibilities for this failure. First, it is possible that the high surface positive charge of nanogels could prevent their effective delivery to the draining lymph

node. Charge is known to modulate complement activation and lymphatic drainage,[109] and primary-amine containing materials were recently shown to induce hematological toxicity characterized by neutrophil activity.[110] Second, it is possible that the poor stability of the NHS-SS-NHS cross-linker under biological pH is preventing controlled co-delivery of antigen-loaded nanogels to the draining lymph node. Premature degradation of the nanogels could release polymer and antigen at the injection site, leading to poor responses analogous to that of **Figures 3.4-3.5**. Two potential approaches to prevent degradation could be to conjugate nanogels to the surface of carrier cells[77] or simply to store the nanogels under more acidic pH. While further work is needed to optimize this system, the nanogel platform remains promising for immunotherapy.

Overall, the design of cationic polymer adjuvants that activate the NLRP3 inflammasome proved to be a greater challenge than anticipated. Six approaches were attempted using a variety of polymer scaffolds and adjuvant dopants, but none met both requirements of (1) high efficacy and (2) chemical tunability necessary for this project. Nevertheless, there are several insights for future iterations of this work. First, the PAI scaffold was highly efficacious and could find success as an adjuvant for cancer immunotherapy (**Figure 3.1-3.2**) despite its lengthy and challenging synthesis. Future efforts could be taken to develop this platform with simpler carbohydrate-based monomers. Second, particle size of ~50-100 nm and co-administration with other TLR agonists appear to be requirements for NLRP3 inflammasome activation and *in vivo* adjuvanticity of cationic polymers (**Table 3.1**). With these design principles in mind, and a clear set of successful and unsuccessful synthetic approaches defined in this chapter, improved cationic polymers could be defined. Finally, inflammasome activating polymer adjuvant lead candidates must be confirmed *in vivo* early in experimental testing. While the nanogel platform appeared to meet both design principles outlined *in vitro*, it failed when used for vaccination, likely due to poor chemical stability under biological pH. Cationic polymers remain exciting as a chemically modular platform for inflammasome-activating adjuvants, and this chapter provides design principles that could lead to future success in this domain.

3.4 Materials and Methods.

Mice and Materials. All reactions were conducted under dried nitrogen or argon stream. Anhydrous solvents were purchased in capped DriSolv™ bottles and stored under air-free conditions. 6-azidohexanoic acid was purchased from Click Chemistry Tools, PEG linkers were purchased from Quanta Biodesign, and Fmoc-protected amino acids were purchased from Aapptec. All other solvents and reagents were obtained from Sigma Aldrich or Thermo Fisher and used without further purification unless otherwise noted. All glassware was flame-dried before use. Silica gel column chromatography was performed using pre-loaded silica gel columns and a CombiFlash purification system. All cell culture reagents unless otherwise noted were purchased from Thermo Fisher. THP-1 and E.G7-OVA cells were purchased from ATCC. HEK Blue IL-1β cells were purchased from InvivoGen. BMDCs were isolated from C57Bl6/J mice as described below. The following antibody clones and dyes were purchased from BioLegend for use in flow cytometry: Zombie NIR Viability Dye, anti-CD16/32 (Clone 93), PE anti-mouse CD3 (Clone 17A2), APC anti-mouse CD4 (Clone RM4-5), APC anti-mouse CD8 (Clone 53-6.7), PerCP/Cy5.5 anti-mouse IL-4 (Clone 11B11), AF488 anti-mouse IFN-γ (Clone XMG1.2), FITC anti-mouse CD86 (Clone GL-1), PE anti-mouse MHC-I:SIINFEKL (Clone 25-D1.16), APC anti-mouse CD40 (Clone 3/23). C57Bl/6J, Nu/J, B6.129S6-Nlrp3tm1Bhk/J, and Balb/C mice (5-week-old) were purchased from Jackson Laboratory (JAX). Mice were housed in an AAALAC accredited animal facility. All animal procedures were performed under a protocol approved by the University of Chicago Institutional Animal Care and Use Committee (IACUC). All compounds used in-vivo were tested for endotoxin prior to use. The animals were allowed to rest for 7 days post receipt prior to injections. All data unless otherwise noted are analyzed and plotted in GraphPad Prism 9.

Synthesis and Characterization of Small Molecules. Synthetic procedures and NMR characterization of all small molecules are described in **Section 3.5**. Proton nuclear magnetic resonance (^{1}H-NMR) spectra were recorded at 300 MHz on a Varian Mercury 300, at 400 MHz

on a Bruker DRX instrument equipped with a BBO probe using Topspin 1.3, or at 500 MHz on a Bruker Avance-II+ spectrometer equipped with a QNP probe using Topspin 2.1 and analyzed using MestreNova software. All ^{1}H-NMR spectra were referenced to the residual solvent peak. Carbon (^{13}C) NMR spectra were recorded at 126 MHz on a Varian Inova 500 spectrometer with tetramethylsilane (TMS) carbon signal as the standard. Electrospray ionization mass spectrometry (ESI-MS) was conducted using a Waters LCT Premier™ XE system or a Agilent 6130 system using 50:50 water:acetonitrile as the solvent. Matrix-assisted laser desorption/ionization mass spectrometry (MALDI-TOF MS) was conducted using a Bruker Ultraflextreme MALDI-TOF-TOF system using Super DHB as a solid support matrix.

Solid Phase Peptide Synthesis. Fmoc-solid phase peptide synthesis of TAT-PEG$_6$-GWWWG and neoantigen peptides was performed using a Liberty Blue peptide synthesizer (CEM) using Rink amide resin (100−200 mesh) as the solid support and DIC/Oxyma activation at 90 °C. For the synthesis of TAT-P6-GWWWG, the N-terminus was capped with azidohexanoic acid using standard peptide coupling procedures to allow conjugation to the alkyne-containing poly(orthoester) scaffold. Double coupling and extended coupling times were used to couple the arginines and the hexaethylene glycol linker. Peptides were deprotected using a mixture of 85% TFA mixed with 5% water, 5% anisole, and 5% thioanisole. Following deprotection, the crude peptide was precipitated in cold diethyl ether. The crude peptide was then purified using a Phenomenex Luna C18 column (5 μm, 100 Å, 250 × 21.2 mm) on a Gilson preparative HPLC using a gradient of acetonitrile (containing 0.1% TFA) in water (containing 0.1% TFA). The purified peptides were lyophilized and characterized using MALDI-TOF MS.

Synthesis of sugar poly(orthoester) (SPOE). The synthesis of functional glucose co-poly(orthoester) (SPOE) was performed based on previously reported synthetic protocol.[111] To a Schlenk flask was added **Monomer 1** (0.20 g, 0.54 mmol)**, Monomer 2**, (0.05 g, 0.11 mmol), anhydrous CH_2Cl_2 (5 mL), tetrabutylammonium iodide (TBAI) (0.199 g, 0.54 mmol) and *N,N*-diisopropylethylamine (DIPEA, 0.21 g, 1.63 mmol). The reaction mixture was refluxed under argon

atmosphere for 20 h. The solvent was removed by reduced pressure. The polymer was precipitated three times using a mixture of water/methanol (9/1, v/v) at 4 °C to afford the SPOE as a white powder (0.18 g, 70%). M_n^{SEC} = 6.3 kDa, PDI =1.3. ^{1}H-NMR (500 MHz, $CDCl_3$) δ = 5.71 (d, 1H), 5.13 (m, 1H), 4.92-4.90 (t, 1H), 4.42 (s, 1H), 4.27 (m, 1H), 3.80 – 3.78 (m, 1H), 3.62 – 3.55 (m, 2H), 2.44 (t, 1H), 2.11 (m, 3H), 2.07 (s, 3H), 1.69 (s, 3H). ^{13}C-NMR (126 MHz, CDCl3) 169.99, 169.51, 121.34, 97.30, 80.06, 72.81, 70.09, 68.35, 67.81, 63.25, 21.12, 20.68, 20.59.

Synthesis of Polymeric Activators of Inflammasomes (PAIs). Synthesis of the alkyne-modified sugar poly(orthoester) (SPOE) backbone and azide modified adjuvants were synthesized and characterized by proton nuclear magnetic resonance (^{1}H-NMR) and mass spectrometry (MS) as described in the Supplementary Information. The synthesis of PAI was performed by sequential Cu(I) catalyzed Huisgen cycloaddition reaction with the SPOE scaffold. In a representative example, alkyne-containing SPOE (0.037 g, M_n^{SEC} = 7.2 kDa, 0.021 mmol alkynes) and 2BXy-N_3 (0.006 g, 0.013 mmol) were added to a 10 mL, flame-dried Schlenk flask in anhydrous THF (3.0 mL). After three cycles of freeze-pump-thaw, Cu(I)Br (1.0 mg, 0.0063 mmol) and *N,N,N′,N′,N″*-pentamethyldiethylenetriamine (4.73 mg, 0.0273 mmol) were added. The reaction was stirred at 37 °C for 12 h. The reaction mixture was purified by passing through neutral alumina and then further precipitated in diethyl ether (3×10 mL) to afford the product (2Bxy-SPOE) as a very light brown powder (0.035 g, 80%). 2Bxy-SPOE was then reacted with azido-TAT-P6-GWWWG (0.023 mg, 0.008 mmol in anhydrous DMF (3.0 mL). After three cycles of freeze-pump-thaw, $Cu^{(I)}$Br (1.0 mg, 0.0063 mmol) and *N,N,N′,N′,N″*-pentamethyldiethylenetriamine (4.73 mg, 0.0273 mmol) were added. The reaction was stirred at 37 °C for 12 h following which the reaction mixture was dialyzed in EDTA solution followed by dialysis in DI water. The solution was lyophilized to obtain a brown powder. PAIs with varied ratios of 2BXy: TAT-PEG_6-GWWWG were prepared analogously by varying the molar ratios of these components.

Nanoassembly of PAIs. PAIs were dissolved in DMSO (1.5 mL) and stirred at room temperature overnight. The solution volume was then subjected to dialysis against endotoxin-free

PBS for 24 h to afford NP solution. Following this the particles were stored at 4 °C. The stability of the nanoparticles was monitored using TEM over a period of eight weeks at 4 °C.

Size Exclusion Chromatography. Size exclusion chromatography (SEC) analyses of poly(orthoesters) were conducted using a Viscotek SEC system equipped with a VE 3580 RI detector, VE 112 solvent delivery system, and a column system comprised of one PAS102 and one PAS103 column (Polyanalytik Inc.). The system was equilibrated at 35 °C in DMF, which served as the polymer solvent and eluent with a flow rate of 1.0 mL min^{-1}. Polymer solutions were prepared at a known concentration (ca. 6 mg/mL) and an injection volume of 100 µL was used. Data collection and analyses were performed by OmniSEC software system from Malvern Inc. The SEC system was calibrated using poly(styrene) standards having molecular weights of 2.5 5.0, 9.0, 17.0 and 50.0 kDa (Supelco). SEC analysis of other polymers in DMF were conducted similarly using 0.01 M LiBr additive at 50 ºC using a Tosoh EcoSEC pump. The system was equipped in series with Tosoh SuperAW3000 and Tosoh SuperAW4000 columns, and samples were eluted with a flow rate of 0.3 mL min^{-1}. Polymer molecular weight was calculated relative to poly(methyl methacrylate) standards (Supelco) using the Tosoh EcoSEC analysis software. SEC analyses in aqueous conditions were conducted similarly using an Agilent Infinity 1260 analytical HPLC equipped with a BioBasic 150 × 7.8 mm SEC 120 column (Thermo Fisher). The system was equilibrated at 20 °C in nanopure water using a flow rate of 0.35 mL min^{-1} and calibrated with Protein Standard Mix 15 - 600 kDa (Supelco). A curve of elution time and $\log_{10}$(Mn) was generated in MATLAB, and elution time was used to determine Mn of experimental compounds.

Transmission Electron Microscope. Transmission Electron Microscopy (TEM) was performed using a FEI Tecnai F30 300 kV FEG(s) TEM microscope. Carbon-coated copper grids were treated with oxygen plasma before deposition of the samples. The samples were deposited on the carbon grids for 1 min, and excess samples were wicked away. The samples were allowed to dry under ambient conditions and subsequently stained with uranyl acetate prior to imaging.

Dynamic Light Scattering. Dynamic light scattering (DLS) measurements were performed by a Wyatt Mobiuζ DLS instrument. Measurements were performed at 25°C using a laser wavelength of 532 nm. Scattered light was collected at a fixed angle of 163.5°

High Performance Liquid Chromatography. High performance liquid chromatography (HPLC) was employed to evaluate the composition of PAIs using an Agilent Infinity 1260 analytical HPLC equipped with a Phenomenex Luna C18 column (5 µm, 100 Å, 150 × 4.6 mm) and a UV-VIS detector. First, TAT-P6-GWWWG and 2BXy were injected to determine the elution time and molar absorption coefficient at 280 nm of each component. Then, PAIs were degraded by incubating in 0.1% TFA in 1:1 DMSO:water for 4 h. The degraded PAI solution was then injected to the HPLC, and the area under the curve of each component peak was referenced to the standard curves to quantify presence of TAT-PEG_6-GWWWG and 2BXy in the polymer scaffold.

Fourier Transfer Infrared Spectroscopy (FT-IR). Infrared spectra of polymers were recorded on a Shimadzu IR Tracer Fourier Transform-Infrared Spectrometer in attenuated total reflection (ATR) mode. Freeze-dried samples were placed directly onto the crystal for analysis.

Synthesis of Polymers Containing 2-hydroxypropyl methacrylate (HPMA). All monomers and other chemicals were used as received unless noted. Polymers were prepared using glycidyl methacrylate (GMA) as a functional azide handle or propargyl methacrylate (PrMA) as a functional alkyne handle. PrMA was synthesized as described in the **Synthetic Methods**. Prior to use, inhibitors were removed from monomers by passing samples through a column of basic alumina (150 mesh). CPADB (1 eq), ACVA (0.1 eq), uninhibited monomers, and a stir bar were then added to a 5 mL round bottom flask and dissolved in 1 mL dry DMF (or 1 mL dioxane, in the case of PrMA containing polymers). The reaction was subjected to three freeze-pump-thaw cycles and then heated to 60 °C, where the reaction proceeded with rapid stirring for 16 h. The resultant polymer was precipitated three times in 1:1 diethyl ether:acetone, dialyzed against dH_2O

for 24 h, and freeze dried to obtain the polymer as a powder. The molecular weight and dispersity were characterized by SEC and the composition characterized by ^{1}H-NMR in D_2O.

Modification of Glycidyl-containing Polymers with Sodium Azide. Ring opening of the epoxy moieties in polymers containing GMA was conducted with sodium azide. Polymers (1 eq of epoxy), ammonium chloride (3 eq), and sodium azide (3 eq) were added to a round bottom flask with a stir bar, dissolved in 1 mL DMF, and reacted at 50 °C for 48 h. (NOTE: heating sodium azide is an explosion hazard, and care must be taken to ensure that the solution is handled under basic condition). The reaction was then cooled and precipitated into 1:1 ethyl acetate:acetone. The crude product was collected, dialyzed against dH_2O overnight, and freeze dried. Incorporation of azide groups was confirmed by FT-IR, where the intensity of the characteristic azide peak (2100 cm^{-1}) was used to approximate the density of azide on the surface.

Grafting of Peptides to Polymers with Cu-Mediated Click Chemistry. TAT peptide containing an N-terminal alkyne or azide and azide- or alkyne-bearing polymers were added to a round bottom flask, dissolved in 1 mL dry DMF, and sparged with argon for 15 min. Meanwhile, CuBr and PMDETA were dissolved in 100 uL dry DMF. After sparging was complete, copper solution was added to the reaction mixture and the reaction stirred at 37°C overnight. To remove unreacted materials, crude product was dialyzed for 24 h against 0.5 M EDTA followed by dialysis for 24 h longer against dH_2O to remove residual EDTA. The product was then freeze dried and characterized by ^{1}H-NMR (when a suitable solvent could be identified) and/or FT-IR.

On-resin Modification of Peptides with Acrylamide Handle. KLA peptide (KLAKLAKKLAKLAK) and TAT-PEG_6-GWWWG peptide (YGRKKRRQRRR-PEG_6-GWWWG-alkyne) were prepared using Rink Amide on a 10 mmol scale. Prior to deprotection, the resin was collected in a Poly-Prep Column (Bio Rad) and reacted with an acrylate handle. For KLA peptide, a cocktail with 30 mmol acrylic acid, 29 mmol 2-benzotriazol-1-yl-1,1,3,3-tetramethyluronium hexafluorophosphate (HBTU), and 60 mmol diisopropylethylamine (DIPEA) was prepared in 8 mL dry DMF. After stirring for 5 min, the cocktail was added to the resin-containing Poly-Prep Column,

which was sealed and stirred for 40 h. After 40 h, the end cap was removed, and the resin was collected at the bottom of the column. For TAT-PEG_6-GWWWG, 3-azidopropyl acrylate (10 mmol), $CuSO_4$ (10 mmol), and tris(hydroxypropyltriazolylmethyl)amine (THPTA, 10 mmol) were dissolved in 8 mL DMF. The reagent mixture was added to the resin-containing Poly-Prep Column. Then, ascorbic acid (30 mmol) was quickly added, the headspace was purged, and the mixture was reacted for 40 h. Following both reactions, the resins were washed with 3 x 10 mL DMF and then 3 x 10 mL DCM, and they were deprotected and purified as described above.

Synthesis of Peptide Acrylamide Co-polymers via PET-RAFT. KLA peptide acrylamide and TAT-PEG_6-GWWWG peptide acrylamide were synthesized as described above. 25 mg of peptide acrylamide, 10 mg of N,N-dimethylacrylamide, 0.175 mg of 4-Cyano-4-(phenylcarbonothioylthio)pentanoic acid (3.5 µL of a 50 mg/mL stock solution in DMF; 1 eq) as chain transfer agent, 0.075 mg Eosin Y (1.5 µL of a 10 mg/mL stock solution in DMF; 0.1 eq) as photocatalyst, and a stir bar were added to a round bottom flask and sealed under argon. 1 mL DMF was added to the reaction mixture, and the solution was subjected to three freeze-pump-thaw cycles before being irradiated with a 450 nm LED strip (Figure A) and stirring at room temperature overnight. Ambient heating from the LED caused heating to 30 °C over the course of the reaction. After 18 h, the reaction was stopped by removing the LED and exposing the reaction to air, and the reaction was solvent transferred and purified by dialysis against dH2O using 6-8 kDa MWCO tubing for 72 h (changing dialysate daily). The purified polymer was lyophilized to achieve a pink powder and characterized by 1H-NMR (in D_2O) and/or DMF-SEC. For synthesis of TAT peptide acrylamide as used in **Figure S6.18**, an analogous procedure was conducted, except cyanopentanoic acid dithiobenzoate was used as the chain transfer agent. In this reaction, five freeze-pump-thaw cycles were conducted prior to 450 nm irradiation.

High Throughput PET-RAFT Polymerization with cp-DIBAC. Acrylamide polymers containing the cp-DIBAC end group (**12**) were synthesized in a method adapted from Li et al.[68] During a typical 50 mg scale synthesis, liquid monomers were passed through a column of

alumina and pipetted into a white polypropylene 96-well plate (Nunc). Stock solutions of cp-DIBAC CTA (50 mg/mL, 1 eq) and 5,10,15,20-Tetraphenyl-21H,23H-porphine zinc (ZnTPP) (10 mg/mL, 0.02 eq) were added to the appropriate wells and then diluted to a final volume of 200 µL with DMSO. The 96-well plate was sealed with well plate tape and irradiated with a 565 nm mounted LED (Thorlabs) 1 inch from the light source for 4 h. Reaction mixtures were then precipitated into 1.2 mL diethyl ether in a 1.5 mL tube, centrifuged at 10,000 G for 10 min to remove unreacted start materials, and then decanted to achieve an oily polymer in DMSO. The polymers were subsequently redissolved in 500 µL DMSO and UV-VIS was used to confirm the presence of the cyclopropenone-protected end-group. Upon confirmation that the end group was in-tact, polymers were returned to the 96-well plate, and the cyclopropenone group was removed by irradiating the well plate with a 365 nm mounted LED (Thorlabs) 1 inch from the light source for 30 min. Cyclopropenone group remove was again confirmed by UV-VIS. Next, 2 equivalents of azide terminated TAT-PEG_6-GWWWG dissolved in DMSO (50 mg/mL) were added to the appropriate wells. The well plate was again sealed, placed on a well-plate shaker set to 1000 rpm, and reacted for 24 h. Upon completion of the reaction, UV-VIS was used to confirm reaction of the cyclooctyne moiety. Solutions were diluted in 10 mL dH_2O, and unreacted peptide and DMSO were removed by passing the solutions thrice through a 3k MWCO centrifugal filter (Amicon). Finally, solutions were freeze dried to obtain peptide-modified acrylamides as a brown powder. Polymers were characterized by DMF-SEC and ^{1}H-NMR.

Bicinchoninic Acid (BCA) Assay. Peptide-polymer conjugates were dissolved at 1,000 µg/mL in dH_2O and tested using Pierce BCA Kit (Thermo Fisher) according to the manufacturer's instructions. Because the amino acid content of TAT-PEG_6-GWWWG is different from the full-length protein standard provided, TAT-PEG_6-GWWWG peptide (1,000-25 µg/mL) was used as a standard. After developing the assay for 30 min, the plate was read on a Multiskan FC plate reader (Thermo Scientific) at 562 nm.

HEK IL-1β Production Assay. THP-1 cells and HEK Blue IL-1β cells were incubated at 37 °C and 5% CO_2. THP-1 cells were cultured in RPMI medium with 10% heat-inactivated fetal bovine serum (HI-FBS), while HEK Blue IL-1β cells were cultured in DMEM medium with 10% HI-FBS and selection antibiotics (Normocin and Zeocin, which were removed during HEK detection assay). For the assay, THP-1 cells were passaged, resuspended in fresh medium at 10^6 cells/mL, and plated at 180,000 cells/well in a 96 well plate. To the cells was then added 20 µL of a 10x solution of ultrapure LPS-EB (InvivoGen, working concentration of 100 EU/mL). Cells were treated with LPS for 3 h, then medium was removed and replaced with 180 µL of fresh medium. 20 µL of 10x polymer solutions were added as indicated. Cells were incubated with the polymers for 5 h. Medium was then collected, and 50 µL of the THP-1 medium was added to HEK Blue IL-1β cells in 150 µL of their medium (150,000 cells/well in a 96 well plate, plated at least 24 h before start of experiment). HEK Blue IL-1β cells were incubated overnight, and then 50 µL of their medium was collected and incubated with150 µL QUANTI-Blue™ (InvivoGen) detection reagent for 1-4 h at 37 °C in a 96 well plate. The plate was checked every 30 min, and upon sufficient development of the detection reagent (top standard ~1.5 A.U.), the plate was read on a Multiskan FC plate reader (Thermo Scientific) at 620 nm.

Cationic Polymer Vaccination Studies. 8-week-old female C57Bl/6J mice were vaccinated intramuscularly in the left flank with 50 µL total volume of the indicated formulations. For Toll-like receptor adjuvanted vaccines, the formulations contained 50 µg ovalbumin (OVA), 10 µg polymer, and either 10 µg MPLA-SM (InvivoGen) in 25 µL AddaVax (InvivoGen) or 25 µg CpG 1018 (Integrated DNA Technologies) in 25 µL PBS. For alum adjuvanted vaccines, the formulations contained 100 µg ovalbumin (OVA), 100 µg Adju-Phos (InvivoGen), and 10 µg polymer in 25 µL PBS. For all studies, mice were vaccinated at experiment onset and again on day 14. 2 and 24 h after the initial injection, mice were bled via the submandibular vein, and systemic cytokines in the serum were assayed via LEGENDplex™ Mouse M1 Macrophage Panel 8-plex (BioLegend). At day 27, mice were bled via the submandibular vein and anti-OVA

antibodies were assayed via anti-Ovalbumin (Gal d 2) total Ig's (A+G+M) ELISA Kit (Alpha Diagnostic International). On day 28, mice were sacrificed, and spleens were harvested for tetramer staining and/or intracellular cytokine staining. Staining protocols, including antibody panels and gating strategies, are described in detail in the **Intracellular Cytokine Staining** and **Tetramer Staining** methods.

Intracellular Cytokine Staining. From each mouse, $5x10^6$ splenocytes were plated in a 96-well plate in 200 µL of T cell medium (RPMI + 10% HI-FBS + 10 mM HEPES buffer + 1x MEM non-essential amino acids + 55 µM β-mercaptoethanol) and restimulated with SIINFEKL (10 µg/mL) and OVA323-339 (10 µg/mL) (prepared in-house via solid-phase peptide synthesis as shown in **Figure S3.31**) for 8 h. In the final 6 h of restimulation, 0.2 µL of GolgiPlug protein transport inhibitor (BD Biosciences) was added. Cells were then washed, stained with a viability marker in PBS, washed, and stained with cell surface markers and Fc receptor blocking antibodies in 50 µL staining buffer (PBS + 2% FBS). Cells were then washed, fixed using Cytofix/Cytoperm (BD Biosciences), and stained for intracellular cytokines according to the manufacturer's protocol. Finally, cells were resuspended in 200 µL staining buffer and analyzed via flow cytometry. Data were collected with a Novocyte Penteon (Agilent) flow cytometer and analyzed using FlowJo v10.8.1. Antibodies used included: Live/Dead Fixable Violet (Thermo Fisher), anti-mouse CD16/32 (Clone 93), BUV395 anti-mouse CD3 (Clone 17A2), BV605 anti-mouse CD4 (Clone GK1.5), AF700 anti-mouse CD8 (Clone 53-6.7), AF647 anti-mouse IFN-γ (Clone XMG1.2), PE anti-mouse IL-4 (Clone 11B11), AF488 anti-mouse IL-2 (Clone JES6-5H4), and PE/Cy7 anti-mouse TNF-α (Clone MP6-XT22). All antibodies were purchased from BioLegend unless indicated otherwise.

Tetramer Staining. From each mouse, $5x10^6$ splenocytes were plated in 200 µL of PBS in a 96-well plate. Cells were stained with a viability marker in PBS, washed, and treated with an Fc receptor blocking antibody in 100 µL staining buffer (PBS + 2% FBS). Meanwhile, SIINFEKL:H-$2K^b$ tetramers were prepared according to the manufacturer's protocol. Cells were washed and

then treated with the tetramers in 50 µL staining buffer for 15 min at 37 °C. Other cell surface markers were then added in 50 µL staining buffer, and the cells were incubated 45 min longer at 4 °C. Cells were then washed, resuspended in 200 µL staining buffer, and analyzed via flow cytometry. Data were collected with a Novocyte Penteon (Agilent) flow cytometer and analyzed using FlowJo v10.8.1. Antibodies and stains used included SIINFEKL:H-2K^{b} APC-labelled tetramers (TetramerShop), Live/Dead Fixable Violet (Thermo Fisher), anti-mouse CD16/32 (Clone 93), FITC anti-mouse CD3 (Clone 17A2), PE anti-mouse CD4 (Clone GK1.5), AF700 anti-mouse CD8 (Clone 53-6.7), and BV711 anti-mouse/human CD44 (Clone IM7). All antibodies were purchased from BioLegend unless indicated otherwise.

Nanogel Synthesis and Purification. OVA and polymers were dissolved at 10 mg/mL in PBS (pH = 6.8), while 2BXy and cross-linkers were dissolved at 10 mg/mL in DMSO. 3 mL of OVA, 1 mL of polymer, and 30 µL of 2BXy were added to a 20 mL scintillation vial. Under rapid stirring, 300 uL of cross-linker was added, and the reaction was allowed to proceed for 4 h. After 4 h, the reaction was diluted 10x in PBS and purified by 5 rounds of centrifugal filtration against a 100 kDa Amicon filter. The nanogels were freeze dried and resuspended at 1 mg/mL for analysis. When further purified by dialysis, 1 mg/mL nanogel solution was dialyzed against dH_2O for 48 h, changing dialysate twice daily.

Antigen Presentation Assay. BMDCs were isolated and differentiated from C57Bl/6J mouse femurs for 6 d as described previously.[45] On day 6, BMDCs were released from the plate by mechanical agitation, resuspended in RPMI + 10% HI-FBS, counted, and plated at 500,000 cells/well in 500 µL medium in a 24 well plate. BMDCs were allowed to rest for 2 h, then treated with 100 µg/mL of nanogels for 20 h. Cells were then washed, stained with Live/Dead Fixable Violet (Thermo Fisher), anti-mouse CD16/32 (Clone 93), FITC anti-mouse CD86 (Clone GL-1), PE anti-mouse H-2K^{b} bound to SIINFEKL (Clone 25-D1.16), and APC anti-mouse CD40 (Clone 3/26), and analyzed *via* flow cytometry on a BD Fortessa LSR-II. Data were analyzed using FlowJo v10.8.1. All antibodies were purchased from BioLegend unless indicated otherwise.

T cell Proliferation and Cytokine Assay. BMDCs were isolated and differentiated from C57Bl/6J mouse femurs for 6 d as described previously.[45] On day 6, BMDCs were released from the plate by mechanical agitation, resuspended in RPMI + 10% HI-FBS + 10 mM HEPES buffer + 55 μM β-mercaptoethanol, counted, and plated at 5 x 10^5 cells/well in 500 μL medium in a 24 well plate. BMDCs were allowed to rest for 2 h, then treated with 100 μg/mL of nanogels for 5 h. Meanwhile, spleens from OT-I mice (C57BL/6-Tg(TcraTcrb)1100Mjb/J, Jackson laboratories) were isolated and digested into a single cell suspension as described above. T cells were isolated via magnetic separation using EasySep™ Mouse T Cell Isolation Kit (STEMCELL) and subsequently stained using CellTrace CFSE according to the manufacturer's procedures. After 5 h, nanogel-treated BMDCs were washed, resuspended in media, and 1.5 x 10^6 OT-I T cells were added to each well. The co-cultures were incubated for 3 d, then the supernatant was collected and analyzed *via* Legendplex Mouse Inflammation 13-plex according to the manufacturer's procedure. Meanwhile, cells were collected, stained with Live/Dead Fixable Far Red to exclude dead cells, and analyzed via flow cytometry. Data were collected with a Novocyte ACEA (Agilent) flow cytometer and analyzed using FlowJo v10.8.1.

SDS-PAGE Gel Electrophoresis. 15 μL of samples (1 mg/mL) and 5 μL of 4x loading buffer were mixed in PCR tubes and heated for 5 min at 95 °C using a thermocycler. Samples were then loaded into a 4-15% Mini-PROTEAN® TGX™ Precast Gel (Bio-Rad) and run at 100 V in TGS buffer. The gel was then stained with One-Step Blue Protein Gel Stain (Biotium) for 1 h, washed with deionized water for 1 h, and imaged using an Azure 400 gel imager. Images were processed in ImageJ.

IL-1β ELISA. BMDCs were isolated and differentiated from C57Bl/6J mouse femurs for 6 d as described previously.[45] On day 6, BMDCs were released from the plate by mechanical agitation, resuspended in RPMI + 10% HI-FBS, counted, and plated at 180,000 cells/well in 180 μL medium in a 96 well plate. 20 μL of a 10x solution of ultrapure LPS-EB (InvivoGen) was added (100 EU/mL working concentration). After 3 h, cells were pelleted, washed once with PBS,

resuspended 180 µL media, and treated in triplicate nanogels. After 5 h, the supernatant was collected and subjected to mouse IL-1β ELISAMAX Kit (Biolegend) according to the manufacturer's procedures.

3.5 Synthetic Methods.

3.5.1 Synthesis of 2,3,4-tri-O-acetyl-α-D-glucopyranosyl bromide (1).

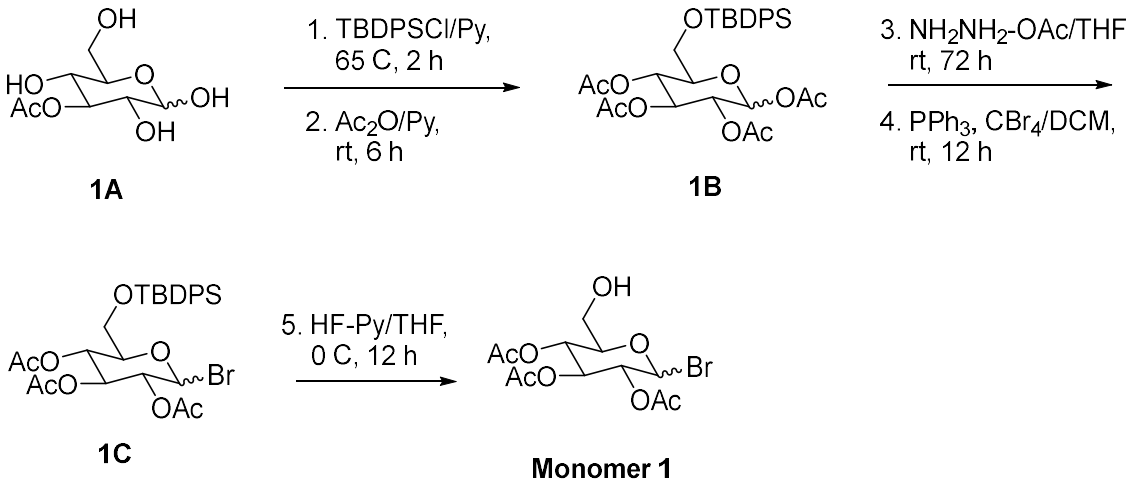

1A **1B** **1C** **Monomer 1**

The synthesis of monomer I was performed based on previously reported synthetic protocol.[111] Briefly, in a 50 mL disposable polypropylene tube, 2,3,4-tri-*O*-acetyl-6-*O*-*tert*-butyldiphenylsilyl-α-D-glucopyranosyl bromide (1.0 g, 1.65 mmol) was added to anhydrous tetrahydrofuran (7 mL). HF-Py (0.82 g, 70% HF in pyridine, 0.57 g HF, 29 mmol HF) was subsequently added. The reaction was stirred under nitrogen at 4 °C for 12 h. The solvent and excess HF-Py was removed by sparging N_2 gas at 4 °C and the residue was purified by silica gel column chromatography (hexanes/ethyl acetate = 6/4, R_f = 0.3) to afford the product as a white powder (0.38 g, 62%).^{1}H-NMR (300 MHz, $CDCl_3$) δ 6.64 (d, 1H), 5.59 (dd, 1H), 5.14 (dd, 1H), 4.78 (dd, 1H), 4.10 (m, 1H), 3.74 (ddd, 1H), 3.60 (ddd, 1H), 2.29 (dd, 1H), 2.06 (s, 3H), 2.05 (s, 3H), 2.02 (s, 3H). ^{13}C-NMR (126 MHz, $CDCl_3$) δ 170.80 (C=O), 170.03 (C=O), 170.01 (C=O), 87.07 (α-C1), 74.57 (C-5), 71.04 (C-2), 69.98 (C-3), 67.85 (C-4), 60.53 (C-6), 20.90 (-OAc), 20.88 (-OAc). ESI-MS: 391.00, 393.00 expected, 391.12, 393.13 observed.

3.5.2 Synthesis of 3-propargyl-2,4-di-*O*-acetyl-α-D-glucopyranosyl bromide (2).

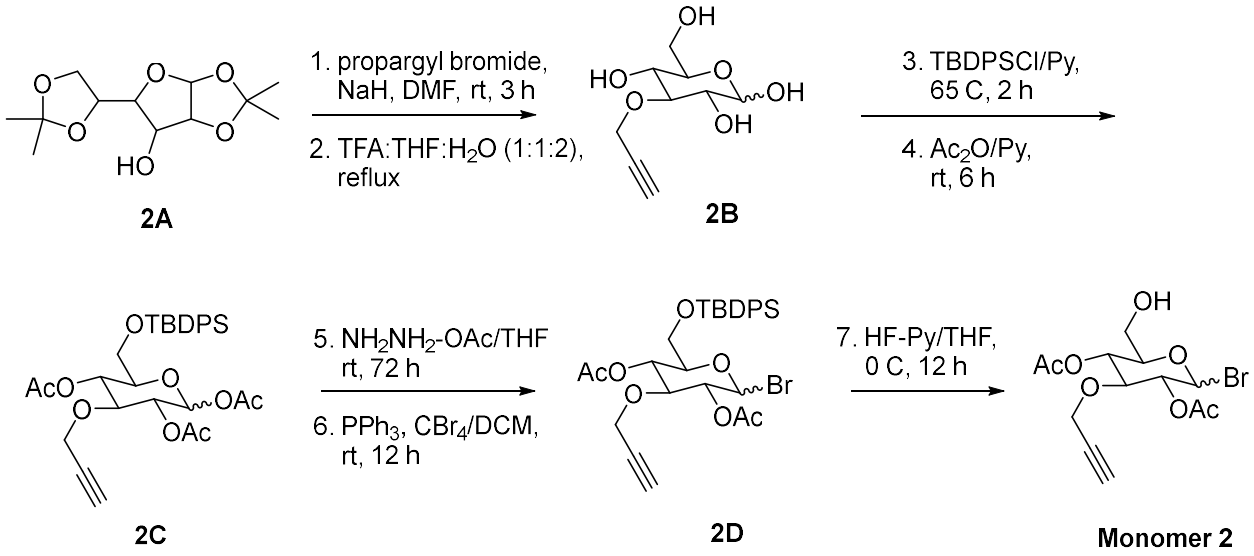

The synthesis of **Monomer 2** was performed based on previously reported synthetic protocol.[111] Briefly, in a 50 mL disposable polypropelene tube, 3-propargyl-2,4-di-*O*-acetyl-6-*O*-*tert*-butyldiphenylsilyl -α-D-glucopyranosyl bromide (1.0 g, 1.7 mmol) was added to anhydrous tetrahydrofuran (7.0 mL). HF-Py (0.82 g, 70% HF in pyridine, 0.57 g HF, 29 mmol HF) was subsequently added. The reaction was stirred under nitrogen at 4 °C for 12 h. The solvent and excess HF-Py was removed by sparging N_2 gas at 4 °C and the residue was purified by silica gel chromatography (hexanes/ethyl acetate = 6/4, R_f = 0.3) to afford the product as a white powder (0.40 g, 66%). ^{1}H-NMR (500 MHz, $CDCl_3$) δ 6.64 (d, 1H), 5.02 (m, 1H), 4.68 (dd, 1H), 4.31 (m, 2H), 4.12 (dd, 1H), 3.96 (m, 1H), 3.69 (ddd, 1H), 3.58 (ddd, 1H), 2.49 (t, 1H), 2.14 (s, 3H), 2.11 (s, 3H), ^{13}C-NMR (126 MHz, $CDCl_3$) δ 170.66, 169.27, 88.47, 79.54, 76.33, 74.77, 72.73, 68.69, 61.08, 60.31, 20.86. ESI-MS: 388.17 expected, 388.06 observed.

3.5.3 Synthesis of 2BXy (3) and 2BXy-Azide (4).

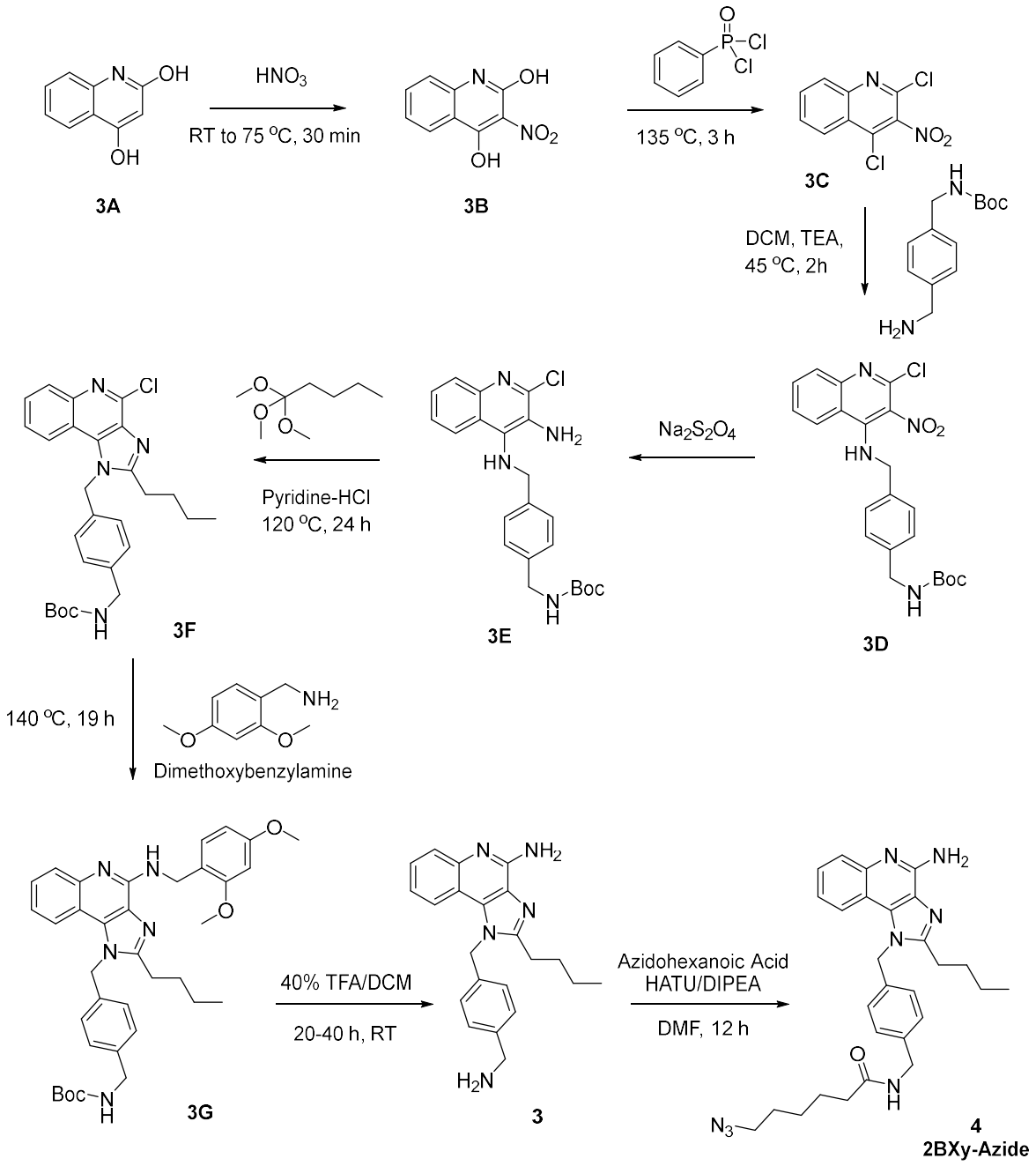

The synthesis of compound **3** was performed based on previously reported synthetic protocol *via* the scheme shown above.[112] Compound **3** (100 mg, 0.28 mmol) and azidohexanoic acid (48.41 mg, 0.31 mmol) were then dissolved in anhydrous DMF following which DIPEA (73.2 µL, 0.42 mmol) and HATU (159.70 mg, 0.42 mmol) were added to the reaction under argon. The reaction mixture was stirred for 12 h at room temperature following which the solvent was removed

under vacuo and the product was purified by silica gel chromatography using a gradient of 0-5% methanol in DCM, giving compound **4** as a yellow powder (104.8 mg, 0.21 mmol, 75 % yield). ^{1}H-NMR (500 MHz, $CDCl_3$) δ 8.52 (s, 1H), 8.22 (d, 1H), 8.03 (d, 1H), 7.67 (d, 1H), 7.44 (t, 1H), 7.25 (d, 2H), 7.20 (m, 1H), 6.97 (d, 2H), 6.21 (s, 1H), 5.75 (s, 2H), 4.41 (d, 2H), 3.75 (m, 2H), 3.22 (t, 2H), 2.87 (t, 2H), 2.22 (m, 2H), 1.86 (s, 2H), 1.80 (m, 2H), 1.65 (m, 2H), 1.56 (m, 2H), 1.42 (m, 2H), 1.38-1.33 (m, 2H), 1.26 (s, 1H) 0.93 (t, 3H). ESI-MS: 499.64 expected, 499.65 observed.

3.5.4 Synthesis of Propargyl Methacrylate (5)

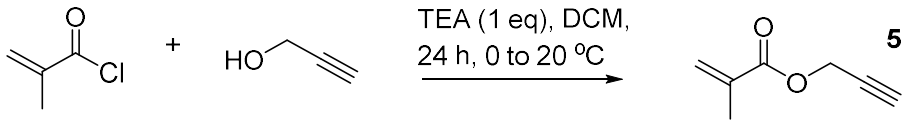

Propargyl Methacrylate (**5**) was prepared using a literature preparation *via* the scheme shown above and obtained as a colorless oil as reported previously.[113] ^{1}H-NMR (400 MHz, $CDCl_3$) δ 6.17 (s, 1H), 5.63 (s, 1H), 4.75 (d, 2H), 2.48 (t, 1H), 1.97 (s, 3H).

3.5.5 Synthesis of 2-(((butylthio)carbonothioyl)thio)propanoic acid (BTPA) (6) and azide derivatized chain transfer agent (7)

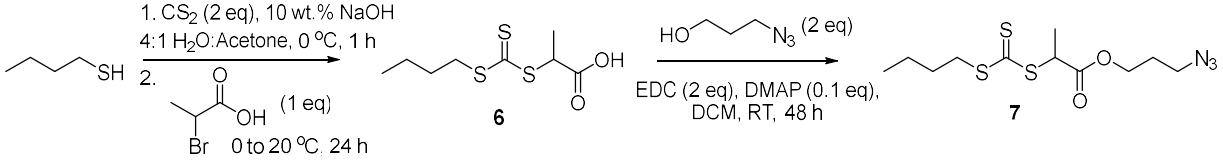

Synthesis of (6). Synthesis and purification of **6** was conducted according to a reported literature preparation and obtained as a yellow crystalline solid.[114] 1H-NMR (400 MHz, CDCl3) δ 7.58 (br s, 1H), 4.86 (q, 1H), 3.37 (t, 2H), 1.69 (m, 2H), 1.63 (d, 3H), 1.44 (m, 2H), 0.94 (t, 3H).

Synthesis of (7). A 100 mL flask was charged with 148 mg **6** (0.62 mmol, 1 eq), 120 µL 3-azidopropan-1-ol (1.2 mmol, 2 eq), 241 mg EDC·HCl (1.2 mmol, 2 eq), 7.1 mg 4-dimethylaminopyridine (0.06 mmol, 0.1 eq), and a stir bar, sealed under argon, and stirred at room

temperature for 48 h. The reaction was subsequently opened to air, the organic phase washed with 3 x 100 mL $NaHCO_3$, and solvent removed under reduced pressure. The crude product was redissolved in 15 mL 1:1:1 water:acetone:methanol, filtered, and purified by reversed phase HPLC on a Phenomenex Luna C18 column (5 µm, 100 Å, 250 × 21.2 mm) (50-100% ACN in water with 0.1% TFA). The pooled product fractions were freeze dried to obtain **7** as a yellow oil. ^{1}H-NMR (400 MHz, $CDCl_3$) δ 4.82 (q, 1H), (qt, 2H), 3.38 (m, 4H), 1.92 (m, 2H), 1.69 (m, 2H), 1.60 (d, 3H), 1.43 (m, 2H), 0.94 (t, 3H).

3.5.6 Synthesis of cyclopropenone-protected dibenzocyclooctyne chain transfer agent (cp-DIBAC CTA) (8-12)

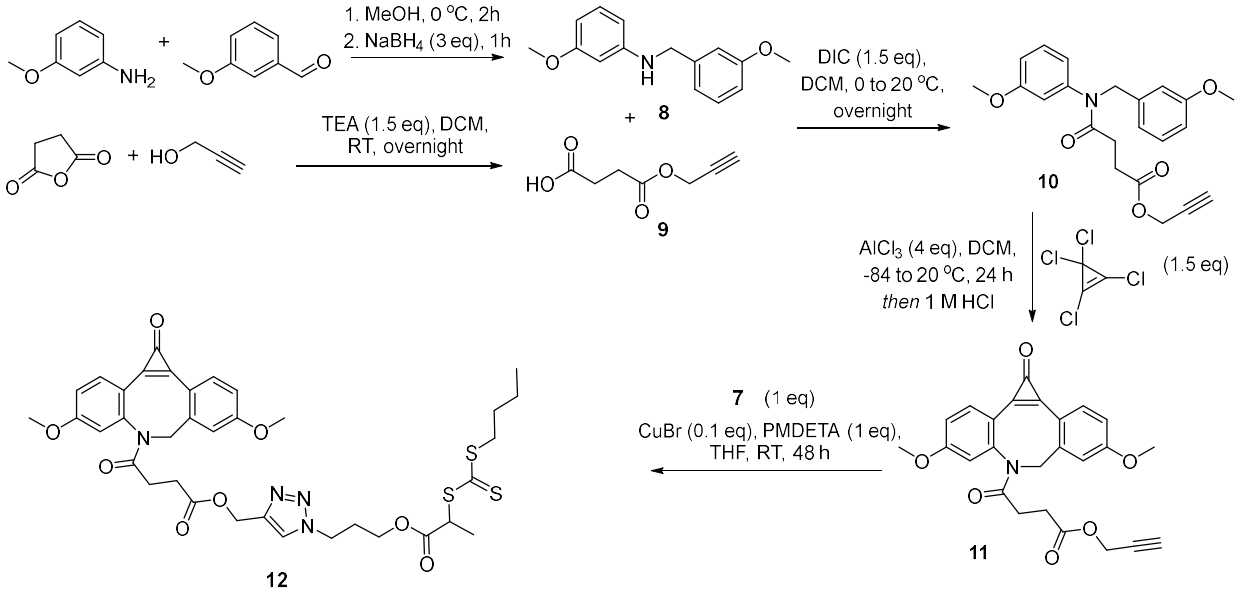

Synthesis of (8). To a 250 mL round bottom flask was added 5.0 mL m-anisidine (45 mmol, 1.1 eq), 5.0 mL m-anisaldehyde (41 mmol, 1 eq), and 100 mL methanol. The reaction mixture was stirred on ice for 2 h until the start material was confirmed to be consumed by TLC. 7.0 g $NaBH_4$ was subsequently added in several 1 g portions over 30 min, and then the reaction was allowed to warm to RT and stirred for 1 h. The reaction was quenched with H_2SO_4 (until pH < 2.0), partitioned between water and ethyl acetate, and the product extracted 3x into ethyl

acetate. The combined organic phases were washed sequentially with 1 M NaOH, water, and brine, dried over $MgSO_4$, and filtered. The solvent was removed under reduced pressure, the crude product was purified by gradient silica gel chromatography of ethyl acetate (0-40%) in hexanes, and the product fractions were dried under reduced pressure to yield a colorless viscous oil **8**. ^{1}H-NMR (400 MHz, $CDCl_3$) δ 7.23 (t, 1H), 7.06 (t, 1H), 6.93 (t, 2H), 6.80 (d, 1H) 6.25 (t, 2H), 6.18 (s, 1H), 4.28 (s, 2H), 3.78 (s, 3H), 3.74 (s, 3H).

Synthesis of (9). Succinic anhydride (10.0 g, 100 mmol, 1.1 eq) was suspended in 100 mL dry DCM, and the reaction vessel was sealed under an argon. 12.7 mL triethylamine (90 mmol, 1 eq) was added followed by addition of 5.1 mL propargyl alcohol (90 mmol, 1 eq), and the reaction was stirred overnight. The reaction was quenched by addition of 2 M aqueous HCl and stirring for 30 min. The organic phase was collected, and aqueous phase was extracted with 2 x 100 mL DCM. Combined organic phases were washed with water followed by brine, dried over $MgSO_4$, filtered, and the solvent removed under reduced pressure. The crude product was purified by gradient silica gel chromatography of ethyl acetate (0-40%) in hexanes and dried under reduced pressure to yield a waxy solid **9**. ^{1}H-NMR (400 MHz, $CDCl_3$) δ 11.20 (br s, 1H), 4.71 (d, 2H), 2.69 (m, 4H), 2.50 (t, 1H).

Synthesis of (10). To a flame dried flask was added 2.5 g **8** (10 mmol, 1 eq), 1.9 g **9** (10 mmol, 1.2 eq), 100 mL dry DCM and a stir bar. The reaction was sealed under argon and cooled to 0 °C with rapid stirring. N,N'-diisopropylcarbodiimide (2.4 mL, 1.5 eq) was added dropwise over 5 min. After complete addition, the reaction vessel was warmed to room temperature and stirred overnight. After complete consumption of starting materials was confirmed by TLC, stirring was stopped and reaction mixture was extracted sequentially with 300 mL $NaHCO_3$, 300 mL water, and 300 mL brine. The organic phase was then dried over $MgSO_4$, filtered, loaded onto silica, and purified by gradient silica gel chromatography of acetone (20-40%) in hexanes. The product fractions were pooled together, and solvent was removed under reduced pressure to obtain **10**

as a colorless oil. ^{1}H-NMR (400 MHz, $CDCl_3$) δ 7.23 (t, 1H), 7.17 (t, 1H), 6.85-6.57 (Ar, 6H), 4.84 (s, 2H), 4.68 (d, 2H), 3.76 (s, 3H), 3.72 (s, 3H), 2.69 (t, 2H), 2.45 (t, 1H), 2.42 (t, 2H).

Synthesis of (11). To an oven-dried flask was added 1.68 g $AlCl_3$ (13 mmol, 4 eq), 25 mL dry DCM, and a stir bar. The flask was placed under an addition funnel, sealed under argon, and cooled to -78 °C, at which point 0.62 mL tetrachlorocyclopropene (5 mmol, 1.5 eq) was added in a single portion and stirred for 30 min. 1.2 g **10** (3 mmol, 1 eq) was then dissolved in 10 mL dry DCM, transferred to the addition funnel, and added dropwise to the reaction mixture over 45 min. The reaction mixture was stirred for 1 h at -78 °C, then warmed to room temperature and stirred for 24 h. The reaction was quenched by opening the reaction to air followed by slow addition of 25 mL 1 M HCl. The organic phase was collected and separated, and the aqueous phase was extracted with 2 x 25 mL DCM. Combined organic phases were washed with 2 x 100 mL water followed by 2 x 100 mL brine, then dried over $MgSO_4$, filtered, and solvent removed under reduced pressure. The crude product was purified by gradient silica gel chromatography of ethyl acetate (65-100%) in hexanes, and product fractions were pooled and dried under reduced pressure to obtain **11** as an orange powder. ^{1}H-NMR (500 MHz, $CDCl_3$) δ 8.01 (br s, 1H), 7.90 (br s, 1H), 7.29-6.91 (m, 4H), 5.20 (d, 1H), 4.65 (d, 1H), 4.52 (d, 1H), 4.13 (d, 1H), 3.95-3.87 (d, 6H), 2.84-2.67 (m, 2H), 2.46 (s, 1H), 2.42 (d, 1H), 1.96 (d, 1H). ^{13}C-NMR (100 MHz, $CDCl_3$, d1 = 5 s) δ 171.9, 171.7, 163.2, 162.7, 152.7, 145.8, 143.4, 141.6, 139.2, 136.0, 135.3 118.2, 115.7, 115.5, 115.2, 114.5, 113.8, 77.6, 75.1, 56.5, 56.2, 55.7, 52.2, 29.2, 29.0. ESI-MS calculated for $C_{25}H_{22}NO_6^+$ ($M+H^+$) as 432.1; observed 432.0.

Synthesis of cp-DIBAC CTA (12). A flame dried flask was charged with 50.0 mg **11** (0.12 mmol, 1 eq), 37.3 mg **7** (0.12 mmol, 1 eq), 1.7 mg CuBr (0.012 mmol, 0.1 eq), 24 µL PMDETA (0.12 mmol, 1 eq), and a stir bar. The vessel was sealed, purged, and backfilled with argon prior to addition of 10 mL dry THF. The reaction was subjected to three freeze-pump-thaw cycles and stirred at room temperature for 48 h. Consumption of monomer was confirmed by LC-MS, at which point the reaction was quenched by exposure to air. The crude reaction was filtered and purified

by reversed phase HPLC on a Phenomenex Luna C18 column (5 µm, 100 Å, 250 × 21.2 mm) (50-100% ACN in water with 0.1% TFA). Product-containing fractions were pooled and freeze dried to obtain **12** as a yellow powder. ^{1}H-NMR (400 MHz, $CDCl_3$) δ 8.03 (d, 1H), 7.91 (d, 1H), 7.60 (s, 1H), 7.23-6.94 (m, 4H), 5.20 (d, 1H), 5.15 (d, 2H), 4.81 (q, 1H), 4.44 (t, 2H), 4.24-4.10 (m, 3H), 3.93 (d, 6H), 3.36 (m, 2H), 2.77-2.58 (m, 2H), 2.41 (dt, 1H), 2.29 (m, 2H), 1.95 (dt, 1H), 1.67 (m, 2H), 1.61 (d, 3H), 1.42 (m, 2H), 0.92 (t, 3H). ESI-MS calculated for $C_{36}H_{41}N_4O_8S_3^+$ ($M+H^+$) as 753.2; observed 753.0.

3.5.7 Synthesis of NHS-SS-NHS Cross-linker.

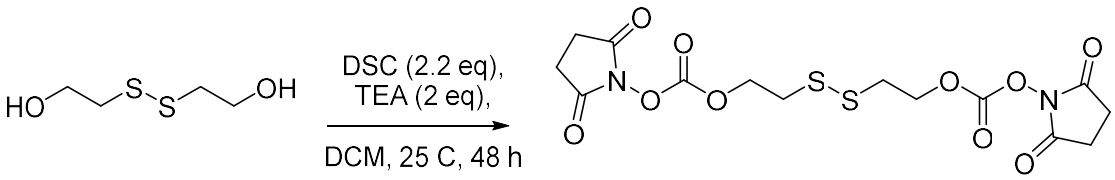

A beaker was charged with disuccinimidyl carbonate (4.6 g, 18 mmol, 2.2 eq), 75 mL dry DCM, and a stir bar. The reaction was sealed under argon, and with rapid stirring, 2-hydroxyethyl disulfide (1 mL, 8.2 mmol, 1 eq) was added dropwise over 15 min. The reaction was stirred for 48 h, at which point the reaction was concentrated under reduced pressure and filtered. The crude product was loaded onto silica and purified via gradient silica gel chromatography (0→10% MeOH in DCM). The product containing fractions, were pooled, concentrated, and recrystallized from hexanes to obtain bis[2-(N-succinimidyl-oxycarbonyloxy)ethyl] disulfide (NHS-SS-NHS) as a white crystalline solid. ^{1}H-NMR (400 MHz, $CDCl_3$) δ = 4.58 (t, 4H), 3.05 (t, 4H), 2.84 (s, 8H).

3.5.8 Synthesis of AEMA-containing Polymers

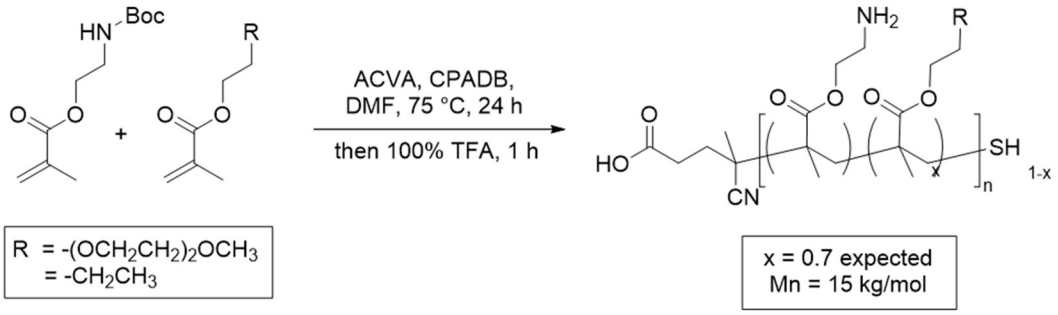

Polymers were synthesized on a 1 g scale. Triethylene glycol methyl ether methacrylate (TEGMA) and butyl methacrylate (BMA) were passed through a column of basic alumina prior to use. Boc-(2-aminoethyl) methacrylate (BocAEMA) was synthesized as described in Chapter 2 and recrystallized from 1:1 hexanes:DCM prior to use. All other materials were used as received. Reagents and a stir bar were loaded into a flame-dried round bottom flask and dissolved in 2.5 mL DMF. The vessel was sealed and stirred until all reagents were dissolved. Upon complete dissolution, the reaction was sparged for 30 min with argon and then placed in a pre-heated oil bath at 75 °C. The reaction was allowed to proceed for 24 h, then cooled and exposed to air to quench the reaction. 25 µL aliquots were collected for size exclusion chromatography. The polymers were protonated by addition of 500 µL TFA, precipitated into 97 mL of 1:1 diethyl ether:hexanes, and collected by centrifugation. All polymers were then treated with 3 mL TFA for 1 h to remove Boc protecting groups or as a control. After 1 h, the polymers were re-precipitated into 97 mL of 1:1 diethyl ether:hexanes, collected by centrifugation, and taken up in 5 mL dH_2O. The polymers were dialyzed sequentially for 24 h each against 0.5 M NaCl and dH_2O and then freeze dried to obtain the polymers as white or pink aerogels. Size exclusion chromatography (SEC) was conducted in DMF with 0.01 M LiBr additive at 50 ºC using a Tosoh EcoSEC system as described above. ^{1}H-NMR was conducted at 400 MHz in D_2O as described above.

3.6 Supplementary Information.

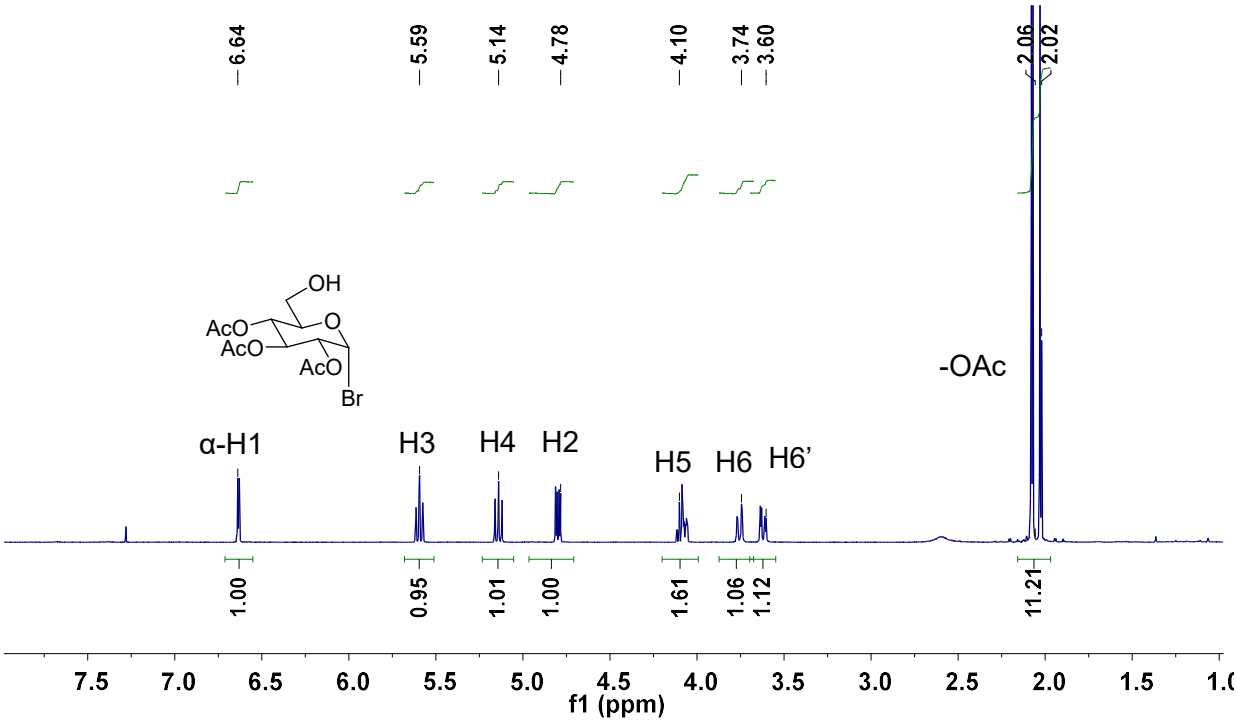

Figure S3.1: ^{1}H-NMR spectrum at 400 MHz in $CDCl_3$ of SPOE monomer I.

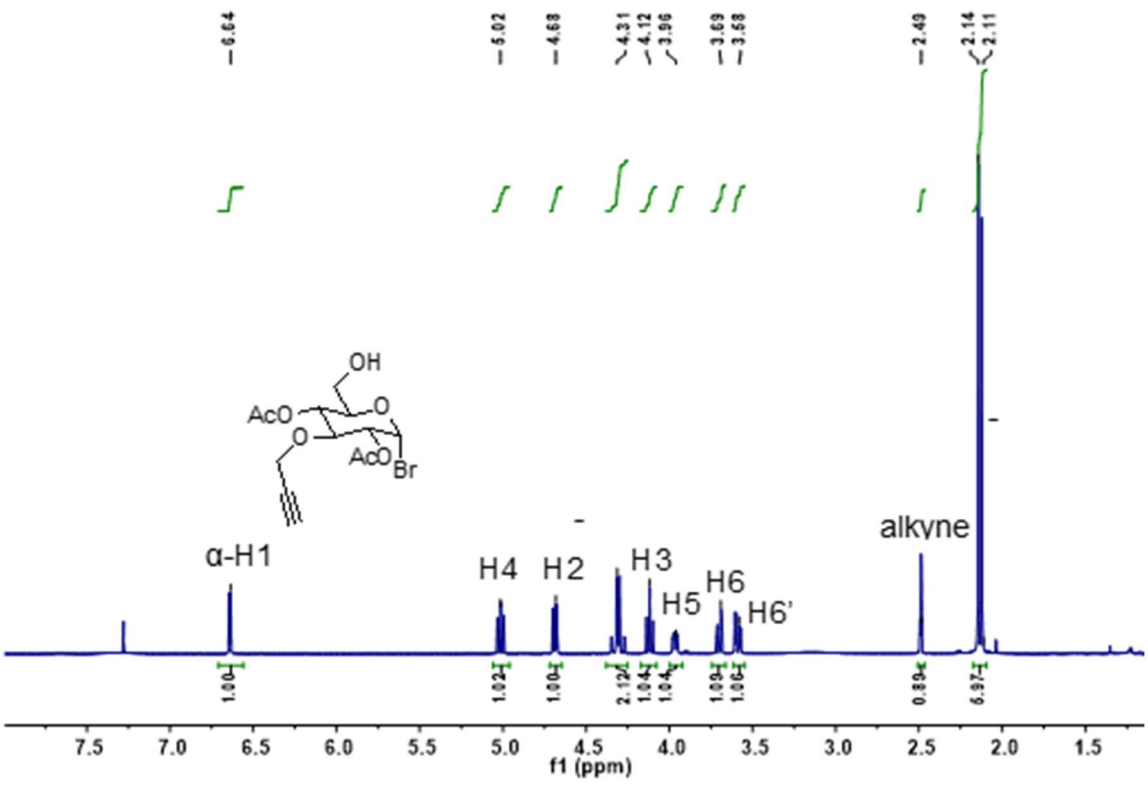

Figure S3.2: ^{1}H-NMR spectrum at 400 MHz in $CDCl_3$ of SPOE monomer II.

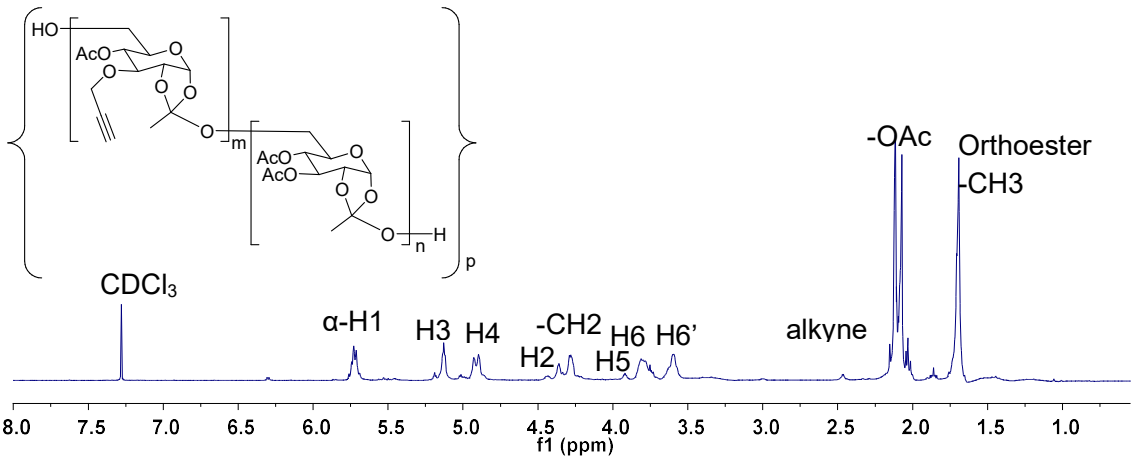

Figure S3.3: ^{1}H-NMR at 400 MHz in $CDCl_3$ of SPOE co-polymer.

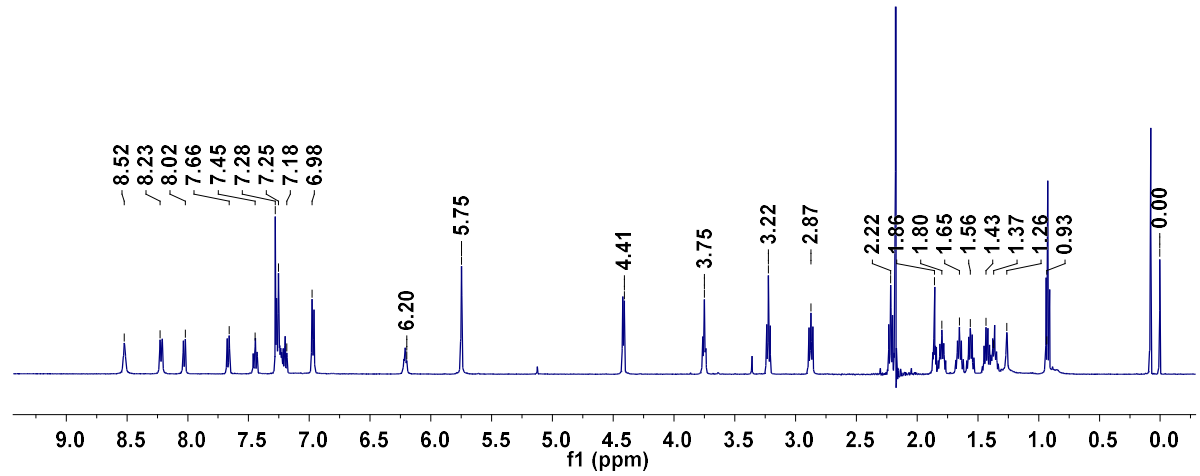

Figure S3.4: ^{1}H-NMR at 400 MHz in $CDCl_3$ of 2BXy azide (4).

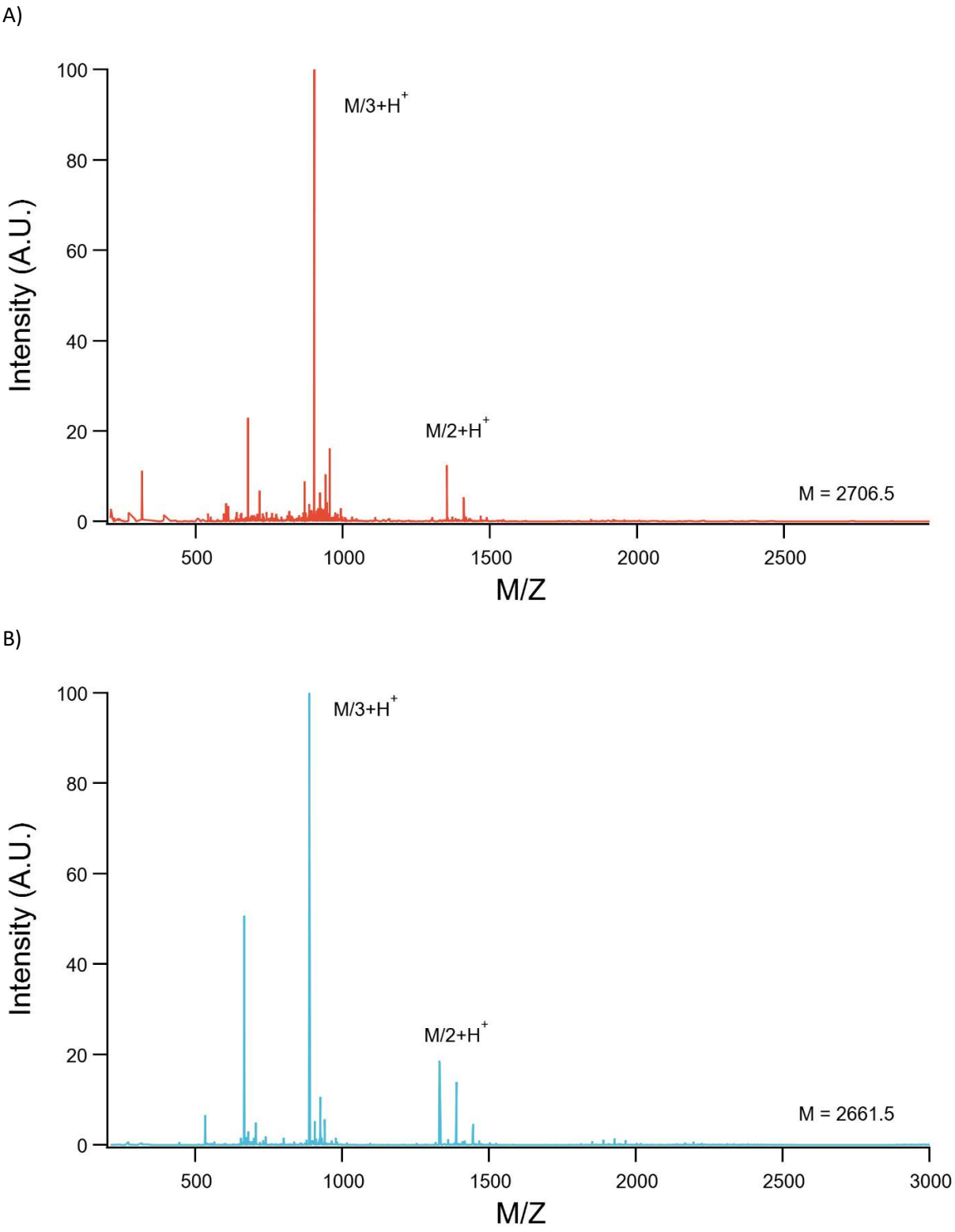

Figure S3.5: ESI-MS spectra of TAT-PEG_6-GWWWG prepared with N-terminal azide or alkyne functionalities using 6-azido-1-hexanoic acid or hex-5-yn-1-oic acid, respectively.

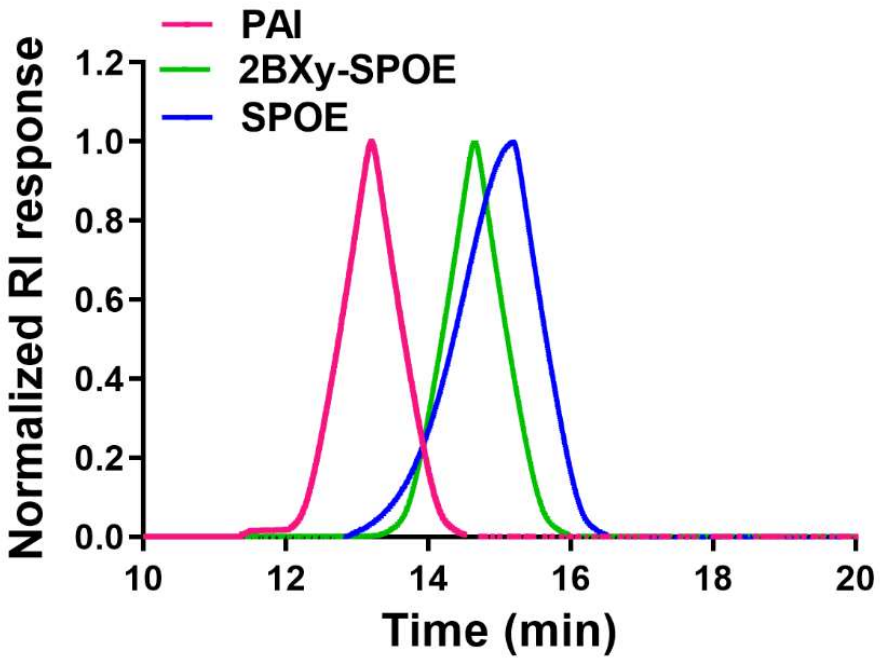

Figure S3.6: GPC analysis of SPOE, 2BXy-SPOE and PAI in DMF.

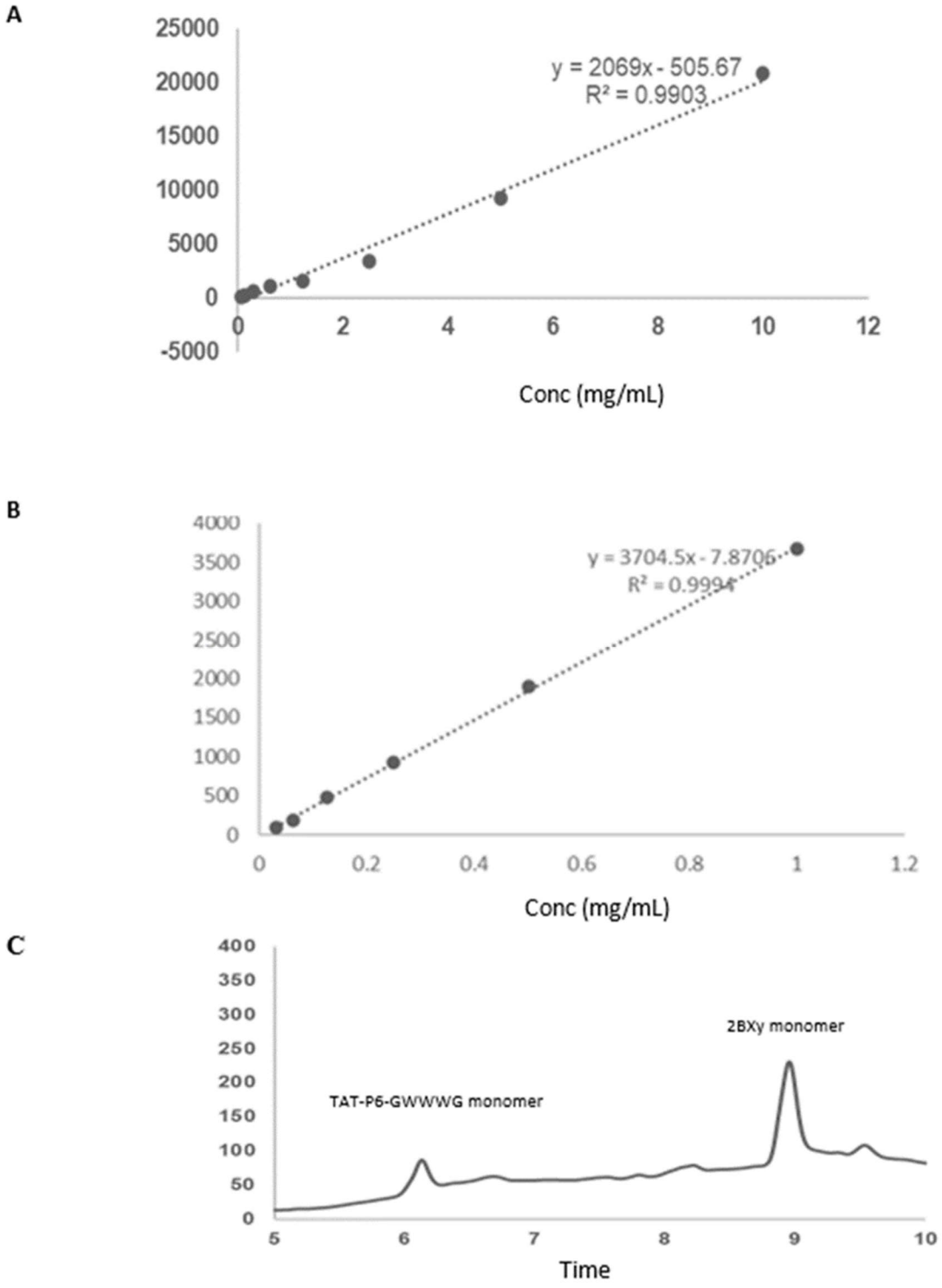

Figure S3.7: HPLC analysis of PAI. PAI was degraded by incubating in 0.1% TFA in 1:1 DMSO:water for 4 h. The resultant solution was injected in a C8 column on an Agilent analytical HPLC and monitored at 280 nm using the UV-vis detector. Two peaks were observed and confirmed as TAT-P6-GWWWG-glucose and 2BXy-glucose by ESI-MS. The concentration of TAT-P6-GWWWG peptide and 2Bxy in the polymer were determined by peak integration (C) based on standard curves for TAT-PEG_6-GWWWG (A) and 2BXy (B).

Entry	Theoretical calculation			Experimental quantification		
	Ratios	TLR7/8a	TATGWWWG	TLR 7/8a	TATGWWWG	Ratios
1	(0.5:1)	1	2	0.8	1.8	(0.44:1)
2	(1:1)	2	2	2.1	1.8	(1.2:1)
3	(1.5:1)	3	2	2.7	1.8	(1.5:1)
4	(2:1)	4	2	3.9	1.8	(2.2:1)

Figure S3.8: Ratio of TLR7/8 agonist and TAT-PEG_6-GWWWG in polymer library as determined by HPLC.

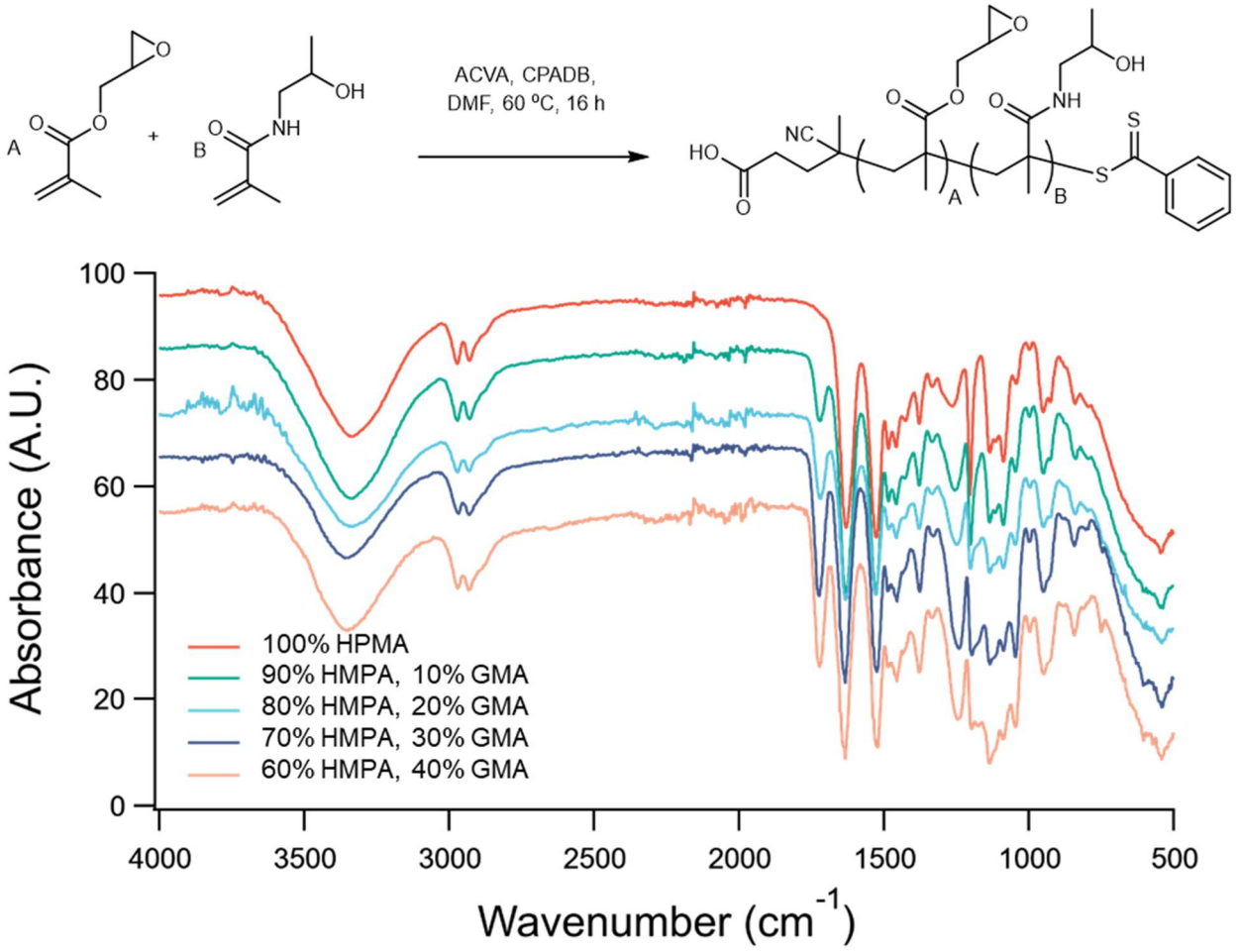

Figure S3.9: FT-IR characterization of HPMA-GMA co-polymers with 0-40% glycidyl content. Presence of ester peak at 1640 cm^{-1} increases proportionally with increasing GMA molar ratio, indicating successful formation of copolymers.

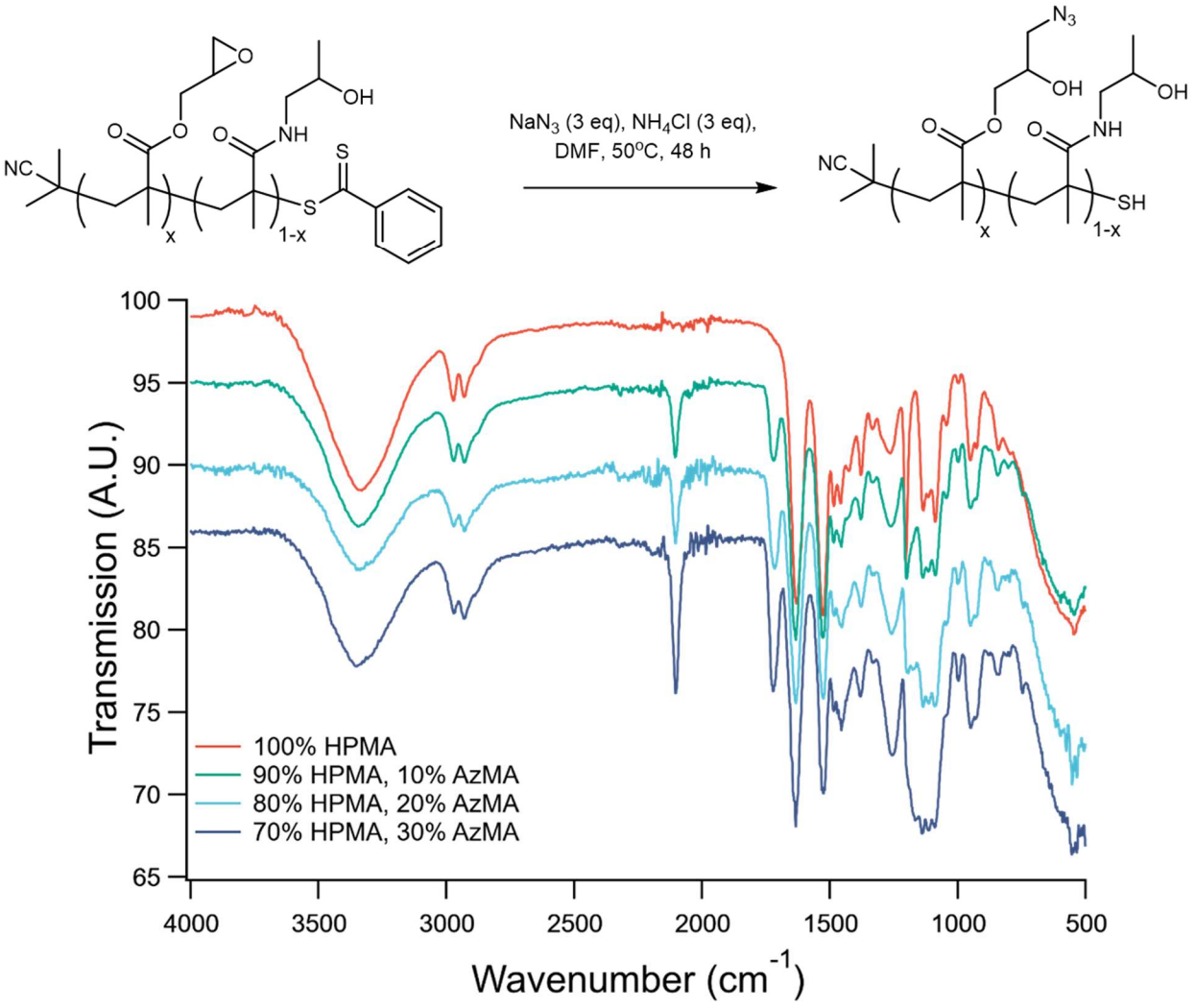

Figure S3.10: FT-IR characterization of HPMA-GMA co-polymers with 0-40% glycidyl content after ring opening reaction with sodium azide. The spectra show presence of an increasing azide peak (2100 cm^{-1}) as glycidyl content in the native polymer backbone increases.

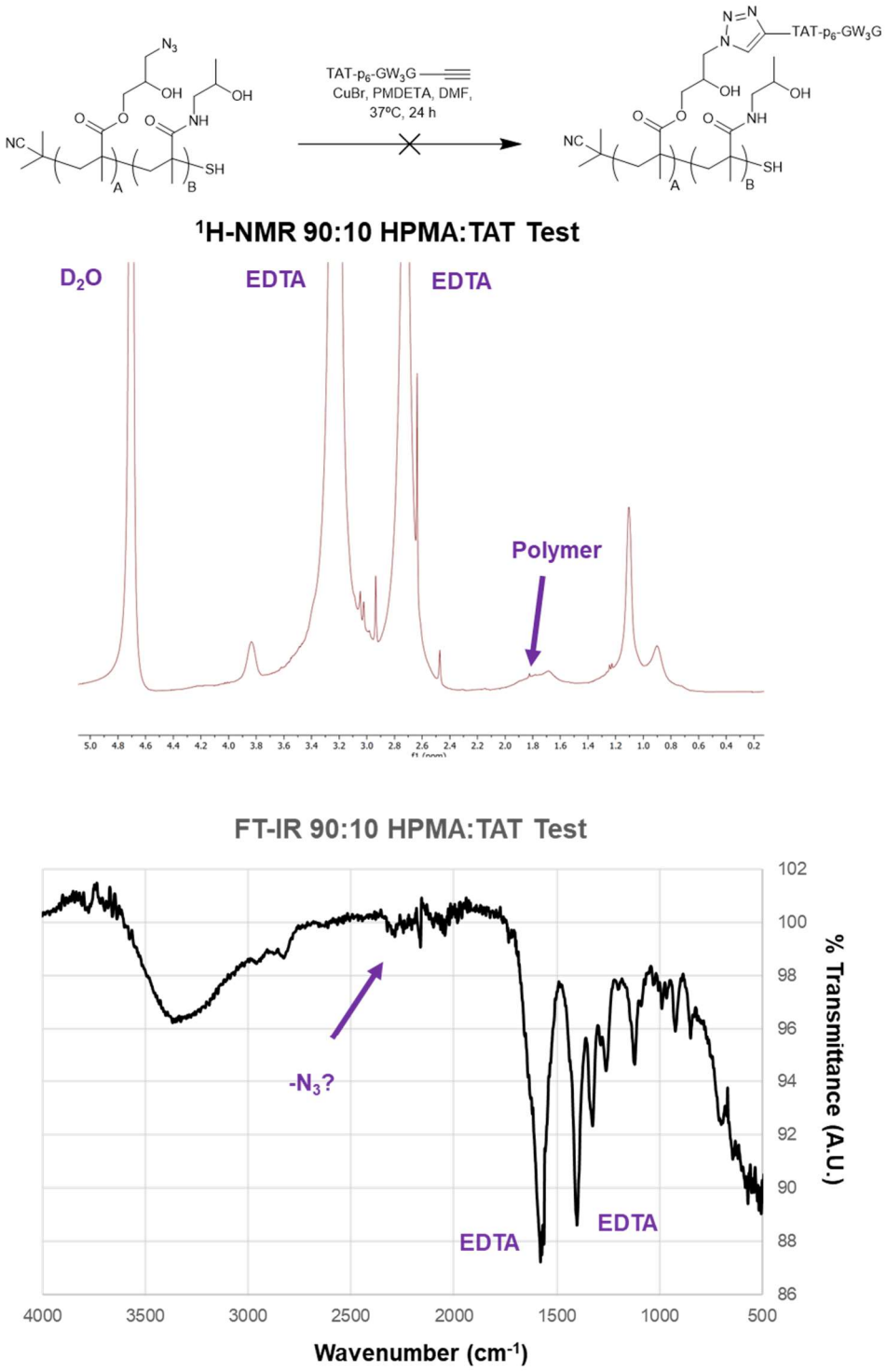

Figure S3.11: ^{1}H-NMR (top, 400 MHz in D_2O) and FT-IR (bottom) characterization of residues collected after Cu(I)-mediated click reaction between TAT-PEG6-GWWWG-alkyne and azide-modified methacrylates. Functionalized polymers were purified by dialysis against 0.5 M EDTA to remove copper ions followed by deionized water to remove EDTA; however, based on these characterization data, it was observed that EDTA chelates the methacrylate polymer backbone and could not be effectively removed.

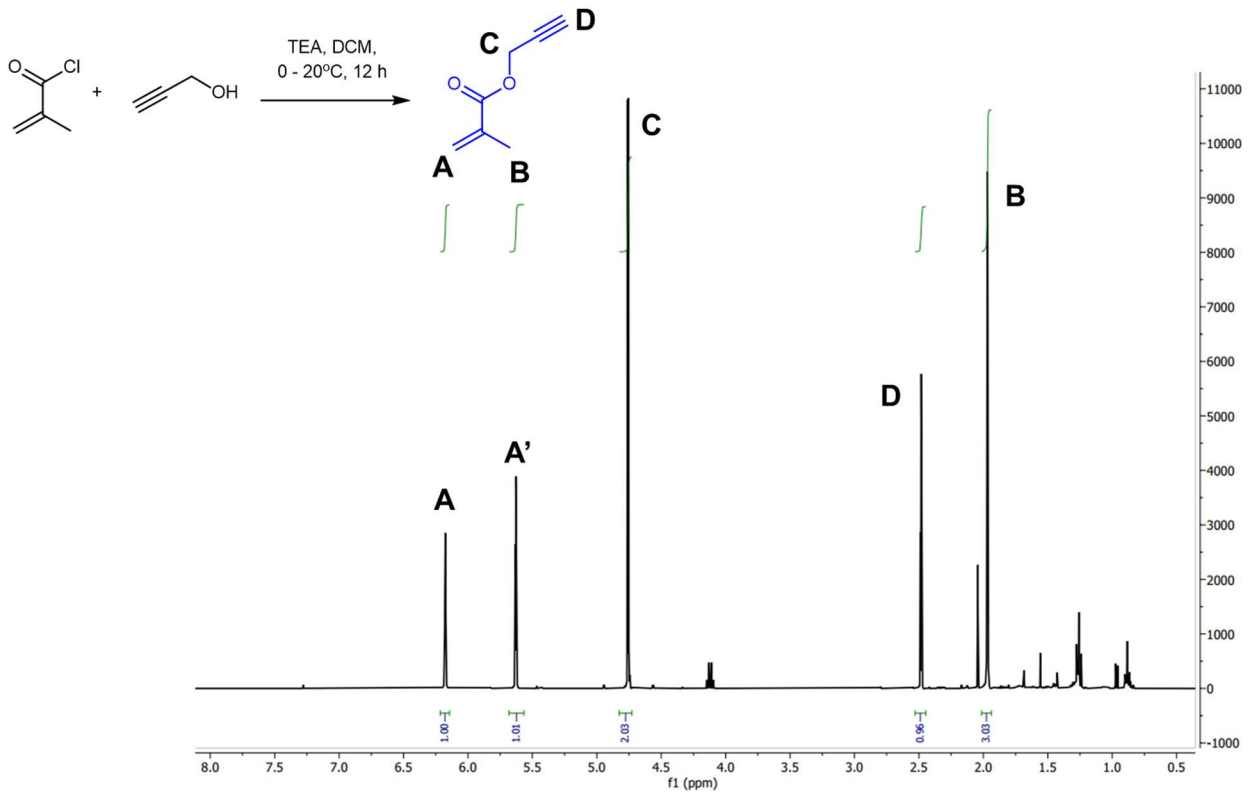

Figure S3.12: ^{1}H-NMR at 400 MHz in $CDCl_3$ of propargyl methacrylate (PrMA) monomer.

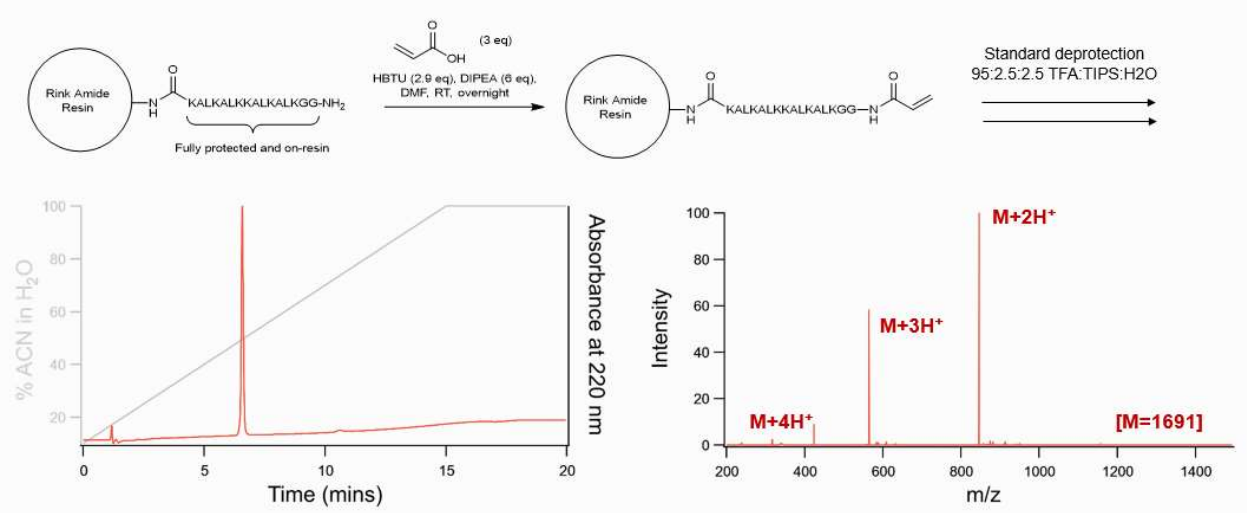

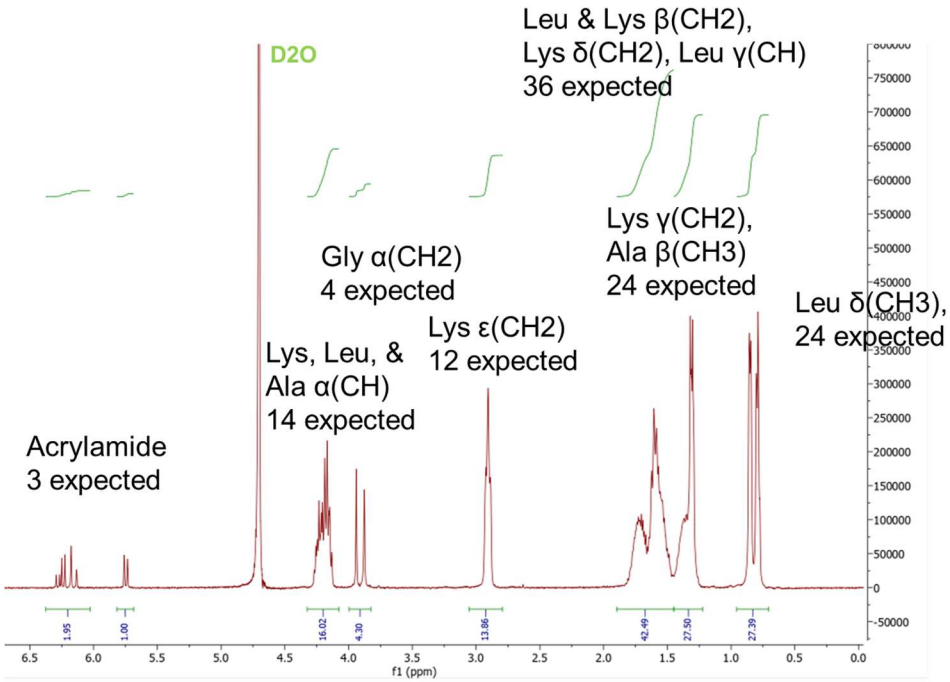

Figure S3.13: Characterization of KLA peptide. Scheme for the on-resin modification of KLA peptide with acrylic acid, along with HPLC purity analysis, ESI-MS molecular weight determination, and ^{1}H-NMR compositional analysis at 500 MHz in D_2O.

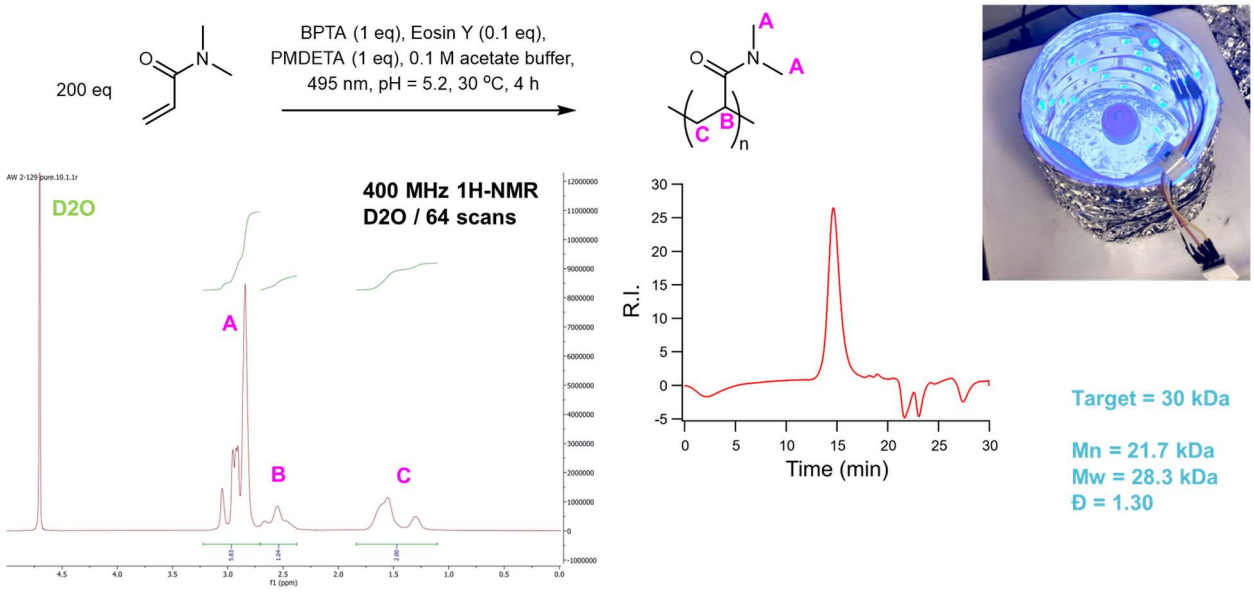

Figure S3.14: Validation of the effectiveness of the LED reactor for PET-RAFT synthesis of DMA. DMA was synthesized in acetate buffer using the reactor vessel shown and characterized by ^{1}H-NMR at 400 MHz in D_2O and GPC in DMF.

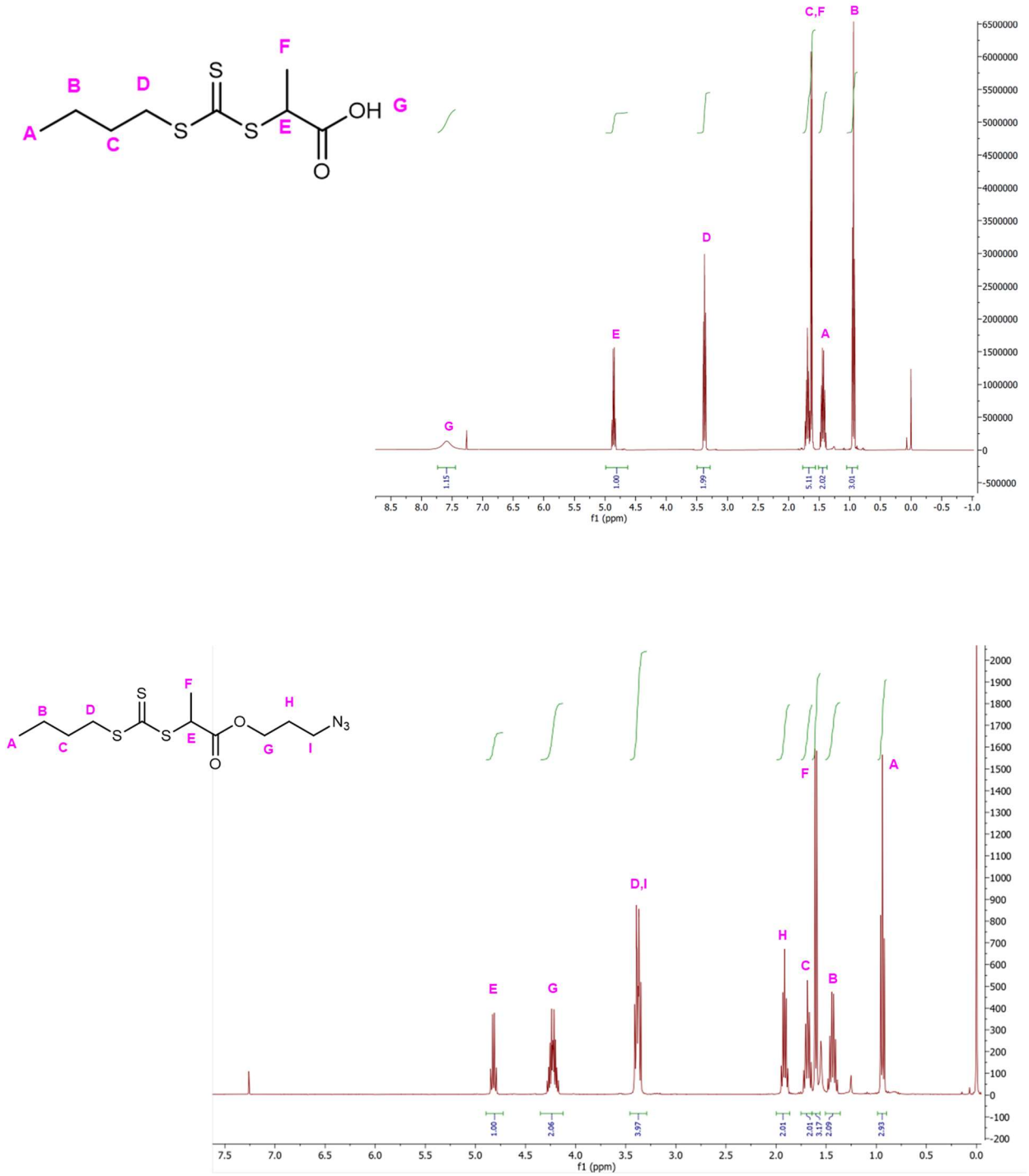

Figure S3.15: ^{1}H-NMRs at 400 MHz in $CDCl_3$ of **6** and **7**.

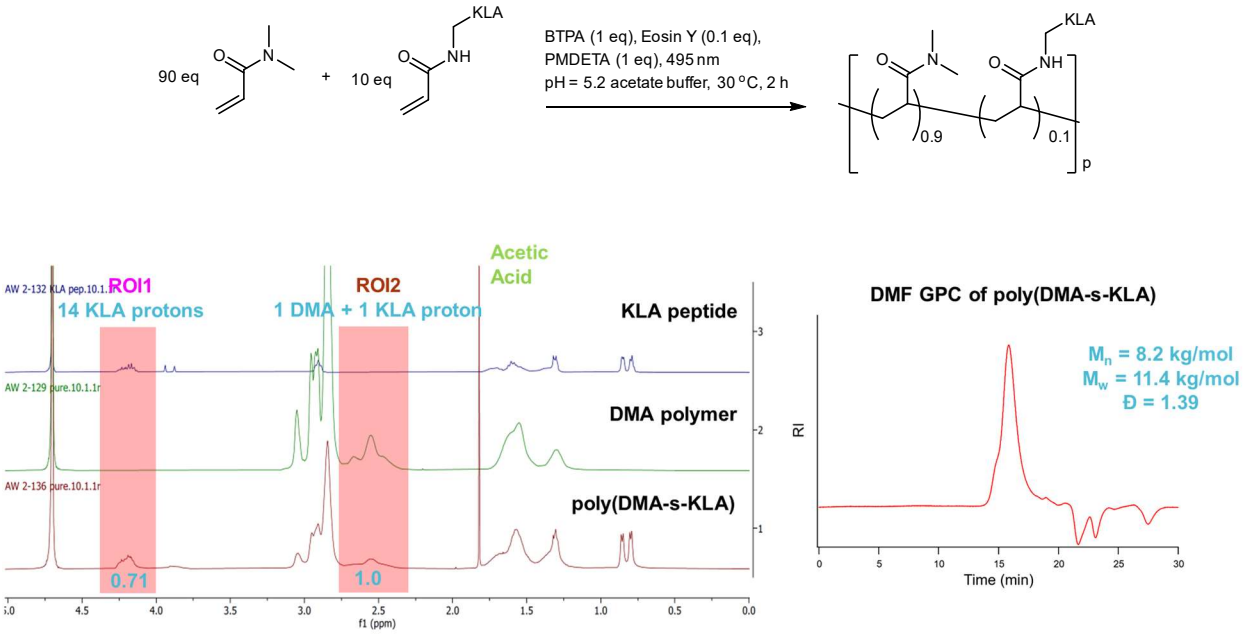

Figure S3.16: Polymerization of a poly(DMA-s-KLA) co-polymer using peptide acrylamide-based monomers. The polymers were characterized by ^{1}H-NMR at 400 MHz in D_2O (with peaks referenced relative to a poly(DMA) and KLA peptide controls) and DMF GPC.

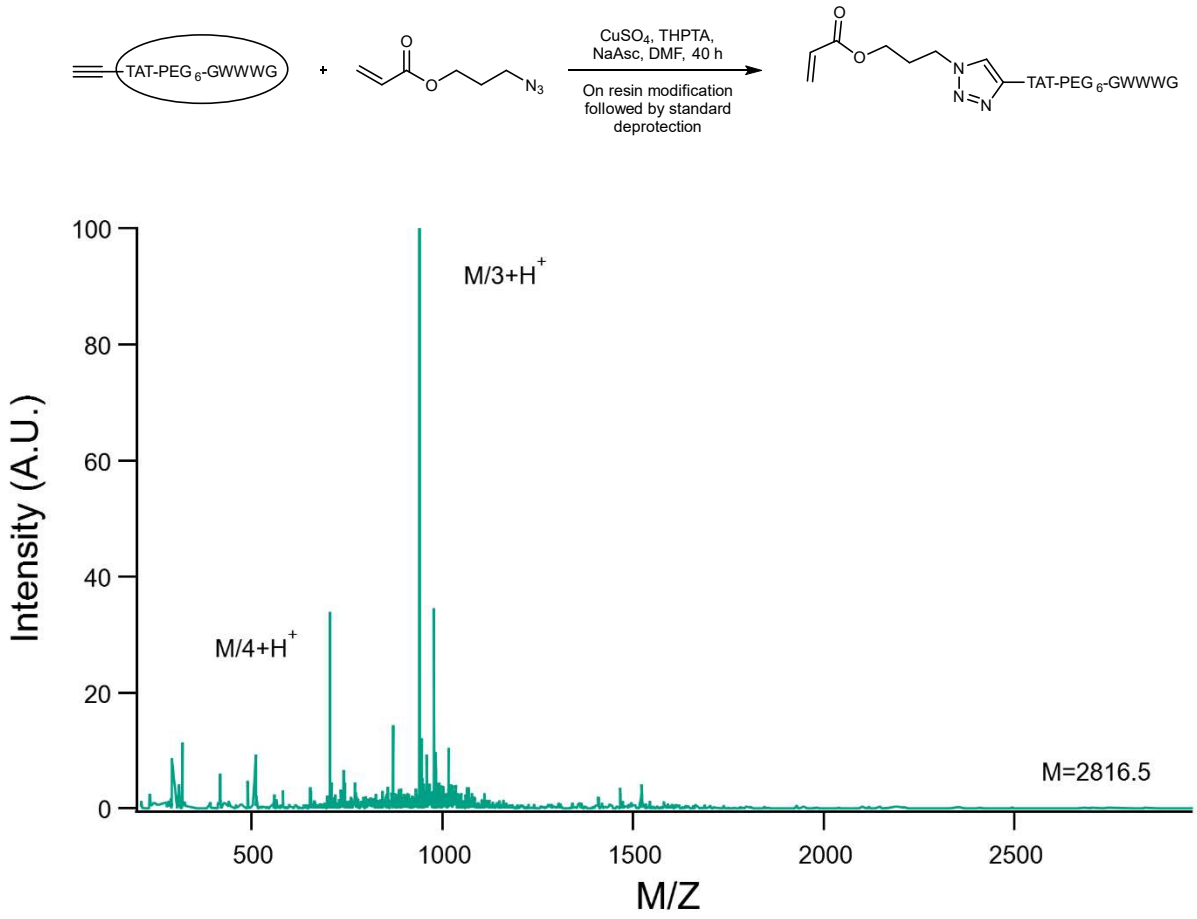

Figure S3.17: Scheme and ESI-MS characterization of successful functionalization after deprotection and purification of TAT-acrylamide monomer.

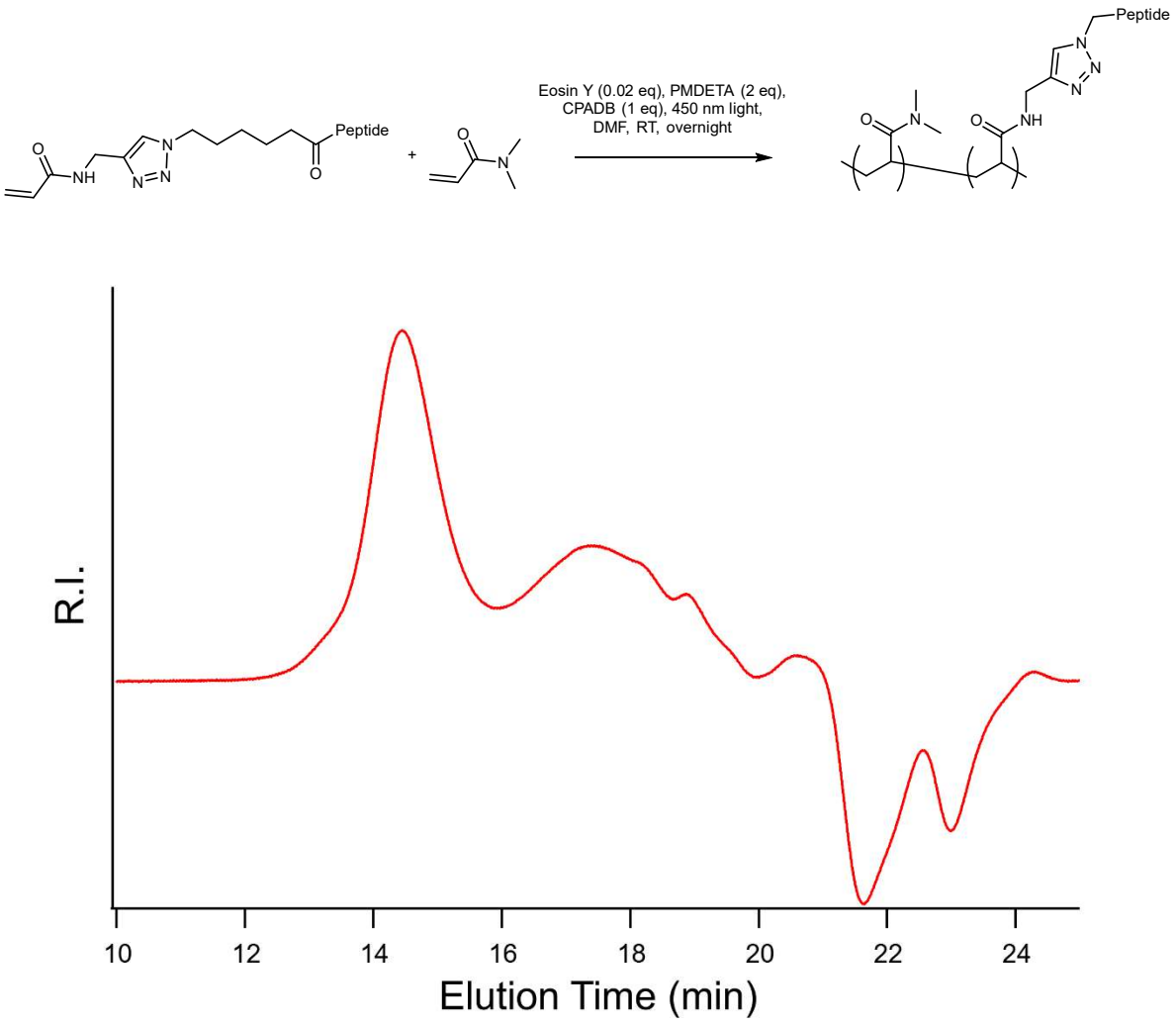

Figure S3.18: Scheme and crude GPC trace of TAT-acrylamide polymerized with benzodithioate CTA. Based on the GPC, it was found that the major product containing peak had a Mn ≈ 26,000 g/mol and Đ ≈ 1.3.

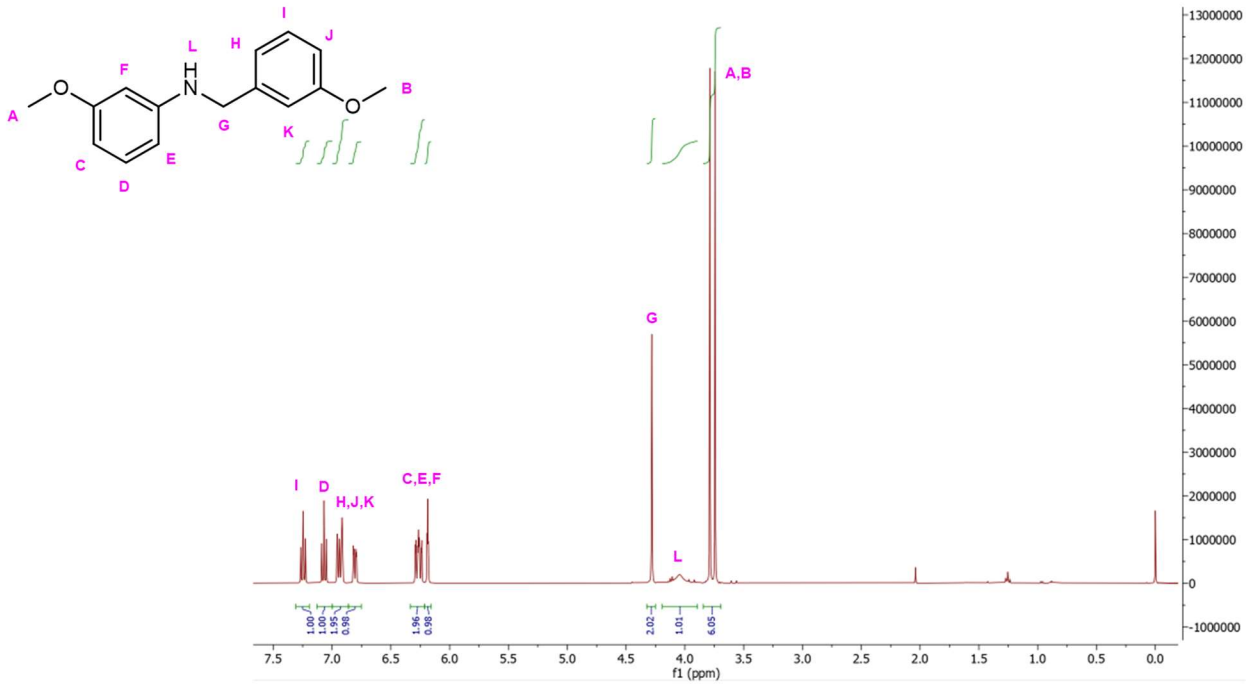

Figure S3.19: ^{1}H-NMR at 400 MHz in $CDCl_3$ of **8**.

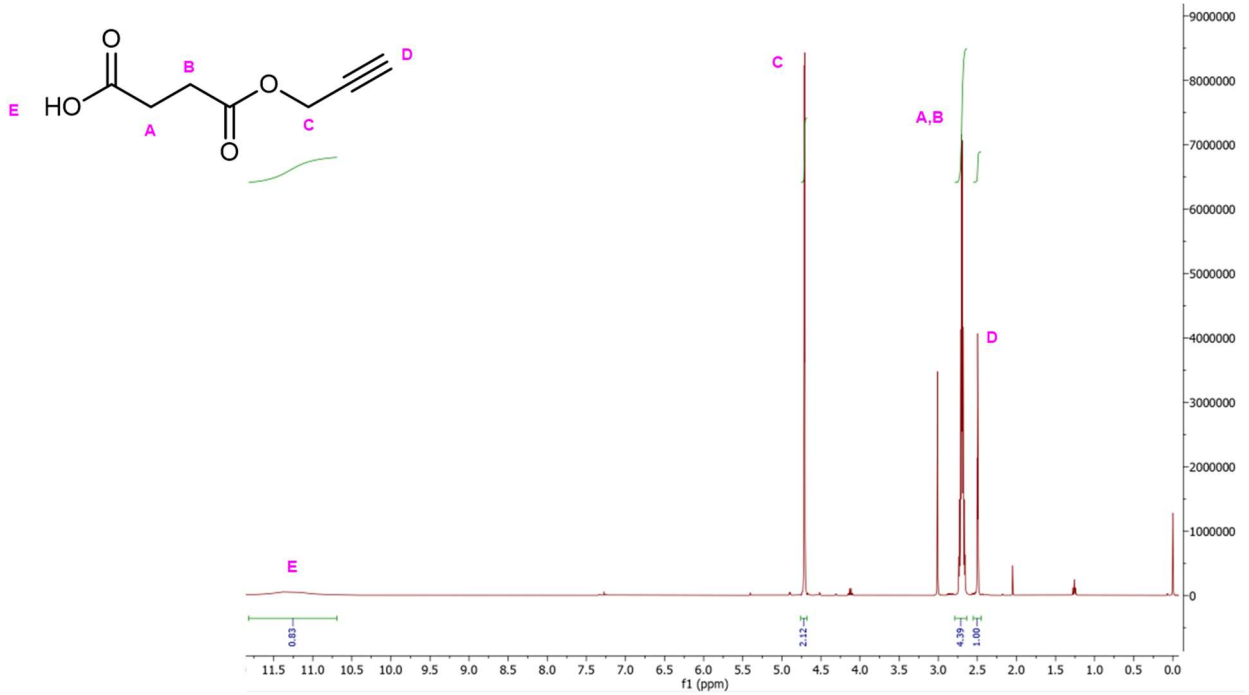

Figure S3.20: ^{1}H-NMR at 400 MHz in $CDCl_3$ of **9**.

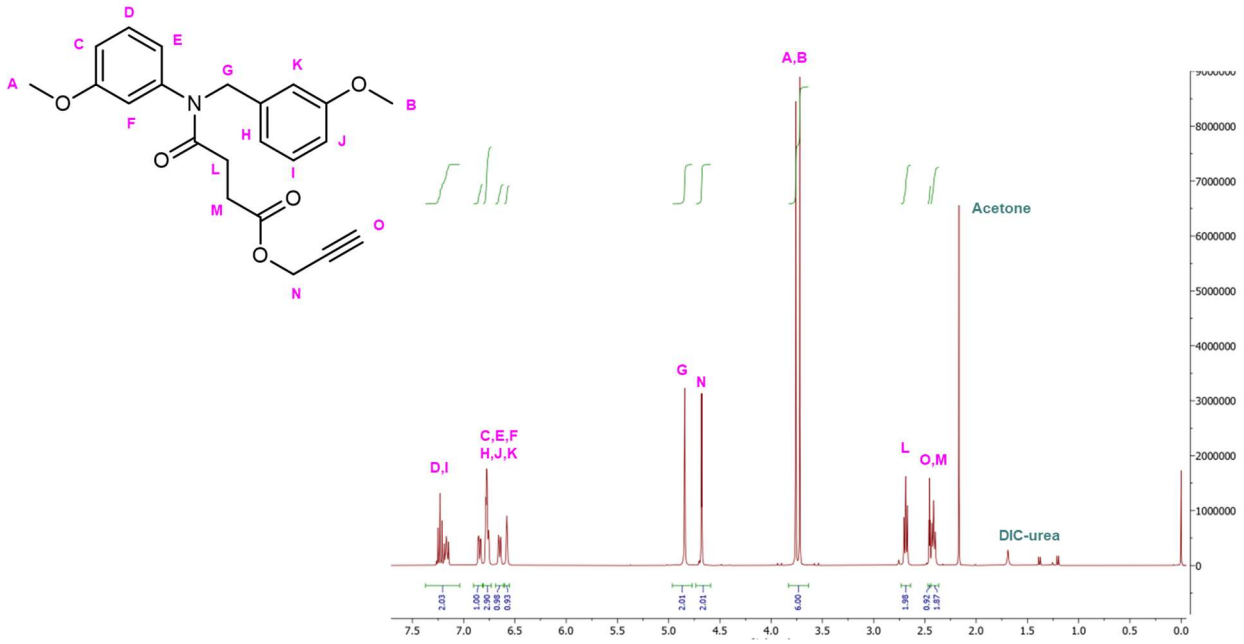

Figure S3.21: ^{1}H-NMR at 400 MHz in $CDCl_3$ of **10**.

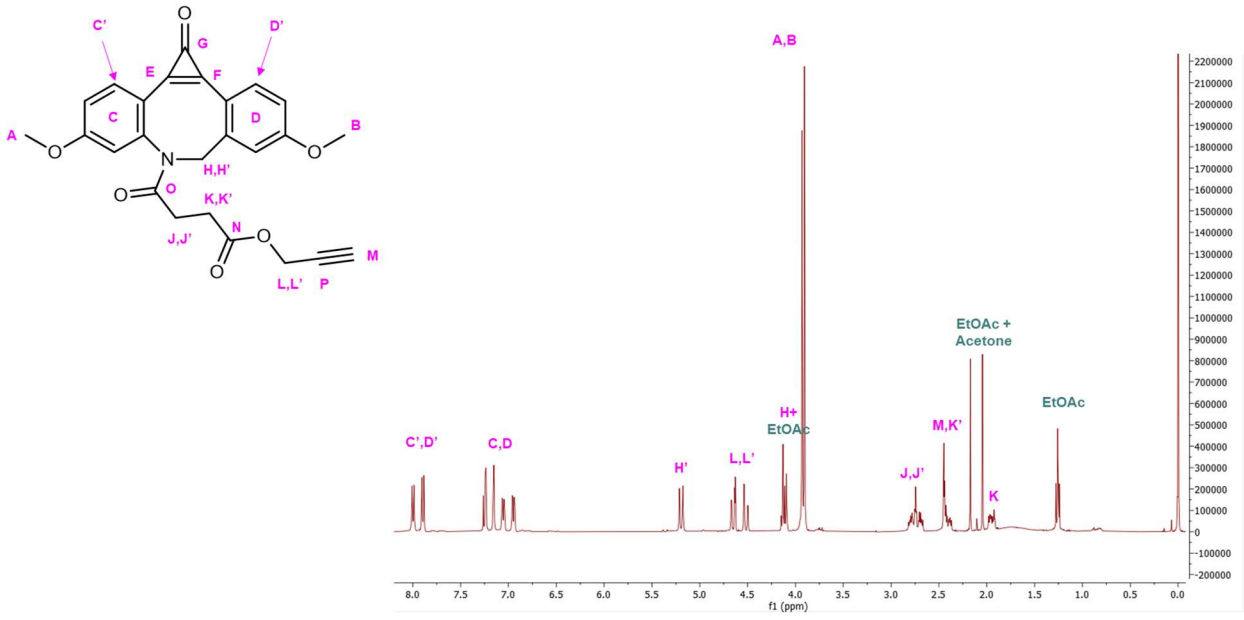

Figure S3.22: ^{1}H-NMR at 400 MHz in $CDCl_3$ of **11**.

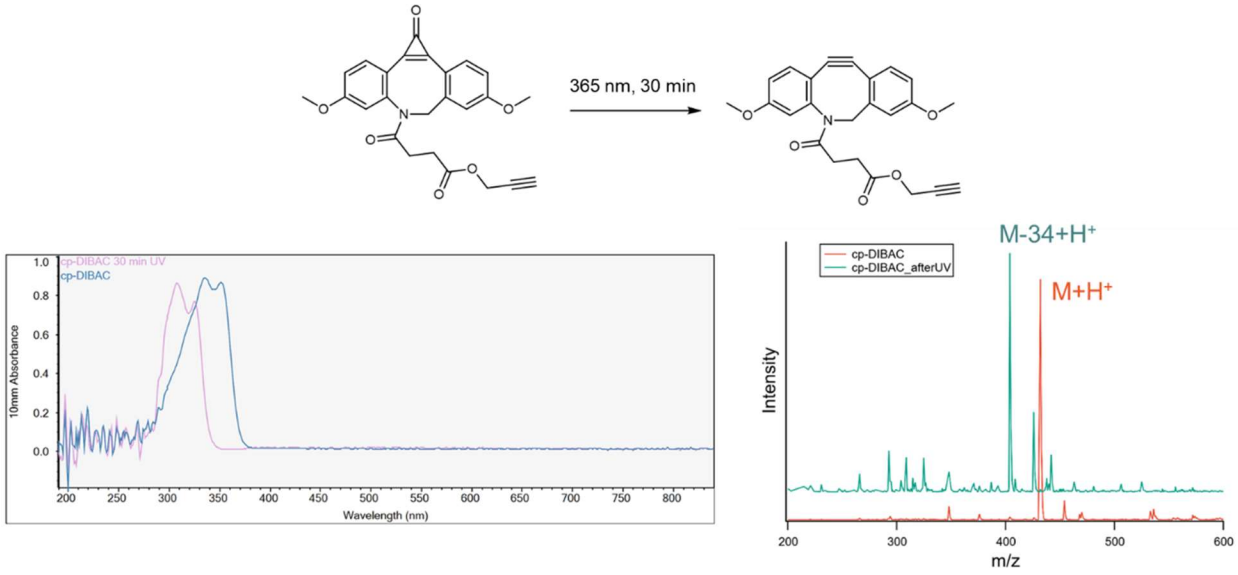

Figure S3.23: Deprotection of cp-DIBAC (**11**) was confirmed by UV-VIS and ESI-MS.

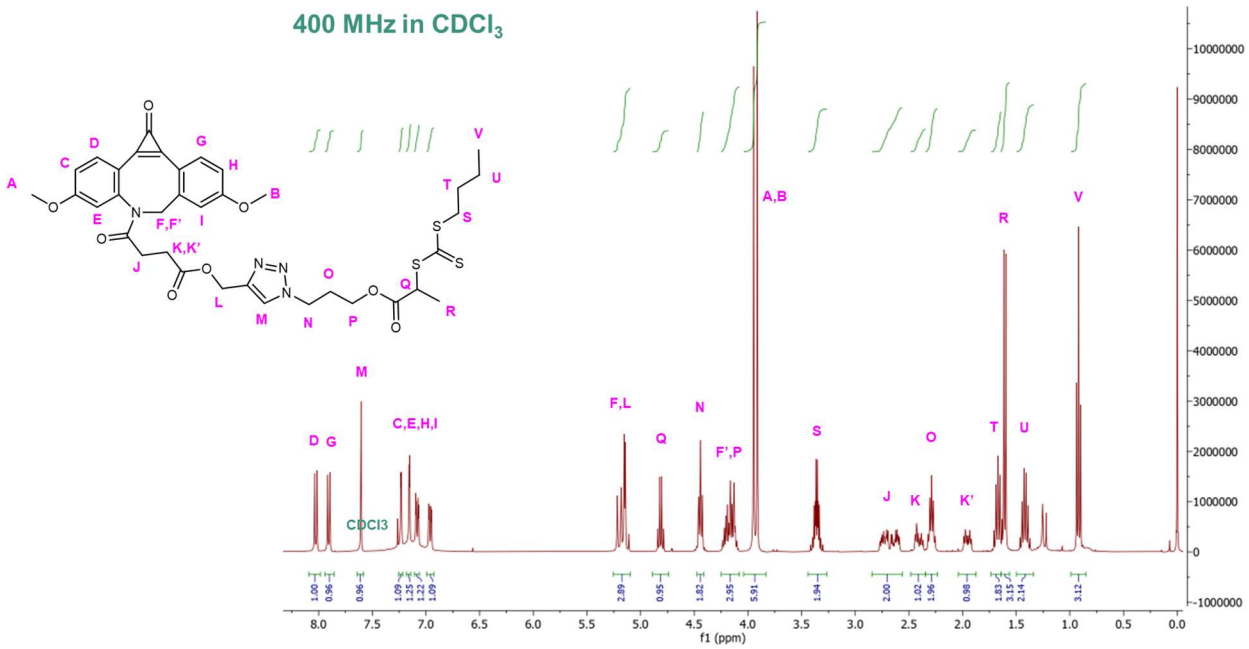

Figure S3.24: ^{1}H-NMR at 400 MHz in $CDCl_3$ of **12**.

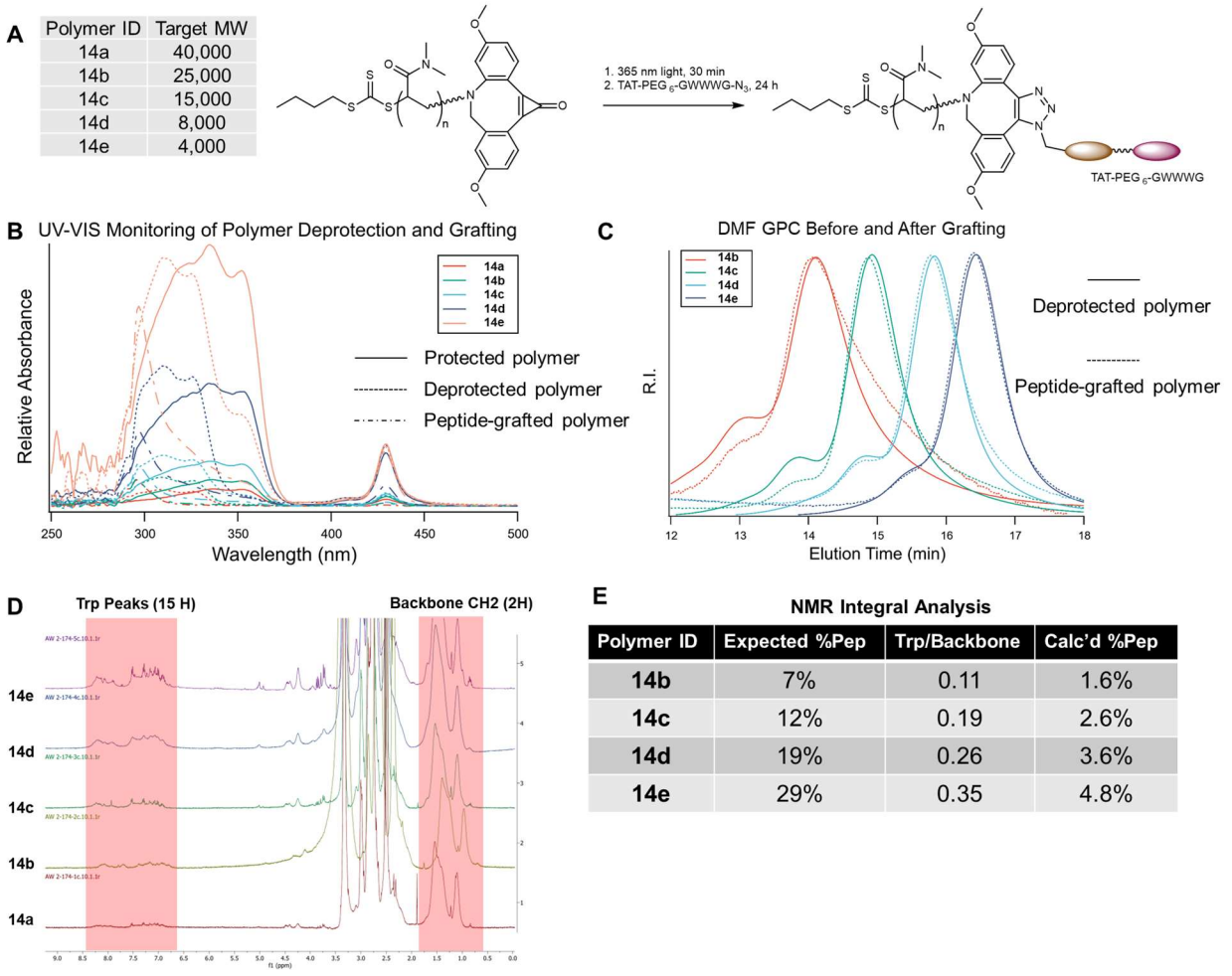

Figure S3.25: Synthesis and characterization of **14a-e**. A) Scheme of synthetic strategy and target molecular weights. B) UV-VIS monitoring of cp-DIBAC at each point in the synthesis. C) GPC of polymers before and after grafting of peptides via Cu-free click chemistry. D) ^{1}H-NMR spectra (400 MHz in DMSO-d6) and E) integral analysis to estimate the percentage of peptide groups grafted to the polymer using tryptophan peaks as a proxy.

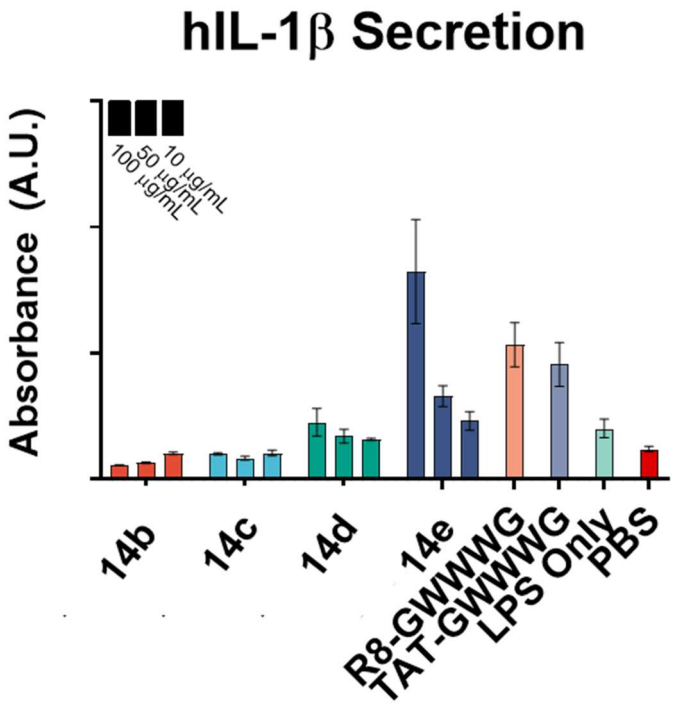

Figure S3.26: In-vitro characterization of **14b-e** using HEK Blue IL-1β assay. Lower graft densities of TAT-PEG_6-GWWWG resulted in lower IL-1β production.

ID	Mon/MW/#pep	Mn (GPC)	Đ (GPC)
15a	DEA/10k/1	8,500	1.72
15b	DEA/8k/1	8,300	1.57
15c	DEA/6k/1	6,600	1.88
15d	DEA/4k/1	3,600	2.49
15e	TEGA/10k/1	11,200	1.21
15f	TEGA/8k/1	10,600	1.19
15g	TEGA/6k/1	7,600	1.18
15h	NIPAm/12k/1	24,700	1.31
15i	NIPAm/8k/1	15,700	1.66
15j	NIPAm/6k/1	11,900	1.26

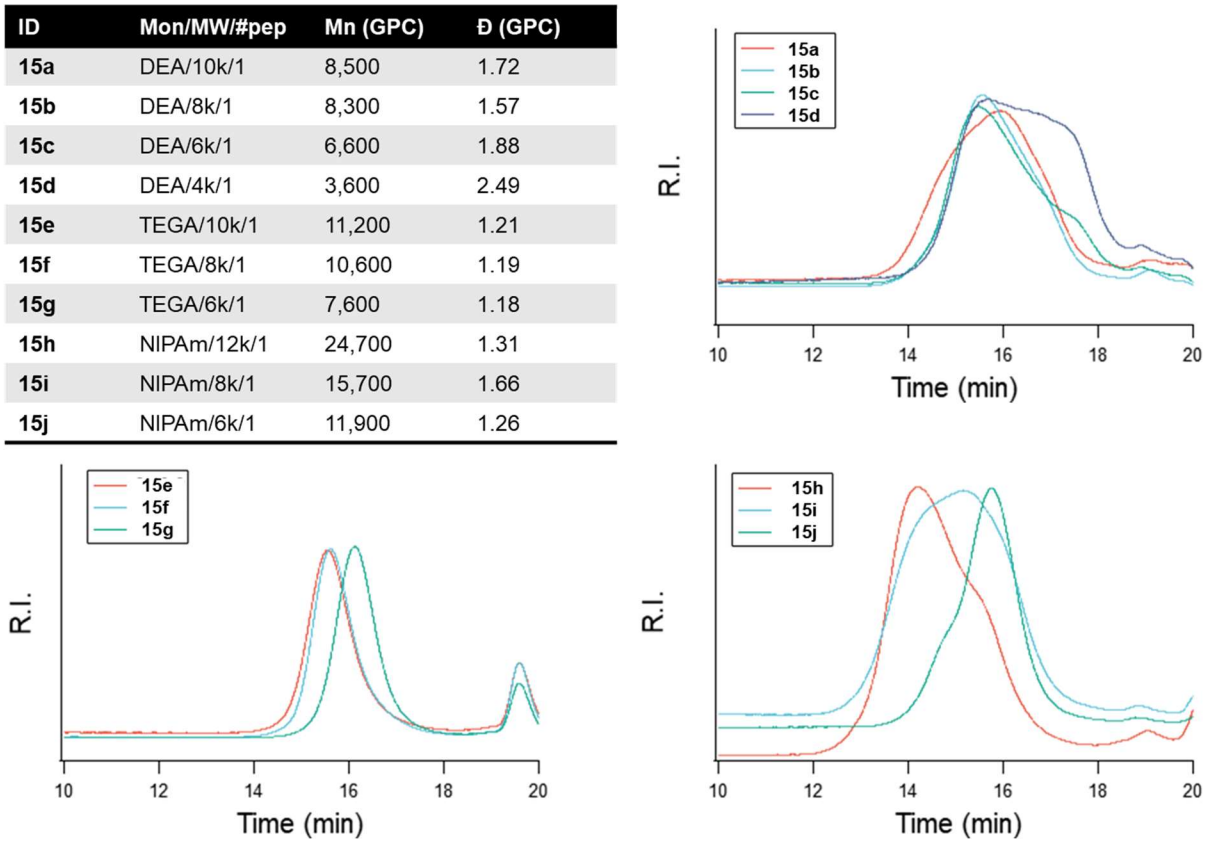

Figure S3.27: Synthesis of various polymers with cp-DIBAC CTA. A small library of polymers **15a-j** were synthesized using the cp-DIBAC CTA and various monomers, including N,N-diethylacrylamide (DEA), Triethylene glycol methyl ether acrylamide (TEGA), and N-isopropyl acrylamide (NIPAm) at different molecular weights. Only the TEGA containing polymers were found to polymerize with narrow dispersities, based on GPC analysis of the crude reaction mixtures in DMF.

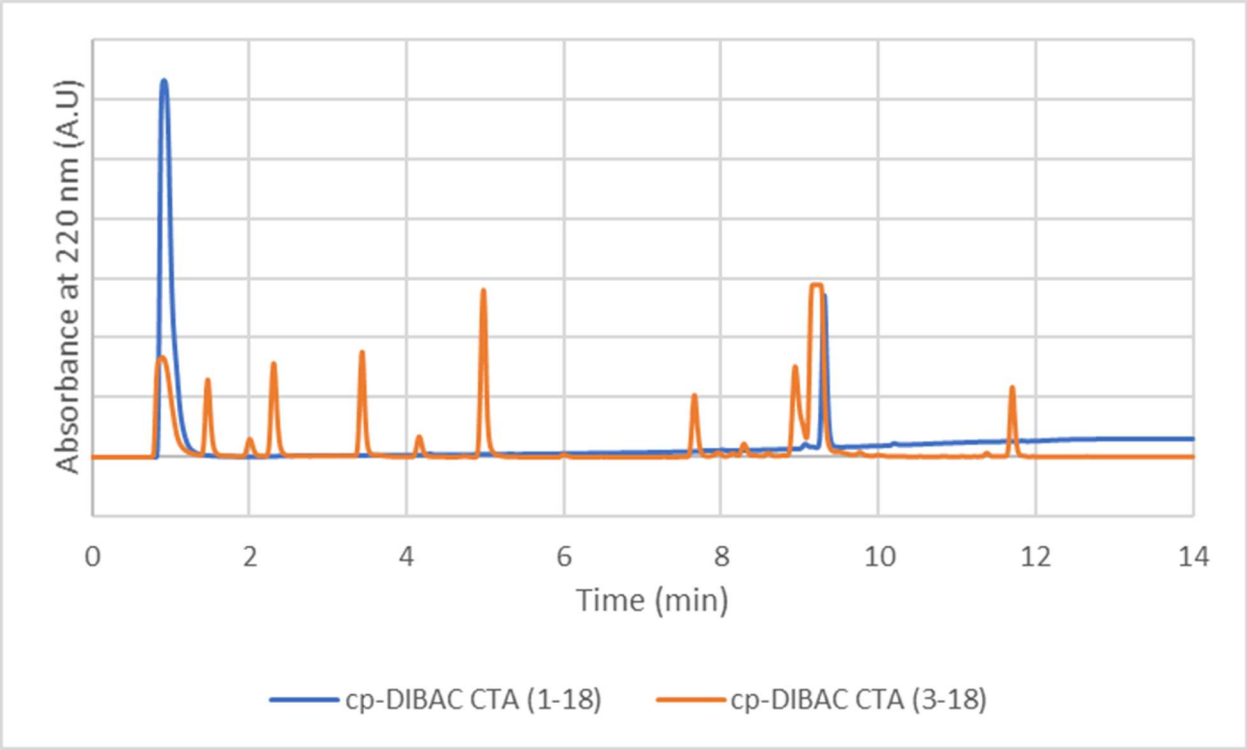

Figure S3.28: HPLC trace demonstrating decomposition of **12** over two months (Jan 18, 2021 to March 18, 2021) while stored at -80 °C in anhydrous DMSO. 5 nmol of a DMSO (5 µL of 1 mM stock) was injected onto an Agilent Poroshell 120 EC-C18 column (3 µm, 100 Å, 50 x 4.6 mm) and analyzed using a 10 min gradient elution (10-100% ACN in water with 0.1% TFA).

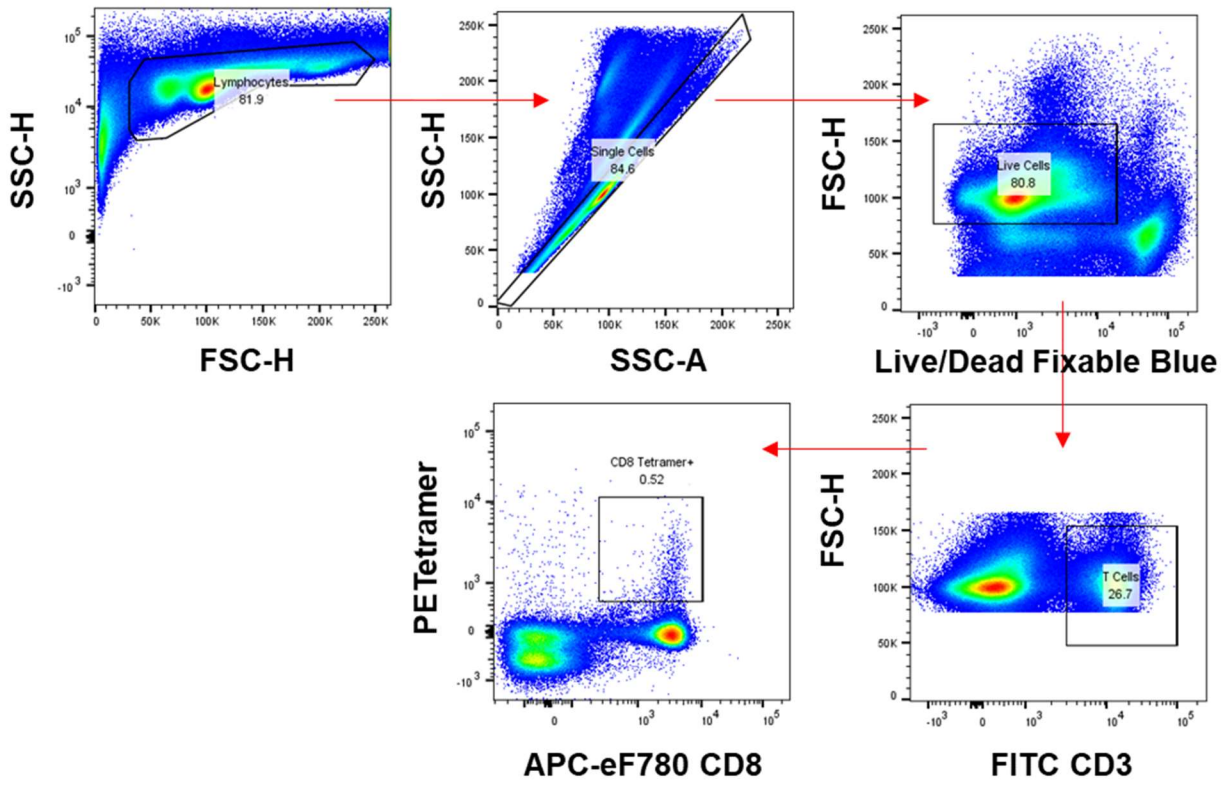

Figure S3.29: Gating strategy for tetramer staining data presented in **Figure 3.4E**.

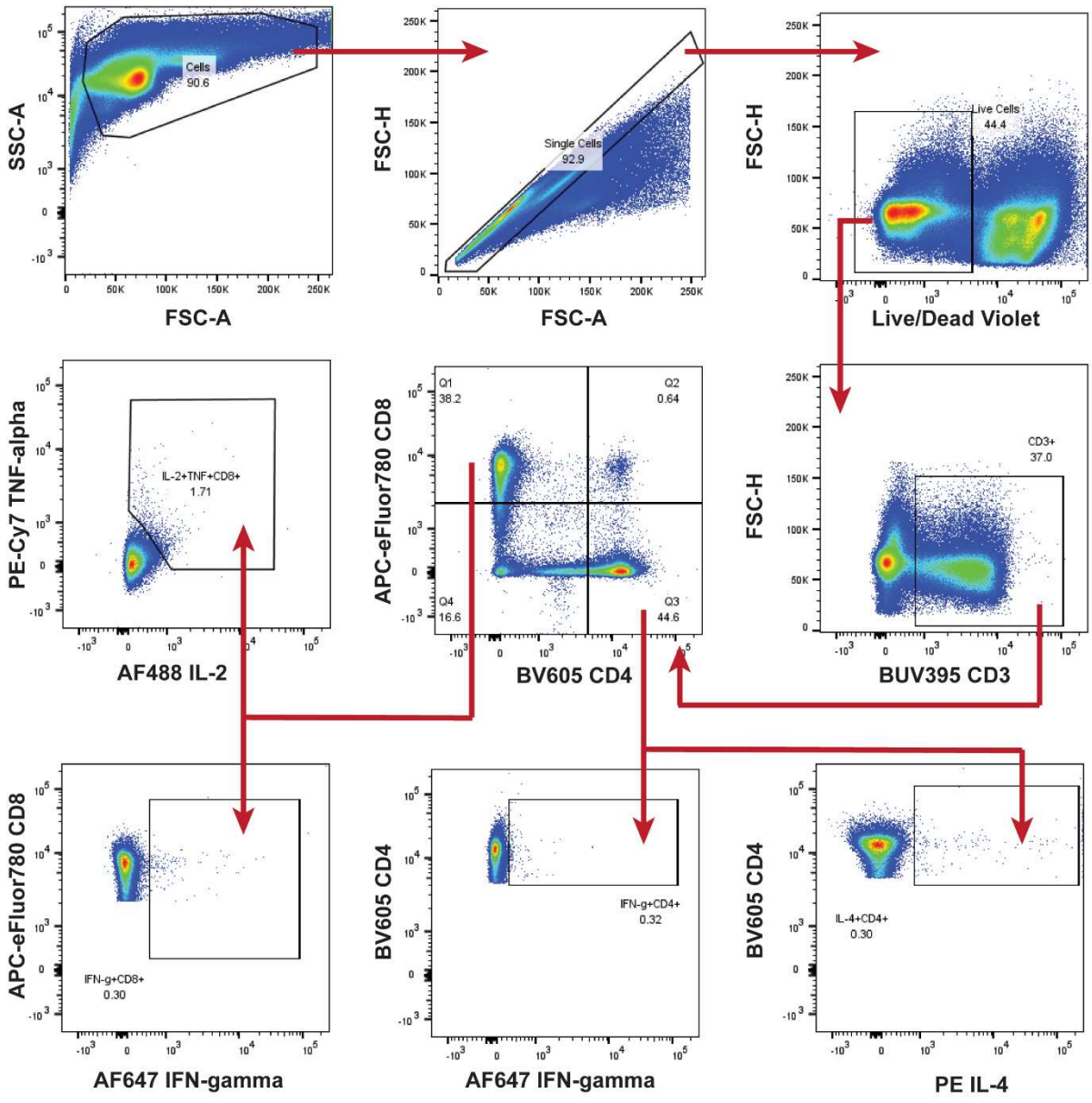

Figure S3.30: Gating strategy for intracellular cytokine secretion data presented in **Figure 3.5D**.

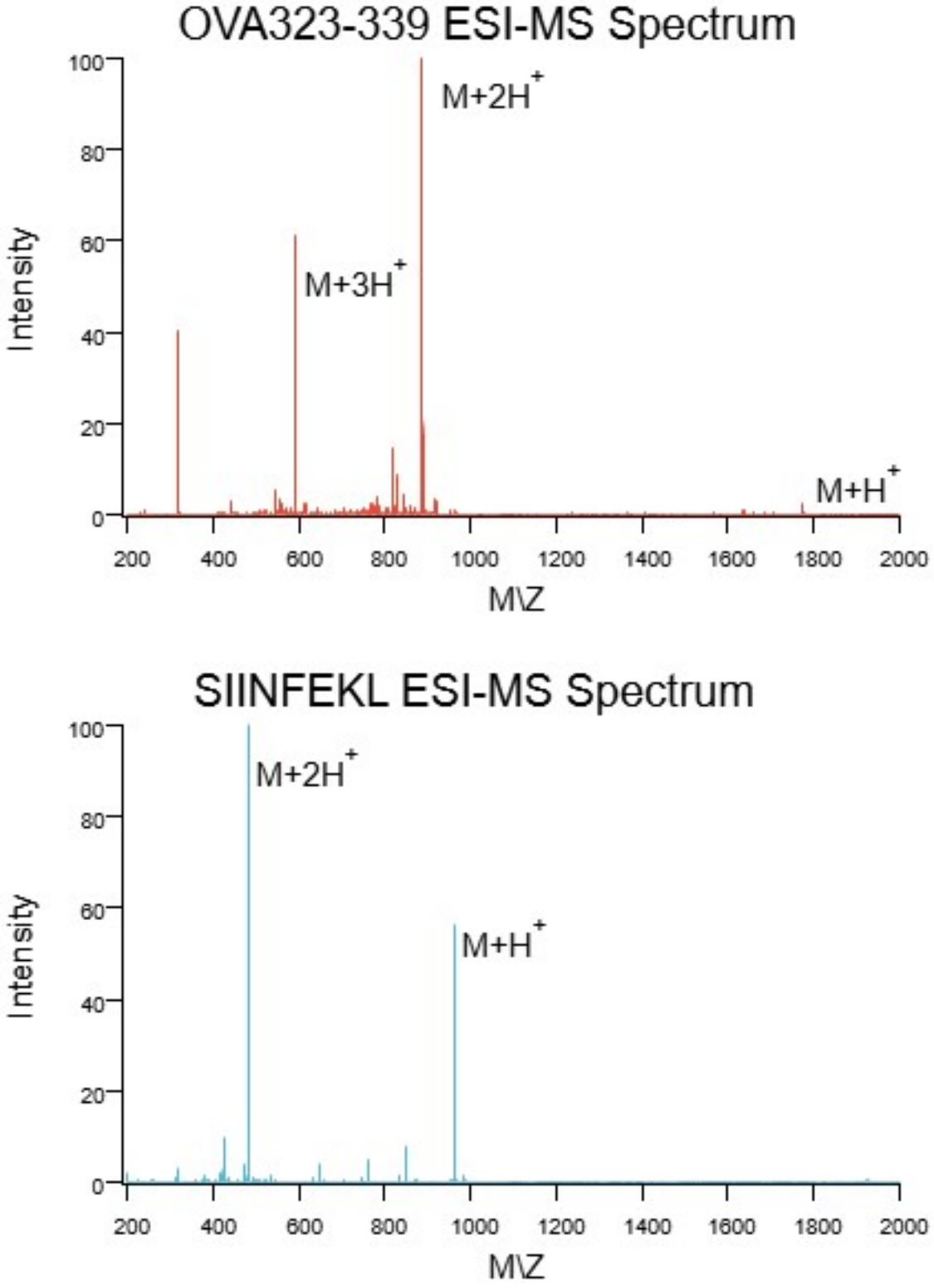

Figure S3.31: ESI-MS Spectra of SIINFEKL and OVA323-339 peptides prepared via solid-phase peptide synthesis for T cell restimulation studies.

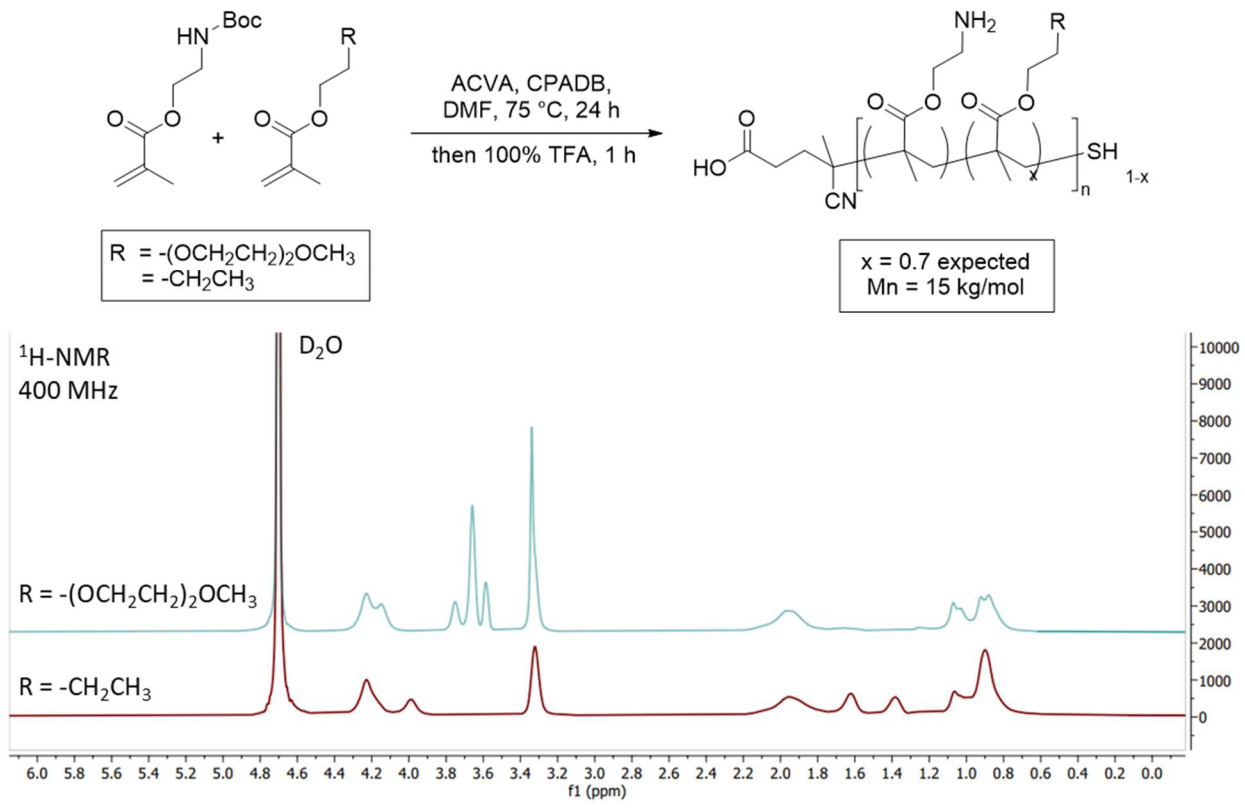

Figure S3.32: Synthesis and characterization of 15 kg/mol polymers for nanogel studies. ^{1}H-NMRs were conducted at 400 MHz in D_2O.

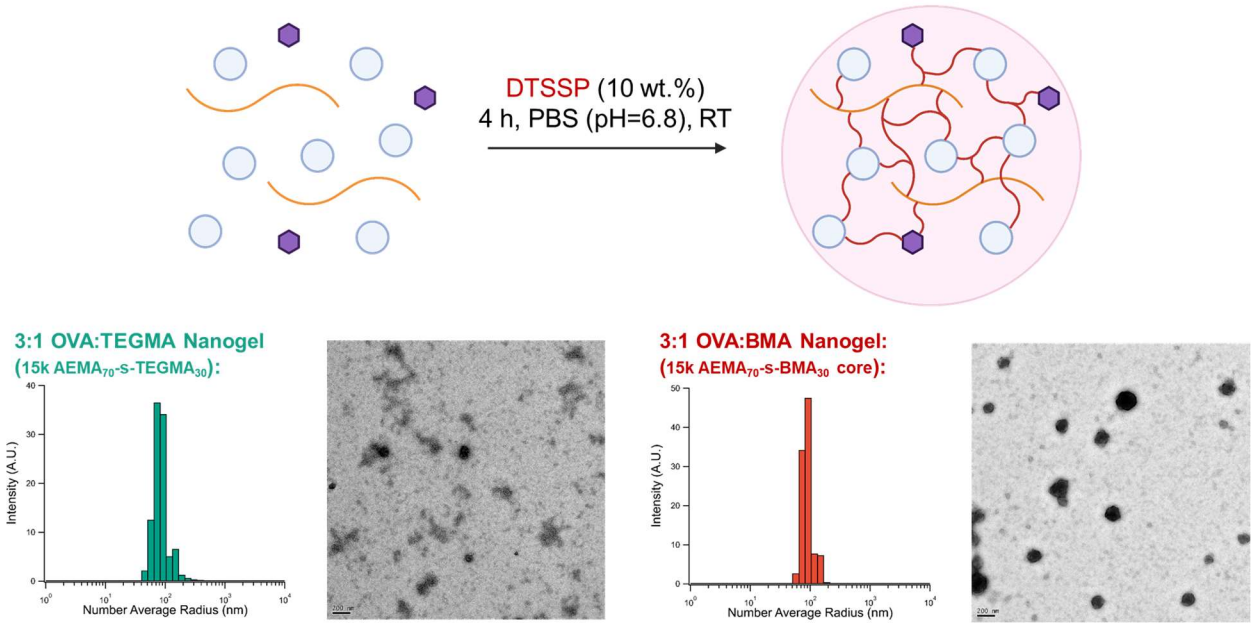

Figure S3.33: Synthesis and characterization of first-generation nanogels from 15 kg/mol polymers, ovalbumin, and DTSSP. The resulting structures were characterized by transmission electron microscopy with uranium acetate staining and dynamic light scattering.

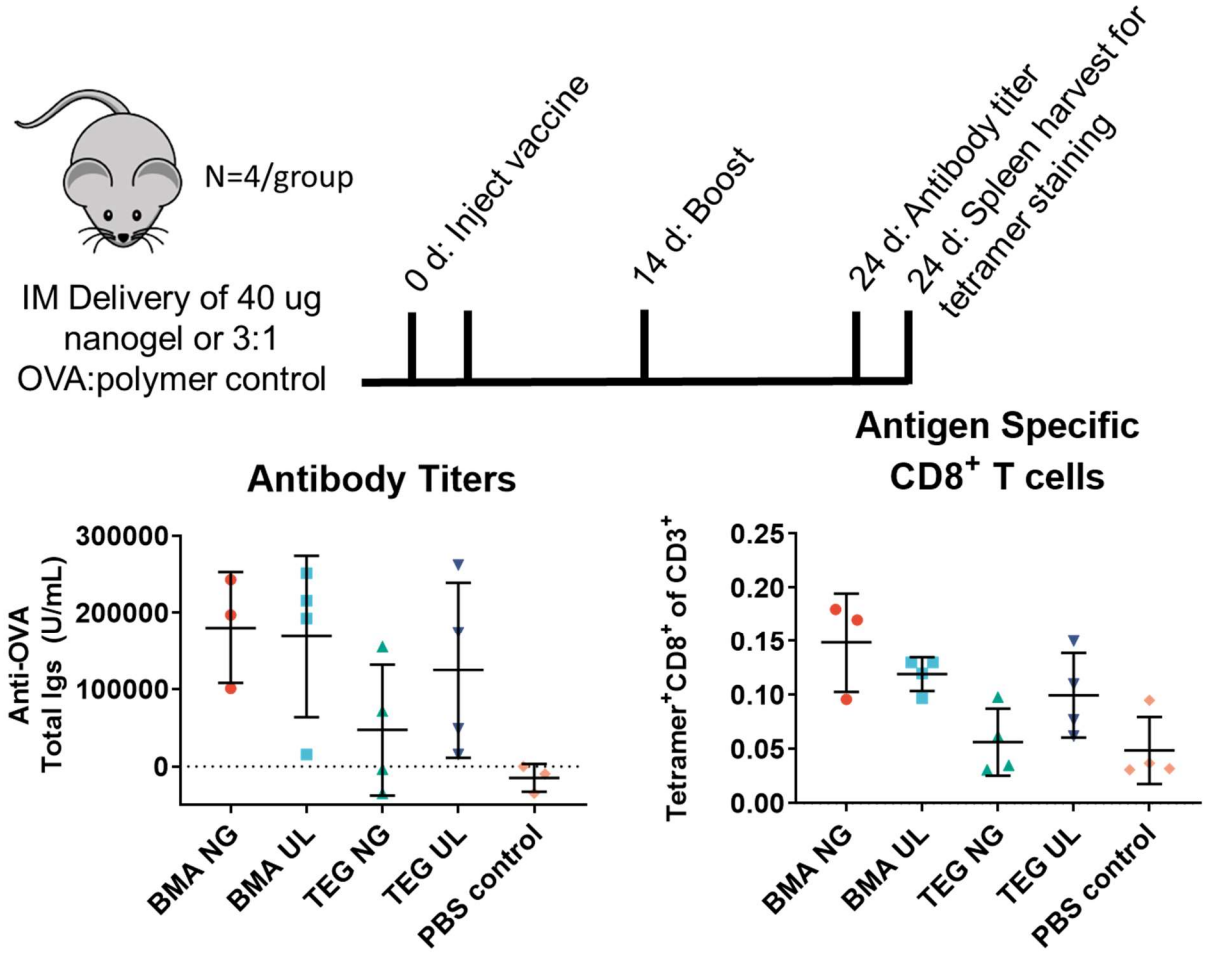

Figure S3.34: Vaccine study with first generation nanogels. Vaccine schedule and *in vivo* responses generated toward first generation nanogels (NG) or unlinked controls (UL) containing 15 kg/mol poly(AEMA-*s*-BMA) (BMA) or 15 kg/mol poly(AEMA-*s*-TEGMA) (TEG) cross-linked with DTSSP. Antibody titers were measured in the serum, while antigen specific $CD8^+$ T cells were measured in spleens using SIINFEKL-specific tetramers.

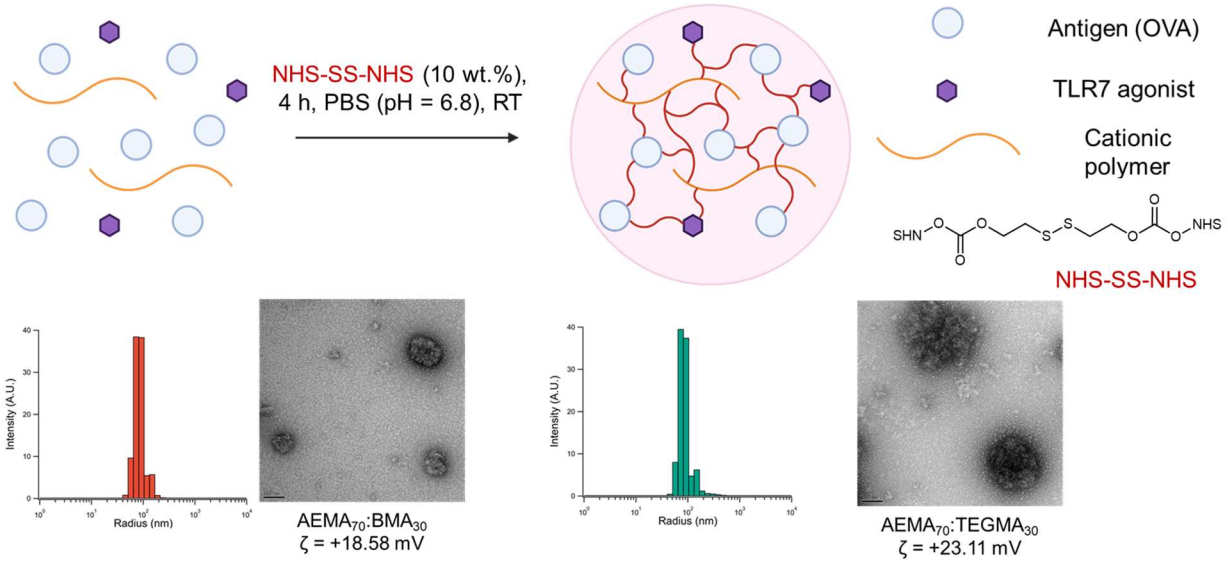

Figure S3.35: Synthesis and characterization of second-generation nanogels from 15 kg/mol polymers, ovalbumin, and NHS-SS-NHS. The resulting structures were characterized by transmission electron microscopy with uranium acetate staining and dynamic light scattering.

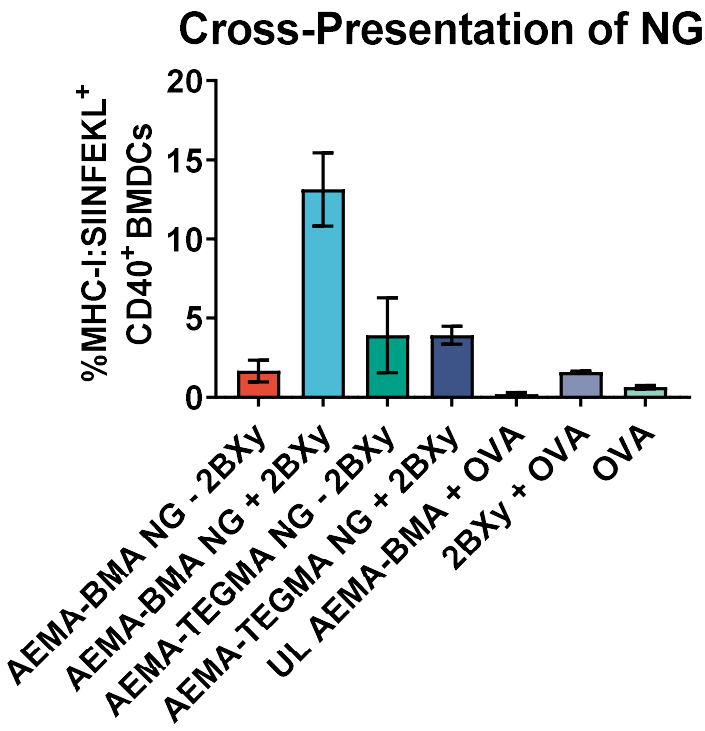

Figure S3.36: Activity of second-generation nanogels (prepared as shown in **Figure S3.35**) was confirmed in BMDCs using an antigen presentation assay. BMDCs were incubated with nanogels for 5 h and then stained with anti-MHC-I:SIINFEKL, anti-CD40, and a viability dye. The percentage of live, CD40+MHC-I:SIINFEKL+ cells were then analyzed via flow cytometry. Representative flow gating is presented, and averaged data is representative of four independent trials.

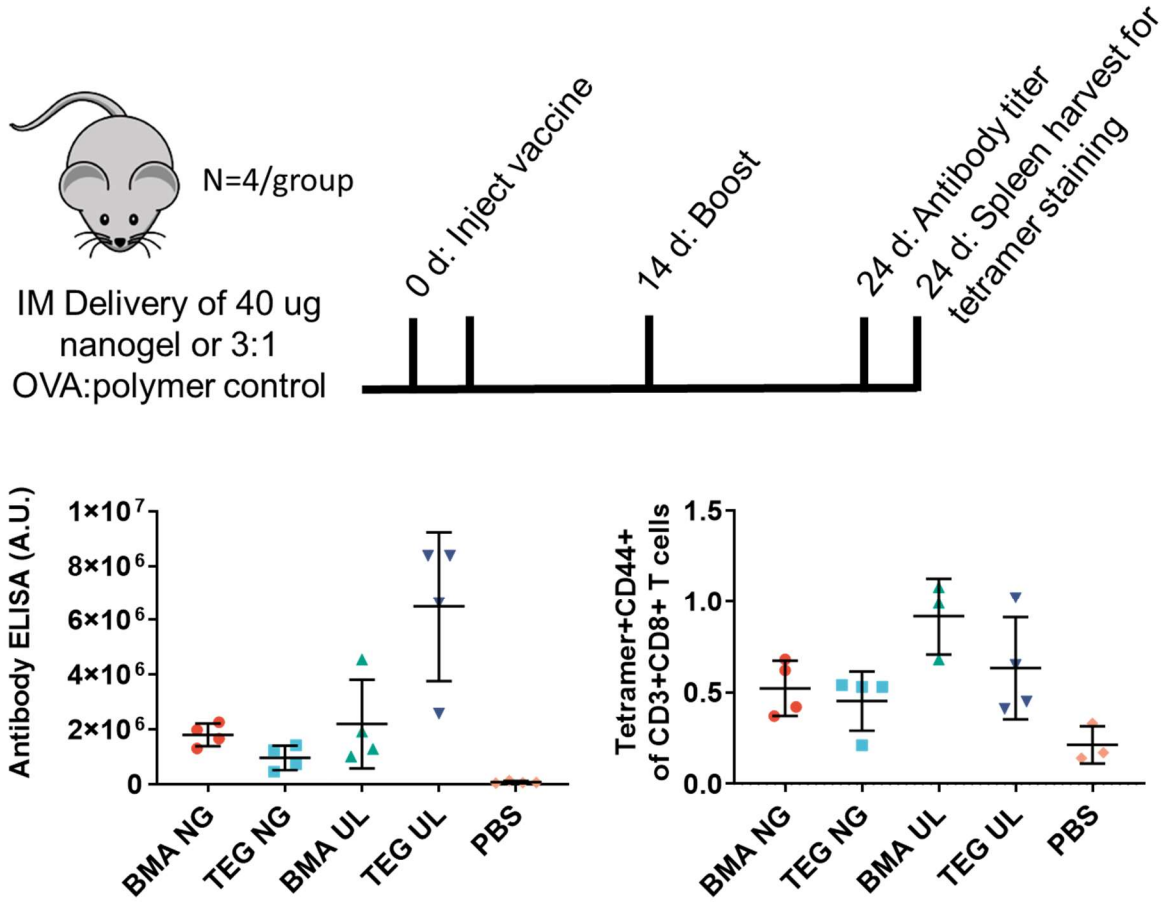

Figure S3.37: Vaccine schedule and *in vivo* responses generated toward second generation nanogels (NG) or unlinked controls (UL) containing 15 kg/mol poly(AEMA-*s*-BMA) (BMA) or 15 kg/mol poly(AEMA-*s*-TEGMA) (TEG) cross-linked with NHS-SS-NHS. Antibody titers were measured in the serum, while antigen specific $CD8^+$ T cells were measured in the spleens using SIINFEKL-specific tetramers.

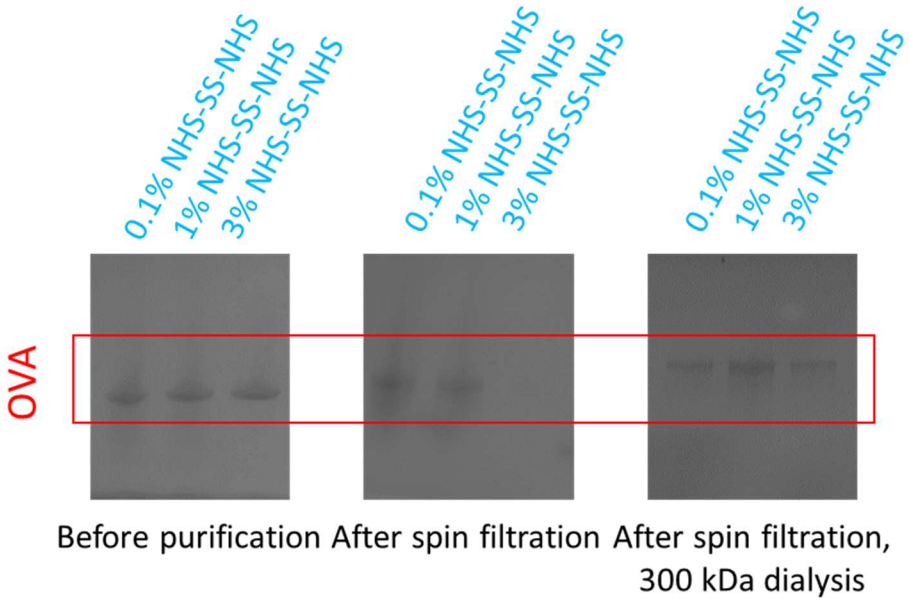

Figure S3.38: SDS-PAGE gel electrophoresis studies on nanogels to evaluate their purity. Nanogels were purified using the indicated strategies, denatured at 95 °C for 5 min (in the absence of reducing agent, which would cleave disulfide cross-linkages), and then analyzed using a 4-15% bis-acrylamide gel to evaluate removal of unreacted OVA. It was observed that NHS-SS-NHS cross-linker was unstable in aqueous-buffer, releasing unreacted OVA despite extensive purification, while DTSSP-linked nanogels were able to be purified.

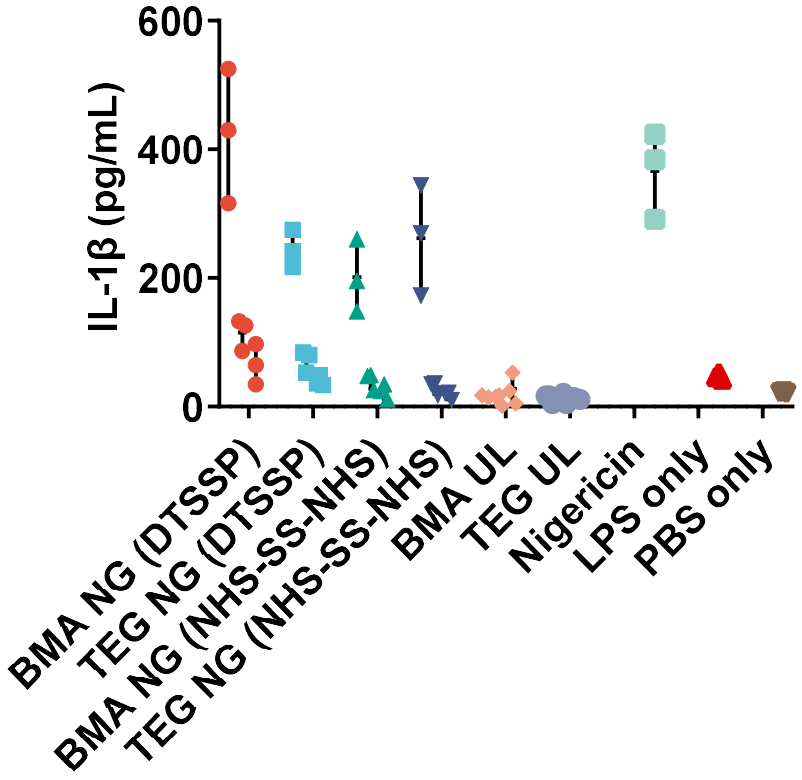

Figure S3.39: *In-vitro* IL-1β production of nanogels. Nanogels were incubated with LPS-primed BMDCs overnight. Supernatant was collected and analyzed *via* IL-1β ELISA. Experiments were conducted 100, 10, and 1 μg/mL (left to right) of nanogels (NG) or equivalent concentrations of unlinked controls (UL).

3.7 References.

1. Manna, S.; Maiti, S.; Shen, J.; Weiss, A. M.; Mulder, E. J.; Esser-Kahn, A. P., Nano-vaccine that activates the NLRP3 Inflammasome Enhances Tumor Specific Activation of Anti-Cancer Immunity. *Biomaterials* **2023**, *296*, 122062.

2. Pollard, A. J.; Bijker, E. M., A guide to vaccinology: from basic principles to new developments. *Nat Rev Immunol* **2020**, 21 (2), 83-100.

3. Lauring, A. S.; Jones, J. O.; Andino, R., Rationalizing the development of live attenuated virus vaccines. *Nat Biotechnol* **2010,** *28* (6), 573-579.

4. Moyle, P. M.; Toth, I., Modern subunit vaccines: development, components, and research opportunities. *ChemMedChem* **2013,** *8* (3), 360-376.

5. McShane, H., Insights and challenges in tuberculosis vaccine development. *Lancet Respir Med* **2019,** *7* (9), 810-819.

6. Crompton, P. D.; Pierce, S. K.; Miller, L. H., Advances and challenges in malaria vaccine development. *J Clin Invest* **2010,** *120* (12), 4168-4178.

7. Read, A. J.; Erickson, S.; Harmsen, A. G., Role of CD4+ and CD8+ T cells in clearance of primary pulmonary infection with Coxiella burnetii. *Infect Immun* **2010,** *78* (7), 3019-3026.

8. McElroy, A. K.; Akondy, R. S.; Davis, C. W.; Ellebedy, A. H.; Mehta, A. K.; Kraft, C. S.; Lyon, G. M.; Ribner, B. S.; Varkey, J.; Sidney, J.; Sette, A.; Campbell, S.; Stroher, U.; Damon, I.; Nichol, S. T.; Spiropoulou, C. F.; Ahmed, R., Human Ebola virus infection results in substantial immune activation. *Proc Natl Acad Sci U S A* **2015,** *112* (15), 4719-4724.

9. Henao-Restrepo, A. M.; Camacho, A.; Longini, I. M.; Watson, C. H.; Edmunds, W. J.; Egger, M.; Carroll, M. W.; Dean, N. E.; Diatta, I.; Doumbia, M.; Draguez, B.; Duraffour, S.; Enwere, G.; Grais, R.; Gunther, S.; Gsell, P.-S.; Hossmann, S.; Watle, S. V.; Kondé, M. K.; Kéïta, S.; Kone, S.; Kuisma, E.; Levine, M. M.; Mandal, S.; Mauget, T.; Norheim, G.; Riveros, X.; Soumah, A.; Trelle, S.; Vicari, A. S.; Røttingen, J.-A.; Kieny, M.-P., Efficacy and effectiveness of an rVSV-vectored vaccine in preventing Ebola virus disease: final results from the Guinea ring vaccination, open-label, cluster-randomised trial (Ebola Ça Suffit!). *Lancet* **2017,** *389* (10068), 505-518.

10. Amanat, F.; Krammer, F., SARS-CoV-2 Vaccines: Status Report. *Immunity* **2020,** *52* (4), 583-589.

11. Polack, F. P.; Thomas, S. J.; Kitchin, N.; Absalon, J.; Gurtman, A.; Lockhart, S.; Perez, J. L.; Perez Marc, G.; Moreira, E. D.; Zerbini, C.; Bailey, R.; Swanson, K. A.; Roychoudhury, S.; Koury, K.; Li, P.; Kalina, W. V.; Cooper, D.; Frenck, R. W., Jr.; Hammitt, L. L.; Tureci, O.; Nell, H.; Schaefer, A.; Unal, S.; Tresnan, D. B.; Mather, S.; Dormitzer, P. R.; Sahin, U.; Jansen, K. U.; Gruber, W. C.; Group, C. C. T., Safety and Efficacy of the BNT162b2 mRNA Covid-19 Vaccine. *N Engl J Med* **2020**, *383* (27). 2603-2615.

12. Baden, L. R.; El Sahly, H. M.; Essink, B.; Kotloff, K.; Frey, S.; Novak, R.; Diemert, D.; Spector, S. A.; Rouphael, N.; Creech, C. B.; McGettigan, J.; Kehtan, S.; Segall, N.; Solis, J.; Brosz, A.; Fierro, C.; Schwartz, H.; Neuzil, K.; Corey, L.; Gilbert, P.; Janes, H.; Follmann, D.;

Marovich, M.; Mascola, J.; Polakowski, L.; Ledgerwood, J.; Graham, B. S.; Bennett, H.; Pajon, R.; Knightly, C.; Leav, B.; Deng, W.; Zhou, H.; Han, S.; Ivarsson, M.; Miller, J.; Zaks, T.; Group, C. S., Efficacy and Safety of the mRNA-1273 SARS-CoV-2 Vaccine. *N Engl J Med* **2020**, *384* (5), 403-416

13. Tom, J. K.; Albin, T. J.; Manna, S.; Moser, B. A.; Steinhardt, R. C.; Esser-Kahn, A. P., Applications of Immunomodulatory Immune Synergies to Adjuvant Discovery and Vaccine Development. *Trends Biotechnol* **2019,** *37* (4), 373-388.

14. Jackson, S.; Lentino, J.; Kopp, J.; Murray, L.; Ellison, W.; Rhee, M.; Shockey, G.; Akella, L.; Erby, K.; Heyward, W. L.; Janssen, R. S.; Group, H. B. V. S., Immunogenicity of a two-dose investigational hepatitis B vaccine, HBsAg-1018, using a toll-like receptor 9 agonist adjuvant compared with a licensed hepatitis B vaccine in adults. *Vaccine* **2018,** *36* (5), 668-674.

15. Heineman, T. C.; Cunningham, A.; Levin, M., Understanding the immunology of Shingrix, a recombinant glycoprotein E adjuvanted herpes zoster vaccine. *Curr Opin Immunol* **2019,** *59*, 42-48.

16. Di Pasquale, A.; Bonanni, P.; Garcon, N.; Stanberry, L. R.; El-Hodhod, M.; Tavares Da Silva, F., Vaccine safety evaluation: Practical aspects in assessing benefits and risks. *Vaccine* **2016,** *34* (52), 6672-6680.

17. Manji, G. A.; Wang, L.; Geddes, B. J.; Brown, M.; Merriam, S.; Al-Garawi, A.; Mak, S.; Lora, J. M.; Briskin, M.; Jurman, M.; Cao, J.; DiStefano, P. S.; Bertin, J., PYPAF1, a PYRIN-containing Apaf1-like protein that assembles with ASC and regulates activation of NF-kappa B. *J Biol Chem* **2002,** *277* (13), 11570-5.

18. Martinon, F.; Burns, K.; Tschopp, J., The Inflammasome: A Molecular Platform Triggering Activation of Inflammatory Caspases and Processing of proIL-1β. *Molecular Cell* **2002,** *10* (2), 417-426.

19. Agostini, L.; Martinon, F.; Burns, K.; McDermott, M. F.; Hawkins, P. N.; Tschopp, J., NALP3 Forms an IL-1β-Processing Inflammasome with Increased Activity in Muckle-Wells Autoinflammatory Disorder. *Immunity* **2004,** *20* (3), 319-325.

20. Swanson, K. V.; Deng, M.; Ting, J. P., The NLRP3 inflammasome: molecular activation and regulation to therapeutics. *Nat Rev Immunol* **2019,** *19* (8), 477-489.

21. Petrilli, V.; Papin, S.; Dostert, C.; Mayor, A.; Martinon, F.; Tschopp, J., Activation of the NALP3 inflammasome is triggered by low intracellular potassium concentration. *Cell Death Differ* **2007,** *14* (9), 1583-9.

22. Martinon, F.; Petrilli, V.; Mayor, A.; Tardivel, A.; Tschopp, J., Gout-associated uric acid crystals activate the NALP3 inflammasome. *Nature* **2006,** *440* (7081), 237-241.

23. Mariathasan, S.; Weiss, D. S.; Newton, K.; McBride, J.; O'Rourke, K.; Roose-Girma, M.; Lee, W. P.; Weinrauch, Y.; Monack, D. M.; Dixit, V. M., Cryopyrin activates the inflammasome in response to toxins and ATP. *Nature* **2006,** *440* (7081), 228-232.

24. Zhou, R.; Tardivel, A.; Thorens, B.; Choi, I.; Tschopp, J., Thioredoxin-interacting protein links oxidative stress to inflammasome activation. *Nat Immunol* **2010,** *11* (2), 136-140.

25. Munoz-Planillo, R.; Kuffa, P.; Martinez-Colon, G.; Smith, B. L.; Rajendiran, T. M.; Nunez, G., K(+) efflux is the common trigger of NLRP3 inflammasome activation by bacterial toxins and particulate matter. *Immunity* **2013,** *38* (6), 1142-1153.

26. Liu, X.; Zhang, Z.; Ruan, J.; Pan, Y.; Magupalli, V. G.; Wu, H.; Lieberman, J., Inflammasome-activated gasdermin D causes pyroptosis by forming membrane pores. *Nature* **2016,** *535* (7610), 153-158.

27. Ghiringhelli, F.; Apetoh, L.; Tesniere, A.; Aymeric, L.; Ma, Y.; Ortiz, C.; Vermaelen, K.; Panaretakis, T.; Mignot, G.; Ullrich, E.; Perfettini, J. L.; Schlemmer, F.; Tasdemir, E.; Uhl, M.; Genin, P.; Civas, A.; Ryffel, B.; Kanellopoulos, J.; Tschopp, J.; Andre, F.; Lidereau, R.; McLaughlin, N. M.; Haynes, N. M.; Smyth, M. J.; Kroemer, G.; Zitvogel, L., Activation of the NLRP3 inflammasome in dendritic cells induces IL-1beta-dependent adaptive immunity against tumors. *Nat Med* **2009,** *15* (10), 1170-1178.

28. Pang, I. K.; Ichinohe, T.; Iwasaki, A., IL-1R signaling in dendritic cells replaces pattern-recognition receptors in promoting CD8(+) T cell responses to influenza A virus. *Nat Immunol* **2013,** *14* (3), 246-253.

29. Van Den Eeckhout, B.; Van Hoecke, L.; Burg, E.; Van Lint, S.; Peelman, F.; Kley, N.; Uze, G.; Saelens, X.; Tavernier, J.; Gerlo, S., Specific targeting of IL-1beta activity to CD8(+) T cells allows for safe use as a vaccine adjuvant. *NPJ Vaccines* **2020,** *5*, 64.

30. Chung, Y.; Chang, S. H.; Martinez, G. J.; Yang, X. O.; Nurieva, R.; Kang, H. S.; Ma, L.; Watowich, S. S.; Jetten, A. M.; Tian, Q.; Dong, C., Critical regulation of early Th17 cell differentiation by interleukin-1 signaling. *Immunity* **2009,** *30* (4), 576-587.

31. Bruchard, M.; Rebe, C.; Derangere, V.; Togbe, D.; Ryffel, B.; Boidot, R.; Humblin, E.; Hamman, A.; Chalmin, F.; Berger, H.; Chevriaux, A.; Limagne, E.; Apetoh, L.; Vegran, F.; Ghiringhelli, F., The receptor NLRP3 is a transcriptional regulator of TH2 differentiation. *Nat Immunol* **2015,** *16* (8), 859-870.

32. Yao, Y.; Chen, S.; Cao, M.; Fan, X.; Yang, T.; Huang, Y.; Song, X.; Li, Y.; Ye, L.; Shen, N.; Shi, Y.; Li, X.; Wang, F.; Qian, Y., Antigen-specific CD8(+) T cell feedback activates NLRP3 inflammasome in antigen-presenting cells through perforin. *Nat Commun* **2017,** *8*, 15402.

33. Chakraborty, R.; Chandra, J.; Cui, S.; Tolley, L.; Cooper, M. A.; Kendall, M.; Frazer, I. H., CD8(+) lineage dendritic cells determine adaptive immune responses to inflammasome activation upon sterile skin injury. *Exp Dermatol* **2018,** *27* (1), 71-79.

34. Dostert, C.; Ludigs, K.; Guarda, G., Innate and adaptive effects of inflammasomes on T cell responses. *Curr Opin Immunol* **2013,** *25* (3), 359-365.

35. Evavold, C. L.; Kagan, J. C., How Inflammasomes Inform Adaptive Immunity. *J Mol Biol* **2018,** *430* (2), 217-237.

36. Deets, K. A.; Vance, R. E., Inflammasomes and adaptive immune responses. *Nat Immunol* **2021,** *22*, 412–422.

37. Welsby, I.; Detienne, S.; N'Kuli, F.; Thomas, S.; Wouters, S.; Bechtold, V.; De Wit, D.; Gineste, R.; Reinheckel, T.; Elouahabi, A.; Courtoy, P. J.; Didierlaurent, A. M.; Goriely, S.,

Lysosome-Dependent Activation of Human Dendritic Cells by the Vaccine Adjuvant QS-21. *Front Immunol* **2016,** *7*, 663.

38. Marty-Roix, R.; Vladimer, G. I.; Pouliot, K.; Weng, D.; Buglione-Corbett, R.; West, K.; MacMicking, J. D.; Chee, J. D.; Wang, S.; Lu, S.; Lien, E., Identification of QS-21 as an Inflammasome-activating Molecular Component of Saponin Adjuvants. *J Biol Chem* **2016,** *291* (3), 1123-1136.

39. Didierlaurent, A. M.; Laupeze, B.; Di Pasquale, A.; Hergli, N.; Collignon, C.; Garcon, N., Adjuvant system AS01: helping to overcome the challenges of modern vaccines. *Expert Rev Vaccines* **2017,** *16* (1), 55-63.

40. Didierlaurent, A. M.; Collignon, C.; Bourguignon, P.; Wouters, S.; Fierens, K.; Fochesato, M.; Dendouga, N.; Langlet, C.; Malissen, B.; Lambrecht, B. N.; Garcon, N.; Van Mechelen, M.; Morel, S., Enhancement of adaptive immunity by the human vaccine adjuvant AS01 depends on activated dendritic cells. *J Immunol* **2014,** *193* (4), 1920-30.

41. Olotu, A.; Fegan, G.; Wambua, J.; Nyangweso, G.; Leach, A.; Lievens, M.; Kaslow, D. C.; Njuguna, P.; Marsh, K.; Bejon, P., Seven-Year Efficacy of RTS,S/AS01 Malaria Vaccine among Young African Children. *N Engl J Med* **2016,** *374* (26), 2519-29.

42. Keech, C.; Albert, G.; Cho, I.; Robertson, A.; Reed, P.; Neal, S.; Plested, J. S.; Zhu, M.; Cloney-Clark, S.; Zhou, H.; Smith, G.; Patel, N.; Frieman, M. B.; Haupt, R. E.; Logue, J.; McGrath, M.; Weston, S.; Piedra, P. A.; Desai, C.; Callahan, K.; Lewis, M.; Price-Abbott, P.; Formica, N.; Shinde, V.; Fries, L.; Lickliter, J. D.; Griffin, P.; Wilkinson, B.; Glenn, G. M., Phase 1-2 Trial of a SARS-CoV-2 Recombinant Spike Protein Nanoparticle Vaccine. *N Engl J Med* **2020**.

43. Shinde, V.; Cho, I.; Plested, J. S.; Agrawal, S.; Fiske, J.; Cai, R.; Zhou, H.; Pham, X.; Zhu, M.; Cloney-Clark, S.; Wang, N.; Zhou, B.; Lewis, M.; Price-Abbott, P.; Patel, N.; Massare, M. J.; Smith, G.; Keech, C.; Fries, L.; Glenn, G. M., Comparison of the safety and immunogenicity of a novel Matrix-M-adjuvanted nanoparticle influenza vaccine with a quadrivalent seasonal influenza vaccine in older adults: a phase 3 randomised controlled trial. *Lancet Infect Dis* **2022**, *22* (1), 73-84.

44. Tahtinen, S.; Tong, A. J.; Himmels, P.; Oh, J.; Paler-Martinez, A.; Kim, L.; Wichner, S.; Oei, Y.; McCarron, M. J.; Freund, E. C.; Amir, Z. A.; de la Cruz, C. C.; Haley, B.; Blanchette, C.; Schartner, J. M.; Ye, W.; Yadav, M.; Sahin, U.; Delamarre, L.; Mellman, I., IL-1 and IL-1ra are key regulators of the inflammatory response to RNA vaccines. *Nat Immunol* **2022,** *23* (4), 532-542.

45. Manna, S.; Howitz, W. J.; Oldenhuis, N. J.; Eldredge, A. C.; Shen, J.; Nihesh, F. N.; Lodoen, M. B.; Guan, Z.; Esser-Kahn, A. P., Immunomodulation of the NLRP3 Inflammasome through Structure-Based Activator Design and Functional Regulation via Lysosomal Rupture. *ACS Cent Sci* **2018,** *4* (8), 982-995.

46. Fan, Z.; Jan, S.; Hickey, J. C.; Davies, D. H.; Felgner, J.; Felgner, P. L.; Guan, Z., Multifunctional Dendronized Polypeptides for Controlled Adjuvanticity. *Biomacromolecules* **2021**, *22* (12), 5074-5086.

47. Baljon, J. J.; Dandy, A.; Wang-Bishop, L.; Wehbe, M.; Jacobson, M. E.; Wilson, J. T., The efficiency of cytosolic drug delivery using pH-responsive endosomolytic polymers does not correlate with activation of the NLRP3 inflammasome. *Biomater Sci* **2019,** *7* (5), 1888-1897.

48. Nandi, D.; Shivrayan, M.; Gao, J.; Krishna, J.; Das, R.; Liu, B.; Thayumanavan, S.; Kulkarni, A., Core Hydrophobicity of Supramolecular Nanoparticles Induces NLRP3 Inflammasome Activation. *ACS Appl Mater Interfaces* **2021,** *13* (38), 45300-45314.

49. Duewell, P.; Kisser, U.; Heckelsmiller, K.; Hoves, S.; Stoitzner, P.; Koernig, S.; Morelli, A. B.; Clausen, B. E.; Dauer, M.; Eigler, A.; Anz, D.; Bourquin, C.; Maraskovsky, E.; Endres, S.; Schnurr, M., ISCOMATRIX adjuvant combines immune activation with antigen delivery to dendritic cells in vivo leading to effective cross-priming of CD8+ T cells. *J Immunol* **2011,** *187* (1), 55-63.

50. Larena, M.; Holmgren, J.; Lebens, M.; Terrinoni, M.; Lundgren, A., Cholera toxin, and the related nontoxic adjuvants mmCT and dmLT, promote human Th17 responses via cyclic AMP-protein kinase A and inflammasome-dependent IL-1 signaling. *J Immunol* **2015,** *194* (8), 3829-39.

51. Lonn, P.; Kacsinta, A. D.; Cui, X. S.; Hamil, A. S.; Kaulich, M.; Gogoi, K.; Dowdy, S. F., Enhancing Endosomal Escape for Intracellular Delivery of Macromolecular Biologic Therapeutics. *Sci Rep* **2016,** *6*, 32301.

52. Maiti, S.; Manna, S.; Shen, J.; Esser-Kahn, A. P.; Du, W., Mitigation of Hydrophobicity-Induced Immunotoxicity by Sugar Poly(orthoesters). *J Am Chem Soc* **2019,** *141* (11), 4510-4514.

53. Shukla, N. M.; Mutz, C. A.; Ukani, R.; Warshakoon, H. J.; Moore, D. S.; David, S. A., Syntheses of fluorescent imidazoquinoline conjugates as probes of Toll-like receptor 7. *Bioorg Med Chem Lett* **2010,** *20* (22), 6384-6.

54. Presolski, S. I.; Hong, V. P.; Finn, M. G., Copper-Catalyzed Azide-Alkyne Click Chemistry for Bioconjugation. *Curr Protoc Chem Biol* **2011,** *3* (4), 153-162.

55. Lusty, E.; Poznanski, S. M.; Kwofie, K.; Mandur, T. S.; Lee, D. A.; Richards, C. D.; Ashkar, A. A., IL-18/IL-15/IL-12 synergy induces elevated and prolonged IFN-gamma production by ex vivo expanded NK cells which is not due to enhanced STAT4 activation. *Mol Immunol* **2017,** *88*, 138-147.

56. Wei, H.; Pahang, J. A.; Pun, S. H., Optimization of brush-like cationic copolymers for nonviral gene delivery. *Biomacromolecules* **2013,** *14* (1), 275-284.

57. Ebbesen, M. F.; Schaffert, D. H.; Crowley, M. L.; Oupický, D.; Howard, K. A., Synthesis of click-reactive HPMA copolymers using RAFT polymerization for drug delivery applications. *J Polym Sci A Polym Chem* **2013,** *51* (23), 5091-5099.

58. Santander-Borrego, M.; Green, D. W.; Chirila, T. V.; Whittaker, A. K.; Blakey, I., Click functionalization of methacrylate-based hydrogels and their cellular response. *J Polym Sci A Polym Chem* **2014,** *52* (13), 1781-1789.

59. Kopecek, J.; Kopeckova, P., HPMA copolymers: origins, early developments, present, and future. *Adv Drug Deliv Rev* **2010,** *62* (2), 122-49.

60. Tsarevsky, N. V.; Bencherif, S. A.; Matyjaszewski, K., Graft Copolymers by a Combination of ATRP and Two Different Consecutive Click Reactions. *Macromolecules* **2007,** *40* (13), 4439-4445.

61. Pickens, C. J.; Johnson, S. N.; Pressnall, M. M.; Leon, M. A.; Berkland, C. J., Practical Considerations, Challenges, and Limitations of Bioconjugation via Azide-Alkyne Cycloaddition. *Bioconjug Chem* **2018,** *29* (3), 686-701.

62. Sun, H.; Choi, W.; Zang, N.; Battistella, C.; Thompson, M. P.; Cao, W.; Zhou, X.; Forman, C.; Gianneschi, N. C., Bioactive Peptide Brush Polymers via Photoinduced Reversible-Deactivation Radical Polymerization. *Angew Chem Int Ed Engl* **2019,** *58* (48), 17359-17364.

63. Gianneschi, N. C.; Sun, H.; Cao, W.; Zang, N.; Clemons, T.; Scheutz, G.; Hu, Z.; Thompson, M.; Liang, Y.; Vratsanos, M.; Zhou, X.; Choi, W.; Sumerlin, B.; Stupp, S., Proapoptotic Peptide Brush Polymer Nanoparticles via Photoinitiated Polymerization-Induced Self-Assembly. *Angew Chem Int Ed Engl* **2020**, *59* (43), 19136-19142

64. Mori, H.; Takahashi, E.; Ishizuki, A.; Nakabayashi, K., Tryptophan-Containing Block Copolymers Prepared by RAFT Polymerization: Synthesis, Self-Assembly, and Chiroptical and Sensing Properties. *Macromolecules* **2013,** *46* (16), 6451-6465.

65. Larson, B. C.; Pomponio, J. R.; Shafaat, H. S.; Kim, R. H.; Leigh, B. S.; Tauber, M. J.; Kim, J. E., Photogeneration and Quenching of Tryptophan Radical in Azurin. *J Phys Chem B* **2015,** *119* (29), 9438-9449.

66. Mattheis, C.; Wang, H.; Meister, C.; Agarwal, S., Effect of guanidinylation on the properties of poly(2-aminoethylmethacrylate)-based antibacterial materials. *Macromol Biosci* **2013,** *13* (2), 242-255.

67. Lodge, T. P.; Hiemenz, P. C., *Polymer Chemistry*. 2 ed.; CRC Press: Boca Raton, FL, 2013.

68. Li, Z.; Kosuri, S.; Foster, H.; Cohen, J.; Jumeaux, C.; Stevens, M. M.; Chapman, R.; Gormley, A. J., A Dual Wavelength Polymerization and Bioconjugation Strategy for High Throughput Synthesis of Multivalent Ligands. *J Am Chem Soc* **2019,** *141* (50), 19823-19830.

69. Upadhya, R.; Kanagala, M. J.; Gormley, A. J., Purifying Low-Volume Combinatorial Polymer Libraries with Gel Filtration Columns. *Macromol Rapid Commun* **2019,** *40* (24), e1900528.

70. Chanput, W.; Mes, J. J.; Wichers, H. J., THP-1 cell line: an in vitro cell model for immune modulation approach. *Int Immunopharmacol* **2014,** *23* (1), 37-45.

71. Gavin, A. L.; Hoebe, K.; Duong, B.; Ota, T.; Martin, C.; Beutler, B.; Nemazee, D., Adjuvant-enhanced antibody responses in the absence of toll-like receptor signaling. *Science* **2006,** *314* (5807), 1936-1938.

72. Franchi, L.; Nunez, G., The Nlrp3 inflammasome is critical for aluminium hydroxide-mediated IL-1beta secretion but dispensable for adjuvant activity. *Eur J Immunol* **2008,** *38* (8), 2085-2089.

73. McKee, A. S.; Munks, M. W.; MacLeod, M. K.; Fleenor, C. J.; Van Rooijen, N.; Kappler, J. W.; Marrack, P., Alum induces innate immune responses through macrophage and mast cell

sensors, but these sensors are not required for alum to act as an adjuvant for specific immunity. *J Immunol* **2009,** *183* (7), 4403-4414.

74. Flach, T. L.; Ng, G.; Hari, A.; Desrosiers, M. D.; Zhang, P.; Ward, S. M.; Seamone, M. E.; Vilaysane, A.; Mucsi, A. D.; Fong, Y.; Prenner, E.; Ling, C. C.; Tschopp, J.; Muruve, D. A.; Amrein, M. W.; Shi, Y., Alum interaction with dendritic cell membrane lipids is essential for its adjuvanticity. *Nat Med* **2011,** *17* (4), 479-487.

75. Hutchison, S.; Benson, R. A.; Gibson, V. B.; Pollock, A. H.; Garside, P.; Brewer, J. M., Antigen depot is not required for alum adjuvanticity. *FASEB J* **2012,** *26* (3), 1272-1279.

76. Oleszycka, E.; Lavelle, E. C., Immunomodulatory properties of the vaccine adjuvant alum. *Curr Opin Immunol* **2014,** *28*, 1-5.

77. Tang, L.; Zheng, Y.; Melo, M. B.; Mabardi, L.; Castano, A. P.; Xie, Y. Q.; Li, N.; Kudchodkar, S. B.; Wong, H. C.; Jeng, E. K.; Maus, M. V.; Irvine, D. J., Enhancing T cell therapy through TCR-signaling-responsive nanoparticle drug delivery. *Nat Biotechnol* **2018,** *36* (8), 707-716.

78. Chang, T. Z.; Stadmiller, S. S.; Staskevicius, E.; Champion, J. A., Effects of ovalbumin protein nanoparticle vaccine size and coating on dendritic cell processing. *Biomater Sci* **2017,** *5* (2), 223-233.

79. Li, A. W.; Sobral, M. C.; Badrinath, S.; Choi, Y.; Graveline, A.; Stafford, A. G.; Weaver, J. C.; Dellacherie, M. O.; Shih, T. Y.; Ali, O. A.; Kim, J.; Wucherpfennig, K. W.; Mooney, D. J., A facile approach to enhance antigen response for personalized cancer vaccination. *Nat Mater* **2018,** *17* (6), 528-534.

80. Badrinath, S.; Dellacherie, M. O.; Li, A.; Zheng, S.; Zhang, X.; Sobral, M.; Pyrdol, J. W.; Smith, K. L.; Lu, Y.; Haag, S.; Ijaz, H.; Connor-Stroud, F.; Kaisho, T.; Dranoff, G.; Yuan, G. C.; Mooney, D. J.; Wucherpfennig, K. W., A vaccine targeting resistant tumours by dual T cell plus NK cell attack. *Nature* **2022,** *606* (7916), 992-998.

81. Super, M.; Doherty, E. J.; Cartwright, M. J.; Seiler, B. T.; Langellotto, F.; Dimitrakakis, N.; White, D. A.; Stafford, A. G.; Karkada, M.; Graveline, A. R.; Horgan, C. L.; Lightbown, K. R.; Urena, F. R.; Yeager, C. D.; Rifai, S. A.; Dellacherie, M. O.; Li, A. W.; Leese-Thompson, C.; Ijaz, H.; Jiang, A. R.; Chandrasekhar, V.; Scott, J. M.; Lightbown, S. L.; Ingber, D. E.; Mooney, D. J., Biomaterial vaccines capturing pathogen-associated molecular patterns protect against bacterial infections and septic shock. *Nat Biomed Eng* **2022,** *6* (1), 8-18.

82. Li, T.; Zehner, M.; He, J.; Prochnicki, T.; Horvath, G.; Latz, E.; Burgdorf, S.; Takeoka, S., NLRP3 inflammasome-activating arginine-based liposomes promote antigen presentations in dendritic cells. *Int J Nanomedicine* **2019,** *14*, 3503-3516.

83. Munoz-Wolf, N.; Ward, R. W.; Hearnden, C. H.; Sharp, F. A.; Geoghegan, J.; O'Grady, K.; McEntee, C. P.; Shanahan, K. A.; Guy, C.; Bowie, A. G.; Campbell, M.; Roces, C. B.; Anderluzzi, G.; Webb, C.; Perrie, Y.; Creagh, E.; Lavelle, E. C., Non-canonical inflammasome activation mediates the adjuvanticity of nanoparticles. *Cell Rep Med* **2022**.

84. Gong, N.; Zhang, Y.; Teng, X.; Wang, Y.; Huo, S.; Qing, G.; Ni, Q.; Li, X.; Wang, J.; Ye, X.; Zhang, T.; Chen, S.; Wang, Y.; Yu, J.; Wang, P. C.; Gan, Y.; Zhang, J.; Mitchell, M. J.;

Li, J.; Liang, X. J., Proton-driven transformable nanovaccine for cancer immunotherapy. *Nat Nanotechnol* **2020,** *15* (12), 1053-1064.

85. Chen, B.; Yan, Y.; Yang, Y.; Cao, G.; Wang, X.; Wang, Y.; Wan, F.; Yin, Q.; Wang, Z.; Li, Y.; Wang, L.; Xu, B.; You, F.; Zhang, Q.; Wang, Y., A pyroptosis nanotuner for cancer therapy. *Nat Nanotechnol* **2022,** *17* (7), 788-798.

86. Munoz-Wolf, N.; Ward, R. W.; Hearnden, C. H.; Sharp, F. A.; Geoghegan, J.; O'Grady, K.; McEntee, C. P.; Shanahan, K. A.; Guy, C.; Bowie, A. G.; Campbell, M.; Roces, C. B.; Anderluzzi, G.; Webb, C.; Perrie, Y.; Creagh, E.; Lavelle, E. C., Non-canonical inflammasome activation mediates the adjuvanticity of nanoparticles. *Cell Rep Med* **2023,** *4* (1), 100899.

87. Gan, P.; Gao, Z.; Zhao, X.; Qi, G., Surfactin inducing mitochondria-dependent ROS to activate MAPKs, NF-kappaB and inflammasomes in macrophages for adjuvant activity. *Sci Rep* **2016,** *6*, 39303.

88. Wegmann, F.; Gartlan, K. H.; Harandi, A. M.; Brinckmann, S. A.; Coccia, M.; Hillson, W. R.; Kok, W. L.; Cole, S.; Ho, L. P.; Lambe, T.; Puthia, M.; Svanborg, C.; Scherer, E. M.; Krashias, G.; Williams, A.; Blattman, J. N.; Greenberg, P. D.; Flavell, R. A.; Moghaddam, A. E.; Sheppard, N. C.; Sattentau, Q. J., Polyethyleneimine is a potent mucosal adjuvant for viral glycoprotein antigens. *Nat Biotechnol* **2012,** *30* (9), 883-888.

89. Wang, X.; Chang, C. H.; Jiang, J.; Liu, Q.; Liao, Y. P.; Lu, J.; Li, L.; Liu, X.; Kim, J.; Ahmed, A.; Nel, A. E.; Xia, T., The Crystallinity and Aspect Ratio of Cellulose Nanomaterials Determine Their Pro-Inflammatory and Immune Adjuvant Effects In Vitro and In Vivo. *Small* **2019,** *15* (42), e1901642.

90. Eisenbarth, S. C.; Colegio, O. R.; O'Connor, W.; Sutterwala, F. S.; Flavell, R. A., Crucial role for the Nalp3 inflammasome in the immunostimulatory properties of aluminium adjuvants. *Nature* **2008,** *453* (7198), 1122-1126.

91. Li, H.; Willingham, S. B.; Ting, J. P.; Re, F., Cutting edge: inflammasome activation by alum and alum's adjuvant effect are mediated by NLRP3. *J Immunol* **2008,** *181* (1), 17-21.

92. Marichal, T.; Ohata, K.; Bedoret, D.; Mesnil, C.; Sabatel, C.; Kobiyama, K.; Lekeux, P.; Coban, C.; Akira, S.; Ishii, K. J.; Bureau, F.; Desmet, C. J., DNA released from dying host cells mediates aluminum adjuvant activity. *Nat Med* **2011,** *17* (8), 996-1002.

93. Kool, M.; Soullie, T.; van Nimwegen, M.; Willart, M. A.; Muskens, F.; Jung, S.; Hoogsteden, H. C.; Hammad, H.; Lambrecht, B. N., Alum adjuvant boosts adaptive immunity by inducing uric acid and activating inflammatory dendritic cells. *J Exp Med* **2008,** *205* (4), 869-882.

94. Orr, M. T.; Khandhar, A. P.; Seydoux, E.; Liang, H.; Gage, E.; Mikasa, T.; Beebe, E. L.; Rintala, N. D.; Persson, K. H.; Ahniyaz, A.; Carter, D.; Reed, S. G.; Fox, C. B., Reprogramming the adjuvant properties of aluminum oxyhydroxide with nanoparticle technology. *NPJ Vaccines* **2019,** *4*, 1.

95. Forster III, J.; Nandi, D.; Kulkarni, A., mRNA-carrying lipid nanoparticles that induce lysosomal rupture activate NLRP3 inflammasome and reduce mRNA transfection efficiency. *Biomater Sci* **2022,** *10* (19), 5566-5582.

96. Wang, J.; Chen, H. J.; Hang, T.; Yu, Y.; Liu, G.; He, G.; Xiao, S.; Yang, B. R.; Yang, C.; Liu, F.; Tao, J.; Wu, M. X.; Xie, X., Physical activation of innate immunity by spiky particles. *Nat Nanotechnol* **2018,** *13* (11), 1078-1086.

97. Seubert, A.; Calabro, S.; Santini, L.; Galli, B.; Genovese, A.; Valentini, S.; Aprea, S.; Colaprico, A.; D'Oro, U.; Giuliani, M. M.; Pallaoro, M.; Pizza, M.; O'Hagan, D. T.; Wack, A.; Rappuoli, R.; De Gregorio, E., Adjuvanticity of the oil-in-water emulsion MF59 is independent of Nlrp3 inflammasome but requires the adaptor protein MyD88. *Proc Natl Acad Sci U S A* **2011,** *108* (27), 11169-11174.

98. Pizzuto, M.; Bigey, P.; Lachages, A. M.; Hoffmann, C.; Ruysschaert, J. M.; Escriou, V.; Lonez, C., Cationic lipids as one-component vaccine adjuvants: A promising alternative to alum. *J Control Release* **2018,** *287*, 67-77.

99. Seydoux, E.; Liang, H.; Dubois Cauwelaert, N.; Archer, M.; Rintala, N. D.; Kramer, R.; Carter, D.; Fox, C. B.; Orr, M. T., Effective Combination Adjuvants Engage Both TLR and Inflammasome Pathways To Promote Potent Adaptive Immune Responses. *J Immunol* **2018,** *201* (1), 98-112.

100. Yang, M.; Flavin, K.; Kopf, I.; Radics, G.; Hearnden, C. H.; McManus, G. J.; Moran, B.; Villalta-Cerdas, A.; Echegoyen, L. A.; Giordani, S.; Lavelle, E. C., Functionalization of carbon nanoparticles modulates inflammatory cell recruitment and NLRP3 inflammasome activation. *Small* **2013,** *9* (24), 4194-4206.

101. Niikura, K.; Matsunaga, T.; Suzuki, T.; Kobayashi, S.; Yamaguchi, H.; Orba, Y.; Kawaguchi, A.; Hasegawa, H.; Kajino, K.; Ninomiya, T.; Ijiro, K.; Sawa, H., Gold nanoparticles as a vaccine platform: influence of size and shape on immunological responses in vitro and in vivo. *ACS Nano* **2013,** *7* (5), 3926-3938.

102. Lu, F.; Mencia, A.; Bi, L.; Taylor, A.; Yao, Y.; HogenEsch, H., Dendrimer-like alpha-d-glucan nanoparticles activate dendritic cells and are effective vaccine adjuvants. *J Control Release* **2015,** *204*, 51-9.

103. Hernandez-Franco, J. F.; Mosley, Y. C.; Franco, J.; Ragland, D.; Yao, Y.; HogenEsch, H., Effective and Safe Stimulation of Humoral and Cell-Mediated Immunity by Intradermal Immunization with a Cyclic Dinucleotide/Nanoparticle Combination Adjuvant. *J Immunol* **2021,** *206* (4), 700-711.

104. Swaminathan, G.; Thoryk, E. A.; Cox, K. S.; Meschino, S.; Dubey, S. A.; Vora, K. A.; Celano, R.; Gindy, M.; Casimiro, D. R.; Bett, A. J., A novel lipid nanoparticle adjuvant significantly enhances B cell and T cell responses to sub-unit vaccine antigens. *Vaccine* **2016,** *34* (1), 110-119.

105. Swaminathan, G.; Thoryk, E. A.; Cox, K. S.; Smith, J. S.; Wolf, J. J.; Gindy, M. E.; Casimiro, D. R.; Bett, A. J., A Tetravalent Sub-unit Dengue Vaccine Formulated with Ionizable Cationic Lipid Nanoparticle induces Significant Immune Responses in Rodents and Non-Human Primates. *Sci Rep* **2016,** *6*, 34215.

106. Sharp, F. A.; Ruane, D.; Claass, B.; Creagh, E.; Harris, J.; Malyala, P.; Singh, M.; O'Hagan, D. T.; Petrilli, V.; Tschopp, J.; O'Neill, L. A.; Lavelle, E. C., Uptake of particulate

vaccine adjuvants by dendritic cells activates the NALP3 inflammasome. *Proc Natl Acad Sci U S A* **2009,** *106* (3), 870-875.

107. Huang, C. H.; Mendez, N.; Echeagaray, O. H.; Weeks, J.; Wang, J.; Vallez, C. N.; Gude, N.; Trogler, W. C.; Carson, D. A.; Hayashi, T.; Kummel, A. C., Conjugation of a Small-Molecule TLR7 Agonist to Silica Nanoshells Enhances Adjuvant Activity. *ACS Appl Mater Interfaces* **2019,** *11* (30), 26637-26647.

108. Dissanayake, S.; Denny, W. A.; Gamage, S.; Sarojini, V., Recent developments in anticancer drug delivery using cell penetrating and tumor targeting peptides. *J Control Release* **2017,** *250*, 62-76.

109. Reddy, S. T.; van der Vlies, A. J.; Simeoni, E.; Angeli, V.; Randolph, G. J.; O'Neil, C. P.; Lee, L. K.; Swartz, M. A.; Hubbell, J. A., Exploiting lymphatic transport and complement activation in nanoparticle vaccines. *Nat Biotechnol* **2007,** *25* (10), 1159-1164.

110. Toy, R.; Pradhan, P.; Ramesh, V.; Di Paolo, N. C.; Lash, B.; Liu, J.; Blanchard, E. L.; Pinelli, C. J.; Santangelo, P. J.; Shayakhmetov, D. M.; Roy, K., Modification of primary amines to higher order amines reduces in vivo hematological and immunotoxicity of cationic nanocarriers through TLR4 and complement pathways. *Biomaterials* **2019,** *225*, 119512.

111. Maiti, S.; Manna, S.; Shen, J.; Esser-Kahn, A. P.; Du, W., Mitigation of hydrophobicity-induced immunotoxicity by sugar poly (orthoesters). *J Am Chem Soc* **2019,** *141* (11), 4510-4514.

112. Manna, S.; Maiti, S.; Shen, J.; Du, W.; Esser-Kahn, A. P., Pathogen-like Nanoassemblies of Covalently Linked TLR Agonists Enhance CD8 and NK Cell-Mediated Antitumor Immunity. *ACS Cent Sci* **2020,** *6* (11), 2071-2078.

113. Akae, Y.; Sogawa, H.; Takata, T., Cyclodextrin-Based [3]Rotaxane-Crosslinked Fluorescent Polymer: Synthesis and De-Crosslinking Using Size Complementarity. *Angew Chem Int Ed Engl* **2018,** *57* (45), 14832-14836.

114. Ferguson, C. J.; Hughes, R. J.; Nguyen, D.; Pham, B. T. T.; Gilbert, R. G.; Serelis, A. K.; Such, C. H.; Hawkett, B. S., Ab Initio Emulsion Polymerization by RAFT-Controlled Self-Assembly. *Macromolecules* **2005,** *38* (6), 2191-2204.

CHAPTER 4 Identification of Small Molecule Inflammasome Activators for Vaccination.

This chapter is in preparation for publication.

4.1 Introduction.

Despite progress in curbing transmission of infectious disease by vaccination, new adjuvants which can safely stimulate robust adaptive immune responses are still needed.[1] Some of the most potent FDA-approved adjuvants, saponins, have been shown to mediate their adjuvanticity in part *via* activation of inflammasomes and subsequent secretion of IL-1 cytokines (IL-1α, IL-1β, IL-18, IL-33, and others).[1-4] Inflammasomes are innate immune danger sensors that, when activated, form polyprotein complexes that catalyze the activation of Caspase 1 (Casp1).[5] Casp1, in the presence of a priming signal such as a Toll-like receptor 4 (TLR4) agonist, cleaves pro-IL-1 cytokines to their active form to induce potent pro-inflammatory signaling. Casp1 also induces a regulated form of inflammatory cell death, termed pyroptosis, through Gasdermin D (GSDMD) N-terminal cleavage.[5] Chronic IL-1 cytokine secretion is associated with various disease pathologies,[6-9] but acute production can promote a Type 1 immune response to afford pathogen clearance in the context of infection or vaccination.[5, 10] Saponin-containing adjuvant formulations, such as $AS01_B$ and Matrix-M, are used in an increasing number of vaccines despite significant side effects in a large percentage of individuals.[11-14] Furthermore, saponins are chemically complex and currently require extraction from the bark of *Quillaja saponaria*, a limited natural resource, for scalable production.[15-17] As such, it is desirable to identify new IL-1 producing adjuvants with greater safety, scalability, and chemical tunability for use in vaccination.

One popular approach toward the identification of novel adjuvants is high throughput screening. Historically, such screens have been conducted with the goal of identifying novel agonists for a pattern recognition receptor (PRR) of interest *via* ligand-binding studies or cell-based assays.[18-20] Alternatively, functional outputs such as cytokine production can be screened in the absence of a specific target receptor. The Esser-Kahn lab recently generated a high

throughput dataset wherein transcription factor activation and cytokine production were assayed *in-vitro* following co-administration of >10,000 drug-like small molecules with PRR agonists.[21] One surprising result from this screen was that many of the tested compounds induced high levels of IL-1β secretion when co-administered with LPS (a TLR4 agonist), pointing to a population of small molecule drug-like compounds that may activate inflammasomes and serve as alternatives to saponin adjuvants. In this study, we characterize these compounds with the goal of identifying and formulating IL-1β-producing small molecules for use in vaccination. These compounds would have advantages of scalable synthesis and tunable structures, allowing for the identification, optimization, and development of next generation inflammasome activating adjuvants.

4.2 Results and Discussion.

4.2.1 Screening and validation of novel IL-1 producing adjuvants.

Identification of small molecule immunomodulators which can enhance IL-1β secretion in concert with TLR4 agonist signaling are desirable as low-cost and tunable alternatives to saponin adjuvant systems, such as AS01 and Matrix-M.[16] In our recent high throughput screen, a library of small molecule immunomodulator compounds were co-administered to THP-1 monocytes with the TLR4 agonist, bacterial lipopolysaccharide (LPS, 100 nM), or PBS. Six cytokines (IL-1β, IL-12, IP-10, CCL4, TNF-α, IFN-β) were assayed in the supernatant following overnight treatment using AlphaPlex bead-based assays.[21] The results were reported as fold-change increase or decrease in cytokine production relative to cells treated with LPS or PBS alone. From the results of this screen, we selected 11 compounds that maximized fold-change increase in IL-1β secretion for further analysis (**Table S4.1**). Compounds with low solubility were excluded, while six additional compounds that target similar signaling pathways as the top-performing compounds were also included for analysis (**Table S4.1**). The compounds selected predominantly included statins, cell cycle modulators, and kinase inhibitors, suggesting similar mechanisms of action.

With a library of 17 candidate compounds in hand, we first validated the activity of these compounds in bone marrow-derived macrophages (BMDMs) derived from C57Bl/6J mice. LPS-primed or -unprimed BMDMs were treated with each compound in serial two-fold dilutions of 1.9-500 μM to identify the concentration where maximum LPS-dependent IL-1β secretion was observed. Toxicity was assayed using secreted lactate dehydrogenase (LDH), while IL-1β secretion was assayed using ELISA (**Figure S4.1**). While statins identified during the primary screen did not induce high levels of IL-1β secretion in BMDMs, treatment with many of the top-performing cell cycle modulators and kinase inhibitors resulted in robust concentration-dependent IL-1β secretion, suggestive of inflammasome activation. Statins may induce IL-1β signaling in specific cell subsets or biological contexts outside the scope of this study. We also screened production of other pro-inflammatory cytokines when LPS-primed or -unprimed bone marrow-derived dendritic cells (BMDCs) were treated with our candidate compounds at 100 μM (**Figure S4.2**). 100 μM was selected as the concentration of peak activity for many compounds in our preliminary IL-1β screen. Again, many top-performing cell cycle modulators and kinase inhibitors induced high levels of IL-1α, IL-1β, IL-6, and TNF-α, pro-inflammatory cytokines associated with inflammasome activation and immunogenic cell death, supporting their further study as adjuvants.

Based on the results of this initial screen, the Cyclin-Dependent Kinase (CDK) inhibitors, Ribociclib, Palbociclib, Flavopiridol, and CDKI-73, were identified as potent inducers of IL-1β. CDK inhibitors are FDA-approved cancer therapeutics that interrupt cell cycle progression, resulting in senescence and apoptosis.[22-24] In addition to their senescence-inducing properties, CDK inhibitors are well-reported to induce a Senescence Associated Secretory Phenotype (SASP) characterized by release of pro-inflammatory cytokines (canonically IL-1α and IL-6).[25, 26] Using the SASP in adjuvant development has yet to be explored, though at least one study has demonstrated that SASP-mediated IL-1 secretion is mediated by inflammasomes.[25] The CDK4/6 inhibitors, Palbociclib and Ribociclib, have also been reported to enhance $CD8^+$ T cell responses through poorly defined mechanisms.[23, 27-31] We hypothesized that this immunostimulatory activity

could stem in part from activation of inflammasomes and be enhanced through synergistic co-delivery of TLR agonists to facilitate an adjuvant effect for vaccination. We therefore selected Ribociclib as a desirable candidate for further development as an adjuvant. Ribociclib activity was re-screened in LPS-primed or -unprimed BMDCs at 1.9-500 μM, and a peak concentration of secreted IL-1β (>3,000 pg/mL) was observed at 125 μM (**Figure 4.1A-B**). While cell death was observed in both LPS-unprimed and -primed cells treated with Ribociclib, high levels of pro-inflammatory cytokines required LPS priming (**Figure 4.1C**). Finally, Ribociclib was found to induce IL-1β secretion in LPS-primed human THP-1 monocytes, though priming with adjuvants targeting other PRRs induced low or undetectable levels of IL-1β secretion (**Figure S4.3**). These data encouraged further exploration into the mechanism of Ribociclib-mediated IL-1β secretion.

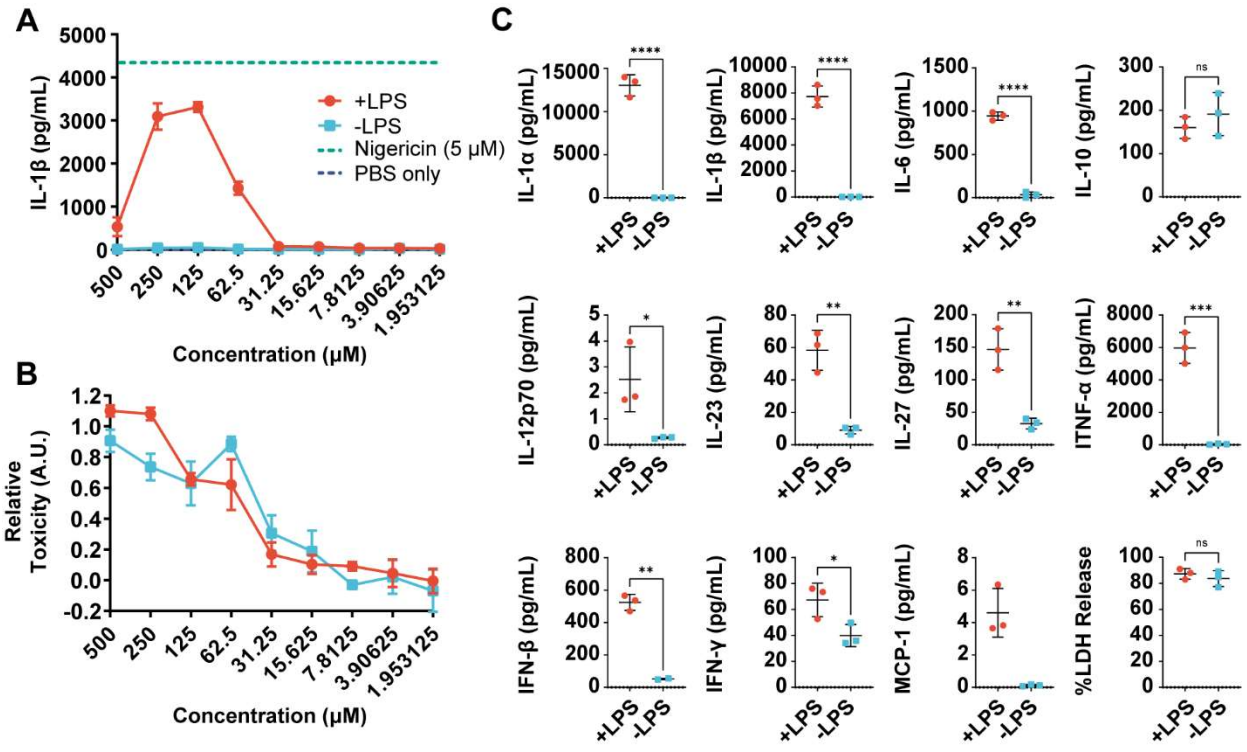

Figure 4.1: Identification of Ribociclib as a potent, IL-1 producing adjuvant. A) IL-1β and B) LDH release when LPS-primed or -unprimed BMDCs were treated with Ribociclib at various concentrations. C) LPS-primed or -unprimed BMDCs were treated with Ribociclib at 125 μM, which was found to be a concentration of maximum activity. Cytokine production was assayed using Legendplex Mouse Inflammation 13-plex, and unpaired t-tests were used to determine differences between groups. IL-17 and GM-CSF are not shown, as neither of these cytokines were observed in any of the treatment conditions.

4.2.2 Identifying mechanisms of Ribociclib-mediated IL-1 production in-vitro.

Having identified Ribociclib as a promising target compound, we next probed whether IL-1β secretion was resulting from activation of known inflammasome pathways. We first repeated IL-1β secretion studies in BMDCs in the presence of various chemical inhibitors. The NACHT, LRR and PYD domains-containing protein 3 (NLRP3) inflammasome is the most common and well-studied inflammasome, though a host of other inflammasomes with similar effector functions and roles in adaptive immunity have been reported.[5] NLRP3 is activated by a variety of signals that disrupt homeostasis, such as lysosomal destabilization, cellular ion fluxes, or intracellular reactive oxygen, which all result in NLRP3 conformational changes and downstream effector functions.[32] When BMDCs were pre-treated with homeostatic inhibitors prior to addition of our target compounds, few changes in IL-1β secretion were observed (**Figure 4.2A**). In contrast, treatment with direct inhibitors of NLRP3 or Caspases dramatically reduced IL-1β secretion (**Figure 4.2A**). To query the role of NLRP3 more definitively, we repeated assays in BMDC-KOs lacking components of inflammasome machinery: NLRP3, Caspase-1 (Casp1), and Gasdermin D (GSDMD) (**Figure 4.2B**). Knockout of these inflammasome components reduced IL-1β secretion, though some IL-1β was still observed suggesting a role for multiple, overlapping cell death pathways (or leaky gene knockouts). In contrast, knockout of IL-1R, which should have no effect on IL-1β secretion and was therefore used as a control, did not affect IL-1β secretion after treatment with Ribociclib (**Figure 4.2B**). Similar trends were observed with other CDK inhibitors and hit compounds (**Figures S4.4-S4.6**). Western Blots of BMDC lysates for cleavage products of active inflammasome machinery show that treatment with Ribociclib induced active Casp1 production followed by cleavage of GSDMD and IL-1β to their active form after 4 h (**Figure 4.2C** and **Figure S4.7**). Additional Western Blots for phosphorylated MLKL (a marker of necroptosis)[33] or phosphorylated Rb protein (a protein which is inhibited during CDK-induced senescence)[31] did not indicate activation of alternative cell death pathways. These data, in total, provide evidence

that Ribociclib and other CDK inhibitors activate inflammasomes to mediate IL-1β secretion, though further work is needed to understand the mechanism behind this novel mode of activation.

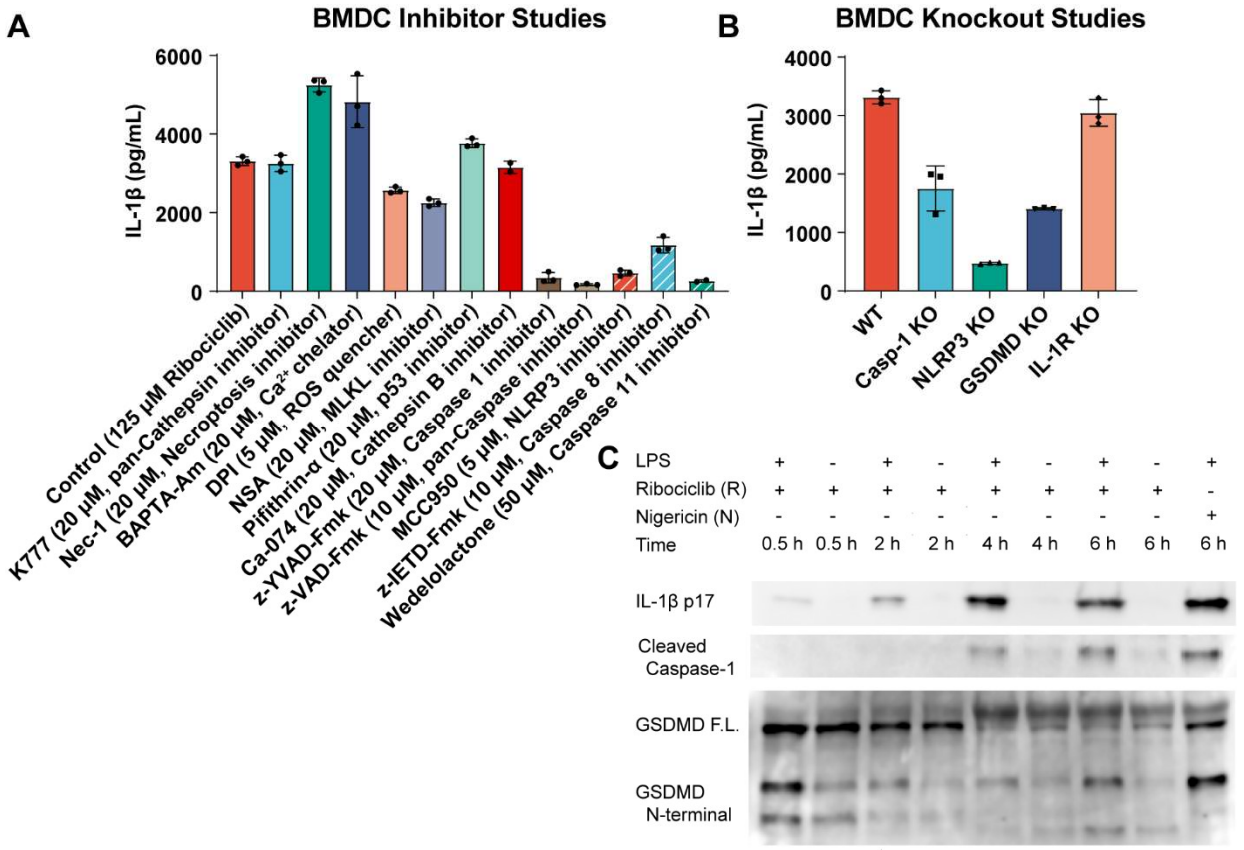

Figure 4.2: Evaluation of Ribociclib's mechanism of IL-1 cytokine production. A) LPS-primed BMDCs were pre-treated with the indicated inhibitor compounds for 30 min, then treated with 125 μM (or 15.6 μM, in the case of DPI) Ribociclib. IL-1β was measured in the supernatant *via* ELISA. B) LPS-primed BMDCs isolated from the indicated KO mice were treated with 125 μM Ribociclib, and IL-1β was measured in the supernatant *via* ELISA. C) LPS-primed or -unprimed BMDCs were treated with 125 μM Ribociclib (R) or a control, 5 μM Nigericin (N), for the indicated timepoints, then lysed with M-PER and analyzed *via* Western Blot. Full blots and conditions for antibody treatment are provided in **Figure S4.7**.

4.2.3 Formulation of Ribociclib for vaccination.

Having generated strong evidence of inflammasome activation *in vitro*, Ribociclib was formulated for vaccination in C57Bl6/J mice using a prophylactic ovalbumin (OVA) model. As inflammasome-activating adjuvants typically require both a TLR agonist signal an activating signal, Ribociclib (50 nmol/dose) was co-delivered with a TLR4 agonist, MPLA (5 μg/dose), that

has improved safety relative to LPS and is approved for use in humans. A saponin adjuvant, Quil-A, that is related to GSK's AS01 formulation, was similarly co-formulated with MPLA and used as a positive control. In a pilot study, the indicated formulations were injected intramuscularly with 50 μg OVA, mice were boosted at day 13, and experiments were terminated at day 26 (**Figure S4.8A**). Here, Ribociclib-adjuvanted vaccines were found to enhance early IFN-γ production at 24 h relative to Quil-A, though IL-6 and MCP-1 levels were reduced relative to Quil-A (**Figure S4.8B**). Evaluation of the adaptive response revealed that, while Ribociclib induced minor increases in OVA-specific B and T cell responses, these responses were an order of magnitude lower than the Quil-A containing formulations (**Figure S4.8C-E**). In a follow-up study, Ribociclib formulations containing 10, 100, or 1,000 nmol/dose were employed (**Figure S4.9**). Here, Ribociclib induced a modest increase in splenic, antigen-specific $CD8^+$ T cell production at 10 and 100 nmol relative to MPLA alone, though it still did not perform at an equivalent level to Quil-A. These results were encouraging, but we hypothesized that the high bioavailability of Ribociclib (which was originally designed as an orally available drug) resulted in poor retention at the injection site, limiting its effects during intramuscular injection. With this limitation in mind, we set off to improve the formulation of Ribociclib for vaccination by encapsulating it into liposomes.

Liposomal formulations have become common tools to modify the physicochemical properties of active pharmaceutical ingredients (APIs) and control their delivery to specific cell and organelle subsets. In liposomes, hydrophilic APIs can be loaded into the aqueous core or lipid shell, but poor loading of aqueous APIs hinders control over loading and delivery of large quantities of payload.[34] To better control the loading and delivery of Ribociclib, a lipid-modified version of Ribociclib containing a 1,2-dipalmitoyl-*sn*-glycero-3-phosphoethanolamine (DPPE) tail, which we refer to as Ribo-L, was prepared in two steps (**Figure 4.3A** and **S4.10**). DPPE can be cleaved by lysosomal phospholipases[35] to release Ribociclib with a four-atom modification at the piperazine terminus, a site that was found to be amenable to modification in previous structure-activity studies.[36] Lipid functionalization was found to reduce IL-1β secretion from ~3,000 pg/mL

to ~1,000 pg/mL at 125 μM (**Figure S4.11**), though it was reasoned that the enhanced delivery of Ribo-L would serve as a net benefit *in-vivo*. Ribo-L was then incorporated alongside MPLA into DPSC liposomes, which were prepared *via* thin film rehydration and extrusion through a 200 nm filter.[34] Liposomes loaded with 1000, 200, or 40 μg/mL of Ribo-L (henceforth referred to as Hi, Mid, and Lo) were found to have similar size, charge, and shape as MPLA control liposomes (**Figure 4.3B-C** and **S4.12-S4.15**), supporting their use in downstream biological assays.

Having successfully prepared Ribociclib-loaded liposomes, prime-boost vaccination studies were repeated to evaluate if these formulations could enhance vaccine efficacy relative to soluble formulations. Ribo-L, MPLA, and empty liposomes or unlinked controls were injected intramuscularly, and cellular and humoral immune responses were evaluated (**Figure 4.3D**). Ribo-L liposomes dramatically enhance the pro-inflammatory cytokines, IL-6 and TNF-α, 2 h after initial injection (**Figure 4.3E**). Quil A, meanwhile, was the only treatment to induce increased levels of IFN-γ at 24 h post-initial injection (**Figure 4.3E**). Hypothesizing that Ribo-L liposomes enhanced IFN-γ production at later timepoints than those tested, mice were also bled at 72 h post-boost. In this case, Ribo-L liposomes increased IFN-γ levels in a Ribo-L dose-dependent fashion (**Figure S4.16**), confirming that these formulations enhanced IFN-γ at later points than Quil-A. The Ribo-L liposomes resulted in comparable antibody titer levels to MPLA liposomes (**Figure 4.3H**); however, Ribo-L liposomes enhanced both $CD4^+$ and $CD8^+$ antigen-specific T cell responses relative to MPLA liposomes as measured by tetramer staining (**Figure 4.3I-J**). In a second independent study, Ribo-L liposomes were also found to enhance antigen-specific germinal center B cells responses to levels comparable with Quil-A (**Figures S4.17-S4.19**). These data, in total, support the notion that Ribociclib enhances cell-mediated immune responses.

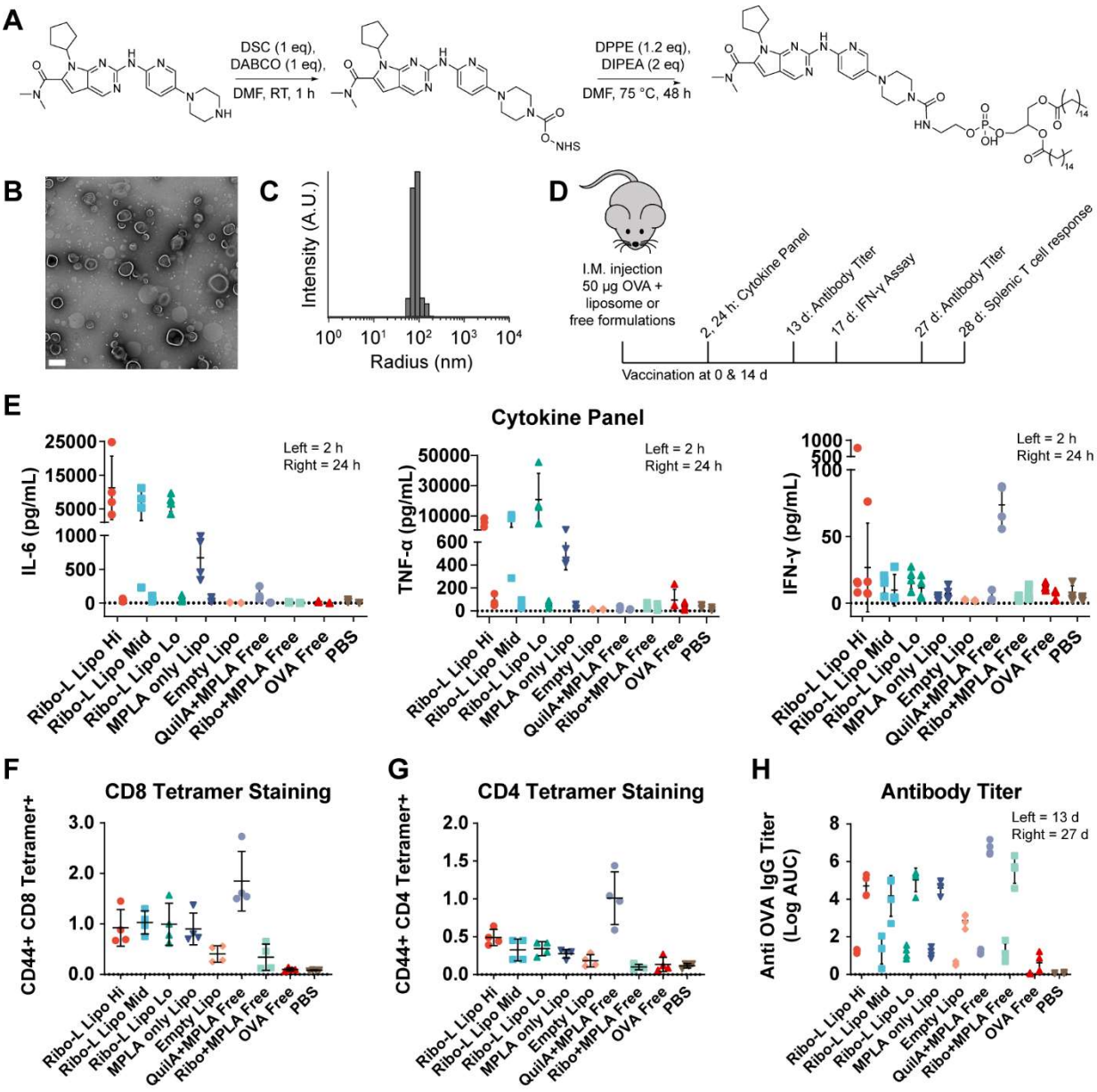

Figure 4.3: Synthesis, formulation, and *in vivo* responses of Ribociclib lipid derivatives. A) Synthetic scheme for the preparation of Ribo-L in two steps from commercially available Ribociclib. B) TEM image of Ribo-L formulated at 40 µg/mL within DSPC and MPLA containing liposomes (scale bar = 250 nm). C) Representative DLS of monodisperse liposome formulation. D) Vaccination schedule for the characterization of Ribo-L formulations *in vivo*. HI, MED, and LO correspond to 50, 10, and 2 nmol/dose of Ribo-L in liposomes. E) Cytokine production 2 h (left) and 24 h (right) after injection with the indicated formulations. F) Splenic, antigen specific CD8 and G) CD4 T cell responses 28 d after initial vaccination. H) Anti-OVA IgG titer 13 d (left) and 27 d (right) after initial vaccination.

4.2.4 Evaluating in-vivo responses toward Ribociclib-adjuvanted vaccines.

Having successfully developed a Ribociclib-containing formulation for vaccination, further efforts were undertaken to understand the mechanisms of Ribo-L liposomes *in-vivo*. First, we asked whether these liposomes enhance activation of dendritic cells in the draining lymph node. Mice were injected intramuscularly with vaccines containing OVA or DQ-OVA adjuvanted with liposomal or free Ribociclib, Quil A, or PBS, and the draining inguinal lymph node was dissected 5 d later (modeling a recent study by Li, *et al.*)[37] for immunophenotypic analysis. DQ-OVA is a self-quenched fluorescent OVA derivative which becomes fluorescent upon endosomal processing and protease-mediated cleavage.[38] It was observed that the Ribo-L containing liposomes upregulated surface expression of CD86 and presentation of the immunodominant OVA antigen, SIINFEKL, on dendritic cells, whereas free Ribociclib did not facilitate this productive innate immune response (**Figure 4.4A-B**). Moreover, DQ-OVA processing was also enhanced by Ribo-L liposomes relative to free Ribociclib (**Figure S4.20**). We then asked whether this response was dependent on IL-1 receptor (IL-1R) signaling. IL-1R-deficient mice or wild-type (WT) controls were vaccinated with OVA containing $AS01_B$ (which was obtained from Shingrix) or Ribo-L liposomes as adjuvants (**Figure 4.4C**). No differences in systemic TNF-α or IL-6 production were observed between IL-1R-deficient and WT mice after treatment with $AS01_B$ or Ribo-L liposomes at 2 or 24 h after injection (**Figure 4.4D-E**). Despite this lack of early cytokine response, IL-1R-deficient mice had reduced OVA-specific $CD8^+$ T cell responses relative to their WT counterparts after treatment with both $AS01_B$ or Ribo-L liposome adjuvanted vaccines (**Figure 4.4F** and **S4.21**). Moreover, IL-1R-deficient mice had reductions in anti-OVA IgG responses after treatment with Ribo-L liposomes, but not $AS01_B$ (**Figure 4.4G** and **S4.22**). While total IgG and CD8 T cell responses were reduced in IL-1R-KO mice, these changes did not correspond with differences between groups in the IgG2c/IgG1 ratio, a feature which is often associated with a Th1-biased responses (**Figure S4.22**). Moreover, the differences in total IgG and CD8 T cell responses did not correspond with changes in antigen-specific germinal center B cell production

(**Figure S4.23**). Altogether, these results support the hypothesis that Ribo-L liposomes induce IL-1 cytokine production in the draining lymph node to facilitate upregulation of cell surface markers and enhanced antigen presentation by dendritic cells. Moreover, these studies provide the first evaluation of adaptive immune responses toward $AS01_B$, a highly potent and commercially relevant adjuvant, in IL-1R deficient mice. While the role of inflammasomes in the adjuvanticity of $AS01_B$ is still debated, these studies provide additional insight into its mechanism of action.

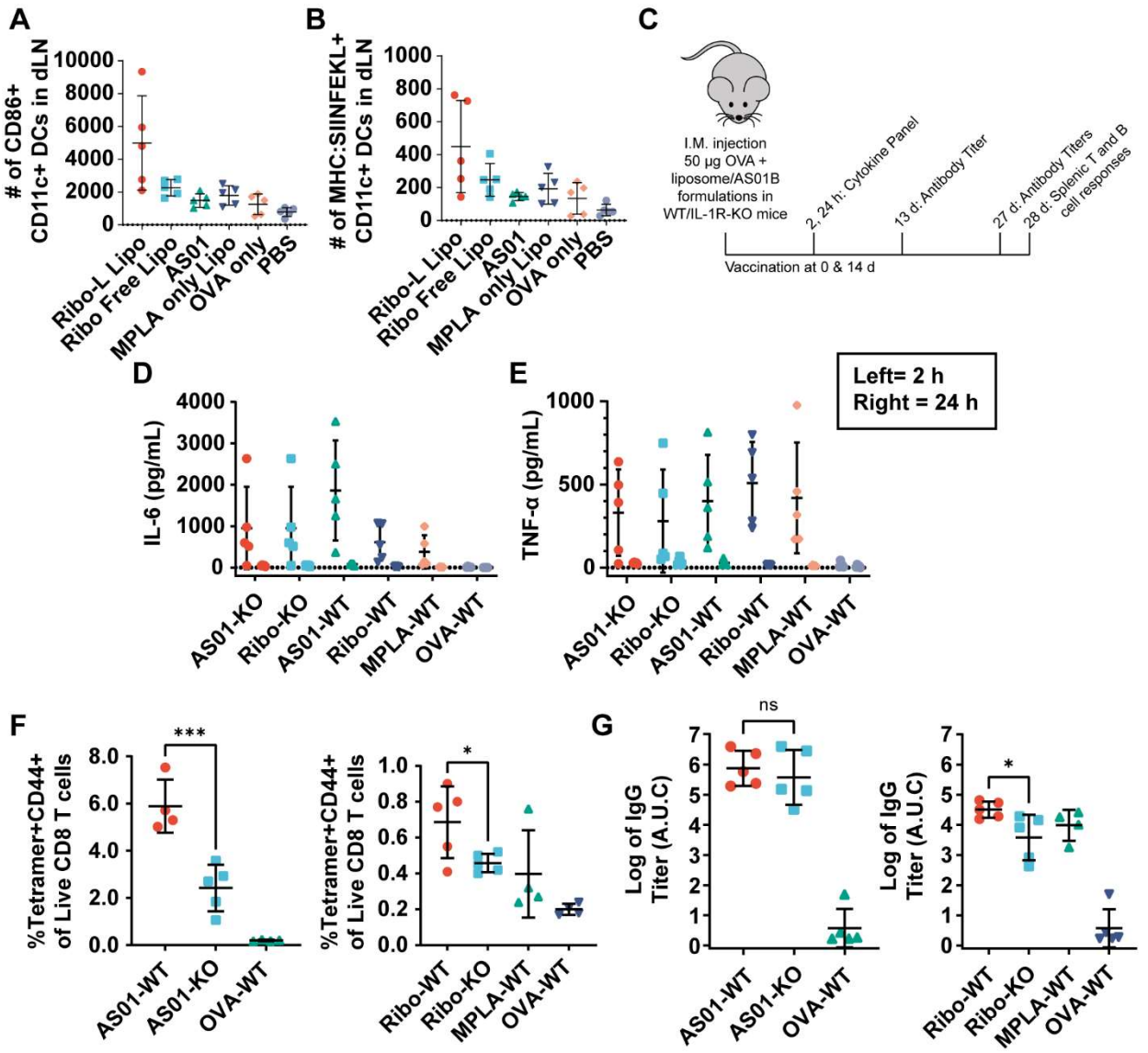

Figure 4.4: In-vivo mechanism of Ribociclib-mediated immunity. A) Upregulation of the cell surface markers, CD86 and MHC-II, and B) enhanced presentation of MHC-I restricted antigen on dendritic cells in the draining inguinal lymph node of mice injected intramuscularly with the indicated formulations. C) Vaccination schedule for a comparative study between wild-type (WT) and IL-1R deficient (KO) C57Bl6/J mice. D) Systemic IL-6 and E) TNF-α in the serum of WT or KO mice vaccinated with the indicated formulations after 2 or 24 h. Other cytokines tested were below baseline levels and are therefore not reported. F) Splenic, antigen-specific CD8 T cell responses to the indicated formulations. G) Total IgG titers generated in response to the indicated formulations. For F-G, the comparisons were conducted between WT and IL-1R KO mice, so separate statistical analyses (one-way ANOVA with Sidak's multiple comparisons test) were conducted using the sets of data shown.

We then tested the Ribo-L liposomes as prophylactic vaccines against herpes zoster (Shingles) infection. A direct head-to-head comparison was conducted to Shingrix, which is an

AS01$_B$ adjuvanted recombinant vaccine used clinically in individuals >50 years old.[12] Mice were vaccinated using 1/10th of the human dose as reported previously,[39] and the recombinant glycoproptein antigen (gE) used commercially was employed for all experimental groups. In this study, it was found that Ribo-L liposomes performed comparably to MPLA liposomes and were less effective than AS01-adjuvanted vaccines, offering no additional protection in terms of antibody titers or antigen-specific T cell responses (**Figures 4.5** and **S4.24**). Only CD4$^+$ T cell responses were observed, suggesting that gE is CD4-restricted in C57Bl6/J mice – a feature which may limit the efficacy of IL-1 producing adjuvants in this model. Additional work must be conducted to understand the limitations of the Ribo-L liposomal formulation to optimize this system for new applications. While future work is needed to fully demonstrate the Ribo-L platform, the data herein provide compelling evidence that this (and other) IL-1 producing small adjuvant(s), when formulated appropriately, could prove as valuable tools for vaccination.

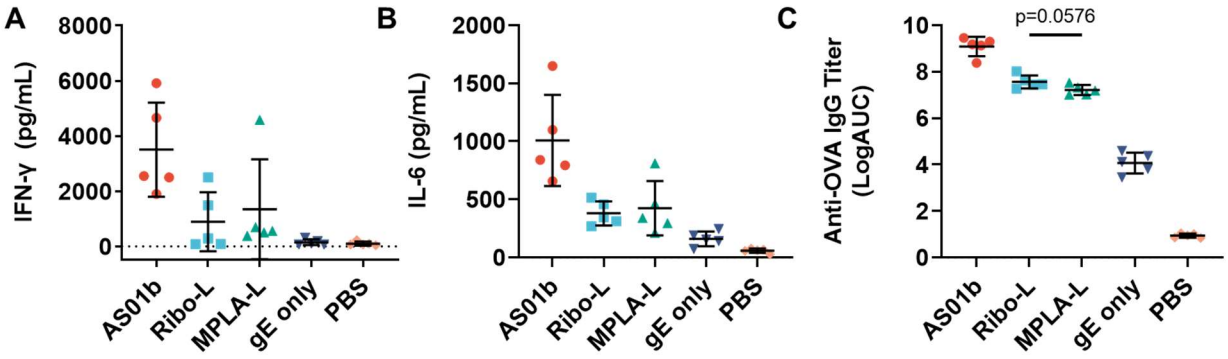

Figure 4.5: Adaptive responses toward shingles vaccine formulations. A-B) Splenocytes were harvested and restimulated with 5 μg/mL of gE antigen for 4 d. Supernatant was then collected and analyzed for T the cell polarizing cytokines, A) IFN-γ or B) IL-6. C) Serum was collected 14 d after boost, and IgG titers were performed using ELISA plates coated with gE antigen.

4.3 Conclusion and Future Directions.

In this study, we report the identification of CDK4/6 inhibitors as novel inflammasome activating adjuvants for vaccination using a high throughput screening approach. Ribociclib, an

FDA-approved small molecule inhibitor, was found to induce IL-1β secretion in dendritic cells in a Caspase-, NLRP3-, and GSDMD-dependent fashion through both inhibitor and knock-out studies. When co-formulated in liposomes with a TLR4 agonist, MPLA, and used for vaccination with a model antigen, OVA, Ribociclib enhanced antigen specific CD4 and CD8 T cell responses relative to controls. Ribociclib also enhanced T cell and antibody responses in a manner partially dependent upon IL-1R signaling. This system did not translate to a clinically relevant Shingles model, nor did it reach levels of efficacy achieved by the AS01 formulation, highlighting a need for optimization of Ribociclib liposome platform toward different antigens or delivery contexts (or identification of other IL-1 producing small molecule adjuvant formulations). Nevertheless, this system could serve as a low-cost, tunable adjuvant platform for vaccination. More globally, these results highlight the potential of high throughput screening to identify novel inflammasome activating vaccine adjuvants that overcome the limitations of saponin adjuvants.

Several studies have identified that Ribociclib and other CDK inhibitors enhance cell-mediated adaptive immune responses when used to induce cell cycle arrest in the context of cancer therapy.[27-30] In this study, we report inflammasome activation as an additional immune-potentiating effect of Ribociclib. CDK inhibitors have long been shown to induce high levels of pro-inflammatory cytokine production *via* the SASP, and it is likely based on the work herein that these effects are mediated, at least in part, by activation of inflammasomes.[25] Co-administration of Ribociclib with TLR4 agonists was shown to bolster IL-1 secretion through Caspase dependent mechanisms *in vitro* and enhance antigen presentation *in vivo*. Moreover, Th1-biased immune responses were enhanced after prime-boost vaccination when Ribociclib was formulated into liposomes. Enhanced Th1 responses are a key feature of some NLRP3 ligands,[10] though correlating inflammasome activation to the adjuvant activity of vaccine formulations has proven challenging.[2] Given that inflammasome activation results in pyroptosis, a rapid and inflammatory mode of cell death, it is challenging to ascribe inflammasome activation to a kinase-dependent or -independent mechanism using traditional methods. Genetic ablation of the interaction between

CDK4/6 and Cyclin D is embryonic lethal.[40, 41] While we provide evidence suggestive of Caspase and NLRP3 inhibition by Ribociclib, future work must be conducted to understand how these compounds mediate this phenotype. Kinase screening in parallel with proteomics and transient genetic knockdowns could provide critical information toward achieving this goal, though these assays are well beyond the scope of this pilot screening study.

More globally, this study supports the identification of novel small molecule adjuvants targeting the NLRP3 inflammasome and/or IL-1β for use in vaccination. Many FDA-approved vaccine APIs have been shown in recent years to activate inflammasomes, including saponins and the ionizable lipid component of mRNA lipid nanoparticles.[2, 3, 42] While these compounds have shown remarkable success in vaccination, they are challenging and expensive to prepare, and they induce immunotoxic side effects in many individuals – all hindering widespread adoption of these platforms. Small molecules, on the other hand, are often less costly and more easily tunable. Development of small molecule inflammasome activators would allow for better control over inflammasome activation, induce safer and/or more efficacious responses, and improve vaccine accessibility to a larger population. Ribociclib, for example, can be prepared on an industrial scale in 5-6 synthetic steps,[43] and the lipid modification reported herein requires only two additional steps. While further optimization of the Ribociclib structure and formulation or identification of more potent compounds may still be needed, this work provides proof of concept that small molecule inflammasome activators can hold great potential in next-generation vaccines.

The identification of Ribociclib as an inflammasome activating adjuvant holds great potential for future study both in vaccine development and in cancer immunology. It is of great interest to determine if inflammasome activation contributes to cell-mediated immunity generated by CDK inhibitors in a clinical setting. Goel *et al.* report that CDK inhibitors enhance type-III interferon production and inhibit regulatory T cell proliferation,[27] while Deng *et al.* report that CDK inhibitors derepress NFAT signaling to facilitate effector T cell function.[28] If inflammasome activation is confirmed to be important for these effector T cell responses, then future studies may

consider co-delivery of Ribociclib (or other CDK inhibitors) with neoantigens for dual therapy generating both cell cycle arrest and anti-tumor immunity. This hypothesis can be tested in a preliminary fashion by probing tumor growth and T cell infiltration in WT or IL-1R-KO mice treated with Ribociclib. Additionally, future work will be needed to optimize the formulation both for cancer immunotherapy and vaccination. Ribociclib is a highly polar, orally available drug. In this study, we overcome this limitation by modifying Ribociclib with stimulus responsive lipid-based linkers which afford high loading efficiency into liposomes; however, a 3-fold reduction in activity was observed after this modification (**Figure S4.11**). More work is needed to conclusive determine if Ribociclib induces IL-1 secretion through CDK inhibition or an alternative mechanism. In either case, better structure-property relationships will allow for modified Ribociclib derivatives that maintain immunogenicity while still allowing for controlled delivery. Overall, this study provides key insight which will both expand the scope of use for Ribociclib and inspire the development of better inflammasome activating adjuvants for vaccination.

4.4 Materials and Methods.

Mice and Materials. All chemicals and cell culture reagents were obtained from Sigma Aldrich or Thermo Fisher and used without further purification unless otherwise noted. **Table S4.2** provides the sourcing of screening compounds and inhibitors. For synthesis, Ribociclib was purchased in bulk from AmBeed, and N,N'-disuccinimidyl carbonate was purchased from AA Blocks. Lipid reagents for liposomes (including synthetic MPLA-PHAD used in liposomes) were purchased from Avanti Polar Lipids. A table providing the clone and source of all antibodies used for flow cytometry and western blots is provided in **Table S4.3**. The human Shingrix vaccine was purchased from VaccineShop through an approved contract with the IIT Research Institute that allows for animal use. For *in-vitro* assay, cells were maintained at 37 °C and 5% CO2. For *in-vivo* studies, female, 6-week-old C57Bl6/J (WT), B6.129S6-Nlrp3tm1Bhk/J (NLRP3-KO), B6N.129S2-Casp1tm1Flv/J (Casp1-KO), C57BL/6J-Gsdmdem1Vnce/J (GSDMD-KO), and B6.129S7-

Il1r1tm1Imx/J (IL-1R-KO) were purchased from Jackson Labs and allowed to acclimatize for at least 1 week prior to use. Mice were housed in an AAALAC accredited animal facility with controlled light, temperature, and humidity conditions and supplied with food and water *ad libitum*. All animal procedures were performed under a protocol approved by the University of Chicago Institutional Animal Care and Use Committee. Unless otherwise noted, all data are analyzed and plotted in GraphPad Prism 9.

High Throughput Immunomodulator Screen. The high throughput screen was conducted as reported in J.Y. Kim, M.G. Rosenberger, *et al.*[21] using automated high throughput instrumentation. Briefly, RAW Dual cells (InvitroGen) were plated at 50,000 cells/well in 384 well plates in DMEM + 10% HI-FBS. Cells were treated with immunomodulator compounds (10 μM). After 1 h, PRR agonists were added, and cells were incubated for 20 h. Cells were imaged for viability using IncuCyte S3 (Sartorius), and then supernatant was collected. NF-κB was determined using QUANTI-Blue Assay (InvivoGen), and IRF activity was determined using QUANTI-Luc Plus Assay (InvivoGen). From the primary screen, modulators that induced significant changes in NF-κB and/or IRF activity without inducing toxicity (viability > 70%) were selected for secondary screening. In the secondary screen, THP-1 cells (ATCC) were plated at 50,000 cells/well in 384 well plates. Cells were treated with immunomodulator compounds (10 μM). After 1 h, PRR agonists were added, and cells were incubated for 20 h. Supernatant was collected and analyzed for cytokine production (IL-1β, IL-12, IP-10, CCL4, TNF-α, IFN-β) using AlphaPlex Multiplexing Kits (PerkinElmer). Absorbance and luminescence readouts were quantified using a Synergy NEO2 plate reader (BioTek) with AlphaPlex filters for europium (615 nm) and terbium (545 nm) emission where appropriate. Immunomodulator activity was quantified by determining the fold-change relative to controls, which were only treated with PRR agonists.

Selection and Preparation of Hit Compounds. Hit compounds for secondary screening were selected from the high throughput data set by evaluating the fold-change increase in IL-1β secretion in THP-1 cells treated with LPS-EK (100 nM, InvivoGen) with modulators relative to

LPS-EK alone. Compounds with solubility < 10 mM in DMSO were excluded. Palbociclib, Flavopiridol, CDKI-73, Dabrafenib, Bafetinib, and IPI-3063 were also included in the screen based on preliminary data suggesting high levels of activity, while Quil-A was included as a control with known activity *in-vivo*. For all *in-vitro* studies, 10 mM solutions of the inhibitors were prepared in DMSO and diluted in PBS to 10x of the working concentration prior to addition to cells.

Dose-response screening of IL-1β secretion in primary murine cells. Bone-marrow derived macrophages (BMDMs) or dendritic cells (BMDCs) from wild-type or indicated knockout mice were isolated and differentiated as reported previously.[44, 45] After 6 d of differentiation, cells were mechanically detached, washed, and plated in a 96 well plate at 1.8 x 10^5 cells/well in 180 µL fresh medium (RPMI + 10% HI-FBS). Cells were allowed to adhere for 1 h and then treated with 20 µL of 10x ultrapure LPS-EB (working concentration 100 EU/mL) or PBS. After 3 h, cells were washed and resuspended in 180 µL fresh medium. Where relevant, cells were pretreated with inhibitors (2 µL of 100x working concentration in DMSO as noted in the figures) for 30 min. Then 20 µL of 10x hit compounds were added and incubated overnight. After 16 h, supernatants were collected and subjected to CyQUANT™ LDH Cytotoxicity Assay (Thermo Scientific) and ELISA MAX™ Mouse IL-1β Assay (BioLegend) according to the manufacturer's procedures. Absorbance readouts were collected using Multiskan FC plate reader (Thermo Scientific).

Immunoblot Assays. BMDCs were isolated and cultured as described above and plated in untreated 24 well plates at 1x10^6 cells/well. Cells were treated with 100 EU/mL ultrapure LPS-BS (InvivoGen) or PBS for 3 h, then washed and treated with Ribociclib (100 µM) or Nigericin (5 µM) for the indicated times. Supernatant was then collected, and cells were lysed with 200 µL M-PER (Thermo Scientific) with 1x Protease/phosphatase Inhibitor Cocktail (Cell Signaling Technologies). Supernatants and lysates were aliquoted into 20 µL portions and stored at -80 °C until use. For assays, supernatants or lysates were loaded 3:1:0.1 with 4x Laemmli buffer (BioRad) and β-mercaptoethanol, respectively, and boiled for 10 min at 95 °C. They were then loaded alongside Prime-Step Prestained Protein Ladder (BioRad) into 12% Mini-PROTEAN TGX

Precast Gels (BioRad), and 125 V was applied for 60-75 min to separate bands. Blots were transferred to PVDF membranes using Trans-Blot turbo transfer system (BioRad). Membranes were blocked with TBS-T + 5% nonfat milk at RT for 1 h, washed 3 x 5 min with TBS-T, then stained with the indicated antibodies (**Table S4.3**) in TBS-T + 5% BSA overnight at 4 °C. After 16 h, membranes were washed 3 x 5 min with TBS-T and stained with HRP Goat anti-Rabbit or Goat anti-Mouse IgG (Thermo Scientific) in TBS-T + 1% BSA at RT for 1 h in the dark. Finally, membranes were washed 5 x 5 min with TBS-T, treated for 10 min with Supersignal West Dura Extended Duration Chemiluminescent Substrate (Thermo Scientific), and imaged using an Azure 600 imager (Azure Biosystems). Images were processed using ImageJ.

Vaccination Studies. Age matched, 6-to-12-week-old female C57Bl/6J mice were vaccinated intramuscularly in the flank with 50 µL of vaccine formulations. For soluble formulations, vaccines were prepared in 7:2:1 PBS:PEG300:DMSO and filtered through a 200 nm sterile filter prior to injection. For liposomal formulations, dialyzed liposomes were added to lyophilized antigens and briefly vortexed prior to injection to mimic GSK's *Adjuvant System* formulations.[46] Unless otherwise noted, studies with OVA contained 50 µg OVA, 10 µg VacciGrade sMPLA (InvivoGen), and 50 nmol of modulators (SelleckChem) or 10 µg Quil-A (InvivoGen), while liposomes contained 50 µg OVA, 5 µg sMPLA (Avanti Polar Lipids), and 10 nmol of Ribo-Lipid. Where noted, $AS01_B$ and gE antigen were obtained from the licensed Shingles vaccine and used at $1/10^{th}$ of the human dose. Mice were vaccinated at experiment onset and again on day 14. 2 and 24 h after the initial injection, mice were bled via the submandibular vein, and cytokines in the serum were assayed *via* LEGENDplex Mouse Inflammation 13-plex (BioLegend) according to the manufacturer's protocol. At days 13 and 27, mice were bled via the submandibular vein for antibody titers. On day 28, mice were sacrificed, and spleens were harvested for flow cytometry and/or restimulation

IFN-γ Analysis Post-Boost. An adapted form of LEGENDplex Mouse Inflammation 13-plex using IFN-γ capture beads (Biolegend #740153) was used to assay IFN-γ production post-

boost. Briefly, blood was collected from the submandibular vein 72 h post-boost. 25 µL serum (or recombinant IFN-γ controls), 25 µL PBS, and 25 µL of 1x capture beads were added to a V-bottom plate and incubated while shaking at 700 rpm for 2 h. Beads were pelleted by centrifugation at 1000 x G for 2 min, washed with PBS, and then treated with 25 µL of biotinylated anti-IFN-γ antibody (Biolegend #505803, 5 µg/mL). After 1 h, 25 µL of streptavidin-PE (Biolegend #405203, 5 µg/mL) was added and incubated 30 min longer. Beads were pelleted by centrifugation at 1000 x G for 2 min, washed with PBS, and analyzed using a Novocyte ACEA (Agilent) flow cytometer.

Antibody Titers. MaxiSorb ELISA Plates (Nunc) were coated overnight with 5 µg/mL antigen in PBS at 4 °C. After 16 h, plates were washed 3x and then blocked with PBS + 2% BSA. After 2 h, plates were washed 3x and then treated with serial ten-fold dilutions of serum (10^2-10^7 dilution) in PBS + 2% BSA. After 2 h, plates were washed 3x and then treated with Goat anti-Mouse IgG (Thermo Scientific), Goat anti-mouse IgG1 (Southern Biotech), or Goat anti-mouse IgG2c (Southern Biotech) diluted 1:10,000 in PBS + 0.4% BSA. After 1 h, plates were washed 5x and then treated with 100 µL of 1-step Ultra-TMB (Thermo Scientific). After 5 min, 50 µL of 2 M H_2SO_4 was added, and plates were read at 450 nm using Multiskan FC plate reader (Thermo Scientific). Data is reported as the logarithm of area under the curve. Where noted, some antibody responses were also determined *via* direct ELISA. In this case, Mouse Anti-Ovalbumin Ig(A+G+M) ELISA Kit (ADI) was employed according to the manufacturer's procedure.

Restimulation of T cells. Spleens were mechanically ground into a single cell suspension, treated with ACK lysing buffer to remove red blood cells, and counted using CountBright Absolute Counting Beads (Thermo Scientific). 2 x 10^6 splenoyctes were plated in a round-bottom 96 well plate in RPMI + 10% HI-FBS + 10 mM HEPES + 1x MEM non-essential amino acids + 55 µM β-mercaptoethanol. For cytokine analysis, splenocytes were treated with 20 µM of antigen for 72 or 96 h as indicated, and then cytokine production in the supernatant was assayed via CBA Mouse Th1/2/17 Panel (BD Biosciences) according to the manufacturer's protocol. For intracellular cytokine staining of Shingrix vaccinated T cells, cells were incubated

with VZV-gE overlapping peptide pool (JPT, 2 μM) for 2 h, then GolgiBlock (BD) was added and cells were incubated 6 h longer. Cells were then washed and stained for viability and surface markers as described above, then fixed with Cytofix/Cytoperm kit (BD). The fixed cells were then stained for intracellular cytokines, washed, and analyzed by with an Novocyte ACEA (Agilent) flow cytometer. Data were analyzed using FlowJo v10.8.1.

Flow Cytometric Analysis of B and T cell surface markers. Spleens were mechanically ground into a single cell suspension, treated with ACK lysing buffer to remove red blood cells, and counted using CountBright Absolute Counting Beads (Thermo Scientific). 5 x 10^6 cells were stained for viability for 30 mins at ambient temperature, then washed and treated with Fc-receptor blocking antibodies for 15 min at 4 °C. Cell surface markers were then stained, and cells and analyzed with a Novocyte Penteon (Agilent) flow cytometer. MHC tetramers and pentamers were incubated with cells at 37 °C for 30 min prior to addition to other cell surface markers, which were incubated at 4 °C for 30 min. Data were analyzed using FlowJo v10.8.1.

Synthesis and Characterization of Ribo-Lipid. Ribo-lipid was synthesized in two steps from Ribociclib. First, Ribociclib (200 mg, 1.0 eq), 1,4-diazabicyclo [2.2.2]octane (52 mg, 1.0 eq), and 10 mL DMF were added to a flame dried, round bottom flask. Under rapid stirring, N,N′-disuccinimidyl carbonate (118 mg, 1.0 eq) was added and the reaction sealed under argon. After 1 h, solvent was removed under reduced pressure, and the crude product was taken up in DCM. The crude was loaded onto silica and purified by flash chromatography (0 to 10% gradient elution of MeOH in DCM). Product containing fractions were pooled and dried to obtain Ribociclib-NHS Ester as a yellow solid (183 mg, 69% yield). ^{1}H-NMR (400 MHz, DMSO-d6): 9.35 (s, 1H), 8.76 (s, 1H), 8.19 (d, 1H), 8.04 (d, 1H), 7.49 (dd, 1H), 6.60 (s, 1H), 4.73 (m, 1H), 3.72 (br s, 2H), 3.60 (br s, 2H), 3.20 (t, 4H), 3.05 (s, 6H), 2.80 (t, 4H), 1.98 (m, 4H), 1.65 (m, 2H), 1.23 (m, 2H). ESI-MS: $[M]+H^+$ = 576.3 expected, 576.2 observed. NOTE: After chromatographic separation, solvent must be rapidly removed from Riboiclib-NHS Ester to avoid reaction of the NHS Ester with MeOH.

To a glass scintillation vial was added 1,2-dipalmitoyl-*sn*-glycero-3-phosphoethanolamine (229 mg, 1.0 eq), N,N-diisopropylamine (200 µL, excess), and 15 mL DMF. The solution was stirred at 70 °C in an oil bath until all components dissolved, and then Ribociclib-NHS Ester (208 mg, 1.1 eq) was added in a single portion. The reaction was stirred at 70 °C for 48 h, at which point complete reaction was confirmed by LC-MS (70-100% ACN in H_2O + 0.1% TFA, 50x4.6 mm C18 column) and TLC ("Solvent A" = 65:25:4 $CHCl_3$:MeOH:H_2O). DMF was then removed under reduced pressure, and the crude product was taken up in $CHCl_3$. The product was purified using silica gel chromatography (stepwise elution of 20%, 40%, 60% Solvent A in $CHCl_3$). The pooled fractions were concentrated, taken up in 1:1 MeOH:H_2O + 1% TFA, and freeze dried to obtain a yellow solid (135 mg, 35% yield). ^{1}H-NMR (500 MHz, DMSO-d6, T = 50 ºC): 9.67 (br s, 1H), 8.81 (m, 1H), 8.00 (m, 2H), 7.61 (dd, 1H), 6.64 (s, 1H), 5.14 (m, 1H), 4.76 (m, 1H), 4.29 (m, 1H), 4.12 (m, 1H), 3.99 (m, 2H), 3.86 (m, 2H), 3.62 (m, 1H), 3.48 (m, 4H), 3.35 (m, 1H), 3.28 (m, 2H), 3.10 (m, 4H), 3.06 (s, 6H), 2.41 (m, 2H), 2.27 (m, 4H), 2.00 (m, 4H), 1.66 (m, 2H), 1.50 (m, 4H), 1.23 (m, 50H), 0.85 (t, 6H). ESI-MS: $[M]+H^+$ = 1152.7 expected, 1152.8 observed. Phase transition in DMSO = 40 ºC.

Preparation and Characterization of Liposomes. Liposomes were prepared via thin film rehydration and extrusion. Distearoylphosphatidylcholine (DSPC), 1,2-distearoyl-sn-glycero-3-phosphoethanolamine-N-[methoxy(polyethylene glycol)-2000] (18:0 PEG2000 PE), cholesterol, 1,1'-Dioctadecyl-3,3,3',3'-Tetramethylindocarbocyanine Perchlorate (DiI), synthetic MPLA phosphorylated hexa-acyl disaccharide (sMPLA-PHAD), and Ribo-Lipid were dissolved in chloroform, added to 20 mL scintillation vials, and evaporated under reduced pressure to form a thin film (see **Figure S4.13** for reagent quantities used in preparation of 1 mL liposomes). After drying overnight, the thin films were rehydrated in PBS under gentle rotation at 72 °C for 5 min, then extruded through a 200 nm filter to create a uniform size distribution. The liposomes were dialyzed against PBS overnight using 3.5K MWCO Slide-A-Lyzer MINI dialysis cups (Thermo Scientific). Liposomes were characterized using high performance liquid chromatography

(HPLC), dynamic and electrophoretic light scattering (DLS/ELS), and transmission electron microscopy (TEM). For HPLC, liposomes were decomposed *via* 1:1 dilution in methanol, and 20 µL was injected onto an Agilent Infinity 1260 analytical HPLC equipped with a C8 Luna 4.6 x 150 mm column (Phenomenex). A 20 min gradient elution of 30-100% ACN in H_2O + 0.1% TFA was employed, and Ribo-lipid content was determined by evaluating absorbance at 220 nm relative to a standard curve of known concentration. For DLS/ELS, liposomes were diluted 1:5 in PBS and loaded into a quartz cuvette with an electrophoretic cell for analysis using a Wyatt Möbiuζ instrument. Measurements were collected at 25 °C using a laser wavelength of 532 nm. Scattered light was collected at a fixed angle of 163.5°, and each measurement was collected as the average of 4-5 scans. For TEM, liposomes were diluted 1:10 in nanopure water, drop cast on an ultrathin holey carbon-coated copper grid, and stained with 2 wt.% uranyl acetate. The stained sample was immediately imaged using a FEI Technai F30 TEM (TSS Microscopy).

Antigen presentation studies. Age matched, 6-to-12-week-old female C57Bl/6J mice were vaccinated intramuscularly in the flank with 50 µL of vaccine formulations as described above. Where noted, DQ-OVA (Thermo Scientific) was used in place of OVA. After 5 d, the inguinal draining lymph node was collected and enzymatically digested with collagenase (1 mg/mL) and DNAse (100 µg/mL) at 37 °C for 1 h. Digested lymphocytes were passed through a 40 µm cell strainer, pelleted, and resuspended in 200 µL PBS. Cells were stained for viability and cell surface markers and analyzed with a Novocyte Penteon (Agilent) flow cytometer. Flow cytometry data was analyzed using FlowJo v10.8.1.

4.5 Supplementary Information.

Name	Screened?	Solubility in DMSO	IL-1β fold change to PBS	IL-1β fold change to LPS
Plerixafor	NO	NO	0.63726694	145.700745
SP2509	YES	87 mM	8.62795921	141.043521
Pitavastatin Calcium	YES	114 mM	10.7193237	109.424487
Ribociclib (LEE011)	YES	18 mM	0.94492742	97.044902
Fosbretabulin Disodium	NO	NO	3.85996718	86.8531596
MK8353 (SCH900353)	YES	72 mM	50.4689605	60.8457472
Atorvastatin Calcium	YES	87mM	4.80884195	60.3593899
OTX015	NO	199 mM	10.3392994	59.3799347
Nocodazole	YES	25 mM	1103.48136	50.5993418
TW-37	NO	200 mM	4.41052587	47.2520472
Fedratinib (SAR302503)	NO	191 mM	9.4436571	42.494088
Fluvastatin Sodium	YES	201 mM	7.51584017	40.3840081
Golvatinib	YES	32 mM	1.66632749	38.2702418
PLX-4032 (Vemurafenib)	YES	198 mM	3.5283998	33.4206315
Simvastatin	NO	201 mM	3.48087089	32.8255489
KU-60019	YES	183 mM	0.0381261	31.7102192
Lovastatin	NO	198 mM	6.26610177	30.1086918
CGP 57380	YES	197 mM	61.4051523	26.7271027
Palbociclib (PD-0332991) HCl	YES	27 mM	N/A	N/A
Flavopiridol (Alvocidib)	YES	201 mM	N/A	N/A
CDKI-73	YES	200 mM	N/A	N/A
Dabrafenib (GSK2118436)	YES	192 mM	N/A	N/A
Bafetinib (INNO-406)	YES	173 mM	N/A	N/A
IPI-3063	YES	200 mM	N/A	N/A

Table S4.1: Identification of IL-1β producing compounds *via* high throughput screening. The compounds listed were incubated at 10 μM with THP-1 monocytes for 1 h, then 100 nM LPS or PBS were added to cells and incubated overnight. The fold-change reported is relative to treatment with 100 nM LPS or PBS alone. Solubility values were obtained from *SelleckChem.* Six additional compounds presented at the bottom of the table were also included in screening.

A) IL-1β secretion

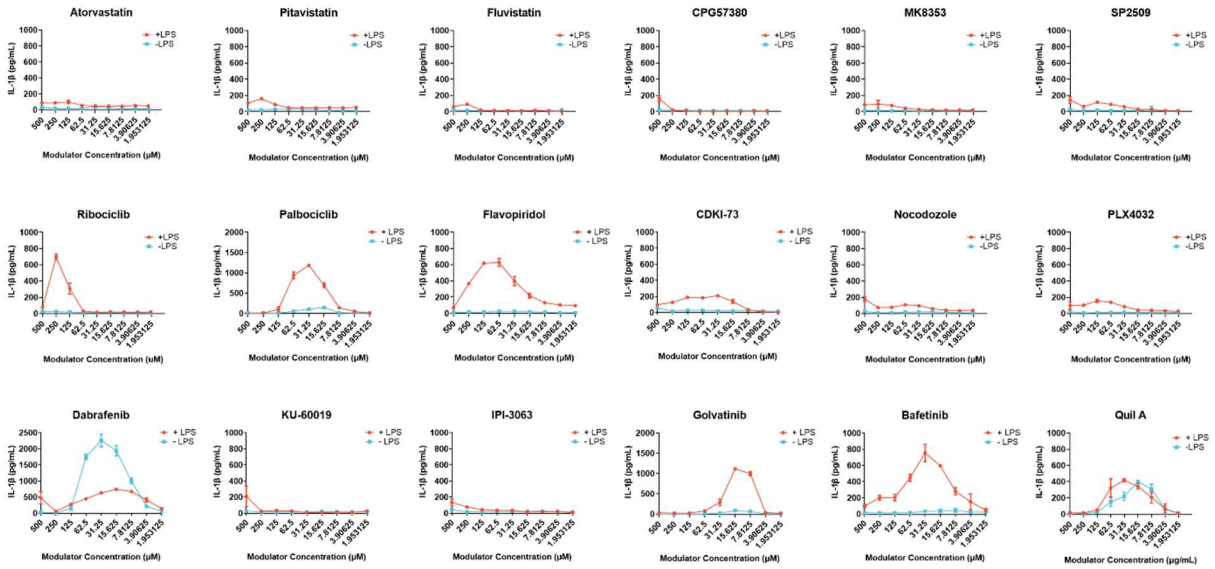

B) Toxicity

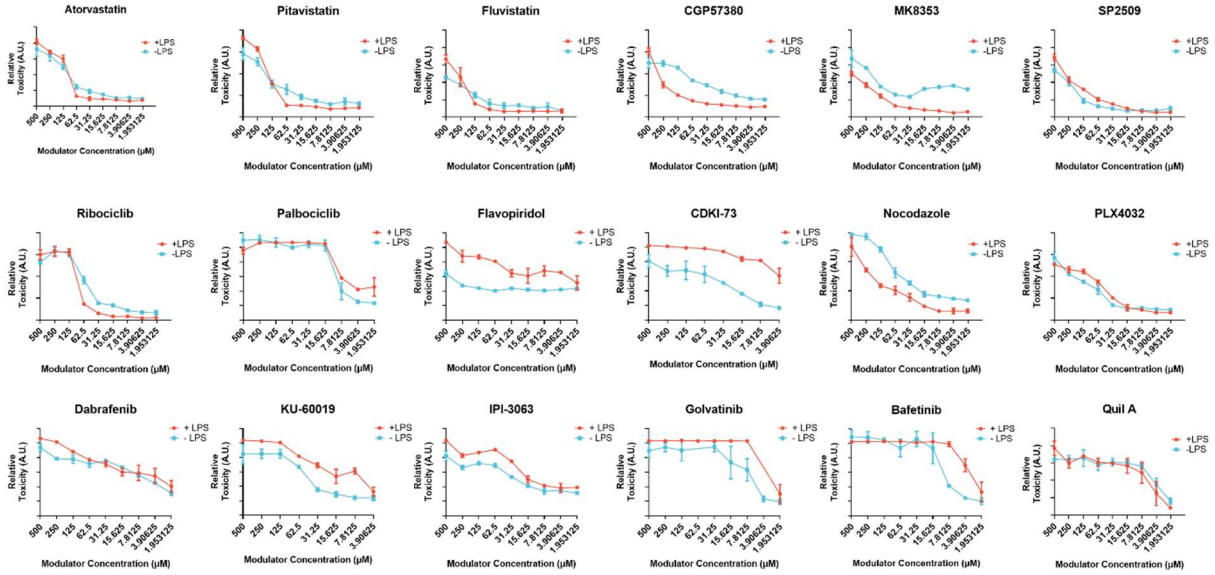

Figure S4.1: Screen of IL-1β secretion and toxicity of compounds identified through high-throughput screening. LPS-primed or -unprimed BMDMs were treated overnight with the 17 analytes and Quil A as a positive control. IL-1β secretion was quantified using ELISA, and toxicity was quantified using secreted lactate dehydrogenase (LDH) assay.

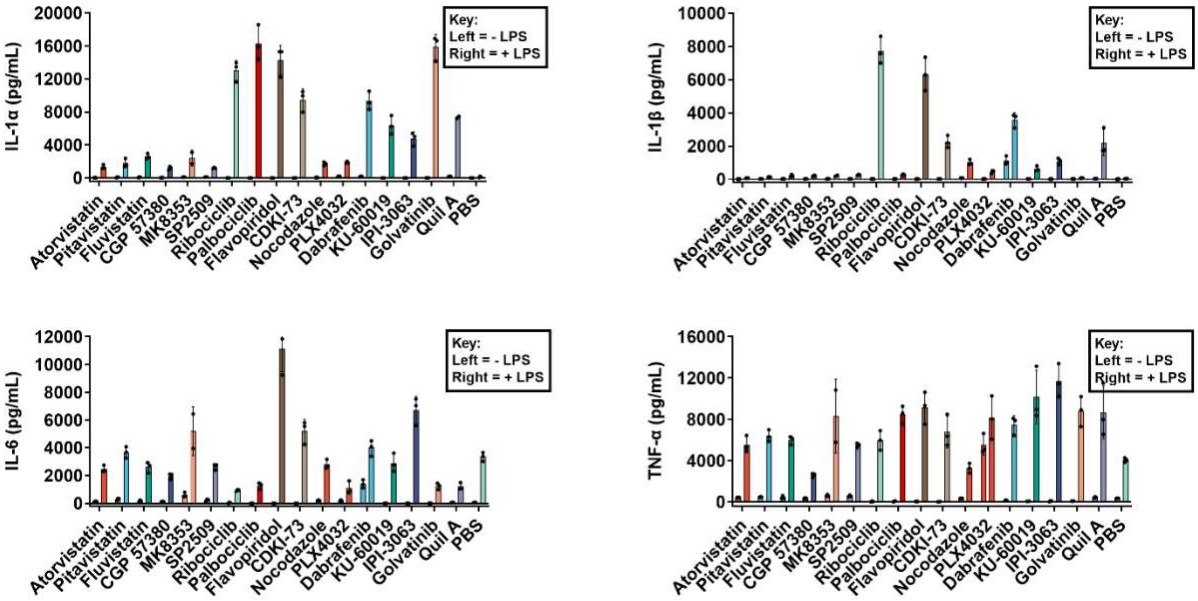

Figure S4.2: Screen of cytokine production induced by top immunomodulators in LPS-primed or -unprimed BMDCs. 500,000 primed or unprimed BMDCs were treated overnight in a 6-well plate with the 17 modulators (100 μM) and Quil A (10 μg/mL) as a positive control. Supernatant was collected and assayed for secreted cytokines using Legendplex Mouse Inflammation 13-plex according to the manufacturer's procedure.

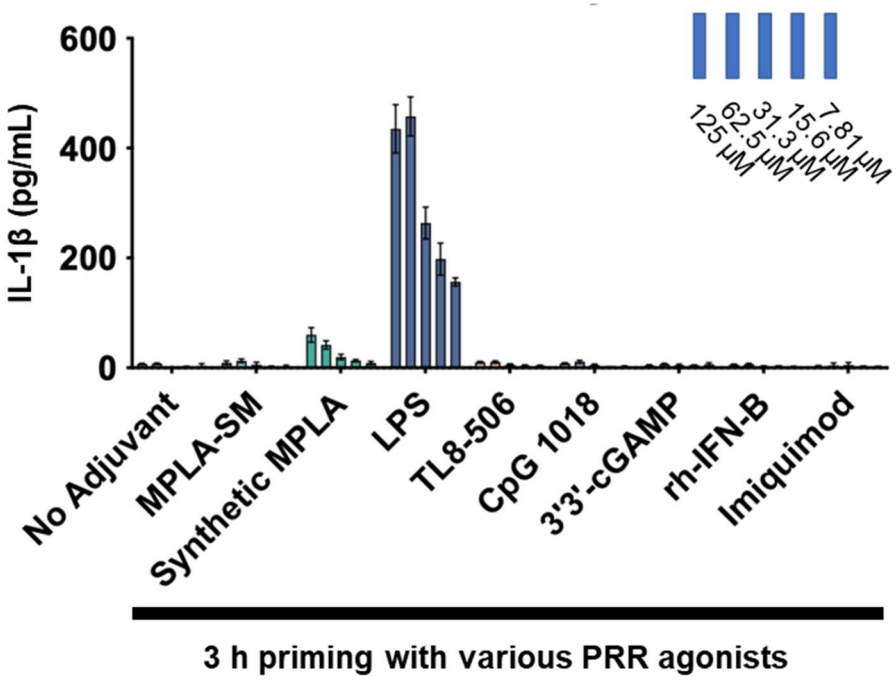

Figure S4.3: Screen of IL-1β secretion in THP-1 human monocytes following priming with the PRR agonists listed (MPLA-SM = 0.25 μg/mL, sMPLA = 0.25 μg/mL, LPS = 0.1 μg/mL, TL8-506 = 0.1 μg/mL, CpG 1018 = 0.25 μg/mL, 3,3'-cGAMP = 10 μg/mL, rh-IFN-B = 1 ng/mL, Imiquimod = 10 μg/mL). MPLA-SM, sMPLA, and LPS are TLR4 agonists, TL8-506 is a TLR8 agonist, CpG 1018 is a TLR9 agonist, 3,3'-cGAMP is a STING agonist, rh-IFN-B is recombinant interferon β, and Imiquimod is a TLR7/8 agonist. IL-1β production was assayed after overnight incubation with Ribociclib at the concentrations listed (7.8-125 μM) by ELISA.

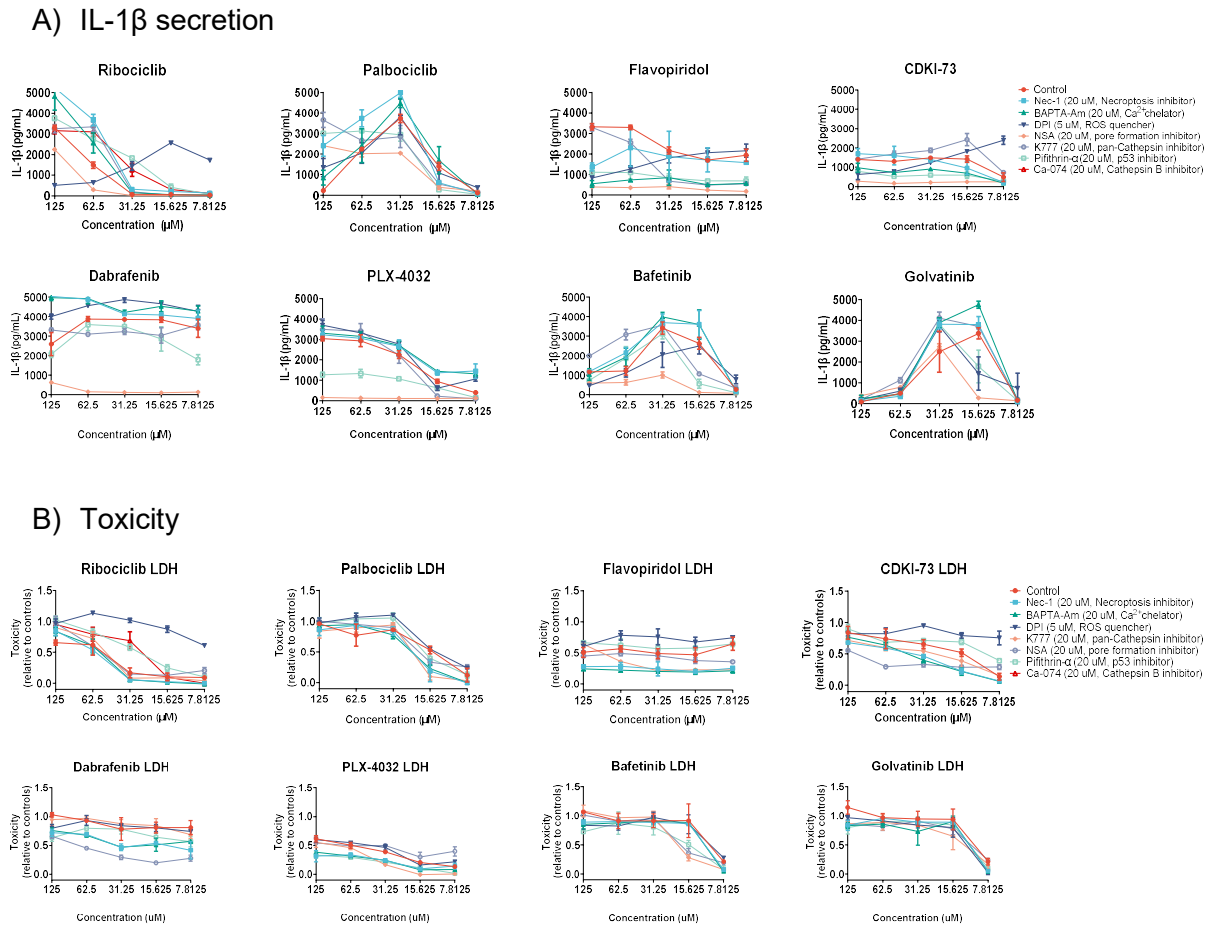

Figure S4.4: Screen of IL-1β secretion and toxicity of compounds in the presence of chemical inhibitors that disrupt homeostatic processes related to NLRP3 inflammasome activation. LPS-primed BMDCs were pre-treated with the indicated inhibitors for 30 min, then incubated with each compound at the indicated concentrations overnight. IL-1β secretion was quantified using ELISA, and toxicity was quantified using secreted lactate dehydrogenase (LDH) assay.

A) IL-1β secretion:

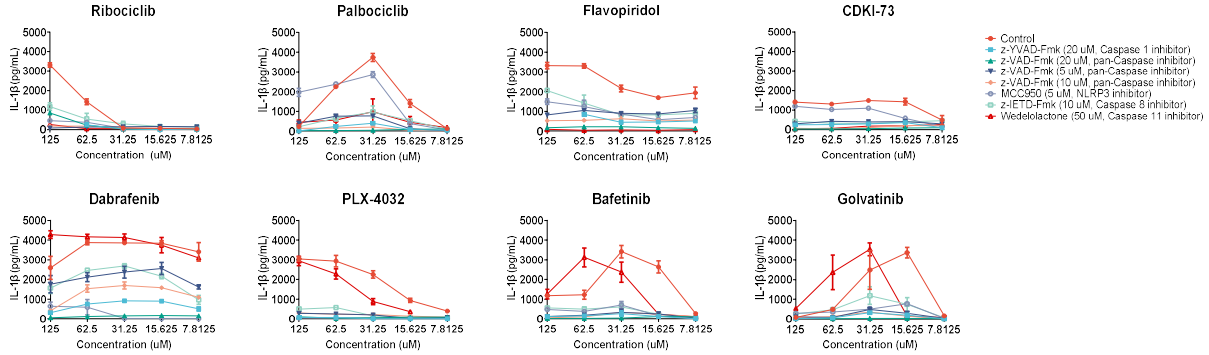

B) Toxicity:

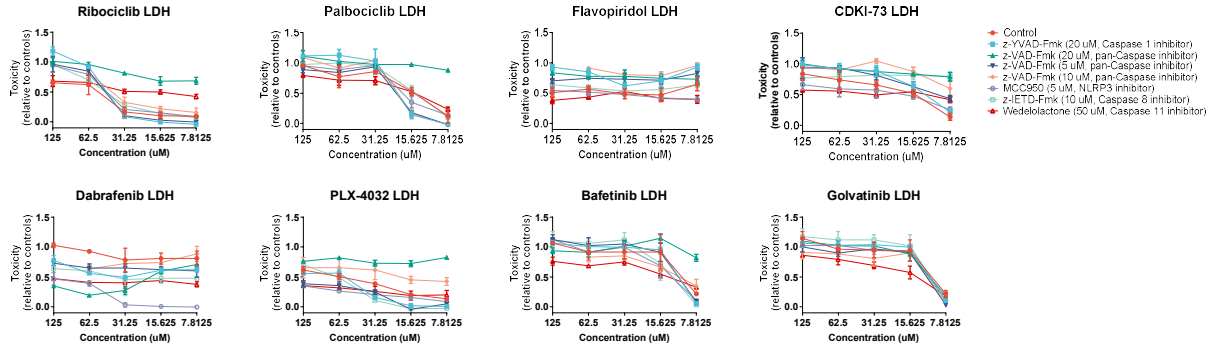

Figure S4.5: Screen of IL-1β secretion and toxicity of compounds in the presence of chemical inhibitors that disrupt effector functions related to NLRP3 inflammasome activation. LPS-primed BMDCs were pre-treated with the indicated inhibitors for 30 min, then incubated with each compound at the indicated concentrations overnight. IL-1β secretion was quantified using ELISA, and toxicity was quantified using secreted lactate dehydrogenase (LDH) assay.

A) IL-1β secretion:

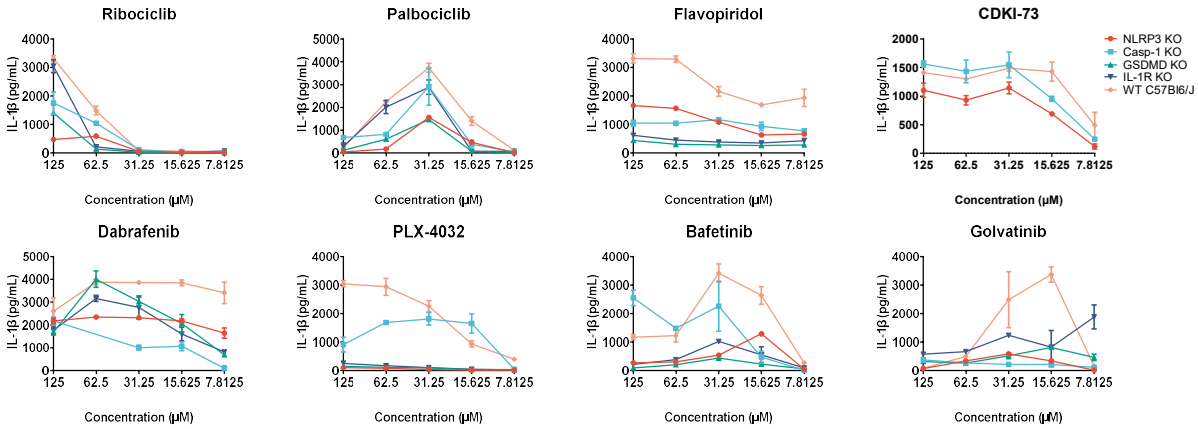

B) Toxicity:

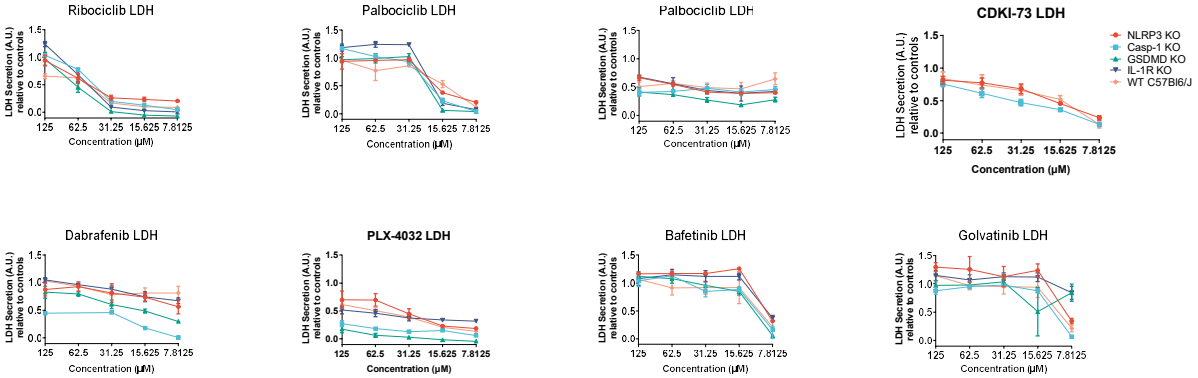

Figure S4.6: Screen of IL-1β secretion and toxicity of compounds in BMDCs from various knockout mice. LPS-primed BMDCs were with each compound at the indicated concentrations overnight. IL-1β secretion was quantified using ELISA, and toxicity was quantified using secreted lactate dehydrogenase (LDH) assay. IL-1R KO mice were employed as a control. GSDMD-KO and IL-1R-KO studies were not performed with CKDI-73 due to insufficient cell counts.

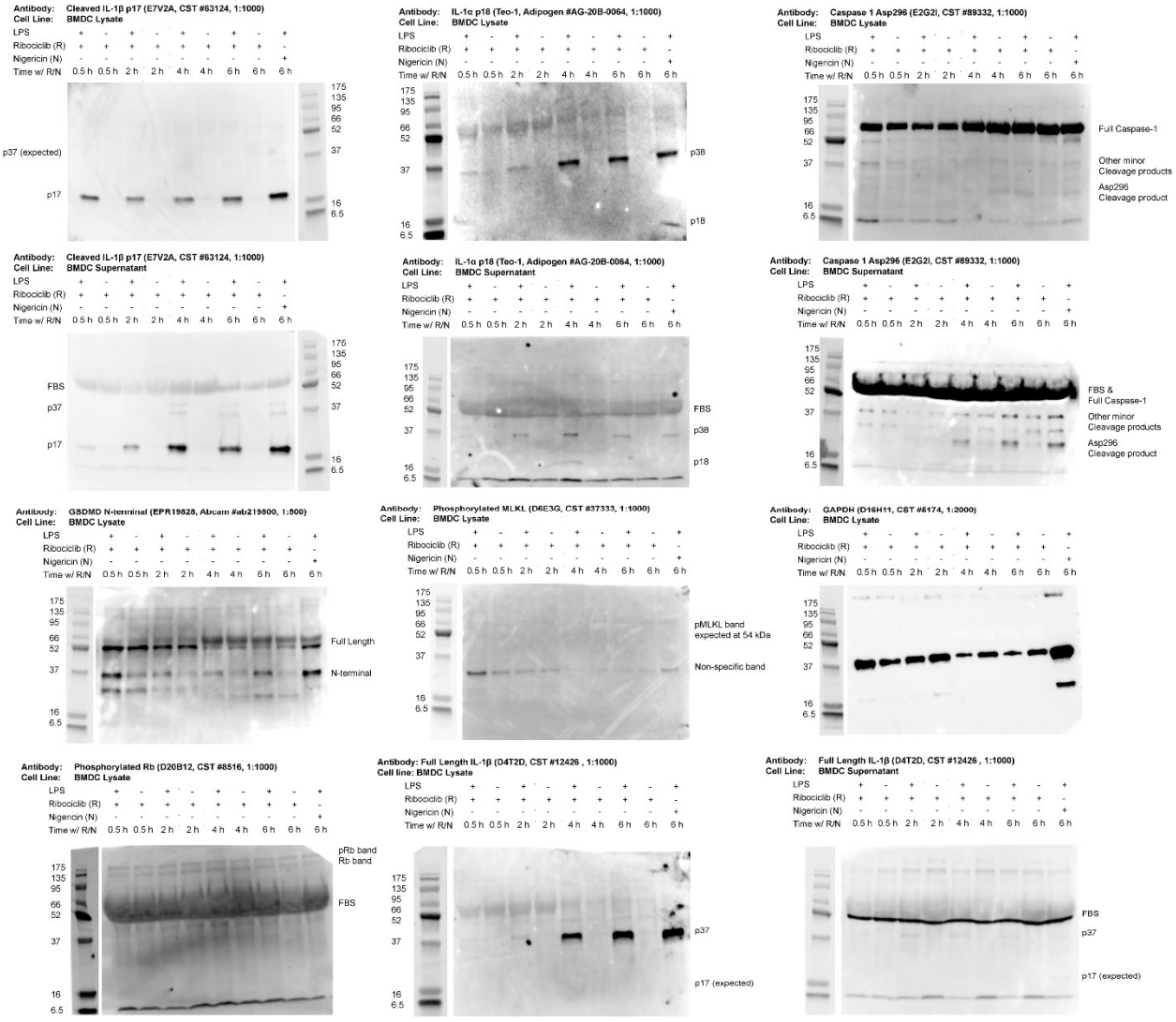

Figure S4.7: Full immunoblots of BMDCs treated with Ribociclib. LPS-primed or -unprimed BMDCs were treated with Ribociclib (R) or Nigericin (N) for the indicated times, then supernatants were collected, and cells were lysed with M-PER for analyses. Samples were eluted on a 12% SDS-PAGE gel, transferred to a PVDF membrane, and stained with the indicated antibodies overnight at 4 °C. Finally, membranes were stained with a HRP conjugated secondary antibody, treated with luminol-based detection substrate, and dried prior to imaging. Samples were imaged immediately using a chemiluminescent detection mode, while protein ladders were imaged using fluorescent detection mode. Images were processed in ImageJ.

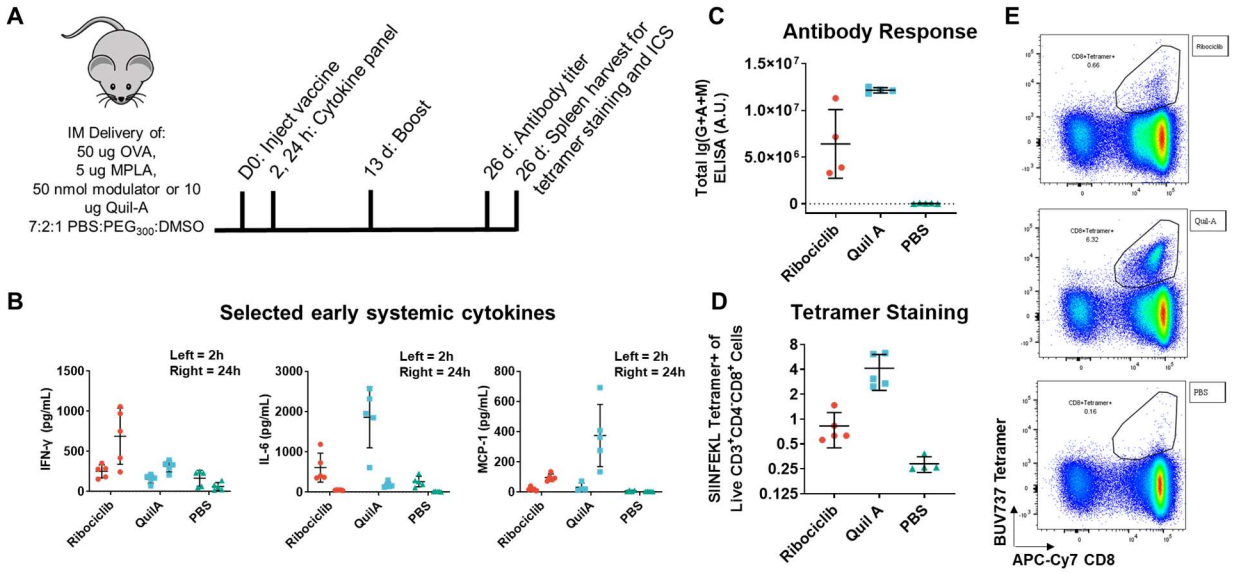

Figure S4.8: Pilot vaccination study using Ribociclib formulation. A) Ribociclib or Quil-A were formulated with MPLA and OVA and injected intramuscularly according to the indicated schedule. B) Systemic cytokines in the serum were assayed 2 and 24 h after injection. C) Total Ig's were assayed in the serum *via* ELISA. D) Splenocytes were harvested, stained, and analyzed using flow cytometry to identify antigen specific $CD8^+$ T cells. E) Representative flow plots from (D).

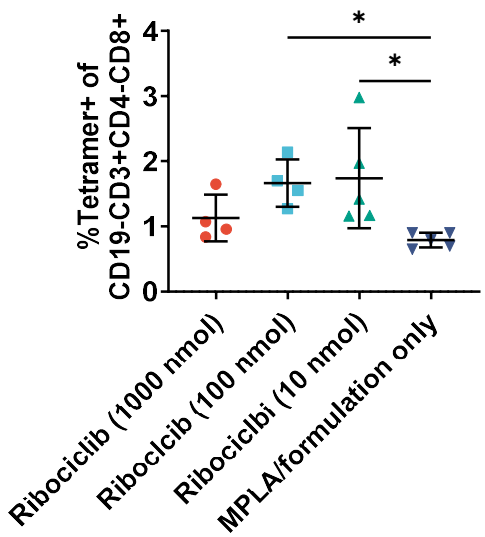

Figure S4.9: Dose-response experiment probing CD8 T cell responses toward Ribociclib. Ribociclib formulations containing the indicated quantities were prepared and used analogously as to **Figure S4.8**, and splenic, antigen specific $CD8^+$ T cells were analyzed using flow cytometry. One way ANOVA with Dunnett's multiple comparisons test was used to determine statistical significance (* = $p<0.05$).

A)

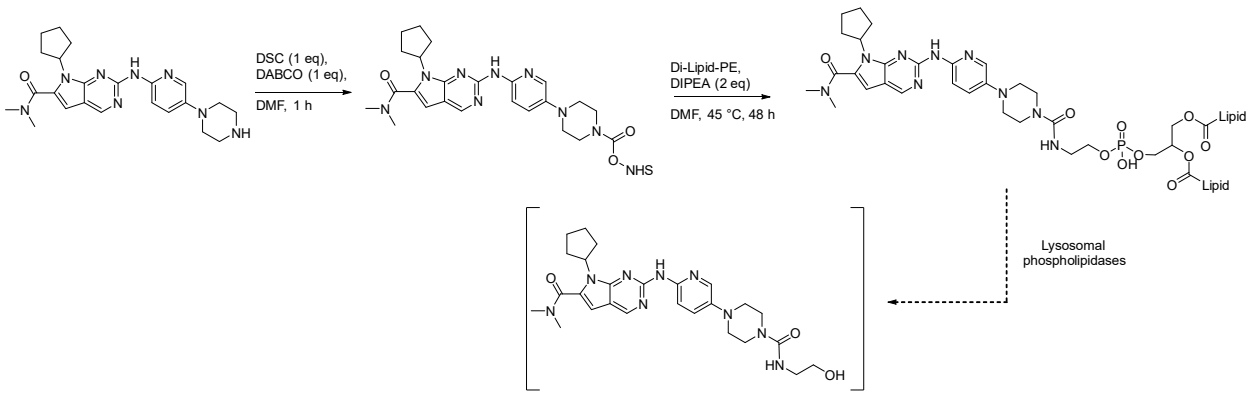

B)

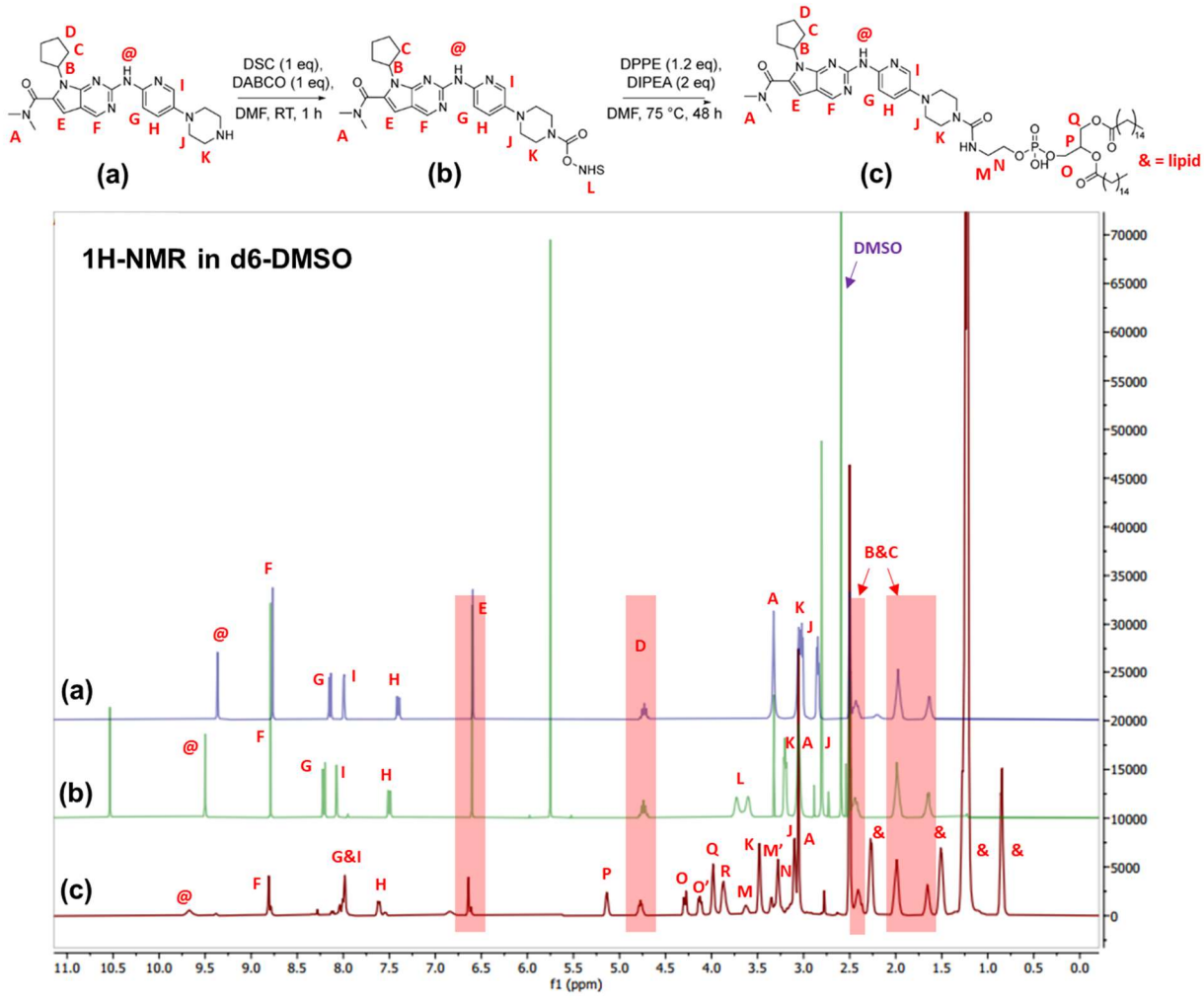

Figure S4.10: Synthesis of Ribo-L. A) Synthetic scheme for preparation of Ribo-L from Ribociclib and proposed cleavage of lipid by endo/lysosomal phospholipidase D. B) ^{1}H-NMR spectrum of Ribo-L and intermediate species in DMSO-d6. (a) and (b) were conducted at 400 MHz and ambient temperature, while (c) required heating at 50 ºC using the 500 MHz instrument for characterization.

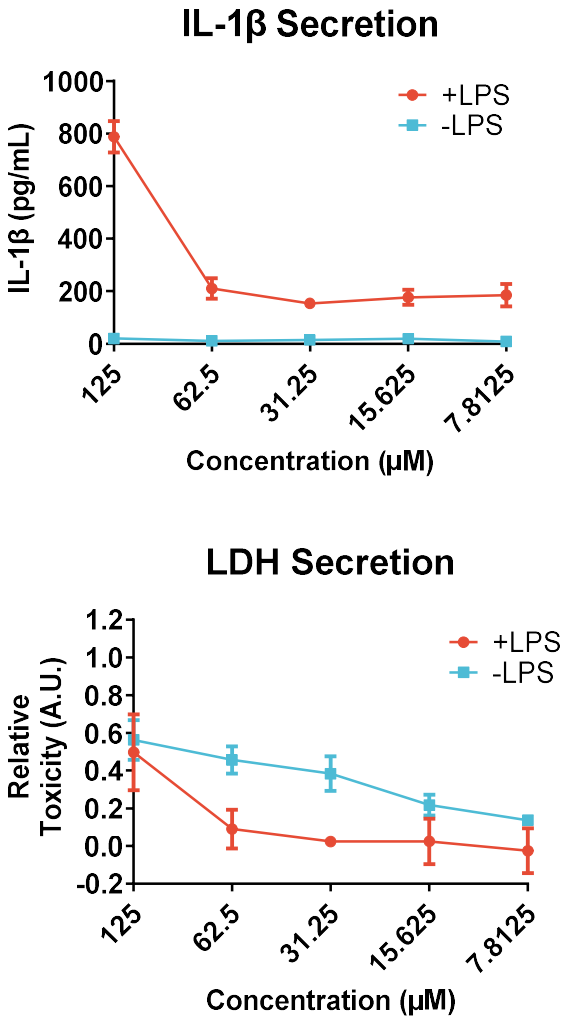

Figure S4.11: In-vitro characterization of Ribo-L. Ribo-L was treated with LPS-primed or -unprimed BMDCs overnight, and supernatant was collected for evaluation by LDH assay and IL-1β ELISA.

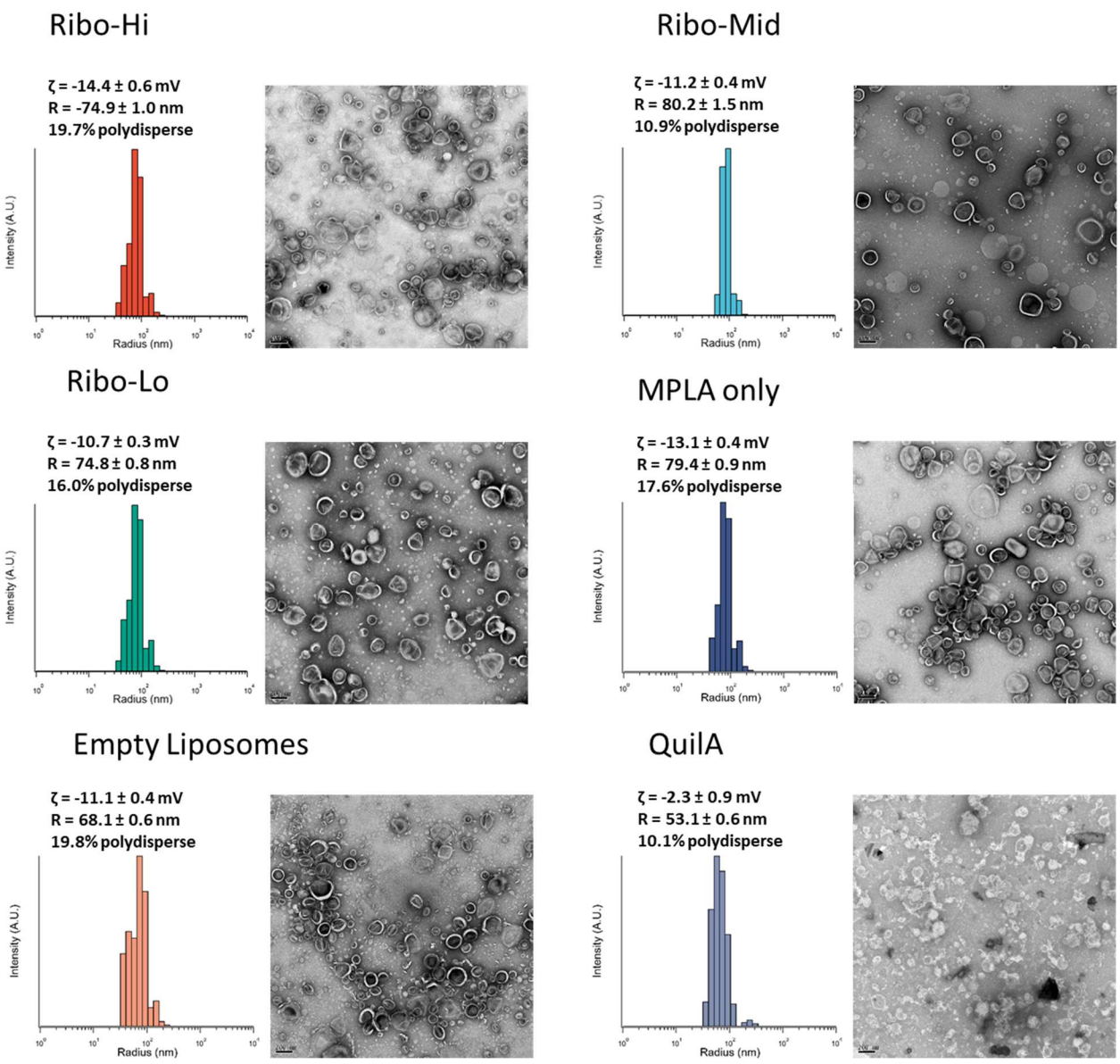

Figure S4.12: Morphological characterization of liposomes. Liposomes containing three different concentrations of Ribo-L (Hi = 200 μg/mL, Mid = 40 μg/mL, Lo = 8 μg/mL) and MPLA (10 μg/mL) were prepared and analyzed *via* DLS and TEM as shown. Radii, zeta potentials, and dispersities are determined as the average of 5 independent light scattering experiments.

	DSPC	DSPC-PEG$_{2000}$	Cholesterol	sMPLA	Ribo-L
Concentration	25 mg/mL	25 mg/mL	20 mg/mL	1 mg/mL	5 mg/mL
Liposome ID					
Ribo-L Hi	300 µL	60 µL	10 µL	200 µL	200 µL
Ribo-L Mid	300 µL	60 µL	10 µL	200 µL	40 µL
Ribo-L Lo	300 µL	60 µL	10 µL	200 µL	8 µL
MPLA Only	300 µL	60 µL	10 µL	200 µL	0 µL
Empty	300 µL	60 µL	10 µL	0 µL	0 µL

Figure S4.13: Quantities of reagents used in the preparation of 1 mL liposomes. Each reagent was loaded at the indicated volume into a 20 mL scintillation vial and evaporated under reduced pressure to form a thin film. The thin films were then rehydrated in 1 mL of PBS under gentle rotation at 70 °C for 5 min and extruded through a 200 nm filter to obtain Ribo-L liposomes.

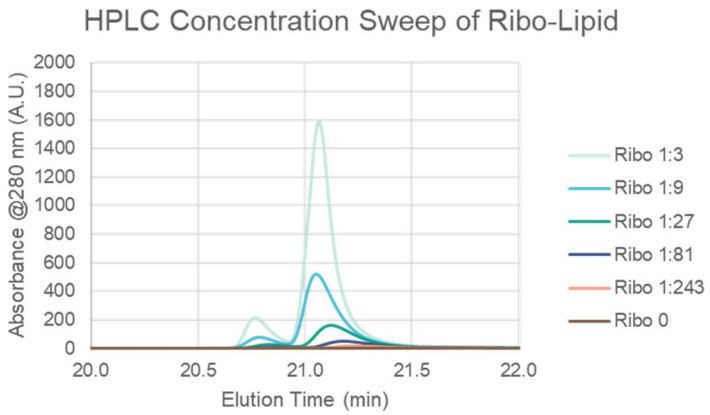

	Absorbance @280 nm	Conc. (mg/mL)	Mass Injected (ng)
Ribo 1:1	n/a	5	50
Ribo 1:3	1589.04	1.67	16.67
Ribo 1:9	519.96	0.56	5.56
Ribo 1:27	161.75	0.19	1.85
Ribo 1:81	50.80	0.06	0.62
Ribo 1:243	17.05	0.02	0.21
Ribo 0	3.59	0.00	0.00

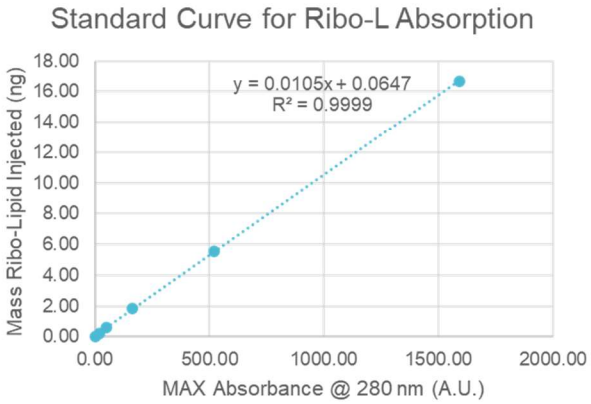

Figure S4.14: Correlation between absorbance and concentration of Ribo-L *via* HPLC. Several 3-fold dilutions of Ribo-L were diluted in $CHCl_3$ from a 5 mg/mL stock and injected onto an analytical C8 column (150 x 4.6 mm), and absorbance at 280 nm was measured. 10 µL of each diluted sample was injected, and a 20 min, 30-100% acetonitrile gradient elution in H_2O + 0.1% TFA with a 5 min hold at 100% acetonitrile was used for elution. Based on the concentration sweep, a standard curve of concentration versus mass of Ribo-L injected was generated.

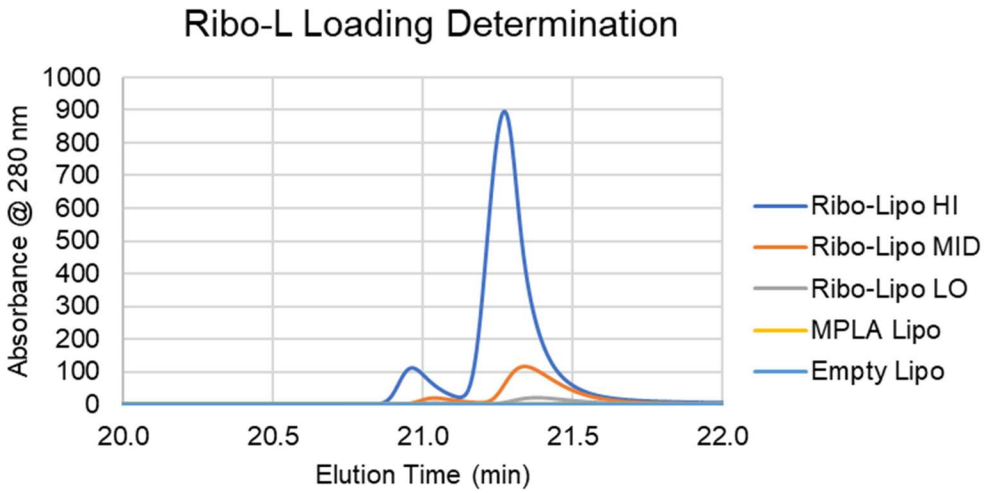

Liposome	MAX Abs @ 280 nm	Mass Ribo-Lipid Injected (ng)	[Ribo-Lipo]/Liposome (mg/mL)	Expected Loading (mg/mL)	Loading Efficiency
Ribo-Lipo HI	896.26	9.48	0.237	0.200	118%
Ribo-Lipo MID	116.36	1.29	0.032	0.040	80%
Ribo-Lipo LO	20.69	0.28	0.007	0.008	88%
MPLA Lipo	1.34	0.08	0.002	0	N/A
Empty Lipo	1.21	0.08	0.002	0	N/A

Figure S4.15: Quantitation of Ribo-L loading in liposomes *via* HPLC. Liposomes were degraded by dilution 1:1 with MeOH, and 20 µL of each diluted sample was injected and subjected to the column conditions described in **Figure S4.14**. The maximum absorbance at 280 nm at 21.0-21.5 min for each liposome was fit to the standard curve and used to determine the loading of Ribo-L. Results are representative of at least three independent experiments.

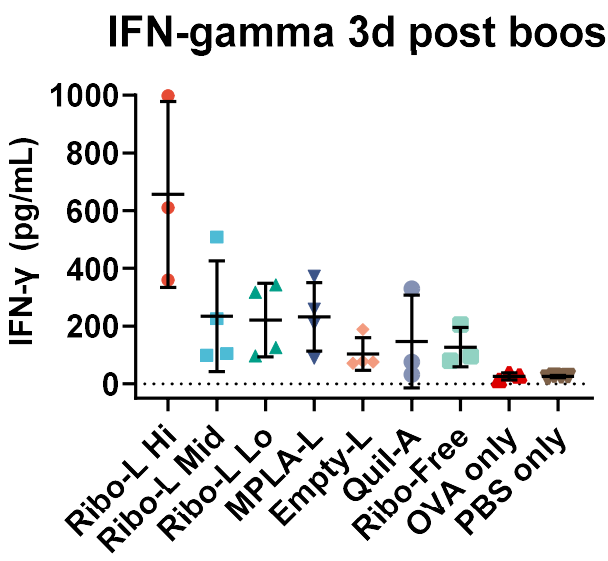

Figure S4.16: IFN-γ production generated by Ribo-L liposomes or controls 3 d post-boost. Serum was collected and analyzed using a modified bead-based assay as described in the **Methods**.

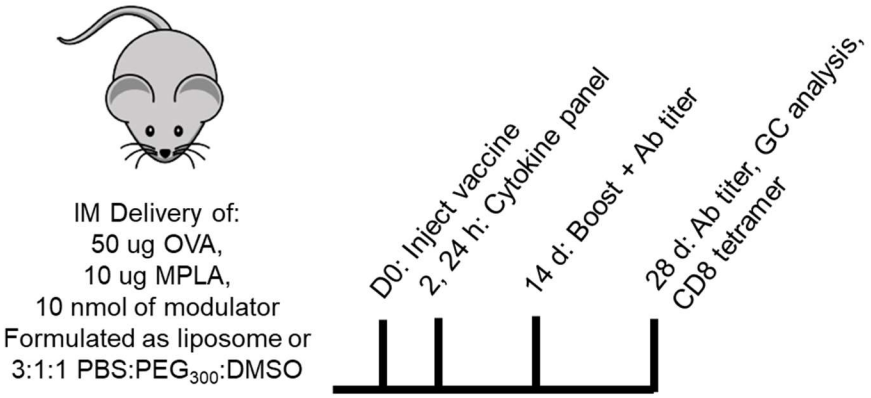

Group	Composition	Function
1	Ribociclib + MPLA (liposome)	Liposomal formulation
2	Ribociclib + MPLA (free)	Ribociclib control
3	Quil-A + MPLA (free)	Positive control
4	MPLA only (free)	Formulation control
5	PBS only	Negative Control

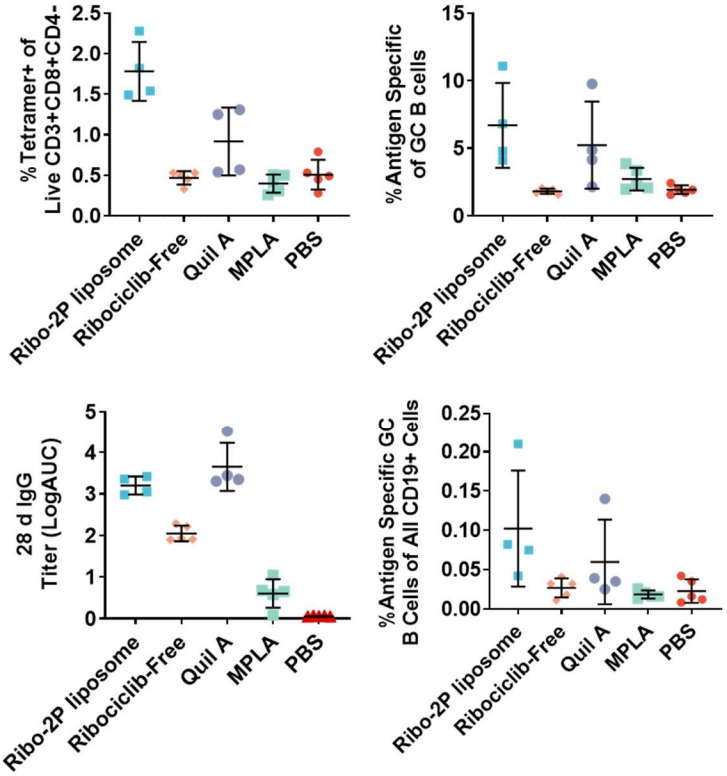

Figure S4.17: Characterization of the adaptive immune response generated toward Ribociclib liposomes relative to various soluble formulations.

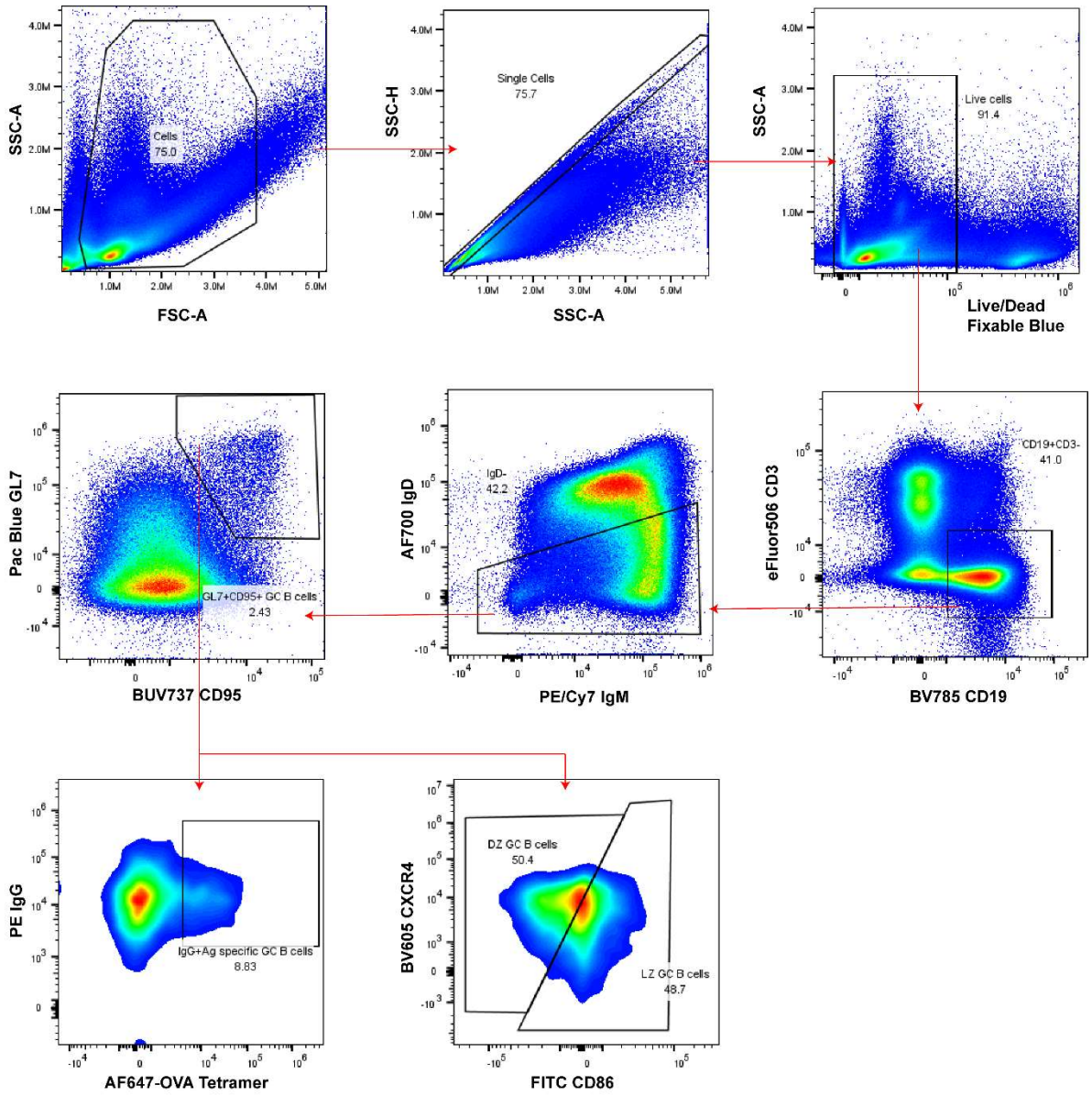

Figure S4.18: Representative flow gating strategy for the characterization of antigen-specific germinal center B cell responses. AF647-OVA tetramers were prepared as described in the **Methods.**

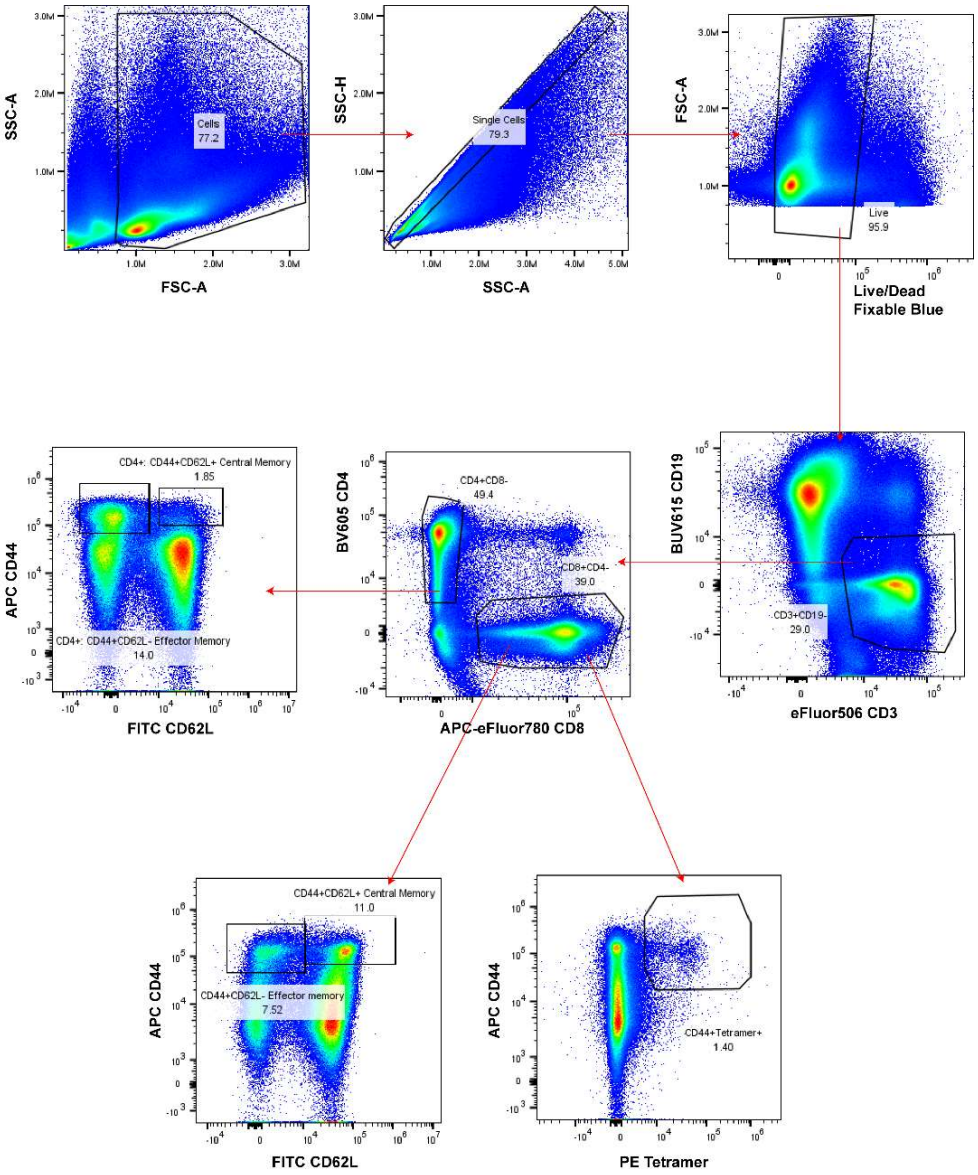

Figure S4.19: Representative flow gating strategy for the characterization of antigen-specific T cells and memory/effector subsets. CD4 Tetramer positive cells were gated analogously to the CD8 Tetramer staining data provided here.

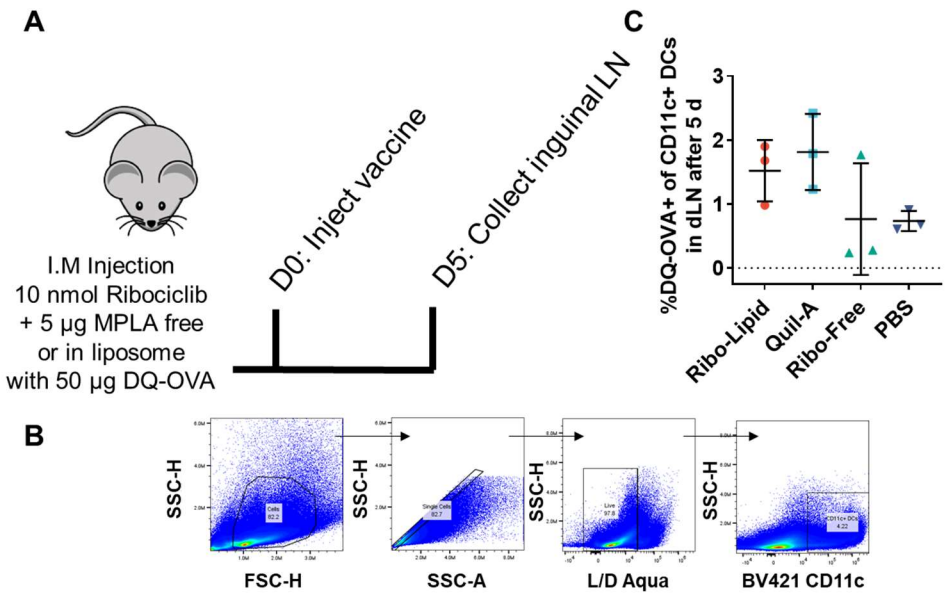

Figure S4.20: Additional characterization of the response toward DQ-OVA in draining inguinal lymph node after vaccination. A) Vaccination schedule and formulations used. B) Gating strategy for characterization of CD11c$^+$ dendritic cells. C) DQ-OVA processing in CD11c$^+$ dendritic cells 5 d after injection.

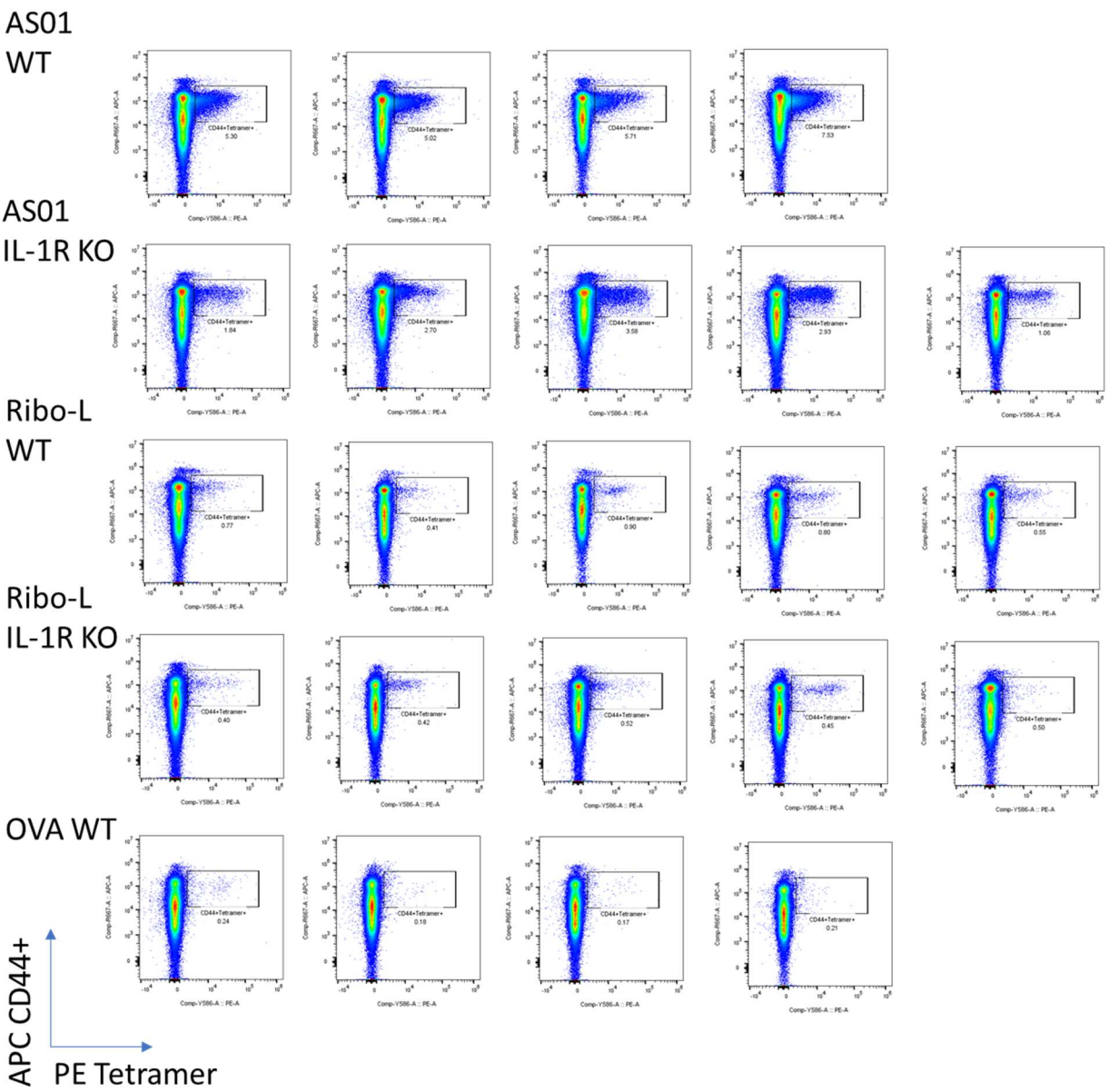

Figure S4.21: Flow cytometry plots depicting CD44^{+}Tetramer^{+} CD8 T cell responses in WT and IL-1R KO mice.

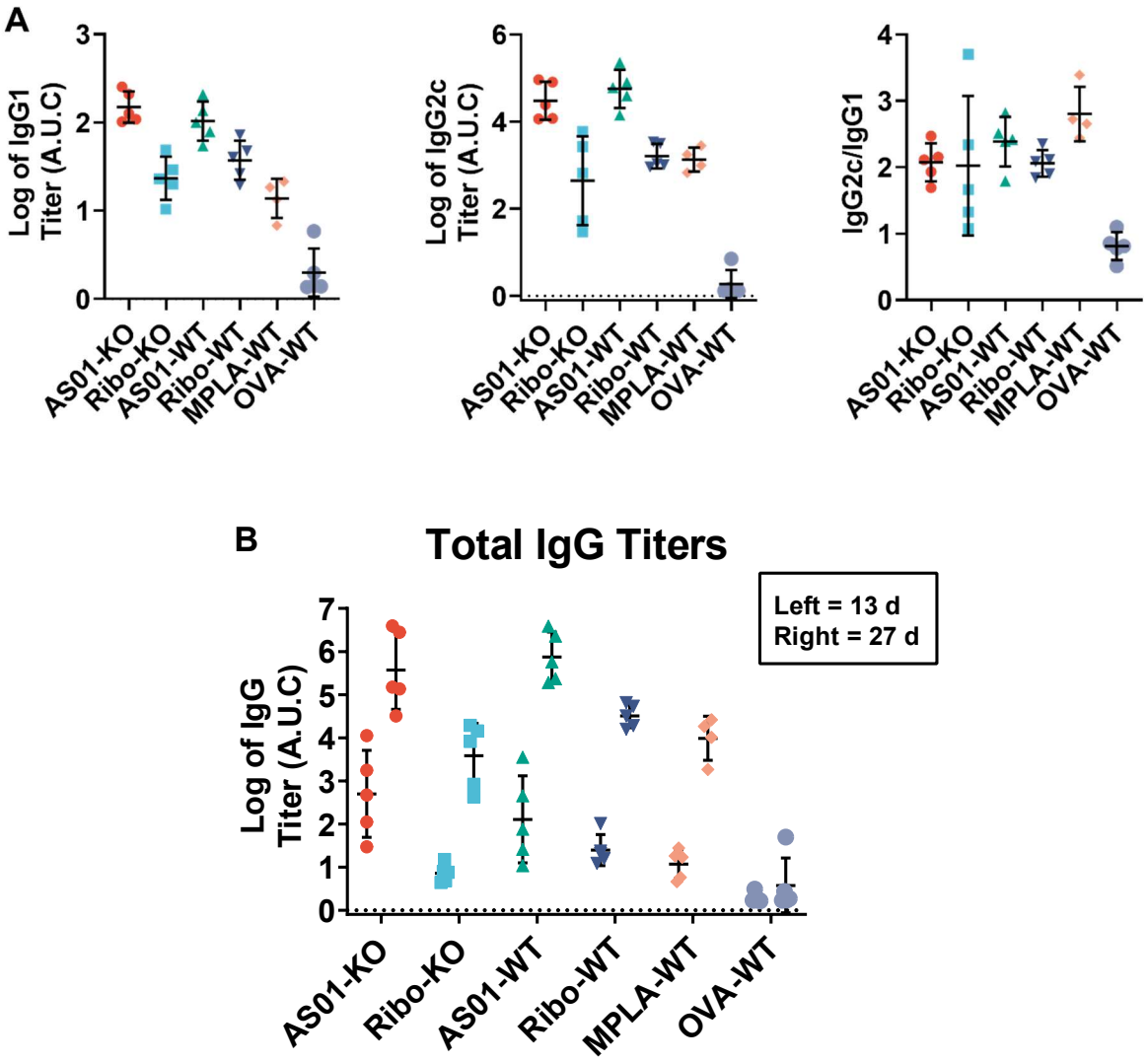

Figure S4.22: Additional characterization of antibody responses in WT and IL-1R-KO mice. A) Isotype-specific antibody responses from IL-1R KO ("KO") or wild type ("WT") mice treated with the indicated formulations. Based on the IgG2c and IgG1 titers shown, the isotype bias (IgG2c/IgG1 ratio) was calculated for each mouse as a proxy for Th1 biased immunity. B) Total IgG titers 13 and 27 d after the initial injection for all groups tested. Selected groups are also presented for statistical analysis in **Figure 4.4G**.

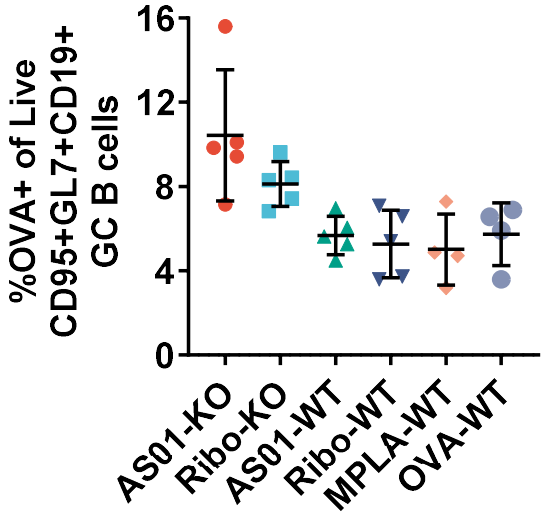

Figure S4.23: Additional characterization of B cell responses in WT and IL-1R KO mice. Percentage of splenic, antigen-specific, germinal center B cell responses determined via flow cytometry from IL-1R KO ("KO") or wild type ("WT") mice treated with the indicated formulations.

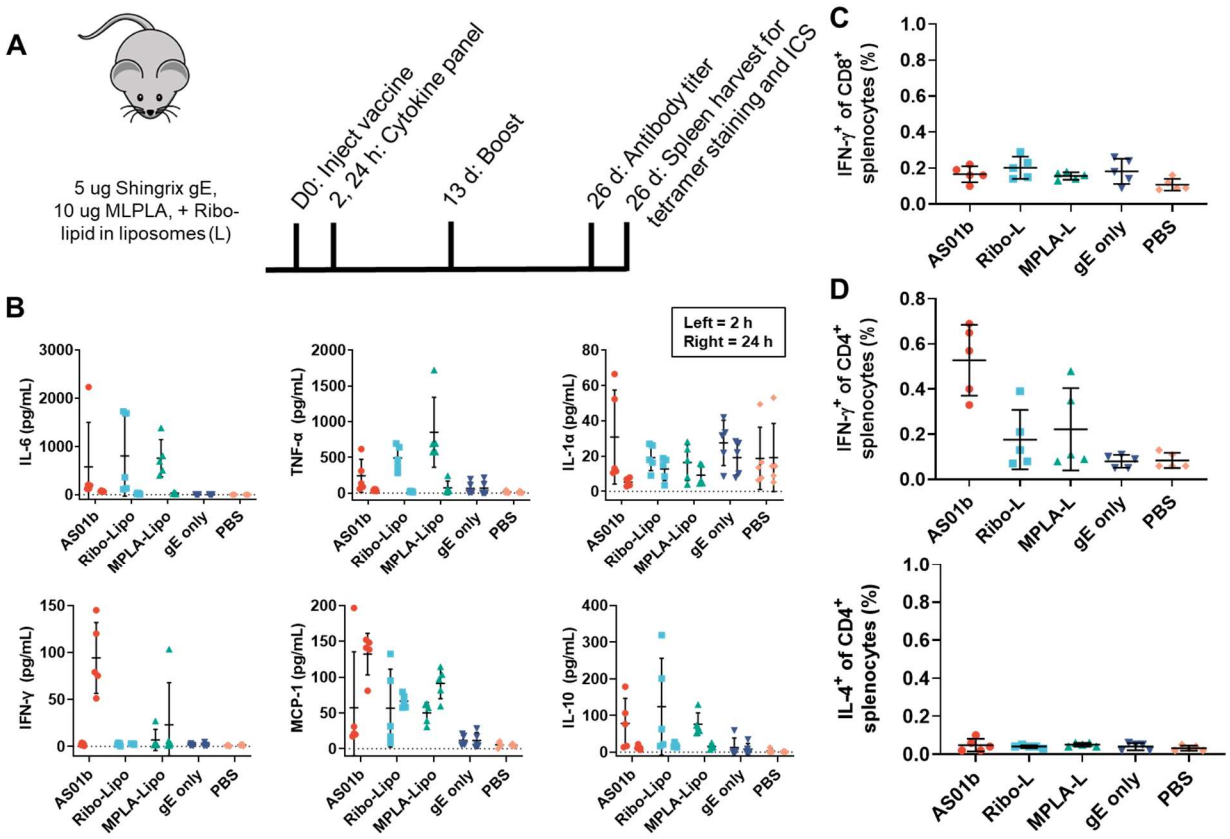

Figure S4.24: Additional data related to the Shingles vaccination study. A) Experimental timeline of the study. B) Cytokines 2 h (left) and 24 h (right) after vaccination. C) Antigen-specific CD8 and D) CD4 T cell responses were assayed by restimulating cells with VZV-gE PepMix overlapping peptide 15mer pool (JPT) for 6 h, blocking cellular protein transport, and staining for intracellular cytokines associated with T cell polarization as shown.

Compound	Vendor	Product Number
Atorvastatin Calcium	SelleckChem	S2077
Bafetinib (INNO-406)	SelleckChem	S1369
BAPTA-Am	ApexBio	B7187
Ca-074	ApexBio	A1926
CDKI-73	MedChemExpress	HY-12445
CGP 57380	SelleckChem	S7421
Dabrafenib (GSK2118436)	SelleckChem	S2807
Diphenyleneiodium Chloride (DPI)	ApexBio	B6326
Flavopiridol (Alvocidib)	SelleckChem	S1230
Fluvastatin Sodium	SelleckChem	S1909
Golvatinib	MedChemExpress	HY-13068
IPI-3063	SelleckChem	S7335
K777	Cayman Chemical	19114
KU-60019	SelleckChem	S1570
MCC950	MedChemExpress	HY-12815
MK-8353 (SCH900353)	SelleckChem	S8701
Necrostatin-1	SelleckChem	S8037
Necrosulfonamide	EMD Millipore	480073
Nigericin	Sigma Aldrich	N7143
Nocodazole	SelleckChem	S2775
Palbociclib (PD-0332991) HCl	SelleckChem	S1116
Pitavastatin Calcium	SelleckChem	S1759
PLX-4032 (Vemurafenib)	SelleckChem	S1267
Quil-A	InvivoGen	vac-quil
Ribociclib (LEE011)	SelleckChem	S7440
SP2509	SelleckChem	S7680
Wedelolactone	MedChemExpress	HY-N0551
Z-IETD-FMK	MedChemExpress	HY-101297
Z-VAD-FMK	ApexBio	A1902
Z-YVAD-FMK	ApexBio	A8955

Table S4.2: List of inhibitors and modulators tested in **Chapter 4** and their vendors.

Antibody	Fluorophore	Clone	Vendor
OVA MHC-I Pentamer	PE	F093	ProImmune
OVA MHC-II Tetramer	PE	TT1010	ProImmune
Anti-mouse/human CD11b	PerCP	M1/70	BioLegend
Anti-mouse CD11c	BV421	N418	BioLegend
Anti-mouse F4/80	BUV396	T45-2342	BD
Anti-mouse I-A/I-E	PE/Cy7	M5/114.15.2	BioLegend
Anti-mouse CD86	AF700	GL-1	BioLegend
Anti-mouse CD40	Super Bright 780	1C10	Thermo
Anti-mouse H-2k^{b}:SIINFEKL	APC	25-D1.16	BioLegend
Live/Dead Fixable Blue	N/A	N/A	Thermo
Live/Dead Fixable Aqua	N/A	N/A	Thermo
Zombie NIR Fixable Viability Dye	N/A	N/A	BioLegend
Anti-mouse CD3	Pac Blue	17A2	BioLegend
Anti-mouse CD4	BV605	RM4-5	BioLegend
Anti-mouse CD8	APC-eFluor780	53-6.7	Thermo
Anti-mouse CD19	PE/Cy7	6D5	BioLegend
Anti-mouse/human CD44	APC	IM7	BioLegend
Anti-mouse CD62L	FITC	MEL-14	BioLegend
Anti-mouse CD3	eFluor506	17A2	Thermo
Anti-mouse CD19	BV785	6D5	BioLegend
Anti-mouse GL7	Pac Blue	GL7	BioLegend
Anti-mouse CD95	BUV737	Jo2	BD
Anti-mouse CD86	FITC	GL-1	BioLegend
Anti-mouse CXCR4	BV605	L276F12	BioLegend
Anti-mouse IgD	AF700	11-26c.2a	BioLegend
Anti-mouse IgM	PE-Cy7	RMM-1	BioLegend
Anti-mouse IgG	PE	Poly4053	BioLegend
Anti-mouse/human CD11b	PE	M1/70	BioLegend
Anti-mouse Ter-119	PE	TER-119	BioLegend
Anti-mouse CD19	PE	6D5	BioLegend
Anti-mouse CD8	PE	53-6.7	BioLegend
Anti-mouse CD4	PE	RM4-5	BioLegend
Anti-mouse CD8	APC	53-6.7	BioLegend
Anti-mouse CD4	APC	RM4-5	BioLegend
Anti-mouse IFN-gamma	AF488	XMG-1.2	BioLegend
Anti-mouse IL-4	AF488	11B11	BioLegend

Table S4.3: List of antibodies used in **Chapter 4** for flow cytometry and Western Blots with vendor and clone.

Antibody	Fluorophore	Clone	Vendor
Phospho-Rb (Ser807/811)	N/A	D20B12	CST
Cleaved Casp-1 (Asp296)	N/A	E2G2I	CST
Goat anti Mouse IgG (H+L)	HRP	N/A	Thermo
Goat anti mouse IgG1	HRP	N/A	Southern Biotech
Goat anti mouse IgG2c	HRP	N/A	Southern Biotech
Goat anti Rabbit IgG (H+L)	HRP	N/A	Thermo
GAPDH	N/A	D16H11	CST
Cleaved IL-1β (Asp117)	N/A	E7V2A	CST
Full Length IL-1β	N/A	D4T2D	CST
Cleaved IL-1α (p18)	N/A	Teo-1	AdipoGen
Phospho-MLKL (Ser345)	N/A	D6E3G	CST
Gasdermin D	N/A	EPR19828	Abcam

Table S4.3 (cont.): List of antibodies used in Chapter 4 for flow cytometry and Western Blots with vendor and clone.

4.6 References.

1. Pulendran, B.; P, S. A.; O'Hagan, D. T., Emerging concepts in the science of vaccine adjuvants. *Nat Rev Drug Discov* **2021,** *20* (6), 454-475.

2. Marty-Roix, R.; Vladimer, G. I.; Pouliot, K.; Weng, D.; Buglione-Corbett, R.; West, K.; MacMicking, J. D.; Chee, J. D.; Wang, S.; Lu, S.; Lien, E., Identification of QS-21 as an Inflammasome-activating Molecular Component of Saponin Adjuvants. *J Biol Chem* **2016,** *291* (3), 1123-1136.

3. Welsby, I.; Detienne, S.; N'Kuli, F.; Thomas, S.; Wouters, S.; Bechtold, V.; De Wit, D.; Gineste, R.; Reinheckel, T.; Elouahabi, A.; Courtoy, P. J.; Didierlaurent, A. M.; Goriely, S., Lysosome-Dependent Activation of Human Dendritic Cells by the Vaccine Adjuvant QS-21. *Front Immunol* **2016,** *7*, 663.

4. Coccia, M.; Collignon, C.; Herve, C.; Chalon, A.; Welsby, I.; Detienne, S.; van Helden, M. J.; Dutta, S.; Genito, C. J.; Waters, N. C.; Deun, K. V.; Smilde, A. K.; Berg, R.; Franco, D.; Bourguignon, P.; Morel, S.; Garcon, N.; Lambrecht, B. N.; Goriely, S.; Most, R. V.; Didierlaurent, A. M., Cellular and molecular synergy in AS01-adjuvanted vaccines results in an early IFNgamma response promoting vaccine immunogenicity. *NPJ Vaccines* **2017,** *2*, 25.

5. Deets, K. A.; Vance, R. E., Inflammasomes and adaptive immune responses. *Nat Immunol* **2021,** *22*, 412-422.

6. Sharma, B. R.; Kanneganti, T. D., NLRP3 inflammasome in cancer and metabolic diseases. *Nat Immunol* **2021**, *22* (5), 550-559.

7. Rodrigues, T. S.; de Sa, K. S. G.; Ishimoto, A. Y.; Becerra, A.; Oliveira, S.; Almeida, L.; Goncalves, A. V.; Perucello, D. B.; Andrade, W. A.; Castro, R.; Veras, F. P.; Toller-Kawahisa, J. E.; Nascimento, D. C.; de Lima, M. H. F.; Silva, C. M. S.; Caetite, D. B.; Martins, R. B.; Castro, I. A.; Pontelli, M. C.; de Barros, F. C.; do Amaral, N. B.; Giannini, M. C.; Bonjorno, L. P.; Lopes, M. I. F.; Santana, R. C.; Vilar, F. C.; Auxiliadora-Martins, M.; Luppino-Assad, R.; de Almeida, S. C. L.; de Oliveira, F. R.; Batah, S. S.; Siyuan, L.; Benatti, M. N.; Cunha, T. M.; Alves-Filho, J. C.; Cunha, F. Q.; Cunha, L. D.; Frantz, F. G.; Kohlsdorf, T.; Fabro, A. T.; Arruda, E.; de Oliveira, R. D. R.; Louzada-Junior, P.; Zamboni, D. S., Inflammasomes are activated in response to SARS-CoV-2 infection and are associated with COVID-19 severity in patients. *J Exp Med* **2021,** *218* (3), e20201707.

8. Ising, C.; Venegas, C.; Zhang, S.; Scheiblich, H.; Schmidt, S. V.; Vieira-Saecker, A.; Schwartz, S.; Albasset, S.; McManus, R. M.; Tejera, D.; Griep, A.; Santarelli, F.; Brosseron, F.; Opitz, S.; Stunden, J.; Merten, M.; Kayed, R.; Golenbock, D. T.; Blum, D.; Latz, E.; Buee, L.; Heneka, M. T., NLRP3 inflammasome activation drives tau pathology. *Nature* **2019,** *575* (7784), 669-673.

9. Martinon, F.; Petrilli, V.; Mayor, A.; Tardivel, A.; Tschopp, J., Gout-associated uric acid crystals activate the NALP3 inflammasome. *Nature* **2006,** *440* (7081), 237-241.

10. Hatscher, L.; Lehmann, C. H. K.; Purbojo, A.; Onderka, C.; Liang, C.; Hartmann, A.; Cesnjevar, R.; Bruns, H.; Gross, O.; Nimmerjahn, F.; Ivanovic-Burmazovic, I.; Kunz, M.; Heger, L.; Dudziak, D., Select hyperactivating NLRP3 ligands enhance the TH1- and TH17-inducing potential of human type 2 conventional dendritic cells. *Sci Signal* **2021,** *14* (680), eabe1757.

11. Papi, A.; Ison, M. G.; Langley, J. M.; Lee, D. G.; Leroux-Roels, I.; Martinon-Torres, F.; Schwarz, T. F.; van Zyl-Smit, R. N.; Campora, L.; Dezutter, N.; de Schrevel, N.; Fissette, L.;

David, M. P.; Van der Wielen, M.; Kostanyan, L.; Hulstrom, V.; Group, A. R.-S.; Group, A. R.-S., Respiratory Syncytial Virus Prefusion F Protein Vaccine in Older Adults. *N Engl J Med* **2023,** *388* (7), 595-608.

12. Lal, H.; Cunningham, A. L.; Godeaux, O.; Chlibek, R.; Diez-Domingo, J.; Hwang, S. J.; Levin, M. J.; McElhaney, J. E.; Poder, A.; Puig-Barbera, J.; Vesikari, T.; Watanabe, D.; Weckx, L.; Zahaf, T.; Heineman, T. C.; Group, Z. O. E. S., Efficacy of an adjuvanted herpes zoster subunit vaccine in older adults. *N Engl J Med* **2015,** *372* (22), 2087-2096.

13. RTS, S. C. T. P., Efficacy and safety of RTS,S/AS01 malaria vaccine with or without a booster dose in infants and children in Africa: final results of a phase 3, individually randomised, controlled trial. *The Lancet* **2015,** *386* (9988), 31-45.

14. Heath, P. T.; Galiza, E. P.; Baxter, D. N.; Boffito, M.; Browne, D.; Burns, F.; Chadwick, D. R.; Clark, R.; Cosgrove, C.; Galloway, J.; Goodman, A. L.; Heer, A.; Higham, A.; Iyengar, S.; Jamal, A.; Jeanes, C.; Kalra, P. A.; Kyriakidou, C.; McAuley, D. F.; Meyrick, A.; Minassian, A. M.; Minton, J.; Moore, P.; Munsoor, I.; Nicholls, H.; Osanlou, O.; Packham, J.; Pretswell, C. H.; San Francisco Ramos, A.; Saralaya, D.; Sheridan, R. P.; Smith, R.; Soiza, R. L.; Swift, P. A.; Thomson, E. C.; Turner, J.; Viljoen, M. E.; Albert, G.; Cho, I.; Dubovsky, F.; Glenn, G.; Rivers, J.; Robertson, A.; Smith, K.; Toback, S.; nCo, V. S. G., Safety and Efficacy of NVX-CoV2373 Covid-19 Vaccine. *N Engl J Med* **2021**, *385* (13), 1172-1183.

15. Wang, P.; Kim, Y. J.; Navarro-Villalobos, M.; Rohde, B. D.; Gin, D. Y., Synthesis of the potent immunostimulatory adjuvant QS-21A. *J Am Chem Soc* **2005,** *127* (10), 3256-3257.

16. Fernandez-Tejada, A.; Tan, D. S.; Gin, D. Y., Development of Improved Vaccine Adjuvants Based on the Saponin Natural Product QS-21 through Chemical Synthesis. *Acc Chem Res* **2016,** *49* (9), 1741-1756.

17. Willyard, C. The Bumpy Road to Malaria Vaccination, *Nature* [Online], 2022. https://www.nature.com/articles/d41586-022-04343-7.

18. Guan, Y.; Omueti-Ayoade, K.; Mutha, S. K.; Hergenrother, P. J.; Tapping, R. I., Identification of novel synthetic toll-like receptor 2 agonists by high throughput screening. *J Biol Chem* **2010,** *285* (31), 23755-23762.

19. Chan, M.; Hayashi, T.; Mathewson, R. D.; Nour, A.; Hayashi, Y.; Yao, S.; Tawatao, R. I.; Crain, B.; Tsigelny, I. F.; Kouznetsova, V. L.; Messer, K.; Pu, M.; Corr, M.; Carson, D. A.; Cottam, H. B., Identification of substituted pyrimido[5,4-b]indoles as selective Toll-like receptor 4 ligands. *J Med Chem* **2013,** *56* (11), 4206-4223.

20. Liu, B.; Tang, L.; Zhang, X.; Ma, J.; Sehgal, M.; Cheng, J.; Zhang, X.; Zhou, Y.; Du, Y.; Kulp, J.; Guo, J. T.; Chang, J., A cell-based high throughput screening assay for the discovery of cGAS-STING pathway agonists. *Antiviral Res* **2017,** *147*, 37-46.

21. Kim, J. Y.; Rosenberger, M. G.; Chen, S.; Ip, C. K.; Bahmani, A.; Chen, Q.; Shen, J.; Tang, Y.; Wang, A.; Kenna, E.; Son, M.; Tay, S.; Ferguson, A. L.; Esser-Kahn, A. P., Discovery of New States of Immunomodulation for Vaccine Adjuvants via High Throughput Screening: Expanding Innate Responses to PRRs. *ACS Cent Sci* **2023**, *9* (3), 427-439.

22. Malumbres, M.; Barbacid, M., Cell cycle, CDKs and cancer: a changing paradigm. *Nat Rev Cancer* **2009,** *9* (3), 153-166.

23. Klein, M. E.; Kovatcheva, M.; Davis, L. E.; Tap, W. D.; Koff, A., CDK4/6 Inhibitors: The Mechanism of Action May Not Be as Simple as Once Thought. *Cancer Cell* **2018,** *34* (1), 9-20.

24. Fassl, A.; Geng, Y.; Sicinski, P., CDK4 and CDK6 kinases: From basic science to cancer therapy. *Science* **2022,** *375* (6577), eabc1495.

25. Acosta, J. C.; Banito, A.; Wuestefeld, T.; Georgilis, A.; Janich, P.; Morton, J. P.; Athineos, D.; Kang, T. W.; Lasitschka, F.; Andrulis, M.; Pascual, G.; Morris, K. J.; Khan, S.; Jin, H.; Dharmalingam, G.; Snijders, A. P.; Carroll, T.; Capper, D.; Pritchard, C.; Inman, G. J.; Longerich, T.; Sansom, O. J.; Benitah, S. A.; Zender, L.; Gil, J., A complex secretory program orchestrated by the inflammasome controls paracrine senescence. *Nat Cell Biol* **2013,** *15* (8), 978-990.

26. Faget, D. V.; Ren, Q.; Stewart, S. A., Unmasking senescence: context-dependent effects of SASP in cancer. *Nat Rev Cancer* **2019,** *19* (8), 439-453.

27. Goel, S.; DeCristo, M. J.; Watt, A. C.; BrinJones, H.; Sceneay, J.; Li, B. B.; Khan, N.; Ubellacker, J. M.; Xie, S.; Metzger-Filho, O.; Hoog, J.; Ellis, M. J.; Ma, C. X.; Ramm, S.; Krop, I. E.; Winer, E. P.; Roberts, T. M.; Kim, H. J.; McAllister, S. S.; Zhao, J. J., CDK4/6 inhibition triggers anti-tumour immunity. *Nature* **2017,** *548* (7668), 471-475.

28. Deng, J.; Wang, E. S.; Jenkins, R. W.; Li, S.; Dries, R.; Yates, K.; Chhabra, S.; Huang, W.; Liu, H.; Aref, A. R.; Ivanova, E.; Paweletz, C. P.; Bowden, M.; Zhou, C. W.; Herter-Sprie, G. S.; Sorrentino, J. A.; Bisi, J. E.; Lizotte, P. H.; Merlino, A. A.; Quinn, M. M.; Bufe, L. E.; Yang, A.; Zhang, Y.; Zhang, H.; Gao, P.; Chen, T.; Cavanaugh, M. E.; Rode, A. J.; Haines, E.; Roberts, P. J.; Strum, J. C.; Richards, W. G.; Lorch, J. H.; Parangi, S.; Gunda, V.; Boland, G. M.; Bueno, R.; Palakurthi, S.; Freeman, G. J.; Ritz, J.; Haining, W. N.; Sharpless, N. E.; Arthanari, H.; Shapiro, G. I.; Barbie, D. A.; Gray, N. S.; Wong, K. K., CDK4/6 Inhibition Augments Antitumor Immunity by Enhancing T-cell Activation. *Cancer Discov* **2018,** *8* (2), 216-233.

29. Petroni, G.; Formenti, S. C.; Chen-Kiang, S.; Galluzzi, L., Immunomodulation by anticancer cell cycle inhibitors. *Nat Rev Immunol* **2020,** *20* (11), 669-679.

30. Heckler, M.; Ali, L. R.; Clancy-Thompson, E.; Qiang, L.; Ventre, K. S.; Lenehan, P.; Roehle, K.; Luoma, A.; Boelaars, K.; Peters, V.; McCreary, J.; Boschert, T.; Wang, E. S.; Suo, S.; Marangoni, F.; Mempel, T. R.; Long, H. W.; Wucherpfennig, K. W.; Dougan, M.; Gray, N. S.; Yuan, G. C.; Goel, S.; Tolaney, S. M.; Dougan, S. K., Inhibition of CDK4/6 Promotes CD8 T-cell Memory Formation. *Cancer Discov* **2021,** *11* (10), 2564-2581.

31. Jin, X.; Ding, D.; Yan, Y.; Li, H.; Wang, B.; Ma, L.; Ye, Z.; Ma, T.; Wu, Q.; Rodrigues, D. N.; Kohli, M.; Jimenez, R.; Wang, L.; Goodrich, D. W.; de Bono, J.; Dong, H.; Wu, H.; Zhu, R.; Huang, H., Phosphorylated RB Promotes Cancer Immunity by Inhibiting NF-kappaB Activation and PD-L1 Expression. *Mol Cell* **2019,** *73* (1), 22-35.

32. Swanson, K. V.; Deng, M.; Ting, J. P., The NLRP3 inflammasome: molecular activation and regulation to therapeutics. *Nat Rev Immunol* **2019,** *19* (8), 477-489.

33. Grootjans, S.; Vanden Berghe, T.; Vandenabeele, P., Initiation and execution mechanisms of necroptosis: an overview. *Cell Death Differ* **2017,** *24* (7), 1184-1195.

34. Kraft, J. C.; Freeling, J. P.; Wang, Z.; Ho, R. J., Emerging research and clinical development trends of liposome and lipid nanoparticle drug delivery systems. *J Pharm Sci* **2014,** *103* (1), 29-52.

35. Tao, X.; Jia, N.; Cheng, N.; Ren, Y.; Cao, X.; Liu, M.; Wei, D.; Wang, F. Q., Design and evaluation of a phospholipase D based drug delivery strategy of novel phosphatidyl-prodrug. *Biomaterials* **2017,** *131*, 1-14.

36. Rondla, R.; PadmaRao, L. S.; Ramatenki, V.; Haredi-Abdel-Monsef, A.; Potlapally, S. R.; Vuruputuri, U., Selective ATP competitive leads of CDK4: Discovery by 3D-QSAR pharmacophore mapping and molecular docking approach. *Comput Biol Chem* **2017,** *71*, 224-229.

37. Li, A. W.; Sobral, M. C.; Badrinath, S.; Choi, Y.; Graveline, A.; Stafford, A. G.; Weaver, J. C.; Dellacherie, M. O.; Shih, T. Y.; Ali, O. A.; Kim, J.; Wucherpfennig, K. W.; Mooney, D. J., A facile approach to enhance antigen response for personalized cancer vaccination. *Nat Mater* **2018,** *17* (6), 528-534.

38. Jones, L. J.; Upson, R. H.; Haugland, R. P.; Panchuk-Voloshina, N.; Zhou, M.; Haugland, R. P., Quenched BODIPY dye-labeled casein substrates for the assay of protease activity by direct fluorescence measurement. *Anal Biochem* **1997,** *251* (2), 144-152.

39. Dendouga, N.; Fochesato, M.; Lockman, L.; Mossman, S.; Giannini, S. L., Cell-mediated immune responses to a varicella-zoster virus glycoprotein E vaccine using both a TLR agonist and QS21 in mice. *Vaccine* **2012,** *30* (20), 3126-3135.

40. Kozar, K.; Ciemerych, M. A.; Rebel, V. I.; Shigematsu, H.; Zagozdzon, A.; Sicinska, E.; Geng, Y.; Yu, Q.; Bhattacharya, S.; Bronson, R. T.; Akashi, K.; Sicinski, P., Mouse development and cell proliferation in the absence of D-cyclins. *Cell* **2004,** *118* (4), 477-491.

41. Malumbres, M.; Sotillo, R.; Santamaria, D.; Galan, J.; Cerezo, A.; Ortega, S.; Dubus, P.; Barbacid, M., Mammalian cells cycle without the D-type cyclin-dependent kinases Cdk4 and Cdk6. *Cell* **2004,** *118* (4), 493-504.

42. Tahtinen, S.; Tong, A. J.; Himmels, P.; Oh, J.; Paler-Martinez, A.; Kim, L.; Wichner, S.; Oei, Y.; McCarron, M. J.; Freund, E. C.; Amir, Z. A.; de la Cruz, C. C.; Haley, B.; Blanchette, C.; Schartner, J. M.; Ye, W.; Yadav, M.; Sahin, U.; Delamarre, L.; Mellman, I., IL-1 and IL-1ra are key regulators of the inflammatory response to RNA vaccines. *Nat Immunol* **2022,** *23* (4), 532-542.

43. Poratti, M.; Marzaro, G., Third-generation CDK inhibitors: A review on the synthesis and binding modes of Palbociclib, Ribociclib and Abemaciclib. *Eur J Med Chem* **2019,** *172*, 143-153.

44. Manna, S.; Howitz, W. J.; Oldenhuis, N. J.; Eldredge, A. C.; Shen, J.; Nihesh, F. N.; Lodoen, M. B.; Guan, Z.; Esser-Kahn, A. P., Immunomodulation of the NLRP3 Inflammasome through Structure-Based Activator Design and Functional Regulation via Lysosomal Rupture. *ACS Cent Sci* **2018,** *4* (8), 982-995.

45. Ajit, J.; Cassaidy, B.; Tang, S.; Solanki, A.; Chen, Q.; Shen, J.; Esser Kahn, A. P., Temporal Control of Trained Immunity via Encapsulated Release of β-Glucan Improves Therapeutic Applications. *Adv Healthc Mater* 2022, *11* (18), e2200819

46. Garcon, N.; Chomez, P.; Van Mechelen, M., GlaxoSmithKline Adjuvant Systems in vaccines: concepts, achievements and perspectives. *Expert Rev Vaccines* **2007,** *6* (5), 723-739.

CHAPTER 5 Site-specific antigen-adjuvant conjugation using cell-free protein synthesis enhances antigen presentation and $CD8^+$ T-cell response.

This chapter has been published, in part, in Scientific Reports.[1]

5.1 Introduction.

Synthetic subunit vaccines that invoke potent cellular immune responses are desirable for the safe and scalable prevention of disease. Early vaccines were composed of whole pathogens attenuated by heat inactivation or chemical modification. Traditional attenuated vaccines are highly potent, and their administration has led to reductions in morbidity from many diseases. Despite their potency, attenuated vaccines pose a safety risk resulting from the presence of live pathogens, limiting use in elderly or immunocompromised individuals.[2] Furthermore, attenuated vaccines can contain harmful pathogenic material, undergo spontaneous mutations to revert to their infectious form, and risk infecting the host if incompletely inactivated.[3] Thus, there is interest in designing synthetic alternatives to attenuated vaccines.

Subunit vaccines comprising a protein antigen do not contain live pathogenic material and therefore serve as desirable alternatives to attenuated vaccines. Subunit vaccines are composed of poorly immunogenic protein antigens co-administered with one or more adjuvants which bind pattern-recognition receptors (PRRs) to activate innate immunity.[3-6] Innate immune activation is critical for cross-presentation of proteolyzed antigen on MHC by antigen-presenting cells (APCs) and recognition by antigen-specific T-cells, resulting in protective adaptive immune responses.[5] FDA-approved subunit vaccines containing synthetic adjuvants have been developed for hepatitis B and shingles, among others.[7, 8]

Despite the success of subunit vaccines, they have been limited by weak immunogenicity of the antigen, necessitating co-administration of large doses of adjuvant. Synthetic PRR agonists often generate adverse inflammatory profiles when used as adjuvants, resulting in poor translation to clinical use.[9] One method to reduce the dose of agonist is through co-delivery of antigen and

adjuvant to the same APC.[10] Co-delivery allows adjuvant-mediated activation of the APC along with concurrent antigen processing and presentation, resulting in efficient T-cell responses and dose sparing.[11] Precise control over the amount of adjuvant administered with the antigen can prevent adverse responses and improve efficiency of subunit vaccines.

Co-delivery of antigen and adjuvant through conjugation can facilitate efficient activation of APCs and enhanced antigen exposure using a single construct, enhancing proliferation of antigen-specific T-cells.[10, 12-14] Oligodeoxynucleotides, such as unmethylated CpG, activate the innate immune system by binding endosomal toll-like receptor 9 (TLR9) to enhance cross-presentation of antigenic components.[15] TLR9 agonists conjugated to ovalbumin (OVA) were shown to enhance both cross-presentation and antigen-specific $CD8^+$ T-cell production.[10, 14] However, these systems were limited by poor control over the modification site and aggregation resulting from over-conjugation of ODN adjuvants. To overcome this limitation, we hypothesized that cell-free protein synthesis would allow scalable production of dose controlled, site-specific antigen-adjuvant conjugates that would not affect protein folding or disrupt major epitopes. Moreover, we were interested to explore how conjugation of alternative TLR agonists to antigen could be used to modulate the adaptive immune response (*e.g.*, facilitating Th1/2 biasing), as most literature to date has focused on TLR9.

Cell-free protein synthesis (CFPS) is an efficient, *E.coli*-derived platform to express and purify unglycosylated proteins containing non-native amino acids (nnAA) in their natively-folded state. The translational machinery provided by the cellular lysate supplemented with energy sources and plasmid DNA facilitates *in-vitro* synthesis of proteins that are unnatural, insoluble, or toxic to living systems.[16] Historically, CFPS systems were limited by feedback inhibition caused by byproducts resulting from use of ATP as an energy source.[17] Recently, the XpressCF$^+$ CFPS system (Vaxcyte, Inc.) has overcome these limitations by using pyruvate as an alternative energy source to allow scalable production of complex proteins.[17, 18] By using an orthogonal tRNA and aminoacyl synthetase pairing, this technology allows site-specific incorporation of nnAAs with

reactive side chains into the folded protein.[18-20] Using this system, we aimed to test if scalable production of site-specific antigen-adjuvant conjugates could induce production of a $CD8^+$ killer T cell response in a vaccination model.

Herein, we describe a novel strategy to generate a model antigen-adjuvant conjugate subunit vaccine using CFPS. OVA-2pAMF, an unglycosylated OVA mutant containing two site-specific *p*-azidomethyl-L-phenylalanine (pAMF) mutations at K20 and K370, was synthesized using XpressCF$^+$ on a 14 mg scale. A TLR9 agonist, CpG1018, was conjugated to the pAMF sites using azide-alkyne click chemistry to generate the conjugate vaccine, OVA-CpG. Functionally, the conjugate vaccine enhanced antigen cross-presentation and APC activation *in-vitro* and promoted $CD8^+$ T-cell responses *in-vivo* without showing aggregation or cytotoxicity. Most importantly, these studies demonstrate that large quantities of mutant proteins containing nnAAs at specific sites in the folded protein can be prepared using CFPS and that conjugating a CpG oligonucleotide TLR agonist to these sites can enhance antigen-specific $CD8^+$ T-cell production in a vaccination model.

5.2 Results and Discussion.

5.2.1 Synthesis of OVA-CpG Conjugates Using CFPS.

CFPS is a versatile approach to synthesize protein antigens with site-specific mutations for antigen-adjuvant conjugation. To demonstrate the applicability of CFPS and to provide an appropriate comparison to previous antigen-adjuvant co-localization experiments,[10-14, 21, 22] we used a model antigen, OVA. Noting that a pioneering study of non-specific conjugation of CpG to OVA at a ≥2:1 ratio induced aggregation and reduced antigen presentation,[14] we introduced two site-specific conjugatable handles on one OVA protein to overcome this limitation of non-specific conjugation. We selected the human-mouse cross-reactive CpG1018 as a clinically relevant TLR9 agonist and appended a commercially available 5'-thiol handle for conjugation.[7]

In selecting the conjugation sites, we considered the structure of OVA with a focus on its immunodominant MHC epitopes, SIINFEKL ($OVA_{257-264}$) and ISQAVHAAHAEINEAGR ($OVA_{323-339}$). We hypothesized that epitope blocking and aggregation could be mitigated by introducing spatially-isolated and solvent-exposed conjugation sites away from the immunodominant epitopes. K20 and K370 were therefore selected as optimal conjugation sites (**Figure 5.1A-B**). The handles were introduced by replacing lysine codons with amber codons in the coding sequence for OVA. Using an orthogonal tRNA and synthetase pair, we selectively incorporated *p*-azidomethyl-L-phenylalanine (pAMF) at these sites to generate one protein with two azide reactive sites, OVA-2pAMF. A TEV protease cleavage site coupled to a poly-Histidine tag was expressed at the C terminus to facilitate purification of the protein by sequential combination of affinity and size-exclusion chromatography. Protein expression conditions were optimized to a temperature of 25°C (**Figure 5.1C**) and the purity of the purified protein was confirmed by SDS-PAGE (**Figure 5.1D** & **Figure S5.1**). The protein was further characterized by Q-TOF MS and MALS (**Figure 5.1D-F**). CFPS was subsequently scaled up to generate 14 mg of the purified protein. After purification, endotoxin was removed using Triton X-114 to a level <1.5 EU/mL.[23] A recovery yield of 78% for the endotoxin purification step was achieved (**Figure S5.2**), permitting use of milligram-scale OVA-2pAMF in later biological experiments.

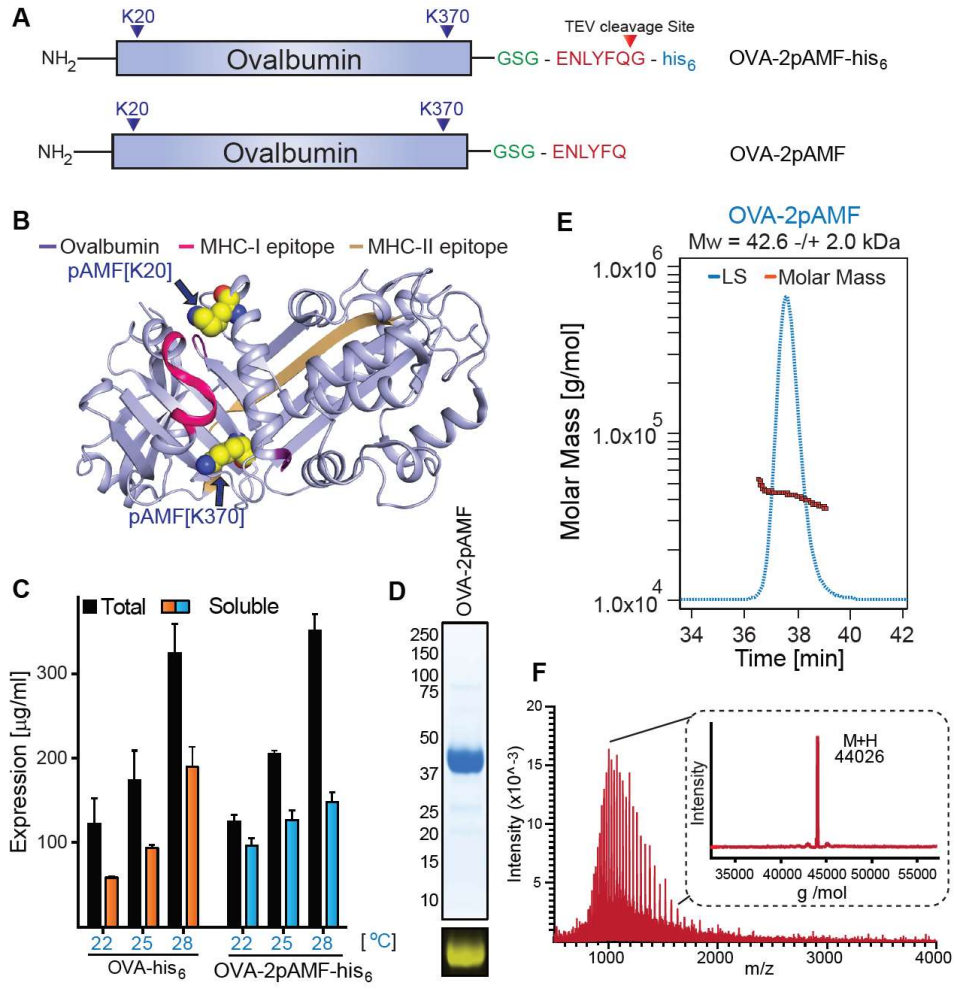

Figure 5.1: Expression purification, and characterization of OVA-2pAMF. A) Modular architecture and expression construct design of OVA-2pAMF with B) the K20 and K370 pAMF conjugation sites noted. C) Optimization of OVA-2pAMF expression conditions. D) SDS-PAGE demonstrates > 95% purity, and DBCO-TAMRA labeling confirms pAMF incorporation. Biophysical characterization of purified OVA-2pAMF using E) SEC-MALS indicates a monodisperse protein preparation and F) Q-TOF ESI-MS (deconvoluted in inset) indicates close agreement with the expected mass, 44,026 Da.

After synthesizing and purifying OVA-2pAMF, we conjugated the 5'-thiol modified CpG1018 through a DBCO-Maleimide linker (**Figure 5.2A-B** & **Figure S5.3**). Copper-free click chemistry was employed to facilitate this reaction under aqueous conditions. Unreacted CpG-DBCO was removed by centrifugal filtration, and the OVA-CpG conjugates were characterized using SDS-PAGE gel chromatography. Three batches of OVA-CpG were prepared, and loading densities of 1.2, 1.5, and 1.3 CpGs/OVA were obtained (**Figure 5.2C** & **Figure S5.4**). It should

be noted that SDS-PAGE revealed two distinct peaks for the 1 CpG/OVA component; while both components were included in the densitometry analysis, we believe these species correspond to different charge states of the K20 or K370 conjugation sites after reaction with CpG which may have resulted in minor electrostatic variations during electrophoresis. We also attempted to improve loading by increasing reaction temperature, but these efforts resulted in degradation of OVA-2pAMF observed through the presence of large, low molecular weight bands ≤ 37 kDa in SDS-PAGE gels of the crude product (not shown). Addition of excess CpG-DBCO or prolonging the reaction were also found to be insufficient to drive the reaction to completion; we believe that the negative charge of CpG could shield the pAMF sites during later stages of the reaction to result in this effect. Unreacted CpG was found to be sufficiently removed using size-exclusion HPLC of the purified product (**Figure S5.5**). Preparative anion exchange chromatography using a 0-1 M NaCl gradient in a method previously described by the Chertok group was shown to remove unreacted OVA-2pAMF from the reaction mixture; however, components containing one and two CpG/OVA eluted together (**Figure S5.6**).[14] With the limited benefit to this purification strategy, we opted to use the unpurified heterogeneous mixtures in future studies; thus, site-specific OVA-CpG conjugates containing 1.2-1.5 CpG/OVA were achieved for use in later assays.

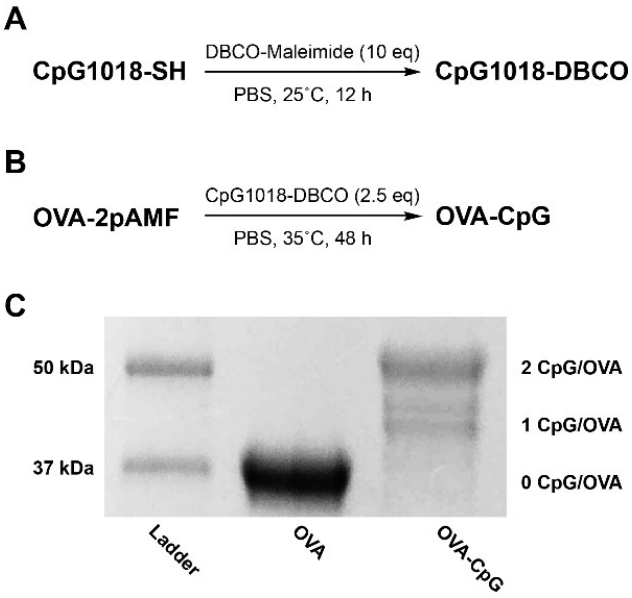

Figure 5.2: Synthesis of OVA-TL9 agonist constructs. A) Synthesis of CpG-DBCO and B) conjugation of CpG-DBCO to OVA-2pAMF. C) SDS-PAGE gel of OVA-CpG conjugates visualized using One-Step Blue protein gel staining demonstrates loading of 1.5 OVA/CpG in batch one of the OVA-CpG conjugate.

5.2.2 In-vitro Immunostimulatory Activity of CpG Conjugates.

Having successfully synthesized OVA-CpG, we validated its *in-vitro* immune activity of our linked systems relative to unlinked controls using RAW-Blue and HEK mTLR9 reporter cell lines. Conjugation of PRR agonists to a macromolecule can alter receptor binding, and it is therefore important to validate activity after conjugation. We first tested activity using HEK mTLR9 reporter cells. OVA-CpG conjugates exhibited enhanced mTLR9 activation relative to unlinked OVA + CpG (**Figure 5.3A**). For all in-vitro studies, the dose of OVA and CpG used in the OVA+CpG treatment was designed to match that of the linked OVA-CpG conjugate. Native EndoFit Ovalbumin (InvivoGen) was used for all *in-vitro* and *in-vivo* experiments as a non-immunogenic control; though OVA-2pAMF is not expected to induce an immune response, such controls could prevent aberrant activation in control groups from non-specific immunostimulatory activity of OVA-2pAMF. We then used the RAW-Blue NF-κB reporter cells to test downstream signaling of the TLR9 receptor. Again, signaling induced by OVA-CpG was increased relative to unlinked controls (**Figure 5.3B**). These results validated that conjugation of CpG to OVA-2pAMF enhanced TLR9

signaling. TLR9 is expressed in the endocytic compartment; thus, the divalency of the OVA-CpG construct both facilitates enhanced endosomal uptake through conjugation and increases TLR activation in the endosome to facilitate activation of APCs. Indeed, linked antigen-adjuvant formulations have been shown previously to enhance APC activation *in-vitro*.[13]

After confirming activity of our conjugates, we tested their capability relative to unlinked controls to induce cross-presentation and activate dendritic cells *in-vitro.* The DC2.4 dendritic cell line was used as APCs, and cross-presentation was quantified by co-culturing with B3Z hybridoma T-cells. These T-cells specifically recognize the OVA MHC-I epitope motif, SIINFEKL, presented on H-2K^{b}. Upon recognition, β-galactosidase is produced which is quantified using a colorimetric substrate, CPRG. At concentrations ≥ 10 μg/mL, linked OVA-CpG incubated with the DC2.4 cells for 5 h invoked greater cross-presentation than unlinked controls (**Figure 5.3C**). Indeed, the unlinked OVA + CpG was unable to induce cross-presentation even at the highest dose tested; we believe that this unexpected result might occur due to changes in the kinetics of OVA-CpG uptake relative to soluble CpG at the 5 h timepoint as well as enhanced TLR9 binding resulting from co-localization of OVA and CpG in a single endosome. These results highlight the importance of enhanced uptake and high endosomal adjuvant concentrations in facilitating cross-presentation.

To further demonstrate that TLR9 signaling is at the basis of the enhanced CD8^{+} T cell activation, we then evaluated dendritic cell activation resulting from treatment with our conjugates. CD80 and CD86 are common cell surface markers which would serve as a viable proxy of activation. OVA-CpG or unlinked controls were incubated with DC2.4 cells at 50 μg/mL for 20 h, and cells were subsequently stained and analyzed using flow cytometry. The DC2.4 cells showed enhanced cell surface expression of CD80, but not CD86, when treated with OVA-CpG relative to unlinked controls (**Figure 5.3D-E** & **Figure S5.7**). Previous studies have shown that both mature and immature DC2.4 cells highly express CD86, but not CD80, which could explain differences in their expression patterns in this model.[24] Moreover, a distinct activated DC

population marked by an increase in granularity was observed by flow cytometry after treating the cells with linked conjugates relative to their unlinked controls, further validating the activated phenotype (**Figure 5.3F** & **Figure S5.8**). Higher cross-presentation and activation efficiency at lower CpG concentration demonstrates effectiveness of our conjugation strategy.

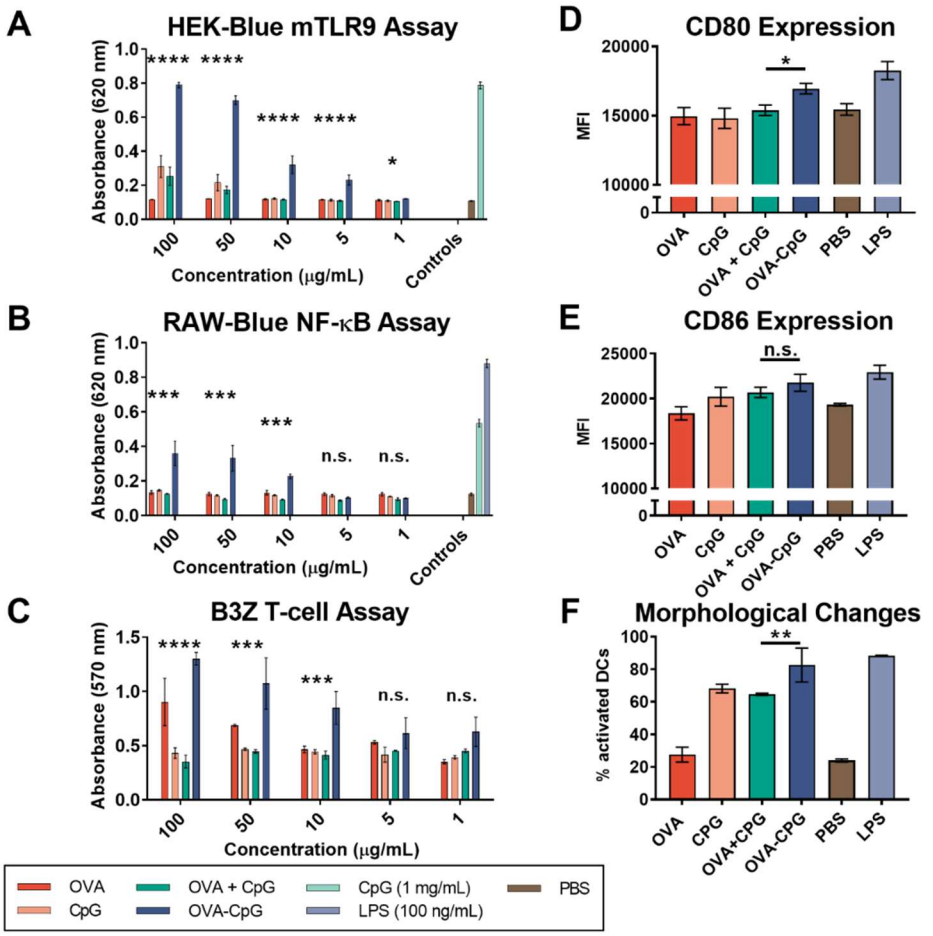

Figure 5.3: *In-vitro* characterization of OVA-CpG. TLR9 activity of OVA-CpG conjugates in A) HEK mTLR9 and B) RAW-Blue NF-κB reporter cell activity was enhanced in OVA-CpG conjugates relative to unlinked controls. C) Cross-presentation of OVA-CpG on DC2.4 cells was enhanced relative to unlinked controls as measured using the B3Z T-cell hybridoma model. Flow cytometry evaluating mean fluorescent intensity of D) CD80 and E) CD86 as well as F) morphological changes associated with activation after stimulation with 50 μg/mL OVA-CpG or unlinked controls. Statistics were conducted using one- or two-way ANOVA with multiple comparisons testing to evaluate OVA-CpG relative to OVA + CpG.

5.2.3 In-vivo Vaccination Experiments Using CpG Conjugates.

After characterizing our conjugates *in-vitro*, we designed an *in-vivo* experiment to assay cellular and humoral immune responses to the conjugate OVA-CpG systems. Previous experience in our laboratory indicated that 10-50 μg of OVA and 25-50 μg of CpG are optimal for murine vaccination; however, given the linked nature of our conjugates, these doses were infeasible. We therefore implemented a dose of 1 nmol of the OVA-CpG conjugate (44 μg OVA and 12 μg CpG for a loading of 1.5 CpG/OVA) and corresponding amount of unlinked controls (44 μg EndoFit Ovalbumin and 12 μg uncapped CpG-SH). 1 nmol of unadjuvanted OVA and PBS were used as controls. A boost was administered 14 d after initial intramuscular injection, and humoral and cellular immune responses were assayed after 21 and 28 d, respectively.

In response to the vaccination schedule (described in **Figure S5.9A**), no changes in body weight were observed, although OVA-CpG conjugates induced increased IFN-γ and MCP-1 production 24 h after injection (**Figure S5.9**). This could result from greater TLR9 stimulation in the draining lymph nodes afforded by conjugation to OVA, as observed with other nanoparticulate constructs.[6] After 21 d, no differences in total or IgG1/IgG2c antibody titers were observed between the linked and unlinked groups (**Figures S5.10** & **S5.11**), indicating that the conjugates did not improve humoral immunity or induce Th1/Th2 bias in the immune response. The ability of antigen-adjuvant conjugates to enhance antibody production is disputed in the literature.[10, 14, 15] Our result suggests that OVA-TLR9 agonist linkage enhances the efficiency of endosomal uptake and TLR activation rather than global antigen recognition, providing little advantage for humoral immunity. After 28 d, spleens were harvested, cultured, and stained using antigen-specific MHC tetramers to assay the cellular response. The conjugates showed >3x enhancement in antigen-specific T-cell production (**Figure S5.11**) indicating enhanced *in-vivo* cellular immune responses.

Given these results, we reduced the dose of our linked vaccine system, running additional experiments at 1.0, 0.1, and 0.01 nmol (10 μg, 1.0 μg and 0.1 μg CpG for a loading of 1.2 CpG/OVA) using batch 2 of the OVA-CpG conjugates (as well as unlinked controls as described

above) to observe the efficiency of our linked systems in generating cellular immunity (**Figure 5.4A**). Again, serum anti-OVA antibody titers showed no differences after 21 d (**Figure 5.4B**), while splenic antigen-specific $CD8^+$ T-cell production was enhanced relative to unlinked controls at the 1.0 nmol dose. Intriguingly, a modest antigen-specific $CD8^+$ T-cell response was also observed using the reduced 0.1 nmol OVA-CpG amount, which is less than one tenth of the CpG commonly used as an adjuvant. In contrast, minimal antigen-specific $CD8^+$ T-cell production was observed using 1.0 or 0.1 nmol of unlinked control (**Figure 5.4C-D**). Based on these results, we conclude CFPS is a scalable platform for generating antigens with site-specific nnAAs for conjugation to adjuvants. Our OVA-CpG conjugates reduced the quantity of adjuvant needed to invoke antigen-specific $CD8^+$ T-cell production in our vaccine model.

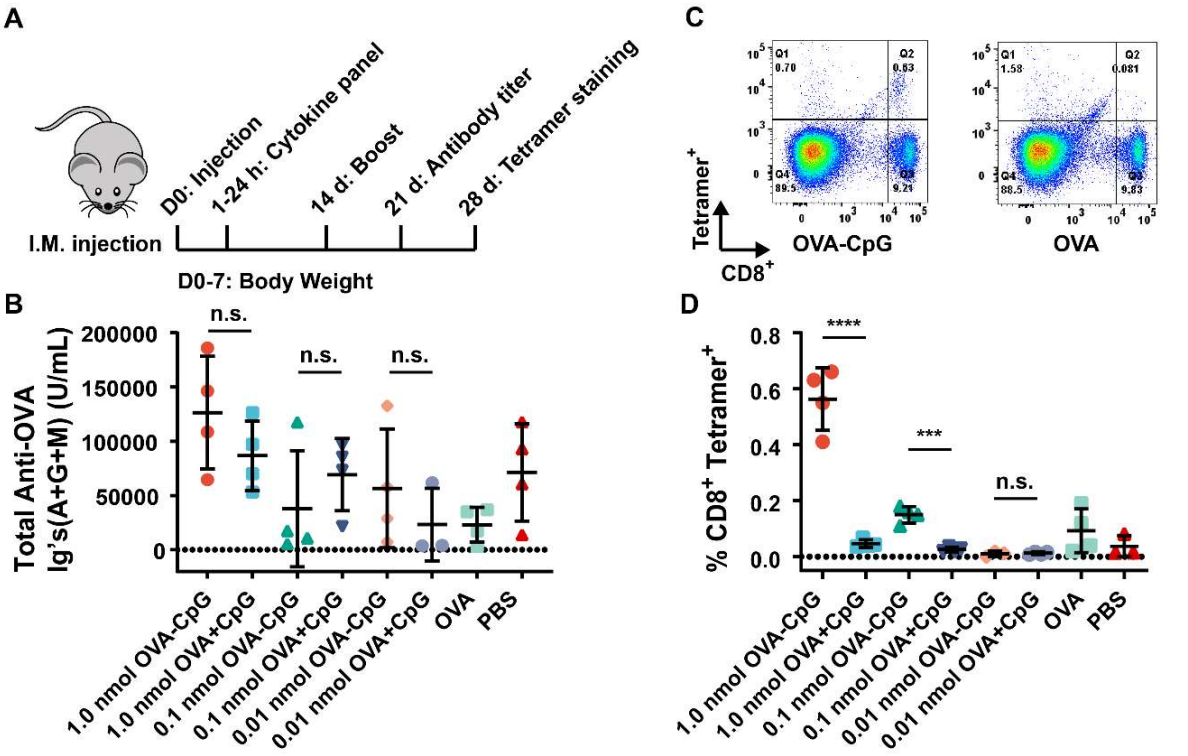

Figure 5.4: In-vivo characterization of OVA-CpG in an OVA vaccination model. A) *In-vivo* experiment overview. B) No significant differences in anti-OVA total antibody titers were observed 21 d after injection ($p > 0.05$). C) Representative flow cytometry gating for evaluation of antigen specific $CD8^+$ T-cell production. D) Summary statistics for all flow cytometry gated as shown in (C) demonstrating enhanced antigen specific $CD8^+$ T-cell production of OVA-CpG conjugates relative to unlinked controls. Statistics were conducted using student's t-test to evaluate OVA-CpG relative to OVA + CpG.

5.2.4 Synthesis of OVA-2BXy Constructs and Preliminary In-vivo Characterization.

Given the efficacy of OVA-CpG constructs, we sought to identify if other TLR agonists could be used for antigen-adjuvant conjugation using the CFPS platform. Other TLR agonists can induce different innate immune signaling pathways to afford Th1- or Th2-biased adaptive immune responses that might be of interest in protecting against infections.[6] Moreover, combinations of adjuvants can be employed to recapitulate the immunostimulatory profile of natural pathogens.[6, 25] In an initial pilot study, azide-modified TLR2/6 and TLR7 agonists, Pam2CSK4-N_3 and 2BXy-PEG_4-N_3 (**Figure S5.12**), were obtained and conjugated to OVA-2pAMF on a 100 µg scale using conditions analogous to those in **Figure 5.2B**. Both reactions were found to be successful *via* SDS-PAGE gel chromatography (**Figure 5.5A**), demonstrating that other TLR agonists are amenable to conjugation using this platform. With that said, the OVA-Pam2CSK4 construct had a dramatic decrease in solubility and was therefore unsuitable for further study (not shown). We then characterized the activity of the OVA-PEG_4-2BXy construct using a RAW-Blue NF-κB reporter assay. In contrast to OVA-CpG, the OVA-PEG_4-2BXy construct showed a dramatic reduction in activity relative to unlinked 2BXy (**Figure S5.13**). Previous results in our lab and others[26] have suggested that short, PEG-based linkers can reduce the activity of TLR7 agonists, so we obtained a second 2BXy construct containing a G_4S linker that has been reported to retain activity in-vitro. The 2BXy-G_4S construct was conjugated to OVA (OVA-G_4S-2BXy) using an analogous approach (**Figure S5.14**), providing two different OVA-TLR7 agonists for future study.

Having designed two OVA-TLR7 agonist constructs, we characterized the activity of these constructs relative to their unlinked controls in a murine vaccination model (**Figure 5.5B**). Mice were vaccinated with OVA-G_4S-2BXy, OVA-PEG_4-2BXy, or the appropriate unlinked controls (1 nmol OVA equivalents/dose) on days 0 and 14, and B and T cell responses were characterized on days 21 and 28, respectively. Surprisingly, it was observed that OVA-PEG_4-2BXy displayed enhanced OVA-specific antibody production relative to its unlinked counterpart, whereas OVA +

2BXy-G_4S displayed greater activity than its linked counterpart (**Figure 5.5C**). This result again highlights the critical importance of linker chemistry in the adjuvanticity of covalent formulations.[25-27] Only unlinked 2BXy and 2BXy-G_4S induced antigen-specific $CD8^+$ T cell production (**Figure 5.5D**). Given these results, we hypothesized that the limited efficacy of TLR7 agonists could be tied to the different dosages of antigen and adjuvant that are facilitated by site-specific conjugation. Typically, 2BXy is employed at the 50-100 nmol range *in-vivo*, a 25- to 50-fold excess of that used in this experiment. While antigen-adjuvant conjugation can reduce the needed dose, this low quantity of 2BXy was likely insufficient to facilitate an adjuvant effect in this study.

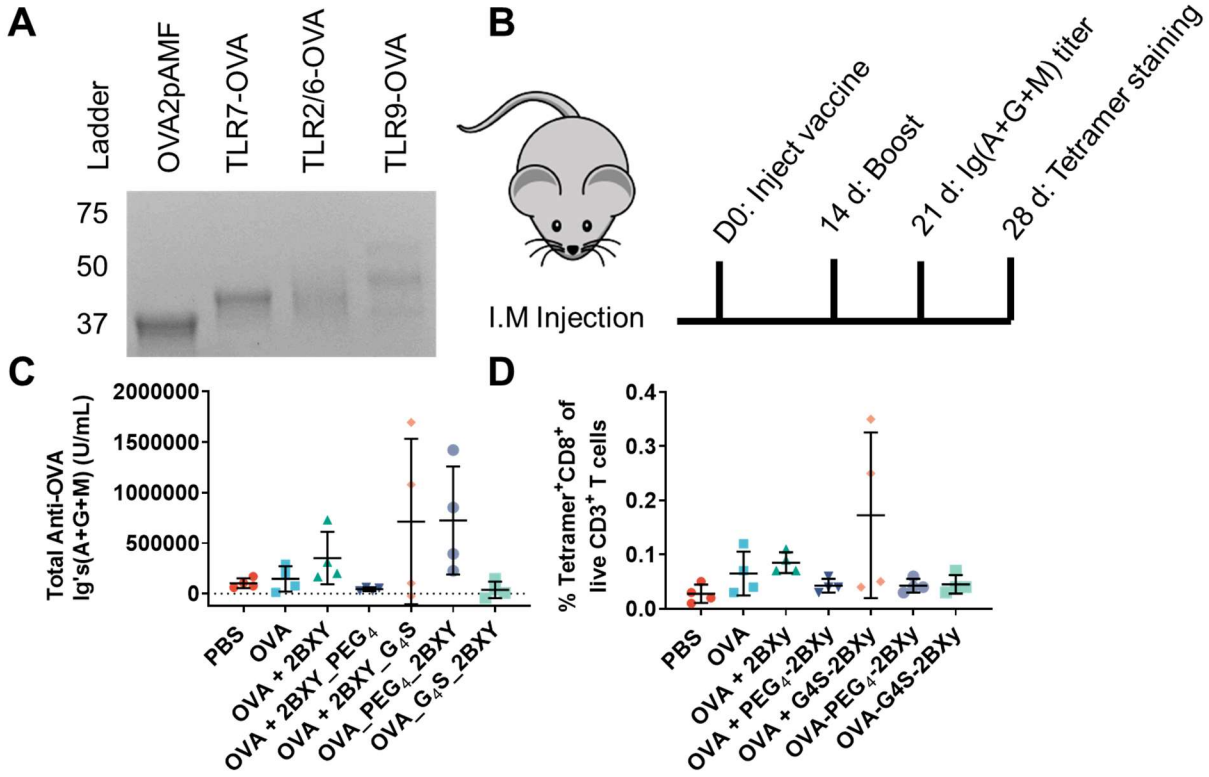

Figure 5.5: Synthesis and *in-vivo* characterization of OVA-TLR7, OVA-TLR2/6, and OVA-TLR9 agonist conjugates. The structures of the agonists used are provided in **Figure S5.12**. A) OVA-TLR7, OVA-TLR2/6, and OVA-TLR9 agonist conjugates were successfully prepared. OVA-TLR7 and OVA-TLR2/6 reactions go to completion, while only 1.2 TLR7 agonists per OVA were successfully engrafted; however, the solubility of OVA-TLR2/6 was too low to allow for further use. B) Vaccination schedule for OVA-TLR7 agonist studies. C) Antibody titers and D) $CD8^+$ tetramer staining from OVA-TLR7 agonist studies. No statistically significant differences between groups were observed using one-way ANOVA with multiple comparisons testing.

To increase the activity of TLR7 agonists in the antigen-adjuvant conjugate platform, we envisioned a water-soluble, multimeric, peptide-based platform that could be used to increase the quantity of 2BXy conjugated to OVA-2pAMF. Previous work in the Esser-Kahn lab identified that multimers of 2BXy and dopamine, a small molecule which has been proposed to inhibit NF-κB signaling, can enhance innate immunostimulatory activity while reducing toxic side effects.[28] A similar scaffold, $(2BXy)_5$-$(Dopa)_5$-DBCO, was synthesized to contain a DBCO handle for functionalization to the OVA-2pAMF scaffold and confirmed by MALDI-TOF MS (**Figure 5.6A-B** and **Figure S5.15**). To achieve this construct, 2BXy containing a C6 spacer and amine reactive group (2BXy-C6-NH_2) was conjugated to a Glutamate-Glycine peptide pentamer ($(GluGly)_5$) via HATU peptide coupling. A control containing only the dopamine multimer, $(Dopa)_5$-DBCO, was also synthesized (**Figure S5.15** and **S5.16**). The oligomers were then conjugated to OVA-2pAMF. To overcome the solubility limitations of $(2BXy)_5$-$(Dopa)_5$-DBCO in PBS, multimers were dissolved in DMSO, diluted 1:1 with PEG300 as a solubilizing agent, and finally added in a 1:4 ratio with OVA-2pAMF in PBS. Following successful reaction, DMSO, PEG, and unreacted multimers were removed *via* dialysis, and OVA constructs were analyzed via SDS-PAGE gel chromatography. To our delight, the OVA-$(Dopa)_5$ and OVA-$(Dopa)_5$-$(2BXy)_5$ reactions appeared successful, validating this approach (**Figure 5.6C**). Having demonstrated the potential of this approach, future efforts will be conducted with our collaborators to use $(2BXy)_5$-$(Dopa)_5$-DBCO and $(Dopa)_5$-DBCO in clinically relevant antigen-adjuvant conjugates.

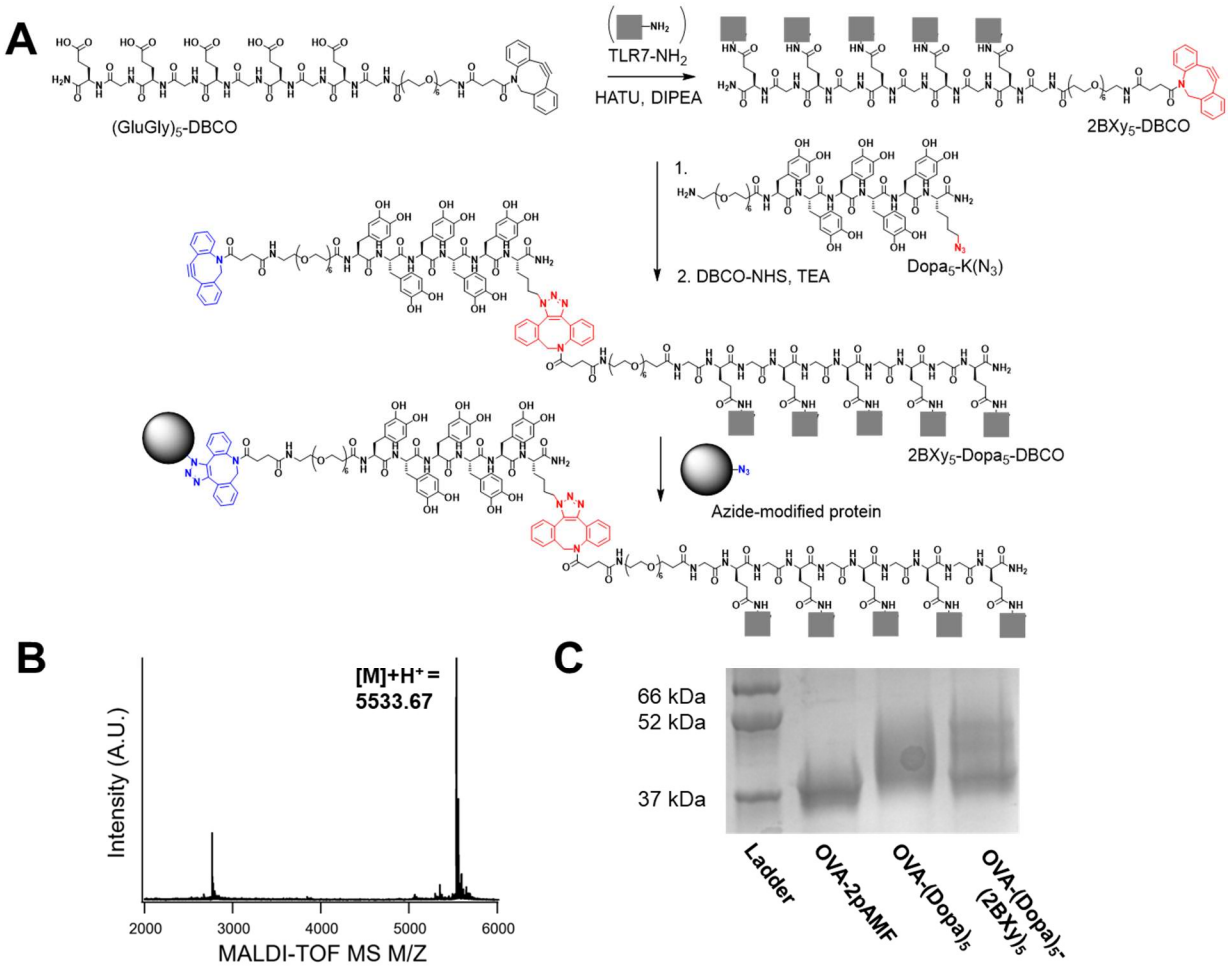

Figure 5.6: Synthesis and characterization of 2BXy oligomers and their conjugation to OVA-2pAMF. The structure of 2BXy is provided in **Figure S5.12**. A) Synthetic scheme for preparation of OVA-$(Dopa)_5$-$(2BXy)_5$ from $(GluGly)_5$-DBCO using sequential click chemistry reactions. $(GluGly)_5$-DBCO, $(Dopa)_5$-$K(N_3)$, and $(Dopa)_5$-DBCO were prepared in-house *via* solid-phase peptide synthesis. B) MALDI-TOF mass spectrum of $(2BXy)_5$-$(Dopa)_5$-DBCO demonstrating its correct mass and purity. C) Model reactions of OVA-2pAMF with $(Dopa)_5$-DBCO and $(2BXy)_5$-$(Dopa)_5$-DBCO were analyzed *via* SDS-PAGE under reducing conditions and visualized using One-Step Blue protein gel stain. Increases in mass confirm successful reactions.

5.3 Conclusion and Future Directions.

We demonstrate herein that CFPS is a facile technique to synthesize large quantities of protein containing site-specific nnAAs for antigen-adjuvant conjugation without disrupting protein folding or epitope recognition. Our OVA-CpG conjugates enhanced cross-presentation compared to unlinked controls *in-vitro*, corresponding to increased antigen-specific $CD8^+$ T-cell production *in-vivo*. Moreover, our OVA-CpG conjugates reduced the dose of CpG needed to invoke antigen-

specific $CD8^+$ T-cell production tenfold. These results suggest that CFPS can be used as a reliable method to produce antigenic proteins with efficient, site-specific conjugation of adjuvants. Given the need to generate potent $CD8^+$ T-cell responses in both prophylactic and protective vaccines, future work using the antigen-adjuvant conjugation strategy described herein will focus on translating this model system to clinically relevant vaccines against disease. In particular, the antigen-adjuvant conjugation strategy holds promise to enhance responses at reduced doses in vaccines protecting against viral infections, such as influenza, where $CD8^+$ T-cell responses are critical but inflammation limits the use of synthetic TLR agonists at efficacious doses. This strategy also holds promise to improve robustness of protective responses in bacterial polysaccharide conjugate vaccines, such as those targeted against pneumococcal or streptococcal bacteria, which suffer from poor immunogenicity. This method can overcome the limitations of conventional antigen-adjuvant conjugation and will be useful for the treatment and prevention of disease.

Future goals in research will be to expand the scope of the CFPS antigen-adjuvant conjugation platform to allow incorporation of different antigens and adjuvants. While OVA is a useful model platform on account of its low cost and immunodominant T cell epitopes, other clinically relevant antigens are desirable to demonstrate translation of this technology in humans and to develop prophylactic therapeutics. Current work is underway with our collaborators to apply this technology in prophylactic COVID-19 and therapeutic chlamydia vaccinations. The inspiration behind both vaccines is that incorporation of antigen with a conserved protein subunit will enhance immunogenicity of less immunodominant antigens and increase the universality of the adaptive response. Alternatively, incorporation of different PRR agonists will allow us to use antigen-adjuvant conjugation to bias the adaptive immune response. For example, TLR2/6 agonists such as Pam2CSK4 are known to induce a Th2 bias,[29] whereas TLR9 agonists induce potent Th1 biases.[12, 25] Dosing and solubility concerns must be overcome to allow incorporation of agonists with different physicochemical properties, as was observed with TLR2/6 and TLR7 agonists in our small screen. One approach that we envision to overcome these limitations is the design of

peptide- or polymer-agonist multimers.[27] As a proof of concept for this approach using the CFPS platform, we prepared peptide-based pentamers, $(2BXy)_5$-$(Dopa)_5$-DBCO and $(Dopa)_5$-DBCO, which contain a DBCO handle for functionalization, and conjugated them to OVA-2pAMF. Related antigen-adjuvant conjugates are now being used by our collaborators for chlamydia vaccination. Overall, the CFPS platform holds great promise for future subunit vaccine development, and we await the development of more sophisticated platforms for implementation in clinical settings.

5.4 Materials and Methods.

Materials and Mice. All chemical reagents unless noted were obtained from Sigma Aldrich. 5'ThioMC6-capped CpG1018 was obtained from IDT Tech. DBCO-Maleimide (Catalog# A108) was obtained from Click Chemistry Tools. 2BXy and Pam2 conjugates were generous gifts from Drs. Flora Kimani and Naorem Nihesh. RAW-Blue NF-κB, HEK mTLR9 SEAP-reporter cells, and EndoFit Ovalbumin (Catalog# vac-pova) used for control assays were obtained from InvivoGen. DC2.4 cells were obtained from EMD Millipore. B3Z T-cell hybridomas were obtained as a gift from N. Shastri (UC Berkeley). All cell culture reagents were obtained from Thermo Fisher Scientific. Anti-CD16/32 (clone 2.4G2), FITC anti-CD86 (clone PO3), and APC anti-CD80 (clone 16-10A1) were obtained from BioLegend. DC2.4 cells were cultured in RPMI-1640 supplemented with 10% FBS, 10 mM HEPES, 100 μM non-essential amino acids and 50 μM β-mercaptoethanol. B3Z cells were cultured in RPMI-1640 supplemented with 10% FBS and 50 μM β-mercaptoethanol. RAW-Blue and HEK mTLR9 cells were cultured in DMEM supplemented with 10% FBS and selective antibiotics. Cells were maintained at 37°C and 5% CO_2. C57Bl/6J mice were obtained from Jackson Laboratories and acclimatized for 1 week prior to experimentation. All experiments were conducted with approval of the University of Chicago Institutional Animals Care and Use Committee and in accordance with ARRIVE guidelines, and animals were maintained in accordance with guidelines and regulations defined by the National Institutes of Health. All statistical analyses were performed using GraphPad Prism.

Cloning, Expression, and Purification of OVA-2pAMF. The codon-optimized gene for the expression of OVA containing two non-native amino acid, *p*-azidomethyl phenylalanine (pAMF) sites, K20pAMF and K370pAMF, was synthesized at ATUM (Menlo Park, CA) and subcloned with an N-terminal methionine into a proprietary vector. The final gene for OVA-[K20pAMF/K370pAMF]-TEV-his_6 contains a C-terminal TEV protease site (ENLYFQG) followed by a his_6-affinity tag for purification. *In-vitro* protein expression using cell free protein synthesis was performed as described elsewhere.[18] For titer estimates, expression of native or pAMF-containing OVA genes was monitored by incorporation of ^{14}C-leucine (GE Life Sciences, Piscataway, NJ). Autoradiography (Storm 840 PhosphoImager) was used to estimate total and soluble fractions of each protein. For large scale expression of OVA [K20/K370-pAMF]-TEV-his_6, the DASbox Mini Bioreactor System (Eppendorf AG) was used. Expression was performed at 25°C and pH 7.2 for 10 h with stirring at 650 rpm while sparging 30% oxygen in air through the reaction. After 10 h, the reaction mixtures were ultracentrifugated at 15,000 G at 4°C for 30 min and filtered using a 0.45 µm filter. The crude filtrate was loaded onto a 5 ml HisTrap column and equilibrated in 10 mM imidazole in Buffer A (50 mM Tris, 10% Glycerol, 150 mM NaCl). The protein was eluted using a step gradient of 10-500 mM imidazole in Buffer A. The eluent was pooled, concentrated, and incubated with his_6-tagged TEV protease overnight under dialysis against Buffer A. The dialyzed cleavage reaction was loaded onto a second pre-equilibrated, 5 ml HisTrap column and untagged OVA-2pAMF was collected. The crude OVA-2pAMF was concentrated and purified on a size exclusion column (Superdex 200 26/60 and Superdex 75 26/60 columns connected in tandem) pre-equilibrated with Buffer A. Finally, OVA-2pAMF containing fractions were pooled, 3x diluted in Buffer B (50 mM Tris, 10% Glycerol, pH 8.0), and loaded onto Capto Q ImpRes anion exchange column pre-equilibrated with Buffer B. The bound protein was eluted using a linear gradient of 0-1 M NaCl in Buffer B. The eluent containing purified OVA-2pAMF was pooled and frozen at -80^{o}C for further use.

Multi-Angle Light Scattering (MALS) Analysis. The SEC MALS UV-RI setup consists of an Agilent HPLC 1100 degasser, temperature-controlled auto-sampler (4°C), column compartment (25°C), and UV-VIS diode array detector (Agilent) in line with a DAWN-HELEOS multi-angle laser light scattering detector and Optilab T-rEX differential refractive interferometer (Wyatt Technology) coupled to three TOSOH columns in series: TSKgel Guard PWXL 6.0 mm ID x 4.0 cm long, 12 µm particle; TOSOH TSKgel 6000 PWXL 7.8 mm ID x 30 cm long, 13 µm particle; and a TSKgel 3000 PWXL 7.8 mm ID x 30 cm long, 7µm particle. A mobile phase consisting of 0.2 µm filtered PBS was used at a 0.5 mL/min flow rate and 50-100 µg sample was injected for analysis. Agilent Open Lab software was used to control the HPLC, and Wyatt Astra 7 software was used for data collection and molecular weight analysis.

pAMF site confirmation using DBCO-TAMRA labeling. Purified OVA-2pAMF (50 µM) was incubated with excess of Dibenzocyclooctyne-PEG4-tetramethylrhodamine (DBCO-TAMRA) dye (5 mM) for 1 h to label azide moieties. Thereafter, the reactions were analyzed using SDS-PAGE gel and fluorescence readout was recorded using a Syngene G-box gel imager.

Mass spectrometry of OVA-2pAMF. Positive mode analysis of proteins was performed on a Waters Xevo G2 XS Q-TOF mass analyzer. A 5 min gradient from 0% B to 97% B was used to elute the protein off a Waters BEH phenyl 300 Å stationary phase at 0.2 ml/min. Mobile buffers were prepared gravimetrically; phase A consisted of 0.1% formic acid in water while phase B was 0.1% formic acid in acetonitrile. Waters Masslynx MaxEnt1 software was used to deconvolute the charge-state ladder into a deconvoluted mass. MALDI-TOF MS of peptide oligomers

Endotoxin Removal. Endotoxin removal was conducted as previously reported with minor alterations.[23] Briefly, a 5% Triton X-114 solution in PBS was cooled in an ice bath, and 100 µL of this solution was added to 400 µL protein solution. The solution was shaken for 40 min at 4°C, warmed to 37°C for 10 min, and ultracentrifugated at 37°C for 10 min at 12,000 G. The top layer containing protein was collected, and the lower layer discarded. This procedure was repeated three times, and protein solution was incubated with SM2 Bio-Beads (Bio Rad) overnight

to remove residual Triton X-114. Endotoxin removal <1.5 EU/mL was validated by diluting 2 µL protein solution with 198 µL LAL Reagent Water and performing 0.015 EU/mL ToxinSensor Single Test Assay Kit (GenScript) according to the manufacturer's procedure. Protein concentration before and after endotoxin removal was determined by Pierce BCA Assay Kit (Thermo Scientific).

Synthesis of CpG-DBCO. To remove the 5' thiol cap, MC6-capped CpG1018 (CpG-S-S-$(CH_2)_6$-OH) was shaken at 1500 rpm overnight with 100 mM tris(2-carboxyethyl)phosphine hydrochloride (TCEP-HCl) in PBS adjusted to pH 8.5 with 1 M NaOH. The oligonucleotide product was precipitated with ethanol, resuspended in PBS, and characterized by ESI-MS. Positive mode analysis of oligonucleotide conjugates was performed on a Waters Xevo G2 XS Q-TOF mass analyzer. A 5 min run in 50 mM pH 7.4 ammonium acetate was used to elute each sample off a Waters BEH 200 Å 150 mm SEC stationary phase at 0.1 mL/min. The concentration of DNA was verified by UV-VIS spectroscopy, and presence of thiol was confirmed by Ellman's assay. A cyclooctyne handle was then introduced using DBCO-Maleimide to react with the free thiol. DBCO-Maleimide was dissolved at 10 mg/mL in DMSO, and 10 eq of this stock solution was added to 1 mL of CpG-SH in PBS. The reaction mixture was shaken at 25°C overnight. Unreacted DBCO-Maleimide and trace DMSO was removed by passing the crude thrice through a 3k MWCO Amicon centrifugal filter, and the product was characterized by ESI-MS ($[M]+H^+$ = 7791 expected, 7791 observed, see **Figure S5.3**). Complete reaction of the thiol was confirmed by Ellman's assay, and concentration of DNA in the product solution was verified by UV-VIS spectroscopy on a Nanodrop 2000 instrument. CpG-DBCO was stored in PBS (1 mg/mL) at -20°C for later use.

OVA-TLR agonist Synthesis. The OVA-CpG conjugate was prepared using azide-alkyne click chemistry. To a 1 mg/mL solution of OVA-2pAMF was added 2.5 eq CpG-DBCO (from the 1 mg/mL stock) at 35°C for 48 h. Unreacted CpG-DBCO was removed by passing the crude thrice through a 30k MWCO Amicon centrifugal filter. The purified product was characterized by SDS-PAGE gel electrophoresis. Samples were treated with 2.5% β-mercaptoethanol, heated to 90°C, and separated by SDS-PAGE gel. Gels were stained with One-Step Blue Protein Gel Stain

(Biotium) and imaged with an Azure c600 Imager (Azure Biosystems). Reaction extent was determined using ImageJ. Analogous procedures were used to prepare OVA-PEG_4-2BXy, OVA-G4S-2BXy, and OVA-Pam2CSK4 constructs. For multimeric constructs, the multimers were dissolved in DMSO at 10 mg/mL and diluted to 5 mg/mL with PEG300 (Selleckchem). Then, 10 eq. of the multimers were added to a 1 mg/mL solution of OVA-2pAMF. The reactions were then conducted, purified, and characterized analogously to other OVA-TLR agonist constructs.

Size-exclusion HPLC. Aggregate and sample purity analysis using size-exclusion HPLC was conducted on an Agilent 1260 Infinity system equipped with a Yarra 3 µm SEC-2000 300 x 4.6 mm LC Column. A 15 min isocratic elution in 100 mM pH 6.8 phosphate buffer was used to separate samples, and samples were monitored at 254 and 280 nm to resolve peaks.

Anion Exchange Chromatography. Separation of OVA-CpG components was conducted using a HiTrap Q FF 1 mL anion exchange column (Cytiva). Briefly, the column was flushed with 5 mL PBS (pH = 6.8). Then, the OVA-CpG mixture was loaded onto the column, and the column was washed with 5 mL PBS. A stepwise elution was subsequently conducted by eluting 5 mL of 0.3, 0.4, 0.5, and 1.0 M NaCl in PBS (pH = 6.8). The fractions were collected and concentrated using 30k MWCO Amicon centrifugal filters. The concentrated fractions were the characterized by SDS-PAGE gel electrophoresis. Fractions were treated with 2.5% β-mercaptoethanol, heated to 90°C, and separated by SDS-PAGE gel. Gels were stained with One-Step Blue Protein Gel Stain (Biotium) and imaged with an Azure c600 Imager (Azure Biosystems). Reaction extent was determined using ImageJ.

RAW-Blue Assay. RAW-Blue cells were passaged and plated in a 96 well plate at 50,000 cells/well in 180 µL DMEM containing 10% HI-FBS and selective antibiotics. The cells were stimulated with the conjugates and unlinked controls for 20 h at 37°C and 5% CO_2. NF-κB activity was measured by a QUANTI-Blue (Invivogen) assay and the absorbance was measured at 620 nm using a Multiskan FC plate reader (Thermo Scientific).

HEK mTLR9 Assay. HEK mTLR9 cells were passaged and plated in a 96 well plate at 100,000 cells/well in 180 µL DMEM containing 10% HI-FBS and selective antibiotics. The cells were stimulated with the conjugates or unlinked controls for 20 h at 37°C and 5% CO_2. TLR9 binding was measured by a QUANTI-Blue (Invivogen) assay and the absorbance was measured at 620 nm using a Multiskan FC plate reader (Thermo Scientific).

In-vitro Cross Presentation Assay. The cross-presentation efficiency of conjugates was measured as described previously with minor changes.[14] DC2.4 cells (100,000 cells/well) were plated in 96-well plates and stimulated with linked OVA-CpG conjugates or unlinked controls for 5 h at 37°C and 5% CO_2. Subsequently, the media was replaced and DC2.4 cells were co-cultured with B3Z T-cell hybridomas (100,000 cells/well) for 18 h. The cells were centrifugated at 500 G for 5 min and the supernatant was removed. The cells were washed twice with 100 µL PBS. 0.15 mM CPRG reagent was prepared in lysis buffer (0.5% (v/v) NP-40 in PBS), 100 µL of the prepared reagent was added to each well, and cells were incubated at 37°C for 12-16 h in the dark. β-gal activity was quantified by measuring absorbance at 570 nm using a Multiskan FC plate reader (Thermo Scientific).

In-vitro DC Activation Assay. DC2.4s (2 million cells/well) were incubated in untreated 24-well plates and stimulated with OVA-CpG conjugates or unlinked controls in 0.5 mL culture media for 20 h at 37°C and 5% CO_2. The cells were mechanically released from the plate and centrifuged at 2500 RPM at 4°C for 10 min. The cell pellet was resuspended in 100 µL cold FACS buffer (10% FBS + 0.1% NaN_3 in PBS) and incubated with anti-CD16/32 (Fc receptor blocking antibody) (1.0 µg/million cells) on ice for 10 min. The cell suspension was pelleted and the supernatant was removed. The cell pellet was then resuspended in cold FACS buffer and incubated with FITC anti-CD86 (1.0µg/million cells) and APC anti-CD80 (0.5 µg/million cells) on ice in darkness for 30 min. Cells were washed twice with 300 µL cold FACS buffer, and then resuspended in FACS buffer (150 µL) and kept on ice until analysis. DC activation was assayed using a Novocyte ACEA (Agilent) flow cytometer. Data were processed using NovoExpress.

In-vivo Characterization. Mice were injected intramuscularly in each flank with 50 μL OVA-CpG conjugates, OVA + CpG, OVA, or PBS (n=4/group). Body weight was measured prior to injection and daily for one week. Mice were bled via facial vein 1 and 24 h after injection, and serum cytokine production was assayed using LEGENDPlex Mouse Inflammation Panel 13plex (BD Biosciences). After 14 d, the same formulation was administered as a boost. After 21 d, serum was collected and antibody production was assayed using mouse Anti-Ovalbumin Ig's total (A+G+M) (Alpha Diagnostic International), Anti-Ovalbumin IgG1 (Alpha Diagnostic International), and Anti-Ovalbumin IgG2c (Chondrex) ELISA kits. After 28 d, mice were sacrificed, and spleens were collected for tetramer staining. Spleens were homogenized, and cells were filtered through a 70 μm strainer. Red blood cells were lysed by incubating with ACK Lysing Buffer for 5 min at 25°C. Splenocytes (2 million cells) were plated in a 96-well plate and incubated with anti-CD16/32 (Fc receptor blocking antibody) (1.0 μg/million cells) for 15 min at 4°C. Splenocytes were washed with FACS buffer (PBS with 2% FBS), resuspended, and stained with APC MHC Class I tetramers (Tetramer Shop) at 37°C in the dark. After 15 mins, FITC anti-CD8 (BD Biosciences) was added and incubated for 30 min longer. Splenocytes were washed and resuspended in FACS buffer. Antigen-specific T-cell production was assayed using a Novocyte ACEA (Agilent) flow cytometer, and data were processed using FlowJo.

Solid Phase Peptide Synthesis. Fmoc-solid phase peptide syntheses of multimer components were performed using a Liberty Blue peptide synthesizer (CEM) using Rink amide resin (100−200 mesh) as the solid support and DIC/Oxyma activation at 90 °C. Azidohexanoic acid (Click Chemistry Tools) was used in place of the N-terminus where relevant. Peptides were deprotected using a mixture of 85% TFA mixed with 5% water, 5% anisole, and 5% thioanisole. Following deprotection, the crude peptide was precipitated in cold diethyl ether. The crude peptide was then purified using a Phenomenex Luna C18 column (5 μm, 100 Å, 250 × 21.2 mm) on a Gilson preparative HPLC using a gradient of acetonitrile (+0.1% TFA) in water (+0.1% TFA). The

purified peptides were lyophilized and characterized using ESI-MS. ESI spectra confirming the purity of peptide components are provided in **Figure S5.15**.

Synthesis of $(GluGly)_5$-DBCO and $(Dopa)_5$-DBCO. $(GluGly)_5$-NH_2 and $(Dopa)_5$-NH_2 were prepared *via* Solid Phase Peptide Synthesis and purified as described. Each of these peptides were dissolved at 10 mg/mL in DMF. 10 eq. of DIPEA and 1.2 eq. of DBCO-NHS Ester (Click Chemistry Tools) were added under rapid stirring, and the reaction was allowed to proceed for 1 h. Complete reaction was confirmed by ESI-MS, and the DBCO-modified peptides were purified using a Phenomenex Luna C18 column (5 µm, 100 Å, 250 × 21.2 mm) on a Gilson preparative HPLC using a gradient of acetonitrile (+0.1% TFA) in water (+0.1% TFA). The purified peptides were lyophilized and characterized using ESI-MS. For $(GluGly)_5$-DBCO, $[M]+H^+$ = 1570.6 expected, 1570.6 observed. For $(Dopa)_5$-DBCO, $[M]+H^+$ = 1535.6 expected, 1535.6 observed. Peptide was confirmed to be >90% pure via HPLC (**Figure S5.16**).

Synthesis of $(2BXy)_5$-DBCO. $(GluGly)_5$-DBCO was dissolved at 10 mg/mL in DMF. 10 eq. of DIPEA and 6 eq. of 2BXy-C6-NH_2 were added, and then, under rapid stirring, 5 eq. of HATU was added in a single portion. The vessel as quickly purged with argon, sealed, and reacted for 4 h. Complete reaction was confirmed by ESI-MS, and the 2BXy-containing peptides were purified using a Phenomenex Luna C8 column (5 µm, 100 Å, 250 × 21.2 mm) on a Gilson preparative HPLC using a gradient of acetonitrile (+0.1% TFA) in water (+0.1% TFA). The purified peptides were lyophilized and characterized using ESI-MS: $[M]+H^+$ = 3843.0 expected, 3843.2 observed.

Synthesis of $(2BXy)_5$-$(Dopa)_5$-DBCO. $(2BXy)_5$-DBCO (1 eq) and $(Dopa)_5$-K(N_3) (1.2 eq) were dissolved in DMF and stirred for 48 h at 40 °C. Complete reaction was confirmed by ESI-MS, and the 2BXy-containing peptides were purified using a Phenomenex Luna C8 column (5 µm, 100 Å, 250 × 21.2 mm) on a Gilson preparative HPLC using a gradient of acetonitrile (+0.1% TFA) in water (+0.1% TFA). The purified $(2BXy)_5$-$(Dopa)_5$-NH_2 was dried under reduced pressure and used immediately. Crude $(2BXy)_5$-$(Dopa)_5$-NH_2 was dissolved in DMF and placed over dried, 4 Å molecular sieves to remove any residual water. After 10 min, 10 eq TEA and 1.2 eq DBCO-

NHS Ester (Click Chemistry Tools) were added under rapid stirring, and the reaction was allowed to proceed for 4 h. Complete reaction was confirmed by ESI-MS, and the adjuvant multimer was purified using a Phenomenex Luna C8 column (5 μm, 100 Å, 250 × 21.2 mm) on a Gilson preparative HPLC using a gradient of acetonitrile (+0.1% TFA) in water (+0.1% TFA). The purified peptides were lyophilized and characterized using MALDI-TOF MS: $[M]+H^+$ = 5533.76 expected, 5533.67 observed (see **Figure 5.6B**). Peptide was also characterized via ESI-MS and confirmed to be >90% pure via HPLC (**Figure S5.17**).

5.5 Supplementary Information.

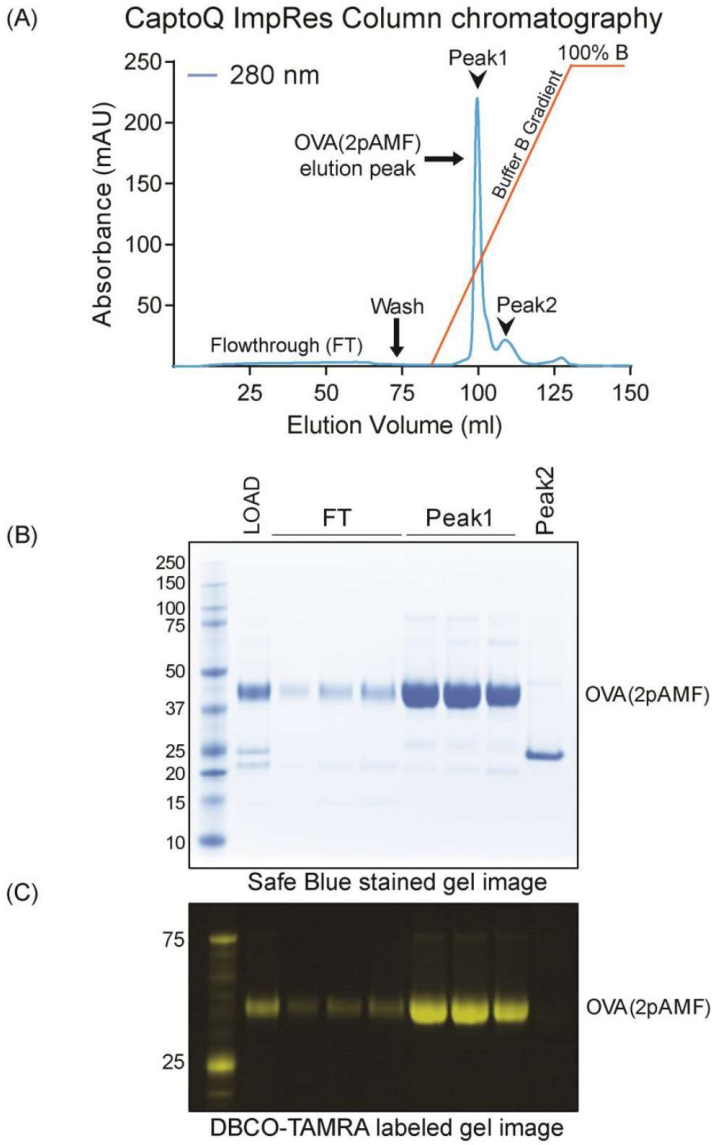

Figure S5.1: Purification of OVA-2pAMF. (A) Anion exchange chromatogram showing the final step of purification followed by (B) safeblue stained and (C) DBCO-TAMRA labeled SDS-PAGE analysis of the FT and elution fractions.

A

B

C

Pre-Endotoxin	2.08 mg
Post-Endotoxin	1.63 mg
Recovery	78% recovered

Figure S5.2: LAL Assay results A) before and B) after endotoxin was removed from OVA-2pAMF using three Triton X-114 washes. Absence of clotting indicates endotoxin decontamination < 1.5 EU/mL. C) BCA Assays conducted before and after endotoxin decontamination reveal 78% recovery after three washes.

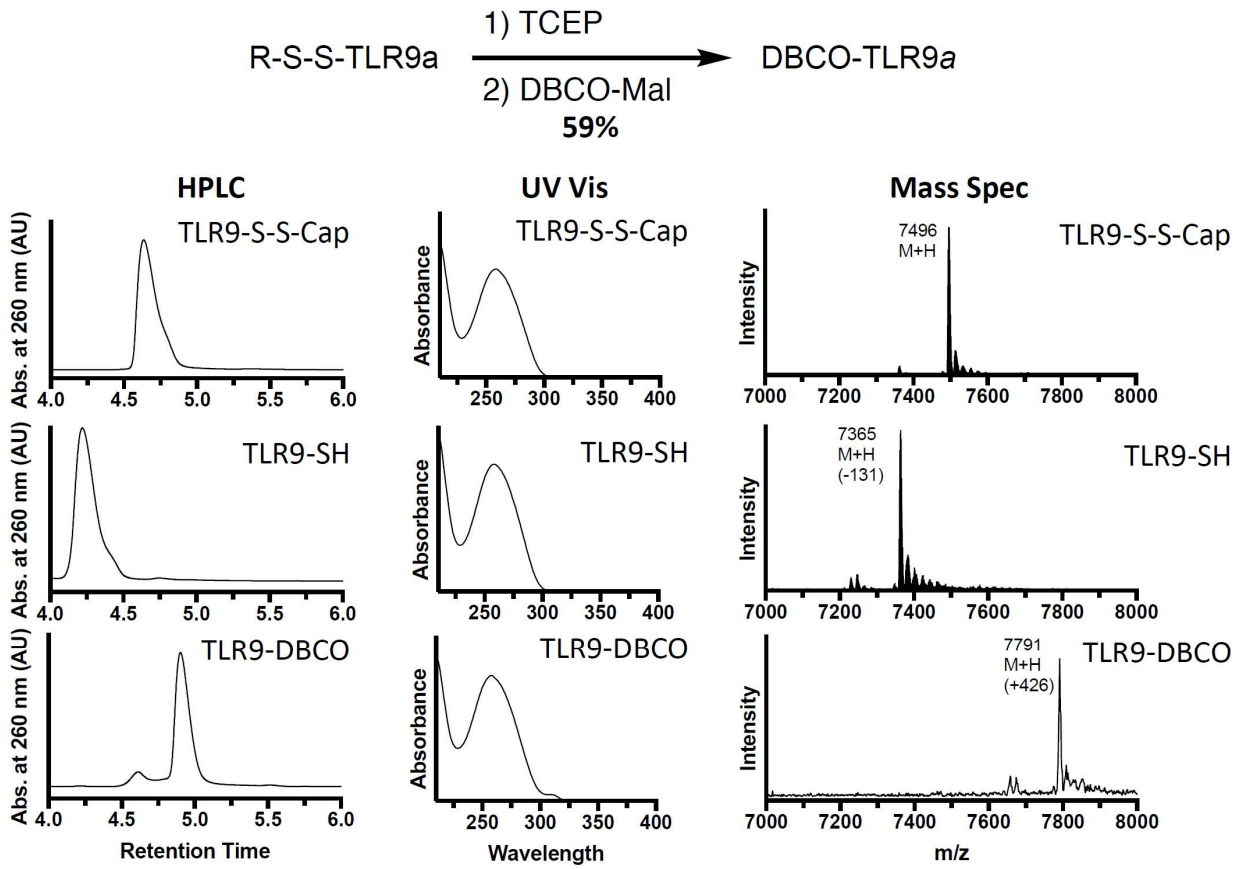

Figure S5.3: Functionalization and characterization of CpG. Capped CpG samples (R = -$(CH_2)_6$-OH) were treated first with TCEP to release the free thiol. The free thiol was subsequently reacted with DBCO-Maleimide to obtain an alkyne-modified derivative. Samples were characterized by HPLC, UV-VIS, and Q-TOF ESI-MS at each characterization step as shown to validate that the modifications were successful.

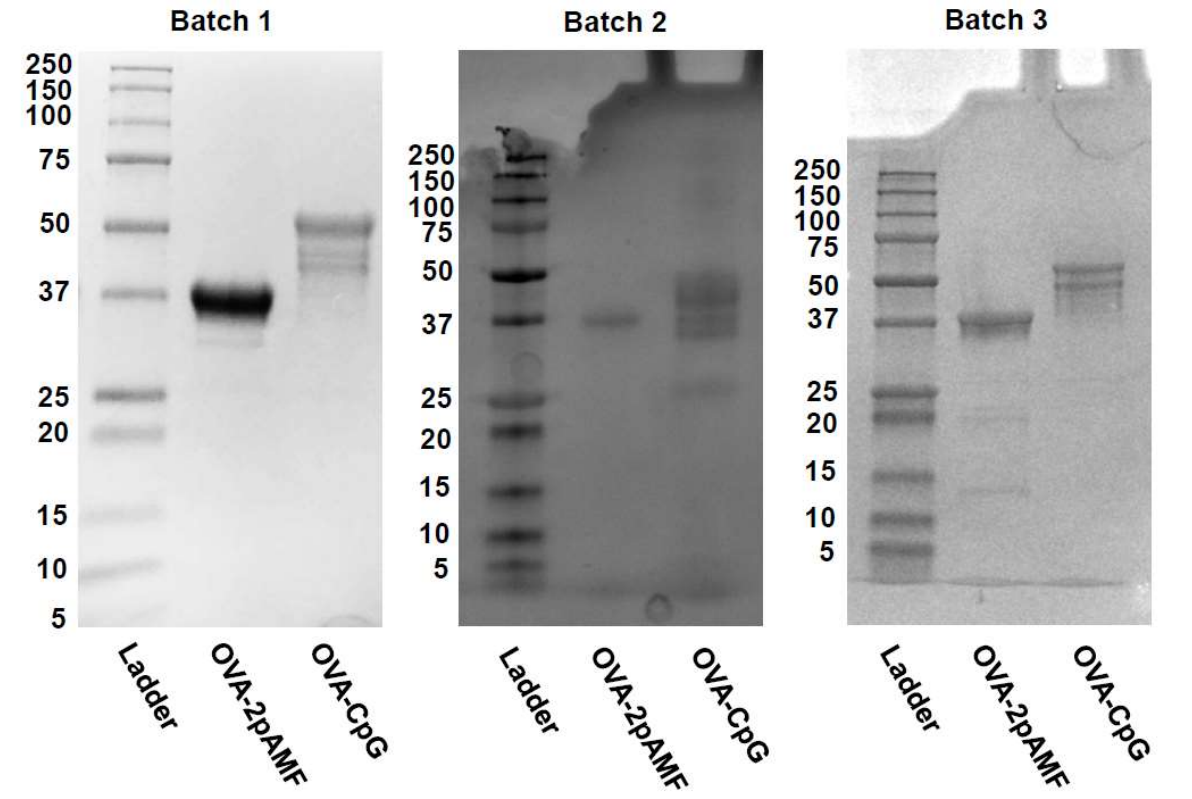

2 CpG/OVA	52%
1 CpG/OVA	39%
0 CpG/OVA	10%
Avg CpG/OVA	1.5

2 CpG/OVA	42%
1 CpG/OVA	33%
0 CpG/OVA	25%
Avg CpG/OVA	1.2

2 CpG/OVA	40%
1 CpG/OVA	49%
0 CpG/OVA	11%
Avg CpG/OVA	1.3

Figure S5.4: Full gels and densitometry of OVA-CpG conjugates. Gels were stained using One-Step Blue Protein Gel Stain, and densitometry was conducted using ImageJ to obtain the CpG content per OVA.

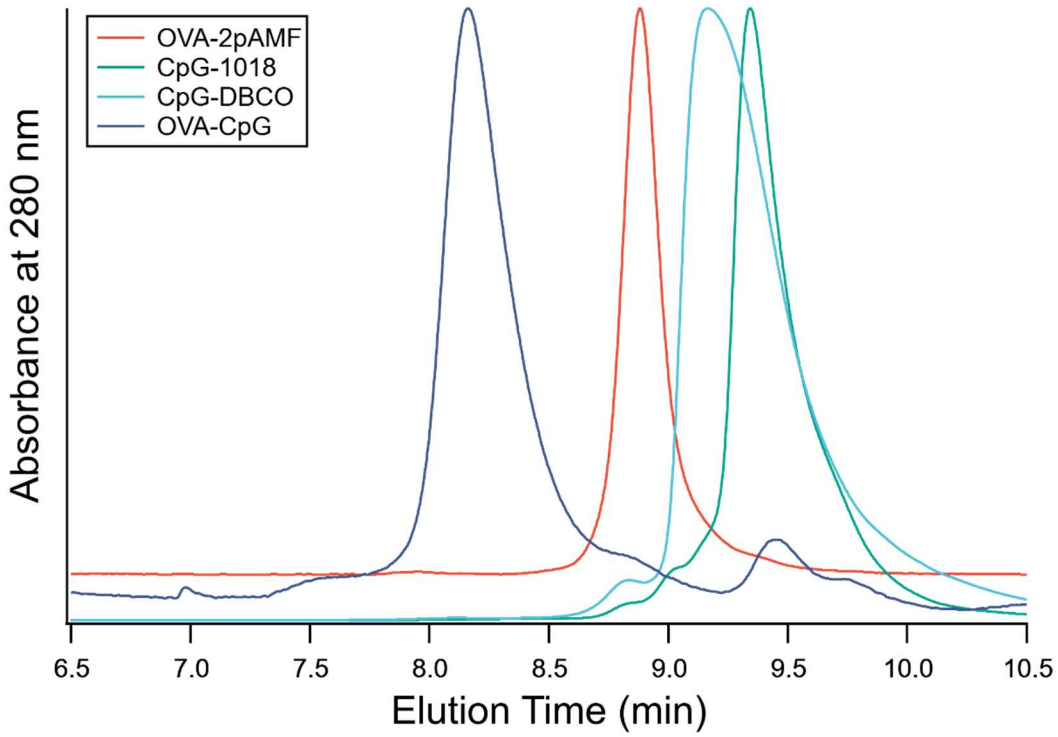

Figure S5.5: Size exclusion HPLC of OVA-CpG and component species reveals sufficient removal of CpG-DBCO and absence of high molecular weight aggregates in the OVA-CpG sample. Samples were eluted using 100 mM pH 6.8 phosphate buffer on a Yarra SEC-2000 300Å column and monitored at 280 nm. It should be noted that OVA-$(CpG)_2$ and OVA-$(CpG)_1$ elute as a single fraction at 8.1 min, which was verified by collecting the fractions and submitting them to SDS-PAGE gel chromatography (not shown).

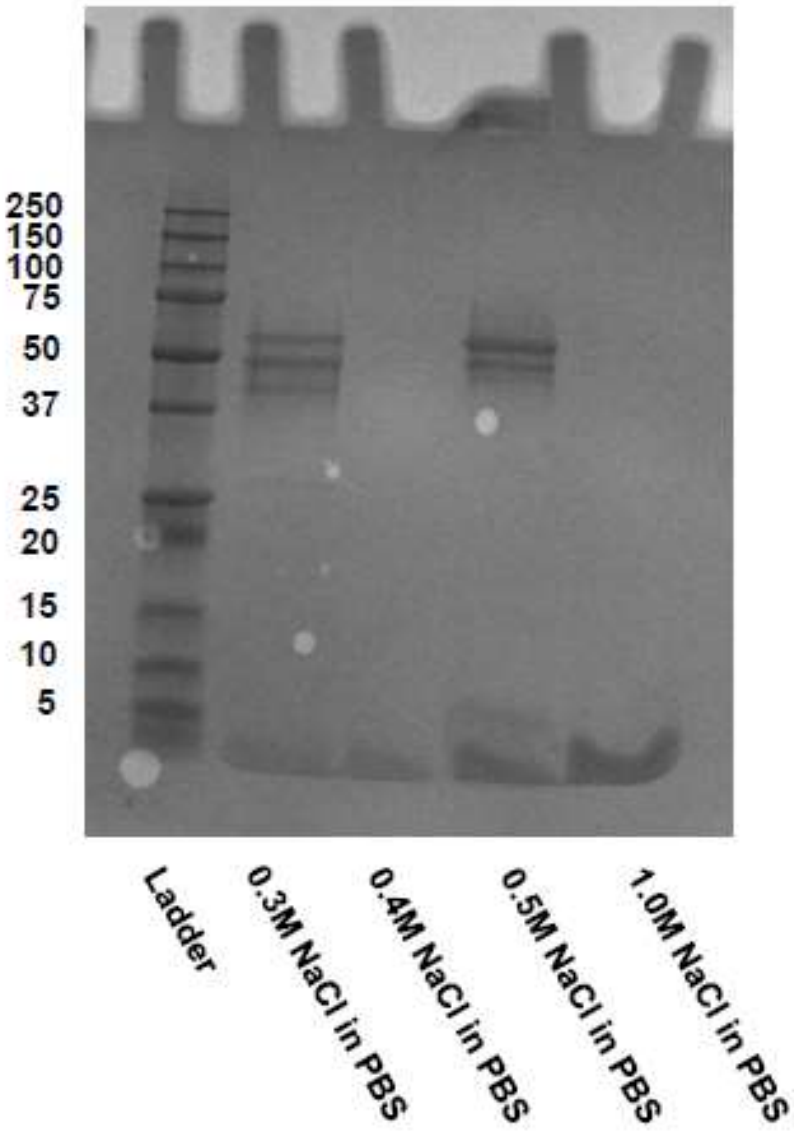

Figure S 5.6: Anion exchange chromatography of OVA-CpG was attempted to isolate OVA-CpG fractions with different loading of CpG, and SDS-PAGE gel chromatography was used to indicate the purification of fractions containing 0, 1, or 2 CpG/OVA. A band containing 1+2 CpG/OVA eluted at a concentration of 0.5 M NaCl in PBS.

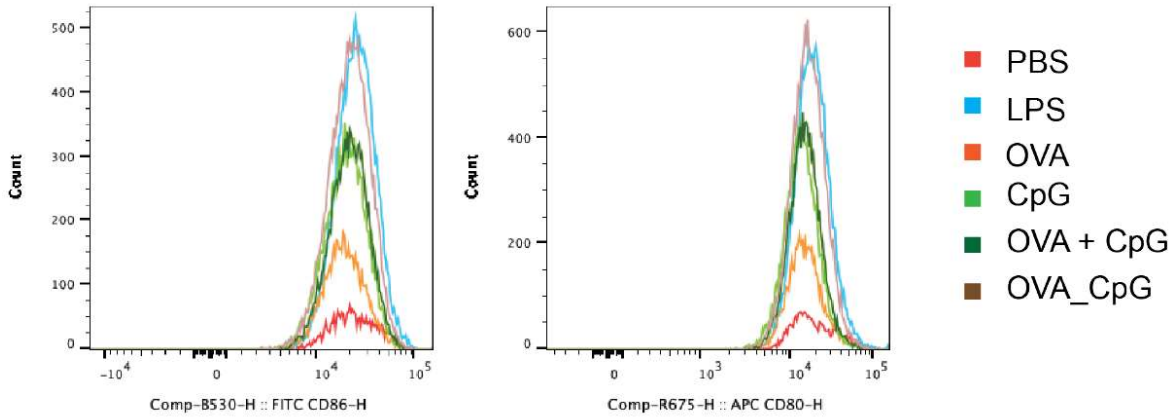

Figure S5.7: Fluorescent intensity plots of CD86 (left) and CD80 (right) expression after DC2.4 cells were incubated for 20 h with 50 µg/mL OVA-CpG or unlinked controls, stained, and analyzed using flow cytometry.

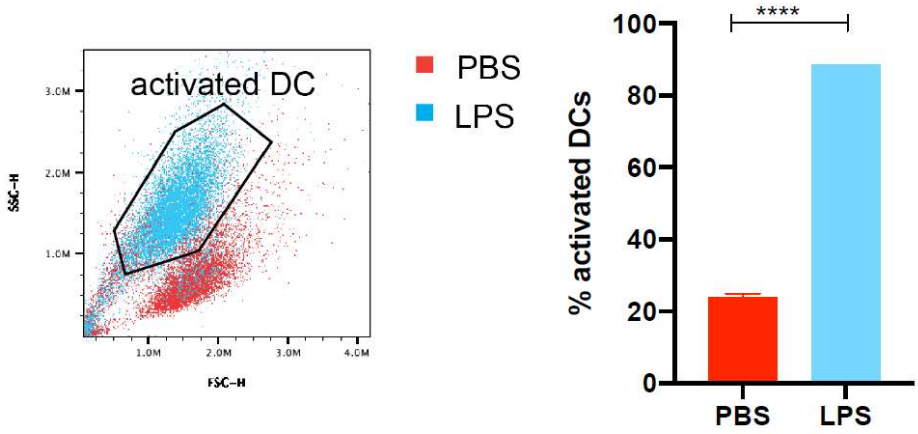

Figure S5.8: Plot of FSC-H against SSC-H in activated (LPS-treated) and control (PBS-treated) treated dendritic cells. Enhanced granularity was observed via flow cytometry in DC2.4 cels after treatment with 100 ng/mL LPS but not PBS. The granular population was used in **Figure 5.3F** to identify activated DCs.

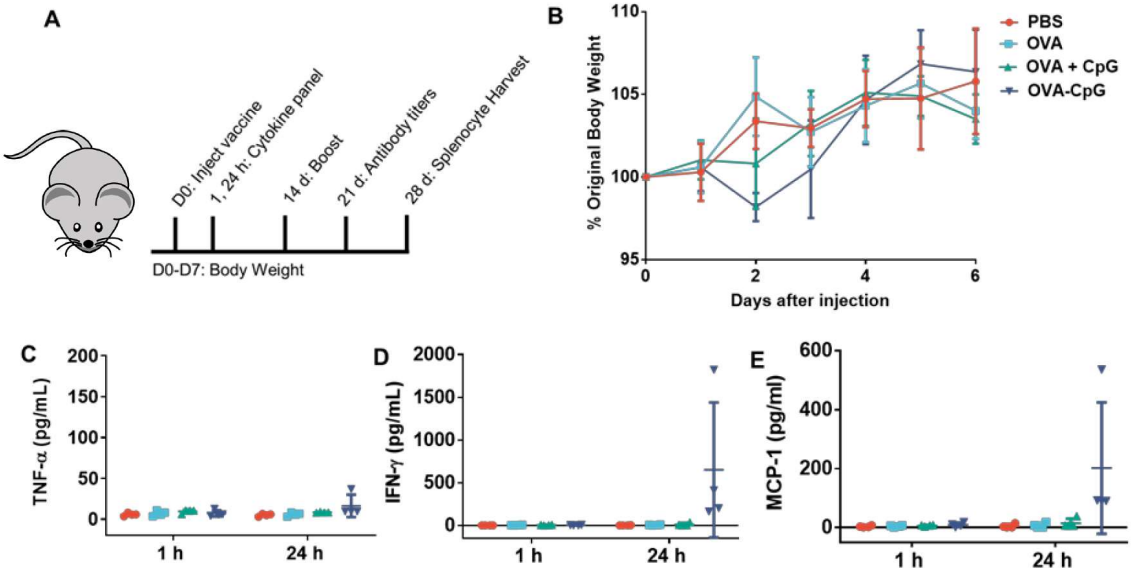

Figure S5.9: Acute inflammatory response to injection of OVA-CpG. A) Mice were vaccinated according to the schedule shown with 1 nmol of OVA-CpG or unlinked controls. B) No significant changes in body weight were observed after injection. C) No significant change in TNF-α secretion was observed 1 or 24 h after injection. After 24 h, significant D) IFN-γ and E) MCP-1 production was observed in mice treated with linked OVA-CpG but not with other control treatments.

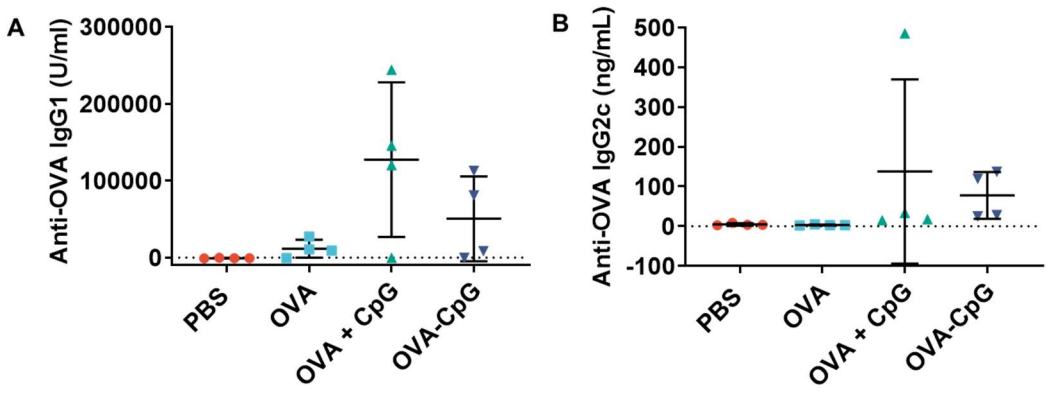

Figure S5.10: Isotype specific antibody titers toward OVA-CpG construct. Mice were vaccinated according to the schedule in **Figure S5.9A**, and serum was collected after 21 d to analyze antibodies *via* ELISA. No differences in A) IgG1 or B) IgG2c specific anti-OVA titers were observed 21 d after injection.

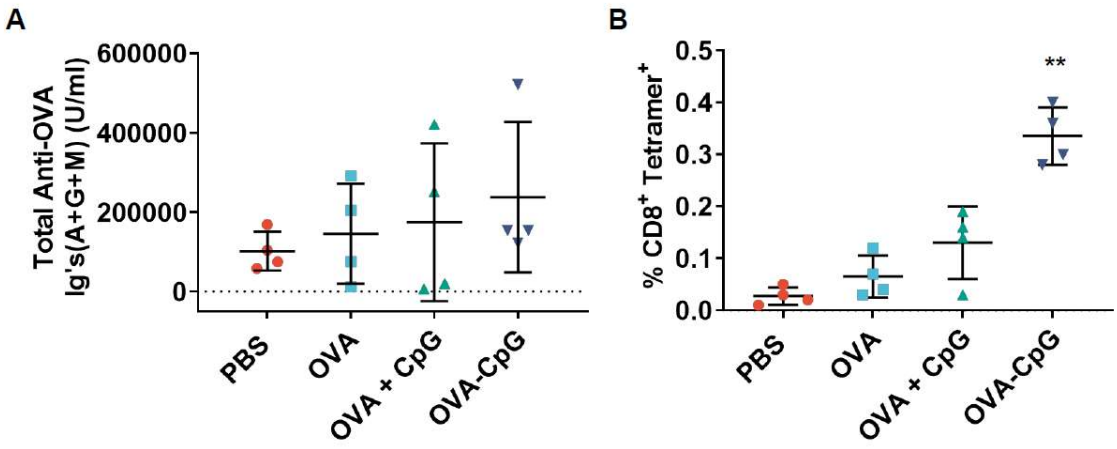

Figure S5.11: Adaptive immune responses toward OVA-CpG construct. Mice were vaccinated according to the schedule in **Figure S5.9A**, and serum was collected after 21 d for ELISAs. Mice were sacrificed after 28 d and T cells were harvested for tetramer staining. A) No differences in total anti-OVA Ig(G+A+M) titers were observed 21 d after injection. B) OVA-CpG induced significant increase (**, $p < 0.01$) relative to OVA + CpG in splenic antigen-specific T-cell production 21 d after injection. Statistics were conducted using student's t-test to evaluate OVA-CpG relative to OVA + CpG.

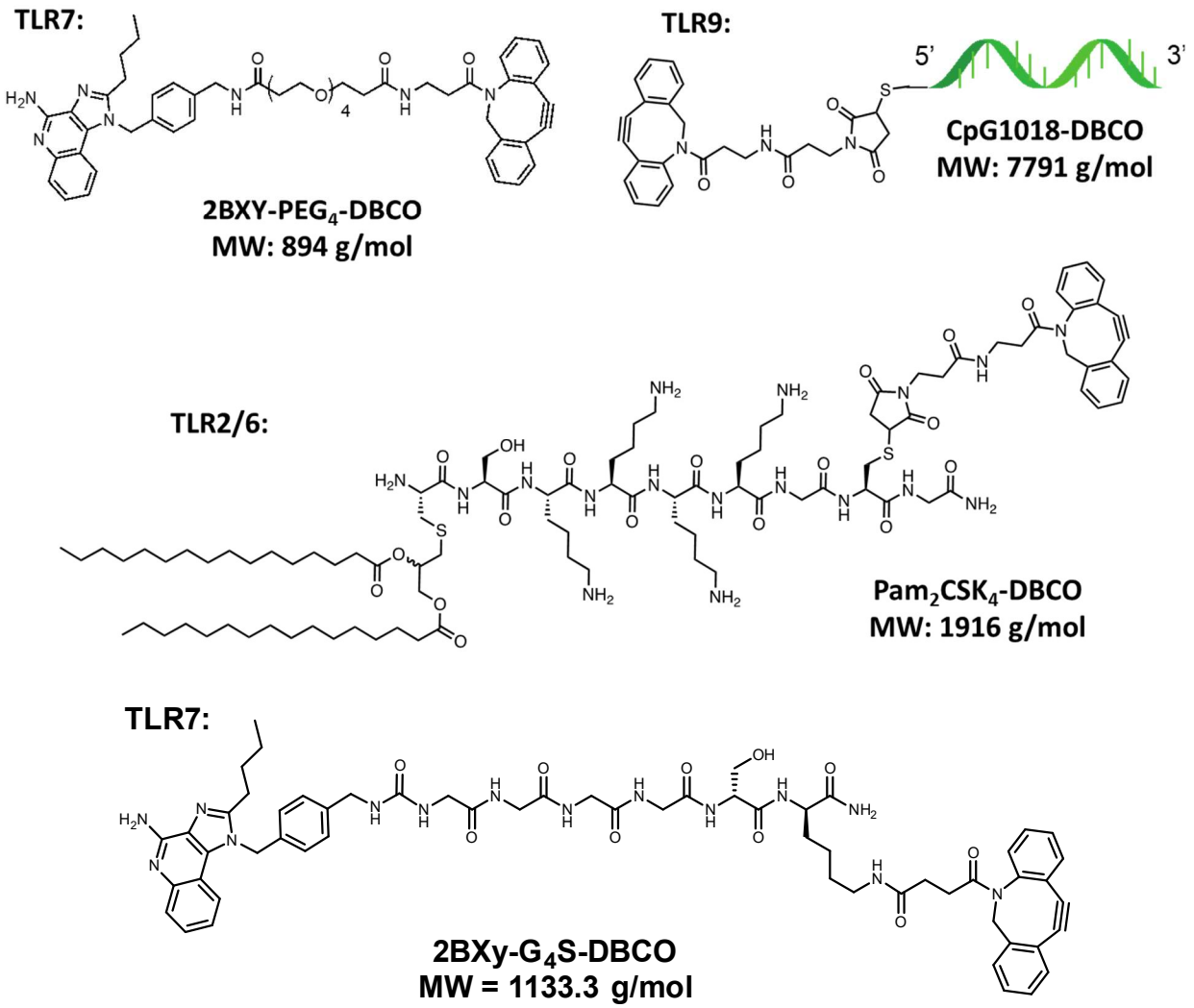

Figure S5.12: Structure of TLR agonists used for model conjugation reactions to OVA-2pAMF.

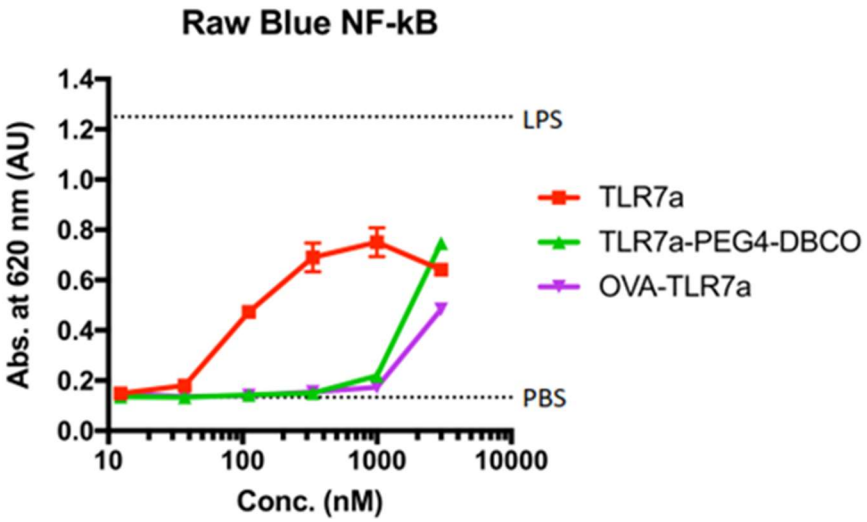

Figure S5.13: Reduction in activity of OVA-PEG$_4$-2BXy construct relative to unlinked 2BXy. Agonists were incubated with RAW Blue cells at the indicated concentrations (molar equivalents of 2BXy) for 20 h, and activity was quantified using QUANTI-Blue assay.

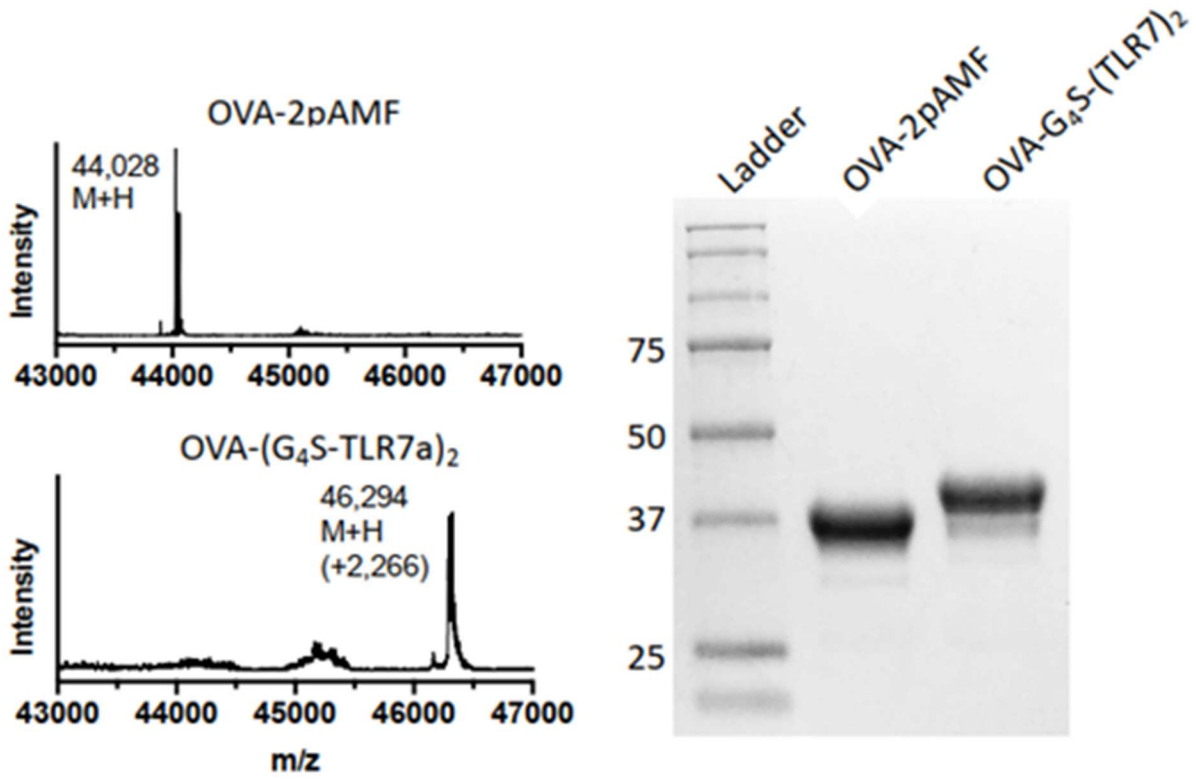

Figure S5.14: Synthesis and characterization of OVA-G_4S-2BXy. Synthesis was conducted according to the scheme described in Figure 5.2, and the product was characterized by mass spectrometry and SDS-PAGE gel chromatography as shown.

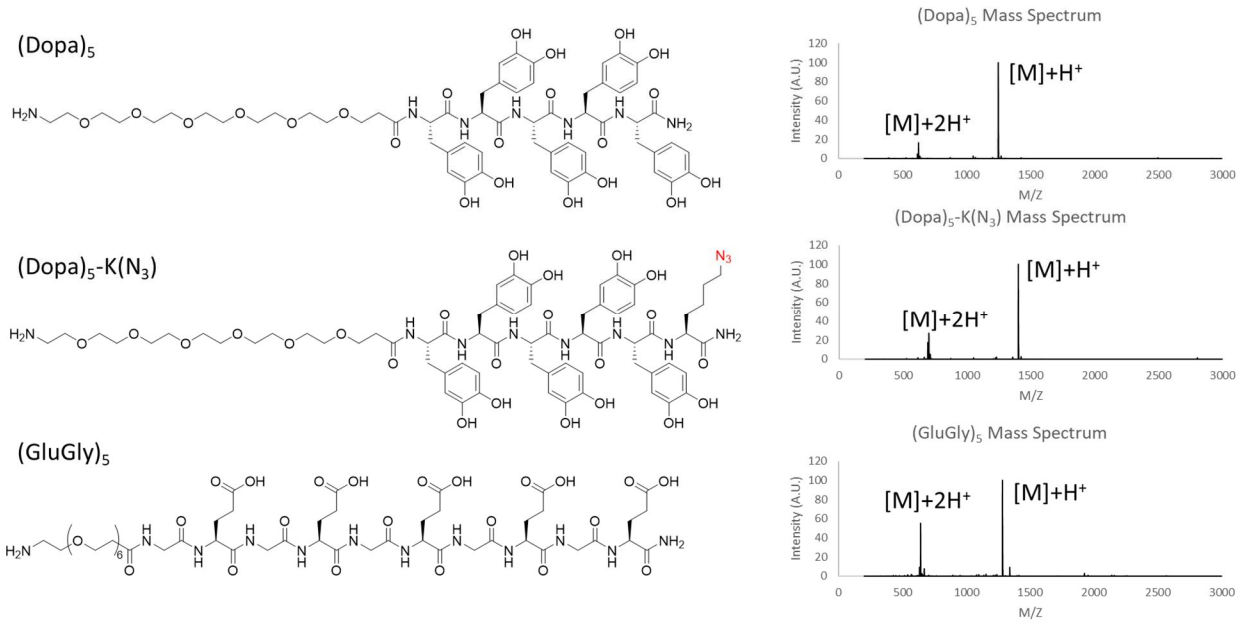

Figure S5.15: Structures and ESI-MS characterization of peptides prepared by solid-phase peptide synthesis as starting materials for $(2BXy)_5$-$(Dopa)_5$-DBCO and $(Dopa)_5$-DBCO.

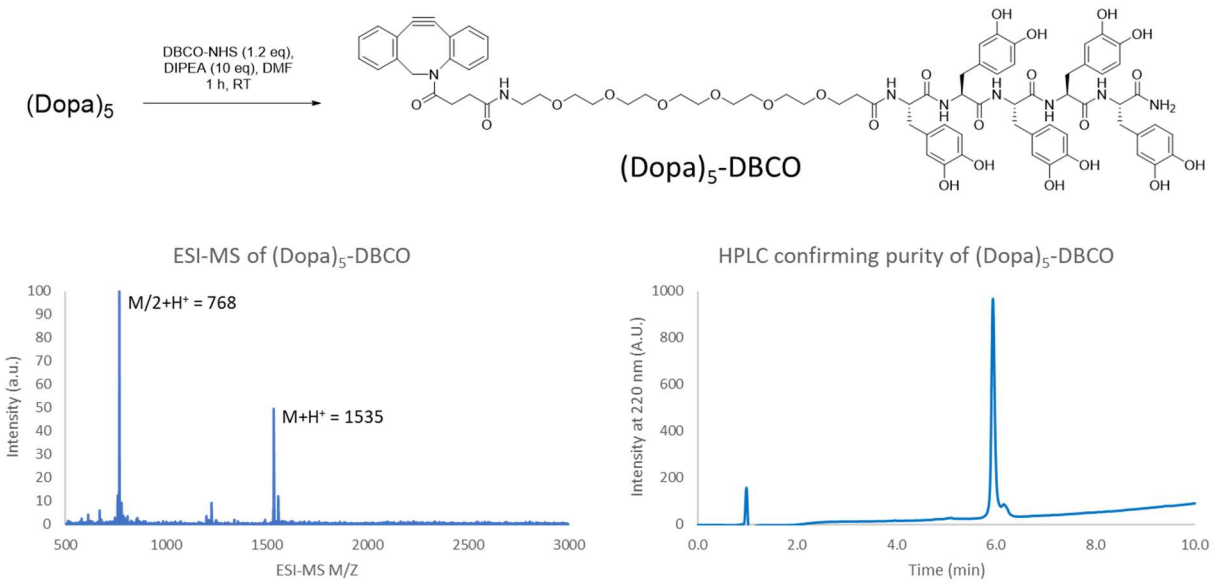

Figure S5.16: Synthetic scheme and characterization by HPLC and ESI-MS of $(Dopa)_5$-DBCO. HPLC purity analysis was conducted using a 50 x 4.6 mm C18 column using a 10 min 10→100% gradient of acetonitrile in water (+0.1% TFA).

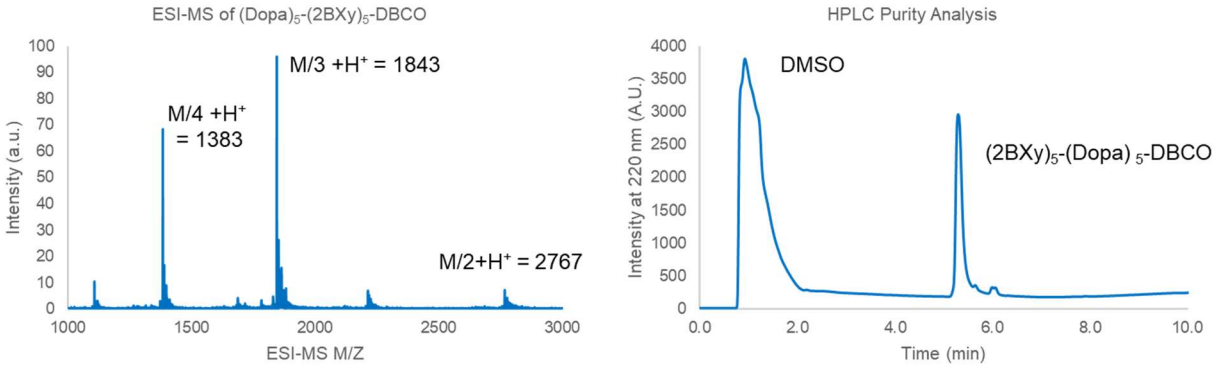

Figure S5.17: Characterization by HPLC and ESI-MS of $(2BXy)_5$-$(Dopa)_5$-DBCO. HPLC purity analysis was conducted using a 50 x 4.6 mm C18 column using a 8 min 10→100% gradient of acetonitrile in water (+0.1% TFA).

5.6 References.

1. Weiss, A. M.; Ajit, J.; Albin, T. J.; Kapoor, N.; Maroju, S.; Berges, A.; Pill, L.; Fairman, J.; Esser-Kahn, A. P., Site-specific antigen-adjuvant conjugation using cell-free protein synthesis enhances antigen presentation and CD8(+) T-cell response. *Sci Rep* **2021,** *11* (1), 6267.

2. Lauring, A. S.; Jones, J. O.; Andino, R., Rationalizing the development of live attenuated virus vaccines. *Nat Biotechnol* **2010,** *28* (6), 573-579.

3. Moyle, P. M.; Toth, I., Modern subunit vaccines: development, components, and research opportunities. *ChemMedChem* **2013,** *8* (3), 360-376.

4. Fearon, D. T.; Locksley, R. M., The instructive role of innate immunity in the acquired immune response. *Science* **1996,** *272* (5258), 50-53.

5. Schulz, O.; Diebold, S. S.; Chen, M.; Näslund, T. I.; Nolte, M. A.; Alexopoulou, L.; Y., A.; R.A., F.; P., L.; Reis e Sousa, C., Toll-like receptor 3 promotes cross-priming to virus-infected cells. *Nature* **2005,** *433* (7028), 887-892.

6. Tom, J. K.; Albin, T. J.; Manna, S.; Moser, B. A.; Steinhardt, R. C.; Esser-Kahn, A. P., Applications of Immunomodulatory Immune Synergies to Adjuvant Discovery and Vaccine Development. *Trends Biotechnol* **2019,** *37* (4), 373-388.

7. Jackson, S.; Lentino, J.; Kopp, J.; Murray, L.; Ellison, W.; Rhee, M.; Shockey, G.; Akella, L.; Erby, K.; Heyward, W. L.; Janssen, R. S.; Group, H. B. V. S., Immunogenicity of a two-dose investigational hepatitis B vaccine, HBsAg-1018, using a toll-like receptor 9 agonist adjuvant compared with a licensed hepatitis B vaccine in adults. *Vaccine* **2018,** *36* (5), 668-674.

8. Heineman, T. C.; Cunningham, A.; Levin, M., Understanding the immunology of Shingrix, a recombinant glycoprotein E adjuvanted herpes zoster vaccine. *Curr Opin Immunol* **2019,** *59*, 42-48.

9. Di Pasquale, A.; Bonanni, P.; Garcon, N.; Stanberry, L. R.; El-Hodhod, M.; Tavares Da Silva, F., Vaccine safety evaluation: Practical aspects in assessing benefits and risks. *Vaccine* **2016,** *34* (52), 6672-6680.

10. Cho, H. J.; Takabayashi, K.; Cheng, P. M.; Nguyen, M. D.; Corr, M.; Tuck, S.; Raz, E., Immunostimulatory DNA-based vaccines induce cytotoxic lymphocyte activity by a T-helper cell-independent mechanism. *Nat Biotechnol* **2000,** *18* (5), 509-514.

11. Nierkens, S.; den Brok, M. H.; Sutmuller, R. P.; Grauer, O. M.; Bennink, E.; Morgan, M. E.; Figdor, C. G.; Ruers, T. J.; Adema, G. J., In vivo colocalization of antigen and CpG [corrected] within dendritic cells is associated with the efficacy of cancer immunotherapy. *Cancer Res* **2008,** *68* (13), 5390-5396.

12. Wille-Reece, U.; Flynn, B. J.; Lore, K.; Koup, R. A.; Kedl, R. M.; Mattapallil, J. J.; Weiss, W. R.; Roederer, M.; Seder, R. A., HIV Gag protein conjugated to a Toll-like receptor 7/8 agonist improves the magnitude and quality of Th1 and CD8+ T cell responses in nonhuman primates. *Proc Natl Acad Sci U S A* **2005,** *102* (42), 15190-15194.

13. Irie, H.; Morita, K.; Koizumi, M.; Mochizuki, S., Immune Responses and Antitumor Effect through Delivering to Antigen Presenting Cells by Optimized Conjugates Consisting of CpG-DNA and Antigenic Peptide. *Bioconjug Chem* **2020**. *31* (11), 2585-2595.

14. Clauson, R. M.; Berg, B.; Chertok, B., The Content of CpG-DNA in Antigen-CpG Conjugate Vaccines Determines Their Cross-Presentation Activity. *Bioconjug Chem* **2019,** *30* (3), 561-567.

15. Maurer, T.; Heit, A.; Hochrein, H.; Ampenberger, F.; O'Keeffe, M.; Bauer, S.; Lipford, G. B.; Vabulas, R. M.; Wagner, H., CpG-DNA aided cross-presentation of soluble antigens by dendritic cells. *Eur J Immunol* **2002,** *32* (8), 2356-2364.

16. Carlson, E. D.; Gan, R.; Hodgman, C. E.; Jewett, M. C., Cell-free protein synthesis: applications come of age. *Biotechnol Adv* **2012,** *30* (5), 1185-1194.

17. Zawada, J. F.; Yin, G.; Steiner, A. R.; Yang, J.; Naresh, A.; Roy, S. M.; Gold, D. S.; Heinsohn, H. G.; Murray, C. J., Microscale to manufacturing scale-up of cell-free cytokine production--a new approach for shortening protein production development timelines. *Biotechnol Bioeng* **2011,** *108* (7), 1570-1578.

18. Kapoor, N.; Vanjak, I.; Rozzelle, J.; Berges, A.; Chan, W.; Yin, G.; Tran, C.; Sato, A. K.; Steiner, A. R.; Pham, T. P.; Birkett, A. J.; Long, C. A.; Fairman, J.; Miura, K., Malaria Derived Glycosylphosphatidylinositol Anchor Enhances Anti-Pfs25 Functional Antibodies That Block Malaria Transmission. *Biochemistry* **2018,** *57* (5), 516-519.

19. Wang, L.; Brock, A.; Herberich, B.; Schultz, P. G., Expanding the genetic code of Escherichia coli. *Science* **2001,** *292* (5516), 498-500.

20. Stafford, R.; Thanos, C.D.; Yang, W. Modified Amino Acids. US Patent US0260137A1. May 19, 2017.

21. Heit, A.; Schmitz, F.; O'Keeffe, M.; Staib, C.; Busch, D. H.; Wagner, H.; Huster, K. M., Protective CD8 T cell immunity triggered by CpG-protein conjugates competes with the efficacy of live vaccines. *J Immunol* **2005,** *174* (7), 4373-4380.

22. Fischer, N. O.; Rasley, A.; Corzett, M.; Hwang, M. H.; Hoeprich, P. D.; Blanchette, C. D., Colocalized delivery of adjuvant and antigen using nanolipoprotein particles enhances the immune response to recombinant antigens. *J Am Chem Soc* **2013,** *135* (6), 2044-2047.

23. Teodorowicz, M.; Perdijk, O.; Verhoek, I.; Govers, C.; Savelkoul, H. F.; Tang, Y.; Wichers, H.; Broersen, K., Optimized Triton X-114 assisted lipopolysaccharide (LPS) removal method reveals the immunomodulatory effect of food proteins. *PLoS One* **2017,** *12* (3), e0173778.

24. Hargadon, K. M.; Forrest, O. A.; Reddy, P. R., Suppression of the maturation and activation of the dendritic cell line DC2.4 by melanoma-derived factors. *Cell Immunol* **2012,** *272* (2), 275-282.

25. Albin, T. J.; Tom, J. K.; Manna, S.; Gilkes, A. P.; Stetkevich, S. A.; Katz, B. B.; Supnet, M.; Felgner, J.; Jain, A.; Nakajima, R.; Jasinskas, A.; Zlotnik, A.; Pearlman, E.; Davies, D. H.; Felgner, P. L.; Burkhardt, A. M.; Esser-Kahn, A. P., Linked Toll-Like Receptor Triagonists Stimulate Distinct, Combination-Dependent Innate Immune Responses. *ACS Cent Sci* **2019,** *5* (7), 1137-1145.

26. Shinchi, H.; Komaki, F.; Yuki, M.; Ohara, H.; Hayakawa, N.; Wakao, M.; Cottam, H. B.; Hayashi, T.; Carson, D. A.; Moroishi, T.; Suda, Y., Glyco-Nanoadjuvants: Impact of Linker Length for Conjugating a Synthetic Small-Molecule TLR7 Ligand to Glyco-Nanoparticles on Immunostimulatory Effects. *ACS Chem Biol* **2022,** *17* (4), 957-968.

27. Lynn, G. M.; Laga, R.; Darrah, P. A.; Ishizuka, A. S.; Balaci, A. J.; Dulcey, A. E.; Pechar, M.; Pola, R.; Gerner, M. Y.; Yamamoto, A.; Buechler, C. R.; Quinn, K. M.; Smelkinson, M. G.; Vanek, O.; Cawood, R.; Hills, T.; Vasalatiy, O.; Kastenmuller, K.; Francica, J. R.; Stutts, L.; Tom, J. K.; Ryu, K. A.; Esser-Kahn, A. P.; Etrych, T.; Fisher, K. D.; Seymour, L. W.; Seder, R.

A., In vivo characterization of the physicochemical properties of polymer-linked TLR agonists that enhance vaccine immunogenicity. *Nat Biotechnol* **2015,** *33* (11), 1201-1210.

28. Nihesh, F. N. Rational Design and Synthesis of Vaccine Adjuvants Using a Combinatorial Approach. Thesis Dissertation. University of Chicago, Chicago, IL, 2022. https://knowledge.uchicago.edu/record/3990

29. Halliday, A.; Turner, J. D.; Guimaraes, A.; Bates, P. A.; Taylor, M. J., The TLR2/6 ligand PAM2CSK4 is a Th2 polarizing adjuvant in Leishmania major and Brugia malayi murine vaccine models. *Parasit Vectors* **2016,** *9*, 96.

CHAPTER 6 In Vitro and in Vivo Analyses of the Effects of Source, Length, and Charge on the Cytotoxicity of Cellulose Nanocrystals.

This chapter has been published, in part, in ACS Biomaterials Science and Engineering.[1]

6.1 Introduction.

Cellulose nanocrystals (CNCs) have emerged as a green nanomaterial with properties that are desirable for a wide range of applications in polymer and materials science. Cellulose is a β(1→4)-linked D-glucose polymer which is predominantly found in the cell walls of plants, providing mechanical reinforcement by forming an ordered, hierarchical structure. This naturally occurring biostructure can be broken down using a series of base, bleach, and acid washes (aided by mechanical agitation) to obtain crystalline nanorods called cellulose nanocrystals, thereby offering a route to a green, abundant, and relatively low-cost source of organic nanomaterials.[2] Depending on the biological source and conditions used during the isolation process, CNCs with a wide range of lengths (50-5,000 nm) and aspect ratios (1-100) can be obtained.[2-4] The resulting crystalline materials are biodegradable and have a property profile that includes low density, mechanical rigidity, and optical transparency when homogenously dispersed in a host matrix.[2, 5, 6] CNCs can also be chemically modified to allow tuning of their properties.[2, 7, 8] CNCs have been investigated in a diverse range of applications from packaging and materials reinforcement to optoelectronic and water purification systems, among others.[2, 8] As such, the annual number of patents filed involving CNCs has increased more than seven-fold between 2013 and 2017, a trend that is expected to continue in the future with increased availability of and interest in CNCs.[9]

Beyond their use in materials engineering applications, CNCs have gained attention as an attractive nanomaterial for biomedicine, owing to their unique physicochemical properties, ease of isolation and functionalization, and abundance in nature. Early studies have shown applications for CNC-based composites in biomaterial scaffolds, antimicrobial dressings, and bioimaging devices.[10-20] For example, poly(vinyl acetate)-CNC composites have been investigated as

mechanically adaptable intracortical probes that display enhanced mechanical compliance between the probes and neural tissue, thereby reducing inflammation and scarring relative to more traditional stiffer silicon-based probes.[17-19] CNCs have also found use in the delivery of small molecules, proteins, and nucleic acids, which can be attached to the CNCs through covalent and non-covalent bonds or delivered using CNCs in hydrogels or micellar formulations.[21-29] Notably, De France and colleagues report that CNC-PEG conjugates can adsorb proteins and be injected to form a hydrogel *in-situ*, remaining at the site of injection for months to allow site-specific release of cargo.[27] With the increased interest in and availability of CNCs, it is imperative to address how CNCs interact with biological systems to ensure safe implementation.

To date, studies that have addressed the biocompatibility of CNCs have been limited predominantly to *in-vitro* or respiratory uptake models. Nanoscale materials often interact with cells and tissues differently than bulk material owing to their high surface area to volume ratios and presence of positive or negative surface charges, which can affect cellular uptake, chemical adsorption, and pharmacological clearance of the materials.[30] In particular, high aspect ratio nanoparticles such as carbon nanotubes[31, 32] and fibrous silica[33] have been the subject of significant concern on account of early reports of pulmonary and cellular toxicity. Indeed, testing on CNCs has indicated that they can exhibit asbestos-like pulmonary toxicity in a murine respiratory uptake model owing to their low density, nanoscale properties, and surface chemistry.[34] It is interesting to note that in these studies and related model pulmonary studies the aspect ratio of the CNCs[35] or whether the CNCs were in an aqueous suspension or powder form[34] does impact the nature of the biological response. While there is still a lot to learn and understand about the potential pulmonary toxicity of CNCs, CNCs differ from carbon nanotubes because they are dispersible in water, potentially allowing for safer handling as aqueous slurries or dispersions. Dispersed wood-derived CNCs have been shown *in-vitro* to have no disruptive effect on cell viability on multiple cell lines at biologically relevant concentrations of < 250 μg/mL,[36] potentially

opening the door to aqueous CNC solutions and their derivatives being investigated in further diagnostic and therapeutic medical devices and drug delivery systems.

Although these results suggest the *in-vitro* biocompatibility of CNCs, they do not address the effects of functionalization, particle shape, or isolation procedures of CNCs *in-vitro* or *in-vivo*. For example, surface charge modification has been shown to alter cellular interactions with CNCs both *in-vitro* and in a zebrafish model.[37-39] Mahmoud *et al.* report that functionalizing CNCs with a positive (RBITC) or negative (FITC) charged fluorophore altered cellular uptake *in-vitro* using HEK and Sf9 cell lines.[37] Particle size was also shown to alter respiratory clearance of CNCs, as CNCs sourced from tunicate (l = 2,244±1,687 nm) invoked greater respiratory inflammation than those sourced from cotton (l = 237±118 nm).[35] Finally, chemical agents or bacterial contamination encountered during the isolation and functionalization process can also confound biological studies if incompletely removed. Labet and Thielemans reported that cleaning CNCs by Soxhlet extraction enhances reproducibility of functionalization reactions, highlighting the importance of removing debris from the surface of CNCs.[40]

With increased interest in the commercial production of CNCs using different sources and isolation procedures, the work reported herein is aimed to more thoroughly examine how parameters, such as charge, length, and cleaning of the CNC surface, impact *in-vitro* and *in-vivo* cytotoxicity and immunocompatibility incurred by the various CNCs. While Colombo *et al.* previously evaluated the *in-vivo* tissue distribution of subcutaneously injected AF647-modified CNCs,[41] this is the first study to our knowledge which evaluates the effects of CNC source on biocompatibility and the first which evaluates the *in-vivo* effects of source and charge after subcutaneous injection. We then explore the use of biocompatible CNCs as a depot-based particulate adjuvant for vaccination.[42-45] We hypothesized that the size and aspect ratio of CNCs would activate the innate immune system and, when co-administered with a peptide antigen, enhance antigen uptake by antigen-presenting cells (APCs) at the injection site to improve adaptive immune responses.

6.2 Results and Discussion.

6.2.1 Synthesis and Characterization of Cellulose Nanocrystals.

To evaluate the effects of CNCs with different sizes and dimensions, CNCs from four different biosources including wood (*w*-), cotton (*c*-), *Miscanthus x. Giganteus* (*MxG*-), and tunicate (*t*-) were targeted for investigation. In addition, CNCs with different surface chemistry affording a variety of charges were targeted (**Figure 6.1**). Finally, CNCs produced via large scale production (*ls)* were compared to those produced on a smaller laboratory scale in order to evaluate whether the method of production would alter the biological response. A total of twelve different CNCs were studied. Uncharged CNCs (*MxG*-CNC-OH, obtained via hydrochloric acid hydrolysis) and CNCs functionalized with sulfate half-esters (*c*-CNC-OSO_3^-, *MxG*-CNC-OSO_3^-, and *t*-CNC-OSO_3^-, obtained via sulfuric acid hydrolysis) were prepared directly from the biosource using literature procedures.[46-48] *c*-CNC-OSO_3^-, *MxG*-CNC-OH, and *t*-CNC-OSO_3^- were further functionalized to yield CNCs with carboxylic acids (CNC-COOH, via TEMPO-based oxidation of the C6 alcohol)[49] or amines (CNC-NH_2, via reaction of epichlorohydrin and ammonia) on their surface.[26] While unfunctionalized CNCs have a slight negative charge, it was hoped that a distribution of charges above and below this baseline would afford a distribution of relevant charges for downstream biological applications of CNCs. Finally, CNCs isolated on a larger, commercially-viable scale from wood (via sulfuric acid hydrolysis, *w*-CNC-$OSO_{3(ls)}^-$)[50, 51] and *Miscanthus x. Giganteus* (via hydrochloric acid hydrolysis, *MxG*-CNC-$OH_{(ls)}$)[52, 53] were obtained to allow a comparative analysis of isolation procedure on the biocompatibility of CNCs.

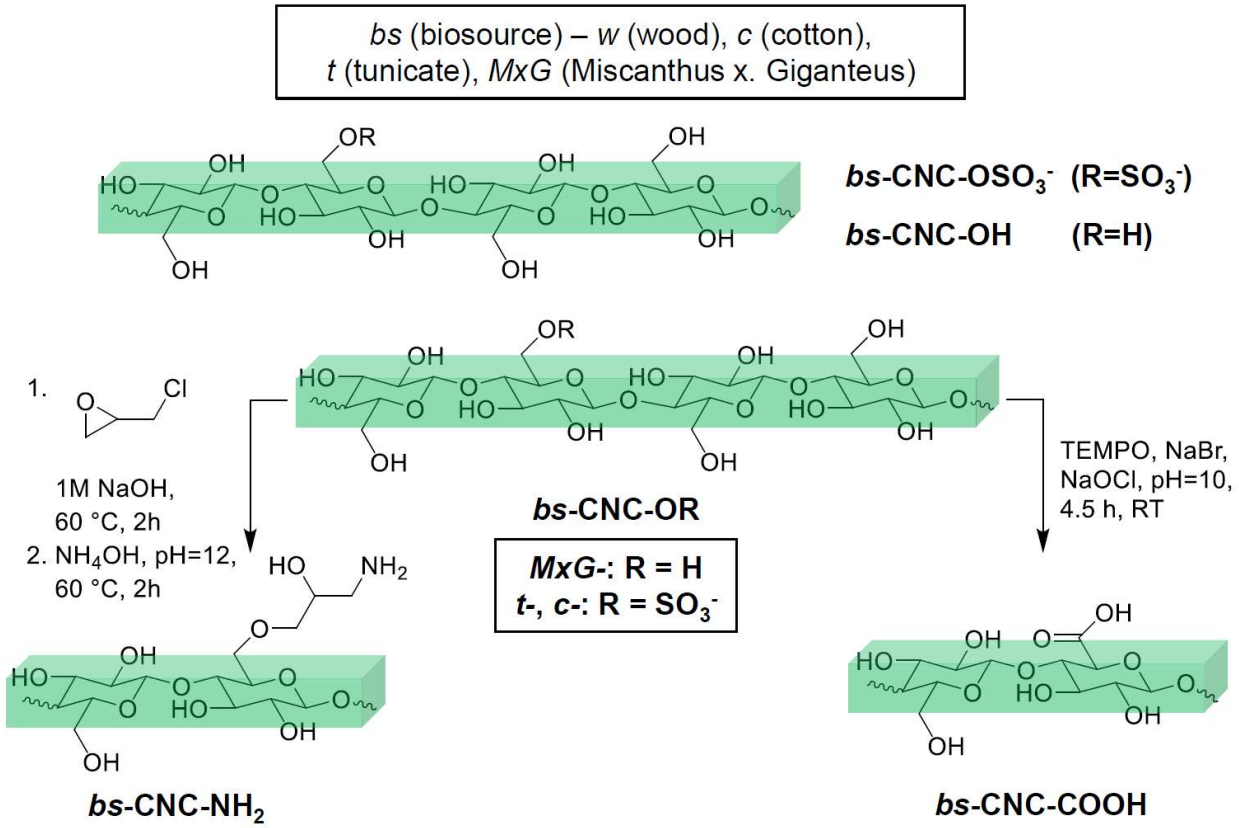

Figure 6.1: Overview of CNC synthesis. CNCs were obtained from tunicate, *MxG*, cotton, and wood to allow study of CNCs with four different lengths. CNCs were then functionalized using epichlorohydrin-mediated amination or TEMPO-oxidation to achieve CNCs with positive and negative charge modifications, respectively, on their surface.

CNCs prepared from each of the four *in-house* procedures and those obtained from the two large scale isolation procedures were characterized by AFM or TEM, wide-angle X-ray scattering (WAXS), thermogravimetric analysis (TGA), and FT-IR to ensure no confounding factors would affect biocompatibility assessments. The length and morphology of the CNCs was evaluated using AFM, except in the case of the uncharged *MxG*-CNC-OH$_{(ls)}$ and *MxG*-CNC-OH samples which were imaged using TEM, as they disperse poorly in solution. As expected, tunicate-based CNCs (*t*-CNCs) were longest (820±400 nm) (**Figure 6.2A** and **Figure S6.1A**), *MxG*-CNCs were shorter (190±60 nm and 120±40 nm for hydrochloric acid hydrolysis and sulfuric

acid hydrolysis, respectively) (**Figure 6.2B-C** and **Figure S6.1B-C**), and cotton-based CNCs (*c*-CNCs) were shortest (90±20 nm) (**Figure 6.2D** and **Figure S6.1D**).[5] The *MxG*-CNC-$OH_{(ls)}$ samples (200±80 nm) were longer than *MxG*-CNC-OH prepared *in house* (**Figure 6.2E** and **Figure S6.1E**); which is possibly a consequence of differences in the length of acid treatment.[3] The *w*-CNC-$OSO_3^-{}_{(ls)}$ samples were 110±40 nm (**Figure 6.2F** and **Figure S6.1F**), commensurate with previous reports.

With the size of the isolated CNCs confirmed, WAXS, TGA, FT-IR, and conductometric titration experiments were subsequently conducted to evaluate the crystallinity index (CI) and chemical composition of the isolated CNCs. Using the peak deconvolution method for WAXS analysis (assuming a Gaussian distribution and modelling the cellulose 1β peaks of 101, 10$\bar{1}$, 021, and 002),[54] it was found that all CNCs were between 85-90% crystalline (**Table 6.1** and **Figures S6.2-S6.6**). Through TGA (**Figure S6.7**), it was observed that all of the sulfated CNC samples had a lower degradation temperature than unfunctionalized *MxG*-CNC-OH and *MxG*-CNC-$OH_{(ls)}$, which is consistent with previous reports.[55] FT-IR spectroscopy revealed no unexpected peaks or lignin contamination (which is observed as peaks at 1,604, 1,512 and 1,462 cm^{-1} that correspond to the aromatic rings of lignin) in the samples (**Figure S6.8**).[47] Finally, conductometric titrations revealed the presence of about 170, 110, and 27 mmol/kg of sulfate half-ester groups on *t*-CNC-OSO_3^-, *MxG*-CNC-OSO_3^-, and *c*-CNC-OSO_3^-, respectively (**Figure S6.9**).

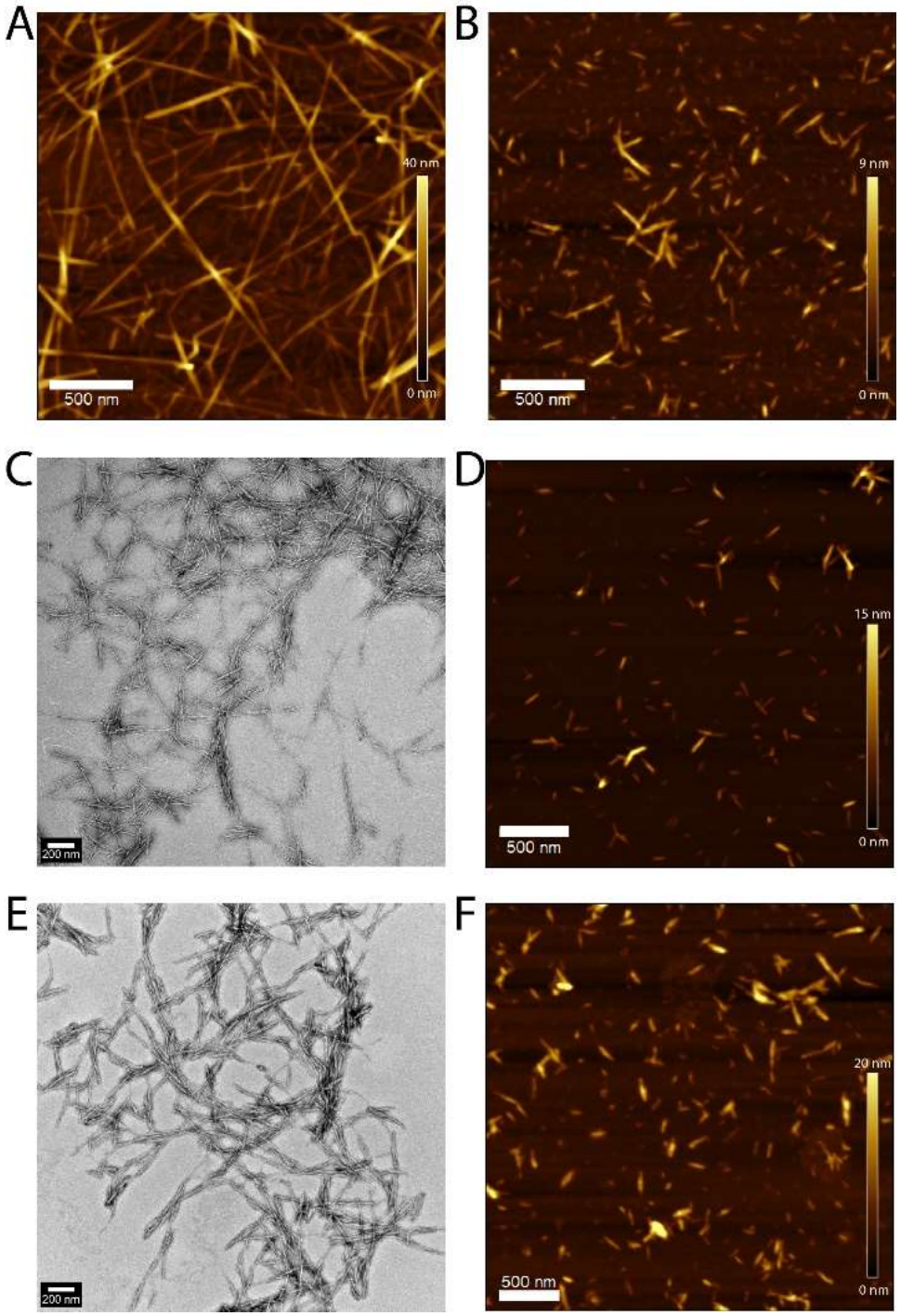

Figure 6.2: Microscopy of CNCs used in this study. A) AFM image of *t*-CNC-OSO_3^-. B) AFM image of *MxG*-CNC-OSO_3^-. C) TEM image of *MxG*-CNC-OH. D) AFM image of *c*-CNC-OSO_3^-. E) TEM image of *MxG*-CNC-$OH_{(ls)}$. F) AFM image of *w*-CNC-$OSO_3^-{}_{(ls)}$. For AFM imaging, samples were drop cast from a dilute aqueous solution onto a poly-lysine coated mica substrate, and for TEM imaging, samples were casted onto a carbon-coated copper grid and stained with uranyl acetate.

The isolated CNCs were subsequently modified to achieve a distribution of surface charges (**Figure 6.1**). *t*-CNC-OSO_3^-, *MxG*-CNC-OH, and *c*-CNC-OSO_3^- were TEMPO-oxidized to yield carboxylic acid-functionalized CNCs (CNC-COOH) or amine-functionalized (CNC-CNH_2 via epichlorohydrin-mediated amination) according to literature procedures and dialyzed for several days to remove impurities.[26, 49] The resulting chemically modified CNCs were characterized by FT-IR (**Figure S6.8**), conductometric titration (**Figure S6.9**), and AFM (**Figure S6.10**), and their purity was assessed by semiquantitative ^{1}H-NMR of a wash solution (**Figure S6.11**). In the FT-IR spectra, characteristic carboxylate peaks were observed at 1,600 cm^{-1} in the CNC-COOH samples while a weak amine wag peak was observed at 850 cm^{-1} in the CNC-NH_2 samples. While the amine wag peak has a high signal to noise ratio and cannot alone justify the presence of surface amines, later zeta potential measurements (**Table 6.1**) confirm that the CNCs functionalized by epichlorohydrin-mediated amination have a positive surface charge which is consistent with the presence of amine groups on the CNC surface. For CNC-COOH samples, conductometric titrations indicated the presence of 900-1,300 mmol/kg carboxylate groups (**Figure S6.9**), providing further validation that the materials were successfully functionalized. AFM studies of the modified CNCs (**Figure S6.10**) confirmed that the dimensions of the CNCs did not change significantly during chemical functionalization, suggesting in tandem with WAXS (**Table 6.1** and **Figures S6.2-S6.6**) that the conditions used for modification retained the crystallinity of the resulting materials. Finally, several of the isolated samples were dispersed in D_2O and subsequently removed from the solution, and the D_2O supernatants were analyzed by ^{1}H-NMR in reference to a 1 mg/mL maleic acid standard (**Figure S6.11**). The isolated and functionalized CNCs were free of contamination in the mmol contaminant/g CNC range, further justifying their use in later studies.

After confirming the chemical modification of the CNCs, electrophoretic light scattering experiments were conducted on a subset of the *MxG*-CNC samples to validate that the CNCs achieved the desired positive or negative charge modifications and further validate the chemical

modification (**Table 6.1** and **Figure S6.12**). Estimating the charge density on CNCs was critical to determine if and how charge properties alter biocompatibility in later analyses. Although electrophoretic light scattering is based off a spherical model, which is a poor description for the long and rigid nanocrystals, the zeta potential (ζ) is directly proportional to the mobility (μ) as shown in equation **(1)**; thus, these data provide a qualitative assessment of the surface charge.[56] *MxG*-CNCs were dispersed by brief ultrasonication in pH = 7 deionized water at a concentration of 1 mg/mL, passed through a 10 μm filter to ensure the complete removal of large aggregates, and immediately analyzed. As expected, TEMPO oxidation imparted a strongly negative charge to the surface of CNCs at pH = 7 (-52.9±3.8 mV) while amination imparted a positive surface charge at pH = 7 (23.7±7.4 mV). Sulfated CNCs bore a comparable or slightly greater negative charge than the unfunctionalized CNCs, which is expected on account of the relatively low density of negatively charged sulfate half-ester moieties.[57, 58] Upon successfully completing characterization of the CNC samples, biological activity could be assayed.

(1) $$\zeta = \frac{3\eta\mu}{2\varepsilon f \kappa R_h}$$

Source	Length	Crystallinity Index	Zeta Potential
t-CNC-OSO_3^-	820±400 nm	87%	-27.4±1.1 mV
MxG-CNC-OSO_3^-	120±40 nm	86%	-19.0±1.3 mV
MxG-CNC-OH	190±60 nm	88%	-16.3±0.4 mV
MxG-CNC-$OH_{(ls)}$	200±80 nm	90%	-17.7±3.2 mV
c-CNC-OSO_3^-	90±20 nm	88%	-16.3±0.3 mV
w-CNC-$OSO_3^-{}_{(ls)}$	110±40 nm	85%	-26.2±1.6 mV
MxG-CNC-COOH	N/A	86%	-52.9±3.4 mV
MxG-CNC-NH_2	N/A	85%	23.7±7.4 mV

Table 6.1: Characterization of CNCs was conducted to evaluate length, crystallinity, and surface charge. The length of the CNCs was calculated for each of the samples using AFM peak height measurements or TEM images in the case of CNC-OH samples. Crystallinity index was calculated by obtaining WAXS spectra of all samples and using peak deconvolution to identify contributions from each of the four major cellulose 1β crystalline peaks (101, 10$\bar{1}$, 021, and 002) as well as the amorphous contribution to the spectrum. Finally, electrophoretic light scattering was used to determine the zeta potential of CNC samples. CNC solutions were dispersed at 1 mg/mL by ultrasonication, and zeta potentials were obtained at 1 V and calculated using the linear polymer model **(1)** at pH=7 in water.

6.2.2 Endotoxin Decontamination.

One challenge with studying the biological response of different CNCs is the possibility that the CNCs contain chemical or biological contaminants which can skew results and complicate data interpretation. Perhaps the most ubiquitous of these contaminants is bacterial endotoxin, a lipopolysaccharide which composes the outer membrane of gram-negative bacteria and induces cytotoxic responses by mTLR4 activation at trace concentrations (< 1 ng/mL).[59] Owing to its abundant presence in nature and amphiphilic nature, bacterial endotoxin previously has been found to adsorb strongly to nanoparticles, including CNCs.[60] The United States Pharmacopiea has reported an acceptable limit of 20 EU/device for medical devices, where EU is a measurement of the activity of endotoxin present in a sample.[61] Preliminary *in-vitro* assays with the CNCs indicated the presence of low-level immune activation and cytotoxicity that was suspected to result from such contamination; as such, methods to identify the presence and subsequently remove endotoxin from the CNC surface were explored.

Quantifying the presence of endotoxin on nanoparticle surfaces poses a unique challenge on account of the interaction of nanoparticles with common endotoxin test reagents.[62, 63] For example, LAL gel clot assay is a common semi-quantitative readout of endotoxin presence which is dependent on the interaction of the coagulin protein with lipopolysaccharide endotoxins to generate clotting. Many nanoparticle samples interact with coagulin, resulting in aberrant clotting and false positive results.[62] Other methods, such as the rabbit pyrogen test, are expensive and impractical for early-stage biocompatibility screening.[63] As such, the HEK mTLR4 cell line was used to quantify the presence of lipopolysaccharide endotoxins, where mTLR4 receptor activation by endotoxins result in the secretion of alkaline phosphatase (SEAP) which can be detected colorimetrically by phosphatase detection reagents. Initial results indicated that *MxG*-CNC-COOH (and other samples) used directly without further purification did show some presence of endotoxin (**Figure 6.3**), albeit at relatively low levels. Nonetheless, it was decided to develop a cleaning procedure for all the CNCs to reduce any complications of endotoxin contamination.

Previous studies have reported the removal of endotoxin by treating nanoparticulate formulations with heat, solvent, or radiation.[55, 62, 64-66] Most commonly, samples are treated with dry heat or autoclave at 175-250 °C for several hours to induce decomposition of the lipopolysaccharide – this approach has proven successful for silicon, titanium, zirconium, and cobalt nanoparticles, as well as alginate-based biomaterials.[64, 65] Other studies have reported that extensive washing with ethanol, acetone, or strong acid removes endotoxin from titanium nanoparticles.[66] While these approaches have been successfully implemented in many cases, the low degradation temperature (approximately 130 °C), poor tolerance for strong acid, and negligible solubility in organic solvents of CNCs provided a unique challenge to remove endotoxin without damaging the CNCs. As such, a procedure using aqueous washes in tandem with ultrasonic treatment was developed based on inspiration from the medical device literature to clean the CNCs.[67] The CNCs were dispersed in endotoxin-free DI water, probe ultrasonicated for 5 min at 25% power (3 s on/off cycles), and then centrifugated to sediment the CNCs. The supernatant was then decanted, and the procedure was repeated for a total of three washes. The samples were then freeze dried, weighed, and dispersed in endotoxin-free water for further use. This procedure afforded ca. 70 wt.% yield of CNCs and could be conducted in about one hour, providing a rapid and simple method to obtain clean samples for biological testing.

Using the described endotoxin removal procedure, all the CNC samples were cleaned and found to have endotoxin levels < 5 EU/mL when incubated at concentrations of 10-100 μg/mL with the HEK mTLR4 reporter cell line (**Figure 6.3**). Having successfully validated a reliable method to remove endotoxin from the samples, the ability of the CNC samples to activate the immune system in future experiments could be assayed.

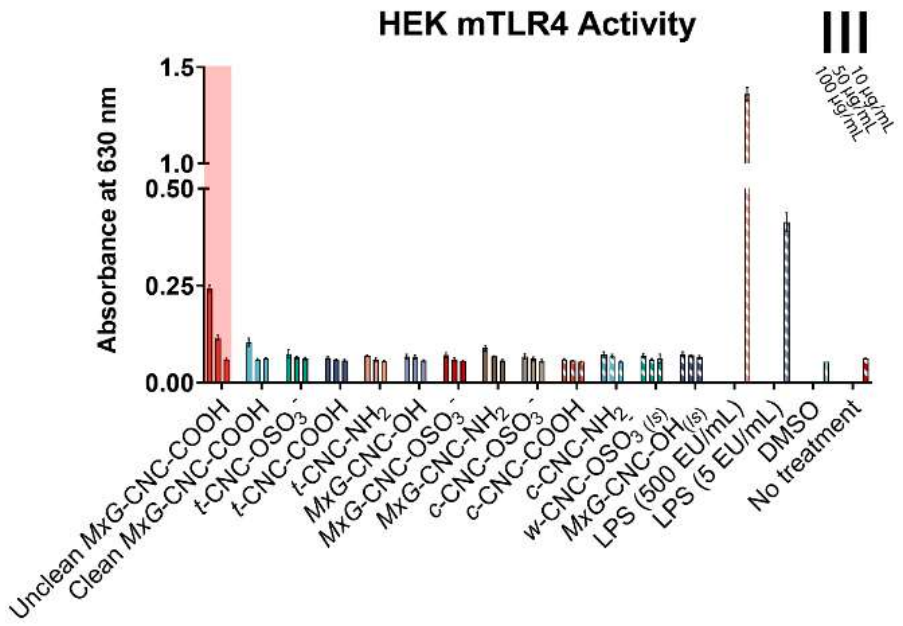

Figure 6.3: Endotoxin removal from CNC samples was validated using the HEK mTLR4 reporter assay (n=3/group). CNC samples were washed three times with endotoxin-free dH_2O by subsequent sonication and ultracentrifugation. The cleaned samples were freeze dried, redissolved in endotoxin-free dH_2O, and incubated with cells at 10-100 µg/mL overnight. HEK mTLR4 activity was indicated using HEK-Blue Detection Medium (InvivoGen), and absorbance was quantified at 620 nm. LPS was used as positive control, and an uncleaned sample (far left in red) with low-level endotoxin contamination is shown as a reference. Error bars indicate standard deviation.

6.2.3 In-vitro biocompatibility of CNCs.

After successfully cleaning the samples, *in-vitro* biocompatibility of all the CNC samples was assayed. Given that CNCs isolated with hydrochloric or sulfuric acid hydrolysis, as well as those which have been further functionalized to achieve different charges or physicochemical properties, have been used in biological studies,[21-29] it was critical to establish a baseline for how different physicochemical parameters (such as charge and particle size) would affect the previously reported biocompatibility of CNCs.[34-38] As an initial test of cytotoxic activity induced by the CNCs with different sources, lengths, and charges, the RAW-Blue macrophage cell line was employed. Cells were incubated with 10-100 µg/mL of CNCs for 24 h, and an MTT assay was used as a colorimetric readout of mitochondrial activity to determine cytotoxicity. No changes in

cytotoxicity were observed (**Figure 6.4A**), validating that altering source or charge of the CNCs had no bearing on cytotoxicity *in-vitro*. It is perhaps a little surprising that the positively charged CNCs did not induce cytotoxicity, as other cationic polymers such as poly(ethyleneimine) have been shown previously to induce cell death *in-vitro*.[68] As such, similar experiments were conducted using an alternative cytotoxicity assay which measures lactate dehydrogenase (LDH) activity. Again, no cytotoxicity was observed using the CNCs from various sources and charges, validating that the CNCs prepared for these studies did not activate cell death pathways under the conditions studied on account of their length or surface functionality (**Figure S6.13**). These results corroborated the prior experiments which suggested that CNCs are not cytotoxic regardless of the source or the charge *in-vitro*; however, it must be cautioned that other functionalization chemistry, such as those which include a longer linker, different pK_a, or greater charge density, might influence cytotoxicity in the case of positively charged CNCs. Moreover, no significant differences between CNCs produced on a small scale or larger, commercially viable scale were observed, indicating that after the above cleaning procedure the method of isolation did not alter cytotoxicity of CNCs *in-vitro*.

After conducting the initial cytotoxicity assessments, immune activity of the 12 CNC samples was assayed. Previous studies have shown that many polymers, such as polystyrene or polycaprolactone, can induce nonspecific inflammation *in-vitro* as measured using RAW-Blue NF-κB activity.[69, 70] It is hypothesized that this nonspecific activation might arise from various physicochemical interactions of the polymers with innate immune cells; as such, it was important to assess whether different CNCs that vary in charge or particle size induce differential immune responses *in-vitro*. RAW-Blue cells have a SEAP reporter coupled to the NF-κB signal transduction pathway which provides a broad readout of immune activation. CNCs were incubated with RAW-Blue cells for 24 h, and then the supernatant was collected and assayed using QuantiBlue detection reagent. No NF-κB signaling was induced by the CNCs with different lengths or charges (**Figure 6.4B**). IL-6 and TNF-α ELISAs were also conducted on supernatants

as a secondary readout of immune activation. Low levels of TNF-α production were observed in most samples, indicating inflammation from cell damage independent of NF-κB signaling, while IL-6 was not induced (**Figures S6.14** and **S6.15**). Taken together, these results suggest that source/size or charge of the CNCs do not induce significant immune activation *in-vitro*.

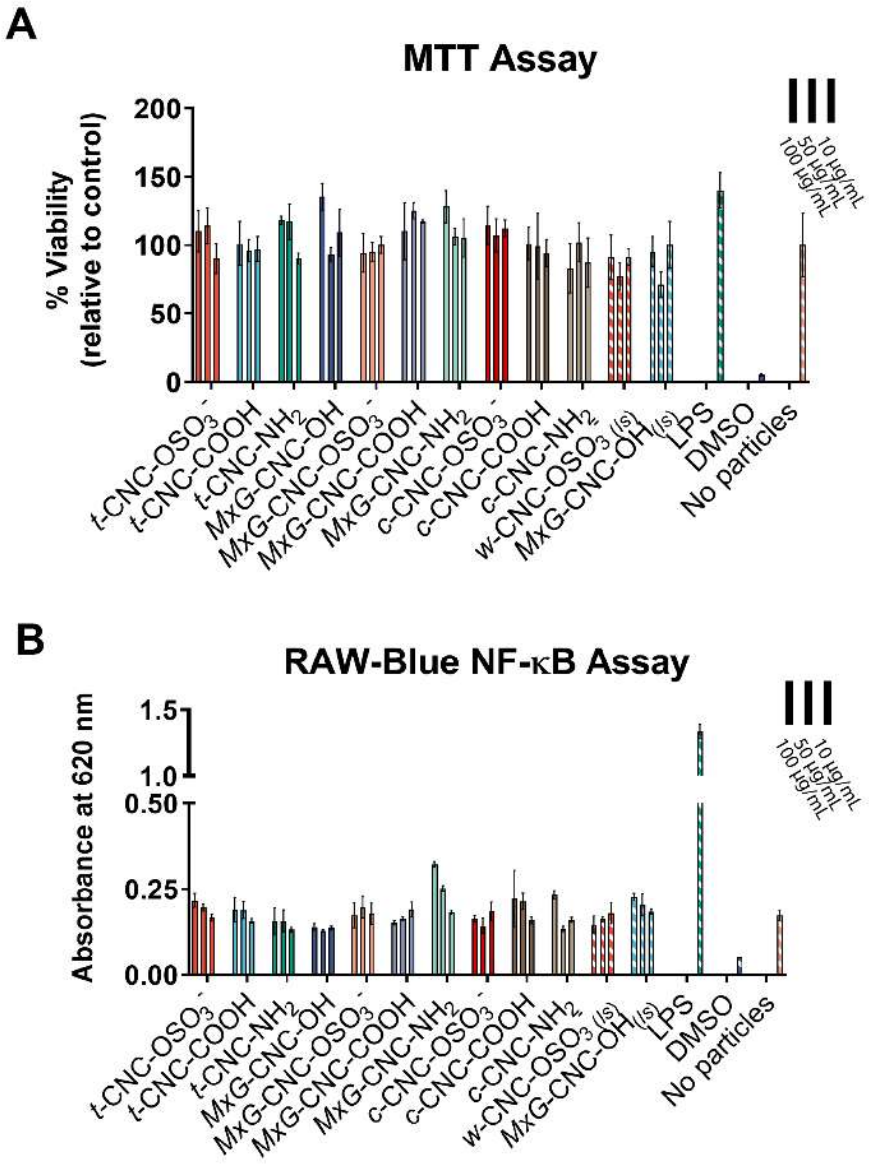

Figure 6.4: *In-vitro* assays assessing biocompatibility of the prepared CNCs (n=3/group). CNCs were incubated with the RAW-Blue macrophage cell line at 10-100 µg/mL for 24 h and (A) immune system activity and (B) cytotoxicity were assayed using RAW-Blue and MTT Assays, respectively. No aberrant immune system activity or cytotoxicity were observed using CNCs from any source or functionalization. Error bars indicate standard deviation.

Though the CNCs appeared to induce minimal immune activation or cytotoxicity *in-vitro*, an additional possibility was that CNCs could precipitate from cell culture media and disrupt cellular division. To test this hypothesis, a BrdU ELISA using RAW macrophages (the parent cell line of RAW-Blue macrophages) was conducted on a subset of the CNC samples to measure the rate of proliferation during incubation with the CNCs. BrdU is a thymidine analog which can be incorporated into host DNA to measure the rate of cell division. CNCs were incubated with the RAW macrophages for 12 h, and then BrdU-containing media was added for an additional 12 h to measure division using an anti-BrdU antibody ELISA. Again, no differences were observed (**Figure S6.16**). During the analyses, however, the presence of large aggregates in the *MxG*-CNC-OH samples were observed using a light microscope (**Figure S6.17**). Given these results, it was hypothesized that aggregation could damage tissue and result in systemic inflammation *in-vivo*, inspiring us to conduct an *in-vivo* biocompatibility assay in mice to test this possibility.

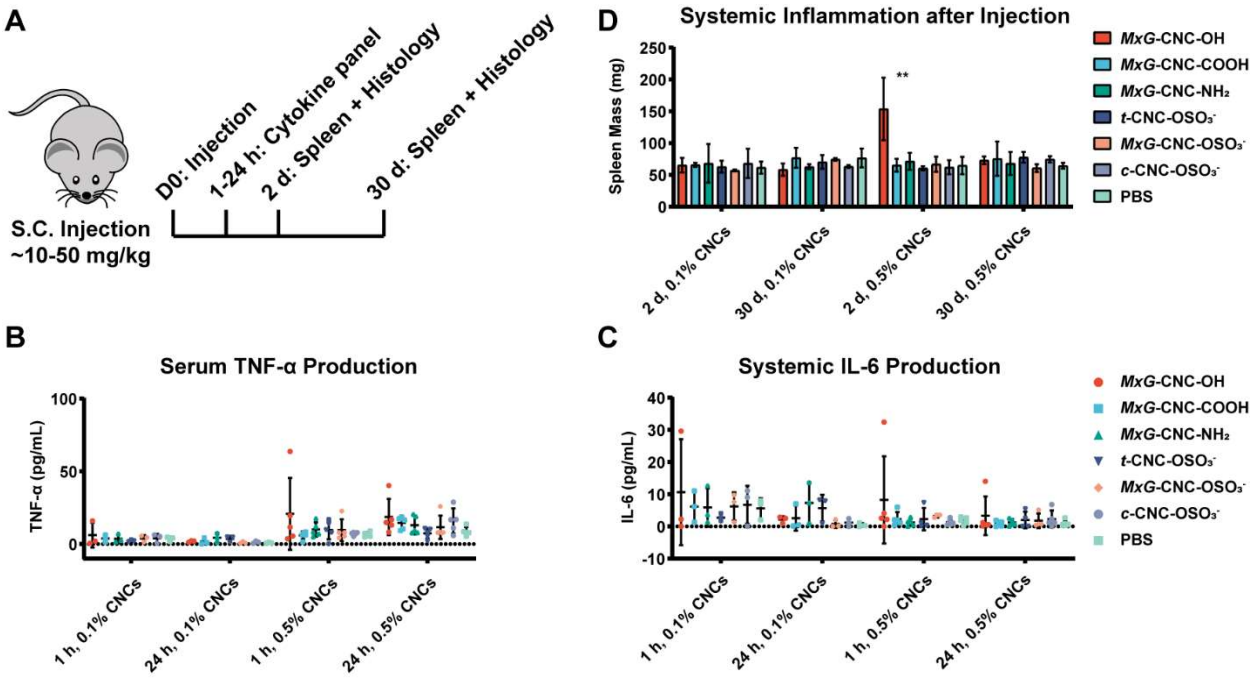

Figure 6.5: A) *In-vivo* experimental design to test inflammation induced by the CNCs (n=3-5/group). No changes in B) TNF-α or C) IL-6 were observed in the CNC samples at either concentration or timepoint analyzed. D) Mice injected with 0.5% *MxG*-CNC-OH had significant splenomegaly after 2 d, suggesting an acute immune response toward the CNCs. Error bars indicate standard deviation. Significant differences between treatments were analyzed by two-way ANOVA with residual multiple comparisons testing. ** = $p < 0.01$

6.2.4 In-vivo biocompatibility of CNCs.

Having replicated and expanded upon previous *in-vitro* work demonstrating the biocompatibility of CNCs, an *in-vivo* experiment was designed using a subset of the CNCs to assay how size and charge would alter the acute inflammatory response towards CNCs in a mouse model. Given that CNCs in *in-vivo* applications have often been administered through subcutaneous routes of administration,[15, 27] six types of CNCs were injected subcutaneously (*t*-CNC-OSO_3^-, *MxG*-CNC-OSO_3^-, *c*-CNC-OSO_3^-, *MxG*-CNC-OH, *MxG*-CNC-COOH, and *MxG*-CNC-NH_2), and the local and systemic immune response was assayed after 2 or 30 d. Two concentrations of CNCs were selected, 0.1% and 0.5%, as these concentrations were observed to be above and below the concentration threshold for dispersibility of the unfunctionalized (*MxG*-CNC-OH) samples. Using these two concentrations, experiments were conducted to evaluate if

the effect of aggregation on *in-vivo* tissue compatibility of the CNCs could be assayed. Mice were injected subcutaneously in the right flank with 300 µL of the prescribed CNC solutions (corresponding to clinically relevant doses of approximately 10 and 50 mg/kg of CNCs), and the systemic immune response was assayed over 2-30 d using acute cytokine production (measured by ELISA), spleen mass, and hematoxylin and eosin staining of tissue from the injection site (**Figure 6.5A**). These outputs would afford a better understanding of systemic inflammation incurred by CNCs which could not be evaluated *in-vitro.*

As a measure of tissue damage and innate immune stimulation incurred by the CNCs, cytokine production was assayed in the serum after injection of the CNC samples. Immunotoxic nanoparticles induce secretion of cytokines into the bloodstream within hours of injection which can invoke a sickness response *in-vivo*.[70, 71] Thus, three pro-inflammatory cytokines (IL-6, TNF-α, and IFN-γ) were analyzed in the serum 1 and 24 h after injection. No significant difference in cytokine production was observed, indicating that the CNCs did not invoke acute serum toxicity at the timepoints analyzed (**Figures 5B-C** and **S6.18**). These results corroborate the earlier *in-vitro* studies using the RAW-Blue cell line and suggest low systemic immunotoxicity of CNCs.

Tissue histology and spleen mass were then measured as indicators of local and systemic pro-inflammatory immune responses, respectively. While cytokine production provides temporal information about the acute inflammatory environment in response to CNCs, histology provides spatial information correlating inflammatory responses to tissue damage incurred by the CNCs. Additionally, spleen mass provides information about the systemic immune response to tissue damage at the site of injection. Mice were sacrificed after 2 or 30 d, and spleens were immediately weighed. In mice dosed with a 0.5% CNC solution, the unfunctionalized *MxG*-CNC-OH samples induced significant splenomegaly 2 d after injection (**Figure 6.5D**). This suggests the production of lymphocytes as an immune response was mounted, which is critical for proper wound healing in response to tissue damage. Further imaging of the injection site post-mortem revealed concurrent inflammation in the subcutaneous tissue of the mice injected with 0.5% *MxG*-CNC-OH

after 2 d (**Figure S6.19**). The subcutaneous tissue was then dissected, fixed, and stained with hematoxylin and eosin. Staining revealed neutrophil infiltration and the presence of large CNC aggregates (> 50 μm) in tissue from the site of injection of mice injected with 0.5% *MxG*-CNC-OH after 2 d (**Figure 6.6**). No aggregates were observed in CNC-NH_2, CNC-COOH, or CNC-OSO_3^- samples at either timepoint, while limited neutrophil infiltration was observed in some samples (**Figure 6.6** and **Figure S6.20**). Given that unfunctionalized CNC-OH are significantly more hydrophobic than CNCs containing amines, carboxylates, or sulfate half-esters, these results suggest that unfunctionalized CNCs have a higher aggregation propensity in tissue which can result in a systemic inflammatory response. Altogether, these results indicate that charged CNCs are nonimmunogenic and therefore viable for use in further biological experiments, while uncharged CNCs can generate undesirable inflammation at high concentrations which can result in tissue damage and sickness response.

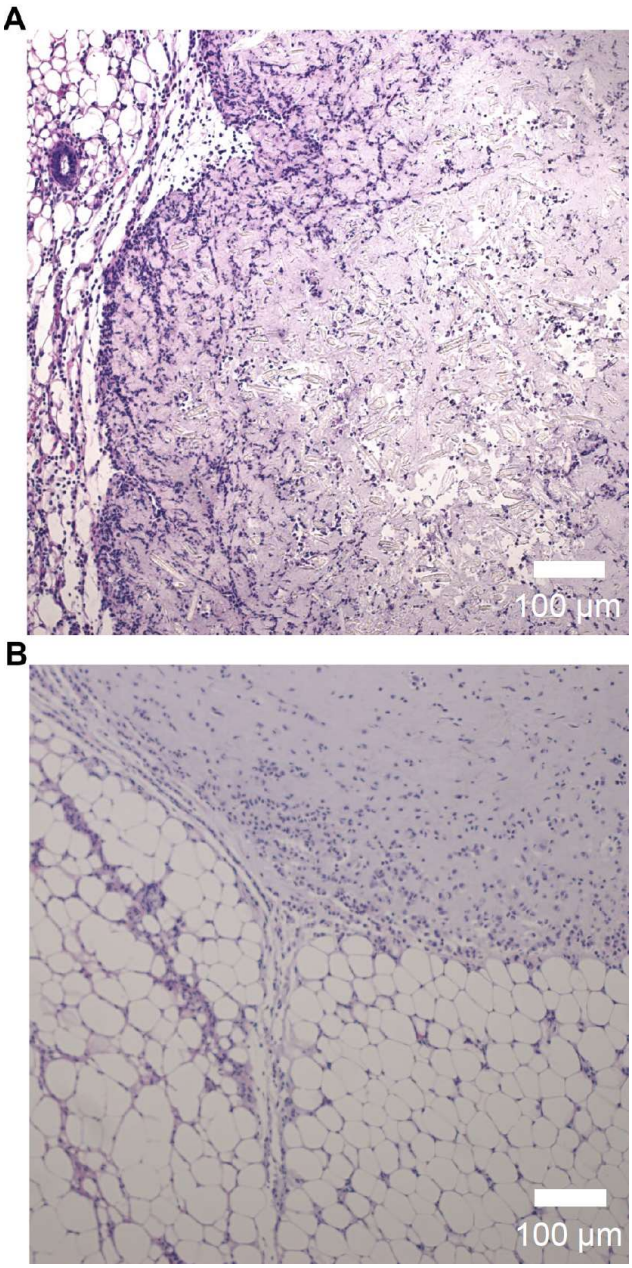

Figure 6.6: Hematoxylin and eosin staining of tissue collected from the injection site of uncharged A) *MxG*-CNC-OH and negatively charged B) *MxG*-CNC-COOH 2 d after injection. Significant neutrophil infiltration and presence of crystallite aggregates was observed in the *MxG*-CNC-OH samples suggesting a pro-inflammatory immune response.

6.2.5 Cellulose Nanocrystals as Adjuvants.

Following confirmation of the biocompatibility of charged CNCs, CNC-antigen conjugates were synthesized with the goal of testing how size and aspect ratio altered the immune response

via the subcutaneous route of injection. While our initial efforts focused on the development of vaccines wherein whole proteins were covalently attached to the CNC surface, this approach was limited for two reasons. First, the size and globular structure of whole proteins resulted in unfavorable kinetics that dramatically slowed the reaction. Second, unreacted protein could not effectively be removed from the CNCs, as both are high molecular weight compounds and poorly soluble in most solvents aside from water. Though asymmetric field flow fractionation or dialysis using high (≥100 kDa) MWCO tubing are often implemented in such scenarios, such approaches were unsuccessful in pilot studies (not shown). Therefore, preliminary efforts were focused on an epitope vaccine model. Epitope vaccines are highly desirable as cancer therapeutics, wherein vaccines induce potent T-cell responsivity against peptide neoantigens to mount an immune response against tumors. SIINFEKL, the immunodominant epitope of the model antigen, ovalbumin, was selected as a target, as it is known to generate robust $CD8^+$ T-cell immunity in a mouse model and provides a common readout against other epitope vaccines models. SIINFEKL was synthesized using solid-phase peptide synthesis (SPPS) with a Rink amide resin and characterized by ESI-MS (**Figure S6.21**).

To conjugate SIINFEKL to the CNCs, an orthogonal approach to graft high densities of peptide to the CNC surface was required. Due to the rigid, rod-like structure of CNCs, surface reactive groups are poorly accessible to macromolecular constructs. Moreover, the solubility of CNCs necessitates that the grafting reactions be conducted in water; as such, many conventional coupling techniques are incompatible with this system. Given these constraints, aldehyde groups were introduced onto the CNC surface by periodate oxidation to afford reactive handles that could react with amines via imine reduction to afford peptide-CNC conjugates (**Figure 6.7A**).[72-74] Periodate selectively oxidizes the C2-C3 carbon bond in (1→4) linked carbohydrates; while periodate can also oxidize the C3-C4 bond at the reducing end of short oligomers to degrade the polymeric chain, the tightly packed semicrystalline structure of the CNCs slows diffusion of reagents into the lattice, protecting interior groups from oxidation.[73] The dialdehyde CNCs (DA-

CNC) were prepared from *MxG*-CNC-OH and characterized by FT-IR and oxime titration to determine the aldehyde density, which was found to be 6400 mmol/kg (**Figure S6.22**). This density corresponds to reaction with ~53% of the C2-C3 bonds in the CNC backbone and is aligned with previous reports. TEM revealed slight degradation of the CNCs after periodate reaction (l = 120±40 nm) (**Figure 6.7B**); however, the rodlike structure was maintained allowing their use for conjugation.

SIINFEKL was then conjugated to DA-CNC by nucleophilic addition of the amine to the newly formed aldehydes followed by aqueous reductive amination with sodium cyanoborohydride, a water-compatible reducing agent.[74] SIINFEKL has two primary amines that are amenable to amination; however, by buffering the solution with 2-(N-morpholino)ethanesulfonic acid MES at pH = 6.0, the more acidic N-terminal amine can be targeted.[75] The product was characterized using FT-IR and bicinchoninic acid (BCA) assay to determine the protein loading density (**Figure 6.7C** and **Figure S6.23**). Using this approach, the grafting density of SIINFEKL was found to be 142 mmol/kg. A limitation of this chemistry is the lack of a secondary output to confirm covalent linkage; however, loss of an NH_2 wag at 836 cm^{-1} in the FT-IR spectrum plausibly indicates formation of a secondary amine (**Figure 6.7C**). With CNC-SIINFEKL conjugates in hand prepared from MxG-CNC-OH as a model system, we conducted a preliminary *in-vivo* vaccination study to evaluate CNC-peptide conjugation as a novel strategy to generate $CD8^+$ T-cell immunity.

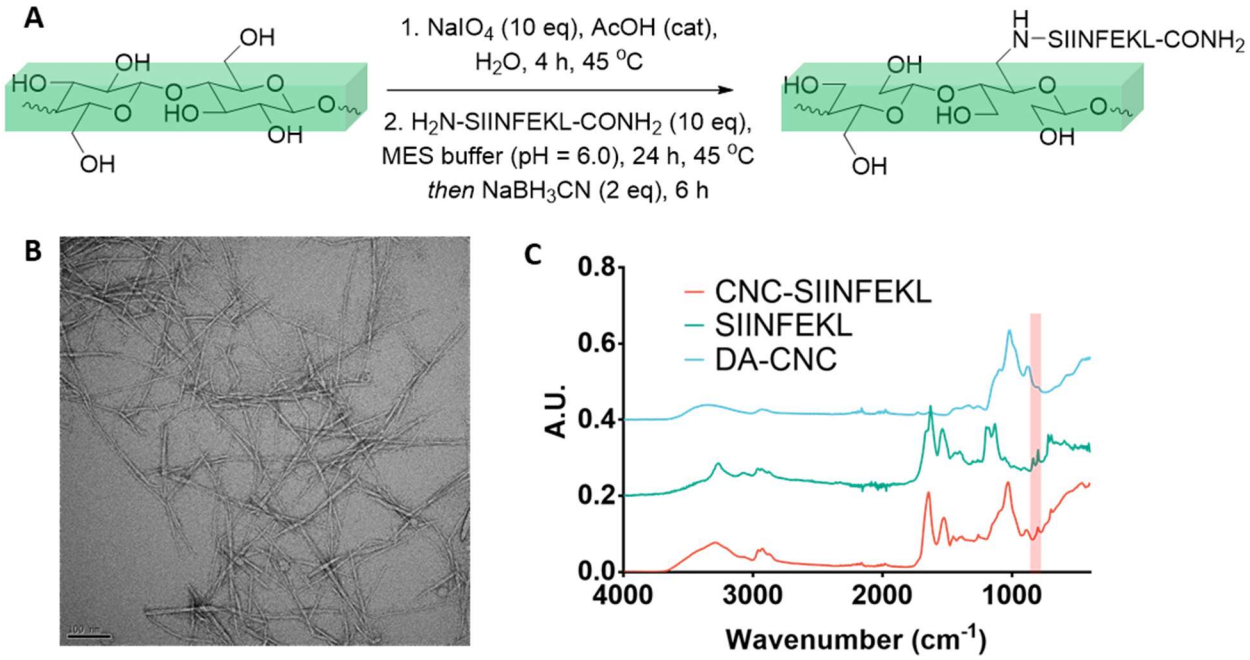

Figure 6.7: Conjugation strategy to produce CNC-SIINFEKL conjugates. A) Conjugates were prepared from MxG-CNC-OH by periodate oxidation followed by imine reduction. A loading density of 142 mmol/kg was achieved for SIINFEKL on the CNC surface. B) TEM demonstrates that the rodlike structure of DA-CNC was maintained after periodate oxidation. C) FT-IR of conjugates suggests successful grafting of SIINFEKL to DA-CNC indicated by loss of an NH_2 wag at 836 cm^{-1}.

Following successful synthesis of the CNC-SIINFEKL conjugates, their efficacy as a particulate adjuvant was explored. While Wang *et al.* previously reported the use of CNCs as an adjuvant during intraperitoneal injection with OVA, this system was limited by extremely high doses of antigen (400 µg) and adjuvant (2 mg), limiting the conclusions that can be drawn from the study.[76] Vaccine formulations containing 50 µg SIINFEKL bound or unbound to CNCs were prepared with 5 µg MPLA and 50 vol.% Addavax. MPLA is a synthetic TLR4 agonist which is often formulated alongside particulate adjuvants to enhance T-cell immunity (as in the FDA-approved $AS01_B$ vaccine formulation); while the synergy between MPLA and particulate adjuvants is not fully understood, NLRP3 inflammasome activation is believed to be involved.[77-79] Again, AddaVax was selected as an emulsifying agent to mimic the dioleoyl phosphatidylcholine and chitosan emulsifier used in $AS01_B$. The SIINFEKL formulations were administered intra-

muscularly as is common using similar carbohydrate delivery vehicles such as chitosan. Acute pro-inflammatory cytokine production was evaluated in the serum 2 and 24 h after injection, and sickness responses were evaluated by recording body weights daily. Mice were administered a boost after 14 d, and after 28 d, blood was collected to analyze anti-OVA antibody titers, and spleens were collected to evaluate antigen-specific T-cell production (**Figure 6.8A**).

In response to the initial vaccination, an initial decrease in body weight was observed in the SIINFEKL and CNC-SIINFEKL groups indicating a minor sickness response. No differences between groups were observed at any of the timepoints tested (**Figure 6.8B**, $p>0.05$). Correspondingly, IL-6 levels were increased in the SIINFEKL and CNC-SIINFEKL groups relative to PBS ($p<0.05$) after 2 h but returned to baseline levels after 24 h ($p>0.05$) (**Figure 6.8C**). These results suggest that an innate immune response was mounted against both the SIINFEKL and CNC-SIINFEKL formulations, which is expected given the presence of MPLA as a TLR4 agonist. After 28 d, neither cellular nor humoral immune responses were observed in the SIINFEKL and CNC-SIINFEKL formulations. Spleens were harvested after 28 d and splenocytes were isolated and cultured. To evaluate antigen-specific T cell production, cells were stained with anti-CD3, anti-CD8, and an MHC-I tetramer specific to SIINFEKL. No differences in the $CD3^+CD8^+Tetramer^+$ population between groups were observed (**Figure 6.8D**). Similarly, when the isolated splenocytes were restimulated with antigen for 48 h and stained for intracellular cytokines, no $CD8^+IFN\text{-}\gamma^+$ population was observed in the SIINFEKL or CNC-SIINFEKL groups (**Figure 6.8E**). Finally, no OVA-specific antibody production was observed in the serum 28 d after vaccination (**Figure 6.8F**). While antibody production is unlikely in the context of a peptide antigen, these results further highlight the failure of the CNC-SIINFEKL conjugation strategy for production of peptide vaccines. Given these results, this work was not pursued further, though we hypothesize that alternative strategies using a CNC-depot based vaccine formulation could be efficacious.

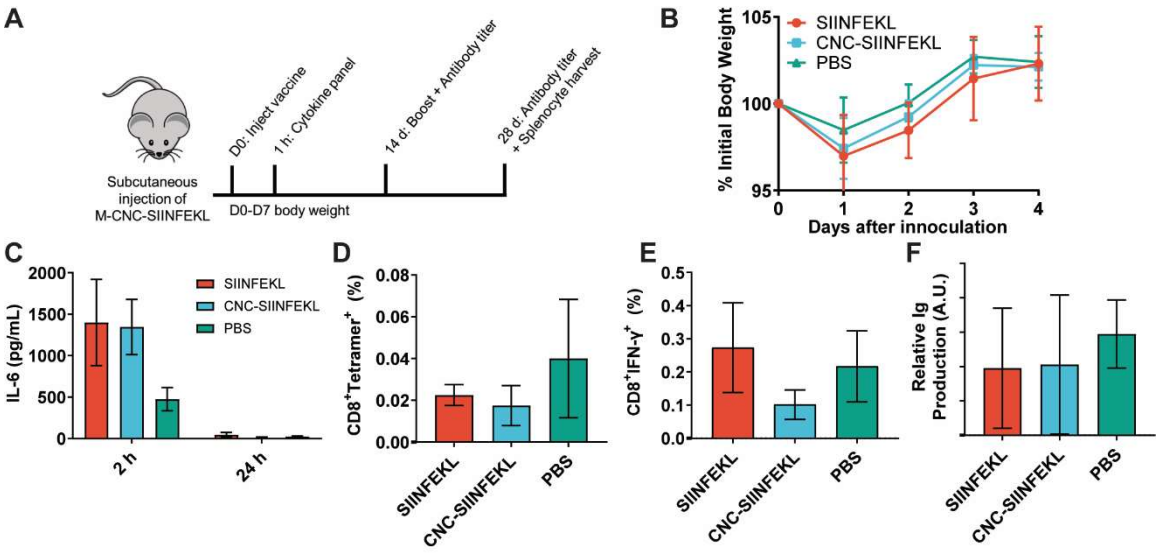

Figure 6.8: Adjuvanticity of CNC-SIINFEKL or CNC+SIINFEKL vaccine formulations was assayed. A) Overview of vaccination strategy. Vaccines were formulated with 50 µg SIINFEKL bound or unbound to CNCs and prepared with 5 µg MPLA and 1:1 AddaVax. B) Body weight was measured in the 4 d after injection of the indicated formulations. C) Mice were bled 2 and 24 h after injection and secreted IL-6 in the serum was assayed. D) Antigen specific $CD8^+$ T cell production was analyzed by tetramer staining and E) intracellular IFN-γ production following restimulation with peptide for 48 h. F) Total immunoglobulin (Ig) production was assayed 28 d after vaccination by ELISA.

6.3 Conclusion and Future Directions.

Reported herein is the *in-vitro* and *in-vivo* biocompatibility studies of CNCs from various biosources and with different surface charges. The CNCs were isolated, functionalized, and characterized from three biosources and obtained from two large-scale producers to yield a series of CNCs with a variety of lengths, charges, and isolation conditions. A simple procedure to remove endotoxin from the CNC surface was developed to allow decontamination prior to their use in biological systems. This procedure was replicated with all CNC samples, and the HEK mTLR4 reporter cell line was used to validate the removal of endotoxin from all samples. Given the increased use of CNCs in biological systems, this low cost and rapid purification procedure should facilitate enhanced reproducibility and validity of results in later biological studies.

The biocompatibility of CNCs with different length, source, and charge was assessed *in-vitro* and *in-vivo*. Unfunctionalized CNCs prepared through hydrochloric acid hydrolysis were

observed to aggregate both in cell culture and in the tissue, resulting in acute systemic inflammation when injected subcutaneously in a murine model. Meanwhile, charged CNCs (achieved through surface modification to place amines, carboxylates, or sulfate half-ester moieties on the CNC surface) did not induce cytotoxicity or systemic inflammation *in-vitro* or *in-vivo*. These results suggest that CNCs functionalized with positive or negative charges are more appropriate for use in biomaterial tissue scaffold composites and hydrogels than unfunctionalized CNCs. Previous reports have indicated that CNCs remain in the tissue for several months after injection,[27] suggesting that these materials could behave as biocompatible depots for the delivery of materials, such as cancer neoantigen epitopes. To test the use of CNCs as antigen depot-based cancer immunotherapies, CNCs were functionalized with a model peptide, SIINFEKL, using periodate oxidation and subsequent reductive amination. Via the subcutaneous route of injection, these materials were unable to induce a productive anti-SIINFEKL immune response; however, additional work optimizing the formulation and chemistry could be used to prepare highly immunogenic CNC-based delivery systems. Understanding how CNCs interact with injection site tissues and biomacromolecular cargoes will be critical to the design principles for new biomaterial systems, such as tissue scaffolds or drug delivery systems, that utilize such nanomaterials.

While these results provide initial information on the biocompatibility of the CNCs studied, it will be critical to better understand how these materials interact with tissue both acutely and chronically. Future work must be conducted to evaluate long term interactions between CNCs and subcutaneous tissue, to study how different functionalization methods alter immune responses, to determine effects of CNCs administered through different routes of injection, and to learn if similar trends persist in higher order animals. Moreover, this work fails to address whether CNCs can effectively be used as an antigen depot for vaccination or cancer immunotherapy. Nonetheless, these results suggest that charged CNCs are compatible with biological tissue and have potential to be used in future biomedical applications.

6.4 Materials and Methods.

Materials and Mice. All chemicals unless otherwise noted were obtained from Sigma Aldrich and used without further purification. Sea tunicates (*Styela Clava*) were harvested from floating docks in Warwick Marina (Warwick, RI). Base-treated pulp from harvested *Miscantus x. Giganteus* was received as a generous gift from Aloterra Energy LLC (Conneaut, OH). Whatman Grade #1 filter paper and 2,2,6,6-Tetramethylpiperidine-1-oxyl (TEMPO) were obtained from Fisher Scientific. (±)-Epichlorohydrin was obtained from Alfa Aesar. Commercial scale *w*-CNC-$OSO_3^-{}_{(ls)}$ were purchased from Blue Goose Biorefineries Inc. (Saskatoon, SK),[50, 51] and *MxG*-CNC-$OH_{(ls)}$ were received as a generous gift from the Materials Engineering Research Facility (MERF) at Argonne National Laboratory (Lemont, IL), who have developed a commercially scalable procedure for the isolation of CNCs from *Miscantus x. Giganteus*.[52, 53] RAW 264.7, RAW-Blue NF-κB reporter, and HEK-Blue mTLR4 reporter cells were obtained from InvivoGen. The cells were cultured in Dulbecco's Modified Eagle's Medium (DMEM) supplemented with 10% (v/v) fetal bovine serum (FBS), 100 U/mL penicillin, 100 µg/mL streptomycin, and selective antibiotics and were maintained at 37 °C and 5% CO_2 atmosphere. All culture reagents were obtained from Thermo Fisher Scientific. For *in-vivo* experiments, six-week-old C57Bl/6J mice were obtained from Jackson Laboratories and acclimatized for 1 week prior to the onset of testing. Animals were housed under controlled light, temperature, and humidity conditions, supplied with food and water *ad libitum*, and monitored daily. All experiments were conducted with approval of the University of Chicago Institutional Animals Care and Use Committee, and animals were maintained in accordance with guidelines and regulations defined by the National Institutes of Health. Statistical analyses were performed using GraphPad Prism.

Isolation of Sulfated CNCs from Sea Tunicate Beak. Sea tunicates (*Styela Clava*) were cleaned and bleached following previously reported procedures.[46] Briefly, tunicates were gutted and their mantles collected. The mantles were washed in 5 wt.% aqueous potassium hydroxide at 80 ℃ for 8 h under continuous stirring. After rinsing with water, the mantles were washed again

with potassium hydroxide solution at 80 ℃ for 16 h. The cleaned mantles were rinsed until the rinse pH was neutral. Bleaching was performed by adding the cleaned mantles (500 g) into 3 L of distilled water (dH_2O) with 5 mL of glacial acetic acid and 10 mL of sodium hypochlorite (>4% chlorine). The temperature was increased to 60 ℃ and the mixture stirred for 1 h. Additional glacial acetic acid (5 mL) and sodium hypochlorite (10 mL) were added in 1 h intervals until the color of the mantles changed to white. Finally, the bleached tunicate mantles were rinsed with water and dried for further use. To hydrolyze the tunicate pulp and obtain crystalline CNCs, 5 g of dry bleached tunicate mantles were pulverized in 500 mL of dH_2O using a kitchen blender to yield a fine cellulose pulp. 500 mL of sulfuric acid (98%) was then slowly added over 60 min with vigorous stirring to a suspension of the tunicate pulp in an ice bath. After the acid addition was completed, the reaction was heated to 60 ℃ and reacted for 1.5 h. The acid hydrolysis was quenched by adding 1 L of cold water to the reaction, and the suspension was then filtered through a fritted glass filter. The crude product was washed with dH_2O until pH > 6. It was re-dispersed in dH_2O at 1 wt.% by ultrasonication and dialyzed against dH_2O for 4 days. Finally, the hydrolyzed tunicate CNCs were recovered by lyophilization to obtain a white aerogel, *t*-CNC-OSO_3^-.

Isolation of Sulfated and Unfunctionalized CNCs from *Miscanthus x Giganteus*. CNCs from *Miscanthus x. Giganteus* (MxG) were isolated from base-treated pulp using previously reported methods with minor changes.[47] MxG pulp was reacted four times with 4.0 L of 2 wt.% sodium hydroxide solution, once at 25 °C and three times at 100 °C for 24 h, filtering and washing with dH_2O after each step until the pH < 8. The resulting pulp was reacted twice with 4.0 L of 2 wt.% sodium hypochlorite (>4% chlorine) and 15 mL of glacial acetic acid for 2 h at 70 °C. The resulting solution was cooled, filtered, washed with dH_2O, and freeze dried to yield 150 g of cellulose fiber as a white pulp. To isolate *MxG*-CNC-OH, the bleached white pulp was hydrolyzed with hydrochloric acid. 3.0 L of 1 M HCl was added to 100 g of the white *MxG* pulp and heated to 75 °C for 15 h. To obtain *MxG*-CNC-OSO_3^-, the bleached white pulp was hydrolyzed with sulfuric acid. 250 mL of 30 wt.% H_2SO_4 was added to 10 g of the *MxG* pulp and heated to 50°C for 3 h.

The resulting mixtures were cooled and filtered through a fritted glass filter. The filtered products were washed with dH_2O until pH > 6, resuspended at 1 wt.%, dialyzed for 72 h against dH_2O, and freeze-dried to yield CNCs (*MxG*-CNC-OH and *MxG*-CNC-OSO_3^-) as white aerogels.

Isolation of Sulfated CNCs from Cotton filter paper. CNCs from Whatman #1 filter paper were isolated using previously reported methods with minor changes.[48] 5.2 g filter paper was initially suspended in 250 mL water and ground into an aqueous pulp using a kitchen blender. The pulp mixture was then placed in an ice bath, and 140 mL 98 wt.% sulfuric acid was added dropwise such that the temperature was held below 20 °C. After addition was complete, the ice bath was removed and the mixture was reacted at 50 °C. After 3.5 h, the reaction was stopped by diluting the mixture with 3.0 L dH_2O. The resulting suspension was filtered and washed using a fritted glass filter until the pH > 6.0. The product was resuspended in dH_2O at 1 wt.%, dialyzed against dH_2O for 72 h, and freeze-dried to yield cotton CNCs as a white aerogel, *c*-CNC-OSO_3^-.

TEMPO Oxidation of CNCs. CNCs from tunicate, *MxG*, and cotton were treated with TEMPO to oxidize the C6 alcohol to a carboxylic acid.[49] As an example, *MxG*-CNC-OH (4.14 g) was dispersed by sonication in 500 mL dH_2O for 30 min. TEMPO (0.412 g) and NaBr (4.02 g) were then added and stirred until dissolved. Then, 10 wt.% of NaOCl (>4% chlorine) was added, and the mixture was stirred for 4.5 h at 25 °C in the dark while holding pH at 10–11 with 5 M NaOH. After the reaction was completed, NaCl (17.0 g) was added and stirred for 10 min. 2 M HCl was added to adjust the pH < 7, and the mixture was filtered through a fine-pore fritted glass filter to yield a crude solid. The solid was resuspended at 1 wt.% in dH_2O and dialyzed against dH_2O for 72 h. The dialyzed solution was freeze-dried to yield a white aerogel, *MxG*-CNC-COOH. This procedure was repeated using tunicate (*t*-CNC-OSO_3^-) and cotton CNCs (*c*-CNC-OSO_3^-) to obtain *t*-CNC-COOH and *c*-CNC-COOH, respectively.

Amine Functionalization of CNCs. CNCs from tunicate, *MxG*, and cotton were functionalized with amines using epichlorohydrin and ammonia according to a previously reported method.[26] As an example, *MxG*-CNC-OH (128 mg) was dispersed in 200 mL water by

ultrasonication for 30 min. It was then reacted with epichlorohydrin (6 mmol/g CNC) at 60 °C for 2 h in the presence of 1 M NaOH to introduce an epoxy moiety to the surface of the CNCs. The product was dialyzed overnight until the pH was <12. The dialyzed product was then adjusted to pH of 12, and 1 mL of 29.4% aqueous NH_4OH was added to the CNCs and reacted for 2 h at 60 °C to aminate the CNCs. The reaction was then cooled and filtered through a fine-pore fritted glass filter. The crude product was dispersed by ultrasonication at 1 wt.% in dH_2O, dialyzed against dH_2O for 72 h, and freeze-dried to obtain a powdery white product, *MxG*-CNC-NH_2. This procedure was repeated using sulfated tunicate (*t*-CNC-OSO_3^-) and cotton CNCs (*c*-CNC-OSO_3^-) to obtain *t*-CNC-NH_2 and *c*-CNC-NH_2, respectively.

FT-IR Spectroscopy. Infrared spectra of unmodified and modified CNCs were recorded on a Shimadzu IR Tracer Fourier Transform-Infrared Spectrometer in attenuated total reflection (ATR) mode. Freeze-dried samples were placed directly onto the crystal for analysis.

Conductometric Titration. Dispersed solutions of CNCs were titrated using NaOH to quantify carboxylate, sulfate half-ester, or aldehyde density on the CNCs. About 30 mg CNCs were dispersed in 50 mL dH_2O. In the case of CNC-COOH samples, the pH was adjusted to pH < 3 using 10 M HCl, and 0.01 M NaOH was added incrementally until pH > 10. In the case of CNC-OSO_3^-, samples, samples were immediately titrated with 0.01 M NaOH in 50 µL increments until the conductivity began to increase. In both cases, the pH and conductivity were recorded at each increment. The quantity of NaOH needed to titrate the carboxylic acid moiteties (pKa ≈ 4.5) was determined by noting the region in the titration curve where conductivity was unchanged and used to quantify the presence of carboxylic acids.[80] The quantity of NaOH needed to titrate the sulfate half-ester moiteties (pKa ≈ 2.5) was determined by noting the initial region at which the conductivity decreased as sulfates were titrated prior to increasing on account of NaOH addition.[81] In the case of aldehydes, aldehyde groups were reacted with hydroxylamine, and an oxime titration was subsequently conducted to quantify the presence of oxime groups as reported previously.[73, 82] 0.1 g DA-CNC and 0.5 g $NH_2OH{\cdot}HCl$ were dispersed into 50 mL of dH_2O by

sonication for 30 min (25% power, 3 s on/off cycle). The pH was then adjusted to 4.5 with 10 M HCl, and the mixture was then titrated using 0.1 M NaOH to determine presence of aldehydes.

Zeta Potential. Electrophoretic light scattering (ELS) was performed to determine zeta potential using a Wyatt Möbiuζ DLS/ELS instrument. CNC samples were dispersed at 1 mg/mL by brief ultrasonication in DI water, and measurements were performed immediately after at 25 °C using a laser wavelength of 532 nm. Scattered light was collected at a fixed angle of 163.5°, and each measurement was collected as the average of 4-5 scans. Correlation functions and zeta potential calculations were analyzed using Wyatt Dynamics software.

Thermogravimetric Analysis. The thermal stability of CNC samples was investigated using a TA Instruments Q500 thermogravimetric analyzer (TGA). About 3 mg of each sample were heated from ambient temperature to 110 °C, held between 110-120 °C for 10 min to remove residual water, and then heated to 600 °C at a heating rate of 10-15 °C/min under a nitrogen atmosphere. The results were analyzed using TRIOS (TA Instruments).

NMR Spectroscopy. CNCs were dispersed at 5 mg/mL in D2O (~5 mL) and sonicated for 15 min to disperse samples and solubilize any trace components (3 s on/off cycles at 25% power). The CNC dispersions were then centrifugated for 30 min at 10,000 G to precipitate the CNCs, and 1 mL supernatant was collected, passed through a 0.22 µm pore-diameter filter, mixed with 10 µL of a 100 mg/mL maleic acid stock (in D_2O) to achieve a concentration of 1 mg/mL, and analyzed via ^{1}H-NMR. NMRs were conducted at 400 MHz (D1 = 42 s) on a Bruker DRX instrument equipped with a BBO probe using Topspin 1.3. Data were plotted with MestReNova.

Imaging. CNC-OSO_3^-, CNC-COOH, and CNC-NH_2 samples were imaged using atomic force microscopy (AFM). 0.01 wt.% of CNCs were dispersed by brief ultrasonication in dH_2O and then prepared on an exfoliated mica substrate. The mica was coated with 50 µL poly-*L*-lysine for 2 min and then washed with dH_2O. 50 µL of CNC solution was then loaded onto the mica and allowed to settle for 2 min before being washed with dH_2O. Samples were dried overnight and imaged with a Cypher ES Environmental AFM (Asylum Research) using FS-1500 probes (Asylum

Research). The length of CNCs was analyzed using height mode with Gwyddion for SPM (Czech Metrology Institute). On account of the low dispersibility of uncharged CNCs in water resulting in large aggregates during AFM imaging, *MxG*-CNC-$OH_{(ls)}$ and *MxG*-CNC-OH samples were instead imaged by transmission electron microscopy (TEM). For TEM imaging, 1.0 mg/mL CNC solutions were dispersed by brief ultrasonication in dH_2O and then passed through a 10 μm pore-diameter filter to remove larger aggregates. About 10 μL of the filtered solution was drop cast on an ultrathin holey carbon-coated copper grid and stained with 2 wt.% uranyl acetate. The stained sample was immediately imaged using a FEI Technai F30 TEM (TSS Microscopy).

Wide Angle X-Ray Scattering. To assess crystallinity of CNC samples, Wide Angle X-ray Scattering (WAXS) was conducted on beamline 12-ID-B using the Advanced Photon Source at Argonne National Laboratory (Lemont, IL) with a Pilatus 300k detector (Dectris) or on a laboratory SAXSLAB GANESHA 300 XL system. On beamline 12-ID-B, samples were irradiated at a voltage of 13.3 KeV for 0.1 s. On the GANESHA system, samples were irradiated using a Cu Kα source (λ = 0.154 nm) at a voltage of 40 kV for 30 min. CNCs were packed in a washer and held in place with Kapton tape. Samples were mounted in a vacuum chamber perpendicular to the collimated beam. Crystallinity Index was determined by the peak deconvolution method after subtracting the Kapton background, and peaks were fit in MATLAB to a Gaussian distribution function at the idealized diffraction peaks for cellulose 1β reported by A.D. French.[54, 83]

WAXS Deconvolution. WAXS data obtained for each of the CNC samples were deconvoluted to a five-term Gaussian fit function (gauss5 function in MATLAB) after subtracting the Kapton tape background, where the Gaussian functions describe the major cellulose 1β peaks of 101, 10$\bar{1}$, 021, and 002 as well as an amorphous background peak. The peaks were centered at the following 2-theta angles (± tolerance), where the location of the amorphous peak was constrained between 18-21° (based on the amorphous cellulose spectra described previously[54]):

(1,0,1): 14.9° ± 0.2°

(1,0,$\bar{1}$): 16.5° ± 0.2°

(0,2,1): 20.4° ± 0.2°

(0,0,2): 22.7° ± 0.2°

Amorphous: 19.5° ± 1.5°

In some cases, the tolerance was reduced to better match the fitted curve to the raw spectra. The bandwidth of peaks was estimated according to Scherrer's equation **(2)** in the Gaussian model, where τ is the width of the CNCs based on AFM imaging, λ is wavelength of incident X-rays, and θ is the Bragg angle used to determine the peak width at full width, half maximum intensity (β).[84] Finally, the amplitudes were modulated in an iterative fashion to best match the fitted curve to the raw spectra, and the crystallinity index was calculated by dividing the crystalline area (the area under the 101, 10$\bar{1}$, 021, and 002 peaks) divided by the total area of the fitted Gaussian function.

(2) $$\beta = \frac{0.9\lambda}{\tau \cos\theta}$$

HEK mTLR4 Assay. HEK mTLR4 cells are used as a semiquantitative readout of endotoxin contamination.[59] CNCs were first washed 3 times with endotoxin-free water. For each wash, CNCs samples were dispersed at approximately 1,000 µg/mL in water, ultrasonicated for 5 min (3 s on/off cycles at 25% power), and subjected to centrifugation at 10,000 G to precipitate the CNCs. The solutions were decanted and re-dispersed after each wash and freeze-dried at the end of cleaning. CNC concentrations of 10-100 µg/mL were used to determine contamination of CNC samples. Particle suspensions of 100 and 1,000 µg/mL were prepared in endotoxin-free water, and 20 µL of each suspension was plated in triplicate in a 96 well plate. LPS-EK (InvivoGen) with a known endotoxin content was used as a positive control. HEK Blue detection media (InvivoGen) was reconstituted in 50 mL endotoxin-free water, heated to 37°C for 30 min, and passed through a 0.22 µm pore-diameter filter. HEK Blue mTLR4 cells were passaged and plated in the 96 well plate at 25,000 cells/well in 180 µL HEK Blue detection media. Cells were incubated with the CNCs at 37 °C and 5% CO_2 overnight. The plate was analyzed after 12 h using a Multiskan FC plate reader (Thermo Scientific), and absorbance was measured at 620 nm.

MTT Assay. RAW-Blue cells were plated in a 96 well plate at 25,000 cells/well in 200 µL DMEM containing 10% HI-FBS and selective antibiotics. Cells were incubated at 37 °C and 5% CO_2 for 24 h. Then, particle suspensions from 100 to 1,000 µg/mL were prepared in endotoxin free water, diluted 1:10 in culture media, and added to the cells. 10% DMSO was used as a positive control. After 24 h, cell culture media was replaced with 50 µL of 3-(4,5-dimethylthiazol-2-yl)-2,5-diphenyl tetrazolium bromide (MTT) reagent (1 mg/mL) and 50 µL of FBS-free media. After incubation for 3 h, formazan crystals were dissolved in 150 µL of a 10% w/v sodium dodecyl sulfate and 0.01 M HCl solution, protected from light, and incubated for 30 min. The absorbance was measured by a Multiskan FC plate reader (Thermo Scientific) at 590 nm.

LDH Assay. RAW-Blue cells were plated in a 96 well plate at 50,000 cells/well in 180 µL DMEM containing 10% HI-FBS and selective antibiotics. Particle suspensions of 1,000 µg/mL were prepared in endotoxin free water, and 20 µL of each treatment was added in triplicate to the cells. After incubation for 20 h, 100 µL supernatant was collected and assayed using a LDH Cytooxicity Assay Kit (Cayman Chemical) according to the manufacturer's procedure. The absorbance was measured by a Multiskan FC plate reader (Thermo Scientific) at 490 nm.

RAW-Blue NF-κB Assay. RAW-Blue cells were passaged and plated in a 96 well plate at 25,000 cells/well in 200 µL DMEM containing 10% HI-FBS and selective antibiotics. Cells were incubated at 37 °C and 5% CO_2 for 24 h. Then, particle suspensions from 100 to 1,000 µg/mL were prepared in endotoxin-free water, diluted 1:10 in DMEM + 10% HI-FBS, and added to the cells. LPS-EK (InvivoGen) was used as a positive control. 24 h after the final addition, 20 µL of the cell supernatant was placed in 180 µL freshly prepared QuantiBlue (InvivoGen) solution and incubated at 37 °C and 5% CO_2 for up to 4 h. The plate was analyzed every hour using a Multiskan FC plate reader (Thermo Scientific) and absorbance was measured at 620 nm.

BrdU Assay. RAW macrophages were plated in a 96 well plate at 25,000 cells/well in 180 µL DMEM containing 10% HI-FBS and selective antibiotics and incubated undisturbed overnight. Particle suspensions of 100 or 1,000 µg/mL were prepared in endotoxin free water, and 20 µL of

each treatment was added in triplicate to the cells. After incubation for 12 h, 20 µL of BrdU reagent was added to each well and incubated for an additional 12 h. Cells were subsequently fixed and BrdU incorporation was assayed using BrdU Cell Proliferation Colorimetric ELISA Kit (Abcam) according to the manufacturer's procedure. The absorbance was measured by a Multiskan FC plate reader (Thermo Scientific) at 450 nm.

Cytokine Assays. RAW-Blue cells were plated in a 96 well plate at 50,000 cells/well in 180 µL DMEM containing 10% HI-FBS and selective antibiotics and incubated undisturbed overnight. Particle suspensions 1,000 µg/mL were prepared in endotoxin free water, and 20 µL of each treatment was added in triplicate to the cells. After incubation for 24 h, supernatants were removed, diluted 1:1 with Assay Diluent, and analyzed using Mouse TNF-α and IL-6 ELISA MAX Deluxe kits (BioLegend) according to the manufacturer's procedure. The absorbance was measured by a Multiskan FC plate reader (Thermo Scientific) at 450 nm.

***In-vivo* biocompatibility experiment.** To assay systemic inflammation incurred by the CNCs, CNCs were injected subcutaneously and assayed acute cytokine production, spleen mass, and inflammation at the site of injection. 0.1% or 0.5% CNC solutions were cleaned using the aforementioned procedure and dispersed in endotoxin-free water. To ensure that all CNCs were injected at the same location, mice were anesthetized under 2-2.5% isoflurane and 2L/min oxygen flow. Mice were then injected in the left flank with the appropriate CNC solution (300 µL of 0.1% or 0.5% CNC/mouse, n=3-5/group). Mice were bled via facial vein 1 or 24 h after injection. Serum was isolated by ultracentrifugation, and cytokine production was analyzed using CBA Mouse Inflammation Cytokine Kit (BD Bioscience) according to the manufacturer's procedure. Flow cytometry was conducted using a Novocyte ACEA (Agilent) flow cytometer, and data was analyzed using GraphPad Prism. To assess tissue compatibility of the CNCs, mice were sacrificed after 2 or 30 d. The subcutaneous tissue was imaged and then collected for histological analysis. Spleens were also collected and weighed as a measure of systemic inflammation. Subcutaneous tissue was immediately fixed in 10% neutral buffered formalin for 36 h, dehydrated

in ethanol, and embedded in paraffin. Tissues were sectioned with a microtome, stained with hematoxylin and eosin, and imaged using an Axio Observer 7 microscope (Carl Zeiss AG) with an Axiocam 506 color camera (Carl Zeiss AG). Based on the images, inflammatory response was assessed qualitatively with the assistance of a histopathologist.

Periodate Oxidation of CNCs. Periodate oxidation of *MxG*-CNC-OH was conducted as described previously.[72, 74] In short, CNCs were dispersed at 1.0 % (wt/vol) in a solution of 10% acetic acid in water by probe sonication for 30 min (25% power, 3 s on/off cycles). The resultant suspension was added to a round bottom flask with a stir bar and heated with rapid stirring to 45 °C. Sodium periodate (10 eq relative to total number of glucose monomers) was then added, and the reaction was stirred in the dark for 5 h. The solution was then stopped, and crude DA-CNCs were collected by filtration through a fine fritted glass filter. DA-CNCs were then resuspended by brief sonication in dH_2O (1.0 % wt/vol) and dialyzed (3.5 kg/mol molecular weight cut-off) for 3 d against dH_2O, changing the dialysate twice daily, to obtain purified DA-CNCs.

Solid Phase Peptide Synthesis. SIINFEKL was prepared on a Liberty Blue automated peptide synthesizer using standard Fmoc solid phase synthesis conditions with DIC/Oxyma activation on a 0.1 mmol scale. Rink amide resin (100-200 mesh) was used as the solid support. After synthesis, the peptide was deprotected using 95:2.5:2.5 (vol/vol) TFA : Triisopropylsilane : Water for 3 h. Following deprotection, the peptide was precipitated in cold diethyl ether and dried under reduced pressure. The crude peptides were then purified using preparative HPLC on a Gilson Gx271 system equipped with a 150 x 21.2 mm Luna PREP-C18(2) 100Å column using a gradient elution of 5-60% acetonitrile in water (+0.1% TFA). Product containing fractions were pooled, freeze dried, characterized using ESI-MS, and stored at -20 °C until use.

Peptide Modification of CNCs. DA-CNC were functionalized with SIINFEKL using reductive amination. DA-CNCs with a known aldehyde content were dispersed in a pH=6 MES buffer solution (10 mM) in water by probe sonication (10 min, 25% power, 3 s on/off cycles). Then, a stir bar was added, and with rapid stirring, 10 eq SIINFEKL (relative to aldehyde) was added to

the reaction mixture. The reaction was warmed to 37 °C and stirred for 48 h. After 48 h, 2.5 eq $NaBH_3CN$ was added over 5 min and the reaction stirred for 6 h longer. The crude product was added to 3.5 kg/mol molecular weight cut-off dialysis tubing and dialyzed against 4 L of dH_2O for one week, changing dialysate twice daily, to obtain purified *MxG*-CNC-SIINFEKL.

Bicinchoninic Acid (BCA) Assay. Peptide grafting density was analyzed using Pierce BCA Protein Assay Kit (Thermo Scientific). MxG-CNC-SIINFEKL was dispersed by sonication at 1 mg/mL in dH_2O. To account for different amino acid content between the provided albumin standards and SIINFEKL, solutions of SIINFEKL (1,000 – 25 µg/mL) were prepared in dH_2O and used to develop a standard curve for accurate determination of grafting efficiency. After incubating MxG-CNC-SIINFEKL and standards with the assay reagent for 30 min, absorbance was measured using a Multiskan FC plate reader (Thermo Scientific) at 562 nm.

***In-vivo* Vaccination Experiment.** Vaccine formulations comprised of 50 µg of SIINFEKL bound or unbound to dose-matched quantity of *MxG*-CNC-OH along with 5 µg of MPLA-SM (InvivoGen) and 50% (vol/vol) AddaVax (InvivoGen) were prepared in PBS. Mice were lightly anesthetized and then injected using an 18G needle in the left flank. Mice were bled after 1 and 24 h, and cytokine production was analyzed in the sera using CBA Mouse Inflammation Cytokine Kit (BD Bioscience) according to the manufacturer's procedure. Flow cytometry was conducted using Novocyte ACEA (Agilent) flow cytometer, and data was analyzed using GraphPad Prism. Mice were boosted with an equivalent formulation 14 d, bled at 28 d, and sacrificed at 28 d. Serum from the 28 d bleed was assayed for OVA-specific antibody production using anti-ovalbumin (Gal d 2) IgG (total Ig's A+G+M) ELISA Kit (Alpha Diagnostic International) according to the manufacturer's protocol. Upon sacrifice, spleens were harvested, digested into a single cell suspension, and plated at 5 x 10^6 cells/well in a 96 well plate. Antigen specific $CD8^+$ T cell production was assayed using MHC-I tetramer staining and intracellular cytokine staining. For tetramer staining, cells were incubated with anti-CD16/32 (Fc receptor blocking antibody, Biolegend, clone 93) (1.0 µg/well) for 15 min at 4 °C. Splenocytes were washed with FACS buffer

(PBS with 2% FBS), resuspended, and stained with APC MHC-Class I tetramers loaded with SIINFEKL (Tetramer Shop) at 37 °C in the dark. After 15 mins, FITC anti-CD8 (BioLegend, clone 53-6.7) was added and incubated for 30 min longer at 4 °C in the dark. Splenocytes were washed, resuspended in FACS buffer, and antigen-specific T-cell production was assayed using a Novocyte ACEA (Agilent) flow cytometer. For intracellular cytokine staining, cells were incubated with SIINFEKL (20 μg/mL) for 48 h. In the last 8 h of incubation, GolgiPlug (BD Biosciences) was added to block intracellular cytokine transport. Following incubation, cells were washed, fixed and permeabilized with Cytofix/Cytoperm kit (BD Biosciences) according to the manufacturer's instructions, and subsequently stained with Alexa Fluor 647 anti-mouse IFN-γ (BioLegend, clone XMG1.2) and FITC anti-CD8 (BioLegend, clone 53-6.7) for 1 h at 4 °C in the dark. Splenocytes were washed, resuspended in FACS buffer, and antigen-specific T-cell production was assayed using a Novocyte ACEA (Agilent) flow cytometer. Data for flow cytometry experiments were analyzed in FlowJo.

6.5 Supplementary Information.

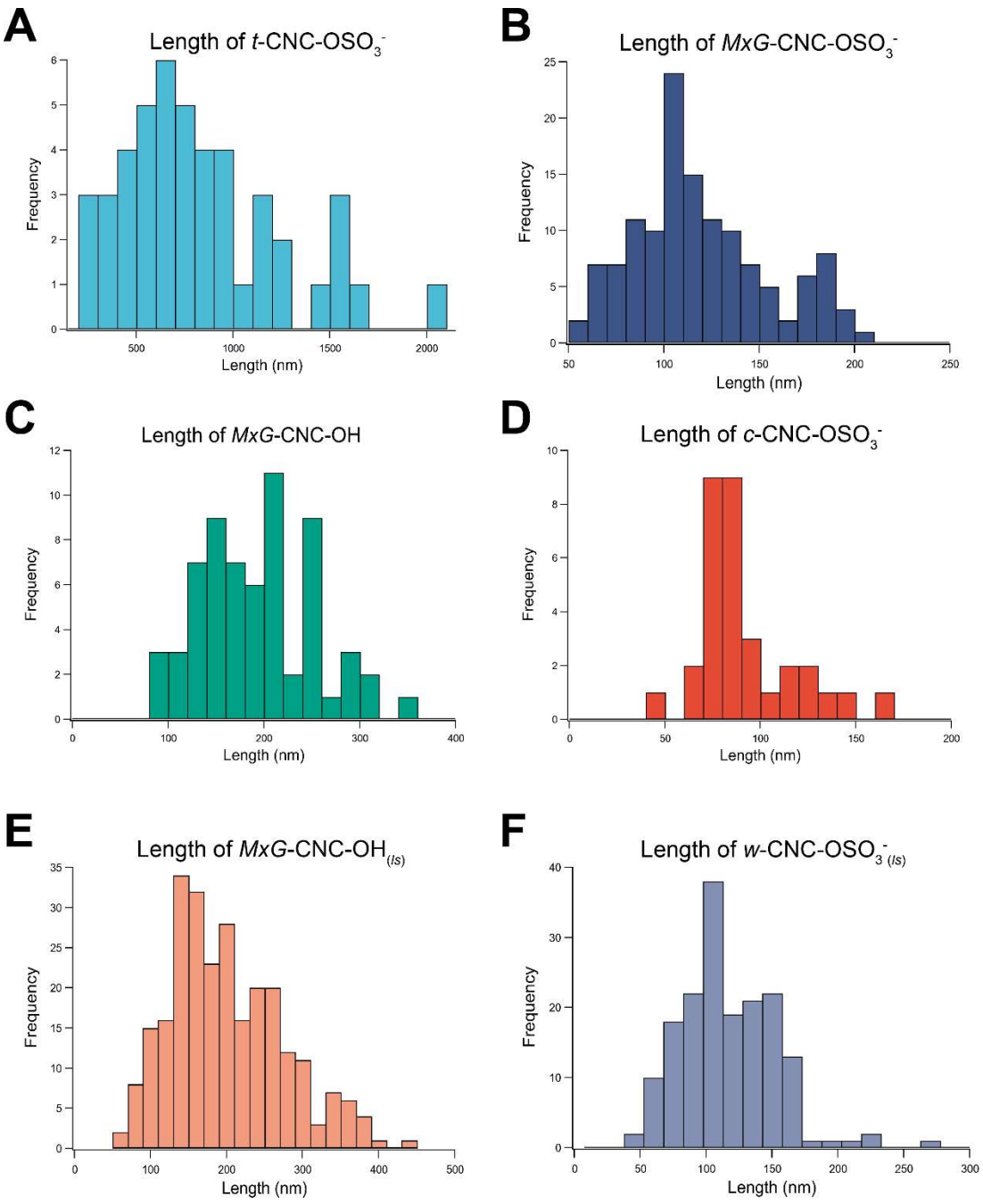

Figure S6.1: Length distributions of CNC samples obtained from each biosource or large-scale production. Samples were imaged using AFM (or TEM for uncharged CNC-OH samples), and the length of individual nanocrystals was evaluated using Gwyddion for SPM (Czech Metrology Institute). At least 50 CNCs were analyzed to determine the length distribution of CNCs.

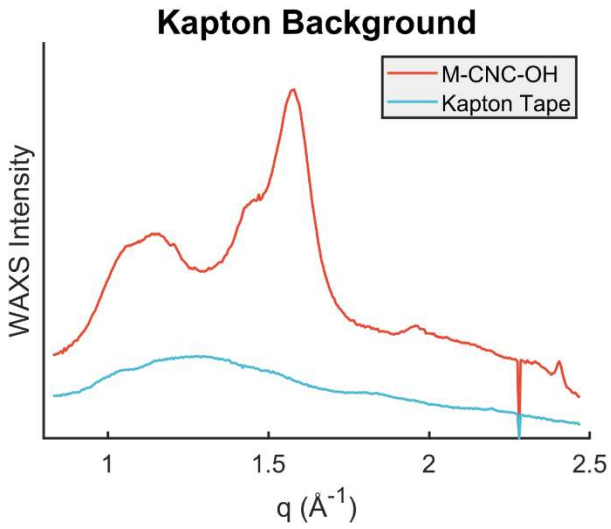

Figure S6.2: Background determination for WAXS measurements. WAXS was conducted by securing CNC samples in a plastic washer using Kapton tape, and the Kapton background spectrum was subtracted prior to determining the crystallinity index of CNC samples (as shown in **Figures S6.3-S6.7**). Here, a representative spectrum of *MxG*-CNC-OH (prior to background subtraction) and Kapton spectrum are shown for reference.

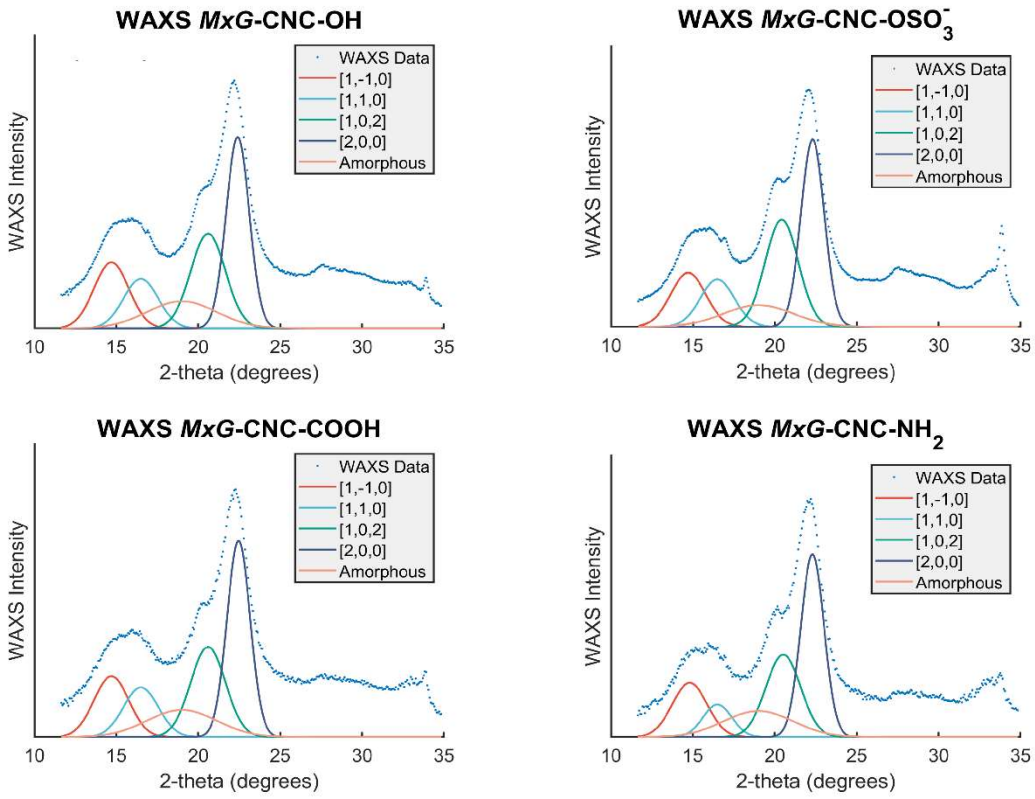

Functionalization	CI
MxG-CNC-OH	86%
MxG-CNC-COOH	86%
MxG-CNC-NH_2	85%
MxG-CNC-OSO_3^-	88%

Figure S6.3: WAXS diffraction patterns of *MxG* CNC samples. The spectra show peak deconvolution used to determine the crystallinity index (CI) of samples. The crystallinity index was calculated by dividing the amorphous peak area by the total area of the fitted function.

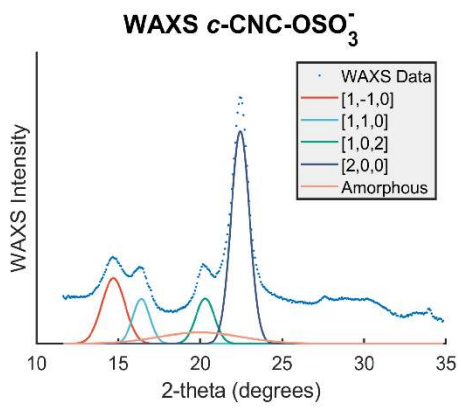

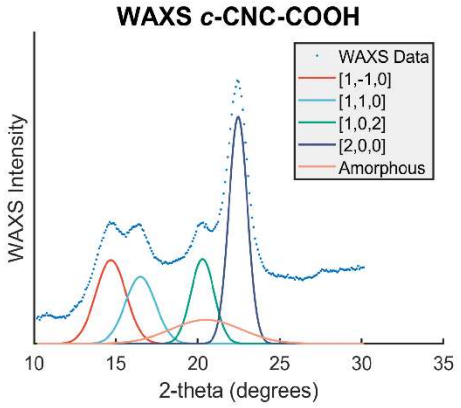

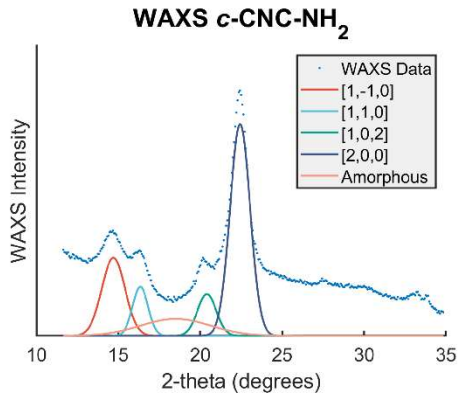

Functionalization	CI
c-CNC-OSO_3^-	88%
c-CNC-COOH	87%
c-CNC-NH_2	87%

Figure S6.4: WAXS diffraction patterns of cotton CNC samples. The spectra show peak deconvolution used to determine the crystallinity index (CI) of samples. The crystallinity index was calculated by dividing the amorphous peak area by the total area of the fitted function.

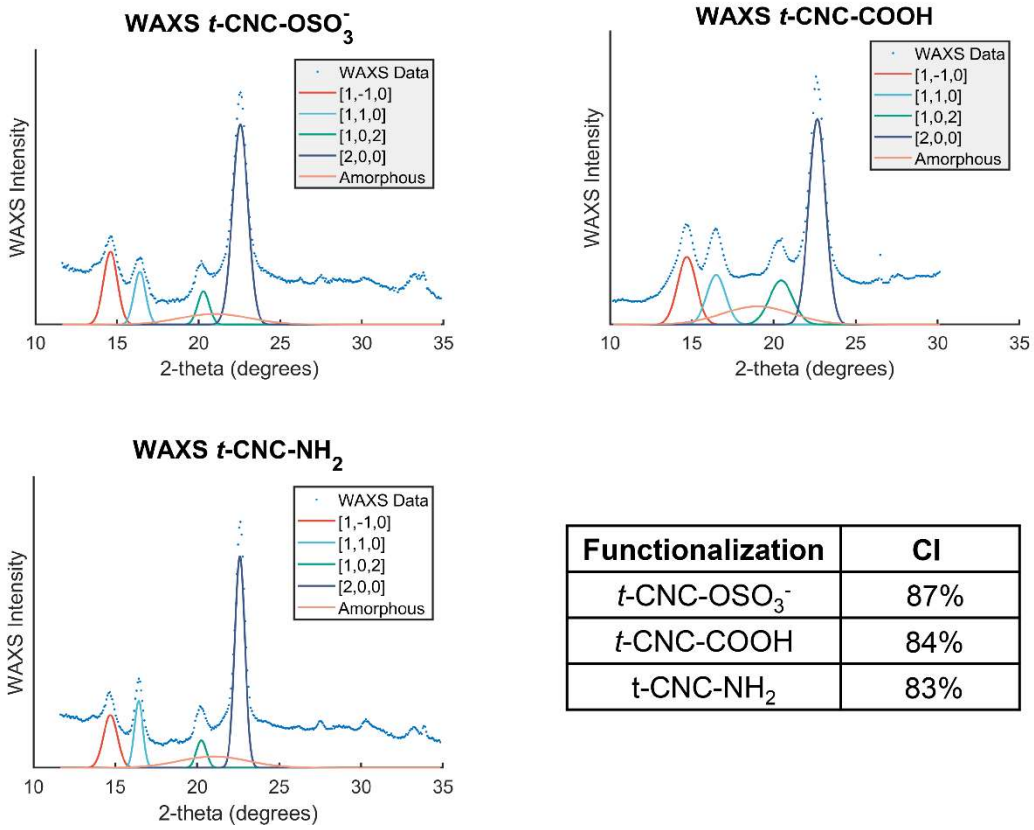

Functionalization	CI
t-CNC-OSO_3^-	87%
t-CNC-COOH	84%
t-CNC-NH_2	83%

Figure S6.5: WAXS diffraction patterns of tunicate CNC samples. The spectra show peak deconvolution used to determine the crystallinity index (CI) of samples. The crystallinity index was calculated by dividing the amorphous peak area by the total area of the fitted function.

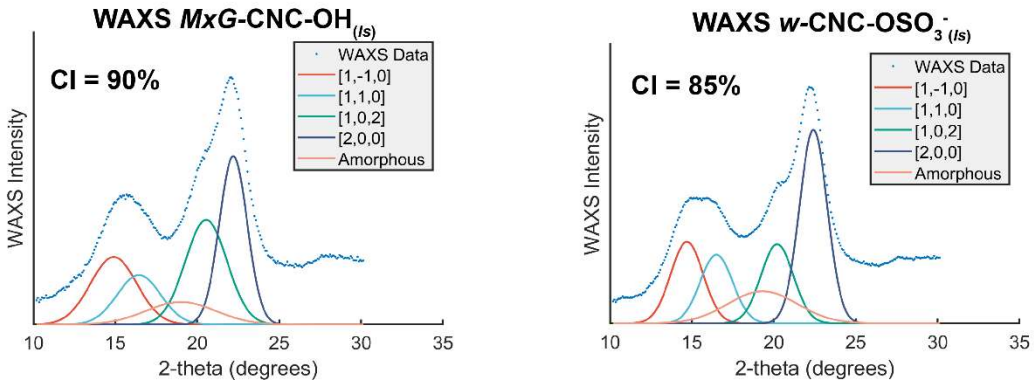

Figure S6.6: WAXS diffraction patterns of commercially sourced CNC samples. The spectra show peak deconvolution used to determine the crystallinity index (C.I.) of samples. The crystallinity index was calculated by dividing the amorphous peak area by the total area of the fitted function.

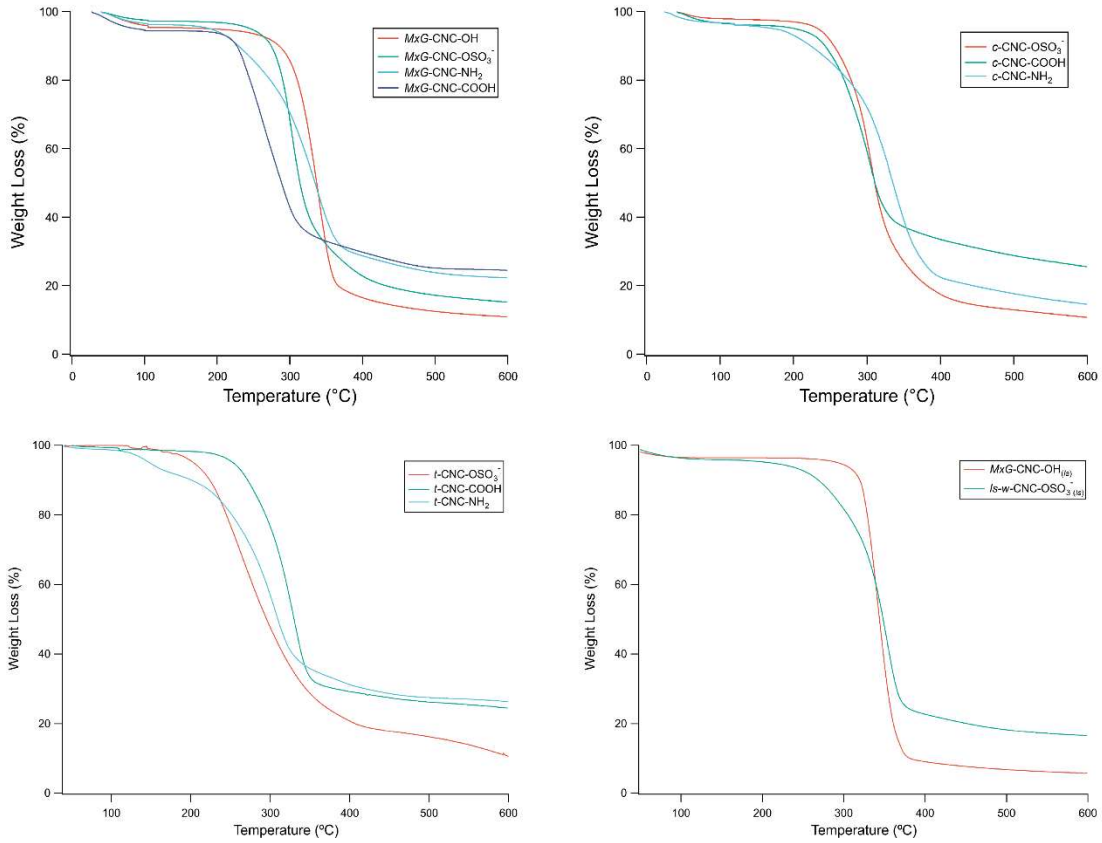

Figure S6.7: Thermogravimetric analysis (TGA) of CNCs. CNCs with different source and functionality were heated at 10-15 °C/min, and weight loss due to thermal decomposition was measured. Sulfated CNCs have a characteristic decrease in the decomposition temperature relative to unfunctionalized CNCs. Amine-functionalized CNCs have a characteristic small amount of decomposition between 200-300 °C. TEMPO-oxidized CNCs have a characteristic increase in residual mass relative to other samples.

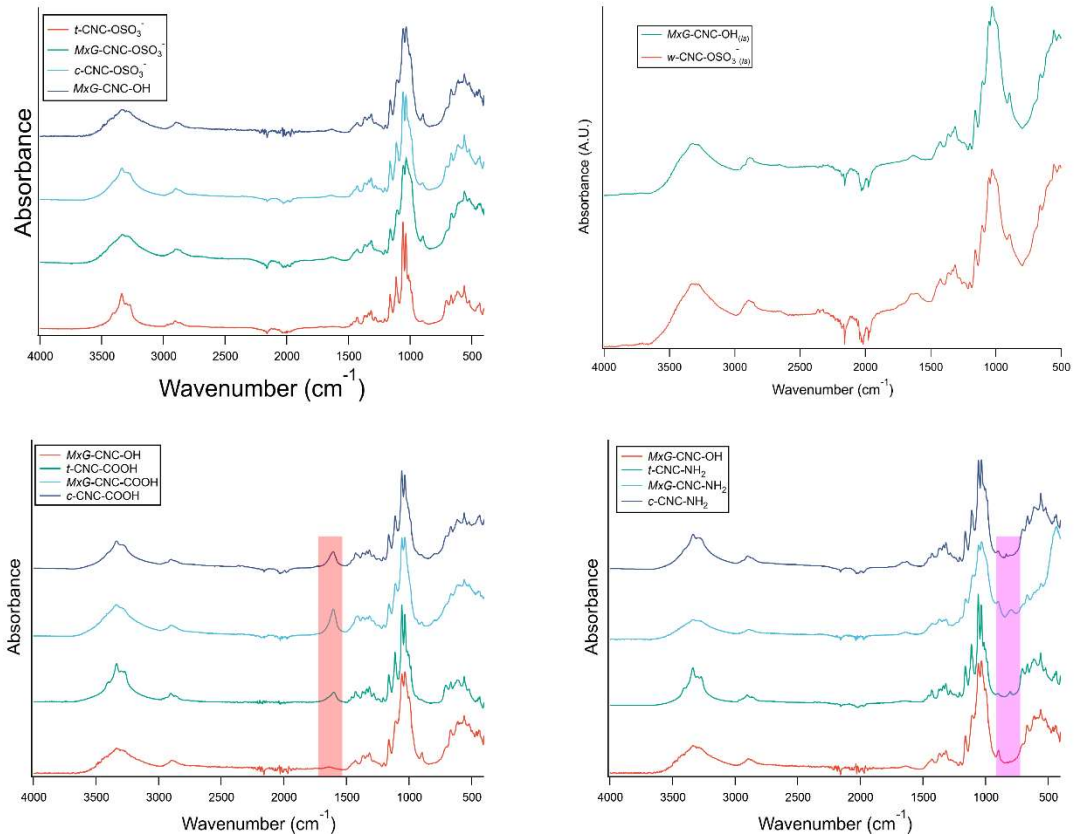

Figure S 6.8: FT-IR of dried CNC samples. FT-IR was conducted to assess chemical groups present in isolated and functionalized materials. TEMPO-oxidized CNCs (CNC-COOH) have a characteristic strong carboxylate peak at ~1600 cm^{-1} (red) while amine-functionalized CNCs (CNC-NH_2) have a characteristic weak amine wag peak at ~800 cm^{-1} (pink).

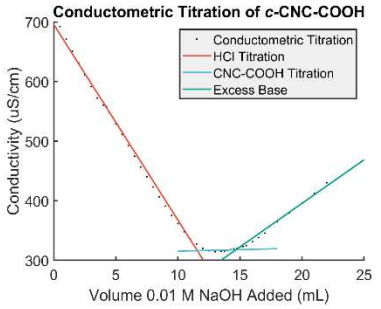

Mass CNCs	20.0 mg
Intercept 1	17.08 mL
Intercept 2	18.91 mL
[CNC-COOH]	920 mmol/kg

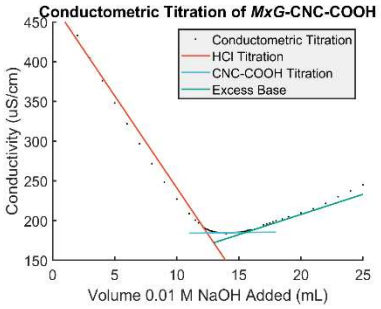

Mass CNCs	30.0 mg
Intercept 1	12.45 mL
Intercept 2	15.53 mL
[CNC-COOH]	1030 mmol/kg

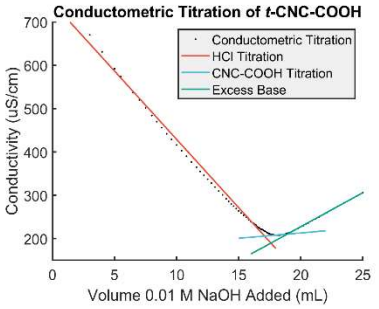

Mass CNCs	23.9 mg
Intercept 1	11.56 mL
Intercept 2	14.68 mL
[CNC-COOH]	1300 mmol/kg

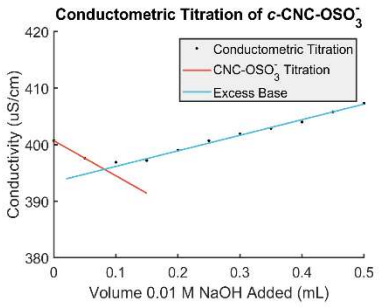

Mass CNCs	44.0 mg
Intercept	0.0815 mL
[CNC-OSO_3^-]	27.2 mmol/kg

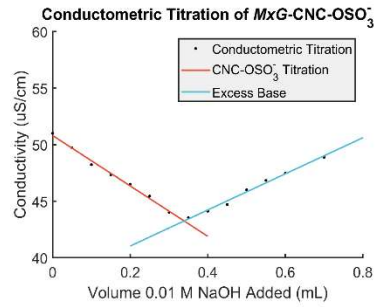

Mass CNCs	44.4 mg
Intercept	0.3390 mL
[CNC-OSO_3^-]	113 mmol/kg

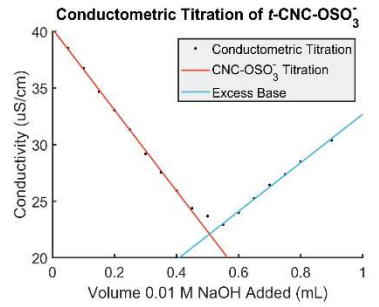

Mass CNCs	30.0 mg
Intercept	0.5061 mL
[CNC-OSO_3^-]	169 mmol/kg

Figure S6.9: Acid-base titrations of CNCs. CNCs containing carboxylic acid or sulfate half-ester modifications were acidified and subsequently titrated using 0.01 M NaOH. Conductivity was assayed throughout the titration to determine and quantify the presence of carboxylate or sulfate half-ester moieties on the CNCs. The region in which conductivity does not change corresponds to titration of carboxylic acids, while the initial decrease in conductivity corresponds to the titration of sulfate half-esters.

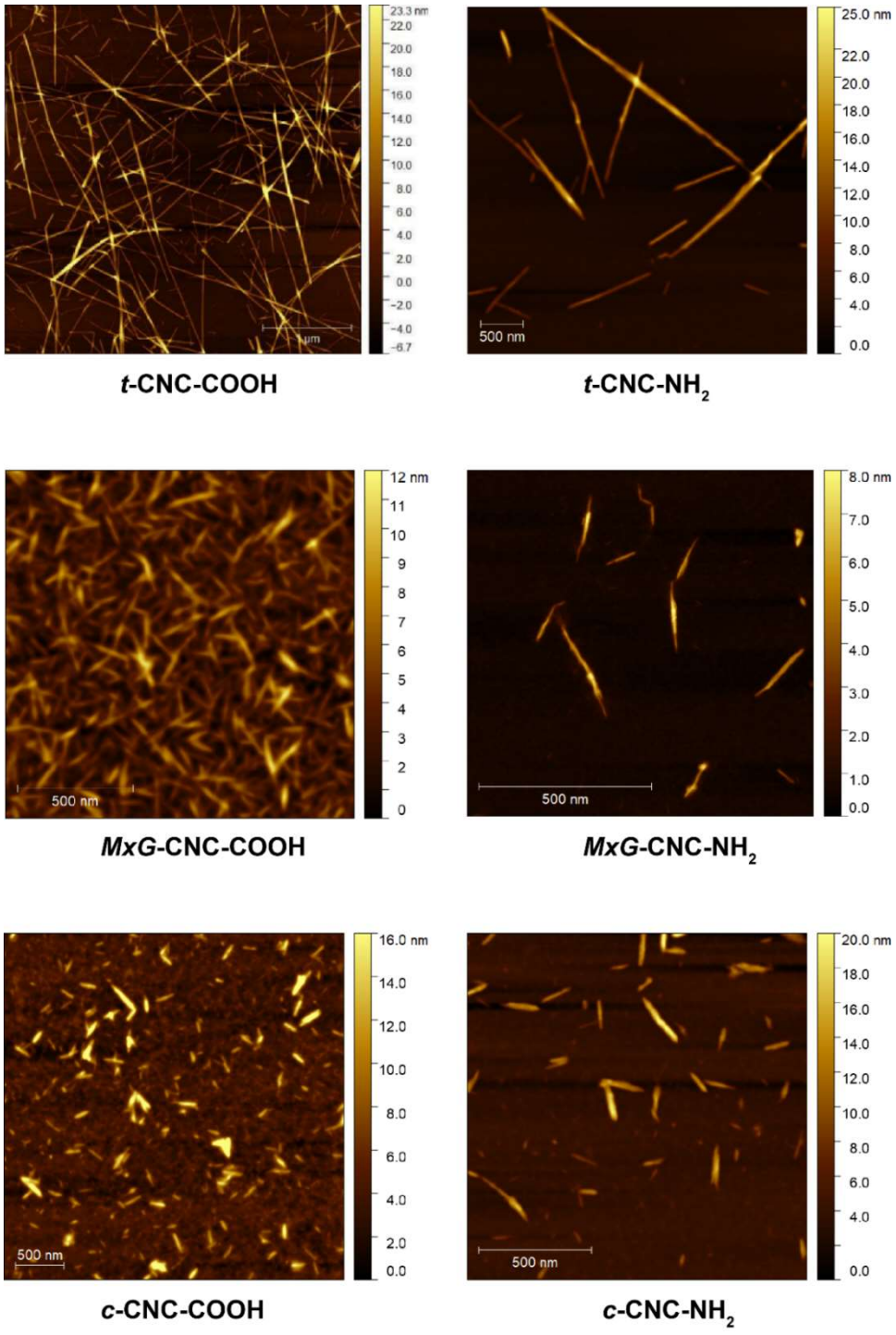

Figure S6.10: AFM images of carboxylic acid and amine-functionalized CNC for morphological analysis. For imaging, samples were drop-casted from a dilute aqueous solution onto a poly-lysine coated mica substrate. The images confirm that structural integrity is not altered via any of the functionalization reactions reported herein.

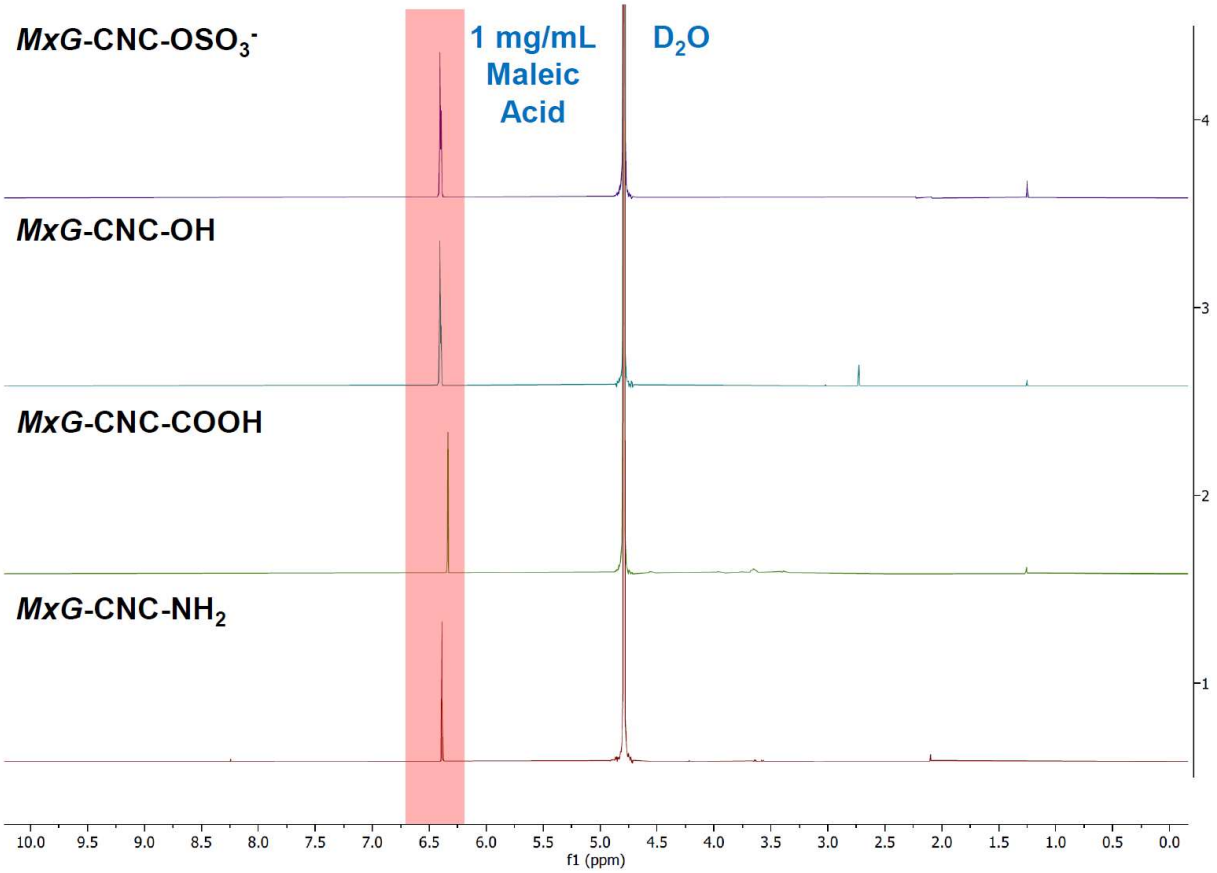

Figure S6.11: ^{1}H-NMR residual analysis of purified CNCs. To confirm the presence or absence of lignin or hemicellulose after isolation and functionalization, a subset of the CNCs were dispersed at 5 mg/mL by sonication in D_2O to solubilize any contaminants. CNCs were then removed by ultracentrifugation and filtration, and the supernatant was analyzed by ^{1}H-NMR using maleic acid as an internal standard to semi-quantitatively analyze any contaminant groups. The internal standard undergoes minor changes in chemical shift due to pH. The materials were confirmed free of contaminants in the mmol contaminant/g CNC range.

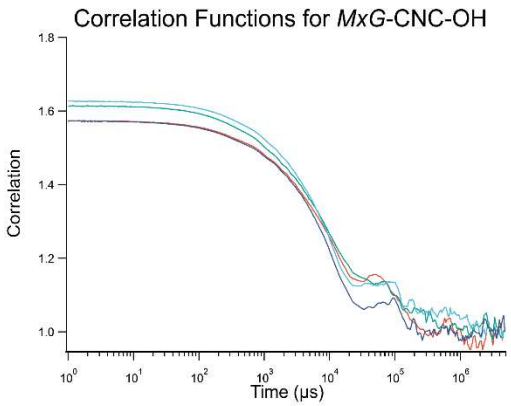

T1	-16.16 mV
T2	-15.94 mV
T3	-16.10 mV
T4	-16.89 mV
Average	-16.3±0.4 mV

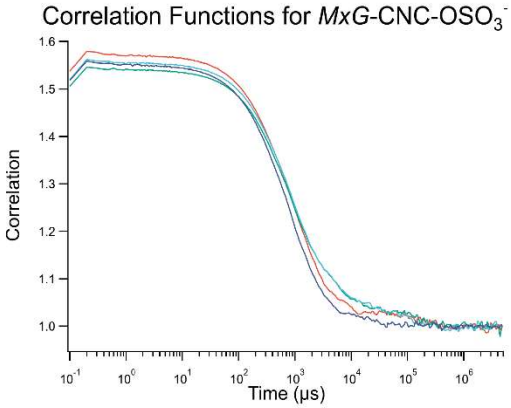

T1	-18.52 mV
T2	-17.54 mV
T3	-19.21 mV
T4	-20.65 mV
Average	-19.0±1.3 mV

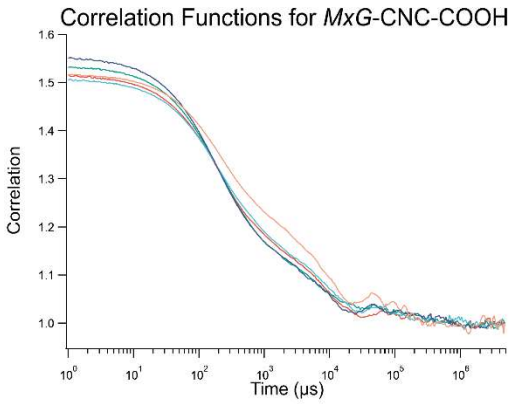

T1	-49.60 mV
T2	-59.41 mV
T3	-51.59 mV
T4	-51.53 mV
T5	-52.59 mV
Average	-52.9±3.8 mV

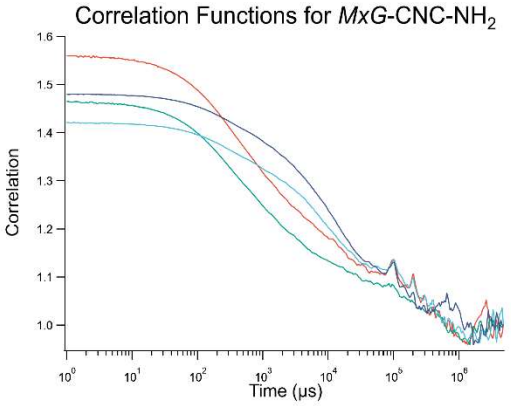

T1	32.91 mV
T2	21.93 mV
T3	24.87 mV
T4	14.93 mV
Average	23.7±7.4 mV

Figure S6.12: Correlation functions and zeta potentials obtained through electrophoretic light scattering experiments.

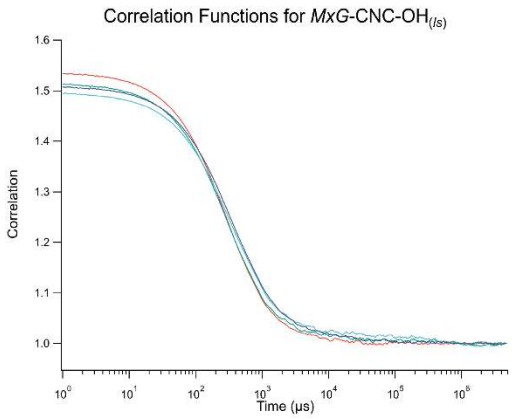

T1	-22.00 mV
T2	-14.47 mV
T3	-17.61 mV
T4	-16.69 mV
Average	-17.7±3.2 mV

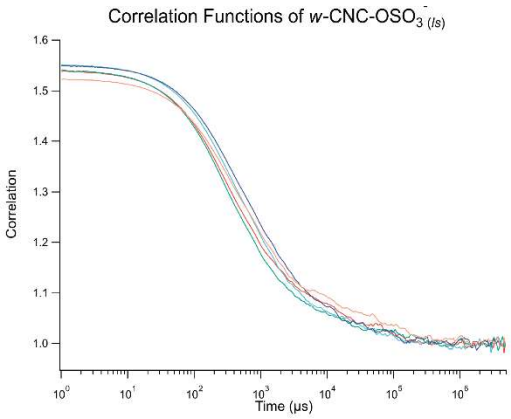

T1	-26.10 mV
T2	-23.69 mV
T3	-26.49 mV
T4	-26.82 mV
T5	-28.13 mV
Average	-26.2±1.6 mV

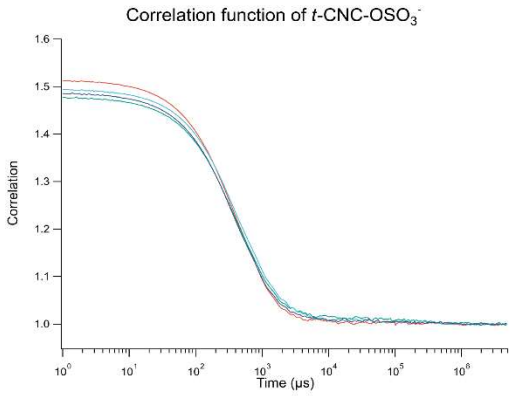

T1	-26.66 mV
T2	-27.67 mV
T3	-28.84 mV
T4	-26.39 mV
Average	-27.4±1.1 mV

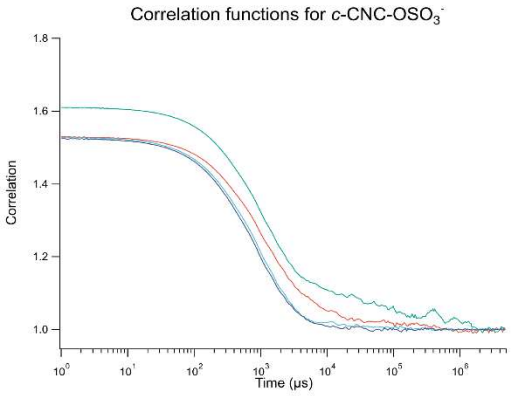

T1	-16.45 mV
T2	-16.07 mV
T3	-16.59 mV
T4	-16.10 mV
Average	-16.3±0.3 mV

Figure S6.12 (cont.): Correlation functions and zeta potentials obtained through electrophoretic light scattering experiments. All experiments were conducted five times at 1 V, and outlying correlation functions were removed to obtain the average datasets.

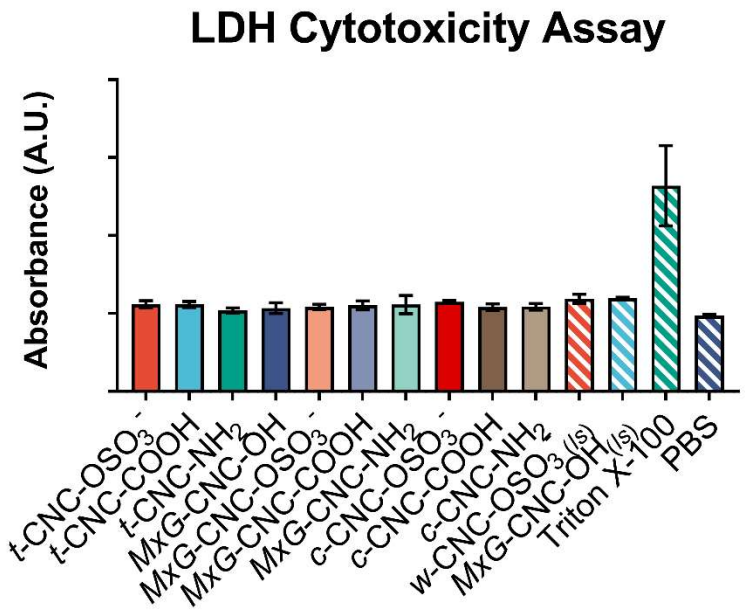

Figure S6.13: LDH Cytotoxicity Assay as a secondary method to measure cytotoxicity induced by CNCs on RAW-Blue cells. CNCs were incubated with cells for 24 h prior to analysis.

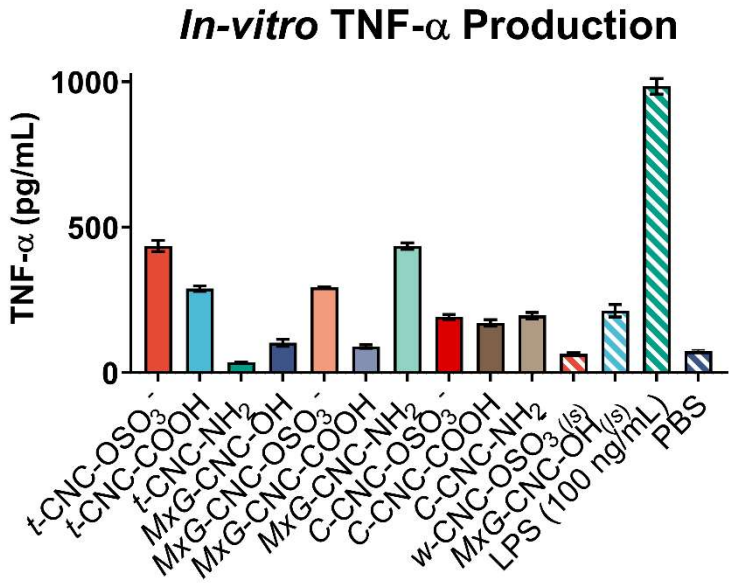

Figure S6.14: TNF-α ELISA of CNCs. Assay of RAW-Blue supernatant after incubation for 24 h with CNCs indicates a low-level nonspecific inflammatory response to CNCs independent of size or charge.

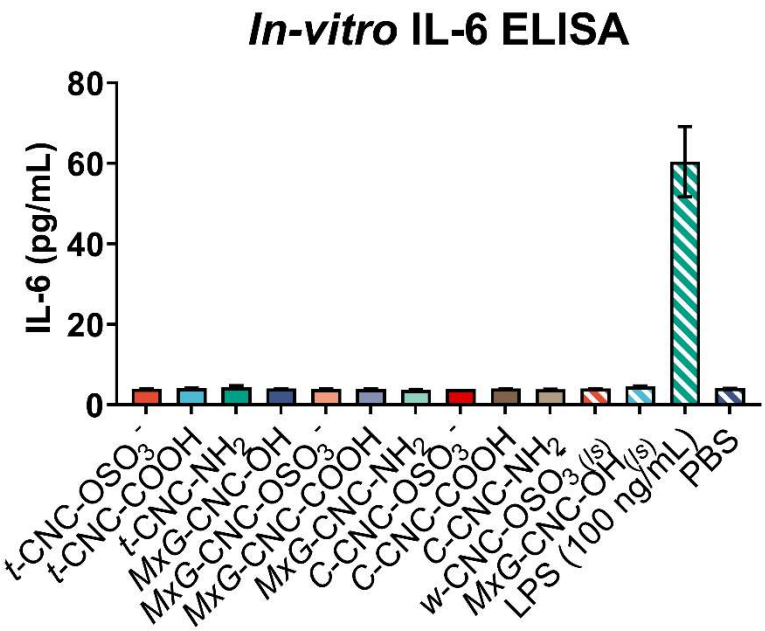

Figure S6.15: IL-6 ELISA of CNCs. Assay of RAW-Blue supernatant after incubation for 24 h with CNCs indicates absence of a pro-inflammatory IL-6 response resulting from charge or size of CNCs.

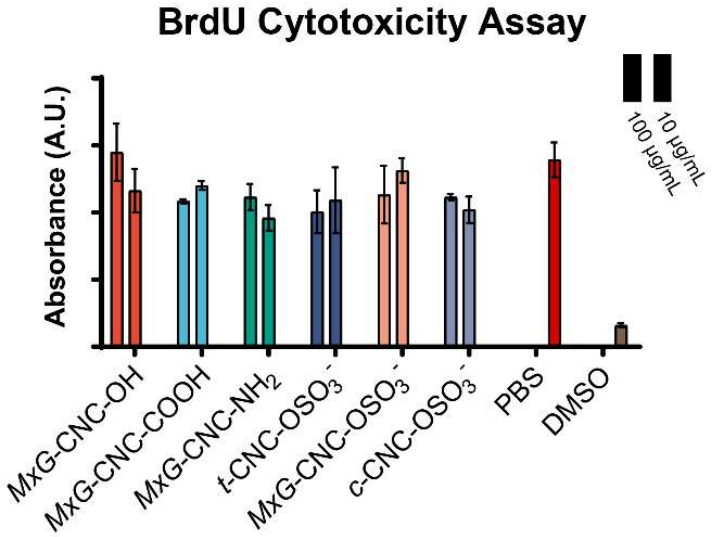

Figure S6.16: A BrdU ELISA was used to determine the effect of CNCs on cellular differentiation *in-vitro*. CNCs were incubated with RAW macrophages for 12 h, then BrdU reagent was added to cell culture media and incubated for an additional 12 h prior to conducting the assay according to the manufacturer's recommendation.

Figure S6.17: Light microscopy of CNC aggregates in cell culture media. Microscopy was used to visualize the presence of aggregates and disrupted cell growth in RAW-Blue cells incubated with A) *MxG*-CNC-OH samples but not with B) *MxG*-CNC-COOH or C) PBS control samples.

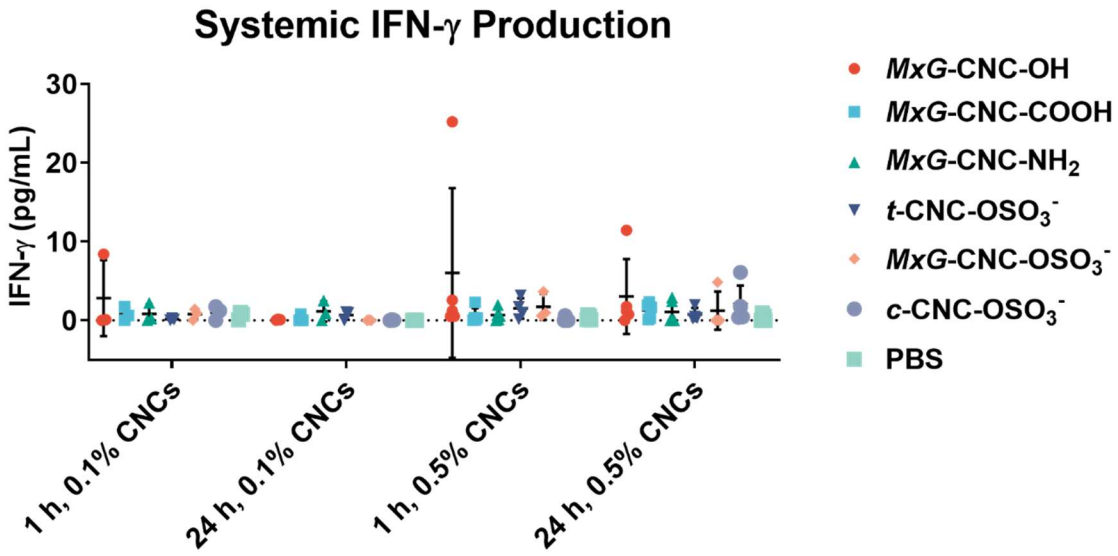

Figure S6.18: Systemic IFN-γ production after injection of CNCs. IFN-γ in the serum was assayed 1 and 24 h after injection of CNCs using Mouse Inflammation CBA (BD Biosciences). No differences were observed between groups.

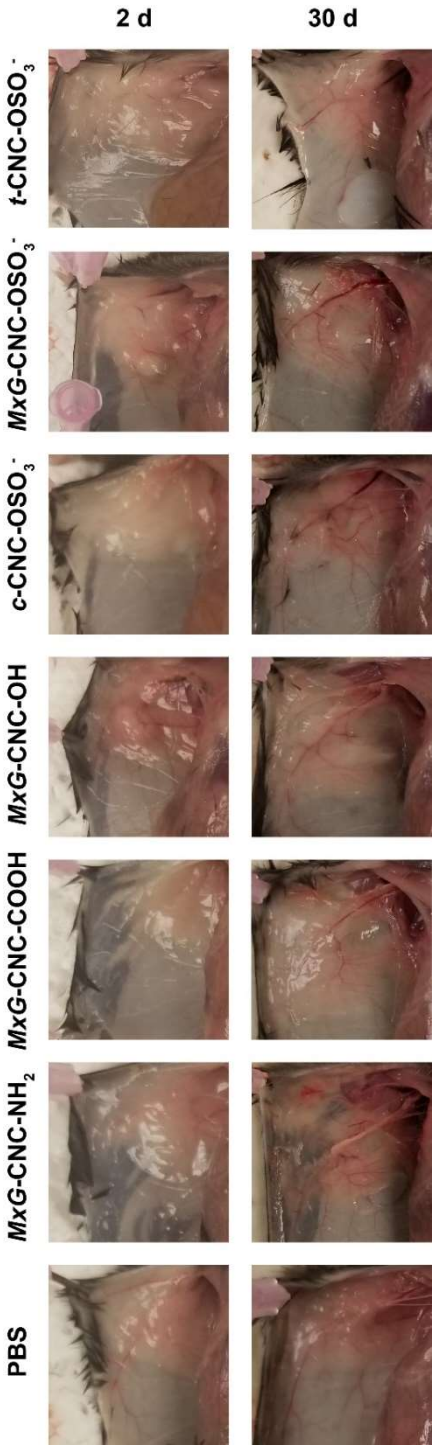

Figure S6.19: Images of subcutaneous tissue from the injection site were collected at the endpoint of the experiment. Imaging reveals redness in MxG-CNC-OH samples after 2 d but not 30 d. No significant inflammation is observed in other samples.

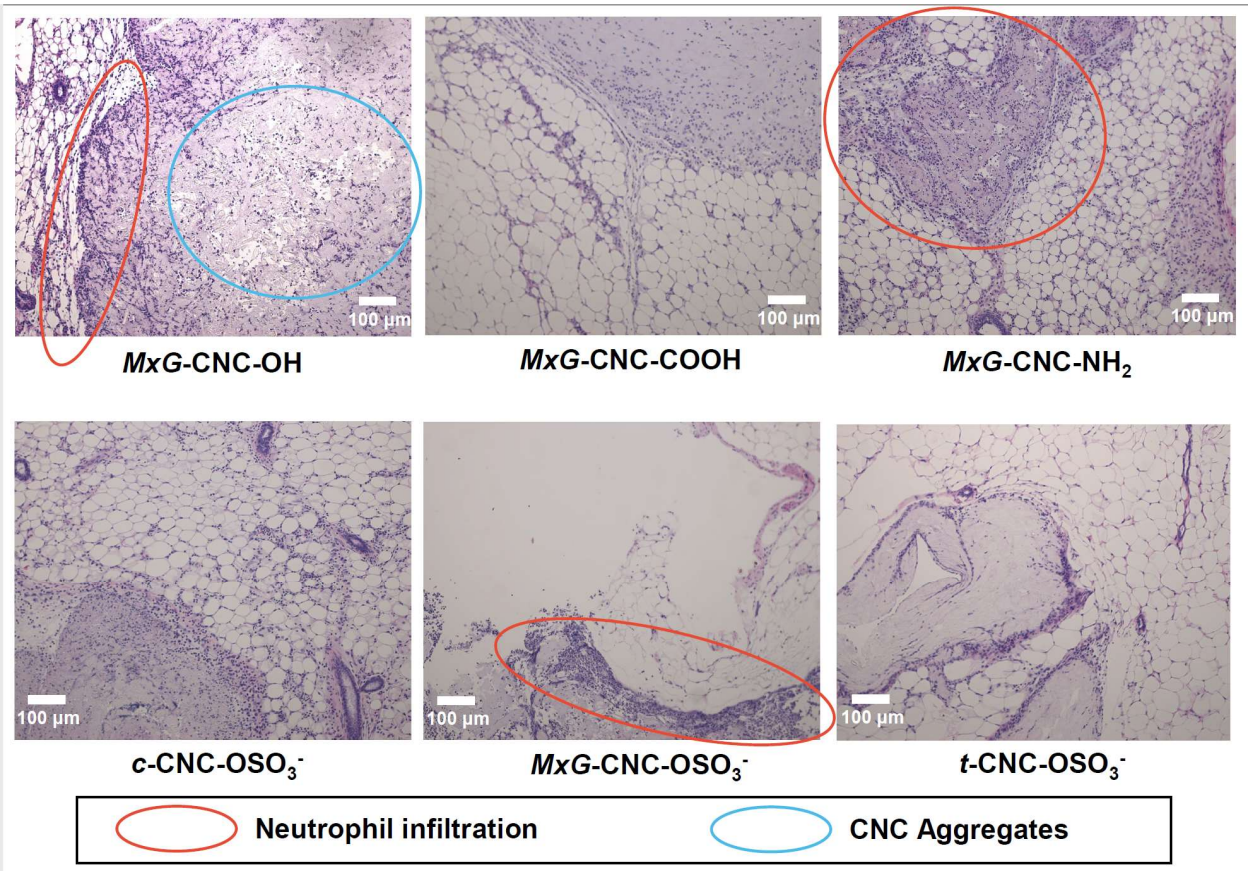

Figure S6.20: Hematoxylin and eosin staining of subcutaneous tissue collected from the injection site was conducted after 2 d for each of the CNCs analyzed *in-vivo* at a concentration of 0.5%. Significant neutrophil infiltration and presence of large aggregates were observed in the *MxG*-CNC-OH samples, suggesting an inflammatory response induced by these CNCs. Images of *MxG*-CNC-OH and *MxG*-CNC-COOH are duplicated from Figure 6 of the main text.

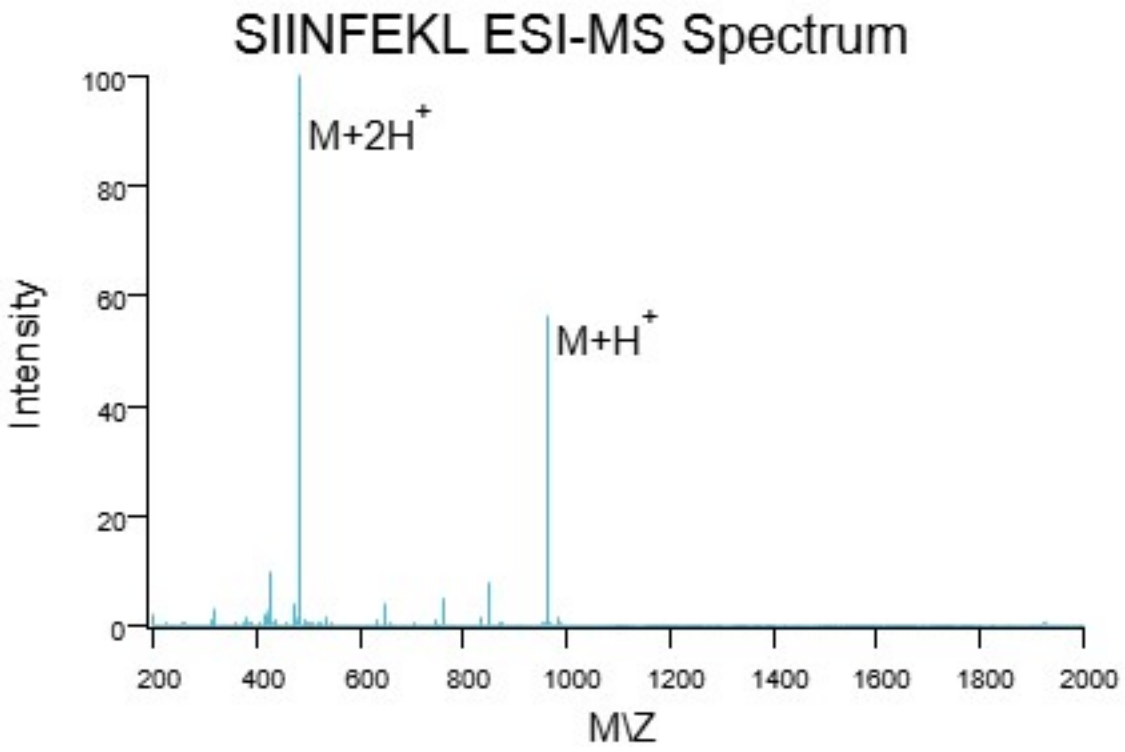

Figure S6.21: ESI-MS Spectra of SIINFEKL prepared via solid-phase peptide synthesis.

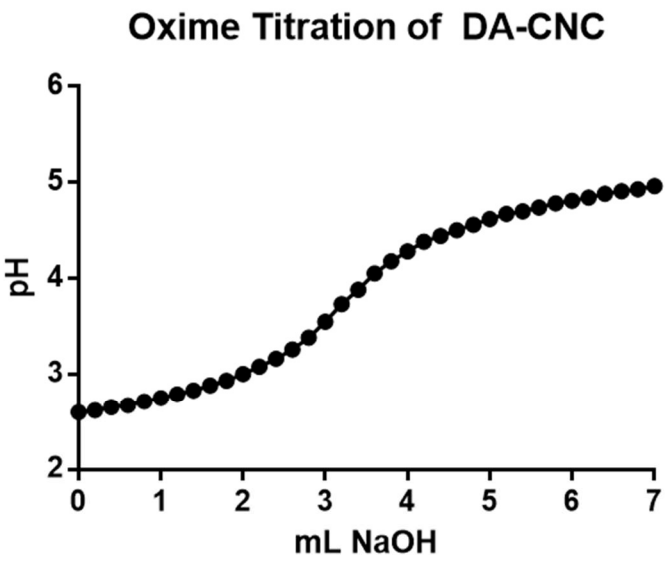

Start mass DA-CNC	55	mg
Volume NaOH at eq pt	3.5	mL
[Aldehyde] in DA-CNC	6400	mmol/kg

Figure S6.22: Oxime titration of DA-CNCs. DA-CNCs were treated with hydroxylamine and then titrated with 0.1 M NaOH to determine the aldehyde content as shown.

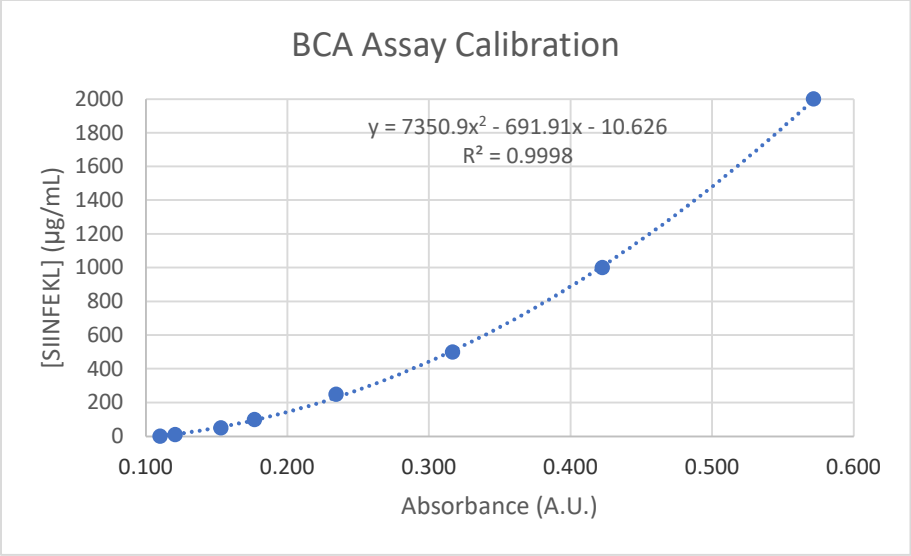

	CNC-SIINFEKL graft density determination
Replicate 1 Absorbance	0.432
Replicate Absorbance	0.570
Replicate Absorbance	0.503
Average Absorbance	0.502
Quantified [SIINFEKL] (ug/mL)	1490
[CNC-SIINFEKL] assayed (mg/mL)	2.00
Graft Density (mmol/kg)	775

Figure S6.23: BCA Assay calibration curve using SIINFEKL standards and graft density determination using CNC-SIINFEKL conjugates.

6.6 References.

1. Weiss, A. M.; Macke, N.; Zhang, Y.; Calvino, C.; Esser-Kahn, A. P.; Rowan, S. J., In Vitro and in Vivo Analyses of the Effects of Source, Length, and Charge on the Cytotoxicity and Immunocompatibility of Cellulose Nanocrystals. *ACS Biomater Sci Eng* **2021**, *7* (4), 1450-1461.

2. Habibi, Y.; Lucia, L. A.; Rojas, O. J., Cellulose nanocrystals: chemistry, self-assembly, and applications. *Chem Rev* **2010,** *110* (6), 3479-500.

3. Elazzouzi-Hafraoui, S.; Nishiyama, Y.; Putaux, J. L.; Heux, L.; Dubreuil, F.; Rochas, C., The shape and size distribution of crystalline nanoparticles prepared by acid hydrolysis of native cellulose. *Biomacromolecules* **2008,** *9* (1), 57-65.

4. Cheng, M.; Qin, Z.; Liu, Y.; Qin, Y.; Li, T.; Chen, L.; Zhu, M., Efficient extraction of carboxylated spherical cellulose nanocrystals with narrow distribution through hydrolysis of lyocell fibers by using ammonium persulfate as an oxidant. *J Mater Chem A* **2014,** *2* (1), 251-258.

5. Calvino, C.; Macke, N.; Kato, R.; Rowan, S. J., Development, processing and applications of bio-sourced cellulose nanocrystal composites. *Prog Polym Sci* **2020** , *103*, 101221.

6. Mariano, M.; El Kissi, N.; Dufresne, A., Cellulose nanocrystals and related nanocomposites: Review of some properties and challenges. *J Polym Sci B Polym Phys* **2014,** *52* (12), 791-806.

7. Tang, J.; Sisler, J.; Grishkewich, N.; Tam, K. C., Functionalization of cellulose nanocrystals for advanced applications. *J Colloid Interface Sci* **2017,** *494*, 397-409.

8. Wohlhauser, S.; Delepierre, G.; Labet, M.; Morandi, G.; Thielemans, W.; Weder, C.; Zoppe, J. O., Grafting Polymers from Cellulose Nanocrystals: Synthesis, Properties, and Applications. *Macromolecules* **2018,** *51* (16), 6157-6189.

9. Charreau, H.; Cavallo, E.; Foresti, M. L., Patents involving nanocellulose: Analysis of their evolution since 2010. *Carbohyd Polym* **2020,** *237*, 116039.

10. Lin, N.; Dufresne, A., Nanocellulose in biomedicine: Current status and future prospect. *Eur Polym J* **2014,** *59*, 302-325.

11. Domingues, R. M.; Gomes, M. E.; Reis, R. L., The potential of cellulose nanocrystals in tissue engineering strategies. *Biomacromolecules* **2014,** *15* (7), 2327-2346.

12. Guo, J.; Liu, D.; Filpponen, I.; Johansson, L. S.; Malho, J. M.; Quraishi, S.; Liebner, F.; Santos, H. A.; Rojas, O. J., Photoluminescent Hybrids of Cellulose Nanocrystals and Carbon Quantum Dots as Cytocompatible Probes for in Vitro Bioimaging. *Biomacromolecules* **2017,** *18* (7), 2045-2055.

13. Imlimthan, S.; Otaru, S.; Keinanen, O.; Correia, A.; Lintinen, K.; Santos, H. A.; Airaksinen, A. J.; Kostiainen, M. A.; Sarparanta, M., Radiolabeled Molecular Imaging Probes for the In Vivo Evaluation of Cellulose Nanocrystals for Biomedical Applications. *Biomacromolecules* **2019,** *20* (2), 674-683.

14. Kumar, A.; Negi, Y. S.; Choudhary, V.; Bhardwaj, N. K., Microstructural and mechanical properties of porous biocomposite scaffolds based on polyvinyl alcohol, nano-hydroxyapatite and cellulose nanocrystals. *Cellulose* **2014,** *21* (5), 3409-3426.

15. Li, W.; Lan, Y.; Guo, R.; Zhang, Y.; Xue, W.; Zhang, Y., In vitro and in vivo evaluation of a novel collagen/cellulose nanocrystals scaffold for achieving the sustained release of basic fibroblast growth factor. *J Biomater Appl* **2015,** *29* (6), 882-893.

16. Zhang, H.; Feng, M.; Chen, S.; Shi, W.; Wang, X., Incorporation of lysozyme into cellulose nanocrystals stabilized beta-chitosan nanoparticles with enhanced antibacterial activity. *Carbohydr Polym* **2020,** *236*, 115974.

17. Nguyen, J. K.; Park, D. J.; Skousen, J. L.; Hess-Dunning, A. E.; Tyler, D. J.; Rowan, S. J.; Weder, C.; Capadona, J. R., Mechanically-compliant intracortical implants reduce the neuroinflammatory response. *J Neural Eng* **2014,** *11* (5), 056014.

18. Nguyen, J. K.; Jorfi, M.; Buchanan, K. L.; Park, D. J.; Foster, E. J.; Tyler, D. J.; Rowan, S. J.; Weder, C.; Capadona, J. R., Influence of resveratrol release on the tissue response to mechanically adaptive cortical implants. *Acta Biomater* **2016,** *29*, 81-93.

19. Capadona, J. R.; Tyler, D. J.; Zorman, C. A.; Rowan, S. J.; Weder, C., Mechanically adaptive nanocomposites for neural interfacing. *MRS Bulletin* **2012,** *37* (6), 581-589.

20. Salimi, S.; Sotudeh-Gharebagh, R.; Zarghami, R.; Chan, S. Y.; Yuen, K. H., Production of Nanocellulose and Its Applications in Drug Delivery: A Critical Review. *ACS Sustain Chem Eng* **2019,** *7* (19), 15800-15827.

21. Dong, S.; Cho, H. J.; Lee, Y. W.; Roman, M., Synthesis and cellular uptake of folic acid-conjugated cellulose nanocrystals for cancer targeting. *Biomacromolecules* **2014,** *15* (5), 1560-1567.

22. Mangalam, A. P.; Simonsen, J.; Benight, A. S., Cellulose/DNA hybrid nanomaterials. *Biomacromolecules* **2009,** *10* (3), 497-504.

23. Wang, H.; He, J.; Zhang, M.; Tam, K. C.; Ni, P., A new pathway towards polymer modified cellulose nanocrystals via a “grafting onto” process for drug delivery. *Polym Chem* **2015,** *6* (23), 4206-4209.

24. Akhlaghi, S. P.; Berry, R. C.; Tam, K. C., Surface modification of cellulose nanocrystal with chitosan oligosaccharide for drug delivery applications. *Cellulose* **2013,** *20* (4), 1747-1764.

25. Abouhmad, A.; Dishisha, T.; Amin, M. A.; Hatti-Kaul, R., Immobilization to Positively Charged Cellulose Nanocrystals Enhances the Antibacterial Activity and Stability of Hen Egg White and T4 Lysozyme. *Biomacromolecules* **2017,** *18* (5), 1600-1608.

26. Dong, S.; Roman, M., Fluorescently labeled cellulose nanocrystals for bioimaging applications. *J Am Chem Soc* **2007,** *129* (45), 13810-13811.

27. De France, K. J.; Badv, M.; Dorogin, J.; Siebers, E.; Panchal, V.; Babi, M.; Moran-Mirabal, J.; Lawlor, M.; Cranston, E. D.; Hoare, T., Tissue Response and Biodistribution of Injectable Cellulose Nanocrystal Composite Hydrogels. *ACS Biomat Sci Eng* **2019,** *5* (5), 2235-2246.

28. Lin, N.; Geze, A.; Wouessidjewe, D.; Huang, J.; Dufresne, A., Biocompatible Double-Membrane Hydrogels from Cationic Cellulose Nanocrystals and Anionic Alginate as Complexing Drugs Codelivery. *ACS Appl Mater Interfaces* **2016,** *8* (11), 6880-6889.

29. Ndong Ntoutoume, G. M.; Grassot, V.; Bregier, F.; Chabanais, J.; Petit, J. M.; Granet, R.; Sol, V., PEI-cellulose nanocrystal hybrids as efficient siRNA delivery agents-Synthesis, physicochemical characterization and in vitro evaluation. *Carbohydr Polym* **2017,** *164*, 258-267.

30. Naahidi, S.; Jafari, M.; Edalat, F.; Raymond, K.; Khademhosseini, A.; Chen, P., Biocompatibility of engineered nanoparticles for drug delivery. *J Control Release* **2013,** *166* (2), 182-94.

31. Poland, C. A.; Duffin, R.; Kinloch, I.; Maynard, A.; Wallace, W. A.; Seaton, A.; Stone, V.; Brown, S.; Macnee, W.; Donaldson, K., Carbon nanotubes introduced into the abdominal cavity of mice show asbestos-like pathogenicity in a pilot study. *Nat Nanotechnol* **2008,** *3* (7), 423-428.

32. Sayes, C. M.; Liang, F.; Hudson, J. L.; Mendez, J.; Guo, W.; Beach, J. M.; Moore, V. C.; Doyle, C. D.; West, J. L.; Billups, W. E.; Ausman, K. D.; Colvin, V. L., Functionalization density dependence of single-walled carbon nanotubes cytotoxicity in vitro. *Toxicol Lett* **2006,** *161* (2), 135-142.

33. Castranova, V.; Porter, D.; Millecchia, L.; Ma, J. Y.; Hubbs, A. F.; Teass, A., Effect of inhaled crystalline silica in a rat model: time course of pulmonary reactions. *Mol Cell Biochem* **2002,** *234-235* (1-2), 177-184.

34. Yanamala, N.; Farcas, M. T.; Hatfield, M. K.; Kisin, E. R.; Kagan, V. E.; Geraci, C. L.; Shvedova, A. A., In Vivo Evaluation of the Pulmonary Toxicity of Cellulose Nanocrystals: A Renewable and Sustainable Nanomaterial of the Future. *ACS Sustain Chem Eng* **2014,** *2* (7), 1691-1698.

35. Endes, C.; Mueller, S.; Kinnear, C.; Vanhecke, D.; Foster, E. J.; Petri-Fink, A.; Weder, C.; Clift, M. J.; Rothen-Rutishauser, B., Fate of cellulose nanocrystal aerosols deposited on the lung cell surface in vitro. *Biomacromolecules* **2015,** *16* (4), 1267-1275.

36. Dong, S.; Hirani, A. A.; Colacino, K. R.; Lee, Y. W.; Roman, M., Cytotoxicity and Cellular Uptake of Cellulose Nanocrystals. *Nano LIFE* **2012,** *2* (3), 1241006.

37. Mahmoud, K. A.; Mena, J. A.; Male, K. B.; Hrapovic, S.; Kamen, A.; Luong, J. H., Effect of surface charge on the cellular uptake and cytotoxicity of fluorescent labeled cellulose nanocrystals. *ACS Appl Mater Interfaces* **2010,** *2* (10), 2924-2932.

38. Sunasee, R.; Araoye, E.; Pyram, D.; Hemraz, U. D.; Boluk, Y.; Ckless, K., Cellulose nanocrystal cationic derivative induces NLRP3 inflammasome-dependent IL-1beta secretion associated with mitochondrial ROS production. *Biochem Biophys Rep* **2015,** *4*, 1-9.

39. Harper, B. J.; Clendaniel, A.; Sinche, F.; Way, D.; Hughes, M.; Schardt, J.; Simonsen, J.; Stefaniak, A. B.; Harper, S. L., Impacts of chemical modification on the toxicity of diverse nanocellulose materials to developing zebrafish. *Cellulose* **2016,** *23* (3), 1763-1775.

40. Labet, M.; Thielemans, W., Improving the reproducibility of chemical reactions on the surface of cellulose nanocrystals: ROP of ε-caprolactone as a case study. *Cellulose* **2011,** *18* (3), 607-617.

41. Colombo, L.; Zoia, L.; Violatto, M. B.; Previdi, S.; Talamini, L.; Sitia, L.; Nicotra, F.; Orlandi, M.; Salmona, M.; Recordati, C.; Bigini, P.; La Ferla, B., Organ Distribution and Bone Tropism of Cellulose Nanocrystals in Living Mice. *Biomacromolecules* **2015,** *16* (9), 2862-2871.

42. Pulendran, B.; P, S. A.; O'Hagan, D. T., Emerging concepts in the science of vaccine adjuvants. *Nat Rev Drug Discov* **2021,** *20* (6), 454-475.

43. Xiang, S. D.; Scholzen, A.; Minigo, G.; David, C.; Apostolopoulos, V.; Mottram, P. L.; Plebanski, M., Pathogen recognition and development of particulate vaccines: does size matter? *Methods* **2006,** *40* (1), 1-9.

44. Flach, T. L.; Ng, G.; Hari, A.; Desrosiers, M. D.; Zhang, P.; Ward, S. M.; Seamone, M. E.; Vilaysane, A.; Mucsi, A. D.; Fong, Y.; Prenner, E.; Ling, C. C.; Tschopp, J.; Muruve, D. A.; Amrein, M. W.; Shi, Y., Alum interaction with dendritic cell membrane lipids is essential for its adjuvanticity. *Nat Med* **2011,** *17* (4), 479-487.

45. Hayashi, M.; Aoshi, T.; Kogai, Y.; Nomi, D.; Haseda, Y.; Kuroda, E.; Kobiyama, K.; Ishii, K. J., Optimization of physiological properties of hydroxyapatite as a vaccine adjuvant. *Vaccine* **2016,** *34* (3), 306-312.

46. Dagnon, K. L.; Shanmuganathan, K.; Weder, C.; Rowan, S. J., Water-Triggered Modulus Changes of Cellulose Nanofiber Nanocomposites with Hydrophobic Polymer Matrices. *Macromolecules* **2012,** *45* (11), 4707-4715.

47. Cudjoe, E.; Hunsen, M.; Xue, Z.; Way, A. E.; Barrios, E.; Olson, R. A.; Hore, M. J.; Rowan, S. J., Miscanthus Giganteus: A commercially viable sustainable source of cellulose nanocrystals. *Carbohydr Polym* **2017,** *155*, 230-241.

48. Capadona, J. R.; Shanmuganathan, K.; Trittschuh, S.; Seidel, S.; Rowan, S. J.; Weder, C., Polymer nanocomposites with nanowhiskers isolated from microcrystalline cellulose. *Biomacromolecules* **2009,** *10* (4), 712-716.

49. Habibi, Y.; Chanzy, H.; Vignon, M. R., TEMPO-mediated surface oxidation of cellulose whiskers. *Cellulose* **2006,** *13* (6), 679-687.

50. Olkowski, A. A.; Laarveld, B.; Arrison, N., Catalytic Biomass Conversion. US Patent US0016179A1, Jan 19 2017.

51. McAlpine, S.; Koneshny, J., Production of Crystalline Cellulose. World Patent WO127938A1, Aug 03 2017.

52. Dahl, E.; Krumdick, G.K.; Pupek, K., Methods of Producing Cellulose Nanocrystals. US Patent US0367704A1, Dec 05 2019.

53. Rowan, S.J.; Hunsen, M.; Way, A., Method for Production of Cellulose Nanocrystals from Miscanthus Giganteus and Composites Therefrom. US Patent US0319043A1, Nov 03, 2016.

54. Park, S.; Baker, J. O.; Himmel, M. E.; Parilla, P. A.; Johnson, D. K., Cellulose crystallinity index: measurement techniques and their impact on interpreting cellulase performance. *Biotechnol Biofuels* **2010,** *3*, 10.

55. Roman, M.; Winter, W. T., Effect of sulfate groups from sulfuric acid hydrolysis on the thermal degradation behavior of bacterial cellulose. *Biomacromolecules* **2004,** *5* (5), 1671-1677.

56. Delgado, A. V.; González-Caballero, F.; Hunter, R. J.; Koopal, L. K.; Lyklema, J., Measurement and Interpretation of Electrokinetic Phenomena (IUPAC Technical Report). *Pure Appl Chem* **2005,** *77* (10), 1753-1805.

57. Araki, J.; Wada, M.; Kuga, S.; Okano, T., Influence of surface charge on viscosity behavior of cellulose microcrystal suspension. *J Wood Sci* **1999,** *45* (3), 258-261.

58. Kargarzadeh, H.; Ahmad, I.; Abdullah, I.; Dufresne, A.; Zainudin, S. Y.; Sheltami, R. M., Effects of hydrolysis conditions on the morphology, crystallinity, and thermal stability of cellulose nanocrystals extracted from kenaf bast fibers. *Cellulose* **2012,** *19* (3), 855-866.

59. Li, Y.; Boraschi, D., Endotoxin contamination: a key element in the interpretation of nanosafety studies. *Nanomedicine* **2016,** *11* (3), 269-287.

60. Nordli, H. R.; Chinga-Carrasco, G.; Rokstad, A. M.; Pukstad, B., Producing ultrapure wood cellulose nanofibrils and evaluating the cytotoxicity using human skin cells. *Carbohydr Polym* **2016,** *150*, 65-73.

61. United States Pharmacopeia and National Formulary (USP31–NF26). *Transfusion and Infusion Assemblies and Similar Medical Devices*, U.S. Pharmacopeial Convention, Rockville, MD, Rockville, MD, 2011. http://www.uspbpep.com/usp31/v31261/usp31nf26s1_c161.asp

62. Smulders, S.; Kaiser, J. P.; Zuin, S.; Van Landuyt, K. L.; Golanski, L.; Vanoirbeek, J.; Wick, P.; Hoet, P. H., Contamination of nanoparticles by endotoxin: evaluation of different test methods. *Part Fibre Toxicol* **2012,** *9*, 41.

63. Dobrovolskaia, M. A.; Neun, B. W.; Clogston, J. D.; Ding, H.; Ljubimova, J.; McNeil, S. E., Ambiguities in applying traditional Limulus amebocyte lysate tests to quantify endotoxin in nanoparticle formulations. *Nanomedicine* **2010,** *5* (4), 555-562.

64. Chansoria, P.; Narayanan, L. K.; Wood, M.; Alvarado, C.; Lin, A.; Shirwaiker, R. A., Effects of Autoclaving, EtOH, and UV Sterilization on the Chemical, Mechanical, Printability, and Biocompatibility Characteristics of Alginate. *ACS Biomat Sci Eng* **2020**, *6* (9), 5191-5201.

65. Marilena, L.; Antonietta, M. G.; Graziana, S.; Paola, Q.; Lucia, M.; Emanuela, M.; Diana, B., Innate defence functions of macrophages can be biased by nano-sized ceramic and metallic particles. *Eur Cytokine Netw* **2004,** *15* (4), 339-346.

66. Schwab, L. P.; Xing, Z.; Hasty, K. A.; Smith, R. A., Titanium particles and surface-bound LPS activate different pathways in IC-21 macrophages. *J Biomed Mater Res B Appl Biomater* **2006,** *79* (1), 66-73.

67. Tarafa, P. J.; Williams, E.; Panvelker, S.; Zhang, J.; Matthews, M. A., Removing Endotoxin from Metallic Biomaterials with Compressed Carbon Dioxide-Based Mixtures. *J Supercrit Fluids* **2011,** *55* (3), 1052-1058.

68. Moghimi, S. M.; Symonds, P.; Murray, J. C.; Hunter, A. C.; Debska, G.; Szewczyk, A., A two-stage poly(ethylenimine)-mediated cytotoxicity: implications for gene transfer/therapy. *Mol Ther* **2005,** *11* (6), 990-995.

69. Moser, B. A.; Steinhardt, R. C.; Esser-Kahn, A. P., Surface Coating of Nanoparticles Reduces Background Inflammatory Activity while Increasing Particle Uptake and Delivery. *ACS Biomater Sci Eng* **2017,** *3* (2), 206-213.

70. Maiti, S.; Manna, S.; Shen, J.; Esser-Kahn, A. P.; Du, W., Mitigation of Hydrophobicity-Induced Immunotoxicity by Sugar Poly(orthoesters). *J Am Chem Soc* **2019,** *141* (11), 4510-4514.

71. Semete, B.; Booysen, L. I.; Kalombo, L.; Venter, J. D.; Katata, L.; Ramalapa, B.; Verschoor, J. A.; Swai, H., In vivo uptake and acute immune response to orally administered chitosan and PEG coated PLGA nanoparticles. *Toxicol Appl Pharmacol* **2010,** *249* (2), 158-165.

72. Sun, B.; Hou, Q.; Liu, Z.; Ni, Y., Sodium periodate oxidation of cellulose nanocrystal and its application as a paper wet strength additive. *Cellulose* **2015,** *22* (2), 1135-1146.

73. Leguy, J.; Nishiyama, Y.; Jean, B.; Heux, L., Ultrastructural Characterization of the Core–Shell Structure of a Wide Range of Periodate-Oxidized Cellulose from Different Native Sources by Solid-State 13C CP-MAS NMR. *ACS Sustain Chem Eng* **2018,** *7* (1), 412-420.

74. Azzam, F.; Galliot, M.; Putaux, J.-L.; Heux, L.; Jean, B., Surface peeling of cellulose nanocrystals resulting from periodate oxidation and reductive amination with water-soluble polymers. *Cellulose* **2015,** *22* (6), 3701-3714.

75. Chen, D.; Disotuar, M. M.; Xiong, X.; Wang, Y.; Chou, D. H., Selective N-terminal functionalization of native peptides and proteins. *Chem Sci* **2017,** *8* (4), 2717-2722.

76. Wang, X.; Chang, C. H.; Jiang, J.; Liu, Q.; Liao, Y. P.; Lu, J.; Li, L.; Liu, X.; Kim, J.; Ahmed, A.; Nel, A. E.; Xia, T., The Crystallinity and Aspect Ratio of Cellulose Nanomaterials Determine Their Pro-Inflammatory and Immune Adjuvant Effects In Vitro and In Vivo. *Small* **2019,** *15* (42), e1901642.

77. Vandepapeliere, P.; Horsmans, Y.; Moris, P.; Van Mechelen, M.; Janssens, M.; Koutsoukos, M.; Van Belle, P.; Clement, F.; Hanon, E.; Wettendorff, M.; Garcon, N.; Leroux-Roels, G., Vaccine adjuvant systems containing monophosphoryl lipid A and QS21 induce strong and persistent humoral and T cell responses against hepatitis B surface antigen in healthy adult volunteers. *Vaccine* **2008,** *26* (10), 1375-1386.

78. Didierlaurent, A. M.; Laupeze, B.; Di Pasquale, A.; Hergli, N.; Collignon, C.; Garcon, N., Adjuvant system AS01: helping to overcome the challenges of modern vaccines. *Expert Rev Vaccines* **2017,** *16* (1), 55-63.

79. Marty-Roix, R.; Vladimer, G. I.; Pouliot, K.; Weng, D.; Buglione-Corbett, R.; West, K.; MacMicking, J. D.; Chee, J. D.; Wang, S.; Lu, S.; Lien, E., Identification of QS-21 as an

Inflammasome-activating Molecular Component of Saponin Adjuvants. *J Biol Chem* **2016,** *291* (3), 1123-1136.

80. Jiang, F.; Esker, A. R.; Roman, M., Acid-catalyzed and solvolytic desulfation of H2SO4-hydrolyzed cellulose nanocrystals. *Langmuir* **2010,** *26* (23), 17919-17925.

81. Way, A. E.; Hsu, L.; Shanmuganathan, K.; Weder, C.; Rowan, S. J., pH-Responsive Cellulose Nanocrystal Gels and Nanocomposites. *ACS Macro Letters* **2012,** *1* (8), 1001-1006.

82. Zhao, H.; Heindel, N. D., Determination of Degree of Substitution of Formyl Groups in Polyaldehyde Dextran by the Hydroxylamine Hydrochloride Method. *Pharmaceutical Research* **1991,** *08* (3), 400-402.

83. French, A. D., Idealized powder diffraction patterns for cellulose polymorphs. *Cellulose* **2013,** *21* (2), 885-896.

84. Flauzino Neto, W. P.; Silvério, H. A.; Dantas, N. O.; Pasquini, D., Extraction and characterization of cellulose nanocrystals from agro-industrial residue – Soy hulls. *Ind Crops Prod* **2013,** *42*, 480-488.

APPENDIX A Full Characterization of Polymer Library.

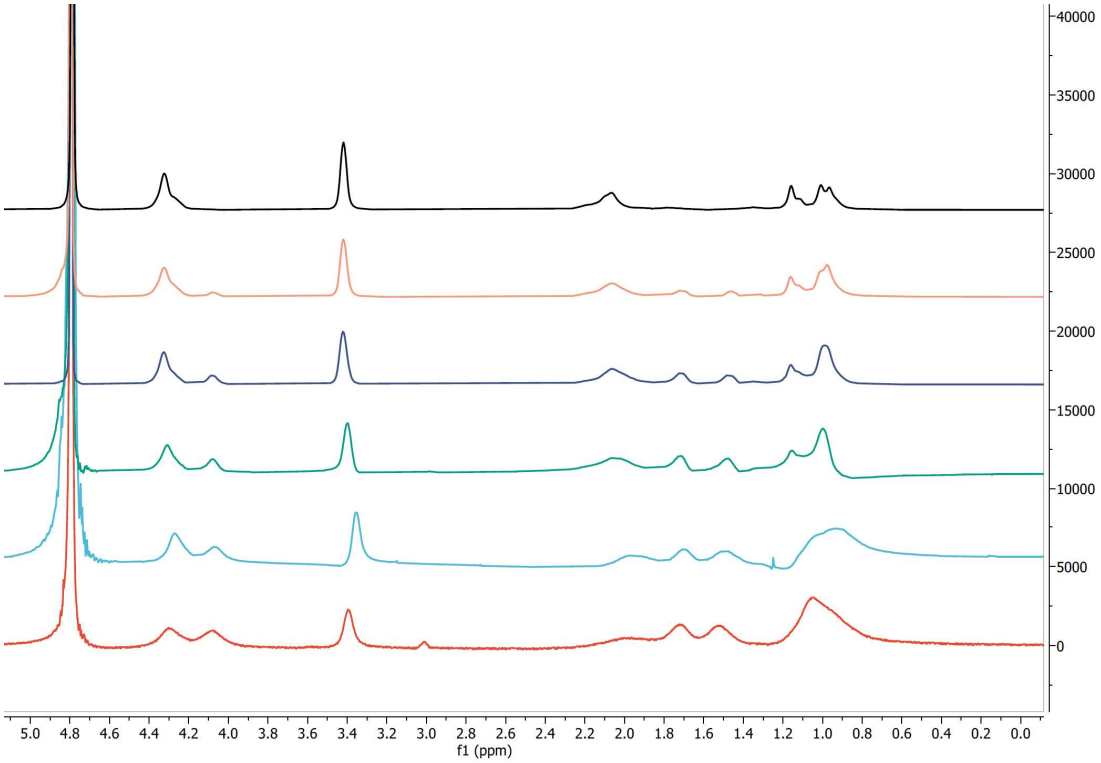

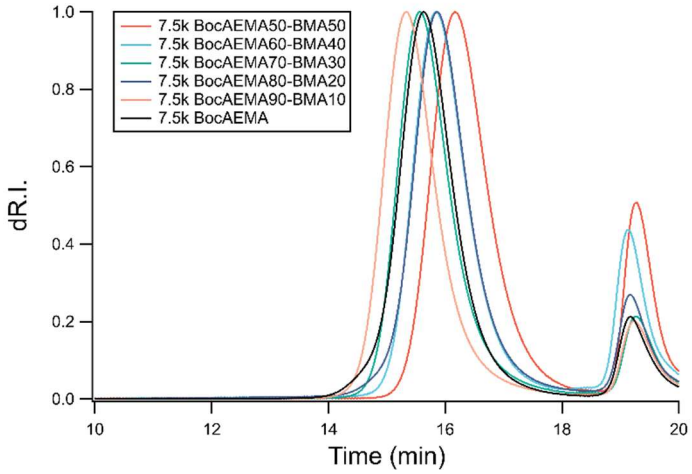

Mon1	Mon2	M_n (th)	%Mon1 (th)	%Mon1 (NMR)	M_n_Boc (SEC)	M_n (SEC)	$Đ$ (SEC)
AEMA	BMA	7,500	50%	52%	6,600	5,000	1.22
AEMA	BMA	7,500	60%	62%	8,900	6,800	1.19
AEMA	BMA	7,500	70%	76%	10,700	7,500	1.22
AEMA	BMA	7,500	80%	82%	8,800	5,900	1.23
AEMA	BMA	7,500	90%	91%	14,200	8,800	1.14
AEMA	N/A	7,500	100%	100%	10,900	6,300	1.22

Figure A1: Characterization of 7.5 kg/mol poly(AEMA-*s*-BMA) polymers.

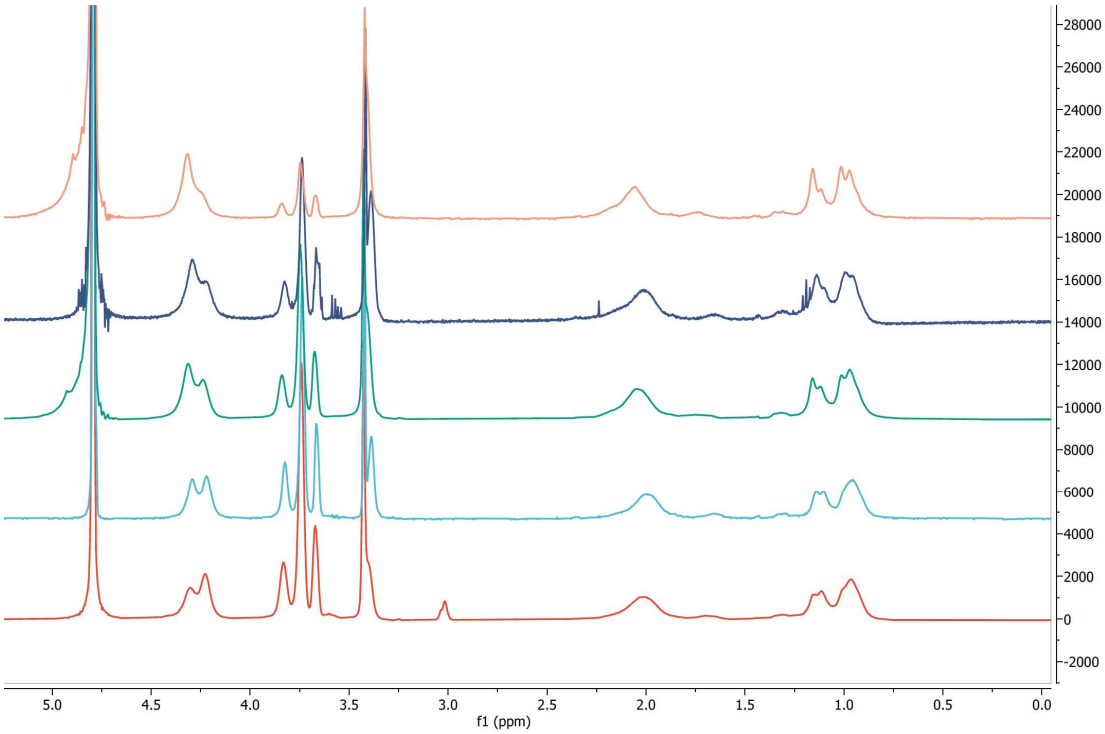

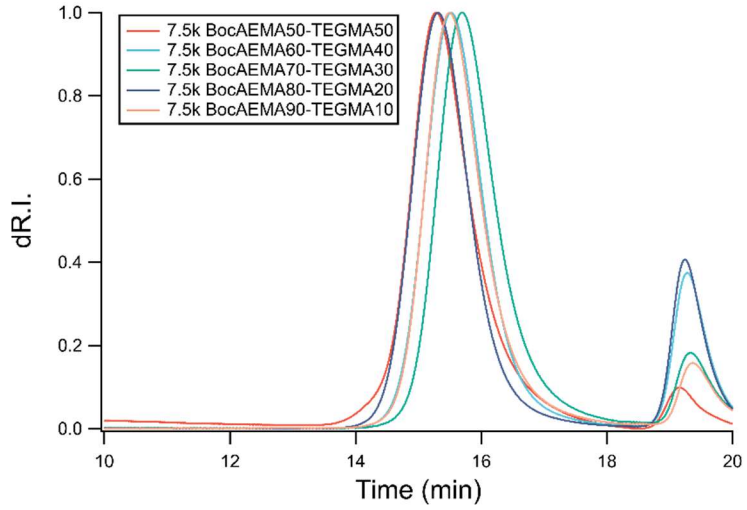

Mon1	Mon2	M_n (th)	%Mon1 (th)	%Mon1 (NMR)	M_n_Boc (SEC)	M_n (SEC)	$Đ$ (SEC)
AEMA	TEGMA	7,500	50%	43%	12,700	10,100	1.30
AEMA	TEGMA	7,500	60%	64%	12,000	8,800	1.19
AEMA	TEGMA	7,500	70%	76%	9,500	6,700	1.26
AEMA	TEGMA	7,500	80%	79%	14,400	9,600	1.16
AEMA	TEGMA	7,500	90%	91%	12,000	7,400	1.18

Figure A2: Characterization of 7.5 kg/mol poly(AEMA-*s*-TEGMA) polymers.

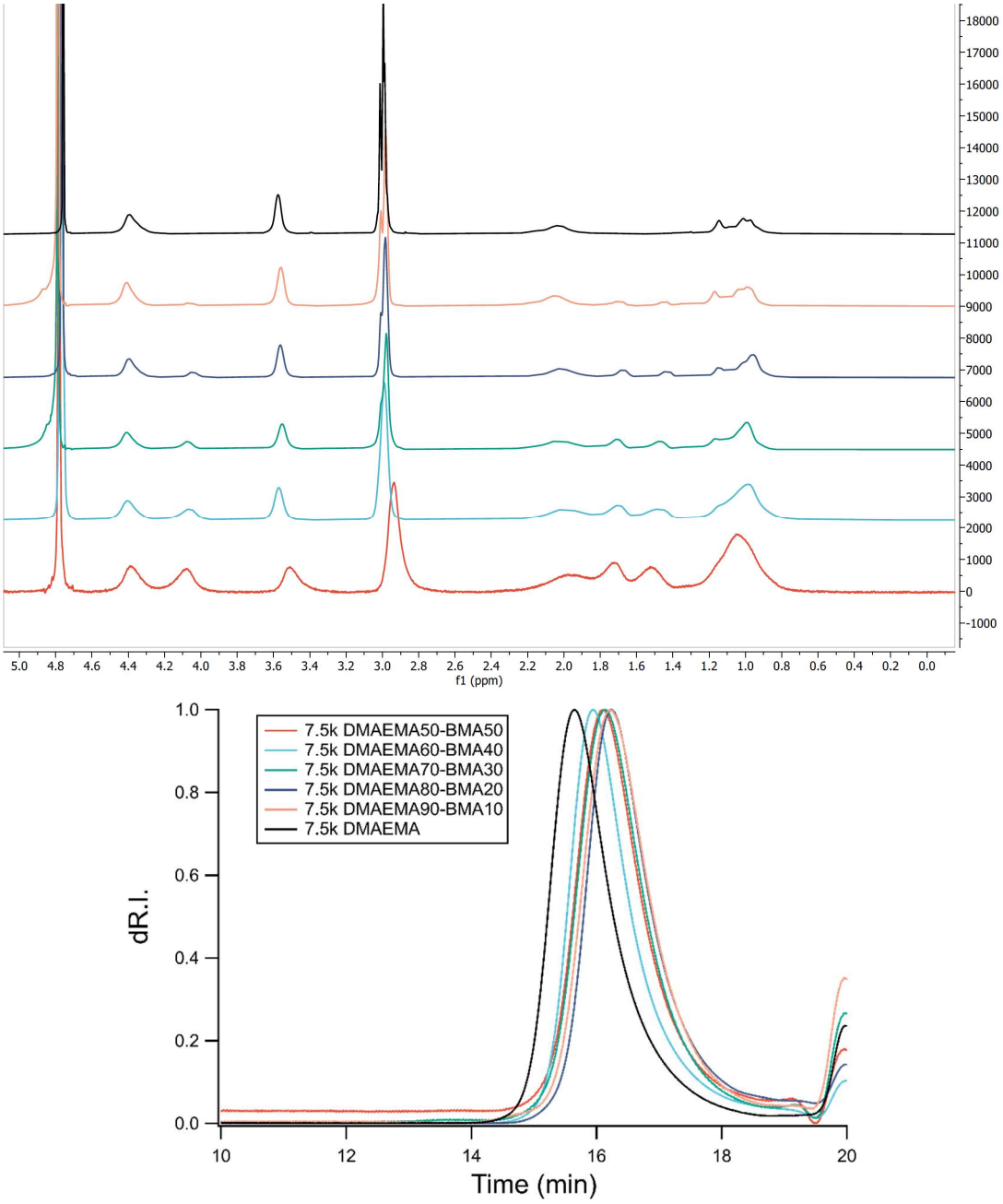

Mon1	Mon2	M_n (th)	%Mon1 (th)	%Mon1 (NMR)	M_n (SEC)	$Đ$ (SEC)
DMAEMA	BMA	7,500	50%	45%	6,000	1.37
DMAEMA	BMA	7,500	60%	59%	7,000	1.35
DMAEMA	BMA	7,500	70%	69%	5,900	1.37
DMAEMA	BMA	7,500	80%	76%	5,600	1.32
DMAEMA	BMA	7,500	90%	91%	5,400	1.37
DMAEMA	N/A	7,500	100%	100%	8,700	1.33

Figure A3: Characterization of 7.5 kg/mol poly(DMAEMA-*s*-BMA) polymers.

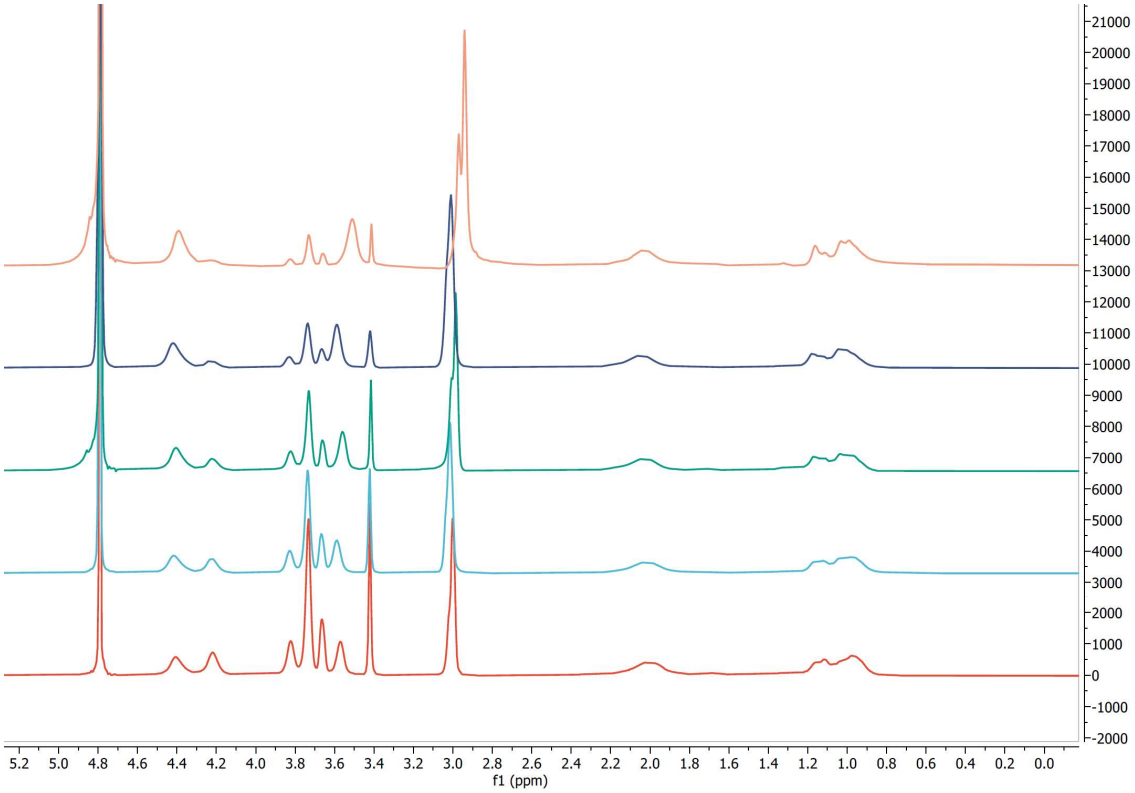

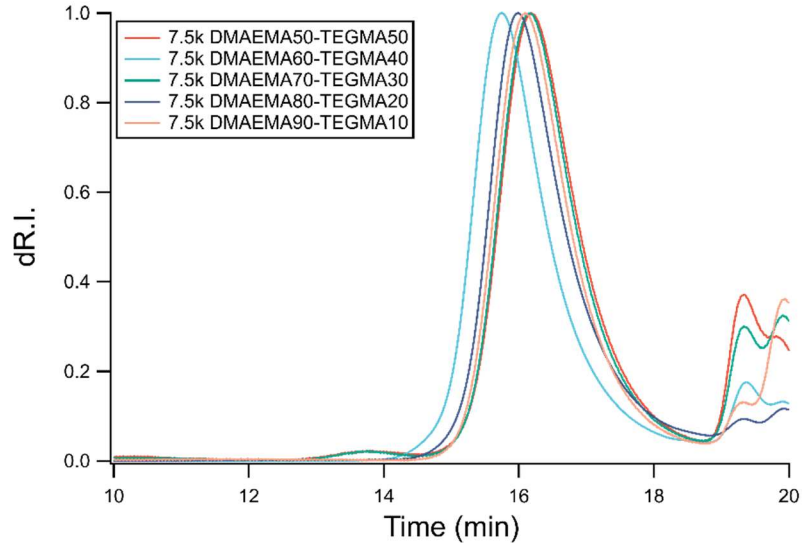

Mon1	Mon2	M_n (th)	%Mon1 (th)	%Mon1 (NMR)	M_n (SEC)	$Đ$ (SEC)
DMAEMA	TEGMA	7,500	50%	51%	5,600	1.37
DMAEMA	TEGMA	7,500	60%	60%	7,800	1.39
DMAEMA	TEGMA	7,500	70%	66%	5,700	1.39
DMAEMA	TEGMA	7,500	80%	81%	6,100	1.45
DMAEMA	TEGMA	7,500	90%	86%	5,900	1.39

Figure A4: Characterization of 7.5 kg/mol poly(DMAEMA-*s*-TEGMA) polymers.

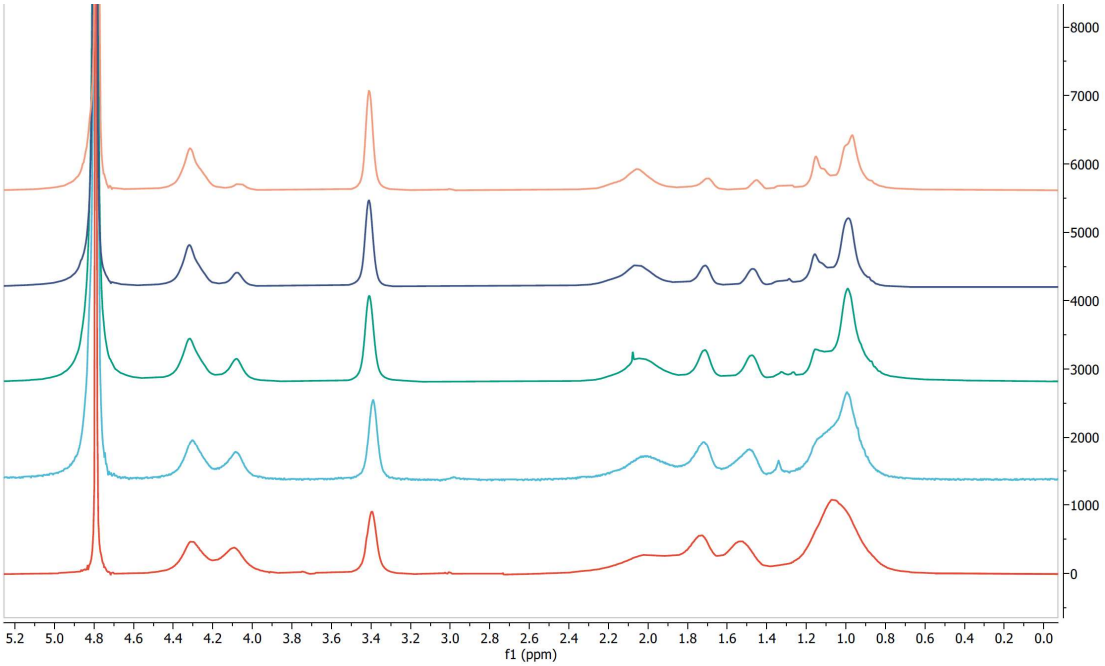

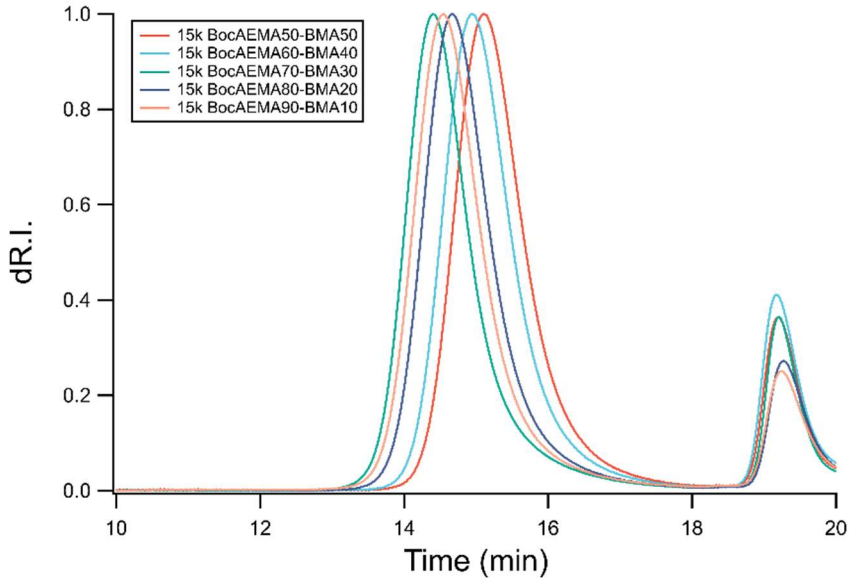

Mon1	Mon2	M_n (th)	%Mon1 (th)	%Mon1 (NMR)	M_n_Boc (SEC)	M_n (SEC)	$Đ$ (SEC)
AEMA	BMA	15,000	50%	54%	16,200	12,700	1.17
AEMA	BMA	15,000	60%	63%	18,200	12,700	1.17
AEMA	BMA	15,000	70%	68%	26,800	18,800	1.17
AEMA	BMA	15,000	80%	81%	22,400	14,700	1.17
AEMA	BMA	15,000	90%	91%	25,700	15,700	1.14

Figure A5: Characterization of 15 kg/mol poly(AEMA-*s*-BMA) polymers.

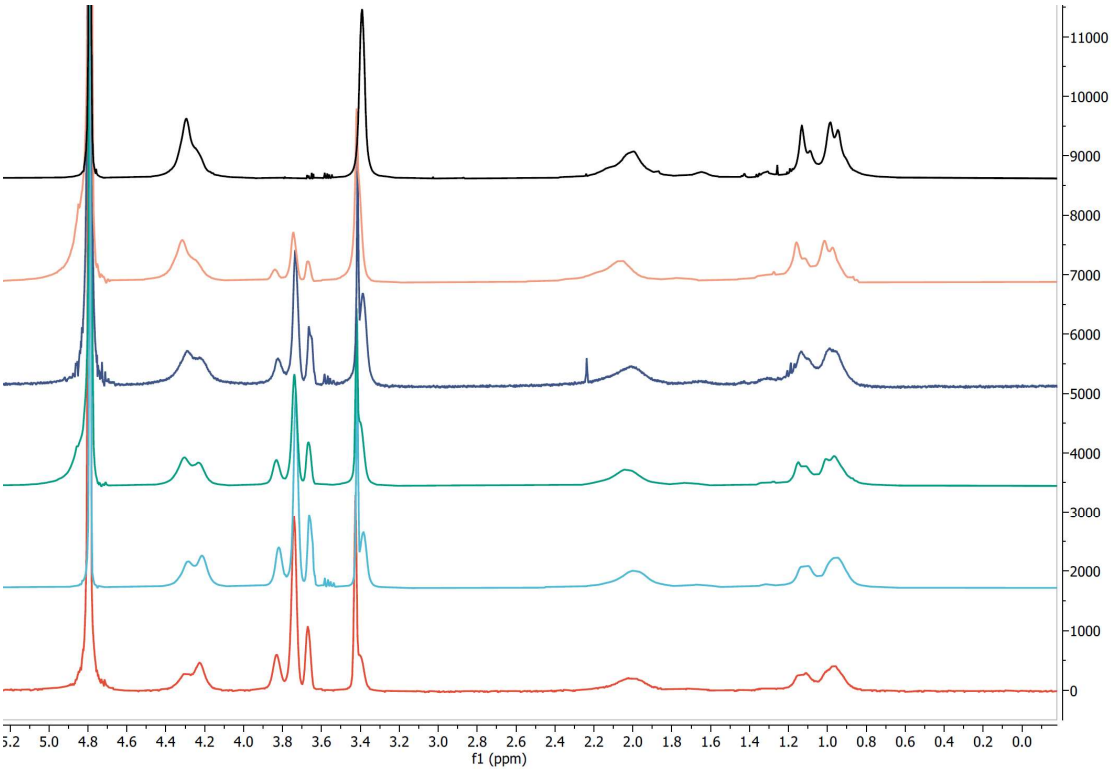

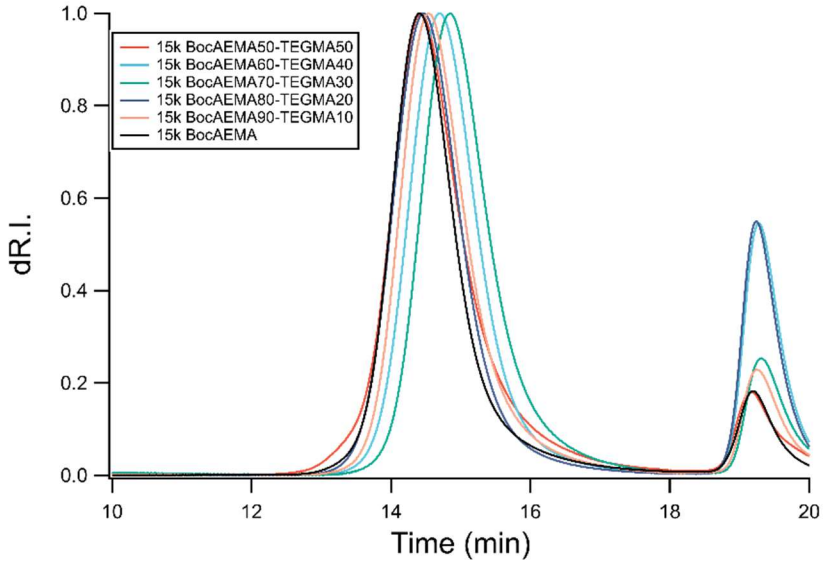

Mon1	Mon2	M_n (th)	%Mon1 (th)	%Mon1 (NMR)	M_n_Boc (SEC)	M_n (SEC)	$Đ$ (SEC)
AEMA	TEGMA	15,000	50%	45%	24,900	19,700	1.25
AEMA	TEGMA	15,000	60%	63%	22,700	16,600	1.17
AEMA	TEGMA	15,000	70%	75%	19,000	13,300	1.21
AEMA	TEGMA	15,000	80%	79%	26,700	17,600	1.18
AEMA	TEGMA	15,000	90%	89%	24,600	15,000	1.18
AEMA	N/A	15,000	100%	100%	25,700	14,600	1.25

Figure A6: Characterization of 15 kg/mol poly(AEMA-*s*-TEGMA) polymers.

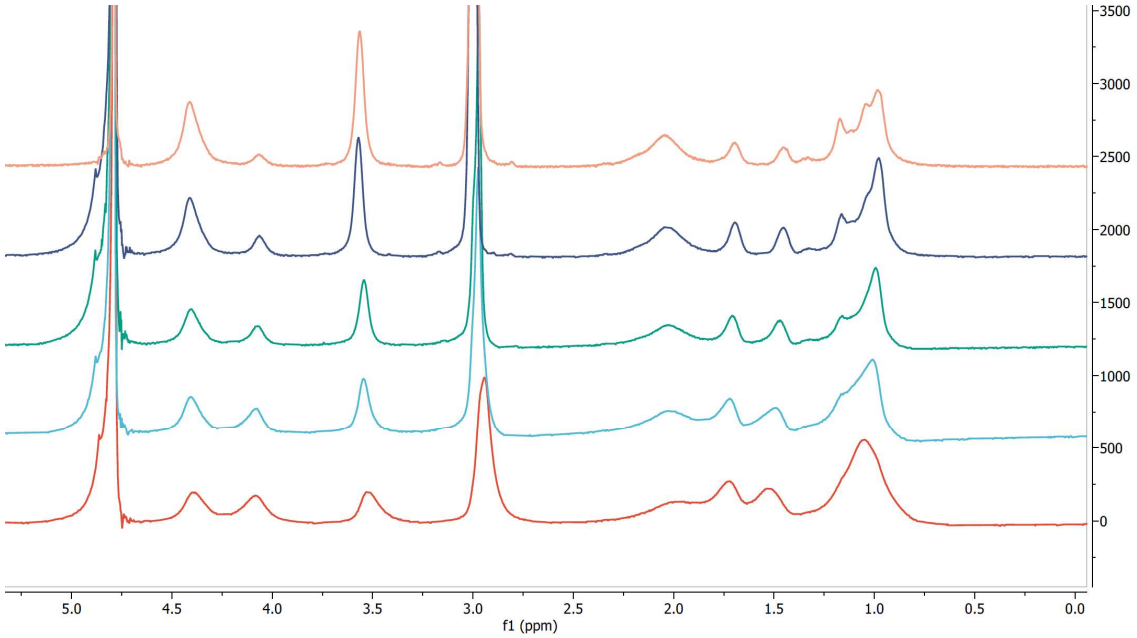

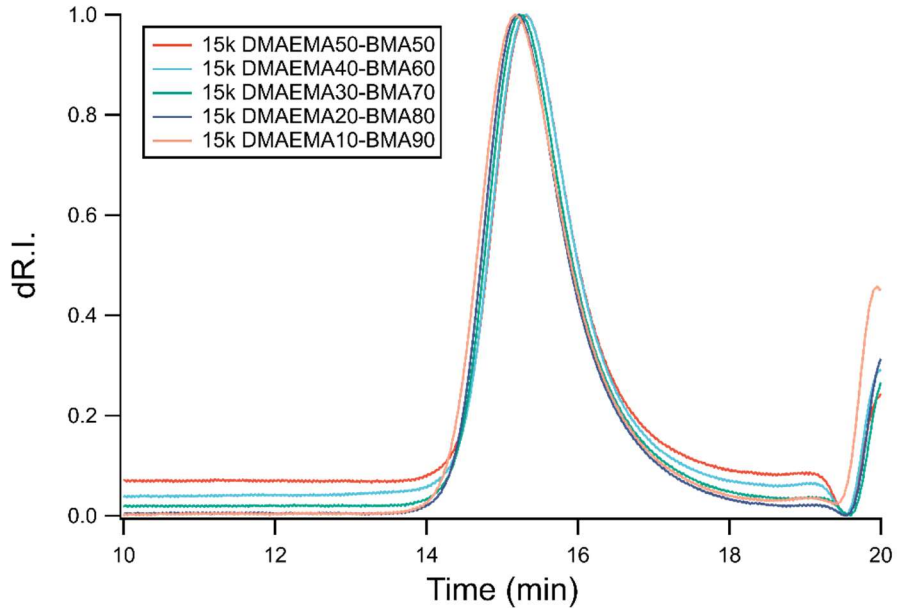

Mon1	Mon2	M_n (th)	%Mon1 (th)	%Mon1 (NMR)	M_n (SEC)	$Đ$ (SEC)
DMAEMA	BMA	15,000	50%	52%	12,300	1.28
DMAEMA	BMA	15,000	60%	65%	11,500	1.35
DMAEMA	BMA	15,000	70%	70%	11,500	1.39
DMAEMA	BMA	15,000	80%	79%	13,200	1.27
DMAEMA	BMA	15,000	90%	93%	13,000	1.32

Figure A7: Characterization of 15 kg/mol poly(DMAEMA-*s*-BMA) polymers.

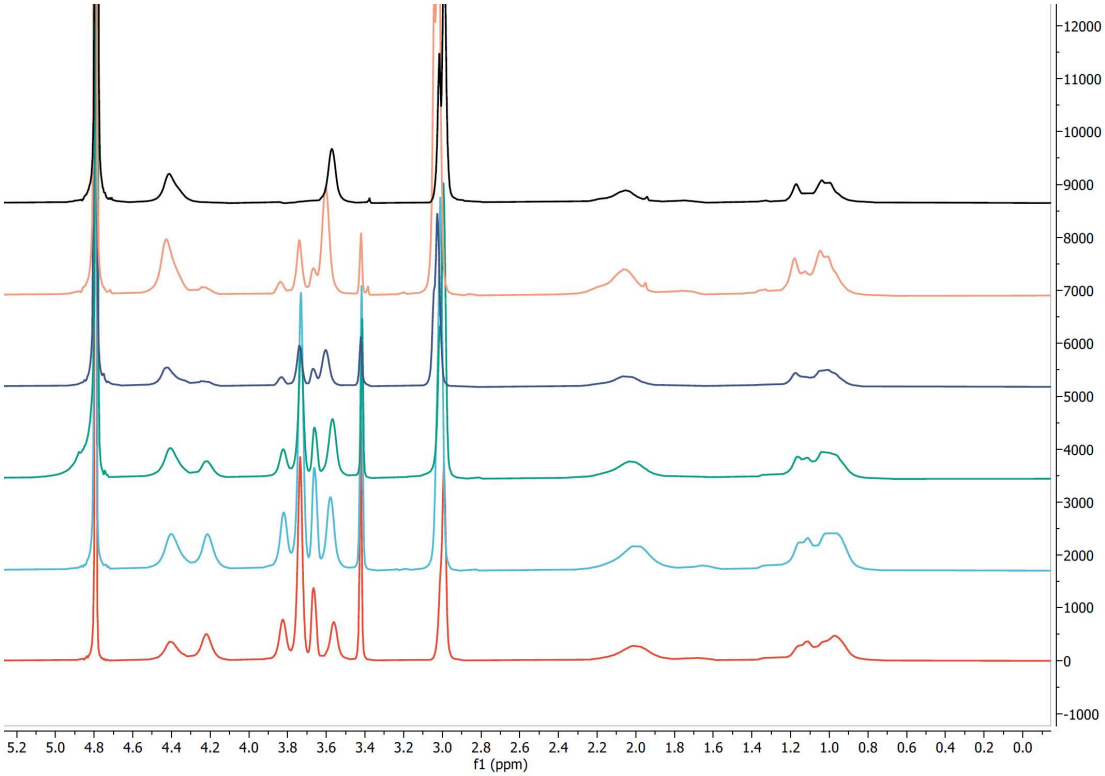

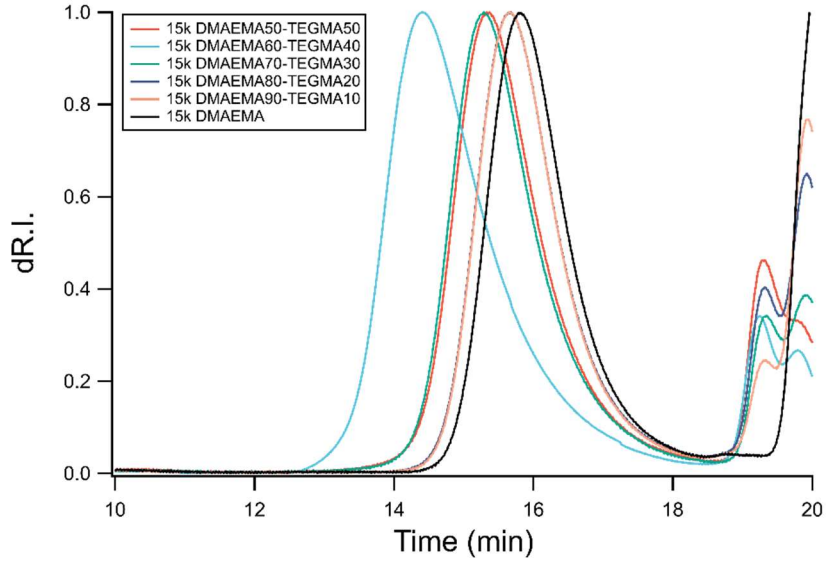

Mon1	Mon2	M_n (th)	%Mon1 (th)	%Mon1 (NMR)	M_n (SEC)	$Đ$ (SEC)
DMAEMA	TEGMA	15,000	50%	50%	11,400	1.36
DMAEMA	TEGMA	15,000	60%	55%	18,700	1.56
DMAEMA	TEGMA	15,000	70%	64%	11,500	1.37
DMAEMA	TEGMA	15,000	80%	79%	9,300	1.20
DMAEMA	TEGMA	15,000	90%	90%	9,700	1.26
DMAEMA	N/A	15,000	100%	100%	10,800	1.32

Figure A8: Characterization of 15 kg/mol poly(DMAEMA-*s*-TEGMA) polymers.

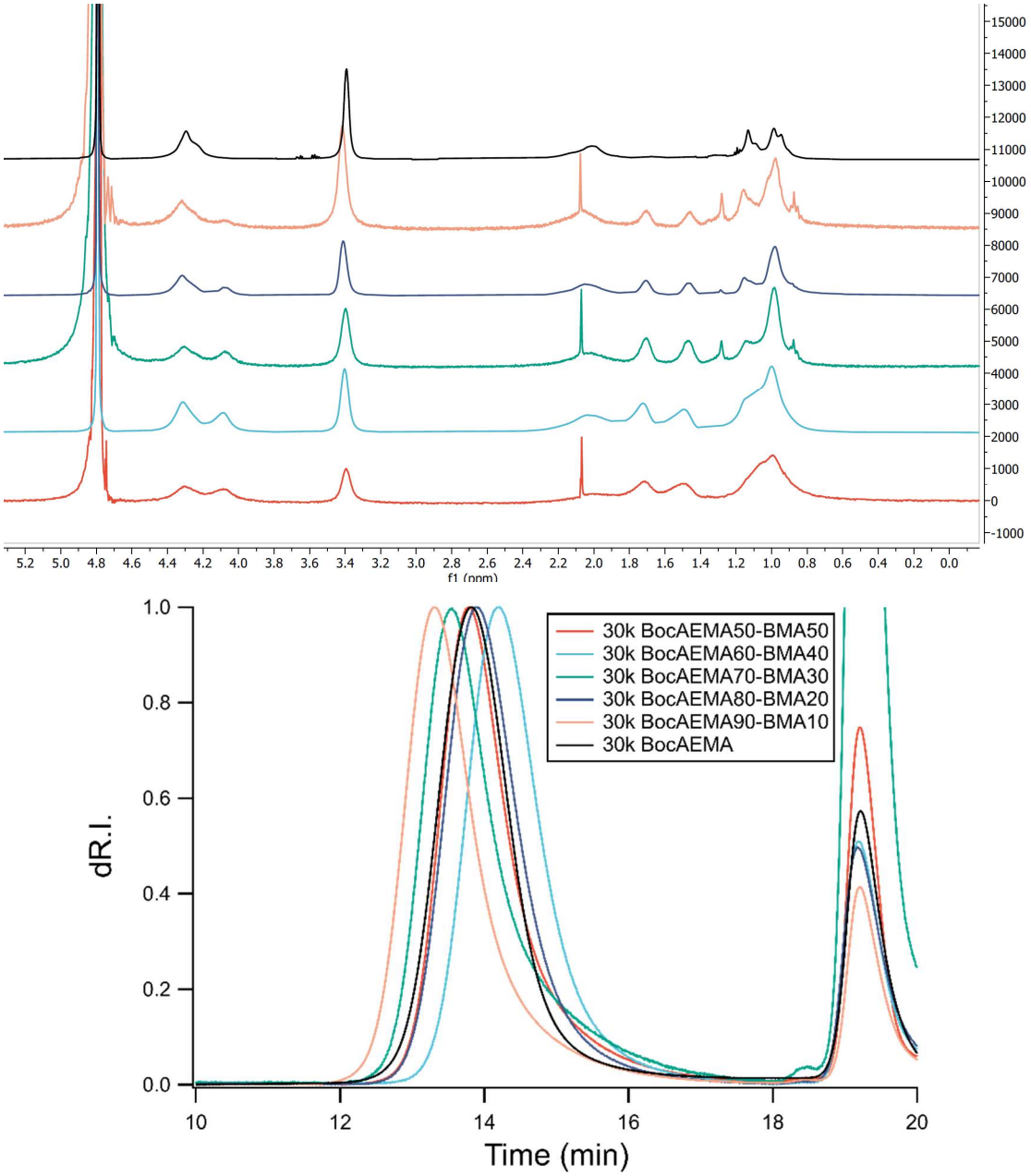

Mon1	Mon2	M_n (th)	%Mon1 (th)	%Mon1 (NMR)	M_n_Boc (SEC)	M_n (SEC)	$Đ$ (SEC)
AEMA	BMA	30,000	50%	44%	40,400	31,800	1.20
AEMA	BMA	30,000	60%	62%	31,300	23,200	1.19
AEMA	BMA	30,000	70%	65%	40,000	27,900	1.36
AEMA	BMA	30,000	80%	83%	38,400	25,100	1.20
AEMA	BMA	30,000	90%	92%	56,900	34,700	1.22
AEMA	N/A	30,000	100%	100%	44,100	25,000	1.16

Figure A9: Characterization of 30 kg/mol poly(AEMA-*s*-BMA) polymers.

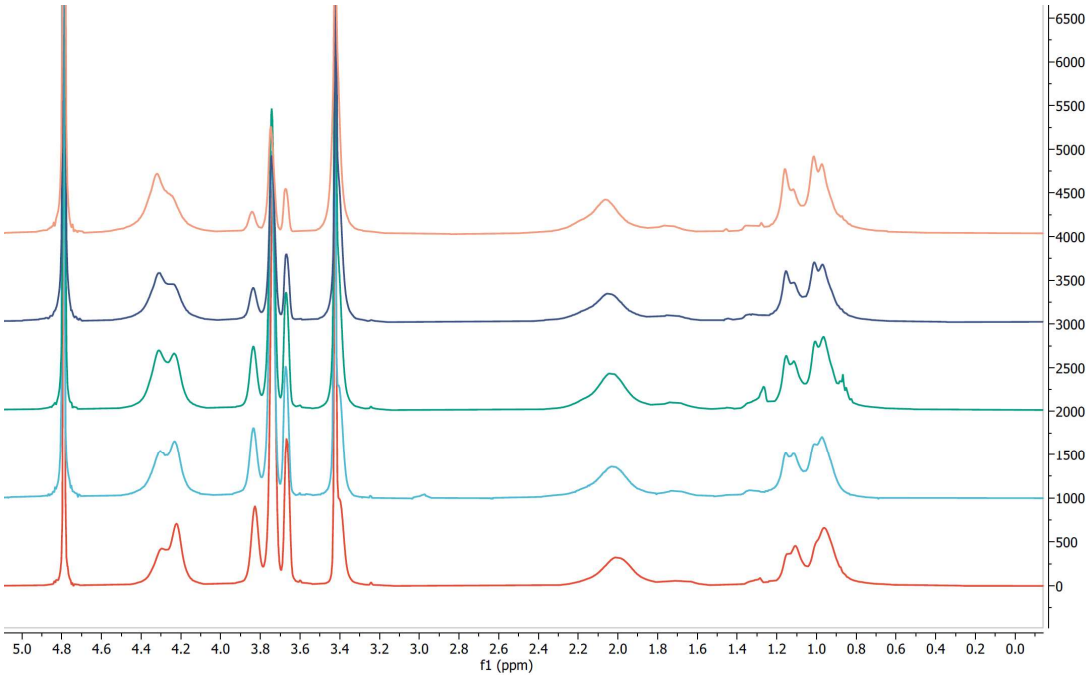

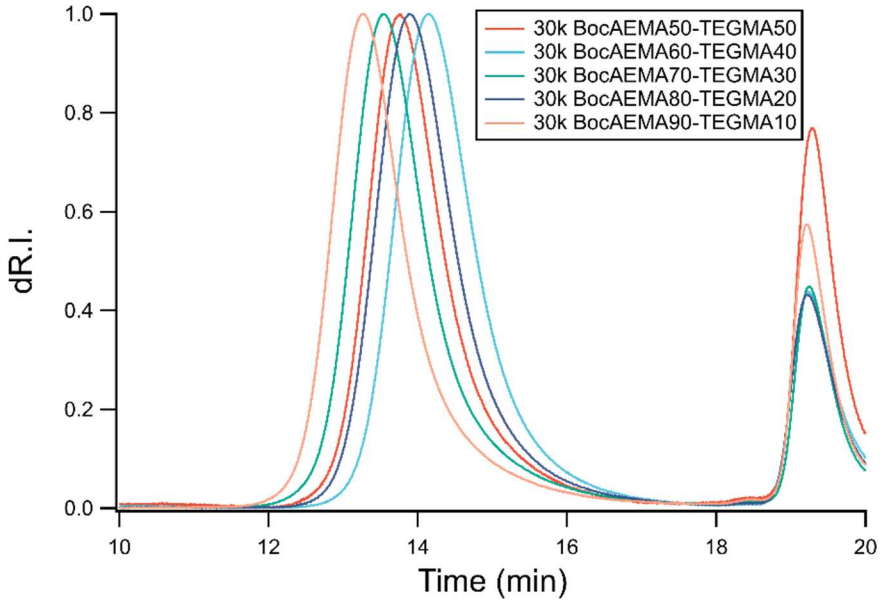

Mon1	Mon2	M_n (th)	%Mon1 (th)	%Mon1 (NMR)	M_n_Boc (SEC)	M_n (SEC)	$Đ$ (SEC)
AEMA	TEGMA	30,000	50%	57%	41,200	32,400	1.22
AEMA	TEGMA	30,000	60%	66%	30,900	22,300	1.24
AEMA	TEGMA	30,000	70%	74%	48,300	33,700	1.22
AEMA	TEGMA	30,000	80%	82%	36,300	23,700	1.25
AEMA	TEGMA	30,000	90%	91%	56,400	34,400	1.26

Figure A10: Characterization of 30 kg/mol poly(AEMA-*s*-TEGMA) polymers.

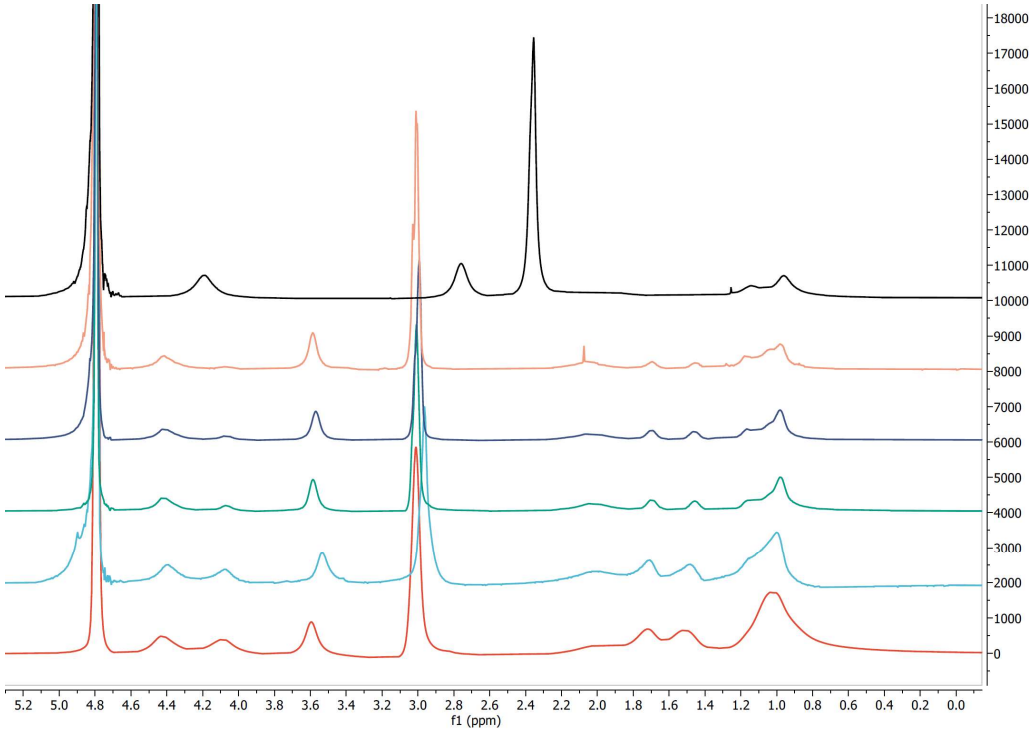

**Note: The 30 kg/mol $DMAEMA_{100}$ polymer was deprotonated prior to ^{1}H-NMR, accounting for the differences observed in its spectrum.

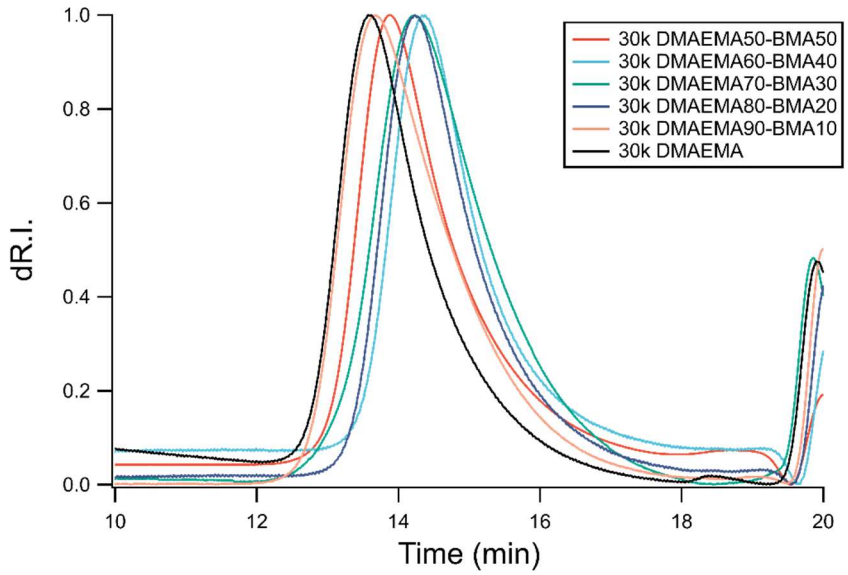

Mon1	Mon2	M_n (th)	%Mon1 (th)	%Mon1 (NMR)	M_n (SEC)	$Đ$ (SEC)
DMAEMA	BMA	30,000	50%	43%	30,900	1.35
DMAEMA	BMA	30,000	60%	62%	23,600	1.31
DMAEMA	BMA	30,000	70%	73%	22,200	1.53
DMAEMA	BMA	30,000	80%	83%	24,000	1.37
DMAEMA	BMA	30,000	90%	86%	30,700	1.49
DMAEMA	N/A	30,000	100%	100%	36,900	1.35

Figure A11: Characterization of 30 kg/mol poly(DMAEMA-*s*-BMA) polymers.

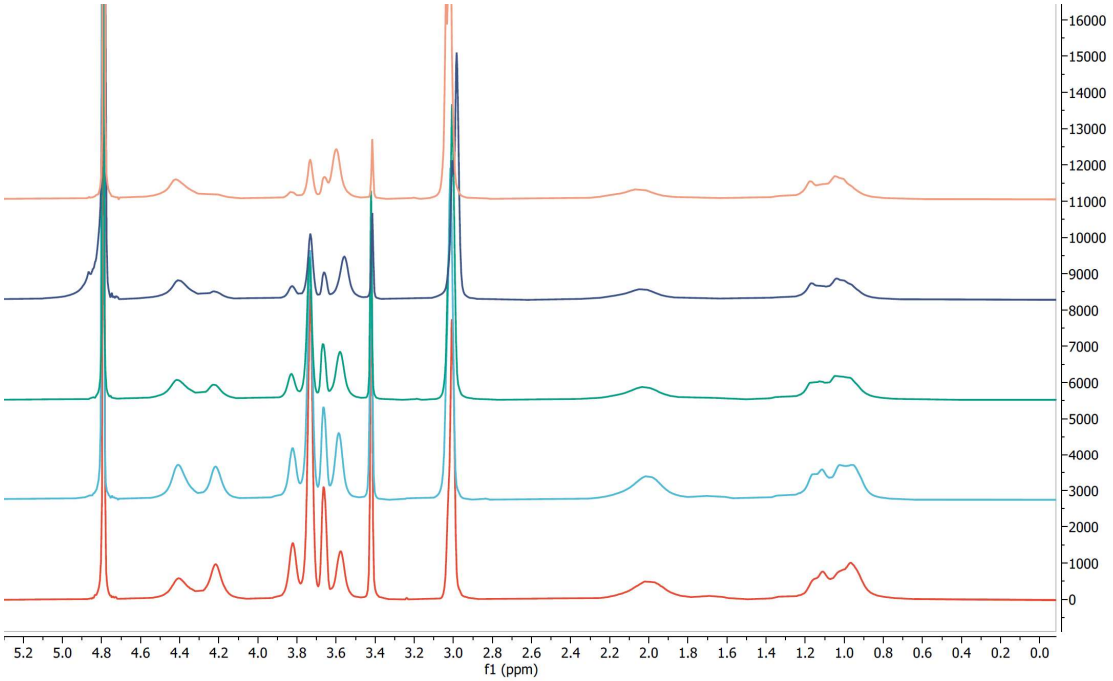

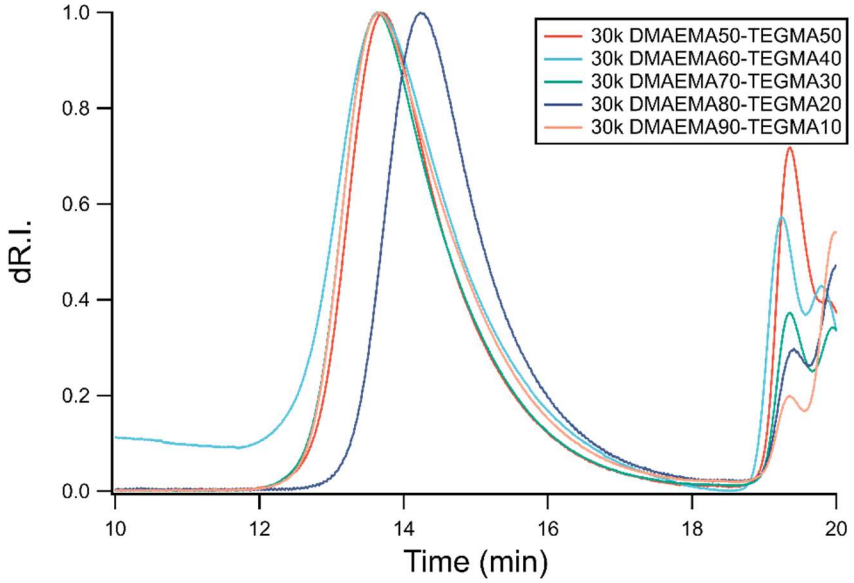

Mon1	Mon2	M_n (th)	%Mon1 (th)	%Mon1 (NMR)	M_n (SEC)	$Đ$ (SEC)
DMAEMA	TEGMA	30,000	50%	50%	32,000	1.47
DMAEMA	TEGMA	30,000	60%	56%	33,900	1.51
DMAEMA	TEGMA	30,000	70%	68%	34,400	1.43
DMAEMA	TEGMA	30,000	80%	74%	21,100	1.53
DMAEMA	TEGMA	30,000	90%	85%	30,800	1.53

Figure A12: Characterization of 30 kg/mol poly(DMAEMA-*s*-TEGMA) polymers.

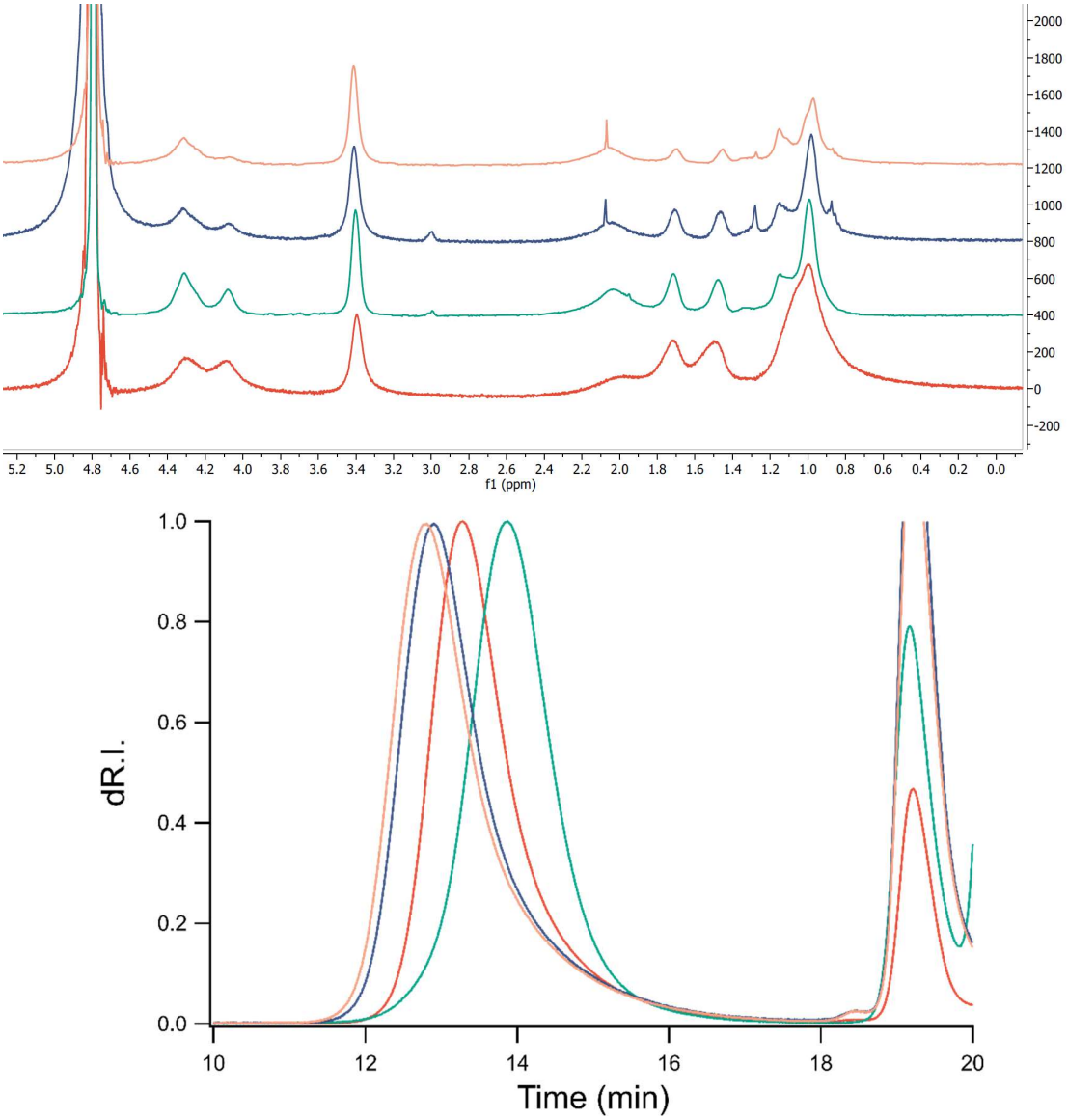

Mon1	Mon2	M_n (th)	%Mon1 (th)	%Mon1 (NMR)	M_n_Boc (SEC)	M_n (SEC)	$Đ$ (SEC)
AEMA	BMA	45,000	50%	42%	53,700	42,200	1.28
AEMA	BMA	45,000	70%	70%	41,800	29,200	1.20
AEMA	BMA	45,000	80%	80%	63,400	41,400	1.40
AEMA	BMA	45,000	90%	92%	68,800	41,900	1.39

Figure A13: Characterization of 45 kg/mol poly(AEMA-*s*-BMA) polymers.

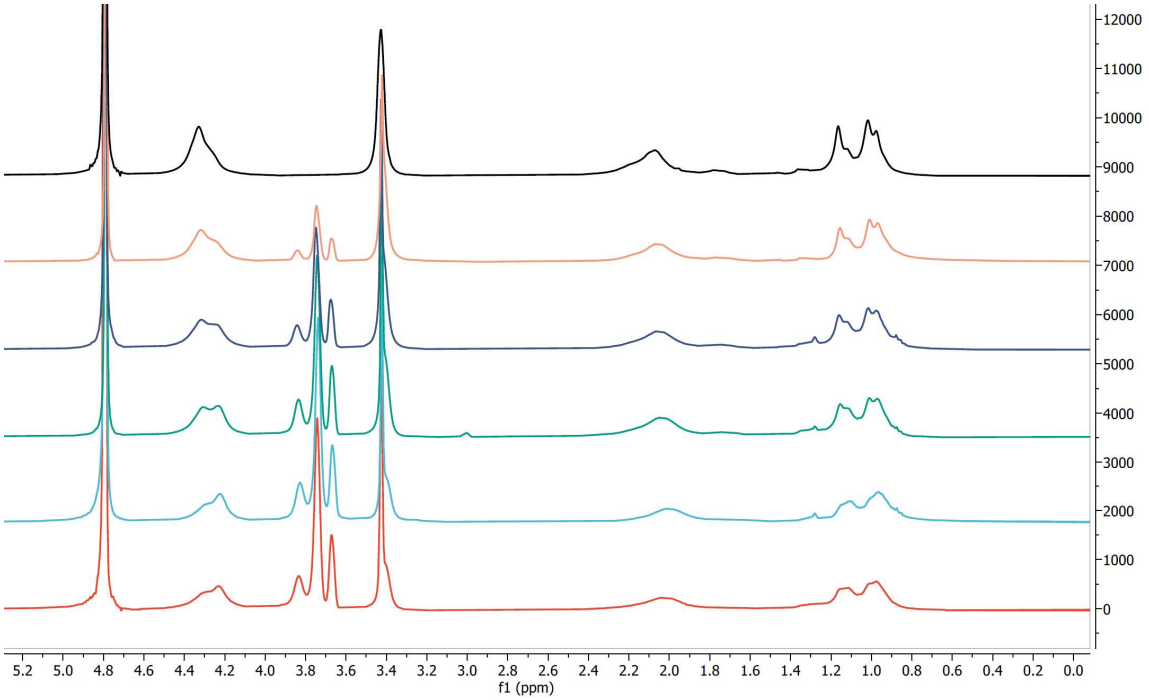

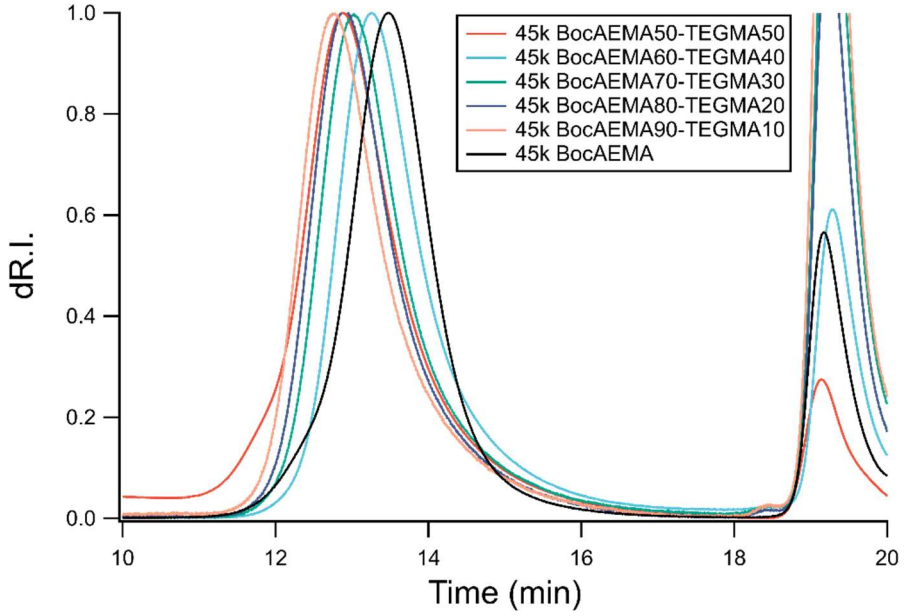

Mon1	Mon2	M_n (th)	%Mon1 (th)	%Mon1 (NMR)	M_n_Boc (SEC)	M_n (SEC)	$Đ$ (SEC)
AEMA	TEGMA	45,000	50%	53%	72,600	53,800	1.40
AEMA	TEGMA	45,000	60%	57%	52,800	41,500	1.34
AEMA	TEGMA	45,000	70%	72%	55,800	38,900	1.47
AEMA	TEGMA	45,000	80%	81%	71,200	46,500	1.29
AEMA	TEGMA	45,000	90%	91%	76,800	46,800	1.32
AEMA	N/A	45,000	100%	100%	58,900	33,300	1.18

Figure A14: Characterization of 45 kg/mol poly(AEMA-*s*-TEGMA) polymers.

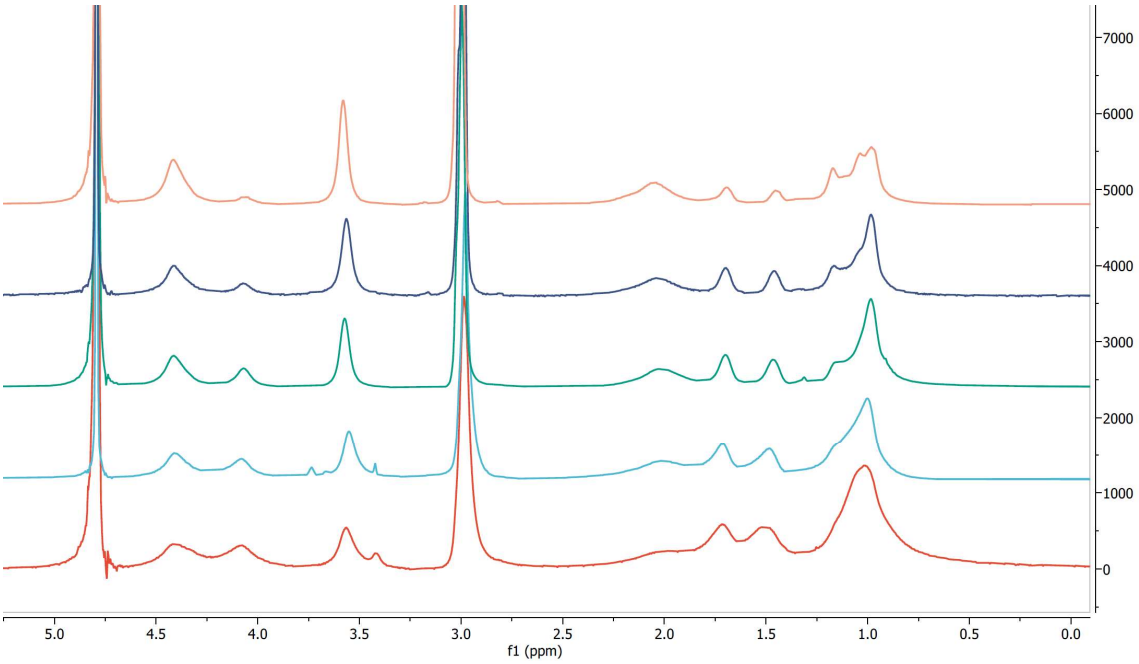

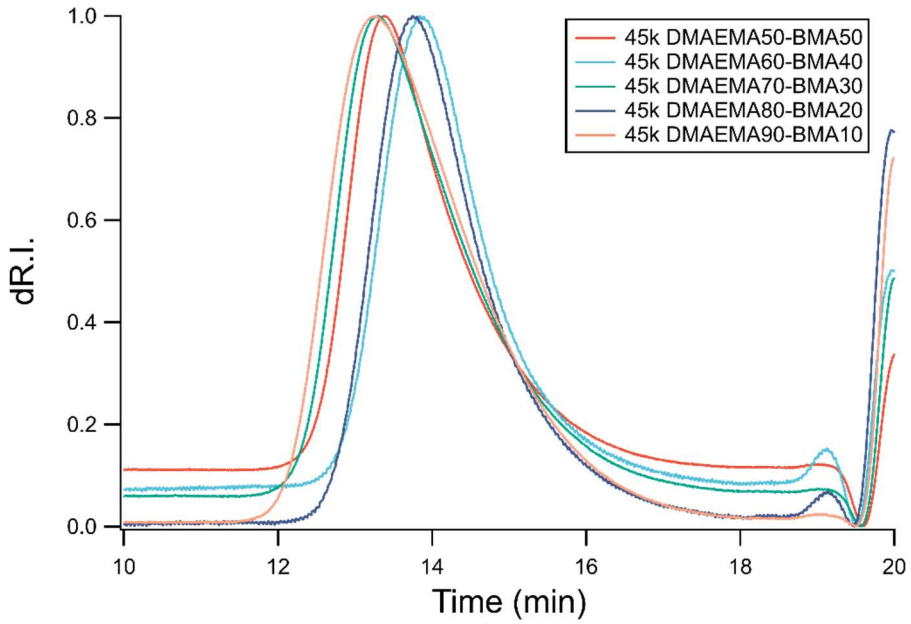

Mon1	Mon2	M_n (th)	%Mon1 (th)	%Mon1 (NMR)	M_n (SEC)	$Đ$ (SEC)
DMAEMA	BMA	45,000	50%	48%	39,600	1.46
DMAEMA	BMA	45,000	60%	61%	34,400	1.32
DMAEMA	BMA	45,000	70%	67%	38,500	1.58
DMAEMA	BMA	45,000	80%	82%	32,000	1.47
DMAEMA	BMA	45,000	90%	91%	38,200	1.66

Figure A15: Characterization of 45 kg/mol poly(DMAEMA-s-BMA) polymers.

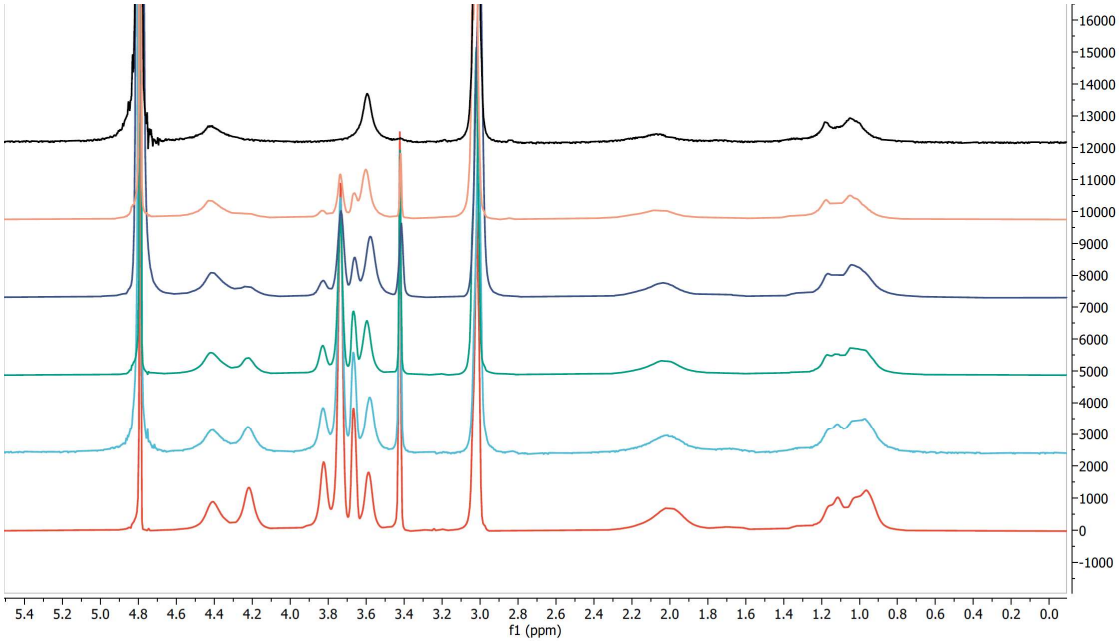

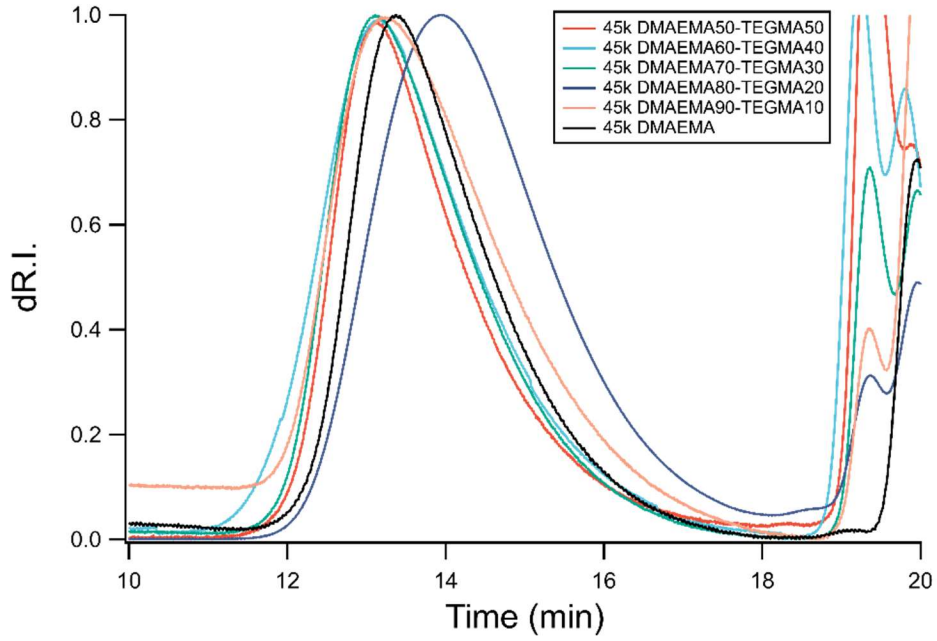

Mon1	Mon2	M_n (th)	%Mon1 (th)	%Mon1 (NMR)	M_n (SEC)	$Đ$ (SEC)
DMAEMA	TEGMA	45,000	50%	51%	42,900	1.65
DMAEMA	TEGMA	45,000	60%	54%	46,100	1.70
DMAEMA	TEGMA	45,000	70%	68%	42,800	1.66
DMAEMA	TEGMA	45,000	80%	76%	35,100	1.43
DMAEMA	TEGMA	45,000	90%	83%	42,500	1.57
DMAEMA	N/A	45,000	100%	100%	40,000	1.51

Figure A16: Characterization of 45 kg/mol poly(DMAEMA-*s*-TEGMA) polymers.

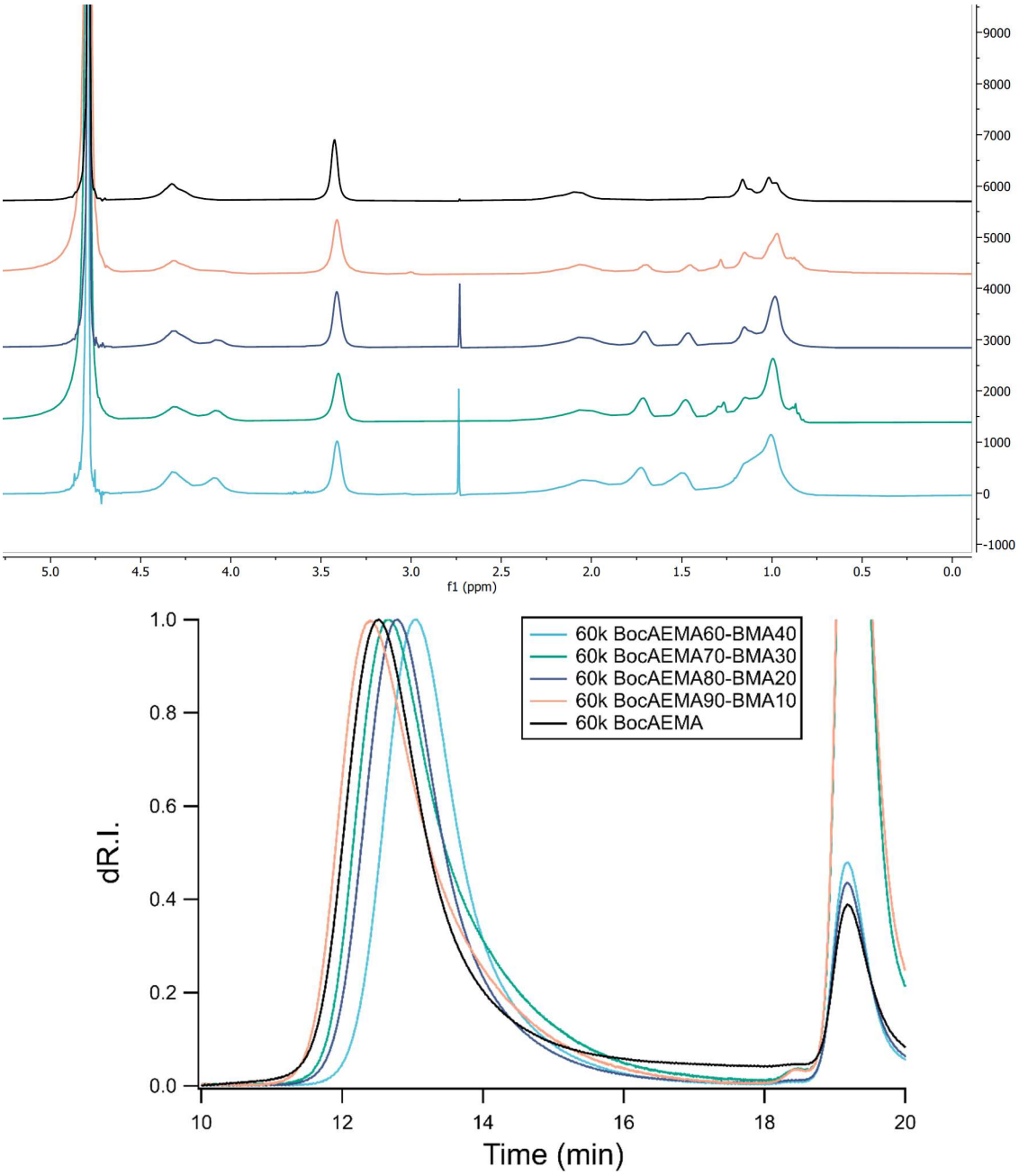

Mon1	Mon2	M_n (th)	%Mon1 (th)	%Mon1 (NMR)	M_n_Boc (SEC)	M_n (SEC)	$Đ$ (SEC)
AEMA	BMA	60,000	60%	60%	66,900	49,500	1.25
AEMA	BMA	60,000	70%	67%	76,800	53,500	1.35
AEMA	BMA	60,000	80%	82%	81,100	52,900	1.26
AEMA	BMA	60,000	90%	88%	76,100	46,300	1.58
AEMA	N/A	60,000	100%	100%	90,100	50,900	1.23

Figure A17: Characterization of 60 kg/mol poly(AEMA-*s*-BMA) polymers.

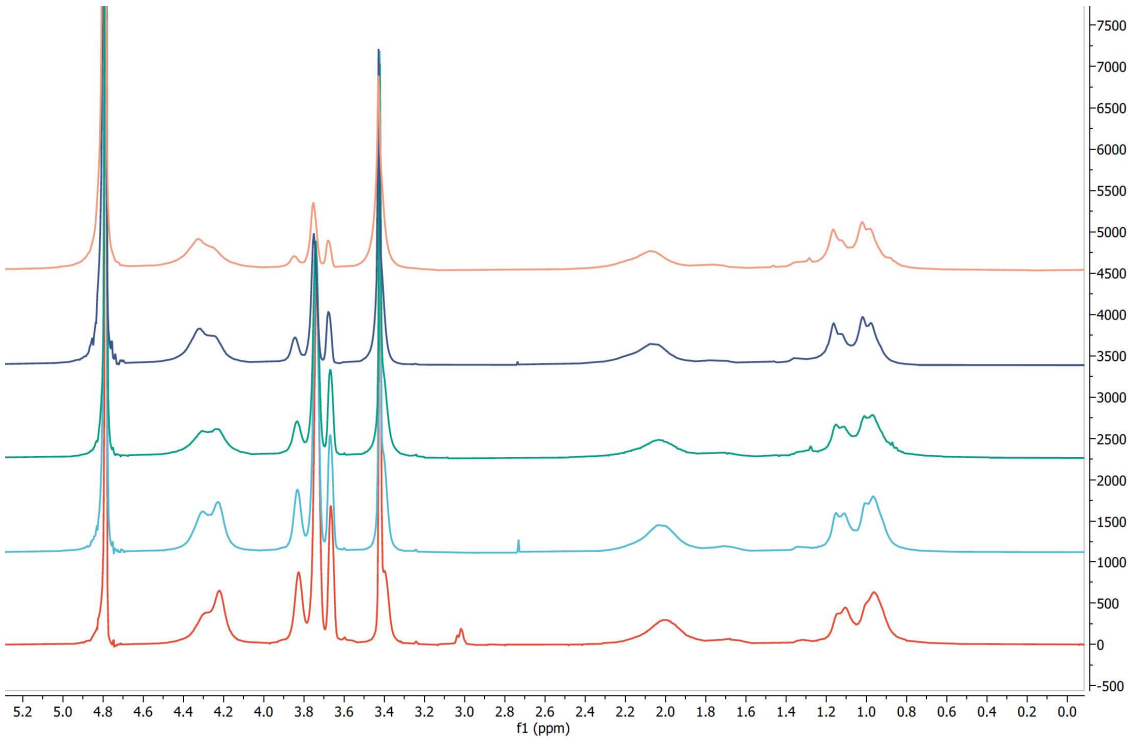

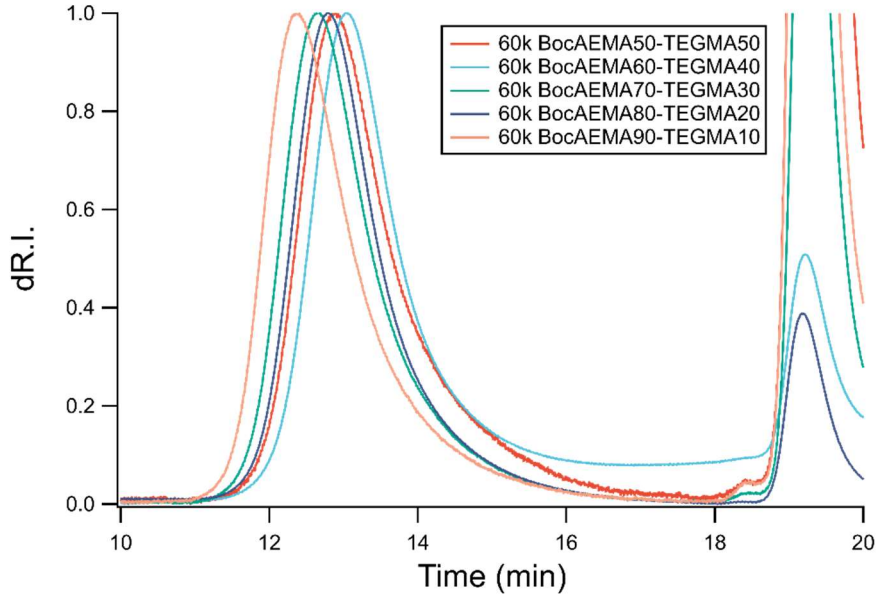

Mon1	Mon2	M_n (th)	%Mon1 (th)	%Mon1 (NMR)	M_n_Boc (SEC)	M_n (SEC)	$Đ$ (SEC)
AEMA	TEGMA	60,000	50%	57%	68,800	54,000	1.31
AEMA	TEGMA	60,000	60%	66%	66,700	49,300	1.26
AEMA	TEGMA	60,000	70%	72%	85,000	59,100	1.31
AEMA	TEGMA	60,000	80%	82%	73,000	47,600	1.37
AEMA	TEGMA	60,000	90%	90%	106,200	64,600	1.27

Figure A18: Characterization of 60 kg/mol poly(AEMA-*s*-TEGMA) polymers.

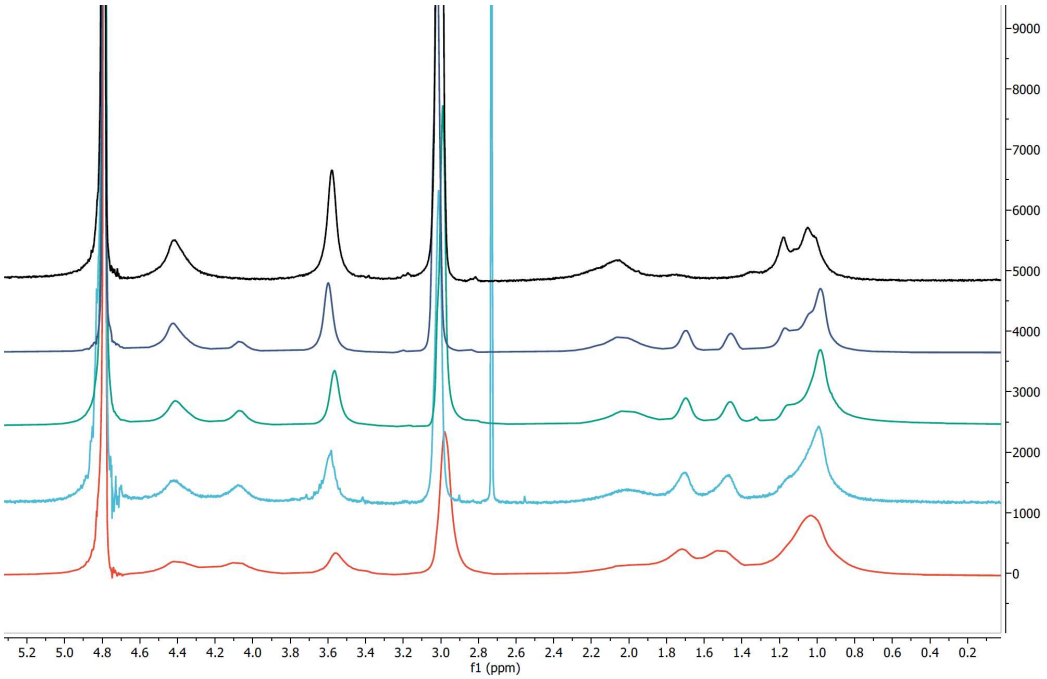

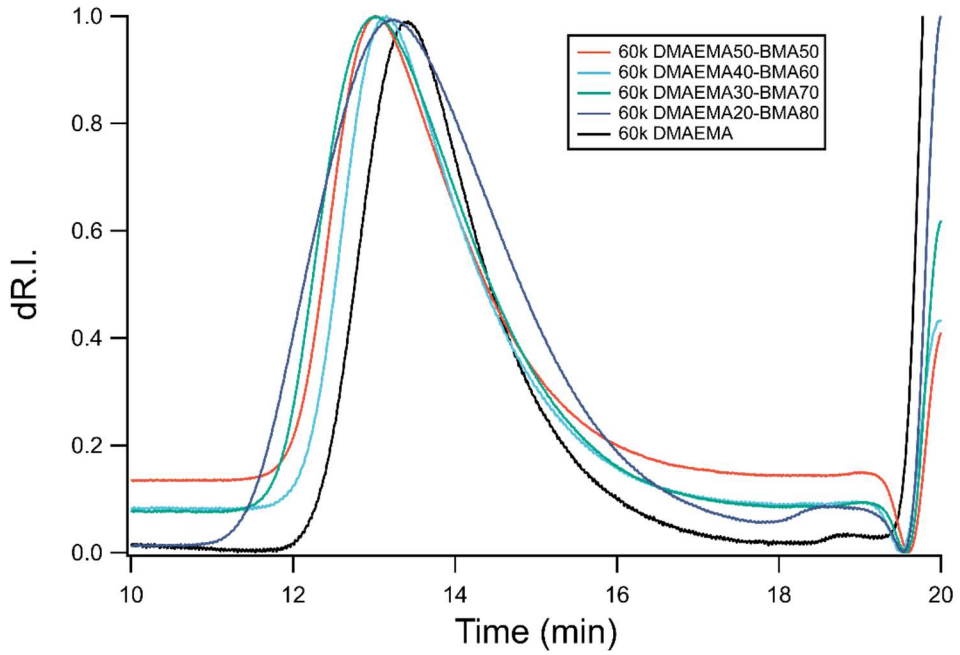

Mon1	Mon2	M_n (th)	%Mon1 (th)	%Mon1 (NMR)	M_n (SEC)	$Đ$ (SEC)
DMAEMA	BMA	60,000	50%	54%	46,400	1.61
DMAEMA	BMA	60,000	60%	67%	48,700	1.44
DMAEMA	BMA	60,000	70%	67%	47,900	1.65
DMAEMA	BMA	60,000	80%	82%	46,900	1.73
DMAEMA	N/A	60,000	100%	100%	45,400	1.36

Figure A19: Characterization of 60 kg/mol poly(DMAEMA-*s*-BMA) polymers.

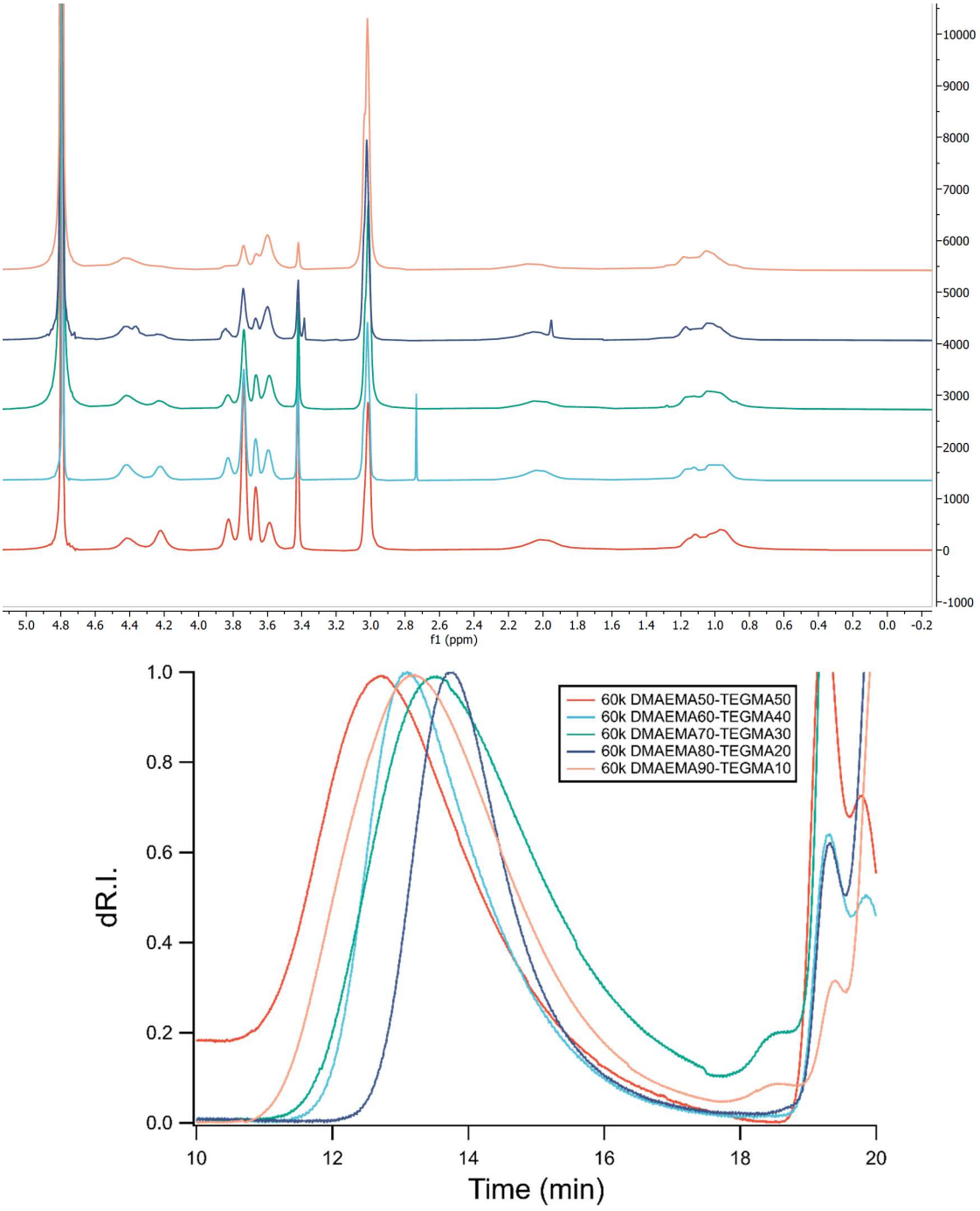

Mon1	Mon2	M_n (th)	%Mon1 (th)	%Mon1 (NMR)	M_n (SEC)	$Đ$ (SEC)
DMAEMA	TEGMA	60,000	50%	48%	78,800	1.58
DMAEMA	TEGMA	60,000	60%	59%	47,200	1.57
DMAEMA	TEGMA	60,000	70%	67%	48,300	1.88
DMAEMA	TEGMA	60,000	80%	79%	50,800	1.24
DMAEMA	TEGMA	60,000	90%	88%	48,200	1.85

Figure A20: Characterization of 60 kg/mol poly(DMAEMA-*s*-TEGMA) polymers.

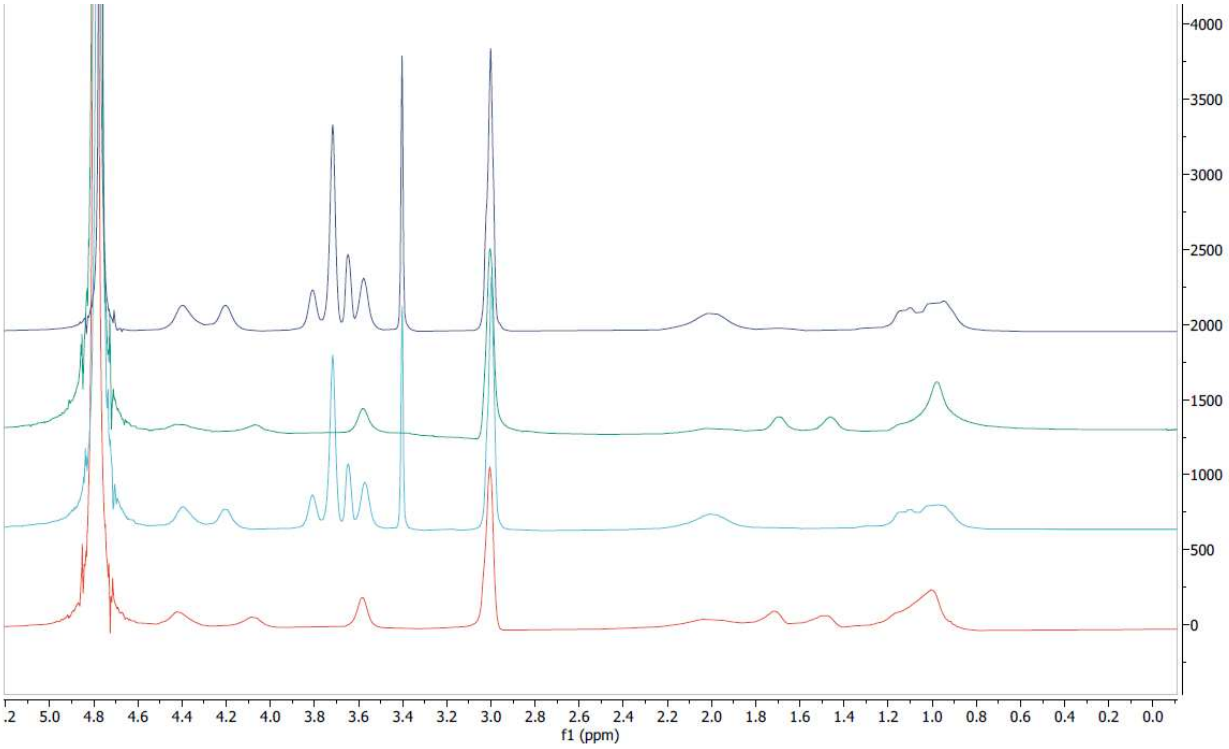

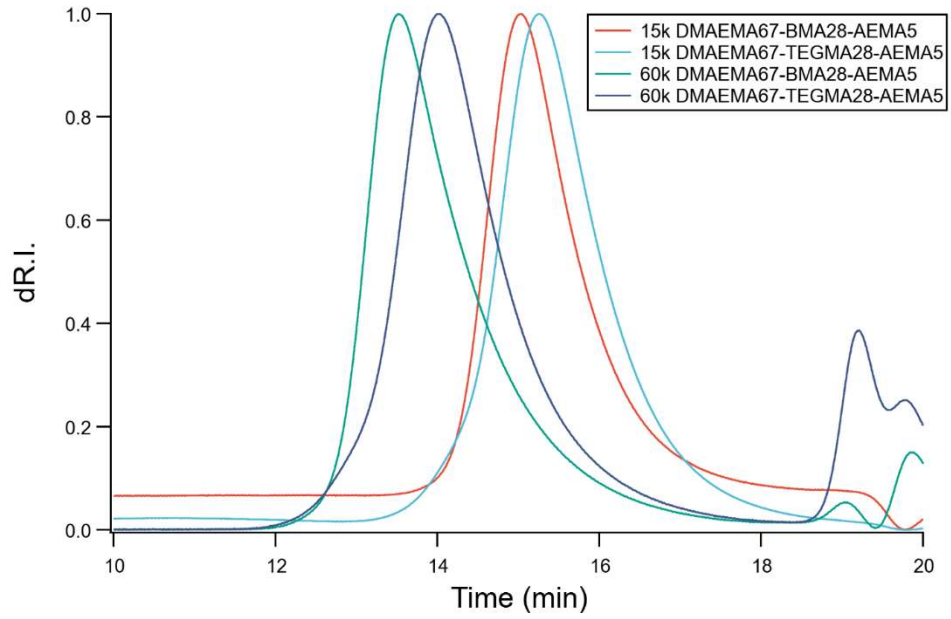

Figure A21: Characterization of polymers containing DMAEMA + 5 mol.% AEMA for fluorescent modification. See **Figure S2.17B** for accompanying quantitative data.